Journal of Turbomachinery

Published Quarterly by ASME

VOLUME 126 • NUMBER 1 • JANUARY 2004

Editor, **DAVID C. WISLER (2008)**
Assistant to the Editor: **ELIZABETH WISLER**
Associate Editors
Gas Turbine (Review Chair)
A. J. STRAZISAR (2004)
Heat Transfer
T. ARTS (2005)
R. BUNKER (2006)
Structures and Dynamics
M. MIGNOLET (2006)
Turbomachinery
R. DAVIS (2005)
S. SJOLANDER (2005)

BOARD ON COMMUNICATIONS
Chair and Vice-President
OZDEN OCHOA

OFFICERS OF THE ASME
President, **REGINALD VACHON**

Executive Director, **VIRGIL R. CARTER**

Treasurer, **R. E. NICKELL**

PUBLISHING STAFF
Managing Director, Engineering
THOMAS G. LOUGHLIN

Director, Technical Publishing
PHILIP DI VIETRO

Production Coordinator
JUDITH SIERANT

Production Assistant
MARISOL ANDINO

TECHNICAL PAPERS

(**Contents continued on inside back cover**)

Transactions of the ASME, Journal of Turbomachinery (ISSN 0889-504X) is published quarterly (Jan., Apr., July, Oct.) by The American Society of Mechanical Engineers, Three Park Avenue, New York, NY 10016. Periodicals postage paid at New York, NY and additional mailing offices. POSTMASTER: Send address changes to Transactions of the ASME, Journal of Turbomachinery, c/o THE AMERICAN SOCIETY OF MECHANICAL ENGINEERS, 22 Law Drive, Box 2300, Fairfield, NJ 07007-2300.
CHANGES OF ADDRESS must be received at Society headquarters seven weeks before they are to be effective. Please send old label and new address.
STATEMENT from By-Laws. The Society shall not be responsible for statements or opinions advanced in papers or ... printed in its publications (B7.1, Par. 3).
COPYRIGHT © 2004 by the American Society of Mechanical Engineers. For authorization to photocopy material for internal or personal use under those circumstances not falling within the fair use provisions of the Copyright Act, contact the Copyright Clearance Center (CCC), 222 Rosewood Drive, Danvers, MA 01923, tel: 978-750-8400, www.copyright.com. Request for special permission or bulk copying should be addressed to Reprints/Permission Department.
INDEXED by Applied Mechanics Reviews and Engineering Information, Inc. Canadian Goods & Services Tax Registration #126148048

This journal is printed on acid-free paper, which exceeds the ANSI Z39.48-1992 specification for permanence of paper and library materials. ∞™
♻ 85% recycled content, including 10% post-consumer fibers.

Downloaded 01 Jun 2010 to 171.66.16.52. Redistribution subject to ASME license or copyright; see http://www.asme.org/terms/Terms_Use.cfm

(**Contents continued**)

Journal of Turbomachinery **Volume 126, Number 1** **JANUARY 2004**

ANNOUNCEMENTS AND SPECIAL NOTES

The ASME Journal of Turbomachinery is abstracted and indexed in the following:

Aluminum Industry Abstracts, Aquatic Science and Fisheries Abstracts, AMR Abstracts Database, Ceramics Abstracts, Chemical Abstracts, Civil Engineering Abstracts, Compendex (The electronic equivalent of Engineering Index), Corrosion Abstracts, Current Contents, Ei EncompassLit, Electronics & Communications Abstracts, Energy Information Abstracts, Engineered Materials Abstracts, Engineering Index, Environmental Science and Pollution Management, Excerpta Medica, Fluidex, Fuel and Energy Abstracts, INSPEC, Index to Scientific Reviews, Materials Science Citation Index, Mechanical & Transportation Engineering Abstracts, Mechanical Engineering Abstracts, METADEX (The electronic equivalent of Metals Abstracts and Alloys Index), Metals Abstracts, Oceanic Abstracts, Pollution Abstracts, Referativnyi Zhurnal, Shock & Vibration Digest, Steels Alert

Backward Traveling Rotating Stall Waves in Centrifugal Compressors

Z. S. Spakovszky
Gas Turbine Laboratory
Department of Aeronautics and Astronautics,
Massachusetts Institute of Technology,
Cambridge, MA 02139

Rotating stall waves that travel against the direction of rotor rotation are reported for the first time and a new, low-order analytical approach to model centrifugal compressor stability is introduced. The model is capable of dealing with unsteady radially swirling flows and the dynamic effects of impeller-diffuser component interaction as it occurs in centrifugal compression systems. A simple coupling criterion is developed from first principles to explain the interaction mechanism important for system stability. The model findings together with experimental data explain the mechanism for first-ever observed backward traveling rotating stall in centrifugal compressors with vaned diffusers. Based on the low-order model predictions, an air injection scheme between the impeller and the vaned diffuser is designed for the NASA Glenn CC3 high-speed centrifugal compressor. The steady air injection experiments show an increase of 25% in surge-margin with an injection mass flow of 0.5% of the compressor mass flow. In addition, it is experimentally demonstrated that this injection scheme is robust to impeller tip-clearance effects and that a reduced number of injectors can be applied for similar gains in surge-margin. The results presented in this paper firmly establish the connection between the experimentally observed dynamic phenomena in the NASA CC3 centrifugal compressor and a first principles based coupling criterion. In addition, guidelines are given for the design of centrifugal compressors with enhanced stability. [DOI: 10.1115/1.1643382]

Winner of the "Best Paper Award," Turbomachinery Committee

Introduction

Extensive studies, mostly experimental, have been conducted on rotating stall and surge in centrifugal compressors. For example, Hunziker and Gyarmathy [1] present an analysis of the effect of subcomponent performance on the operational stability of a centrifugal stage with a vaned diffuser. Lawless and Fleeter [2] show experimental data on rotating stall acoustic signatures in a vaneless and a vaned diffuser. Other publications focus rather on specific system components. Abdelhamid [3] and Frigne and Van Den Braembussche [4] present models for rotating stall in a vaneless diffuser. Impeller stall is discussed in Frigne and Van Den Braembussche [5]. However, little attention has been given in these studies to the impact of impeller-diffuser interaction effects on compression system stability and a detailed dynamic analysis of an entire centrifugal compression system has not been reported. This paper presents the first model that is capable of dealing with both the overall dynamic system effects and the coupling between the system components.

An active control scheme to control rotating stall in a low-speed centrifugal compressor was theoretically investigated by Lawless and Fleeter [6]. A basic assumption in that analysis was that, in its early stages, rotating stall is well represented as a weak, linear disturbance, which grows into a finite stall cell. The same authors investigated the rotating stall acoustic signature experimentally in the same low-speed centrifugal compressor (Lawless and Fleeter [7]). In this investigation the rotating stall behavior exhibited a much more extensive repertoire of excited spatial modes. Similarly the instability pathology of a high-speed centrifugal compressor was analyzed by researchers of the same institution (see Oakes et al. [8]). The results showed the presence of two distinct rotating stall patterns prior to and during surge. The existence of one mode for several hundred revolutions prior to surge initiation suggested an activation parameter for high-speed control schemes.

Definitive success has been achieved in the suppression of surge in centrifugal compressors of laboratory turbocharger rigs, as reported by researchers such as Pinsley et al. [9] and Gysling et al. [10]. Surge control was also demonstrated in working engines by Ffowcs Williams et al. [11] and more recently by Nelson et al. [12]. Nelson et al. [12] actively controlled surge in an engine centrifugal compressor using diffuser air injection. Apart from numerical investigations, for example by Stein et al. [13], surge and rotating stall control has not been reported for high-speed centrifugal compressors. This paper presents the first system stability enhancement of a large flow capacity, high-pressure ratio transonic centrifugal compressor by controlling rotating stall with diffuser air injection.

Scope of the Paper. There are three main objectives of this paper. The first objective is to define and to develop a new modeling approach which is able to capture the key features of surge inception in centrifugal compressors. The second objective is to physically explain the effects of impeller-diffuser interaction on compression system stability and the mechanism of surge inception in radial machines with vaned diffusers. And the third objective is to design a flow control scheme that enhances the compression system stability and to delineate design implications.

A new low-order dynamic model is introduced and is implemented for the NASA Glenn CC3 high-speed centrifugal compressor. Experiments in the same machine are conducted to verify the new theory and to test a flow control scheme that is designed based on the model predictions.

Experimental Setup

All experiments described in this paper were conducted at the NASA Glenn Research Center in the CE-18 high-speed centrifugal compressor test facility. Atmospheric air is drawn into the test facility through an orifice plate and a supply plenum chamber upstream of the test section. Downstream of the centrifugal compressor stage the flow is collected in a collector and regulated with

---

Contributed by the International Gas Turbine Institute (IGTI) of THE AMERICAN SOCIETY OF MECHANICAL ENGINEERS for publication in the ASME JOURNAL OF TURBOMACHINERY. Paper presented at the International Gas Turbine and Aeroengine Congress and Exhibition, Amsterdam, The Netherlands, June 3–6, 2002; Paper No. 2002-GT-30379. Manuscript received by IGTI, December 2001, final revision, March 2002. Associate Editor: E. Benvenuti.

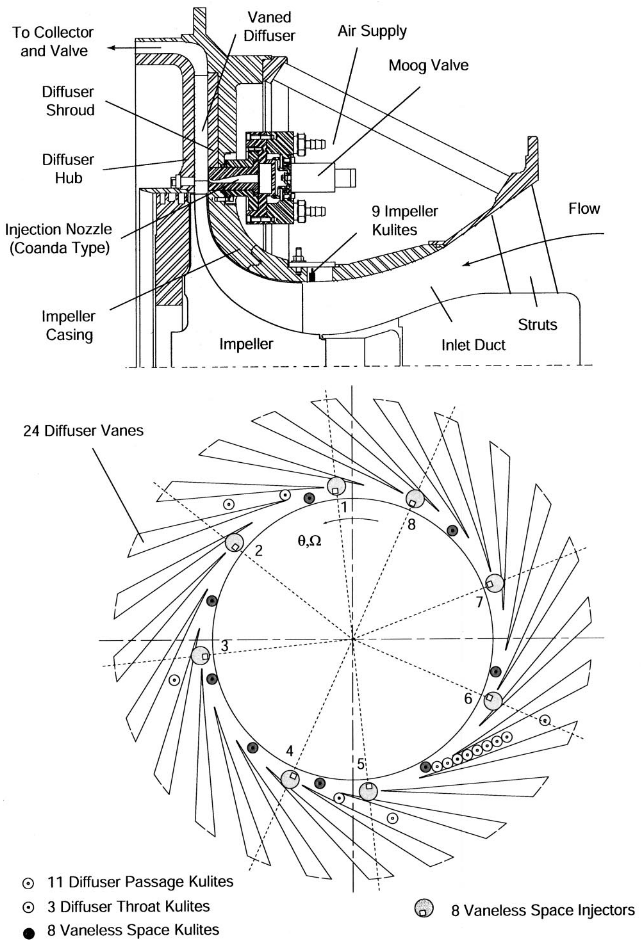

Fig. 1 Cross section and front view of NASA CC3 centrifugal compressor

a throttle valve. The compressor is driven by a high-power electric drive motor through a gear box. The compressor mass flow is controlled by adjusting the exit area of the throttle valve. After passing through the throttle valve, the air is exhausted to the atmosphere.

The test vehicle is the NASA CC3 high-speed centrifugal compressor depicted in **Fig. 1**. The compressor is an Allison Engine Company design (McKain and Holbrook [14]) scaled up to a design flow size of 4.54 kg/s from the original size of 1.66 kg/s. The impeller and vaned diffuser were designed to produce a pressure ratio of 4:1 at the design mass flow. The standard day corrected speed for the design flow condition is 21,789 rpm with an exit tip speed of 492 m/s.

The impeller contains 15 main blades and 15 splitter blades with a backsweep of 50° at the exit. The splitter blade leading edge, located at 30% of the main blade chord, is offset slightly toward the main blade suction surface to provide an even flow split. The inlet tip diameter is 210 mm and the blade height is 64 mm. The exit diameter is 431 mm and the exit blade height is 17 mm. All dimensions are for hot running conditions at 100% corrected design speed. The nominal operating impeller exit clearance is 0.406 mm, or 2.4% of the passage height at the exit.

The vaned diffuser consists of 24 prismatic wedge vanes with the leading edge located at a radius ratio of 1.078 relative to the impeller exit. The vanes have a total divergence angle of 7.8°. The diffuser exit radius is 363 mm and the flow is turned 90° into an annular exit duct and discharged into the plenum (collector).

Instrumentation. Unsteady pressure measurements are obtained from eight circumferentially distributed high-response pressure transducers (50 psia Kulite sensors) located on the front wall (shroud) in the vaneless space at a radius of 1.047 of the impeller exit radius. In addition, 50 psia Kulite sensors are placed at the diffuser vane throat and at various locations inside the diffuser passage on the shroud side as depicted in **Fig. 1**. Nine 15 psia Kulite sensors are circumferentially distributed in the casing immediately upstream of the impeller. All unsteady Kulite sensor signals are sampled at a sample rate of 3 kHz and are signal-conditioned and filtered. The filter gains are set to 1 and the low-pass filter frequencies are set to 1 kHz.

Steady-state compressor performance measurements such as static pressures at various casing, hub (diffuser back wall) and shroud (diffuser front wall) locations, mass flow, pressure and temperature rise and collector valve position are also recorded. Using a high-precision translator system the axial position of the impeller wheel can be varied relative to the casing so that the impeller tip-clearance can be adjusted. Noncontacting RotaData tip-clearance probes were used to measure the axial tip-clearance at the impeller exit and the clearance at the impeller knee.

A New Low-Order Analytical Model for Centrifugal Compressor Stability

The basic idea behind the Moore and Greitzer [15] approach is that rotating stall and surge are the mature forms of small amplitude flow perturbations that are the natural resonances of oscillation in the compression system. These small disturbances grow when background flow conditions are such that their damping becomes negative and the compression system drops into an unstable state, rotating stall or surge.

One of the shortcomings of the ‘‘Moore-Greitzer’’ modeling methodology developed for axial compressors (see Longley [16] for a review) is that the model is limited to a lumped representation of the compressor blade rows. In other words it is not appropriate to model blade rows or compressor blocks where there is significant contribution of the inter-blade-row ducts to the overall compression system dynamics. Furthermore the ‘‘Moore-Greitzer’’ model is not capable of dealing with the radially swirling flows that occur between impeller and vaned diffusers and in vaneless diffusers of centrifugal compressors. It will be shown in this paper that the unsteady flow in the gap between impeller and diffuser plays an important role in the compression system dynamics. Because of the need for this modeling capability, the extension of the Moore-Greitzer methodology and the development of a new model were motivated. The following are the attributes of the new model:

- The approach can model both axial and centrifugal compressors and is capable of dealing with the different mode structures that occur in unsteady radially swirling flows.
- Its modular structure renders modeling flexibility and enables to resolve the dynamics of individual blade-rows, inter-blade-row gaps and intermediate ducts. The new model can thus deal with dynamic interaction effects between components.
- The low-order, analytical nature of the model allows to dissect the dynamic stall phenomena and facilitates the explanation of physical mechanisms.

The derivation of the model equations is omitted here (see Spakovszky [17]) and a short description of the model is given instead.

Model Description. Surge and rotating stall are relatively large length scale and long-time scale fluid dynamic phenomena compared to blade pitch length scale and blade passage convection time scale. In other words instead of focusing on detailed three-dimensional features of the flow (especially in the region of interaction between impeller and vaned diffuser), the long wavelength flow perturbations are considered two-dimensional: for axial flow components in the axial and circumferential directions and for radial flow components in the radial and circumferential

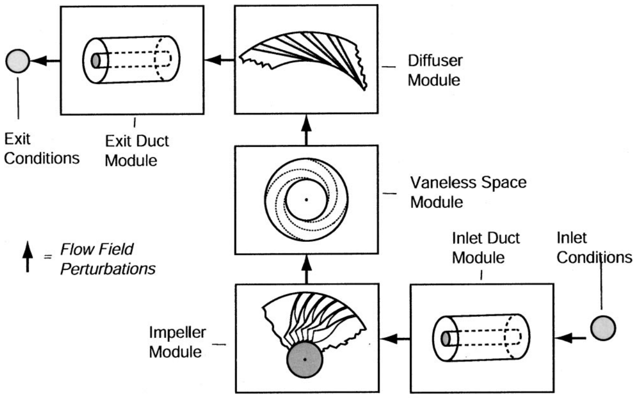

Fig. 2 Implementation of modular, low-order dynamic system model for NASA CC3 centrifugal compressor

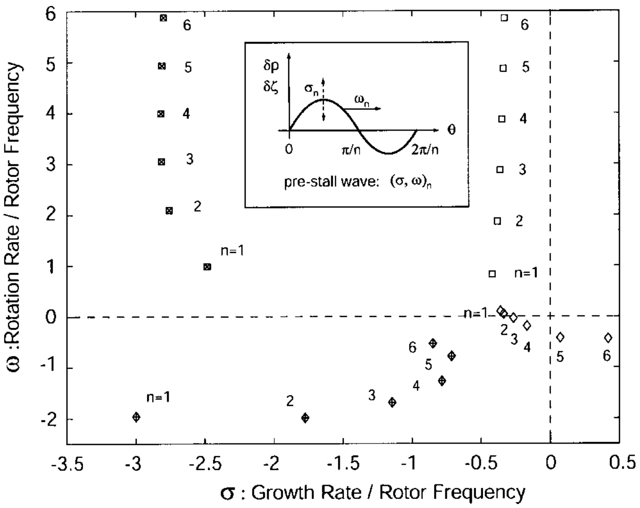

Fig. 3 1st through 6th harmonic system resonances of NASA CC3 centrifugal compressor for an operating point close to stall

directions. Therefore in this paper *impeller-diffuser interaction* is associated with flow effects on the radius scale and this term does not refer to investigations on the blade scale.

Exploiting these facts the general approach to modeling the flow field dynamics is to take the steady-state axisymmetric performance characteristics of the individual compressor components and to combine these with the representation of nonaxisymmetric and unsteady flow effects. In particular, the following assumptions are made: (1) the relevant Mach numbers are low enough that compressibility effects can be neglected, (2) Reynolds number effects are ignored, and (3) effects of viscosity and heat transfer outside the blade rows are neglected.

The objective of the model is to determine the fundamental flow resonances (modes or eigenvalues of the unsteady flow field) that dominate the compression system dynamics. Analyzing the NASA CC3 centrifugal compression system shown in **Fig. 1**, the following compressor components are identified to be important contributors to the dynamic behavior of the system: the axial upstream duct, the impeller, the radial vaneless space between impeller and vaned diffuser, the vaned diffuser and the axial downstream duct. For each of these components (sketched in **Fig. 2**) the governing unsteady equations are linearized and solved analytically. The closed solutions for the flow field perturbations are then cast into a form suitable to be linked to other components. This renders the modular structure of the new model and allows the dynamic interaction between components. A short outline of the solution procedures for the dynamic component models is given below, for more details see Spakovszky [17].

Axial Duct Dynamics. The flow is modeled using the two-dimensional linearized Euler equations in cartesian coordinates. Introducing vorticity and the stream function, switching from the time domain to the frequency domain via a Laplace transform and assuming a Fourier series representation of the flow variables in the circumferential direction allows to transform the Euler equations into two ordinary differential equations. The analytical solution of the unsteady flow field perturbations is then obtained by integration.

Radial Space Dynamics. The radially swirling flow is modeled using the two-dimensional linearized Euler equations in cylindrical coordinates. A complication arises from the fact that the steady background flow is nonuniform. Representing this background flow by a free vortex flow, the governing unsteady equations are solved analytically and the closed solution is cast into a form similar to the case of the axial duct flow dynamics. This is the first time that the fundamental flow resonances which exist in a radially swirling flow are analytically described.

Impeller Dynamics. The flow through the impeller blade passages is essentially modeled as one-dimensional unsteady channel flow along a passage streamline in the rotor frame of reference. The effects of slip (a fundamentally inviscid flow effect), backsweep and inertial effects (including changes in area and density along the gas path) are all accounted for. Unsteady viscous loss effects and inlet swirl sensitivity are also modeled. Unsteady deviation effects are neglected and the blade pitch is assumed small enough so that the exit flow angle is independent of inlet conditions. The connection between the flow perturbations upstream and downstream of the impeller are found from matching conditions across this semi-actuator disk in the absolute frame (mass flow, pressure rise, and flow turning).

Vaned Diffuser Dynamics. The vaned diffuser dynamics are derived similarly to the semi-actuator disk model for the impeller, modeling again unsteady inertia and loss effects, inlet swirl sensitivity, and taking into account changes in area and density along the gas path. The component models depend on the mean flow quantities through the machine and the steady-state blade-row loss characteristics. These are obtained from a mean flow calculation using geometry, velocity triangles and performance data from measurements conducted in the NASA CC3 compressor and from NASA Glenn's centrifugal compressor off-design code (Wood [18]).

An Eigenvalue Problem. The five analytical component models are then connected together to form the overall compression system model. To close the problem, boundary conditions need to be set upstream and downstream of the compression system (see **Figs. 1** and **2**). An infinite-length upstream duct is used as inlet condition, stating that potential perturbations can only decay away from the compressor and that the flow is vorticity-free in the upstream region. The plenum boundary condition is applied at the exit of the finite length downstream duct assuming that the flow inside the plenum is approximately spatially uniform. This yields an eigenvalue problem that needs to be solved in order to find the natural resonances of the compression system (system modes or eigenvalues). Each complex eigenvalue $s=\sigma_n - j\omega_n$ corresponds to a pre-stall wave of sinusoidal shape. The subscript n denotes that the wave has n lobes on the circumference and is thus called an nth spatial harmonic pre-stall wave (see **Fig. 3** for an illustration). The wave rotates around the annulus at a rotation rate ω_n, the imaginary part of the eigenvalue. The real part of the eigenvalue σ_n is the growth rate and indicates whether the wave amplitude grows in time and the resonance is unstable (positive growth rate), or decays in time and the resonance is thus stable

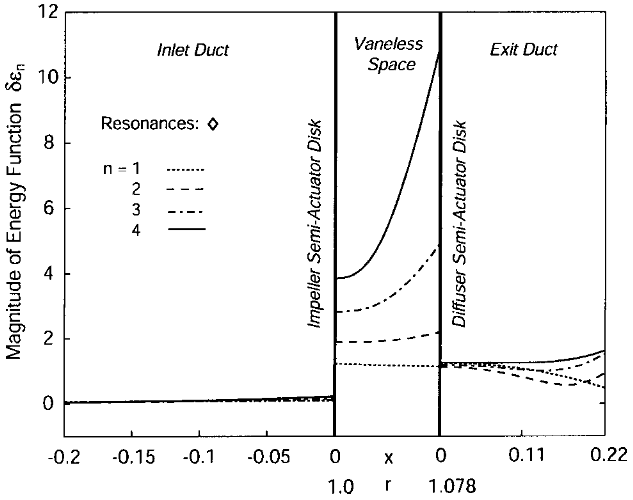

Fig. 4 Energy function 1st through 4th harmonic resonances marked as diamonds in Fig. 3

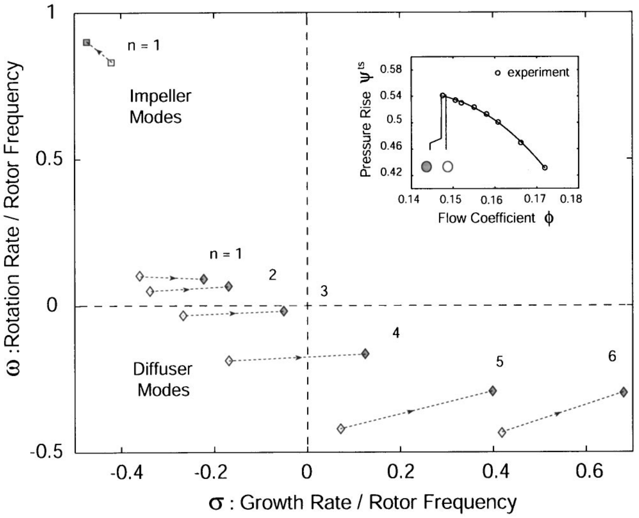

Fig. 5 Motion of system modes when compressor is throttled into stall

(negative growth rate). The least stable of all eigenvalues or natural flow resonances determines the stability of the compression system.

Model Predictions. All flow resonances with $n=1$ through $n=6$ circumferential lobes are found for a compressor operating point close to stall and are plotted in **Fig. 3**. The corresponding harmonic numbers n are plotted next to the resonances and the plot suggests that the system resonances can be gathered into four strings of modes. Put another way there are four resonances per spatial harmonic n and it is instructive to investigate the nature of these four different flow resonances. To help guide the analysis, the spatial distribution of the energy of each resonance is evaluated through the compression system. Defining an energy function of each nth harmonic resonance s as $\delta\varepsilon_n(x,s)=\widetilde{P}_n(x,s)\cdot\widetilde{V}_n(x,s)$ where $\widetilde{V}_n$ is the corresponding complex phasor (essentially based on the eigenvector) of either the axial or the radial velocity perturbation and $\widetilde{P}_n$ is the corresponding complex phasor of the pressure perturbation, the location of the maximum activity can be used to analyze the origin of the resonance. **Figure 4** depicts the magnitude of the energy function through the centrifugal compression system for the first four system resonances marked as open diamonds in **Fig. 3**.

For this string of resonances maximum activity occurs in the vaneless space close to the diffuser. Conducting the same analysis for all four strings yields a group of system resonances which are dominated by perturbations in the impeller (squares) and a group of system resonances which are dominated by perturbations in the diffuser (diamonds). Making use of the analytical form of the model it can be shown for each of the two groups that one of the resonances represents the dynamics associated with the unsteady loss effects. These strings of resonances are additionally marked by pluses in **Fig. 3**.

It is important to note the following three results: (1) For this machine resonances associated with the impeller dynamics are more stable than the ones associated with the diffuser dynamics, and the 5th and 6th harmonic diffuser resonances are unstable (positive growth rates). (2) Diffuser related resonances with a harmonic number of 3 and higher have *negative* rotation rates and travel *against* the direction of impeller rotation. (3) The energy function is strongest in the vaneless space.

To further investigate the pre-stall dynamics of the NASA CC3 centrifugal compressor all system resonances are also computed for the operating point at onset of stall. The resonances are plotted on the same chart to illustrate their motion when the compressor mass flow is reduced. A closer view of the complex plane around the origin is shown in **Fig. 5** and the two operating points are marked on the compressor characteristic. The computation shows that the 4th harmonic resonance associated with the diffuser dynamics becomes unstable when the stall point is approached. Note that this four-lobed pre-stall wave travels *backward* (against the direction of rotor rotation) at a rotation rate of −0.18 times rotor frequency.

Backward Traveling Rotating Stall—Theory of Interaction Waves

The modeling analysis reveals that the unsteady interaction between the impeller and the vaned diffuser plays an important role for centrifugal compressor stability. The radial spacing between impeller and vaned diffuser is also a crucial parameter for the stage matching, and in practice the diffuser leading edge to impeller trailing edge radius ratio can range from 1.035 to 1.215 (see Rodgers [19]). Even if the radial spacing is only on the order of 10% of the impeller exit radius, the high exit swirl[1] yields a relatively long trajectory for fluid particles in the vaneless space. In comparison, axial flow compressors have generally much smaller inter-blade-row gaps between rotors and stators. Fan stages, however, can be comprised of a fan rotor and stator with a considerable axial spacing in between.

Two questions arise from these observations. Can backward rotating stall waves also occur in axial compressors? What is the physical mechanism for the occurrence of this phenomenon?

Flow Resonances in Interacting Axial Rotor-Stator Blade-Rows. To answer the first question the new low-order dynamic model is implemented for a generic axial flow compressor stage that is connected to ducts of infinite length. The rotor blade-row is separated from the stator blade-row by an axial gap of nondimensional length $\Delta x=\Delta\hat{x}/R$, where $\Delta\hat{x}$ is dimensional and R is the mean radius. The goal of the following analysis is to illustrate the influence of the blade-row spacing Δx on the rotating stall wave behavior. To better elucidate this, two limiting cases are considered first.

In the first case the blade-row spacing Δx is set to zero. This results in a system where rotor and stator are closely coupled and refers to the classical Moore-Greitzer problem (Longley [16]). Lumping both blade rows together into a single semi-actuator disk the nth harmonic flow resonance $s=\sigma_n-j\omega_n$ becomes

---

[1] The absolute impeller exit swirl angle can be as high as 70° or 80°, especially for an impeller where the blades have no backsweep.

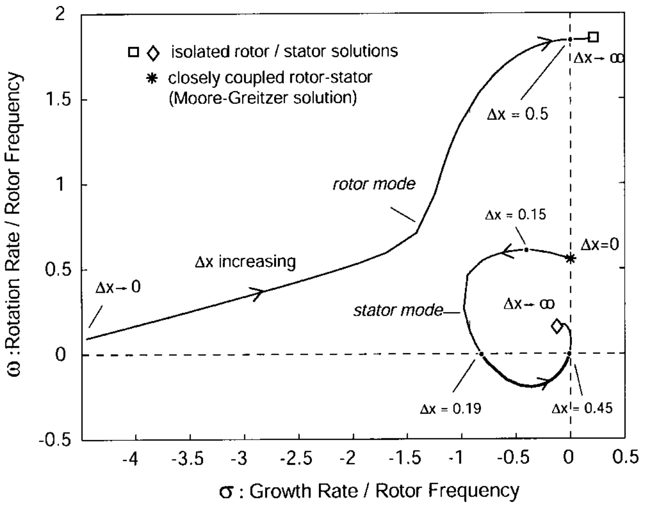

Fig. 6 Motion of third harmonic ($n=3$) resonances of interacting rotor-stator system for variable interblade row spacing $\Delta x=0\ldots1$

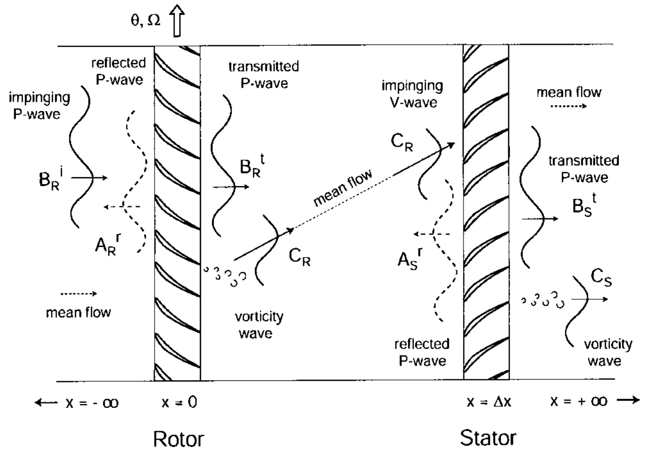

Fig. 7 Wave system for interacting rotor and stator blade-rows

$$\sigma_n=\frac{\frac{\partial\psi^{ts}}{\partial\phi}}{\mu+\frac{2}{n}}\quad\text{and}\quad\omega_n=\frac{\lambda n}{\mu+\frac{2}{n}},\tag{1}$$

where λ and μ are the blade row inertia of the rotor and of the rotor and stator, respectively, and $\partial\psi^{ts}/\partial\phi$ is the slope of the steady-state total-to-static stage pressure rise characteristic with respect to the flow coefficient ϕ. The 3rd harmonic resonance ($n=3$) is plotted as a star in **Fig. 6** for the stage operating at peak pressure rise. The growth rate σ_n is zero since the slope of the compressor characteristic is zero at this operating point.

Then, in the second case, the blade-row spacing Δx is taken to infinity. Now the blade rows are infinitely far apart and can be treated in isolation. Using the early flow model by Stenning [20] for compressor stall, analytical expressions for the modes of an isolated rotor and an isolated stator blade-row can be found. Applying these expressions to the isolated rotor and stator blade rows, the 3rd harmonic rotor resonance and the 3rd harmonic stator resonance are plotted as a square and a diamond, respectively, in **Fig. 6**. The above results show that in both limiting cases ($\Delta x=0$ and $\Delta x=\infty$) the pre-stall waves rotate in the direction of rotor rotation, in concert with the classical rotating stall theory for axial compressors and isolated blade rows.

To investigate the dynamic interaction effects for moderately coupled blade-rows the 3rd harmonic system resonances are computed using the low-order dynamic system model for a range of blade-row spacings. Δx is varied from 0 to 1 and the motion of the rotor and stator resonances is shown in **Fig. 6** by the solid lines. The calculation shows that for very closely coupled blade-rows ($\Delta x=0$) and for weakly coupled blade-rows ($\Delta x=1$) the Moore-Greitzer and Stenning results are confirmed (star and square, diamond, respectively). Note that for $\Delta x=0$ one of the system resonances is very highly damped (very low negative growth rate) and the only resonance contributing to the prestall dynamics is the classical "Moore-Greitzer" resonance. The striking result is that for a range of moderate blade-row spacings ($\Delta x=0.19\ldots0.45$) the resonance associated with the stator dynamics rotates against the direction of rotor rotation. Therefore also in axial flow compressors, there seems to be a coupling regime where backward rotating stall waves can occur.

Physical Mechanism From First Principles. Having demonstrated that the flow field dynamics in the radial gap between impeller and vaned diffuser in centrifugal compressors or in the axial gap between rotor and stator in axial compressors have a strong influence on the compressor pre-stall behavior, the physical mechanism for the occurrence of backward rotating stall waves is investigated next. A first principle based approach is conducted to analyze the wave phenomena in and around the compressor stage and a simple coupling criterion is established that explains the physical mechanism.

The rotor-stator system in **Fig. 7** is again considered where the rotor blade-row is separated from the stator blade-row by an axial spacing Δx. In general there are three fundamental types of modes in a linearized, incompressible, inviscid two-dimensional flow field that constitute the physical flow perturbations (velocities, static pressure, etc.). In this paper the two potential modes A and B are referred as to the upstream and downstream "pressure waves" and the vortical mode C is referred as to the "vortical wave" (for details see Spakovszky [17]). The goal of the following analysis is to show that for moderate coupling the pressure and vorticity waves in this rotor-stator system can interact such that the entire wave system is able to rotate at a negative natural frequency (backward traveling pre-stall wave with $\omega<0$). It is assumed that the axial spacing is large enough so that the pressure wave transmitted through the rotor has little influence on the stator waves. Similarly the pressure wave reflected from the stator is assumed to have little influence on the upstream rotor waves. Under this assumption the rotor and stator wave systems are only coupled through the vorticity wave shed from the rotor blade row and the phase relation between the transmitted rotor pressure wave and the reflected stator pressure wave imposes a matching condition between the two wave systems.

Referring back to **Fig. 7** it is assumed that the upstream flow is vorticity-free and that somewhere upstream a pressure wave is generated. This pressure wave B_R^i impinges onto the rotor where some part of it is reflected (A_R^r) and some part passes through the rotor in the form of a transmitted pressure wave (B_R^t). In addition, the impinging pressure wave sets up a circulation change around the rotor blades which leads to a vorticity wave (C_R) that is convected downstream with the steady mean flow. Upon arrival at the stator the vorticity wave sets up a pressure disturbance in the stator blades which is felt upstream (A_S^r) as well as downstream (B_S^t). To form one interacting wave system that oscillates at a single natural frequency ω, the transmitted (based on B_R^t) and reflected (based on A_S^r) pressure perturbation between the rotor and stator blade rows must line up in phase and match in magnitude. It can be shown analytically that this occurs for a certain axial spacing Δx at a negative natural frequency ω.

A Coupling Criterion For Backward Traveling Rotating Stall Waves. From this first principles analysis a simple crite-

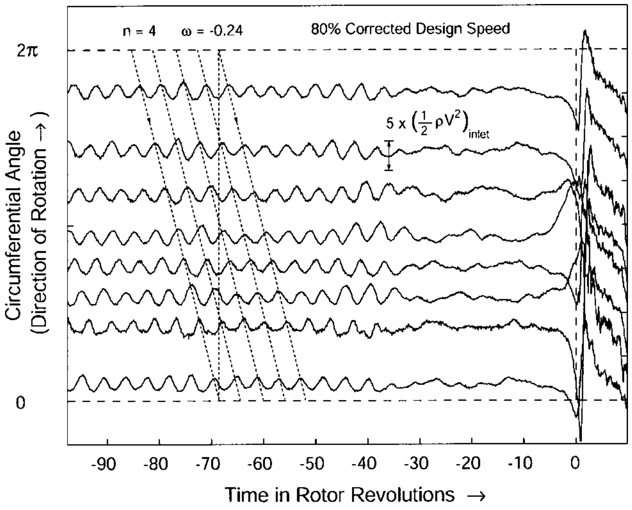

Fig. 8 Unsteady pressure traces in the vaneless space during a stall ramp at 80% corrected design speed

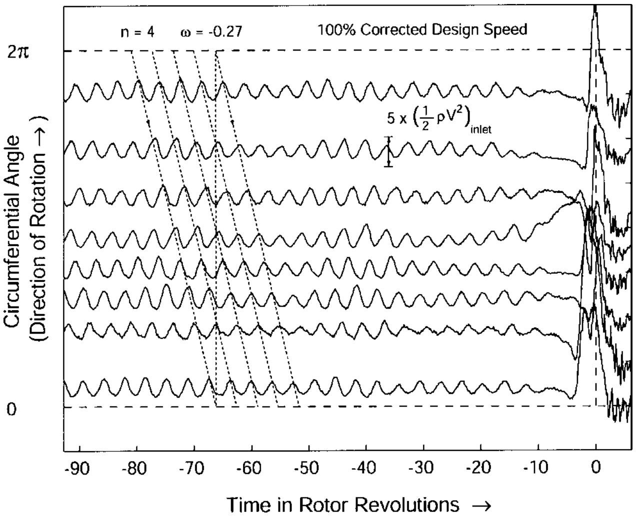

Fig. 9 Unsteady pressure traces in the vaneless space during a stall ramp at 100% corrected design speed

rion is derived that determines the blade-row spacing and critical length scales important for backward traveling rotating stall waves. The coupling criterion is based only on geometry and mean flow values.

It is again considered that an n-th harmonic vorticity wave $\tilde{\zeta}_n$ is shed from the rotor. If the wave is rotating at the frequency ω, the wave amplitude (see Spakovszky [17]) is proportional to

$$\tilde{\zeta}_n(x,t) \sim e^{-j\omega t - j(\omega/\overline{V}_x + n\,\overline{V}_\theta/\overline{V}_x)x}, \tag{2}$$

where $\overline{V}_x$ and $\overline{V}_\theta$ are the axial and tangential mean velocities in the inter-blade row gap. The second expression in the exponent is the total phase shift of the wave as it travels downstream. The first term inside the bracket is the phase shift due to the rotation of the wave and the second term accounts for the phase shift due to the convection with the swirling mean flow. Assuming that the strongest redistribution occurs when the vorticity wave at the stator leading edge (at a nondimensional axial location Δx) is half a wavelength out of phase relative to the initial vorticity wave at the rotor trailing edge $x=0$ (maximum periodic phase shift), the relative phase shift becomes

$$\left(\frac{\omega}{\overline{V}_x} + n\,\frac{\overline{V}_\theta}{\overline{V}_x}\right)\Delta x = \frac{\pi}{n}. \tag{3}$$

Let us assume that for matched pressure fields the natural frequency of the wave system is negative such that $\omega<0$. Using the absolute swirl angle α instead of the axial and tangential velocities and $\Delta x = \Delta\hat{x}/R$, the axial spacing for which this occurs is estimated to be

$$\frac{\Delta\hat{x}}{R} > \frac{\pi}{n^2}\,\frac{1}{\tan\alpha}. \tag{4}$$

It is important to note the following from this coupling criterion: (1) backward traveling waves stem from coupling phenomena on the radius scale, (2) small axial blade-row spacings yield higher harmonic backward rotating stall waves, (3) for high swirl angles in between the blade rows lower harmonic waves are observed that travel against the direction of rotation, and (4) for an axial gap of zero length no backward rotating stall waves can exist, consistent with the classical Moore-Greitzer theory.

Referring back to the interacting rotor-stator example the absolute swirl angle of the flow between rotor and stator of this generic compressor is 65.7 deg. Considering a 3rd harmonic prestall wave as in **Fig. 6** the axial gap sizes for which backward rotating stall waves occur can be estimated using the coupling criterion. The result shows that for $\Delta x > 0.16$ the third harmonic rotation rate can be negative, which is in agreement with the computational results.

The coupling criterion can also be applied to the NASA CC3 centrifugal compressor. The impeller absolute exit swirl angle is estimated to be 79° at this operating point. Assuming $\Delta x = R_2 - R_3 = 0.078$ as the radial spacing between diffuser leading edge and impeller exit, the condition for backward traveling harmonic waves becomes $n > 2.8$. The same observation is made using the full centrifugal compressor model which predicts that pre-stall waves with a harmonic number of 3 and higher travel backward (against the direction of impeller rotation) as shown in **Fig. 5**.

Experimental Validation of Model Predictions[2]

Various stall ramps were conducted at 80% and 100% corrected design speed by gradually closing the collector valve until the compressor surged. **Figure 8** shows the unsteady pressure traces of the eight circumferentially distributed Kulite sensors in the vaneless space (see **Fig. 1**) during a very slow stall ramp at 80% corrected design speed. After removing the mean pressure level from the signal, the unfiltered pressure traces are plotted corresponding to their circumferential position from bottom to top in the direction of impeller rotation. The time into surge is counted in rotor revolutions. Strong periodic fluctuations with a peak-to-peak magnitude of roughly five times the inlet dynamic pressure are visible before surge. Further analysis reveals that the wave fronts of a 4th harmonic pre-stall wave travel against the direction of impeller rotation at about -0.24 times rotor frequency. The wave fronts of the four-lobed spatial periodicity are marked by the dotted lines which are negatively sloped with respect to time[3]. Next, similar stall ramps are repeated at 100% corrected design speed and the unsteady pressure traces are plotted in **Fig. 9**. The periodic pressure disturbances fluctuate again at a magnitude of about five times the inlet dynamic pressure. Again a 4th harmonic pre-stall wave is observed that travels backward at about -0.27 times rotor frequency.

The experimental observations at 80% and 100% corrected design speed compare remarkably well with the model predictions,

---

[2] It has to be emphasized that the modeling effort was undertaken before these experiments were conducted. In other words the discussed modeling results are pure predictions and not a posteriori explanations of experimentally observed phenomena.

[3] It is impossible to align the wave fronts with a positively sloped line which is confirmed by a spectral analysis of the Kulite signals.

Table 1 Model result compared to experimental measurements at 80% and 100% corrected design speed

Model	Data 80% Speed	Data 100% Speed
$n=4$ $\omega=-0.18$	$n=4$ $\omega=-0.24$	$n=4$ $\omega=-0.27$

where the lowest harmonic mode that goes unstable is a 4th harmonic pre-stall wave with a rotation rate of -0.18 times the rotor frequency (see **Fig. 5**). Periodic oscillations of 5th and 6th harmonic waves were also computed by the model but are not observed in the experiment. This suggests that for a periodic wave to exist, the circumferential length scale of the flow nonuniformity has to be long enough such that a blade and its neighbors (two pitches) have similar flow conditions (within a quarter wavelength). Hence, for an impeller blade count of 30, circumferential harmonics up to the 4th are expected to exist in the compression system. This sets a limit to the spatial flow field resolution of the model and is in agreement with similar limitations suggested by Longley [16] for axial compressors. The above experimental measurements and the model results are summarized in **Table 1**. It is important to note that the nondimensional rotation rate is independent of impeller speed, or in other words the mode frequency scales with rotor speed. The 4th harmonic backward traveling resonance is thus one of the incompressible system modes and resembles a four-cell backward traveling rotating stall precursor.

Streamwise Activity of Backward Traveling Waves. **Figure 10** depicts unsteady pressure traces obtained from the Kulite sensors located upstream of the impeller, in the vaneless space, at the diffuser throat and in the diffuser passage at mid chord during the stall ramp at 80% corrected design speed. The 4th harmonic pre-stall wave is also seen at the diffuser throat but with much larger amplitude. However, upstream of the impeller the pressure trace is flat and in the diffuser passage the magnitude of the pressure perturbation is strongly attenuated. This clearly shows that the 4th harmonic backward traveling rotating stall wave is most dominant at the diffuser throat and suggests that this resonance is associated with the diffuser dynamics. The model also predicts the maximum mode activity to occur near the diffuser leading edge: in **Fig. 4** the ratio of the energy function magnitudes between diffuser leading edge and impeller exit and the ratio between diffuser leading edge and diffuser exit are 2.8 and 8.3, respectively. The measurements in **Fig. 10** show similar magnitude ratios of the pressure fluctuations at the respective locations. The pressure magnitude ratios are 2.9 and 5.6.

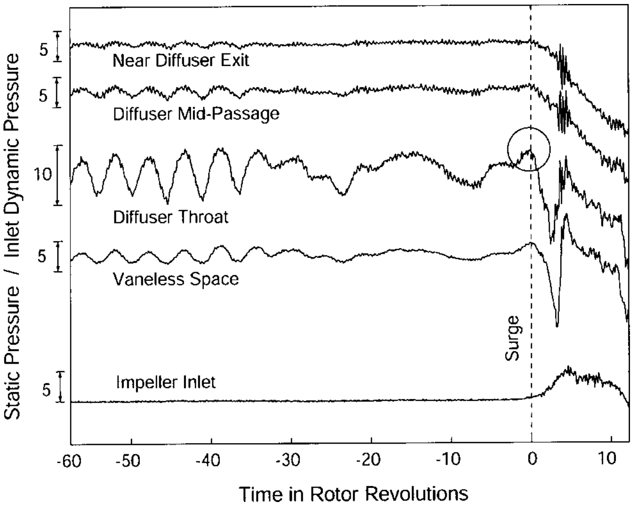

Fig. 10 Pressure traces at impeller inlet, in the vaneless space, at the diffuser throat and in the diffuser passage along the path into instability at 80% corrected design speed

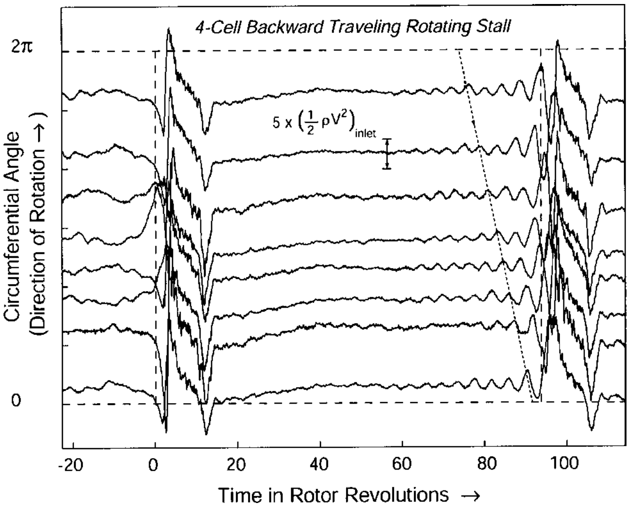

Fig. 11 "Classic Surge": pressure traces in the vaneless space at 80% corrected design speed

The experimental results validate the model predictions and confirm the existence of higher harmonic pre-stall waves that travel in the opposite direction of rotor rotation.

Mechanism of Surge Inception. Along the path into instability the incompressible, backward traveling four-lobed pre-stall wave grows gradually. This incompressible system resonance is most pronounced near the diffuser throat and originates from the unsteady interaction between the impeller and the diffuser. The pre-stall waves in the vaneless space are of large amplitude (about 10 times the inlet dynamic pressure) so that nonlinearities of the compressor characteristic are perceived and nonlinear coupling between the spatial harmonics is introduced. This means that the mode shape of the incompressible resonance is not a purely four-lobed sinusoid but has also a 0th harmonic or surge-like content. **Figure 10** shows that in addition to the large amplitude 4th harmonic backward traveling waves a low-frequency oscillation is superimposed and that a few rotor revolutions prior to surge the periodic fluctuations distort abruptly. The flow starts to break down near the diffuser throat where the steepest pressure drop is observed (see circle in **Fig. 10**). Instants later the pressure starts to rise at the impeller inlet and drops inside the diffuser passage. The surge cycle is initiated.

Pathology of Surge. The B-parameter, defined by Greitzer [21] is a surge stability parameter that determines if the system will go into rotating stall or surge. Put another way, the B-parameter is the ratio of two forces, the pressure difference across the compressor (between plenum and atmospheric pressure upstream of compressor) and the inertial force in the compressor ducting. If the B-parameter of the compression system is very large, the inertial forces are much smaller than the driving force due to the pressure differential and deep surge will occur. On the other hand if the B-parameter of the system is small, the inertial forces are dominant and overcome the pressure differential force. In this case the compressor will exhibit rotating stall.

The B-parameter for the NASA CC3 centrifugal compression system is estimated to be 1.47. In this case the magnitude of the inertial forces and the pressure differential forces are on the same order of magnitude, so that during the surge cycle the machine passes in and out of rotating stall. This is often referred to as "classic surge." **Figure 11** shows the Kulite signals in the vaneless space during this classic surge cycle. The flow breaks down at a nondimensional time of 0 rotor revolutions and the compression system surges. Passing out of surge after about 20 rotor revolutions the compressor operating point climbs up along the steady-state characteristic and at about 60 rotor revolutions stall precursors start to form. The precursor, which is the incompressible resonance with strong 4th harmonic content, starts to rotate against the direction of impeller rotation at a frequency of -0.24 times rotor frequency and grows gradually in amplitude forming four-cell backward traveling rotating stall. Roughly 30 rotor revolutions later the amplitude is so large that the flow through the compression system breaks down again and the surge cycle repeats. Note that the second surge cycle is initiated by a smooth growth of the incompressible mode. This is because during surge the variation in mass flow through the compressor is smoother than when the compressor is throttled into instability by closing the throttle valve.

Flow Control for Enhanced Stability

One of the objectives of this research was to design and implement a flow control scheme in the NASA CC3 centrifugal compressor to enhance the compression system stability. It was suggested by PIV measurements in the same machine (Wernet et al. [22]) that the flow separation and blockage in the diffuser passage, driven by the diffuser hub corner stall on the pressure side, plays an important role during compressor surge. From these steady-state observations, one could argue that air injection in the radial direction upstream of the diffuser or into the diffuser passages might energize the flow and enhance the stability of the machine. Unfortunately later in the test program these flow control concepts were proven unsuccessful. It is demonstrated in this paper that, based on the dynamic model predictions, a properly designed flow control scheme which injects air tangentially between impeller and diffuser is able to enhance the compression system stability.

Model Based Design of Vaneless Space Air Injectors. The idea behind surge control is that air injection can alter the system dynamics and thus dampen the pre-stall resonances, rendering a given unstable operating point stable and extending the operating range. Referring back to the model predictions and unsteady measurement results, the strongest pre-stall activity seems to occur in the vaneless space. **Figures 4** and **10** show that a four-lobed backward traveling rotating stall resonance dominates the compression system dynamics. The focus of the flow control scheme is therefore to change the vaneless space performance by air injection, or more precisely to enhance the diffusion from impeller exit to diffuser throat.

It was found in centrifugal compressors with vaned diffusers that the spanwise (axial) variation of the flow properties at the impeller exit, especially the swirl angle, exert a more significant influence on the diffuser performance than does the unsteady, circumferential variation of the flow (Senoo et al. [23] and Dawes [24]). Furthermore, laser anemometer measurements and CFD calculations for the NASA CC3 impeller (Skoch et al. [25] and Larosiliere et al. [26]) have shown that, at design conditions, the impeller wake is located near the shroud on the blade suction side. This means that, on time-average, the relative velocity at the exit of the impeller is higher near the hub (jet) and lower near the shroud (wake). Considering the velocity triangles at the impeller trailing edge the absolute velocity has a higher swirl angle near the shroud as the flow enters the vaneless space. This situation is sketched in **Fig. 12** (the vaneless space is not to scale) showing the velocity triangle near the shroud (solid) and near the hub (dash). The flow control concept is then to inject air in the tangential direction upstream of the diffuser at the shroud. This further increases the absolute swirl angle near the shroud and therefore decreases the geometric flow area near the impeller. Thus, due to the area ratio effect between impeller exit and diffuser throat, a higher level of diffusion can be obtained near the shroud.

This flow control scheme is implemented using eight injectors circumferentially distributed in between the impeller and the vaned diffuser as shown in **Fig. 1** on the bottom. They are positioned as close as possible to the impeller exit and designed to inject air in the tangential direction as depicted in **Fig. 12**. The injection air is controlled by a valve designed by Berndt [27] and developed by Moog Inc. and MIT. The injector nozzle attached to the valve body directs the flow from the valve to the diffuser. Taking advantage of the Coanda flow effect (Felsing and Moller [28]) the injector nozzles are designed (Strazisar [29]) such that the flow is injected as a sheet that stays attached to the endwall without the nozzle body protruding into the compressor flow. At the nozzle exit the injector slot has a square area of 24.1 mm^2.

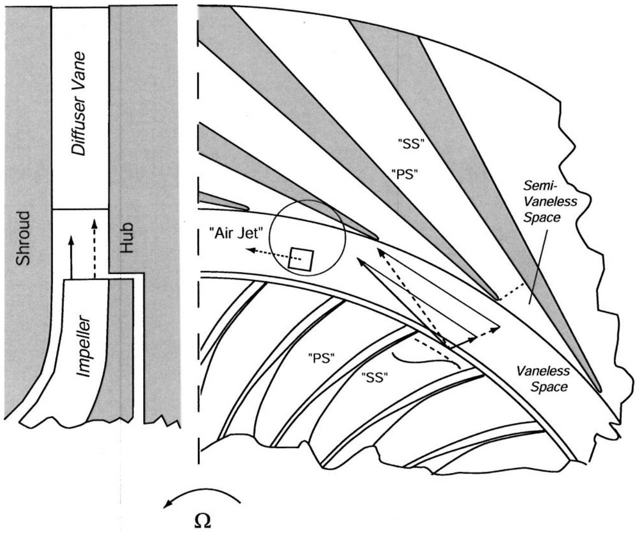

Fig. 12 Velocity triangles at the impeller exit near the diffuser shroud (solid) and near the diffuser hub (dash). The air jet from the tangential injector nozzle is sketched as the dotted line. The vaneless space is not to scale.

Steady-State Experimental Results

The baseline compressor map (no flow control) with speed lines at 80% and 100% corrected design speed is constructed from steady-state measurements and is plotted in **Fig. 13** as circles. The design point and the working line are marked by the full circle and the dashed line, respectively. The surge line (no injection) is plot-

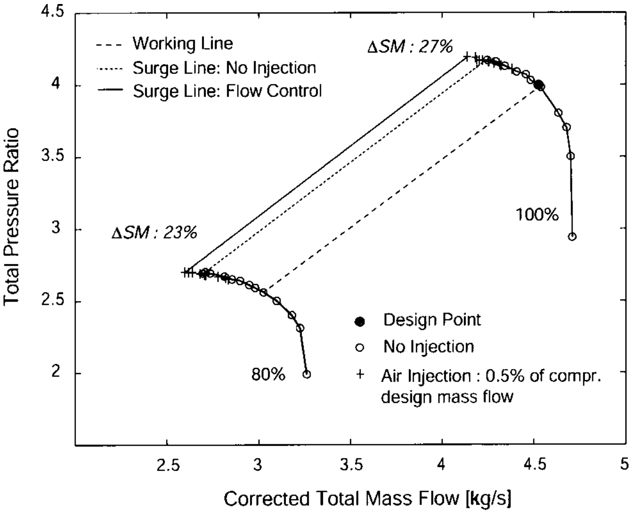

Fig. 13 Speed lines at 80% and 100% corrected design speed: baseline (circles) and with flow control (pluses)

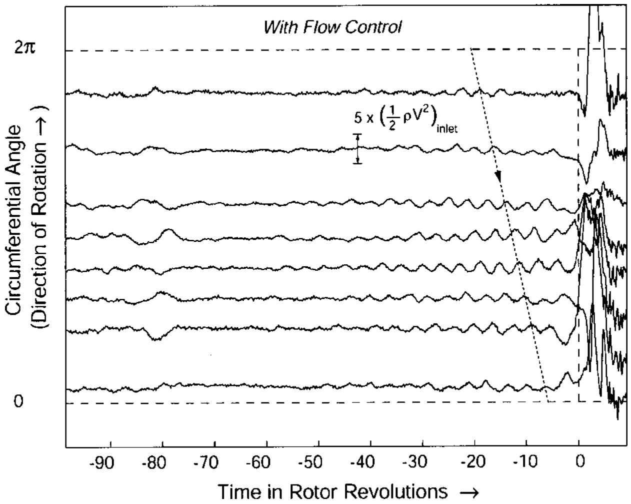

Fig. 14 Pressure traces in the vaneless space during a stall ramp with air injection at 100% corrected design speed

ted as the dotted line. Defining the surge-margin as $\mathrm{SM}=(1-\pi_{\mathrm{work}}/\pi_{\mathrm{surge}}\cdot\dot{m}_{\mathrm{surge}}/\dot{m}_{\mathrm{work}})\times 100\%$, where $\dot{m}$ is the mass flow and π is the total pressure ratio, the surge-margin at part speed and at design speed are 15% and 10%, respectively.

Steady Air Injection Results. The injectors were supplied with external air from the test facility. It has to be mentioned that due to the high total temperature ratio of the centrifugal compressor near surge, the relatively cold injection air had a cooling effect on the impeller wheel (as shown in **Figs. 1** and **12** the injector nozzles are placed close to the impeller exit). The RotaData tip-clearance measurements revealed that the axial impeller exit clearance increased significantly with injector mass flow (the impeller axial blade height shrunk due to the cooling from the injected air). This had a strong impact on the compressor performance. Therefore to maintain the hot running clearance condition, the impeller exit clearance was adjusted to the design value of 2.4% of passage height for each level of injection.

The injected mass flow was measured separately from the compressor mass flow. The total and static pressure measurements from an instrumented nozzle were used together with the individual nozzle discharge coefficients to determine the total injected mass flow. Both the compressor mass flow, measured upstream using an orifice plate, and the injector mass flow were then standard day corrected to the compressor inlet. The sum of the upstream mass flow and the injected mass flow was used to plot the speed lines shown in **Fig. 13**. Stall ramp experiments with air injection were conducted with different levels of injection both at 80% and at 100% corrected design speed. The injection level was varied by adjusting the supply pressure with a valve. From a parametric study the optimum air injection mass flow for the maximum increase in surge-margin was determined to be 0.46% of the compressor design mass flow at part speed and 0.51% of compressor design mass flow at design speed. The compressor map with flow control in the vaneless space is also plotted in **Fig. 13** (pluses). The surge line with a total air injection mass flow of 0.5% of the compressor design mass flow is marked as the solid line. At part speed an increase in surge-margin of 23% is obtained and at design speed the surge-margin is enhanced by 27%.

The enhancement in stability is due to the altered system dynamics and the change in component performance through flow control. This is also observed in the unsteady pressure signals measured during a stall ramp with injection. **Figure 14** depicts the pressure traces in the vaneless space along the path into instability at 100% corrected design speed with an injection mass flow of 0.51% of the compressor design mass flow. The four-lobed backward rotating stall pre-cursors seem to be more damped compared to the case with no air injection (see **Fig. 9**). To link the altered dynamic behavior of the system to changes in performance, the effect of injection on the component performance is analyzed next.

Flow Control Effects on Component Performance. The performance of the impeller and of the diffuser subcomponents

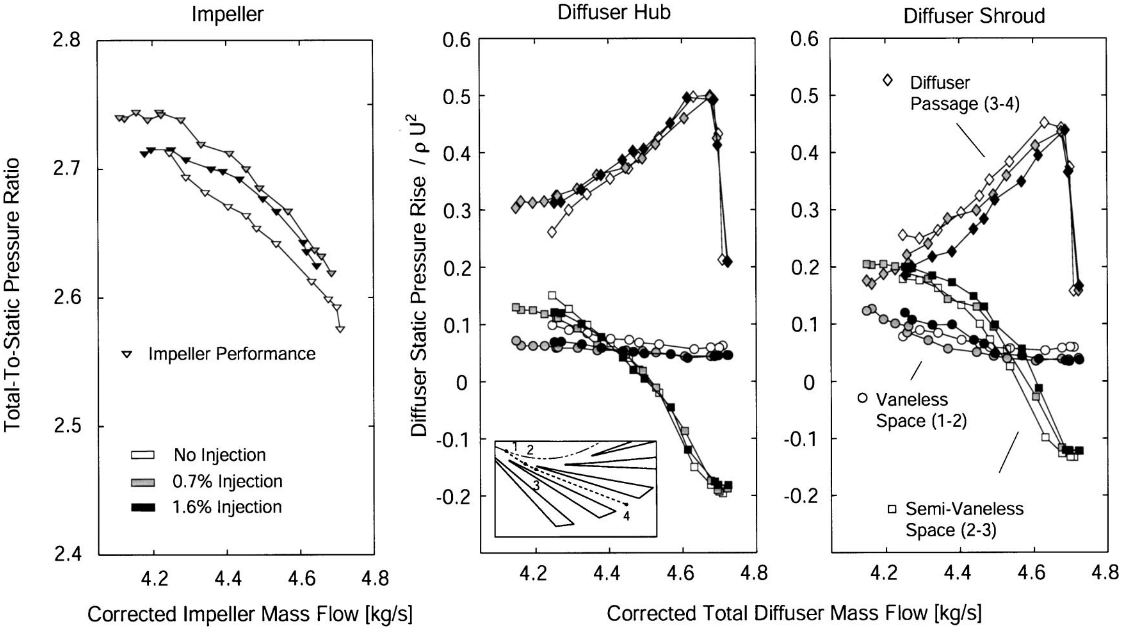

Fig. 15 Impeller total-to-static pressure ratio (left) and diffuser subcomponent pressure rise at the hub (center) and at the shroud (right) for no injection (white symbols) and injected mass flow of 0.7% (gray symbols) and 1.6% of compressor design mass flow (black symbols) at 100% corrected design speed

were carefully mapped out for the baseline case (no injection) and for various levels of air injection. **Figure 15** depicts the impeller total-to-static pressure ratio (left) and the static pressure rise in the vaneless space, in the semi-vaneless space and in the diffuser passage at the hub (center) and at the shroud (right) for no injection (white symbols) and for injected mass flows of 0.7% and 1.6% of the compressor design mass flow (gray and black symbols) at design speed. It is important to note the following from these results:

(1) No Injection. The impeller characteristic (white triangles) has a negative slope[4] over the entire flow range and is thus dynamically stable. The slopes of the vaneless space characteristic (white circles) and the semi-vaneless space characteristic (white squares) at the shroud become zero and positive respectively for very low mass flows while at the hub, the slope is still negative. On average (between hub and shroud) the slope is about zero near surge and it seems that these diffuser subcomponents determine the point of dynamic instability of the compression system. This is in concert with the unsteady measurements and the dynamic modeling results that show maximum pre-stall wave activity near the diffuser throat. Also note that the diffuser passage is unstable (positive slope of pressure rise characteristic) over almost the entire flow range. This is because for lower mass flows the blockage near the throat grows as a consequence of the increasing adverse pressure gradient and the pressure rise in the passage drops.

(2) Air Injection. Air injection affects both impeller and diffuser performance. On the one hand the additional injector mass flow in the vaneless space decreases the mass flow through the impeller and the impeller loading increases, yielding a higher impeller pressure ratio. In addition the tangential momentum from the injection air at the exit of the impeller reduces the relative exit swirl angle and thus reduces the negative slope of the impeller characteristic (less backsweep) destabilizing the impeller. On the other hand the diffusion in the vaneless and semi-vaneless space near the shroud is markedly enhanced and has a stabilizing effect on the components critical for system stability (gray circles and gray squares). A further increase in injection mass flow improves the stability of the vaneless and semi-vaneless space while it destabilizes the impeller. Thus, with relatively high levels of injection (black symbols) the compression system becomes unstable with no improvement in operating range. The dynamic stability of the system is in this case limited by the impeller.

In summary, the measurements suggest that the effect of injection is to extend the flow range over which the vaneless space and the semi-vaneless space are stable (i.e., have negative pressure rise slopes), at the expense of a less stable impeller. Because the resonance responsible for surge inception is concentrated (higher amplitude) in the former regions, stabilizing these components has a beneficial effect on overall system stability. In other words, the critical subcomponent is stabilized by properly designed air injection.

Viability Assessment of Flow Control in Working Engines

To assess the viability of compressor stability enhancement using air injection in a working engine environment, an additional series of experiments was conducted. The impeller exit tip-clearance was increased to test if the flow control scheme was able to enhance the stability of the compression system with deteriorated tip-clearances. Also, in order to keep the flow control expenditure at a minimum a parametric study was conducted with a reduced number of injectors.

Stability Enhancement at Increased Impeller Tip-Clearances. Using the high-precision translator system described earlier, the axial blade tip-clearance at the impeller exit was increased from the design value of 2.4% to 3.6% of the passage height. First the baseline compressor performance with increased tip-clearances was mapped with no injection. The compressor performance deteriorated, reducing the total pressure rise of the machine. At part speed the machine surged at the same mass flow as with the design tip-clearance and the surge-margin decreased by 4%. At design speed, however, the mass flow at surge was reduced. Even though the pressure rise dropped due to the higher tip-clearance, the surge-margin was slightly increased by 7% due to the lower surging mass flow. This is shown in **Fig. 16** as the solid and the shaded diamonds at zero-injected mass flow.

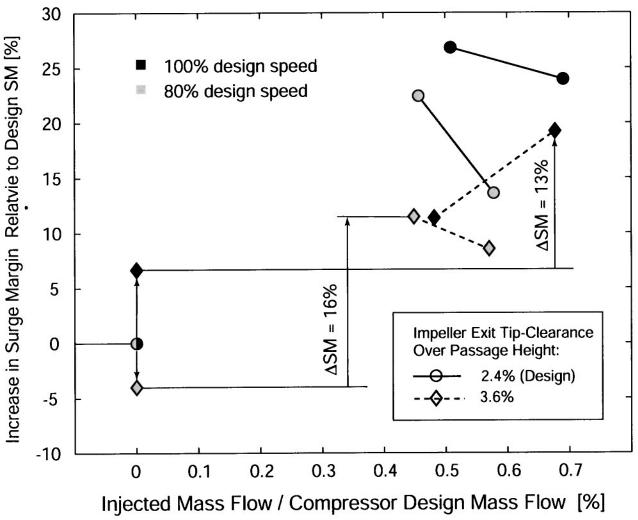

Fig. 16 Effect of impeller exit tip-clearance on surgemargin and on stability enhancement at 80% and at 100% corrected design speed

A series of experiments were then conducted with increased blade tip-clearance using different levels of injection. The measurements revealed that air injection significantly enhanced the compression system stability even with an increased impeller exit tip-clearance. The surge-margin was increased at part speed by 16% and at design speed by 13% relative to the nominal surge-margin with increased tip-clearance. This is summarized in **Fig. 16** (diamonds and dashed lines) together with the results obtained at design conditions (circles and solid lines). The experiments at part speed show that the loss in surge-margin due to the change in tip-clearance is more than recovered.

Stability Enhancement With Reduced Number of Air Injectors. A series of experiments was conducted with a reduced number of injectors to investigate their effectiveness. First, two injectors were physically shut off so that no flow leaked through the actuators. Injectors Nos. 1 and 5 (see **Fig. 1**) were chosen such that the remaining six injectors were as uniformly spaced as possible (see **Fig. 17**). The injection level for best stability enhancement was then determined from stall ramp experiments. Then injectors Nos. 2, 4, 6, and 8 were shut off and the total number of injectors was reduced to 4. In a last experiment the four injectors on the lower half of the circumference were shut off so that an asymmetric distribution of the remaining four injectors was obtained.

The results are summarized in **Fig. 17** and the following can be concluded: (1) A circumferentially uniform spacing between the injectors is crucial for stability enhancement. The measurements with the asymmetric 4 injector configuration showed no enhancement in stability at all (triangles). This is different from the observations by Suder et al. [30] in axial compressors, who found that range extension is related to the total circumferential extent of

---

[4] For high-speed machines the slope of the total-to-static pressure ratio is analogous to the slope of the total-to-static pressure rise coefficient which is the relevant-parameter for rotating stall in low-speed machines (see Eq. (1)).

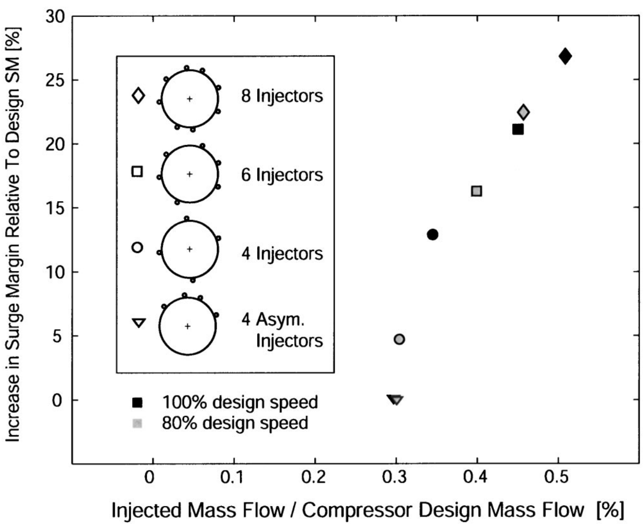

Fig. 17 Stability enhancement at 80% and at 100% corrected design speed with different numbers of injectors

injection but is not related to the circumferential arrangement of injection locations. The reason for the different findings lies in the nature of injection and its effect on the compressor dynamics: in the axial compressor experiments by Suder et al. air was injected upstream of the compressor into a *rotating* blade row, whereas in this case injection occurs in the vaneless space *between* blade rows upstream of a *stationary* blade row. (2) The increase in surge-margin rises with an increased number of injectors. Therefore an increased circumferential coverage improves the effect of tangential air injection in the vaneless space. At design speed a remarkable increase in surge-margin of 13% was achieved using only four injectors with an injection mass flow of 0.35% of the compressor design mass flow (solid circle). (3) As observed in **Fig. 17**, the injector velocity necessary for stability enhancement decreases with the number of injectors. This is because injection in the vaneless space has also an influence on the impeller: Reducing backsweep of the impeller exit flow lessens impeller stability. (4) A minimum of four injectors is required for a benefit in surge-margin.

Design Implications

The unsteady interaction between impeller and diffuser has an important effect on performance and in design practice engineers have used empirical methods to account for this (Rodgers [19]). What is missing from these investigations is the link to compressor stability. This paper demonstrates that the radial gap size is a relevant parameter for backward-traveling rotating stall and has a strong influence on the stability of the compression system. In other words an optimal gap size for improved performance at design conditions does not necessarily guarantee acceptable stability off-design. An enhanced design must take this into account. Having established an understanding for the blade-row interaction effects on system stability the following general recommendations are made for a design with enhanced stability:

- The gap size for optimal performance should be chosen such that impeller and diffuser are closely coupled with $\Delta R < \pi/n^2 \tan\alpha$. This enhances the stability of higher harmonic resonances as shown in **Fig. 6**.
- For a given gap size high impeller exit swirl angles should be avoided to increase the coupling (see coupling criterion in Eq. (4)). Hence highly backswept impeller blades are preferred and generally yield improved dynamic system stability.
- In general a reduced impeller blade count is preferred which increases the blade loading and therefore also slip. Higher slip yields lower absolute impeller exit swirl and, for a given gap size, increased coupling.

It is clear that many design considerations have to be made and some of the above recommendations must be compromised for improved performance and efficiency.

Summary and Conclusions

A new, low-order analytical approach to model centrifugal compressor stability is introduced. Its modular structure renders modeling flexibility and enables to resolve the dynamics of individual blade-rows and thus deals with dynamic interaction effect between components. The low-order, analytical nature of the model allows to dissect the dynamic stall phenomena and facilitates the explanation of physical mechanisms.

The model is implemented for the NASA CC3 high-speed centrifugal compressor and predicts a new signature of stall precursors. The compression system dynamics are dominated by a four-lobed pre-stall resonance that travels against the direction of impeller rotation at a natural frequency of -0.18 times rotor frequency, resembling a four-cell backward traveling rotating stall wave. An energy analysis exhibits that this backward traveling rotating stall wave shows the strongest activity in the vaneless space between impeller and diffuser. The same model is implemented for a generic axial compressor stage and it is demonstrated that backward traveling rotating stall phenomena can also occur in axial machines when the blade-rows are moderately coupled.

A simple coupling criterion is developed from first principles to explain the physical mechanism for the occurrence of backward traveling rotating stall waves and to determine the critical blade-row spacing and the important length scales. It is found that the backward traveling rotating stall resonance stems from the interaction of pressure waves and unsteady vortex shedding driven by the resonant behavior of the impeller and the diffuser wave systems. The coupling criterion states that for blade-row spacings $\Delta\hat{x}/R > \pi/n^2 \tan\alpha$ backward-traveling rotating stall waves can occur.

Experiments are then conducted in the NASA CC3 centrifugal compressor to validate the model predictions. The unsteady pressure measurements show for both part and design speed that an incompressible four-lobed system resonance rotates at about a quarter of rotor speed against the direction of rotation. The experimental results compare remarkably well with the model predictions and confirm the existence of multicell backward-traveling rotating stall.

A flow control scheme for enhanced compression system stability is designed based on the model predictions. The flow control scheme employs steady air injection between impeller and diffuser in the tangential direction. The steady air injection experiments show an increase of 25% in surge-margin with an injection mass flow of 0.5% of the compressor mass flow. Furthermore, it is experimentally demonstrated that this injection scheme is robust to impeller tip-clearance effects and that a reduced number of injectors can be applied for similar gains in surge-margin.

In summary, this paper reports a new phenomenon related to rotating stall in centrifugal compressors. The model findings together with definite measurements explain the mechanism for first-ever observed backward traveling rotating stall in centrifugal compressors with vaned diffusers. The results firmly establish the connection between the experimentally observed dynamic phenomena in the NASA CC3 centrifugal compressor and a first principles based coupling criterion.

Acknowledgments

The author would like to thank Prof. Edward Greitzer for the very useful comments and insightful discussions. The author is most greatly indebted to Dr. Anthony Strazisar, Dr. Michelle

Bright, and Gary Skoch at NASA GRC for their support in this research. Special thanks go also to Tony Zaldana, Tom Jett, Scott Panko, Harry Fuller, and Mark Stevens for their help during compressor testing. This research was conducted under NASA grant NAG3-1457.

References

[1] Hunziker, R., and Gyarmathy, G., 1994, ''The Operational Stability of a Centrifugal Compressor and Its Dependence on the Characteristics of the Subcomponents,'' ASME J. Turbomach., **116**, pp. 250–259.
[2] Lawless, P., and Fleeter, S., 1995, ''Rotating Stall Acoustic Signature in a Low-Speed Centrifugal Compressor: Part I—Vaneless Diffuser,'' ASME J. Turbomach., **118**, pp. 87–96.
[3] Abdelhamid, A., 1980, ''Analysis of Rotating Stall in Vaneless Diffusers of Centrifugal Compressors,'' ASME Paper 80-GT-184.
[4] Frigne, P., and Van Den Braembussche, R., 1980, ''A Theoretical Model for Rotating Stall in the Vaneless Diffuser of a Centrifugal Compressor,'' ASME Paper 84-GT-204.
[5] Frigne, P., and Van Den Braembussche, R., 1984, ''Distinction Between Different Types of Impeller and Diffuser Rotating Stall in a Centrifugal Compressor With Vaneless Diffuser,'' ASME J. Eng. Gas Turbines Power, **106**, pp. 468–474.
[6] Lawless, P., and Fleeter, S., 1991, ''Active Unsteady Aerodynamic Suppression of Rotating Stall in an Incompressible Flow Centrifugal Compressor With Vaned Diffuser,'' Paper No. AIAA-91-1898.
[7] Lawless, P., and Fleeter, S., 1993, ''Rotating Stall Acoustic Signature in a Low-Speed Centrifugal Compressor: Part II—Vaned Diffuser,'' ASME Paper 93-GT-254.
[8] Oakes, W., Lawless, P., and Fleeter, S., 1999, ''Instability Pathology of a High Speed Centrifugal Compressor,'' ASME Paper 99-GT-415.
[9] Pinsley, J., Guenette, G., Epstein, A., and Greitzer, E., 1991, ''Active Stabilization of Centrifugal Compressor Surge,'' ASME J. Turbomach., **113**, pp. 723–732.
[10] Gysling, D., Dugundji, J., Greitzer, E., and Epstein, A., 1991, ''Dynamic Control of Centrifugal Compressor Surge Using Tailored Structures,'' ASME J. Turbomach., **113**, pp. 710–722.
[11] Ffowcs Williams, J., Harper, M., and Allwright, D. J., 1993, ''Active Stabilization of Compressor Instability and Surge in a Working Engine,'' ASME J. Turbomach., **115**, pp. 68–75.
[12] Nelson, E., Paduano, J., and Epstein, A., 2000, ''Active Stabilization of Surge in an Axicentrifugal Turboshaft Engine,'' ASME J. Turbomach., **122**, pp. 485–493.
[13] Stein, A., Niazi, S., and Sankar, L., 2000, ''Computational Analysis of Centrifugal Compressor Surge Control Using Air Injection,'' AIAA Paper No. 2000-3501.
[14] McKain, T., and Holbrook, G., 1997, ''Coordinates for a High Performance 4:1 Presure Ratio Centrifugal Compressor,'' NASA, Technical Report CR-204134.
[15] Moore, F., and Greitzer, E., 1986, ''A Theory of Post-Stall Transients in Axial Compressors: Part I—Development of the Equations,'' ASME J. Eng. Gas Turbines Power, **108**, pp. 68–76.
[16] Longley, J., 1994, ''A Review of Nonsteady Flow Models for Compressor Stability,'' ASME J. Turbomach., **117**, pp. 202–215.
[17] Spakovszky, Z., 2000, ''Applications of Axial and Radial Compressor Dynamic System Modeling,'' Ph.D. thesis, Department of Aeronautics and Astronautics, MIT, Cambridge, MA.
[18] Wood, J., 2000, personal communication, NASA Glenn Research Center.
[19] Rodgers, C., 1982, ''The Performance of Centrifugal Compressor Channel Diffusers,'' ASME Paper 82-GT-10.
[20] Stenning, A., 1980, ''Rotating Stall and Surge,'' ASME J. Fluids Eng., **102**, pp. 14–20.
[21] Greitzer, E., 1976, ''Surge and Rotating Stall in Axial Compressors; Part I: Theoretical Compression System Model,'' ASME J. Eng. Power, **98**, pp. 190–198.
[22] Wernet, M., Bright, M., and Skoch, G., 2001, ''An Investigation of Surge in a High-Speed Centrifugal Compressor Using Digital PIV,'' ASME J. Turbomach., **123**, pp. 418–428.
[23] Senoo, Y., Kinoshita, Y., and Ishida, M., 1977, ''Asymmetric Flow in Vaneless Diffusers of Centrifugal Blowers,'' ASME J. Fluids Eng., **99**, pp. 104–114.
[24] Dawes, W., 1995, ''A Simulation of the Unsteady Interaction of a Centrifugal Impeller With Its Vaned Diffuser: Flow Analysis,'' ASME J. Turbomach., **117**, pp. 213–222.
[25] Skoch, G., Prahst, P., Wernet, M., Wood, J., and Strazisar, A., 1997, ''Laser Anemometer Measurements of the Flow Field in a 4:1 Pressure Ratio Centrifugal Impeller,'' ASME Turbo Expo, Orlando, FL.
[26] Larosiliere, L., Skoch, G., and Prahst, P., 1997, ''Aerodynamic Synthesis of a Centrifugal Impeller Using CFD and Measurements,'' AIAA, ASME, SAE and ASEE Joint Propulsion Conference, Seattle, WA.
[27] Berndt, R. G., 1995, ''Actuation for Rotating Stall Control of High Speed Compressors,'' Master's thesis, Department of Aeronautics and Astronautics, MIT, Cambridge, MA.
[28] Felsing, G., and Moller, P., 1969, ''Coanda Flow Over a Circular Cylinder With Injection Normal to the Surface,'' AIAA J., **7**(5), pp. 842–846.
[29] Strazisar, A., 2000, personal communication, NASA Glenn Research Center.
[30] Suder, K., Hathaway, M., Thorp, S., Strazisar, A., and Bright, M., 2000, ''Compressor Stability Enhancement Using Discrete Tip Injection,'' ASME Turbo Expo, Munich, Germany.

The Effects of Wake-Passing Unsteadiness Over a Highly Loaded Compressor-Like Flat Plate

Xavier Ottavy

Stephane Vilmin

Howard Hodson

Whittle Laboratory,
Cambridge University,
Trumpington Street,
Cambridge CB2 1PZ, UK

Simon Gallimore

Rolls-Royce plc,
Moor Lane,
Derby DE24 8BJ, UK

The present study is concerned with wake-induced unsteady effects in axial-compressor blade rows. The goal is to exploit these effects in order to design high-lift blades without increasing the profile loss, as has been achieved for low-pressure turbine blades. In the first part of this paper, the experimental means and the computational fluid dynamics tools are described. The rig features a flat plate that can be subjected to different velocity distributions representative of the suction side of a real compressor blade. Cylindrical bars mounted on a moving system simulate the incoming wakes from the upstream blade row in the compressor. Results are presented for steady flow and for unsteady compressor-like conditions. In all cases, the separation bubble of the steady flow is suppressed by the turbulence that is induced in the boundary layer by the wakes at approximately 10% of the suction side. Its reappearance is then delayed by a region of stable laminar-like flow and low loss due to the so-called calming effect that follows the wake-induced patch. The paper describes these phenomena in detail for one particular pressure distribution. It is then shown that it should be possible to increase the lift by 35% while keeping the same level of loss as the initial conventional pressure distribution of the study.

[DOI: 10.1115/1.1643384]

Introduction

Modern compressors and turbines have reached efficiency levels that are difficult to improve. In order to decrease the cost of a turbomachine, an attractive alternative is to reduce the weight and production cost of the turbomachine by reducing the number of blades. For low-pressure turbine blade rows, it has been demonstrated that taking into account the unsteadiness created by the passing wakes of upstream bladerows can produce higher lift blades without increasing the profile loss (Schulte and Hodson [1] and Howell et al. [2]). These increases in lift and resulting reductions in blade number were achieved due to wake-induced transition of the boundary layers. The mechanism is as follows. First, the boundary layer separation over the suction side of a high-lift blade is temporarily suppressed by the turbulence induced by the incoming wakes. Second, the so-called calmed regions that trail these wake-induced turbulent flows have a very full velocity profile and yet are laminar like in nature. The calmed zones do not readily separate, thus delaying the reestablishment of the bubble and because they are laminar, they do not produce much loss and so counterbalance any extra losses associated with the same wake-induced turbulence.

The present study is concerned with these phenomena in axial-compressor blades. Nowadays, the design of compressor blades mostly relies on tools that are based on steady flow analysis and assume the blade boundary layers fully turbulent in the turbulent bulk flow, whereas the reality can be very different (Halstead et al. [3]). To study the transition effects over the suction side of an axial-compressor blade in presence of wakes, experimental investigations have been performed on a flat plate subjected to wakes coming from upstream bars.

A range of pressure distributions that go beyond the limits that result from common methods were sought. Usually, the analysis of the steady boundary layer and its resistance to separation in the adverse pressure gradient of the compressor stage leads to a ‘‘ski-slope’’ type pressure distribution, i.e., one that is steep after the suction peak with progressively less diffusion toward the rear of the blade. In looking for the same beneficial unsteady effects from the incoming wakes that have been observed for the turbine blades, the lift has been increased by moving the suction peak downstream and/or by increasing the ratio $V_{\max}/V_{\text{outlet}}$. These two approaches have led to the five configurations that are represented in **Fig. 1**. In this report, the authors have chosen to focus on shape 02 because it presents features that particularly illustrate the study: a large separation bubble in absence of wakes and strong unsteady effects in the case of wake passing. Also, it was tested alongside the development of a computational fluid dynamics (CFD) code that, in conjunction with a prescribed intermittency modeling, is expected to support the analysis of the results and help understand key phenomena.

In a first part of the paper, the experimental rig and the measurement techniques are presented. The CFD program is also introduced. The steady flow and unsteady flow results for shape 02 are then described and discussed in a second part. The analysis then compares profile losses of shape 02 with the other shapes in terms of how they are affected by the lift, the Reynolds number, the reduced frequency and the local diffusion factor.

Experimental and CFD Methods

Experimental Setup. The experimental study has been performed using a moving bar rig with a flat plate as a blade (see **Fig. 2**). The symmetrical pressure distribution imposed on the plate by the top and bottom walls is representative of what may be found on the suction side of a real compressor blade. The wakes downstream of the bars simulate the wakes from the upstream blade row in the compressor.

The plate is built in three parts: an elliptical leading edge, the body (700 mm long and 12.8 mm thick) and a triangular trailing edge (40 mm long, not included in the chord). To test the shapes

---

Contributed by the International Gas Turbine Institute (IGTI) of THE AMERICAN SOCIETY OF MECHANICAL ENGINEERS for publication in the ASME JOURNAL OF TURBOMACHINERY. Paper presented at the International Gas Turbine and Aeroengine Congress and Exhibition, Amsterdam, The Netherlands, June 3–6, 2002; Paper No. 2002-GT-30354. Manuscript received by IGTI, Dec. 2001, final revision, Mar. 2002. Associate Editor: E. Benvenuti.

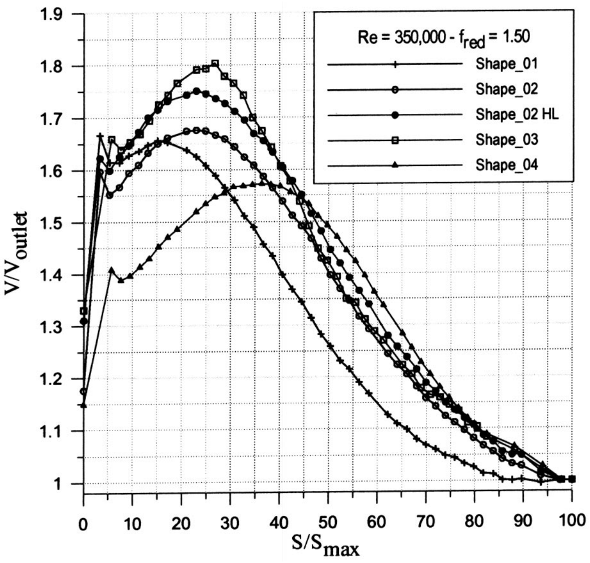

Fig. 1 Tested velocity distributions

01, 02, and 02 highly loaded, the leading edge had a length of 22 mm. It was then replaced with a longer (38 mm) one with more pressure tappings. This was intended to delay the bypass transition onset brought about by the turbulence in the wakes by reducing the size of the leading edge overspeed.

A constant-area section was used upstream of the leading edge of the plate so as to provide a uniform inlet flow. Moreover, this avoids any deformation of the incoming wakes as they convect towards the leading edge of the plate. The outlet section also has a constant area. The ratio between the inlet and the outlet area has been fixed at 0.714 (increased to 0.735 if taking into account the thickness of the plate). A typical value for this ratio is given by the Haller criterion: $V_{\text{outlet}}/V_{\text{inlet}} > 0.72$.

Although the surface of interest is uppermost on the plate, a symmetrical configuration, leading to the same flow on both sides of the plate, has been used. Both leading edges have pressure tappings that were used to set the inlet angle to zero. A symmetrical configuration makes it easier to predict the steady flow pressure distribution using one-dimensional or two-dimensional tools. Moreover, all the inlet probes have been located in the lower path to avoid any perturbation in the upper path (see **Fig. 2**).

Treatment of the Top and Bottom Walls. The top and bottom walls impose the pressure distribution on the flat plate. They were cut from expanded polystyrene. The surface is rough enough to make the boundary layer turbulent and more resistant to separation in presence of an adverse pressure gradient. However, this boundary layer creates a blockage that can be very difficult to take into account when designing the profile of the walls. Also, the comparisons with CFD would be easier if the surface of the top and bottom walls were treated as inviscid, reducing the number of mesh nodes considerably. Therefore, the top and bottom wall boundary layers are bled at several locations using transversal slots, the first one being located just after the throat where the boundary layer thickness starts increasing significantly. No suction device was used. Instead, the pressure inside the test section was made higher than atmospheric so as to assure a mass flow through the slots. This was achieved by placing perforated metal sheets at the exit of the working section so that the resulting pressure distribution over the plate matched the CFD results (see CFD section below).

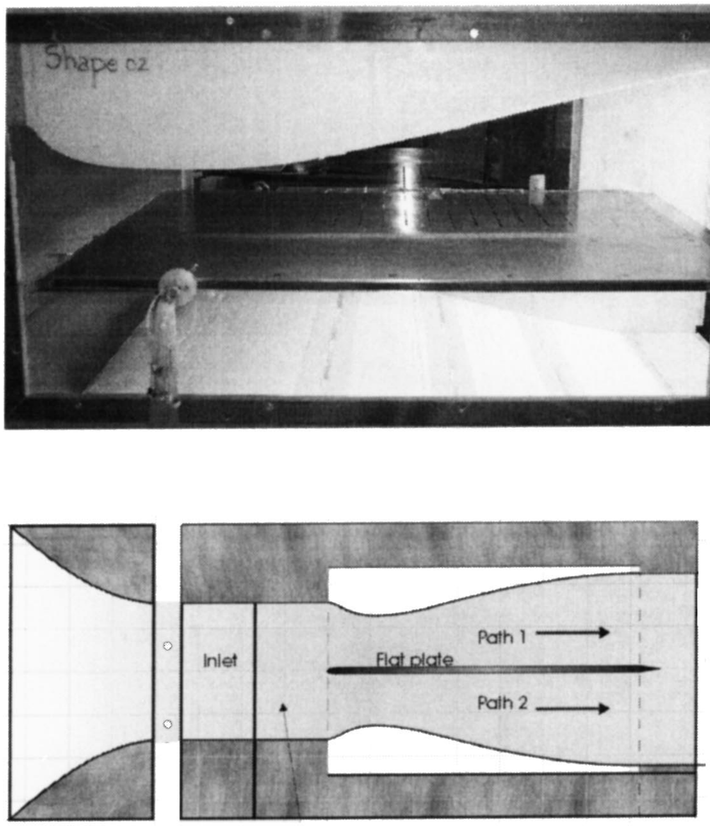

Fig. 2 View of the "wood box" with the plate and the polystyrene walls

The Wake Generator. The upstream wakes are generated by moving bars. The moving bar rig is of the same kind as the one used by Schulte and Hodson [4] and Howell [5]. The bar diameter was set to 7.8 mm, so that the bar loss coefficient is the same as a compressor blade, typically around 4% at midspan. The flow coefficient $V_{\mathrm{inlet}}/U_{\mathrm{bar}}$ has been set to 1.0. A change in the bar spacing was used to change the reduced frequency. The axial distance between the bars and the leading edge of the plate, which was 47% of the plate length or 45 bar diameters, was chosen such that the peak turbulence intensity in the incoming wakes at the leading edge was around 4%–5%.

Flow Conditions. The operating conditions of the presented investigation are given by a Reynolds number of 350,000 or 500,000, and a reduced frequency f_{red} of 0.75 or 1.5. The freestream turbulence intensity is 1.2% at the inlet.

Measurement Techniques

Instrumentation. To measure the static pressure on the profile, the flat plate has been instrumented with 50 pressure tappings located at every 2% of the chord. The results are presented in term of pressure coefficient $C_p=(P_{\mathrm{inlet}}-P_{\mathrm{static}})/(P_{\mathrm{inlet}}-P_{\mathrm{total}})$.

A single-wire probe was used for the boundary layer traverses. It was calibrated in low turbulence, using the Bearman and Cox methods to correct the effects of ambient temperature variations and the effects due to wall proximity, respectively. Hot-wire traverses were performed near the flat plate trailing edge (97.5% surface length). Up to 30 positions through the boundary layer were measured.

With a view to measuring the wall shear stress over the whole surface of the plate, up to 24 hot-film sensors have been attached on the top side of the plate and operated at constant temperature. The pseudo wall shear stress is related to the measured output voltage via the relation due to Hodson et al. [6]

$$\tau_w \propto \left(\frac{E^2-E_0^2}{E_0^2}\right)^3 \tag{1}$$

where E_0 is the output voltage under zero flow conditions

Processed Statistical Quantities. The hot-wire and hot-film data have been identically treated. They are phase-locked averaged by averaging the signal at a fixed time after the trigger pulse over a number of wake periods large enough to get good ensemble data. The trigger was activated using a photocell. The ensemble-averaged variable is

$$\tilde{U}(t)=\frac{\sum_{i=1}^{N}U_i(t)}{N} \tag{2}$$

where N has been set to 64 or 256, depending whether the flow is "without bars" or "unsteady." It is then possible to extract the phase-locked periodic fluctuations by subtracting the ensemble averaged value to the time-averaged value; and also to process the root mean square of the signal at a particular phase by computing the square root of the variance of the quantity:

$$\mathrm{RMS}(t)=\sqrt{\sigma(t)}=\sqrt{\frac{\sum_{i=1}^{N}(U_i(t)-\tilde{U}(t))^2}{N}}. \tag{3}$$

The quantity is the velocity in case of the hot-wire data and the pseudo shear stress τ_w in case of hot-film data. The RMS includes the turbulent fluctuations and also the abrupt variations in space of transition onset. In case of hot film data, its highest value usually indicates a mid-transition boundary layer.

The raw data presented in this paper are taken from the first ensemble of an acquisition session. The raw traces indicate the instantaneous state of the boundary layer. In the case of the hot-film measurements, since the traces are acquired at the same time it is possible to track individual events as they develop in the boundary layer and travel over the flat plate surface.

Hot-Film Nondimensional Results. Because the flow velocity encountered around the flat plate is relatively low (around ten m/s), for each sensor the raw data and the ensemble mean of the quasi shear stress were divided by the maximum ensemble and time mean value of the quasi shear stress of that sensor. There is no relation in terms of absolute values between each sensor. The quasi-shear stress at the wall will be noted τ instead of τ_w for more clarity.

Nondimensional raw data:

$$\tau^*(s,t)=\frac{\tau(s,t)}{\tilde{\tau}_{\max}(s)}. \tag{4}$$

Nondimensional ensemble mean:

$$\tilde{\tau}^*(s,t)=\frac{\frac{\sum_{i=1}^{N}\tau_i(s,t)}{N}}{\tilde{\tau}_{\max}(s)}=\frac{\tilde{\tau}(s,t)}{\tilde{\tau}_{\max}(s)}. \tag{5}$$

Nondimensional variance:

$$\tilde{\sigma}_\tau^*(s,t)=\frac{\tilde{\sigma}_\tau(s,t)}{\tilde{\sigma}_{\tau,\max}(s)}. \tag{6}$$

CFD Method and Strategy

The PUIM Method. The prescribed unsteady intermittency model (PUIM) (Schulte and Hodson [1]) aims to simulate the evolution in time of the laminar, transitional, and turbulent patches which cover the blade while the wake is convected in the inter-blade channel and conveys regions of high freestream turbulence, inducing bypass transition. The laminar-turbulent transition onset is determined by Mayle's correlation, [7], dependent on the turbulence intensity at the boundary layer edge. In case of separation, the transition onset is fixed using a correlation with the momentum-thickness Reynolds number at separation, [7]. The intermittent feature of the transitional flow is modeled by means of an intermittency factor varying from zero (laminar) to one (turbulent). Based on the characteristics of the development of turbulent spots introduced by Emmons [8], it quantifies how often the boundary layer is turbulent at a streamwise position.

The intermittency factor in PUIM is computed either using the concentrated breakdown concept of Narasimha [9], or using a continuous breakdown of the turbulent spots that accounts for the properties of the calmed region (Ramesh and Hodson [10]). This laminar-like flow region of high shear stress, which trails a turbulent spot, as observed by Schubauer and Klebanoff [11], is essential in delaying transition and separation. The correlations used for the spot production rate are Mayle's correlation [7] or Gostelow and Walker's [12] for an attached flow. They are both dependent on the pressure gradient parameter and the turbulence intensity at the boundary layer edge. The spreading of the turbulent spots is prescribed using functions of the edge velocity and the pressure gradient parameter, [13]. For a separated flow, Mayle's correlation gives the spot production rate from the momentum-thickness Reynolds number at separation.

The UNNEWT Solver. Previous Cambridge experimental work has revealed a strong influence of the negative-jet feature of the convected wake on the size and location of the separation bubble. This problem has been investigated prior to the present project using the unstructured-mesh unsteady Navier-Stokes code UNNEWT (Hodson and Dawes [14]).

The code UNNEWT is an unsteady flow version of the unstructured-mesh viscous flow solver NEWT (Dawes [15]). The time marching is performed by the same Runge-Kutta scheme. A two-dimensional version of this code has been written so that the PUIM routines can be used in conjunction with the viscous flow solver. The turbulence model is a *k*-epsilon model introduced by Yang and Shih [16]. To avoid too big a turbulent kinetic energy in

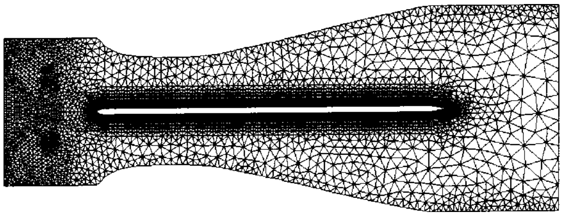

Fig. 3 View of the two-dimensional mesh. 6156 nodes.

the stagnation regions, the treatment introduced by Durbin [17] has been added to the two-equation turbulence model.

The Coupling. The boundary layer parameters and flow variables at the edge of the boundary layer are read from UNNEWT and fed into PUIM that returns a distance-time intermittency field (constant in time in the case of a steady flow simulation). For an unsteady flow, the estimated intermittency at the current time is obtained by the interpolation of the intermittency distributions located at the times that precede and follow the current time in the distance-time field returned by PUIM. The prescribed intermittency factor is then used in the *k*-epsilon turbulence model in UNNEWT via streamwise wall stations built within the unstructured mesh. It acts as a multiplier on the eddy viscosity. It is set to one in the free stream flow and 0.1 in the diffusive terms of the transport equations in the laminar regions. The intermittency is regularly estimated, in different ways depending on the kind of flow that is simulated.

In steady flow, the number of iterations between two calls of PUIM is fixed by the user. In unsteady flow, there are two possible modes. In the first mode, the intermittency evolution in space and time during a wake-period is estimated from the initial solution. In the second mode, the intermittency distribution in distance and in time is updated every number of iterations that corresponds to the elementary time step that is given by the time discretisation in the PUIM routines. The boundary layer parameters and flow variables at the edge of the boundary layer are stored for a whole wake-period. This real-time coupling is probably the more appropriate for unsteady flow simulations, especially when separation is involved.

CFD Mesh and Boundary Conditions. The CFD mesh used for the flow simulation is illustrated in **Fig. 3**. It discretizes the whole chamber since the steady flow solution will be used as initial solution for future unsteady flow simulation. Also, the mesh is relatively fine at the inlet for future modeling of the decay of incoming wakes. Obviously, the modeled steady flow is expected to be symmetric. As boundary conditions, the total pressure, the total temperature, and the flow angle are fixed at the inlet. The static pressure is kept constant at the outlet.

Discussion of the Results

Steady Flow: Shape 02. **Figure 4** is a plot of the experimental measurements compared with numerical predictions. On the experimental pressure distribution, a separation bubble due to the strong diffusion after the throat is clearly indicated by the pressure plateau and the pressure recovery due to laminar-to-turbulent transition. The bubble extends from 35% approximately to midchord of the plate. At the trailing edge, the boundary layer is fully turbulent with a shape factor value of 1.6 approximately. The CFD reproduces these features very satisfactorily on both sides of the plate. The estimated pressure plateau is shorter than in reality. This is because the Mayle correlation seems to give a premature transition onset. This could be due to a slight discrepancy between the predicted location of separation (38% of the chord) and its real position. The pressure distributions do not match exactly after the throat. Also, the limitations of the low Reynolds number *k*-epsilon model for predicting reattached flows are well known. Nevertheless, the predicted displacement and momentum thicknesses near the trailing edge match the experimental measurements. The shape factor is approximately equal to the usual value of 2.5 in the laminar region well upstream of the separation point. It reaches the value of about 3.7 at separation. Once the separated flow un-

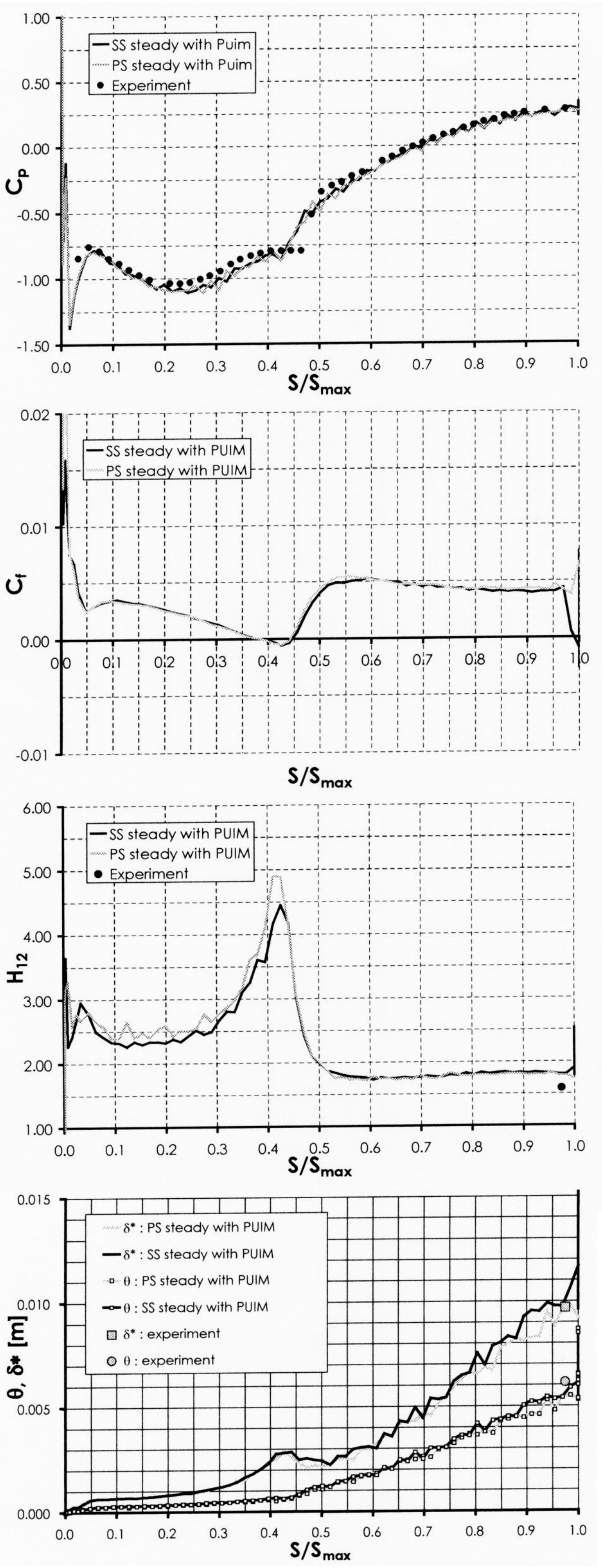

Fig. 4 Measured and simulated steady flow for shape 02, Re =350,000 PS means pressure side, SS means suction side

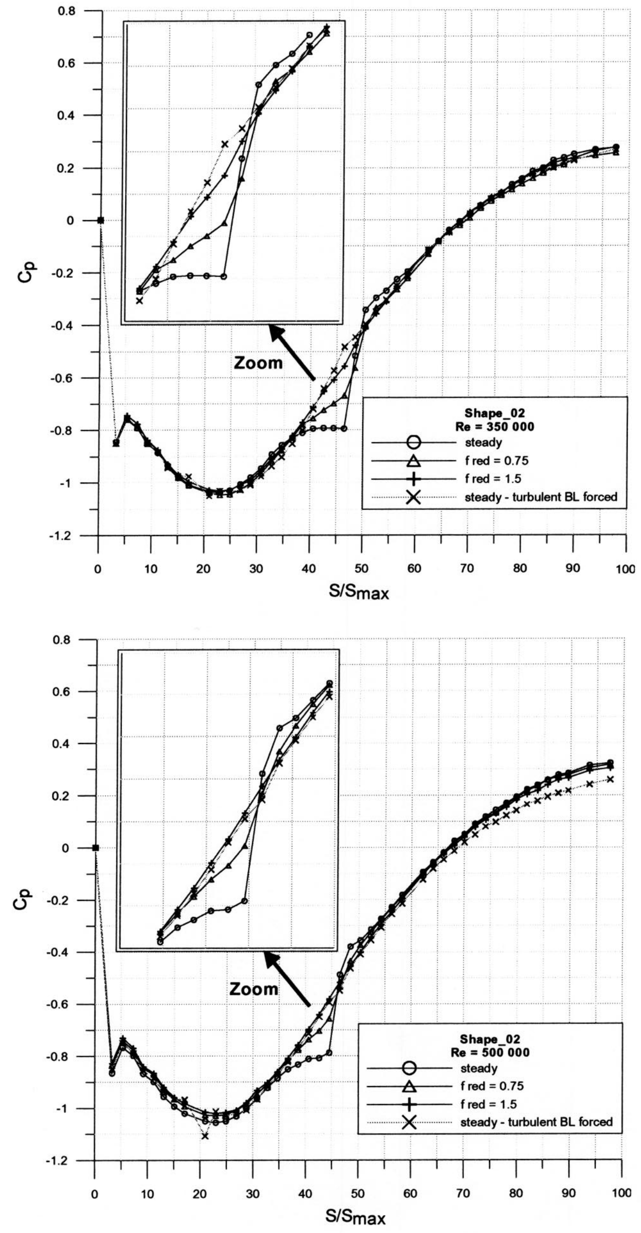

Fig. 5 Experimental C_p distributions with incoming wakes for Re=350,000 and Re=500,000—shape 02

dergoes transition, the shape factor reduces to about 1.7, which is larger than the expected value of 1.4–1.5 for a turbulent boundary layer with no streamwise pressure gradient. The value measured at the trailing edge is about 1.6. This overestimation of the shape factor could be due to the limitations of the low Reynolds number *k*-epsilon model. The discrepancy in the prediction of the bubble size (as had already been observed on other short-bubble test cases for the validation of UNNEWT-PUIM) is not important enough to devalue the clear improvement in the prediction of the boundary layer parameters at the trailing edge compared with a fully turbulent flow simulation. The predictions presented here therefore seem reasonable and this is despite the lack of mesh resolution that manifests itself in the small oscillations in presented data.

Unsteady Flow: Shape 02. The measured pressure distributions for shape 02 for all of the cases with and without the wakes are plotted in **Fig. 5**. With no wakes, there is separation at about 35% of the chord. Increasing the reduced frequency produces a weaker time-averaged perturbation to the pressure distribution. There is no apparent separation with a frequency of 1.5 or in the case where the turbulent boundary layer is made turbulent before the throat using a trip wire.

The corresponding hot-film experimental results are presented for Re=350,000 (see **Fig. 6** and **Fig. 7**). Two types of plots are used to facilitate the interpretation of the data. For these two plots, the time is nondimensionalized so that the units correspond to the bar passing period. This is known as ‘‘wake periodicity.’’ The first type of plot used (at the left side of the figures) is the distance-time or ‘‘S-T’’ diagram. This is a contour plot of the nondimensional ensemble averaged wall quasi-shear stress (called later ensemble mean shear stress for simplicity), showing how it varies with surface distance on abscissa and with time on the ordinate axis. The second type of plot (at the right side of the figures) is a time history of the nondimensional raw signal and of the mean shear stress. The abscissa axis is the nondimensional time. The signals of each sensor have been multiplied by a factor of five and their zero has been positioned on the ordinate axis at the sensor location as a percentage of the surface length. This is another kind of distance-time diagram that superimposes two signals. Note that both signals are nondimensional by their respective maximum value, which is not the same for the raw and the mean data. Four lines have been added on these plots. They correspond to the trajectories of particles traveling at a certain percentage of the local freestream velocity. They are used to show how the transition region develops under the influence of the wake. The wake will convect at the local free stream velocity outside of the boundary (line labeled ‘‘1.00’’). The front of the wake-induced patch travels at the propagation rate of the leading edge of a turbulent spot, i.e., at 88% of the local free stream which is indicated by the line labeled ‘‘0.88.’’ The trailing edge of the same wake-induced patch propagates at the velocity of the trailing edge of a turbulent spot, that is at 50% of the local free stream (line labeled ‘‘0.50’’), and the trailing edge of the calmed regions propagates at around 30% (line labeled ‘‘0.30’’). All these trajectories have been calculated using the experimental pressure distribution along the flat plate. The intercepts of these lines on the time axis have been adjusted manually so as to obtain one single intersection point for all of them. This location approximates to that of transition onset. The lines have no meaning before this event.

The first part of the surface length in **Fig. 6** shows a flow affected by incoming wakes. The raw traces and the intersection point of the four lines show that the wake-induced transition starts very early, i.e., before 10% of the surface length. In the wake-induced path, the mean shear stress has higher values relative to the rest of the time. Traveling along the plate, the boundary layer in the wake-induced path changes its state from transitional to turbulent and finally to one that contains ‘‘old’’ turbulence as indicated on the figure. This designation of states was introduced by Cumpsty et al. [18]. The old turbulent boundary layer is characterized by low values of the mean shear stress (darker zones on the plot) relative to the more recently formed turbulent boundary layers that follow it. Immediately following the wake-induced transition zone is the calmed region that prevents the laminar separation reforming. It is present for more than a third of the wake period at 50% of the surface length. The calmed region can only follow a region of turbulence. The turbulence results from turbulent spot production and growth in the wake-induced path. Therefore the effectiveness of the calmed zone in suppressing flow separation and transition onset between wakes is related to the intermittency levels within the wake-induced path. The effect of the calming zone in **Fig. 6** indicates that transition of the boundary layer in the wake-induced path must be completed very early. This leads to the so-called old turbulent boundary layer at the trailing edge in comparison to the new turbulent boundary layer that develops after the separation. It is worth noticing that

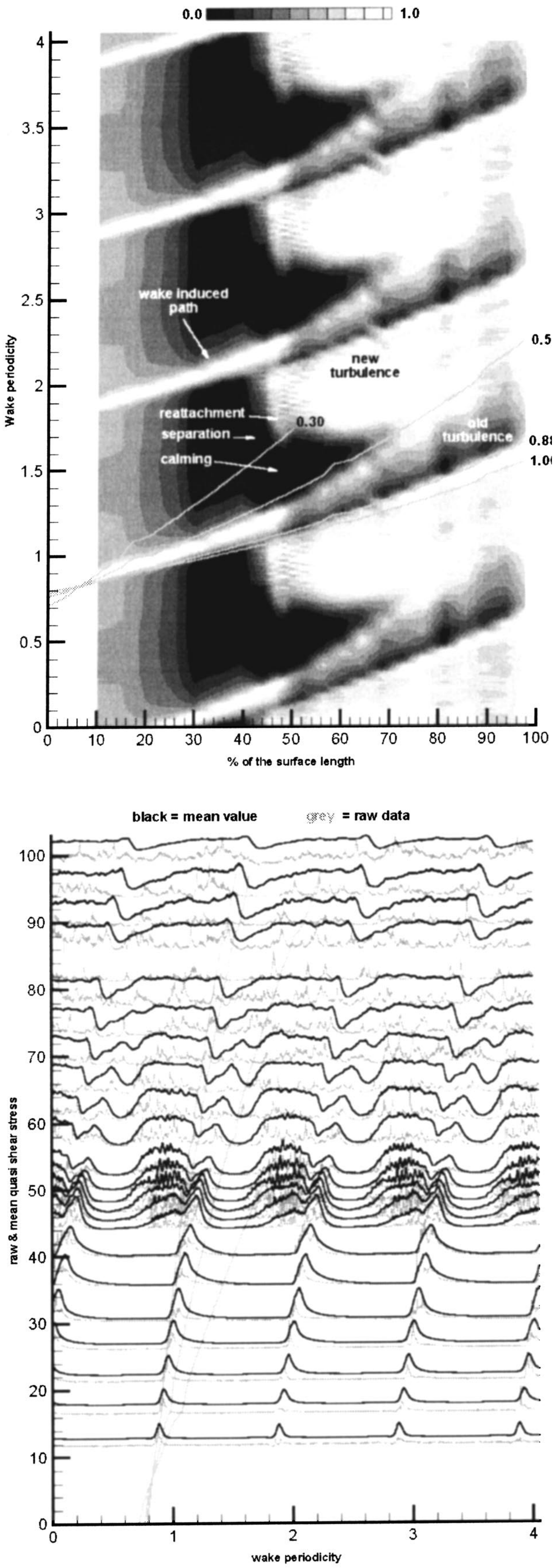

Fig. 6 Hot film data, nondimensional quasi shear stress on the plate—Re=350,000 and $f_{\mathrm{red}}=0.75$—shape 02

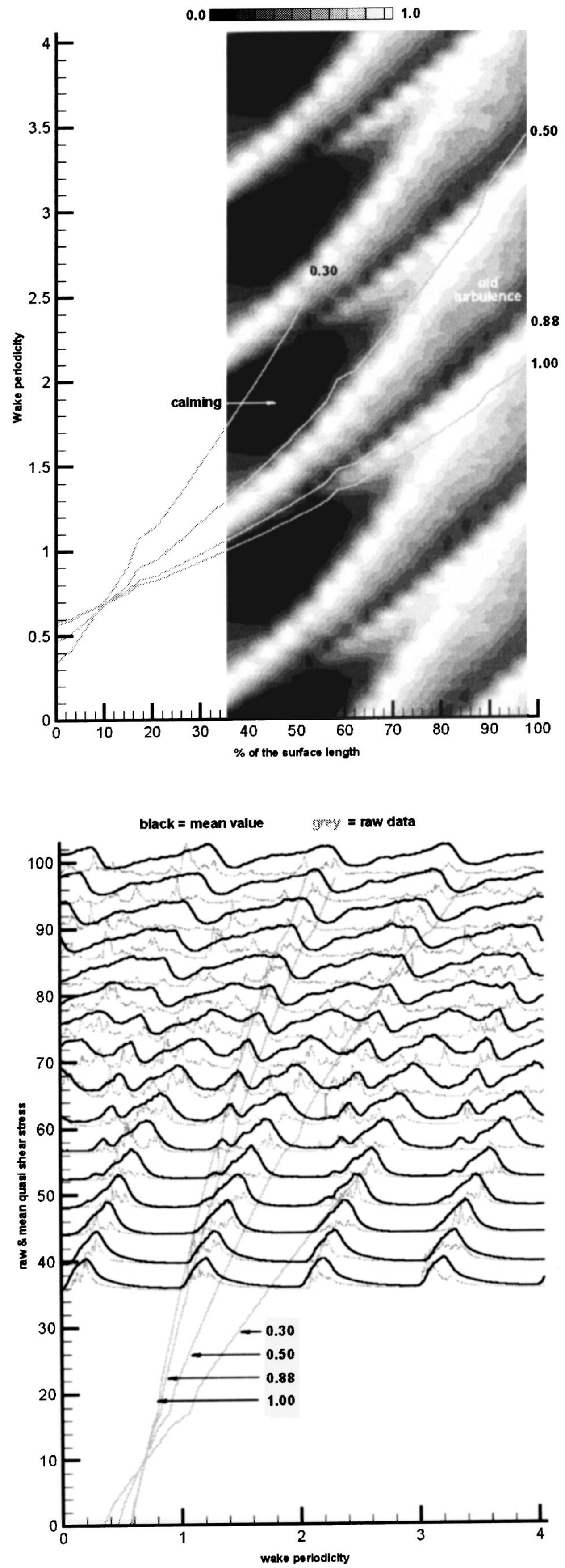

Fig. 7 Hot-film data, nondimensional quasi shear stress on the plate—Re=350,000 and $f_{\mathrm{red}}=1.5$—shape 02

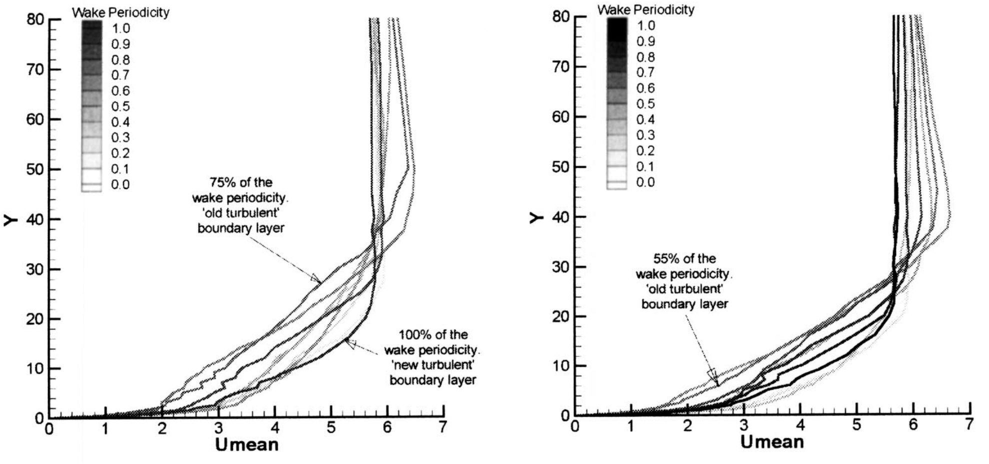

Fig. 8 Boundary layer velocity profile as a function of time—Re=350,000—$f_{\mathrm{red}}=0.75$ and $f_{\mathrm{red}}=1.5$—shape 02

the separation occurs between 40% and 45% of the chord whereas it seems to occur sooner in absence of wakes, between 35% and 40% of the chord.

With a reduced frequency of 1.5 and the same Reynolds number only 16 sensors have been used, as shown in **Fig. 7**. There is no separation because the next wake-induced transition occurs before the end of the calming effect. The wake-induced path is almost the same.

The data plotted in **Fig. 8** are deduced from the hot wire traverses at 97.5% of the chord and represent the time evolution of the boundary layer profile (time as a percentage of the wake periodicity). Ten instants in the period have been plotted. They are differentiated by lines of different gray level. The contour plots of variance, the time histories of the displacement thickness, the momentum thickness and the associated shape factor are plotted versus this non-dimensional time in **Fig. 9** and **Fig. 10**. The dashed lines on these time histories denote the appropriate values obtained from the steady experiments. **Figure 8** to **Fig. 10** show that the boundary layer profiles at the trailing edge clearly change during a wake period.

With reference to the hot film results of **Fig. 6** and **Fig. 7**, it can be seen that the maxima of δ^* and θ, as well as the region of high variance that occurs at the same time (75% of the wake period for $f_{\mathrm{red}}=0.75$; 55% of the wake period for $f_{\mathrm{red}}=1.5$) are all associated with old turbulence region of the wake-induced turbulent zone. Moreover, the boundary layer profiles at these times are typical of a fully turbulent boundary layer.

For the case of $f_{\mathrm{red}}=0.75$, **Fig. 9** shows that δ^* and θ decrease rapidly from their maxima to their respective minimum values at 105% of the wake period. These minima correspond to a boundary layer that follows the region of the strongest calming effect (as indicated in **Fig. 6**). This region therefore produces the ''youngest'' turbulent boundary layer at the trailing edge. The profile originating from the reappearing bubble is indicated in **Fig. 8** ($f_{\mathrm{red}}=0.75$) for a time that corresponds to 100% of the wake period.

Figure 9 shows that the values of δ^* and θ increase to values that are slightly less than the steady flow values by 35% of the wake period. The values then remain essentially constant until they rise at about 60% of the wake period due to the reappearance of the old turbulent flow at the trailing edge. The shape factor is also approximately constant and equal to the steady state value during this period. **Figure 6** indicates that the separation bubble is present for about 40% of the wake period. The attached flow downstream of this steady-state bubble is expected to be delineated by two trajectories that travel at about 88% of the freestream velocity. These two lines correspond to the velocity of the leading edges of the patches of turbulent flow that is created in the bubble

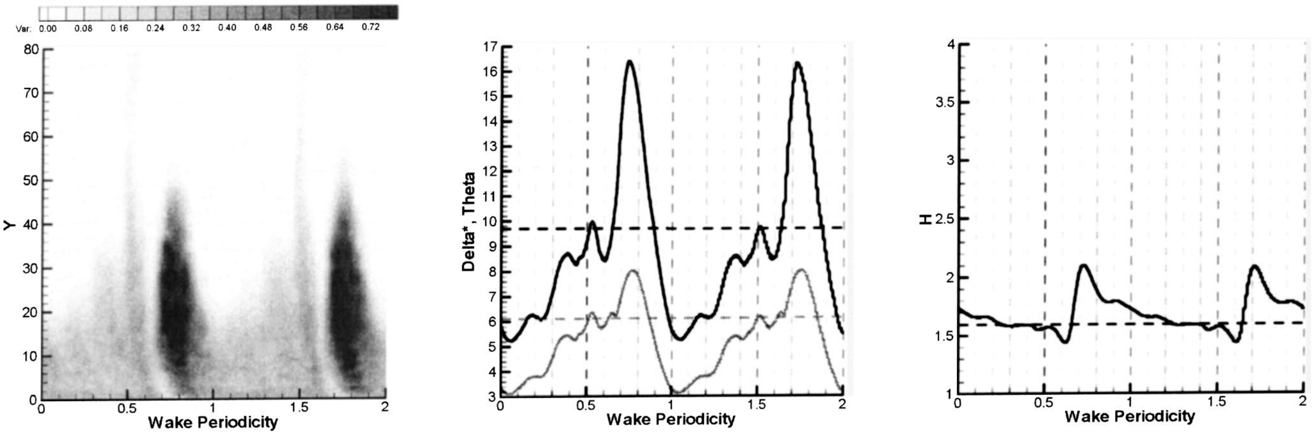

Fig. 9 Hot-wire data at 97.5% of S_{max}. Re=350,000 and $f_{\mathrm{red}}=0.75$—shape 02. Left: variance; center: evolution of displacement thickness (black) and momentum thickness (gray) for two wake periods; right: shape factor.

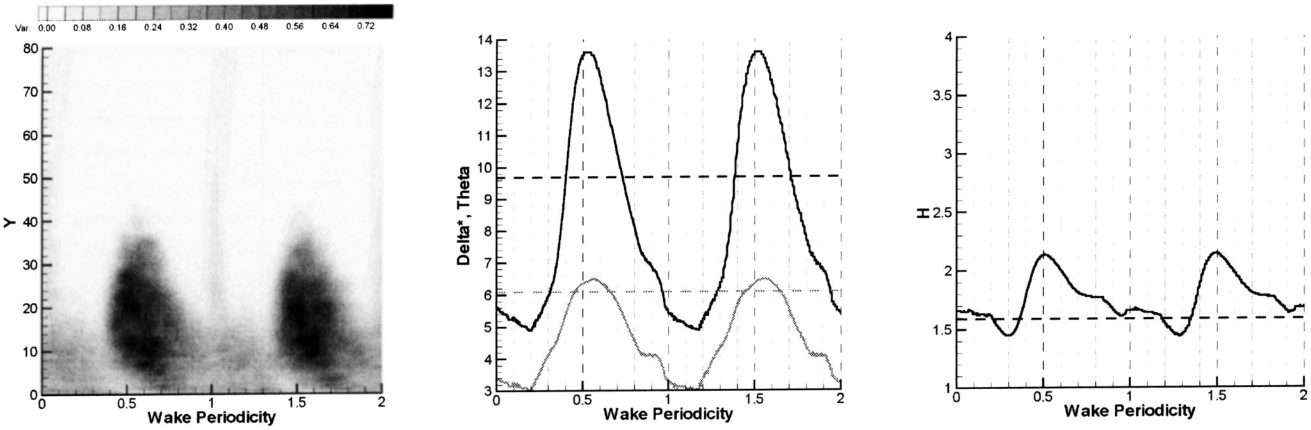

Fig. 10 Hot-wire data at 97.5% of S_{max}. Re=350,000 and f_{red}=1.50—shape 02. Left: variance; center: evolution of displacement thickness (black) and momentum thickness (gray) for two wake periods; right: shape factor.

and that forms due to the wake. The above suggests that separation bubble produces the period of constant integral parameters at the trailing edge. Because the separation and transition are slightly delayed compared to the steady case, δ^* and θ during this period are slightly lower than when the flow is steady.

In the case when $f_{red}=1.5$, **Fig. 7** shows that the leading edge of the next wake-induced turbulent patch arrives at the surface location when the separated flow transition begins to reappear (i.e., near 45% of the chord). As a result, the calmed region maintains its full effect, but the separation bubble is prevented from reappearing. This can be seen in **Fig. 10**, when the minimum valves of δ^* and θ are the same as those in **Fig. 9** and are reached after the same dimensional time has elapsed as in **Fig. 10**. However, no period of essentially constant integral parameters exists.

A steady flow computation was performed to reproduce the characteristics of the old turbulent boundary layer at the trailing edge. Since the bypass transition occurs at approximately 10% of the chord, a numerical trip was placed at this position. Downstream of 10% of the chord, the intermittency was set to 1. Upstream it was set to zero. The case $f_{red}=0.75$ was chosen for comparison of the results. The reason is that, in the case $f_{red}=1.5$, the wake-induced patch catches up with the patch that was created by the previous wake. This can be seen in **Fig. 7**, the line labeled ''0.88'' (leading edge of the patch), translated by one wake-period, intersects the line labeled ''0.50''. (trailing edge of the turbulent patch) at approximately 90% of the chord. This could create some additional blockage in comparison with the case $f_{red}=0.75$, where the boundary layer downstream of the turbulent patch comes from the separation bubble and is less thick. This hypothesis is reinforced by the comparison of the maxima of δ^* and θ in **Fig. 9** and **Fig. 10**. They are smaller in the case $f_{red}=1.5$. This is consistent with an acceleration of the free stream flow due to a blockage effect that is due to merging effects.

At 97.5% of the chord, the maxima of δ^* and θ that were observed at 75% of the wake-period in **Fig. 9** are indeed well predicted by this simulation (see **Fig. 11**). The predicted C_p in the figure shows the blockage due to the thicker boundary layer. It is smaller than the steady flow solution from 60% of the chord. Also, the separation bubble is obviously removed as can be seen in the plots of C_f, H, and C_p. The CFD simulation reinforces the conclusion that the turbulent patch that was induced by the wake at about 10% of the chord propagates towards the trailing edge of the plate. It has the characteristics of a steady turbulent boundary layer starting at 10% of the chord.

Summary—Variation of Loading. The results for shape 02 show that the wakes remove the separation bubble periodically. This is due to the creation of a turbulent patch via the bypass mode of transition at approximately 10% of the plate length. The propagating patch remains attached through the region of the bubble and travels to the end of the plate. It is followed by a strong calming effect that delays the reestablishment of the separation bubble. When the reduced frequency is 0.75, the time between two wakes is sufficiently long that, when the calming zone weakens, the bubble progressively reappears and begins to undergo transition to turbulence. However, the boundary layer does not have time to reach its steady flow state. Furthermore, the separation point is downstream from its steady flow location and the boundary layer parameters at 97.5% of the chord are still smaller than the steady flow values. In case of reduced frequency of 1.5, the separation bubble does not reappear because the wake period is too short.

The momentum thickness is a good indicator of the losses cre-

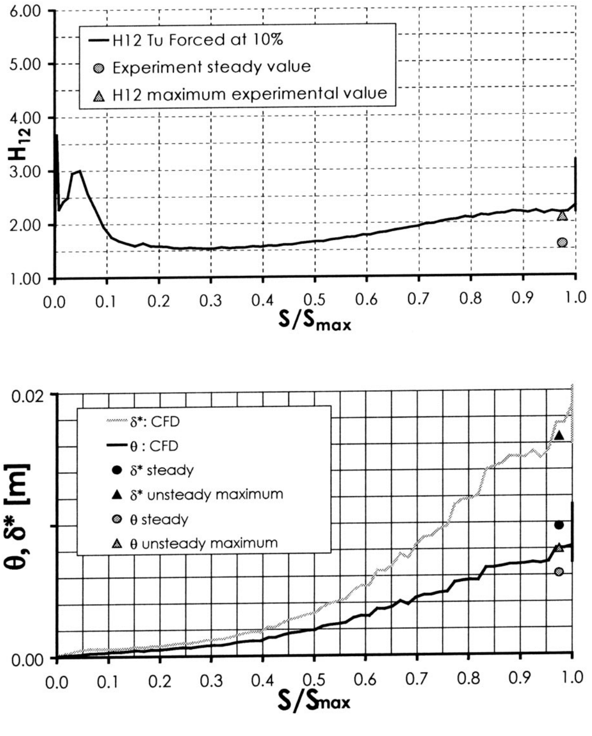

Fig. 11 Measured and predicted flow with forced transition at 10% S_{max}, Re=350,000—shape 02

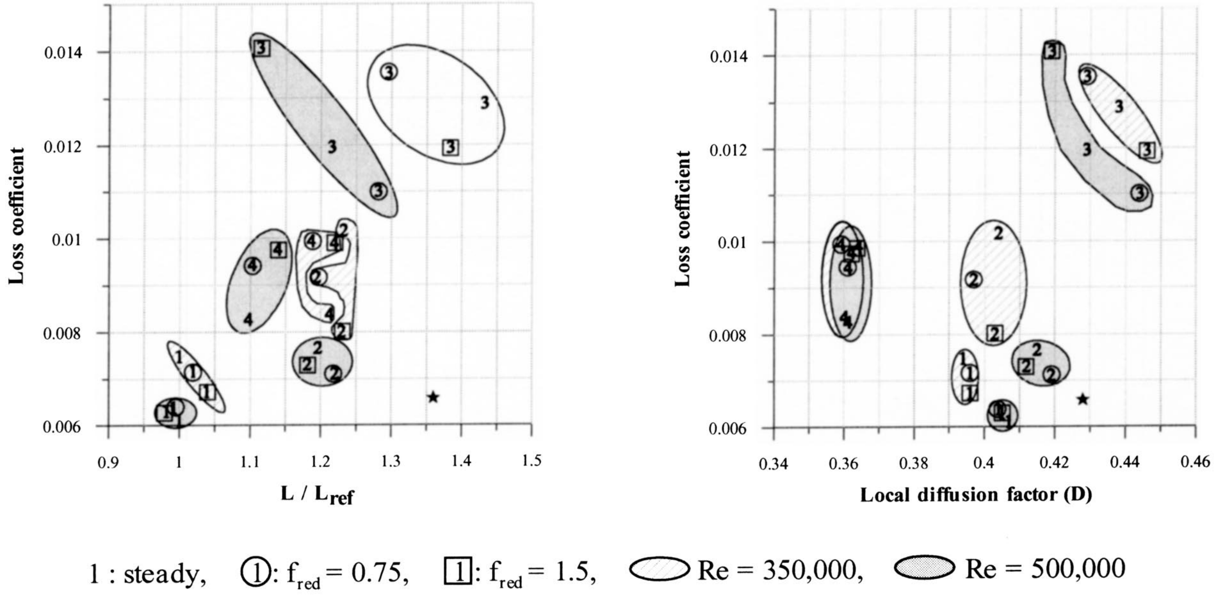

Fig. 12 Summary of the experimental results. Left: results in terms of loss and lift; right: results in terms of loss and local diffusion factor (*D*). 1, 2, 3, 4 for shapes 01, 02, 03, 04, ★ for shape 02 "highly loaded" with Re=350,000 and f_{red}=1.5.

ated by a boundary layer that develops along a blade surface. For a real blade, most of the losses are generated by the suction side (roughly 60%). The results of shape 02 show that the time-averaged momentum thickness at the trailing edge has a lower values than in the steady case, the largest reduction being attained in the case of the higher reduced frequency: a 20% reduction for $f_{red}=1.5$ and a 13.5% reduction for $f_{red}=0.75$. The beneficial effect of the wake unsteadiness has been demonstrated for shape 02.

To compare the profile losses of all the shapes shown in **Fig. 1**, a method based on that introduced by Curtis et al. [19] was used. The loss coefficient is given by

$$\text{Loss} \propto \frac{2\theta/\text{Chord}}{L/L_{\text{ref}}}, \tag{7}$$

where ref stands for shape 01. Shape 01 was chosen as the reference because it has features that are similar to the ones that are used by Rolls Royce for blade design in terms of the accelerating and decelerating parts and the location of the peak suction. The lift of the blade is given by the parameter *L*. It is evaluated using the concept of circulation, where

$$L \propto \oint V \cdot ds. \tag{8}$$

In this study, only the flow over the suction side was measured. The above integral is evaluated by assuming that the velocities over the pressure side would be equal to the velocity at the trailing edge. Since the lift is proportional to the pitch of a bladerow with a given duty, the loss coefficient evaluated in the above manner becomes proportional to that of the equivalent bladerow.

Figure 12 displays the loss as a function of the lift and of the local diffusion factor *D*, for Reynolds numbers of 350,000 and 500,000, for $f_{red}=0.75$ and $f_{red}=1.5$. The cases that were described above are for shape 02, that is indicated on the figure with "2" (steady flow), "2" inside a circle ($f_{red}=0.75$), and "2" inside a square ($f_{red}=1.5$). Compared to the reference case (shape 01), shape 02 has about a 20% increase in lift. It also has an increased loss, although the increase is only slight at the lower Reynolds number.

Shape 02-HL is a high lift version of shape 02. **Figure 1** shows the corresponding velocity distribution. It was tested at a Reynolds number of 350,000 and $f_{red}=1.5$. The data for this test are shown as ★ in **Fig. 12**. It can be seen that shape 02-HL has a value of $V_{max}/V_{outlet}=1.75$, which corresponds to a diffusion factor of almost 0.43. Shape 02-HL has the same level of loss shape 01 and 35% more lift than the reference blade. Shape 02-HL was tested because it was expected that the wake-induced region and the calming region would be more resistant to flow separation because of their elevated levels of shear stress and low shape factor. Studies with Re=500,000 and $f_{red}=0.75$ will be considered in the future. Furthermore, Lieblein's [20] correlation of wake momentum thickness with the diffusion ratio indicates that the wake momentum thickness does not rise rapidly below a local diffusion factor of 0.5. This corresponds to a V_{max}/V_{outlet} of about 1.9. It is suggested that further increases in lift should be sought, with a style similar to that of shape 02-HL.

Aft-loading is an attractive way for delaying the beginning of the wake induced transition and decreasing the wetted surface area exposed to the turbulent boundary layer. Also, the calming effect would be more effective at the trailing edge, inducing low momentum thickness. Shape 04 was tested to investigate this. However, the unsteady flow results present more losses than the steady flow. This is because the location of the wake-induced transition onset did not move downstream as expected. This problem of premature transition was also noticed when varying the Reynolds number. The transition onset did not move downstream with a reduction of Reynolds number. Therefore, the wake-induced turbulent patch at the end of the plate has the characteristics of a turbulent boundary layer that was generated just after the leading edge and that has been subjected to the pressure gradients that exists over the plate. In this case, the acceleration to the suction peak is less than in the case of shape 02, so the momentum thickness is higher than on shape 02 before the deceleration begins after the suction peak. The deceleration is also slightly stronger than shape 02 and this makes the momentum thickness of the patch increase more rapidly and ultimately reach higher values.

To remedy the above problem, the leading edge could be modified again so that the diffusion of velocity that is noticeable on **Fig. 1** is reduced and does not induce a transition onset at around

10% chord when the wake passes. Alternatively, this feature could be used to lock the onset location, which would allow the designer to generate a significantly larger calming effect.

Figure 12 shows that although shape 02-HL and shape 03 have similar local diffusion factors, shape 02-HL and shape 03 produce different losses for $\mathrm{Re}=350{,}000$ and $f_{\mathrm{red}}=1.5$. In the case of shape 03, the losses of the steady flow case are smaller at the higher Reynolds number. As for the other configurations, this is because the separation bubble is smaller and reattaches earlier at the higher Reynolds number. The variation of the lift and the local diffusion factor with the reduced frequency arises due to changes in the mean blockage that occurs as the separation bubble is modified by the wakes.

The general effects of the reduced frequency and the Reynolds number on the losses of shape 03 are similar to those for the other shapes. For example, in case of $\mathrm{Re}=350{,}000$, the higher reduced frequency yields the smaller loss, whereas the opposite is generally true for Re 500,000. In some cases, both unsteady test cases present the lowest losses. In others, this is not so. High losses are generated by the old turbulent boundary layer. The new turbulent boundary layer that develops from the separation bubble, when present between the wakes, produces less loss. The flow that develops from the calmed region produces even lower losses. The dominance of these flow features determines whether the effects of the wakes are beneficial.

In the present experiment, the results have been obtained using only one value of the free stream turbulence intensity (1.2%). This is slightly lower than the values in a turbojet engine. This was chosen in order to highlight and identify the different processes involved in wake-induced transition. Future work should study the influence of higher values of the freestream turbulence intensity.

Conclusions

This project was aimed at developing an understanding of how to design the suction side of an axial compressor blade including the effects of unsteadiness induced by passing wakes. The problem was approached using a flat plate with different imposed pressure distributions and a rig with incoming wakes simulated by moving bars. The Unnewt-Puim CFD tool has produced helpful results in steady simulations. Unsteady simulations using this program are under way.

The results have shown that the incoming wakes have a large influence on the loss. The separation bubble caused by the diffusion after the throat is intermittently suppressed by the wake-induced turbulent region and delayed by the following calmed region. These two regions are more resistant to flow separation because of their elevated levels of shear stress and low shape factor.

When wake-induced transition starts at the early part of the surface, the boundary layer in the wake-induced path soon becomes fully turbulent. This boundary layer is then affected by the pressure gradient as it develops. At the trailing edge, the shear stress associated with this so-called ‘‘old-turbulent’’ boundary layer has relatively low values. High losses are generated within this developing old turbulent boundary layer. The ‘‘new turbulent’’ boundary layer that develops from the separation bubble between the wakes produces less loss. The flow that develops from the calmed region produces even lower losses. The balance between these losses determined whether the effects of the wakes were beneficial.

Because the old turbulent boundary layer will produce the highest part of the losses and has the lowest shape factor, the common approach used in design of assuming that the suction side boundary layer is (almost) fully turbulent remains useful.

Aft-loading needs to be investigated further in order to delay the creation and reduce the losses of that ‘‘old’’ turbulence. In particular, the transition onset location is very influential. It is strongly affected by the shape of the leading edge. This might explain why current industrial practice does not favor aft-loading. Another alternative is to increase the loading. For the configuration that has been presented, this produced excellent performance in terms of ratio lift/loss. This presents a good perspective for future work including further validation of the CFD tool that has been introduced.

Acknowledgments

The authors wish to thank the EPSRC and Rolls-Royce plc for their support.

Nomenclature

Symbols

V = flow velocity
D = ‘‘local’’ diffusion factor$=(V_{\max}-V_{\mathrm{outlet}})/V_{\max}$
Re = Reynolds number based on inlet velocity and plate chord
U_{bar} = bars velocity
s = surface length
t = time
S_{bar} = distance between 2 bars
f_{red} = reduced frequency$=U_{\mathrm{bar}}/S_{\mathrm{bar}}^{*}$Chord$/V_{\mathrm{inlet}}$
u' = turbulent axial velocity fluctuation
Tu = turbulence intensity based on u′ and $V_{x,\mathrm{inlet}}$
C_p = pressure coefficient$=(P_{\mathrm{inlet}}-P_{\mathrm{static}})/(P_{\mathrm{inlet}}-P_{\mathrm{total}})$
τ_w = quasi-shear stress, defined in the text
σ = variance, defined in the text

Subscripts

Inlet = upstream of the leading edge of the flat plate
Outlet = at the trailing edge of the plate
Max = maximum reached along the plate
x = axial component
w = to note a measurement at the wall, i.e., on the plate
i = to identify an ensemble of data
0 = for zero flow condition

Superscripts

$\sim$ = ensemble averaged

References

[1] Schulte, V., and Hodson, H. P., 1998, ‘‘Prediction of the Becalmed Region for LP Turbine Profile Design,’’ ASME J. Turbomach., **120**, pp. 839–845.
[2] Howell, R. J., Hodson, H. P., Schulte, V., Schiffer, H.-P., Haselbach, F., and Harvey, N. W., 2001, ‘‘Boundary Layer Development in the BR710 and BR715 LP Turbines—The Implementation of High Lift and Ultra High Lift Concepts,’’ ASME Paper 2001-GT-0441.
[3] Halstead, D. E., Wisler, D. C., Okiishi, T. H., Walker, G. J., Hodson, H. P., and Shin, H., 1995, ‘‘Boundary Layer Development in Axial Compressors and Turbines Part 1 of 4: Composite Picture,’’ ASME Paper 95-GT-461.
[4] Schulte, V., and Hodson, H. P., 1996, ‘‘Unsteady Wake-Induced Boundary Layer Transition in High Lift LP Turbines,’’ ASME Paper 96-GT-486.
[5] Howell, R. J., 1999, ‘‘Wake—Separation Bubble Interactions in Low Reynolds Number Turbomachinery,’’ Ph.D. dissertation, Cambridge University, Cambridge, UK.
[6] Hodson, H. P., Huntsman, I., and Steele, A. B., 1994, ‘‘An Investigation of Boundary Layer Development in a Multistage LP Turbine,’’ ASME J. Turbomach., **116**, pp. 375–383.
[7] Mayle, R. E., 1991, ‘‘The Role of Laminar-Turbulent Transition in Gas Turbine Engines,’’ ASME Paper 91-GT-261.
[8] Emmons, H. W., 1951, ‘‘The Laminar-Turbulent Transition in a Boundary Layer—Part 1,’’ J. Aerosp. Sci., **18**(7), pp. 490–498.
[9] Narasimha, R., 1957, ‘‘On the Distribution of Intermittency in the Transition Region of a Boundary Layer,’’ J. Aerosp. Sci., **24**, pp. 711–712.
[10] Ramesh, O. N., and Hodson, H. P., 1999, ‘‘A New Intermittency Model Incorporating the Calming Effect,’’ 3rd European Conference on Turbomachinery Fluid Dynamics and Thermodynamics, IMechE, London.
[11] Schubauer, G. B., and Klebanoff, P. S., 1956, ‘‘Contributions on the Mechanics of Boundary-Layer Transition,’’ NACA Report 1289.
[12] Gostelow, J. P., Walker, G. J., Solomon, W. J., Hong, G., and Melwani, N., 1996, ‘‘Investigation of the Calmed Region Behind a Turbulent Spot,’’ ASME Paper 96-GT-489.
[13] Gostelow, J. P., Blunden, A. R., and Walker, G. J., 1992, ‘‘Effects of Free-Stream Turbulence and Adverse Pressure Gradients on Boundary Layer Transition,’’ ASME J. Turbomach., **116**, pp. 392–404.

[14] Hodson, H. P., and Dawes, W. N., 1996, ''On the Interpretation of Measured Profile Losses in Unsteady Wake—Turbine Blade Interation Studies,'' ASME Paper 96-GT-494.

[15] Dawes, W. N., 1992, ''Simulation of Three-Dimensional Viscous Flow in Turbomachinery Geometries Using a Solution-Adaptive Unstructured Mesh Methodology,'' ASME J. Turbomach., **114**, pp. 528–537.

[16] Yang, Z., and Shih, T. H., 1993, ''A Galilean and Tensorial Invariant k-ε Model for Near Wall Turbulence,'' AIAA Paper 93-3105.

[17] Durbin, P. A., 1996, ''On the k-ε Stagnation Point Anomaly,'' Int. J. Heat Fluid Flow, **17**, pp. 89–90.

[18] Cumpsty, N. A., Dong, Y., and Li, Y. S., 1995, ''Compressor Blade Boundary Layers in the Presence of Wakes,'' ASME Paper 95-GT-433.

[19] Curtis, E. M., Hodson, H. P., Banieghbal, M. R., Denton, J. D., Howell, R. J., and Harvey, N. W., 1996, ''Development of Blade Profiles for Low Pressure Turbine Applications,'' ASME Paper 96-GT-358.

[20] Lieblein, S., 1959, ''Loss and Staff Analysis Compressor Cascades,'' ASME J. Basic Eng., **81**, pp. 387–400.

Dennis E. Culley
Michelle M. Bright
NASA Glenn Research Center,
21000 Brookpark Road,
Cleveland, OH 44135

Patricia S. Prahst
AP Solutions, Inc.

Anthony J. Strazisar
NASA Glenn Research Center,
21000 Brookpark Road,
Cleveland, OH 44135

Active Flow Separation Control of a Stator Vane Using Embedded Injection in a Multistage Compressor Experiment

Active flow control has been applied to the suction surface of stator vanes in a low speed axial compressor. Injection from the suction surface has been shown to reduce separation on vanes that were induced to separate by increasing the vane stagger angle by 3° deg. Various configurations were investigated including injector geometry (slots versus holes) and type of injection (steady versus unsteady). Unsteady injection was realized using two different approaches; external actuation through a high frequency valve and embedded actuation using a fluidic device internal to the vane. Using total pressure loss through the vane passage as a metric, reductions in area-averaged loss of 25% were achieved using injected mass flow rates on the order of 1% of compressor throughflow. The development of a tracking control algorithm was also explored for the purpose of closed-loop control. A reliable method of detecting surface separation was implemented using unsteady pressure measurements on the compressor casing near the vane suction surface.
[DOI: 10.1115/1.1643912]

Introduction

In recent external flow control applications, unsteady injection has been shown to generate large eddy structures that greatly enhance mixing between the boundary layer and fluid from the freestream, [1]. Siefert et al. [2] found that for a given level of mixing the injected mass flow could be reduced by an order of magnitude by using unsteady injection rather than steady injection. In a separation control application McManus et al. [3] was able to achieve a 20:1 reduction by using unsteady injection. Amitay and Glezer [4] showed that pulse-width modulated injection was even more efficient at conserving mass flow than sinusoidal injection at a given frequency.

Based on the proven success of flow control in external flows, several research groups have recently begun to investigate the application of aerodynamic flow control to turbomachinery blading. Carter et al. [5] investigated the use of an ejector pump approach to simultaneously apply suction and injection to the suction surface of a cascade blade that was separated under nominal flow conditions. They achieved a 65% reduction in total pressure loss and a 4.5 deg increase in turning when injecting 1.6% of the freestream flow rate. Successful application of the same approach to a subsonic turbine cascade blade experiencing suction side separation at low Reynolds number has also been reported, [6]. Bons et al. [7,8] reported on the application of skewed vortex generator jets to a low-pressure turbine cascade blade to prevent separation at low Reynolds number. They found that pulsed injection with duty cycles as low as 10% was just as effective as harmonic pulsing (duty cycle of 50%) while providing a large reduction in the time-average injected mass flow. This result is similar to that found in an external flow control application, [4].

The long-term objective of our research is to develop and demonstrate flow control methods that utilize air injection in high-speed compressors for control of flow separation within stators. Successful separation control may enable improved performance in two ways: (i) by increasing the range of incidence angles over which total pressure loss is acceptable and (ii) by increasing the loading level at which an acceptable level of loss occurs. The tangible benefits may be an increase in operability and an increase in stator aerodynamic loading, which can lead to reduced engine weight and parts count through lower solidity.

The focus of the present effort is the development of stator vane separation control methods using a low speed compressor. For durability and ease of maintenance it is desired that there be no moving parts within the vane. Since injected air must be bled from the aft stages of the compressor, we desire to minimize the amount of injection required. We therefore explore two approaches to reducing the required mass flow: (i) biased oscillatory injection and (ii) active control of injection (to provide injection only when the vane separates). Biased oscillatory injection, with a nonzero time-average mass flow, is implemented using a motor-driven siren valve mounted in an injection supply line external to the stator vane. An alternative actuation approach is also assessed in which biased oscillatory injection is generated with a fluidic actuator embedded within the vane. While this approach requires a more complicated vane fabrication process, it eliminates the need for an external actuator and achieves unsteady injection with no moving parts, which may be more attractive for implementation on a production compressor.

Finally, the development of an algorithm for use in autonomous control of separation via injection is discussed. Active separation control requires a method of sensing the onset of separation. Results are presented that demonstrate separation sensing using time-averaged vane surface pressure measurements and a second method using time-resolved casing static pressure measurements.

Experimental Setup

A description of the experiment hardware follows in the next three sections. Part 1 describes the existing compressor facility which is used to perform the experiments in this paper. Part 2 describes the flow delivery system which is unique to this investigation. The flow delivery system augments the compressor rig and its hardware and resides wholly outside of the flow field. Components of the control system are also primarily associated

---

Contributed by the International Gas Turbine Institute and presented at the International Gas Turbine and Aeroengine Congress and Exhibition, Atlanta, GA, June 16–19, 2003. Manuscript received by the IGTI December 2002; final revision March 2003. Paper No. 2003-GT-38863. Review Chair: H. R. Simmons.

with this hardware and are described here. Part 3 describes the internal component of the injection system, namely the flow control vane.

Research Compressor. The NASA Glenn Low Speed Axial Compressor (LSAC) facility is used for this study. Air enters the facility through a filtered roof vent, is conditioned for temperature and turbulence, and then passes through a calibrated bellmouth and into the research compressor. Airflow exiting the compressor is controlled by a throttle valve, close-coupled to the collector, and discharged into either an atmospheric or altitude exhaust system. A 1500 hp variable speed motor drives the compressor rotor.

The compressor consists of an inlet guide vane and four identical stages designed for accurate low-speed simulation of the rear stages of a high-speed core compressor. A long entrance duct is used to develop thick endwall boundary layers typical of an embedded stage. The first two stages are used to setup a ''repeating stage'' environment. The third stage is the focus of research measurements, while the fourth stage acts as a buffer to the exit conditions. The flow path has an outer diameter of 1.219 m and a hub-tip radius ratio of 0.80. All stators have inner shrouds with a single labyrinth seal-tooth in the shrouded stator cavity. The nominal rotor tip and stator seal clearances are 1.4% and 0.6% of span, respectively. Rotor tip speed is 61 m/sec and nominal axial velocity is on the order of 25 m/sec. The increased size and low speed of this facility enables intrastage surveys of the flow field thus making possible an increased understanding of the complex flow phenomena within multi-stage axial compressors. A complete description of the LSAC facility is given by Wasserbauer [9].

The blading used for the current tests is based on the Rotor B/Stator B blading designed by General Electric for the NASA Energy Efficient Engine program. Details of the original designs are reported by Wisler [10]. The stators are designed by applying modified 65-series thickness distributions to modified circular-arc meanlines. The NASA stators are slightly modified from the GE design to accommodate a difference in hub-tip radius ratio between the GE and NASA low speed compressor facilities. The NASA stator features a solidity of 1.38, an aspect ratio of 1.32, a stagger angle of 42 deg and a camber of 40.5 deg. The stator chord is 9.4 cm. Stators are sealed at both the hub and tip junctions with the flow path.

Overall performance is expressed in terms of the average pressure rise coefficient, ψ, and flow coefficient, ϕ. The average pressure rise coefficient is determined from inlet and outlet static pressure measurements on the hub and casing. The flow coefficient is defined as the measured mean inlet velocity normalized by the rotor tip speed. The mean inlet velocity is determined from static pressure measurements at the exit of the inlet bellmouth using a previously determined discharge coefficient, and is corrected for humidity. Vane element performance is calculated from total pressure measurements acquired with miniature (1.64 mm) Kiel head probes and static pressure and flow angle measurements acquired with 18 deg wedge probes. All pressure measurements are acquired at midgap of the rotor-stator spacing (the spacing is approximately 35% of axial chord) and are referenced to stagnation conditions measured in the inlet plenum of the facility. The following measurement accuracies are reported by Wellborn [11]: $\Delta\psi = 1.09\%$, $\Delta\phi = 0.39\%$, $\Delta\omega = 2.1\%$.

To reduce the time and expense of exploring several different flow control configurations, all tests are performed under a removable window in the casing over stage three. Two flow control vanes are mounted under the window, with penetrations to the exterior of the casing, which allow for connection to the source of injection air. An experiment reconfiguration is thus achieved without removing the casing by simply disconnecting the air source and removing the window and flow control vanes as a unit.

The flow over the LSAC stator vanes is not prone to strong separation prior to compressor stall. Therefore, the two flow control vanes are installed at a stagger angle increase of approximately 3 deg from nominal to induce early flow separation. Surface pressure measurements acquired from a pair of instrumented stator vanes indicate that at this 3 deg re-stagger the vanes are not separated under open-throttle conditions but suffer a severe separation at lower flow coefficients. All other vanes are installed at the nominal design stagger. The vane restagger is determined from changes in the circumferential position of the vane trailing edge as the vane is rotated about the trunion axis and is accurate to +/−1 deg.

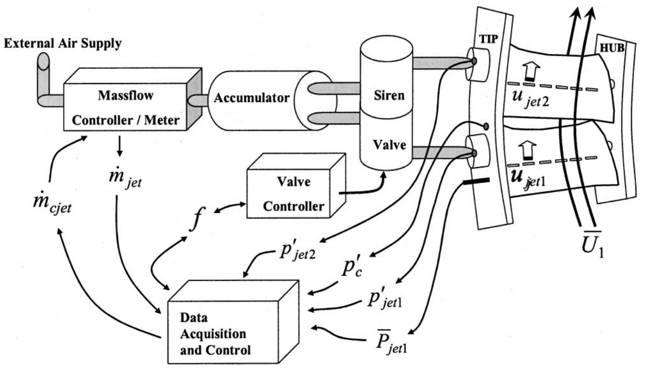

Fig. 1 Schematic of the flow control actuation system

The Flow Delivery System. **Figure 1** is a schematic representation of the overall flow control system including the flow control vanes. Discussion in this section is limited to the details of flow delivery outside of the compressor and the sensing and actuation associated with open or closed-loop control. The various vane configurations tested are described in the next section.

The source of injection fluid in all cases is from a filtered shop air line available in the facility. A remotely operated control valve enables the precise metering of the injected mass flow rate. The flow rate is measured with a mass flow meter to an accuracy of +/−1% full scale. The meter is isolated by a large (volume =5500 cc) accumulator at its output. The accumulator filters out rapid fluctuations in the flow, present during cases of unsteady injection, which will interfere with the accuracy of the flow meter. The accumulator also serves as a stable pressure source for the downstream components of the flow system. There are two independent flow paths from the accumulator to the flow control vanes. Since care is taken to maintain symmetry in the tubing, intermediate fittings, and any other devices inserted between the accumulator and the vanes, an equal distribution of flow to each vane is assumed.

The vane configuration under test determines the exact configuration of the flow delivery system. When externally modulated flow is required a valve is inserted immediately upstream of the flow control vane. This valve, hereafter referred to as the ''siren valve,'' is a high-speed motor-driven device which houses two independent flow modulators on a single spool. Steady flow is supplied to the valve from the accumulator through a 1.7 m length of 0.95 cm inner diameter hard nylon tubing. The flow control vane is connected to the valve output using a 35 cm length of 0.95 cm inner diameter stainless tubing.

When the delivery system is required to provide a constant, steady flow to the flow control vane the same 1.7 meter length of tubing described above connects each vane directly to the accumulator. Note that the embedded-fluidic-vane, described later, also uses this configuration even though the injected flow is actually unsteady.

Also shown in **Fig. 1** are the sensing and control parameters used in open and closed-loop tests. At the tip end of each flow control vane a high frequency piezo-electric pressure transducer is used to measure time-resolved delivery system dynamics. These signals are labeled p'_{jet1} and p'_{jet2}. In some configurations a 1 mm diameter tube is inserted into the internal flow control vane cavity to measure the time averaged total pressure, $\overline{P}_{\text{jet}}$, of the injected flow. Another high frequency piezo-electric pressure signal, p_c', originates in the casing over the stator vane to track fluid disturbances related to vane separation dynamics. The injected mass flow is both a measured value, $\dot{m}_{\text{jet}}$, as well as a controlled parameter, $\dot{m}_{c\text{jet}}$. Finally, the speed of the valve and therefore the injection frequency, f, is controlled. All of these signals are tied to a high bandwidth data acquisition and control system.

Flow Control Vane Design. The last component of the experimental setup is the flow control vane. Several different injection configurations are examined in this investigation. The features of each vane are discussed here in detail.

The shape of the flow control vane is identical (within the tolerance limits of the fabrication process) to that of the standard LSAC vanes. However, injection through the vane surface requires the fabrication of flow passages within the narrow geometry of the vane. This is accomplished using a rapid prototyping process that enables the fabrication of parts with internal passages directly from a solid model CAD design file. The flow control vanes used in the present work are fabricated by a laser-sintering machine that uses powdered polyamide. There are limitations to the process that prevent the precise replication of feature sizes smaller than 0.375 mm. Absolute accuracy of the part geometry is also not assured. However, careful location of the parts to be grown within the laser-sintering machine minimizes these issues and enhances the surface finish and part strength. To further improve the surface finish of the flow control vanes, several coats of primer are applied before installation into the LSAC, yielding a surface finish that is comparable to that of the standard composite glass fiber LSAC vanes. The rapid prototype flow control vanes have been demonstrated to be entirely capable of surviving within the low speed compressor environment.

The optimum injection location on the suction surface for this investigation is 35% of chord. This location was previously determined in a wind tunnel study of separation location performed by the Illinois Institute of Technology using a custom-designed NACA airfoil whose suction surface pressure distribution closely matched that of the standard LSAC stator vane. In all vane configurations the injection angle is pitched at 30 deg relative to the vane surface to impart streamwise momentum to the flow. Three different flow control vanes with injection at this nominal chord location and injection angle are investigated and are shown schematically in **Fig. 2.**

The first vane design is referred to as the slot-vane and is shown in **Fig. 2(*a*).** This design uses a spanwise slot divided into six segments separated by support webs in order to maintain structural rigidity of the vane skin. The slot width and vane skin thickness are each 0.63 mm (0.7% of chord). The spanwise coverage is from approximately 10 to 90% of span and is constrained by the vane cavity design. This vane produces steady injection or unsteady injection when coupled with the external siren valve.

The second design is referred to as the embedded-fluidic-vane and is shown in **Fig. 2(*b*).** This design features three micro-fluidic devices embedded within pockets fabricated on the pressure side of the vane. Each device operates in a bi-stable mode that alternately switches flow entering from the vane trunion to two plenums at the device exit. Each output plenum covers 20% of span and the two plenums are separated by 4% of chord in the streamwise direction. Since each plenum is fed from a narrow output port on the fluidic device, the flow exiting the device must be spread along the length of the plenum before exiting the blade. A row of holes is therefore used in the blade skin over the plenums in lieu of a slot because the higher pressure loss across the holes improves the spanwise uniformity of flow within the plenum. The holes are 0.73 mm in diameter and are separated by 2.3 mm in the spanwise direction. The actuation frequency of each device is fixed at a nominal 2100 Hz. Phase differences between the three embedded-fluidic devices cannot be controlled and steady injection is not possible with this vane.

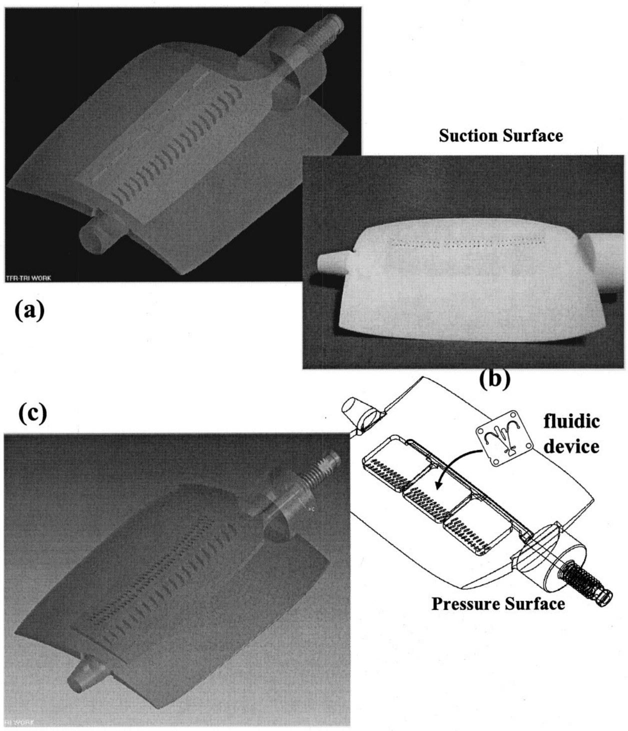

Fig. 2 Flow control vanes. (*a*) Slot-vane; (*b*) embedded-fluidic-vane; (*c*) hole-vane.

The final vane design is referred to as the hole-vane and is shown in **Fig. 2(*c*).** This vane is a hybrid of the first two configurations and is designed to resolve differences in actuation technology and injection geometry between the first two vane styles. Internally, the same cavity design is employed as in the first vane. Externally, the same injection hole array is used as found on the second vane but with hole diameters of 0.55 mm. This vane can produce steady injection or unsteady injection when used with the siren valve.

Nishri and Wygnanski [12] suggest that the most effective forcing frequency for flow control is $F^{+}=fL/\overline{U}_1\approx 1$, where L is the distance between the injection location and the vane trailing edge. The siren valve, which operates over a frequency range of 200–900 Hz ($0.37<F^{+}<1.68$), is used with the first and third vanes to explore this regime of forcing frequencies. The fluidic device is evaluated for several reasons. First, the higher physical frequencies it produces are necessary to achieve an $F^{+}\approx 1$ in future high-speed flow applications. Second, it generates F^{+} values on the order of 3.50 in this application. Investigation of higher frequency excitation is of interest because Amitay et al. [1] showed that excitation at higher frequency produced smaller scale structures in the interaction between the injection jet and mean flow, resulting in lower amplitude lift fluctuations compared to forcing at $F^{+}\approx 1$, thus reducing the structural forces on the airfoil. Third, the fluidic actuator has no moving parts. Finally, since it generates an unsteady flow at the vane surface, its performance is not dependent on the resonance characteristics of the delivery system and vane cavity. As discussed in the Results Section, this is not the case for the siren valve.

Each flow control vane type is calibrated in still air using a hotwire anemometer to measure the exit velocity from the slot or hole at several locations along the span. The calibration establishes the spanwise uniformity of the injected flow and the relative magnitudes of the fluctuating (u_{HW}') and time mean ($\overline{U}_{HW}$) components of the injected flow. When the vane is installed in the LSAC a desired bulk injection velocity, $\overline{U}_{\text{jet}}$, is set using the

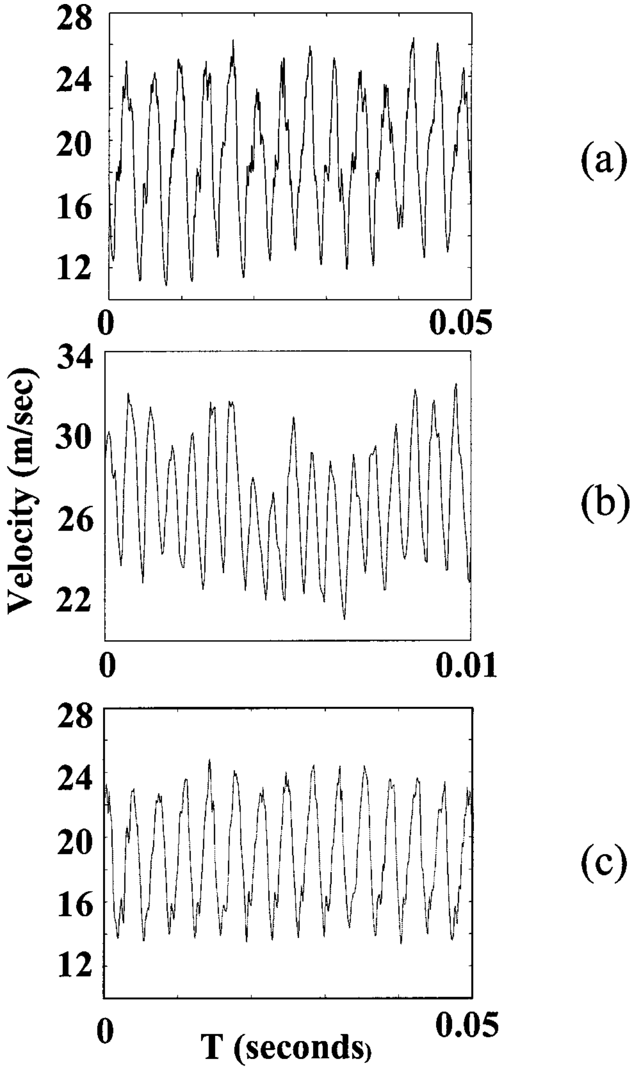

Fig. 3 Comparison of unsteady output generated by the three flow control vanes. (*a*) Slot-vane driven by siren valve; $C\mu = 0.012$ at $F^+ = 0.52$; (*b*) embedded-fluidic-vane; $C\mu = 0.014$ at $F^+ = 3.36$; and (*c*) hole-vane driven by siren valve; $C\mu = 0.011$ at $F^+ = 0.52$.

measured injected mass flow and the total area of the slots or holes. The hot wire measurements are then used to estimate the fluctuating component of the injected flow,

$$u'_{\mathrm{jet}} = \overline{U}_{\mathrm{jet}}(u'_{HW}/\overline{U}_{HW}).$$

Examples of the injected velocity waveform measured with a hotwire anemometer during vane calibration are shown in **Fig. 3** for each type of vane at an injection velocity ratio of $UR \approx 0.75$. The hotwire was located 6 mm (6% chord) downstream of the holes and slots, which corresponds to 8–10 hole diameters. The normal distance between the hotwire and the vane surface corresponded to the location of peak velocity in the injection wall jet, approximately 1 mm from the vane surface. The injection produced from the slot-vane and the hole-vane using the siren valve at 280 Hz ($F^+ = 0.52$) is shown in **Figs. 3(*a*)** and **3(*c*),** respectively. The output is an oscillatory jet with a non-zero mean flow. The output of the embedded-fluidic device is shown in **Fig. 3(*b*),** unfortunately at this level of injection the device is operating below its design point. The predominant frequency is about 1800 Hz ($F^+ = 3.33$) with evidence of some lower frequency components. At higher levels of injection there is an upward shift in the fundamental frequency to 2100 Hz ($F^+ = 3.89$) and little evidence of lower frequency components. By design the fluidic device is expected to fully modulate the injected flow with an 180 deg phase difference between the two output plenums. Additional hotwire measurements acquired closer to the injection holes verify that the instantaneous minimum flow never reaches zero, indicating that the output plenum under the vane skin does not empty in the time it takes the device to switch. The fluidic device therefore produces a harmonic oscillation that is quite similar in character to that produced by the siren valve coupled to the slot-vane and hole-vane.

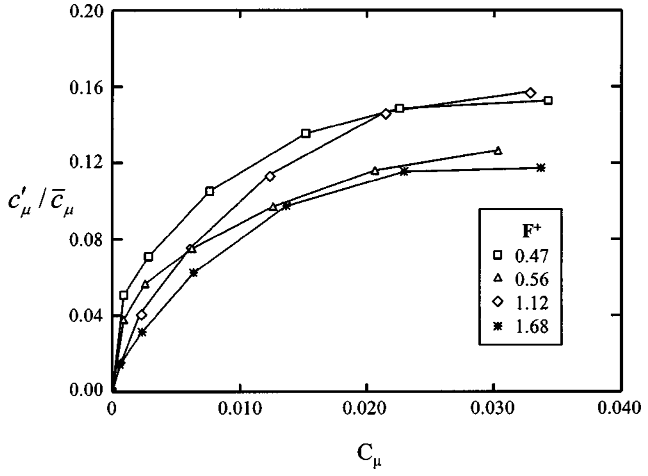

Fig. 4 Injection characteristics of the slot-vane as a function of total momentum

The injected velocity is characterized by its mean and fluctuating components,

$$u_{\mathrm{jet}}(t) = \overline{U}_{\mathrm{jet}} + u'_{\mathrm{jet}},$$

where $\overline{U}_{\mathrm{jet}}$ is the mean velocity and u'_{jet} is the harmonic oscillation imparted by the actuator. Following Nishri and Wygnanski [12], the strength of the injected flow is characterized by a momentum coefficient,

$$C_\mu = \overline{c_\mu} + c'_\mu,$$

where $\overline{c_\mu}$ is the momentum coefficient formed from the mean injected velocity and c'_μ is the momentum coefficient formed from the RMS of the harmonic oscillation. Nishri and Wygnanski performed flow control along the entire span of an airfoil and defined $\overline{c_\mu}$ as

$$\overline{c_\mu} = \frac{2h}{L}\left(\frac{\overline{U_{\mathrm{jet}}^2}}{\overline{U_1^2}}\right),$$

where h is the width of the injection slot. In the present work the injection does not cover the entire span of the vane, and both holes and slots are used. We therefore define a momentum coefficient using the area of injection, A_{jet}, and the airfoil span, s

$$\overline{c_\mu} = \frac{2A_{\mathrm{jet}}}{sL}\left(\frac{\overline{U_{\mathrm{jet}}^2}}{\overline{U_1^2}}\right).$$

The ratio of unsteady (c'_μ) to time-mean momentum ($\overline{c_\mu}$) developed by the jet is plotted against the total momentum (C_μ) in **Fig. 4** for the slot-vane and **Fig. 5** for the two vane styles with holes. The results indicate substantially lower levels of unsteadiness than that used in the external flow control applications mentioned in the introduction. Note that for a synthetic jet, which produces harmonic oscillations with zero mean velocity, c'_μ is

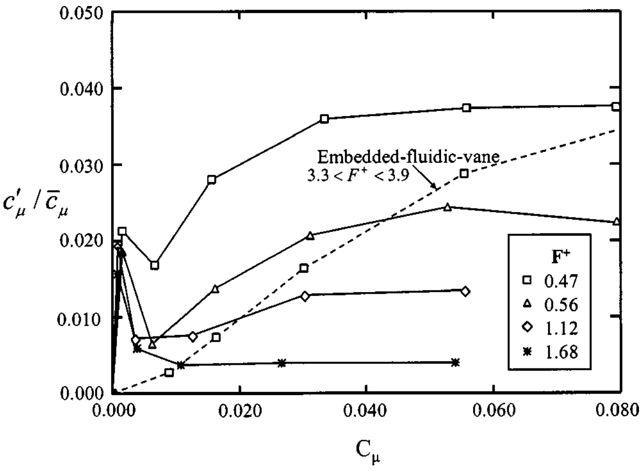

Fig. 5 Injection characteristics of the hole-vane and embedded-fluidic-vane as a function of total momentum for selected test frequencies as a function of total momentum

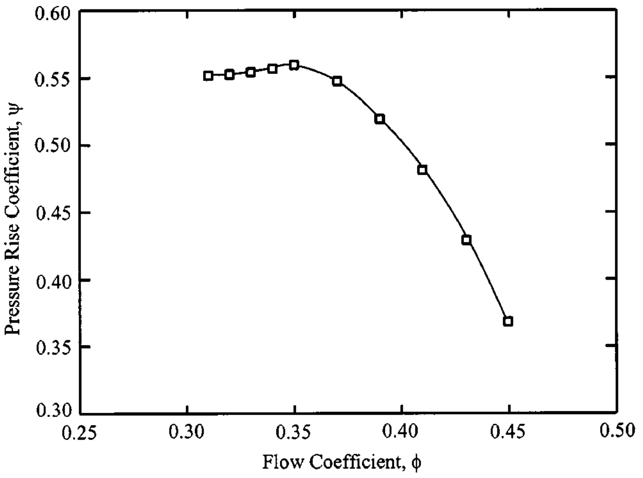

Fig. 6 Overall performance at design speed of the low speed axial compressor rig

100% of C_μ. Unsteady momentum generated by the slot-vane is 12–18% of the time-mean momentum while the unsteady momentum generated by the two hole-vane styles is a maximum of only 4% of the time-mean momentum. The lower unsteady momentum in the vanes with holes may be a result of increased impedance developed by the smaller area of the holes relative to the larger slot area.

The variation in unsteady momentum delivered by the siren valve and slot-vane at various forcing frequencies is a function of the delivery system dynamics and will be discussed in the Results Section. The unsteady momentum generated in the hole-vane by the siren valve decays rapidly in amplitude as frequency is increased, making this actuator/vane combination unsuitable for application in higher speed flows where higher frequencies are required to attain $F^+ \approx 1$. The fluidic device generates low amplitude unsteady momentum at low flow rates because it is not effectively switching flow between its output plenums. As the flow rate increases the internal feedback becomes more effective, generating higher unsteady oscillations. Since the device operates at the higher physical frequencies required for high-speed flow control applications, it holds some promise for use in such applications if the unsteady momentum level can be increased.

Results

All results reported herein are obtained at design speed. For reference, the overall performance curve for this condition is shown in **Fig. 6.** The investigation primarily centers on a flow coefficient of 0.36, which is sufficiently far away from stall yet produces well separated flows across the restaggered flow control vanes.

The effect of vane surface separation is a significant widening and deepening of the vane wake. Circumferential surveys of the downstream total pressure distribution across the vane pitch are used as an indicator of the degree of this separation. **Figure 7** depicts a family of these total pressure profiles for the restaggered slot-vane, at 56% span, using steady injection ($c'_\mu = 0$) over a range of injection momentum coefficients, C_μ. Also shown in the figure is the total pressure profile for the same vane with no injection at nominal stagger. A comparison of the zero injection profiles at both stagger conditions clearly indicates that 3 deg restagger produces a separated flow on the vane suction surface. The investigation uses the zero injection wake profile of the flow control vane under test at restagger as the baseline condition for comparison.

At momentum coefficients $C_\mu < 0.006$ the wake momentum deficit grows relative to the baseline wake because the injected fluid does not carry enough momentum to energize the separation region on the vane suction surface. As the injection is increased a break-even point is reached, and further injection increases energize the separated region and result in wake size reduction. The response of the wake to injection shown in **Fig. 7** is typical for vanes with hole or slot injection geometries. Although the momentum coefficient is the proper measure of injection strength the amount of bleed required to achieve a given C_μ is also of interest since it can impact stage matching. This is shown in **Table 1.**

The benefit to vane performance due to injection is quantified using a total pressure loss coefficient. The conventional definition of loss coefficient for a vane passage with no mass addition is

$$\omega = \frac{P_1 - P_2}{P_1 - p_1}.$$

Here, P_1 and P_2 are the area-averaged total pressure upstream and downstream of the vane and p_1 is the area-averaged static pressure upstream of the vane. This must be corrected to account for the injected flow, which can have a different total pressure than the fluid in the vane passage. With injection present, there are two loss mechanisms within the vane passage: (i) the viscous

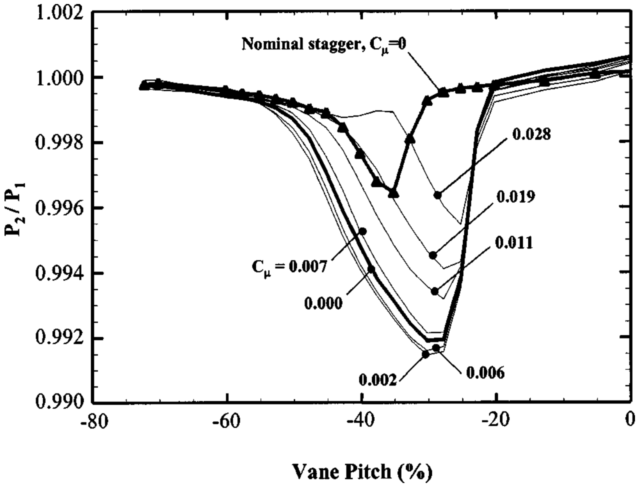

Fig. 7 Wake total pressure profiles for the slot-vane, stagger increased by 3 deg, steady injection, 56% span, $\phi = 0.36$. Also shown is the wake for the slot-vane at nominal stagger, no injection.

Table 1 Injection velocity and total mass flow required per stage as a percent of the freestream for various injection momentum coefficients

C_μ	$\overline{U}_{\rm jet}/\overline{U}_1$	$\dot{m}_{\rm jet}/\dot{m}_1$ (%)
0.002	0.42	0.37
0.006	0.68	0.60
0.007	0.73	0.64
0.011	0.91	0.81
0.019	1.20	1.06
0.028	1.45	1.29

dissipation due to the vane surface boundary layers; and (ii) the mixing loss generated between the injected jet and the freestream flow.

As discussed by Brocher [13], an energy balance across the vane row yields the following total pressure loss coefficient which represents the dissipation generated within the vane passage per unit exit mass flow,

$$\omega=\left(\frac{\dfrac{(\dot{m}_1P_1+\dot{m}_{\rm jet}\overline{P}_{\rm jet})}{\dot{m}_1+\dot{m}_{\rm jet}}-P_2}{P_1-p_1}\right)\left(1+\frac{\dot{m}_{\rm jet}}{\dot{m}_1}\right)$$

where $\overline{P}_{\rm jet}$ is the mean vane cavity pressure, $\dot{m}_{\rm jet}$ is the injected mass flow rate, and $\dot{m}_1$ is the mass flow rate of the freestream entering the vane passage.

The change in loss for the slot-vane restaggered by 3 deg is shown in **Fig. 8** for both steady injection and harmonically oscillating injection generated by the siren valve. The measurement was made at 56% span (which is the spanwise center of one of the injection slots) at a flow coefficient of $\Phi=0.36$. With the vane restaggered by 3 deg the losses associated with the separation on the vane suction surface are the dominant loss mechanism. Steady injection ($F^+=0$) at low injected flow rates increases loss relative to the noninjected case because the injection simply adds more low momentum fluid to a region that is already at or near separation. As injection is increased a break-even point occurs at $C_\mu=0.006$ due to the energizing influence of the injection on the separated flow. Further increases in the injection flow rate produce a reduction in loss for momentum coefficients $C_\mu<0.030$. Increases in injection flow rate beyond this value result in losses that are higher than the noninjected case because the mixing loss increase, which is proportional to $(\overline{U}_{\rm jet}-\overline{U}_1)^3$, is larger than the loss reduction that results from eliminating the suction surface separation.

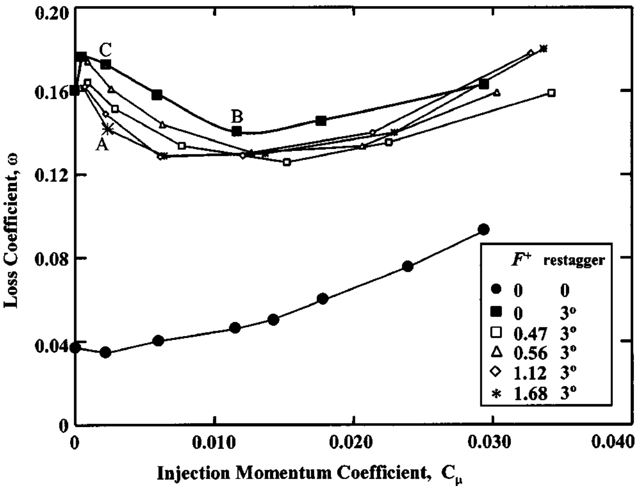

Fig. 8 Loss coefficient as a function of injected momentum for the slot-vane driven by the siren valve actuator, 56% span $\phi=0.36$

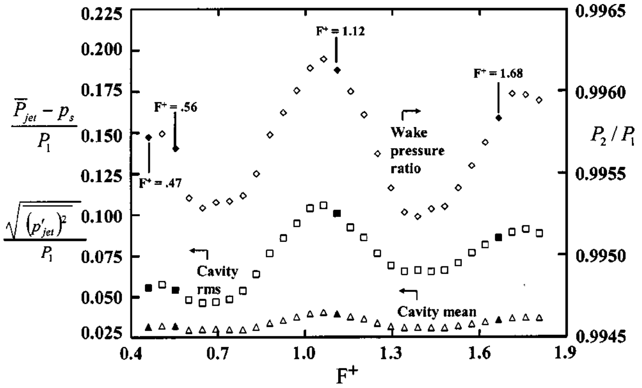

Fig. 9 Flow delivery system dynamics and the wake response as a function of harmonic oscillation frequency

The loss generated with steady injection when the vane is set at its nominal stagger is also shown in **Fig. 8.** At nominal stagger viscous losses are low because the vane suction surface flow is not separated. Injection at very low flow rates ($C_\mu<0.004$) reduces loss by 10% relative the noninjected case. Injection at higher flow rates results in losses that are greater than the non-injected case due to the mixing loss between the injected flow and the freestream.

Figure 8 clearly indicates that the addition of harmonic oscillations improves the effectiveness of the injection. This benefit can be viewed in the following ways:

As a decreased level of injected mass flow required to achieve a given loss reduction: Harmonic oscillations at $F^+=1.68$ for $C_\mu=0.002$ (**Fig. 8,** point A) produce the same loss reduction as steady injection at $C_\mu=0.012$ (**Fig. 8,** point B). This represents an 80% reduction in the steady momentum coefficient, $\overline{c_\mu}$, which in turn corresponds to a 56% reduction in the injected mass flow.

As an increased loss reduction for a given level of injected mass flow: Harmonic oscillations at $F^+=1.68$ for $C_\mu=0.002$ (**Fig. 8**, point A) result in 18% lower loss than steady injection at $C_\mu=0.002$ (**Fig. 8**, point C).

As an decrease in the minimum loss within the vane passage: The minimum loss with harmonically oscillating injection is 0.125 compared to a minimum loss of 0.140 with steady injection.

While an encouraging result, these improvements are far lower improvement than the order of magnitude benefit found in external flow applications, [2,3]. This is most likely due to the fact that for this implementation the unsteady component of the injection momentum coefficient, c'_μ, is less than 20% of the time-mean momentum coefficient, $\overline{c_\mu}$ **(Fig. 4).** In external flow applications using synthetic jets, as shown in Seifert and McManus [2,3] c'_μ was on the order of $\overline{c_\mu}$.

The results in **Fig. 8** also indicate some frequency dependence, with higher frequencies being slightly more effective. As discussed by Kim et al. [14], the forcing from the actuator and the resonance properties of each of the fluid volumes between the actuator and the injection slot determine the injection pressure and velocity at the vane surface. In **Fig. 9** the effect of delivery system resonance on the wake can be seen by comparing the vane cavity pressure to the total pressure measured at a single point on the suction side of the wake. The results shown are for a constant injected mass flow, corresponding to $C_\mu=0.012$, delivered over a range of forcing frequencies. All pressures are normalized by the inlet total pressure to the vane.

The solid symbols in **Fig. 9** depict the same four forcing frequencies that were presented in **Fig. 8.** The results indicate that the difference between the vane cavity total pressure and the vane

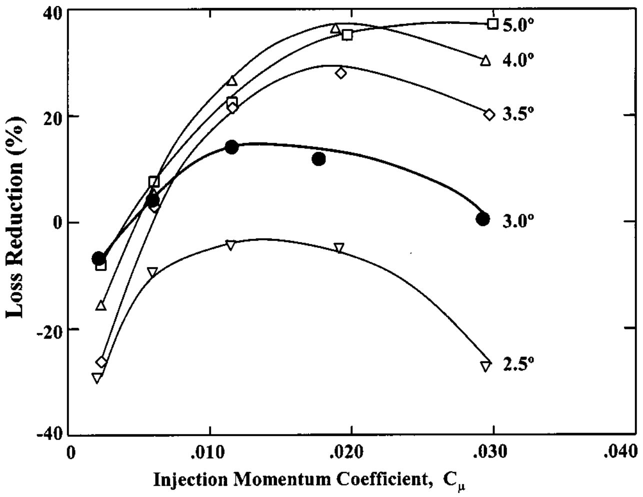

Fig. 10 Sensitivity of loss reduction to vane restagger angle for the slot-vane, steady injection, 56% span, $\phi=0.36$

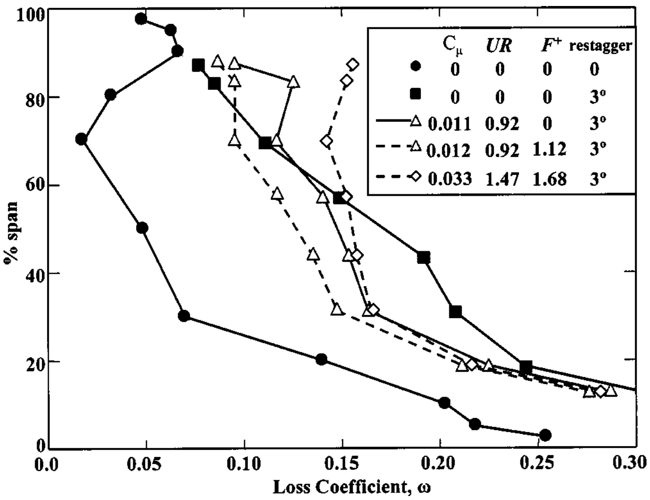

Fig. 11 Reduction in loss coefficient over the vane span for the slot-vane driven by the siren valve actuator, stagger increased by 3 deg, $\phi=0.36$

surface static pressure at the slot location, $(\overline{P}_{\text{jet}}-p_s)$, remains relatively constant. However, the RMS amplitude of the pressure fluctuations in the cavity is two to four times this difference and varies significantly with frequency. This shows that the changes in wake total pressure are highly correlated to changes in RMS amplitude of the cavity pressure and match the loss reduction change with frequency shown in **Fig. 8.** We therefore conclude that the frequency dependence shown in **Fig. 8** is a function of the delivery system resonance rather than a coupling between the forcing frequency and shear layer instability in the separated flow on the vane surface.

The impact of injection on loss reduction shown in **Fig. 8** is quite sensitive to the degree of separation on the vane surface. The loss reduction due to steady injection for a range of blade restagger angles is shown in **Fig. 10.** For restagger less than 3 deg from nominal, there is little or no separation and injection produces increased loss relative to the noninjected case. As blade restagger is increased beyond 3° from nominal, suction surface separation increases viscous losses, injection becomes increasingly effective, and the most effective loss reduction is achieved with injection momentum coefficient greater than $C_\mu=0.012$.

All results discussed so far have been obtained at 56% span. The coverage of injection slots on the vane surface, however, is from 13% to 87% span. The results shown in **Fig. 11** depict the effectiveness of injection across the span at a flow coefficient of $\Phi=0.36$ while varying C_μ and F^+. The loss coefficient of the slot-vane at its nominal stagger angle is also shown for reference. For a steady injection momentum coefficient of $C_\mu=0.011$, loss is reduced across much of the span. Adding harmonic oscillations to the steady injected flow produces benefit at all spanwise locations covered by the slots. In contrast harmonically oscillating injection at a higher momentum coefficient of $C_\mu=0.033$ does not produce loss reduction above 60% span. Injection does not change the fact that losses below 15% span are significantly higher compared to those over the rest of the span. Mixing between the freestream and low-total-pressure fluid emanating from the stator shroud seal cavity generates these high hub endwall losses. The inability of vane surface flow control to lower the level of these losses relative to midspan loss points to the need for separate flow control on the stator endwall.

The results shown in **Fig. 11** reflect the performance of the vane surface flow control at a flow coefficient of $\Phi=0.36$, which represents a highly loaded operating condition **(Fig. 6)** at which the restaggered vane is badly separated. The effectiveness of injection at lower-loaded operating conditions is shown for the slot-vane driven by the siren valve in **Fig. 12.** At the nominal stagger angle, where the vane is unseparated over much of the operating envelope, injection does not provide loss reduction at any flow coefficient. At an increased stagger of 3 deg, both steady and harmonically oscillating injection at a level of $C_\mu=0.011$ provide a loss reduction benefit as loading increases at low flow coefficients. However, both steady and unsteady injection at a higher momentum coefficient of $C_\mu=0.033$ increases loss relative to the noninjected case.

Experiments were repeated under the same conditions for the embedded-fluidic-vane and the hole-vane. The results of these experiments are shown in **Fig. 13** for a blade restagger of 2.5 deg. Recalling that the frequency of the embedded device is not controllable a single curve is used to define its performance. The hole-vane is capable of variable frequency operation and therefore loss data is shown using the same harmonic oscillation frequencies which were chosen for the slot-vane. Unsteady injection using the fluidic device increases the loss of the embedded-fluidic-vane at all injected flow rates. Similarly, steady injection increases the loss of the hole-vane at all injection rates. When driven by the siren valve at $C_\mu<0.015$, the hole-vane loss is reduced relative to that with steady injection. Although this improved loss reduction behavior due to unsteady injection is similar to that of the slot-

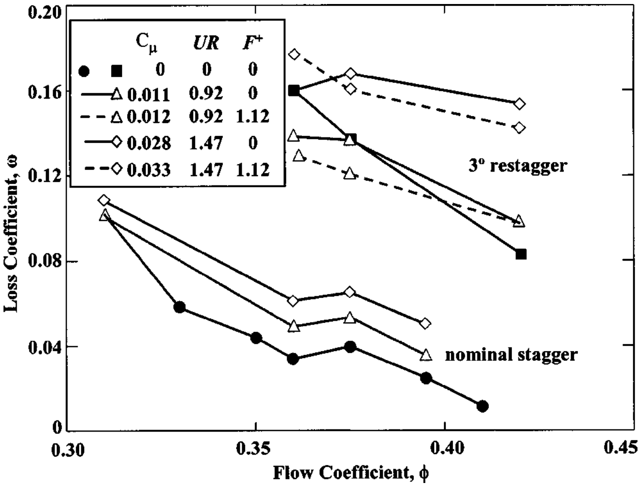

Fig. 12 Reduction in loss coefficient as a function of flow coefficient for the slot-vane driven by the siren valve actuator, stagger angle increased by 3 deg, at 56% span

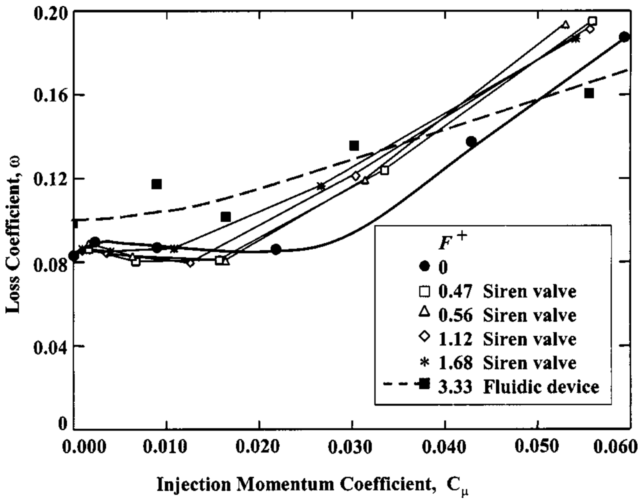

Fig. 13 Loss coefficient as a function of injected momentum for the embedded-fluidic-vane and the hole-vane driven by the siren valve actuator, stagger angle increased by 3 deg, 56% span, $\phi=0.36$

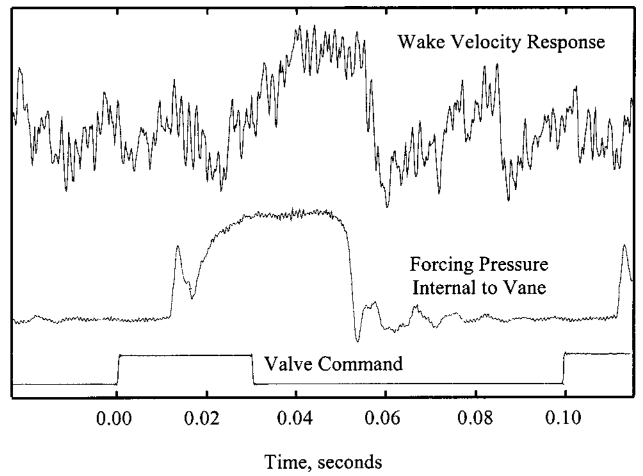

Fig. 15 Time history of the wake response to injection gated with a solenoid valve. Slot-vane, 56% span, $\phi=0.36$.

vane (**Fig. 8**), little or no loss reduction is achieved relative to the noninjected case. The fact that injection increases loss for both hole vane styles is primarily due to the fact that there is little or no separation at this restagger angle. Performance of the two hole vane styles is compared to that of the slot-vane at a larger restagger angle (5 deg) in **Fig. 14**, where the ordinate is the change in loss relative to the noninjected case. At this increased restagger angle all three vane styles reduce loss and the performance of the slot-vane and hole-vane is nearly identical.

Separation Detection and Control. The final task in the present effort is to design and demonstrate a method capable of active sensing and closed loop control of vane surface separation. Closed-loop separation control is desirable because it commands injection only when necessary, thus minimizing the thermodynamic cycle penalty associated with the increased compressor bleed, which is the source of air needed for injection. In an installed compressor, separation is an effect of off-design loading caused by throttle transients, distortion, and increased clearances due to deterioration. In the LSAC, loading changes are induced by closing the rig throttle valve. Our closed-loop control architecture is therefore based on forcing the onset of vane suction surface separation using changes in the throttle position, and reducing the separation using mass flow input to the vane. The signals required to implement control are the mass flow input, $\dot{m}_{\text{jet}}$, the mass flow commanded, $\dot{m}_{\text{cjet}}$, and the pressure, p'_c, measured from a pressure transducer at the casing over the stator vane, and are all shown in **Fig. 1.**

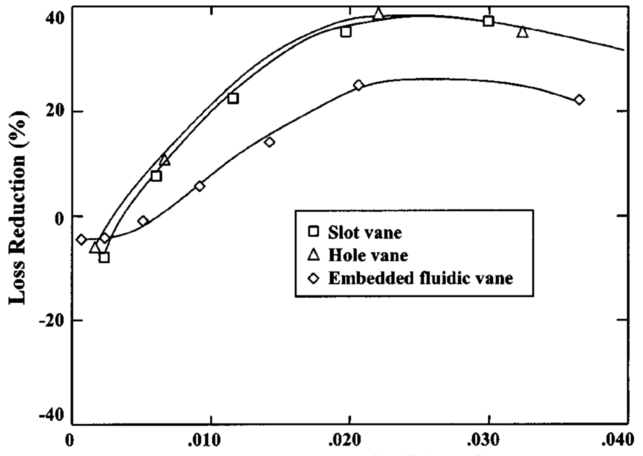

Fig. 14 Comparison of loss reduction for the slot-vane, embedded-fluidic-vane, and hole-vane at 5 deg restagger angle, steady injection, 56% span, $\phi=0.36$

In order to characterize the dynamics associated with a control scheme, open-loop experiments are performed to provide information on the lag between the start of injection and the response of the vane surface separation. The lag is determined by injecting a slug of fluid through the slot-vane using a fast solenoid valve (in place of the siren valve) to gate the flow on and off. The response of the vane surface separation to gated injection is inferred by measuring velocity changes in the suction side of the vane wake. This is accomplished with a hotwire anemometer probe axially located at the stream-wise measurement location used for the total pressure surveys. The internal vane cavity pressure, p'_{jet}, is monitored with the pressure transducer located at the inlet of the cavity (**Fig. 1**). A time history of the solenoid command signal, the wake velocity, and internal vane cavity pressure is shown in **Fig. 15.** The results indicate that the cavity pressure (and therefore the injected velocity) does not attain its peak until 0.025 seconds after the solenoid is opened and that the wake velocity change is complete 0.010 seconds after the cavity pressure peaks. Both of these effects contribute a 0.035 second delay between commanded injection and measured response. This information characterizes the vane dynamics time lag for our control design.

Implementation of a closed-loop control scheme requires a method of detecting separation. Two separation detection schemes were therefore developed. The first scheme employs a flow control vane with suction surface static pressure taps located at 70% and 85% chord and 56% span. The pressure rise between these two locations provides the controller with information on the pressure gradient over the rear of the vane. Measurements of this pressure rise with and without steady injection are acquired over a flow coefficient range of $0.31<\Phi<0.45$ and are shown in **Fig. 16.** Without injection, the pressure rise falls to zero at flow coefficients of $\Phi<0.40$, indicating separation. When injection is activated at an injection level of $C_\mu=0.012$, a pressure rise is restored at flow coefficients of $\Phi<0.40$. The pressure rise is gradually reduced as Φ decreases, and the flow is once again separated at $\Phi=0.31$. When the injection level is increased to $C_\mu=0.030$, the pressure rise is maintained over a wide range of flow coefficients at levels near that experienced at $\Phi=0.45$ without control, and

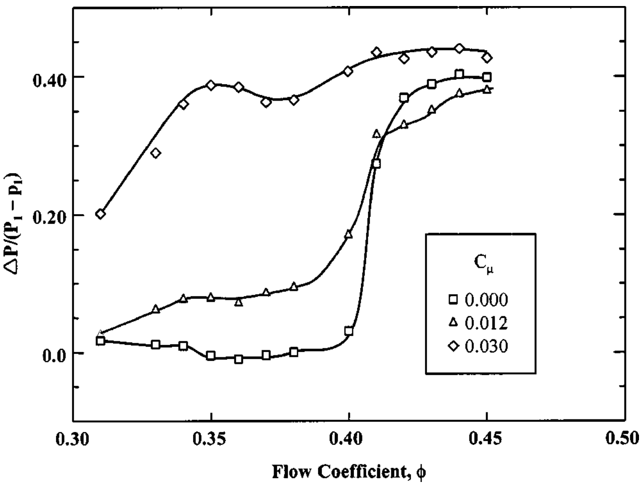

Fig. 16 Vane surface static pressure rise from 70–85% chord with and without steady injection. Slot-vane driven by the siren valve actuator, stagger increased by 3 deg, 56% span.

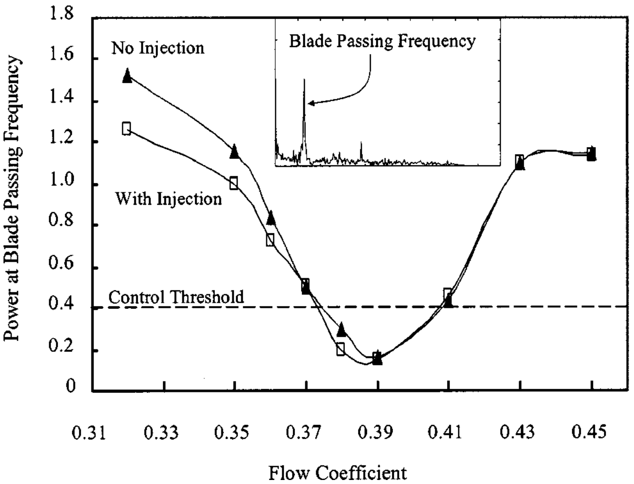

Fig. 17 Power of the first Fourier harmonic of the downstream rotor blade passing frequency is plotted as a function of flow coefficient without injection and with steady injection at $C\mu \approx 0.010$. The inset shows the relative magnitude of the BPF signal at $\phi = 0.36$ with no injection. Slot-vane driven by the siren valve actuator, stagger increased by 3 deg, 56% span.

does not begin to decrease until $\Phi = 0.35$. This type of detection scheme is achieved using static pressure measurements along the vane surface.

The second separation detection scheme investigated uses a pressure transducer located in the casing next to the vane suction surface at 85% chord **(Fig. 1).** This scheme was developed because it requires access to only a casing static pressure. This should therefore be less costly to implement in an engine than the scheme described above which requires an instrumented airfoil. This detection scheme is based on a time-series analysis of the casing static pressure and works as follows. The wake shed from the vane causes an unsteady loading of the downstream rotor. The first Fourier harmonic of the rotor blade passing frequency is a measure of the wake-induced pressure variation generated by the rotor. Since vane surface separation causes increased wake strength, a separation can be detected from the casing static pressure signal by monitoring the power in the first harmonic.

The power measured in the first harmonic over the flow coefficient range of $0.31 < \Phi < 0.45$ with and without injection is shown in **Fig. 17.** A sample power spectrum is shown in the inset of **Fig. 17.** At a flow coefficient of $\Phi = 0.39$, which is near the design point of the compressor, the first harmonic is at a minimum. As the flow coefficient is reduced, vane loading increases and the wake soon begins to grow due to suction surface separation, resulting in increased power in the first harmonic. (The presence of separation for $\Phi < 0.39$ is independently verified by the vane suction surface pressure data shown in **Fig. 16**.) Injection reduces the wake strength for $\Phi < 0.39$ and the power in the first harmonic is reduced. Increasing the flow coefficient above $\Phi = 0.39$ also results in increased power in the first harmonic. In this situation a reduced incidence angle produces a separation on the pressure surface of the vane. Since there is no injection on the pressure side of the vane, the power in the first harmonic does not change with injection. The fact that the power of the first Fourier harmonic increases above and below the design flow coefficient of $\Phi = 0.39$ indicates that additional information about the machine operating condition is necessary in order for a controller to decide if suction surface injection is required.

In a control strategy for the vane, the power of the first Fourier harmonic of the pressure signal is used to determine when to switch injection on or off. When the power of the first Fourier harmonic rises above a threshold level of 0.4 the control computer automatically opens a valve to begin injection. The injected mass flow from the vane surface is then varied proportionally to the casing signal strength. Results from an experiment in which this control strategy is used while the flow coefficient is varied over a range of $0.32 < \Phi < 0.45$ are shown in **Fig. 18.** The power spectral density of the pressure signal p_c' is plotted with and without control. With controlled injection, the amplitude of the power signal is maintained at a level below 0.8. This indicates that the flow is attached using active control.

Summary

Control of stator vane suction surface separation has been demonstrated in a low-speed multistage compressor using steady and unsteady injection on the suction surface. Reductions in exit total pressure loss on the order of 25% were realized using an injected flow equivalent to 1% of the compressor through flow. For a given injection level, the addition of harmonic oscillations to steady injection can reduce the level of injection required to attain a given loss reduction. Although injection was found to be effective across the full span of the vane, the high inner endwall losses typically found in hub-shrouded stators were not significantly reduced by the vane surface injection, pointing to the need for a separate approach to endwall loss reduction. Although injection was found to be effective across a wide range of operating conditions, a given level of injection is most effective when losses are high.

Harmonic oscillations were generated with two types of actuators, a motor-driven siren valve located external to the vane and a bistable fluidic actuator embedded within the vane. In addition, two different injection configurations were evaluated—a spanwise slot and a double row of spanwise holes. The best performance was obtained with the siren valve and slot-vane. Although the siren valve was closely coupled to two vanes, resonance of the fluid volumes between the siren valve and vane surface slots was found to affect the amplitude of the harmonic oscillations generated at the vane surface. This finding suggests caution when supplying injected flow to multiple vanes from a single source of unsteady actuation. As the distance between actuator and vanes increases, the frequency separation between resonance conditions decreases, necessitating careful matching of system volumes between each actuator and vane.

The magnitude of the harmonic oscillation generated by the fluidic actuator evaluated in the present work was attenuated by the small holes in the vane surface. Design of a more effective coupling between the actuator output and the vane surface holds the promise for improved performance compared to the siren

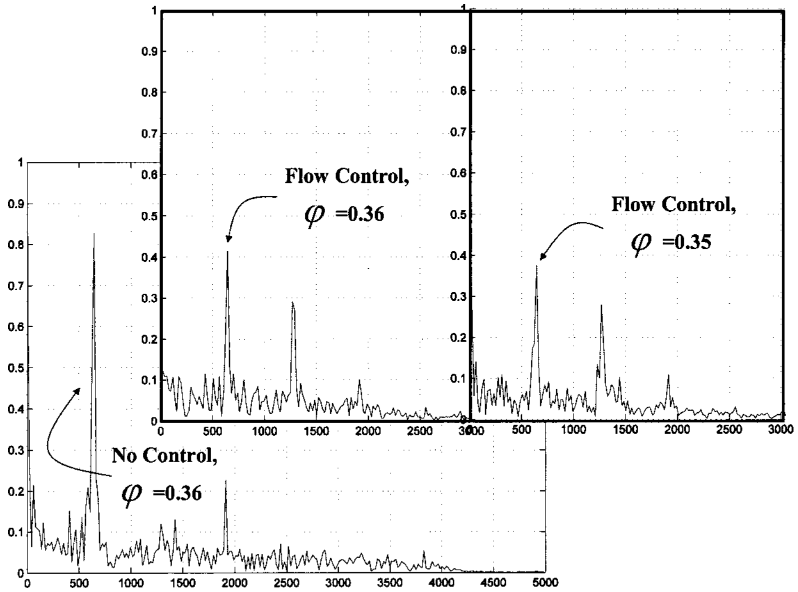

Fig. 18 Power spectral density of the casing static pressure with and without closed loop control. Slot-vane driven by the siren valve actuator, stagger angle increased by 3 deg, 56% span.

valve. Although embedding the fluidic device within the vane entails increased vane fabrication complexity, the device itself has no moving parts and can be driven by a constant pressure source connected to the vane.

Spectral analysis of the casing static pressure measured near the vane-endwall junction was found to provide a reliable indicator of the degree of vane separation. The design of a feedback control system that modulates vane injection to control separation was presented.

A careful cycle study is needed to evaluate the cost/benefit trade of adding flow control vanes to a compressor. The manufacturing cost of the added mechanical complexity of hollow airfoils and embedded or external actuators needs to be assessed against performance benefits. The thermodynamic cycle penalty of recirculating the flow control air within the compressor also needs to be assessed against the performance benefits. Results from this investigation provide an initial quantification of the aerodynamic benefits associated with flow control, which should prove useful when input to a cycle study. Only two flow control vanes in a stage were used in the present work. The next step is to evaluate a full row of flow control vanes, which will enable a study of stage matching issues arising from loss reduction in the stator. Turning changes due to flow control, which will impact stage matching, also need to be quantified.

Acknowledgments

The work reported in this paper is part of the Smart Efficient Components program at NASA Glenn Research Center. In large part, this effort has been funded by the DARPA Micro-Adaptive Flow Control Program, with NASA-GRC, Honeywell Engines & Systems, and the Illinois Institute of Technology as team members.

The authors would like to thank Honeywell Engines & Systems for cooperation in this effort, especially Mukund Acharya for project management and significant contributions to the research, Steve Emo for development of the siren valve actuator and relevant insight into engine systems, John Thurston for development of the embedded-fluidic actuator, and Dan Bugajski for contributions to the control model.

The authors also wish to extend sincere thanks to Dave Williams and his team of students at the Illinois Institute of Technology for extensive contributions to the development of experiment design parameters and analysis of data.

Finally, the authors offer unending gratitude to the crew of test cell W1; Mary Gibson, Rick Senyitko, Bob Davis, and Valarie Roundtree for which without their expertise this research would not have been possible.

DARPA Distribution Statement "A." Approved for Public Release, Distribution Unlimited

Nomenclature

A_{jet} = total area of injector slots or holes
c = chord
$\overline{c_\mu}$ = time-mean momentum coefficient$=(2A_{\text{jet}}/sL)(\overline{U}_{\text{jet}}/\overline{U}_1)^2$
c'_μ = harmonic oscillation momentum coefficient$=(2A_{\text{jet}}/sL)(\sqrt{(u'_{\text{jet}})^2}/\overline{U}_1)^2$
C_μ = total momentum coefficient$=\overline{c_\mu}+c'_\mu$
f = frequency of harmonic oscillation, Hz
F^+ = nondimensional forcing frequency$=fL/\overline{U}_1$
L = distance from injection location to vane trailing edge $=0.65$c
$\dot{m}_1$ = freestream mass flow rate upstream of the vane passage
$\dot{m}_{c\text{jet}}$ = controlled mass flow
$\dot{m}_{\text{jet}}$ = injected mass flow rate
p'_c = unsteady pressure at the compressor casing, Fig. 1
$\underline{p}'_{\text{jet}}$ = unsteady pressure internal to the flow control vane
$\overline{P}_{\text{jet}}$ = time-averaged total pressure internal to the flow control vane
P_1 = area-averaged total pressure upstream of the vane passage
P_2 = area-averaged total pressure downstream of the vane passage
p_1 = area-averaged static pressure upstream of the vane
PR = total pressure ratio$=P_2/P_1$
s = span

$\overline{U}_1$ = mean freestream velocity upstream of the vane passage
$\overline{U}_{\text{jet}}$ = mean jet velocity $= \dot{m}_{\text{jet}}/\rho A_{\text{jet}}$
U_{tip} = rotor tip speed
u'_{jet} = unsteady jet velocity
UR = injection velocity ratio $= \overline{U}_{\text{jet}}/\overline{U}_1$
γ = ratio of specific heat
ρ = density
φ = flow coefficient $=$ (mean inlet velocity)/(compressor tip speed)
ψ = pressure rise coefficient $= (\gamma/\gamma-1)(P_{ref}/\rho_{ref})((P_2/P_1)^{(\gamma-1/\gamma)}-1)(g_c/U_{tip}^2)$
ω = total pressure loss coefficient

References

[1] Amitay, M., Kibens, V., Parekh, D., and Glezer A., 1999, ‘‘The Dynamics of Flow Reattachment Over a Thick Airfoil Controlled by Synthetic Jet Actuators,’’ AIAA Paper No. 99-1001.
[2] Seifert, A., Bachar, T., Koss, D., Shepshelovich, M., and Wygnanski, I., 1993, ‘‘Oscillatory Blowing: A Tool to Delay Boundary-Layer Separation,’’ AIAA J., **31**(11), pp. 2052–2060.
[3] McManus, K., Legner, H., and Davis, S., 1994, ‘‘Pulsed Vortex Generator Jets for Active Control of Flow Separation,’’ AIAA Paper No. 94-2218.
[4] Amitay, M., and Glezer, A., 1999, ‘‘Aerodynamic Flow Control of a Thick Airfoil Using Synthetic Jet Actuators,’’ ASME/JSME Paper FEDSM99-6922.
[5] Carter, C., Guillot, S., Ng, W., and Copenhaver, W., 2001, ‘‘Aerodynamic Performance of a High-Turning Compressor Stator with Flow Control,’’ AIAA Paper 2001-3973.
[6] Stitzel, S., 2002, ‘‘Integrated Ejector Pump Flow Control for Low Pressure Turbine,’’ NASA Phase I SBIR Final Report, NASA-LPT-FR01.
[7] Bons, J., Sondergaard, R., and Rivir, R., 2000, ‘‘Turbine Separation Control Using Pulsed Vortex Generator Jets,’’ ASME J. Turbomach., **123**, pp. 198–206.
[8] Bons, J., Sondergaard, R., and Rivir, R., 2002, ‘‘The Fluid Dynamics of LPT Blade Separation Control Using Pulsed Jets,’’ ASME J. Turbomach., **124**, pp. 77–85.
[9] Wasserbauer, C. A., Weaver, H. F., and Senyitko, R. G., 1995, ‘‘NASA Low Speed Compressor for Fundamental Research,’’ NASA TM4635.
[10] Wisler, D. C., 1977, ‘‘Core Compressor Exit Stage Study: Volume I—Blade Design,’’ NASA CR135391.
[11] Wellborn, S., and Okiishi, T., 1999, ‘‘The Influence of Shrouded Stator Cavity Flows on Multistage Compressor Performance,’’ ASME J. Turbomach., **121**, pp. 486–498.
[12] Nishri, B., and Wygnanski, I., 1998, ‘‘Effects of Periodic Excitation on Turbulent Flow Separation From a Flap,’’ AIAA J., **36**(4), pp. 547–556.
[13] Brocher, E., 1961, ‘‘The Jet-Flap Compressor Cascade,’’ ASME J. Basic Eng., **83**, p. 401.
[14] Kim, B., Williams, D., Emo, S., and Acharya, M., 2002, ‘‘Large Amplitude Pneumatic Oscillator for Pulsed-Blowing Actuators,’’ AIAA Paper 2002-2704.

Aerodynamic Blade Row Interactions in an Axial Compressor—Part I: Unsteady Boundary Layer Development

Ronald Mailach
e-mail: mailach@tus.mw.tu-dresden.de

Konrad Vogeler
e-mail: kvogeler@tus.mw.tu-dresden.de

Dresden University of Technology,
Institute for Fluid Mechanics,
01062 Dresden, Germany

This two-part paper presents experimental investigations of unsteady aerodynamic blade row interactions in the first stage of the four-stage low-speed research compressor of Dresden. Both the unsteady boundary layer development and the unsteady pressure distribution of the stator blades are investigated for several operating points. The measurements were carried out on pressure side and suction side at midspan. In Part I of the paper the investigations of the unsteady boundary layer behavior are presented. The experiments were carried out using surface-mounted hot-film sensors. Additional information on the time-resolved flow between the blade rows were obtained with a hot-wire probe. The unsteady boundary layer development is strongly influenced by the incoming wakes. Within the predominantly laminar boundary layer in the front part of the blade a clear response of the boundary layer to the velocity and turbulence structure of the incoming wakes can be observed. The time-resolved structure of the boundary layer for several operating points of the compressor is analyzed in detail. The topic "calmed regions," which can be coupled to the wake passing, is discussed. As a result an improved description of the complex boundary layer structure is given. [DOI: 10.1115/1.1649741]

1 Introduction

The efficiency of turbomachine bladings and consequently the overall performance of the machine are strongly dependent on the boundary layer (BL) development on the blades. Furthermore the BL state substantially influences the heat transfer between the blade surface and the fluid. For these reasons the knowledge of the boundary layer structure and its development plays an important role for a better understanding and further improvement of turbomachines.

The flow in turbomachines is highly unsteady and turbulent because of the aerodynamic interaction between the rotor and stator blade rows due to wakes and the effect of the potential flow field. In particular the periodic influence of the passing wakes plays an important role for the unsteady BL development on the blades.

Generally there are three fundamental modes for the BL transition from the laminar to the turbulent state (Mayle [1]): The first one is denoted as ''natural'' transition. It is observed for low levels of freestream turbulence. The transition process starts with a weak instability in the laminar BL, which develops through various stages to a fully turbulent BL (Schlichting [2]). The second mode is known as ''bypass'' transition. In this case transition is initiated by disturbances in external flow (e.g., high freestream turbulence, wakes) and bypasses the ''natural'' transition. This is the predominant route of transition in turbomachines, where the natural transition process is periodically disturbed by the incoming wakes (''wake-induced transition''). A third mode occurs if the BL separates. It is therefore known as ''separated flow'' transition and can be found in compressors and low-pressure turbines.

Subject of this paper is the BL development on compressor blades. There are several parameters influencing the BL development on the blades. These are the properties of the incoming wakes, freestream turbulence, blade loading, Reynolds number, the profile pressure distribution and others. Depending on these parameters and as a result of the periodic wake influence an unsteady, highly complex boundary layer behavior can be observed, where a combination of different forms of transition can be found (''multimode transition,'' [1]).

Numerous investigations of the BL for steady and unsteady incoming flow are known from literature. Fundamental investigations of the BL were carried out on flat plates and in cascades with steady inflow conditions. The BL development with periodically disturbed inflow conditions (e.g., by passing bars) is described in the investigations of Pfeil and Herbst [3], Pfeil et al. [4], Mayle and Dullenkopf [5], Liu and Rodi [6], Orth [7], and Teusch et al. [8].

Within recent years an increasing number of experimental investigations of the BL in turbomachines were carried out. In the context of our investigations the publications of Halstead et al. [9] and Walker et al. [10] on the BL behavior on the blades of axial compressors are of relevance. These investigations show extensive regions with predominantly laminar BL in the front part of the compressors blades, which are periodically disturbed by the incoming wakes of the passing blades.

Pfeil and Herbst [3] realized that the unsteady passing of wakes causes the BL to become turbulent during their impingement on the surface. If a wake impinges the leading edge of a turbomachine blade the high turbulence of the wake penetrates into the laminar BL. This way a wake-induced transitional and subsequently turbulent strip is formed, which is moving along the blade independently from the propagation of the wake in the blade passage, [3,5]. Thus a time shift between the wake moving in the blade passage and its influence on the blade surface can be observed.

After the occurrence of turbulent spots a calmed region can be observed (Schubauer and Klebanoff [11]). This calmed region can also appear behind a wake-induced transitional region for unsteady inflow conditions. This was shown by the experiments of Pfeil et al. [4] and Orth [7] on flat plates and is confirmed by the investigations of Halstead et al. [9] and Hodson et al. [12] both for compressor and turbine blades. Within these calmed regions

---

Contributed by the International Gas Turbine Institute and presented at the International Gas Turbine and Aeroengine Congress and Exhibition, Atlanta, GA, June 16–19, 2003. Manuscript received by the IGTI Dec. 2002; final revision Mar. 2003. Paper No. 2003-GT-38765. Review Chair: H. R. Simmons.

disturbances are suppressed. Due to Halstead et al. [9] this is because of the BL profile, which is relaxing from a turbulent to a laminar level of shear stress. On turbomachine blades the calmed regions has the positive effect that possibly separated flow is avoided and the transition point is shifted downstream towards the trailing edge. This way the BL losses are reduced. The reason for the appearance of these calmed regions due to wake passing is not yet well understood. Hodson et al. [12] assume that the acceleration of the flow towards the trailing boundary of the wakes could be responsible for this effect. Up to now this hypothesis could not be verified.

This paper presents experimental investigations of unsteady aerodynamic blade row interactions in the first stage of the four-stage low-speed research compressor of Dresden. In Part I of the paper experiments on the unsteady BL behavior on the stator blades are described. The measurements were carried out on pressure side (PS) and suction side (SS) at midspan using surface-mounted hot-film arrays. Furthermore the flow field upstream the stator blades was investigated, which strongly influences the BL on the considered blades.

The aim of this paper is to improve the understanding of the wake-induced transition process of the BL. The time-resolved structure of the boundary layer will be analyzed for several operating points of the compressor. Special consideration will be taken on the analysis of the time-resolved structure of the incoming flow field and the unsteady BL response. The topic ‘‘calmed regions’’ due to wake passing will be discussed by means of the experimental results. The BL development is compared to the unsteady pressure distribution on the blades, which is the subject of Part II of the paper.

2 Experimental Setup

2.1 Test Facility. The experiments on the BL behavior were performed in the low-speed research compressor of Dresden University of Technology (Dresden LSRC). The compressor consists of four identical stages, which are preceded by an inlet guide vane row, **Fig. 1**. The blading of the compressor was developed on the basis of the profiles of a middle stage of a high-pressure compressor of a gas turbine. Detailed descriptions of the compressor are given by Sauer et al. [13], Müller et al. [14], and Boos et al. [15]. **Table 1** gives a summary of the main design parameters.

2.2 Measuring Techniques and Data Postprocessing. In this part of the paper experiments on the unsteady BL behavior on the first stage stator blades are described. First of all the flow field upstream the considered stator blades was investigated, which strongly influences the BL on the blade. This was done using a single hot-wire probe (*Dantec*). The hot wire was positioned in the middle of the axial gap between rotor 1 and stator 1 at midspan. This way the structure of the incoming wakes was realized.

The measurements of the unsteady BL behavior were carried out on PS and SS of stator 1 at midspan. For these investigations arrays of surface-mounted hot-film sensors were used (*Tao Systems*). Hot-film sensors are a well-established measurement technique for investigating the time-resolved BL development. **Figure 2** shows a hot-film array on the SS of the stator blade at midspan. 16 hot-film bridges (*Baumann*) were operated simultaneously in constant-temperature mode. For data acquisition a workstation with a 16-channel card was used. The sampling rate for the measurements was 51.2 kHz while the frequency response of the sensors is 15 kHz. The blade passing frequency of the rotor blades is 1.05 kHz for design speed.

Both the hot-wire probe and the stator blade equipped with the hot-film sensors were positioned between the wakes of the IGV, which travel through the rotor blade row.

Using the hot-films the heat transfer between the flow and the sensor is utilized. According to Bellhouse and Schultz [16] the relationship between the wall shear stress τ_w and the heat transfer is given in the following form:

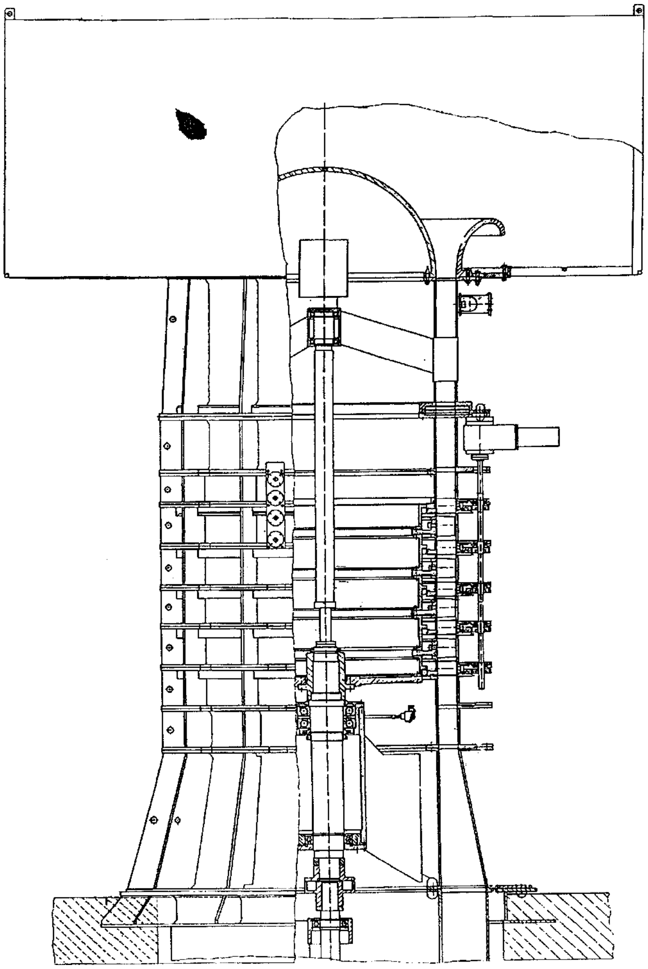

Fig. 1 Sectional drawing of Dresden LSRC

$$\tau_w = K\left(\frac{E^2 - A^2}{\Delta T}\right)^3 \tag{1}$$

where E is the instantaneous voltage of the hot-film anemometer and ΔT is the temperature difference between the flow and the heated sensor. The constants K and A take the heat loss to the substrate into account. Following Hodson et al. [12] qualitative data of the wall shear stress can be calculated in the form

$$\mathrm{QWSS} = C \cdot \tau_w^{1/3} = \left(\frac{E^2 - E_0^2}{E_0^2}\right). \tag{2}$$

In this equation E is the instantaneous anemometer voltage during the test and E_0 is the anemometer voltage for zero-flow conditions. It is common to denote this expression as quasi wall shear stress (QWSS). This parameter is a direct measure to the real wall shear stress.

In a postprocessing the velocity and wall shear stress measuring data were ensemble-averaged with respect to the relative position of the rotor blades. Using this method stochastic and periodic fluctuations can be separated. It can be performed using the equation

$$\langle v(t) \rangle = \frac{1}{N} \sum_{i=0}^{N-1} v_i(t). \tag{3}$$

In our case the data are triggered to an identical rotor blade using a 1/rev-signal and ensemble-averaged $N = 250$ times. The parameter $v_i(t)$ is the instantaneous measured value (velocity, QWSS) at

Table 1 Design parameters of Dresden LSRC

IGV+4 identical stages	
Reynolds number, rotor inlet, midspan (related to rotor chord length)	$5.7 \cdot 10^5$
Mach number, rotor inlet, midspan	0.22
Design speed	1000 rpm
Mass flow, design point	25.35 kg/s
Flow coefficient ϕ, design point	0.553
Enthalpy coefficient Ψ is, design point	0.794
Hub diameter	1260 mm
Hub to tip ratio	0.84
Axial gaps between all blade rows, midspan	32 mm

	IGV	rotor	stator
Blade number	51	63	83
Chord length, midspan	80 mm	110 mm	89 mm
Stagger angle, midspan (versus circumference)	82.8°	49.3°	64.0°
Solidity, midspan	0.941	1.597	1.709

a considered relative position to the point of reference, which is the rotor blade position in this case. The value $\langle v(t) \rangle$ is the resulting ensemble-averaged value.

The ensemble-averaged root mean square-value (RMS) of the measured anemometer voltage is used as a parameter, which reveals information about the stochastic fluctuations of the measured values. It is given by the equation

$$\langle \mathrm{RMS}(t) \rangle = \sqrt{\frac{1}{N} \sum_{i=0}^{N-1} (v_i(t) - \langle v(t) \rangle)^2}. \tag{4}$$

The ensemble-averaged turbulence intensity follows from the ensemble-averaged mean value and its RMS value

$$\langle TI(t) \rangle = \frac{\langle \mathrm{RMS}(t) \rangle}{\langle v(t) \rangle}. \tag{5}$$

Another statistical value, which is used for the description of the BL development, is the skewness. This third-order moment represents a degree of asymmetry of a statistical distribution around its mean value. The ensemble-averaged skewness is given by the equation

$$\langle S(t) \rangle = \frac{\frac{1}{N} \sum_{i=0}^{N-1} (v_i(t) - \langle v(t) \rangle)^3}{\left(\sqrt{\frac{1}{N} \sum_{i=0}^{N-1} (v_i(t) - \langle v(t) \rangle)^2} \right)^3}. \tag{6}$$

The use of these parameters for the analysis of the flow field and the BL state is described in detail in the following sections.

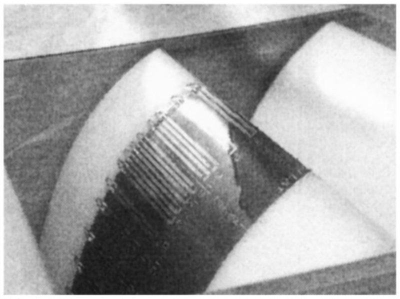

Fig. 2 Surface-mounted hot-film array on a stator blade of first stage, suction side, midspan

3 Model of Wake Structure and Wake Influence on Boundary Layer

The unsteady BL behavior on compressor blades is strongly influenced by the incoming flow field, which is dominated by the wakes of the upstream moving blade row. Within the wake the velocity strongly decreases while the turbulence intensity increases compared to the freestream.

A model showing the influence of the rotor blade wakes on the incoming flow field and the boundary layer of the stator blades is depicted in **Fig. 3**. It shows a single rotor and stator blade as part of the blade rows moving relative to each other. The wake generated at the blade trailing edge can be described as a von Karman vortex street **(Fig. 3)**. The typical features of the vortex street behind compressor blades are shown by several numerical and experimental investigations (Eulitz [17], Sanders et al. [18], and Lehmann [19] in the Dresden LSRC). It consists of two branches with counterrotating vortices. The two wake branches contain the low-momentum fluid stemming from the pressure side (PS) and from the suction side (SS) BL of the blade, respectively. The PS branch of the wake can be found between leading boundary (LB) of the wake and its centreline (CL), while the SS branch is located between the CL and the trailing boundary (TB) of the wake. An asymmetry of the wake around its center-line can occur due to the different BL thickness on PS and SS of the blade. Thus it is

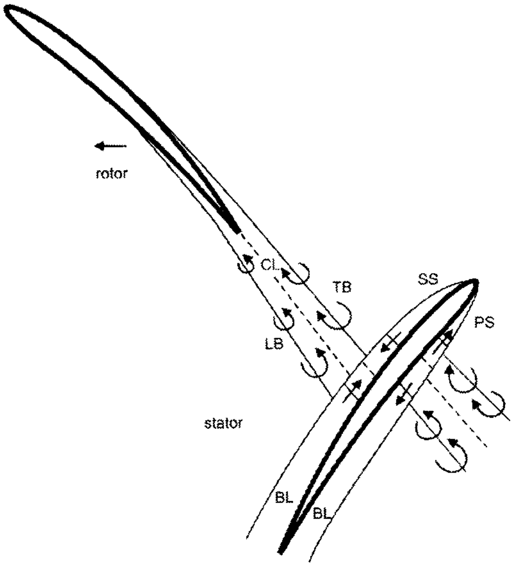

Fig. 3 Rotor blade wake structure and effect on boundary layer of a stator blade in a compressor

depending on the inlet flow angle of the blades; respectively, the operating point of the compressor. Certainly the wake structure develops during the wake propagation.

Due to the induced velocities by the wake and its discrete vortices an increase respectively a decrease of velocity is induced at the wake boundaries within the blade passage as well as within the BL of the blade. As a result of this on the SS of the compressor blade a decrease of velocity can be observed at the LB of the wake, while it increases at the TB of the wake **(Fig. 3)**. In contrast to that on the PS a velocity increase takes place at the LB, while it decreases at the TB of the wake. Because of the induced velocities due to the wake eventually an additional secondary flow system appears within the blade passage, which is directed from SS to PS within the passage (negative jet effect, [17–20]). (As shown by Meyer [20] these velocities are also induced if the wake is not described to consist of discrete vortices.)

Within the BL the wake structure can be observed with a time lag to the propagation of the wakes in the passage. Typical results on the rotor blade wake structure and the BL response on the stator blades are shown in the next sections. More details about the model in **Fig. 3** are discussed there.

4 Incoming Flow Field

To obtain information about the incoming flow field of the stator blades a single hot wire was positioned in the middle of the axial gap at midspan. As an example ensemble-averaged results are shown for the design point of the compressor **(Fig. 4)**. The time t is related to the passing time of a rotor blade passage t_{rotor}. The passing wakes of the upstream rotor blade row can be recognized by a steep velocity decrease. The turbulence intensity starts to increase when the LB of the wake arrives the measuring position. Maximum turbulence intensities of about 15% can be observed, while the freestream value between the wakes is around 2%. The TB of the wake is reached at the end of the steep increase of the velocity, respectively, at that point, where the turbulence intensity returns to the freestream level.

Just before the arrival of the wake LB a decrease of the velocity as well as an increase of the turbulence intensity can be observed. This effect presumably appears due to the induced velocity of the wake. Thus the resulting effect exceeds the wake boundary. After wake passing the highest velocity combined with the lowest turbulence intensity can be observed. These observations correspond to the results of measurements with a laser Doppler anemometer carried out by Lehmann [19] in the Dresden LSRC.

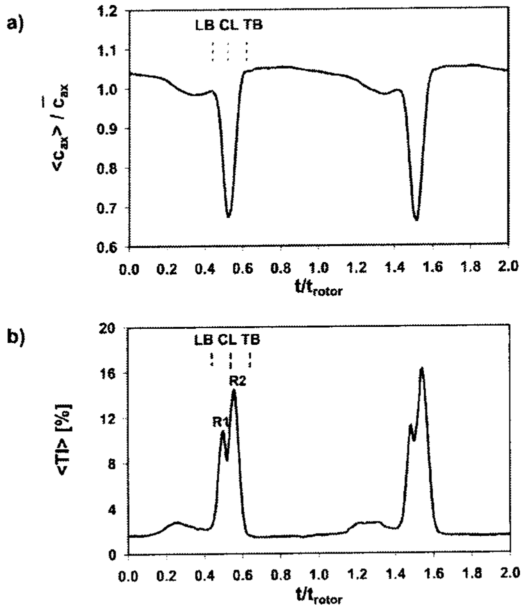

Fig. 4 Flow field parameters upstream stator 1, middle of axial gap between rotor and stator, midspan, design point

A double peak of the RMS value and the turbulence intensity can be observed during wake passing, denoted as R1 and R2. An explanation for this effect is given by Mailach and Vogeler [21,22]: The two points with maximum fluctuations are to be found at the positions with maximum gradients of the ensemble-averaged velocity during wake passing. In the raw data of the velocity (not shown) it can be recognized, that the wake position and the shape of the velocity traces fluctuates for the subsequent passing of an identical blade. These velocity fluctuations and consequently the turbulence intensity are largest at the positions with maximum gradients of the ensemble-averaged velocity. This explains the occurrence of two fluctuation maxima both in the PS branch and SS branch of the wake.

For operating points with reduced mass flow, which is linked with higher aerodynamic loading, the freestream turbulence intensity somewhat grows. The increase of the turbulence intensity in the PS branch of the wake is comparably small. However, the turbulence intensity within the SS branch of the wake as well as the wake width increases considerable due to the higher loading. Hence a stronger influence of the wake and especially its SS branch on the BL of the following stator blade row can be expected.

5 Unsteady Boundary Layer Development on the Suction Side

In this chapter the process of wake-induced transition on the SS of the blades will be considered. In Section 5.1 the typical response of the laminar BL to incoming wakes in the front part of the blade will be discussed for the design point of the compressor. Subsequently the BL development along the whole blade chord for different operating points will be described in Section 5.2.

5.1 Response of the Laminar Boundary Layer to Incoming Wakes.

Following the structure of the incoming wakes and the BL will be compared. Commonly the quasi wall shear stress and the RMS are used as parameters to identify the BL state and development. In our case these values are ensemble-averaged to analyze the unsteady BL development (Eqs. (2)–(4)).

Some explanations will be given for the application of the skewness (Eq. (6)). This parameter represents a degree of asymmetry of a statistical distribution around its mean value. For the fully laminar BL (intermittency $\gamma=0$) the wall shear stress at a given point is evenly distributed and the skewness is zero. If the BL is laminar with some turbulent portions the skewness becomes positive ($0<\gamma<0.5$). This is due to the fact that the wall shear stress increases during the short-duration appearance of turbulent spots within the predominantly laminar BL. If equal portions of laminar and turbulent BL exist in time, the wall shear stress is evenly distributed around its mean value and the skewness becomes zero again ($\gamma=0.5$). If the transition process proceeds, turbulent portions dominate versus laminar ones. The skewness becomes negative in this case ($0.5<\gamma<1.0$). Following the transition process will be completed and the BL is fully turbulent ($\gamma=1$). In this case the wall shear stress is again evenly distributed and the skewness is zero.

Typical results of the BL investigations for a measuring position in the front part of the blade are shown in **Figs. 5(*a–c*)**. For the design point of the compressor the BL at the chosen position at 33% of chord length is laminar, but disturbed by the incoming wakes. In **Fig. 5** it is laminar between $t/t_{\text{rotor}}=0-0.15$, for instance. During this time the QWSS is nearly constant on a low level. The RMS value as a parameter for the fluctuations of the wall shear stress is relatively low as well. For this fraction of time the skewness is zero. This indicates that the BL is fully laminar without any turbulent spots.

The wakes penetrate into the BL when impinging the leading edge of the blade. From this point of time the impact of the wake

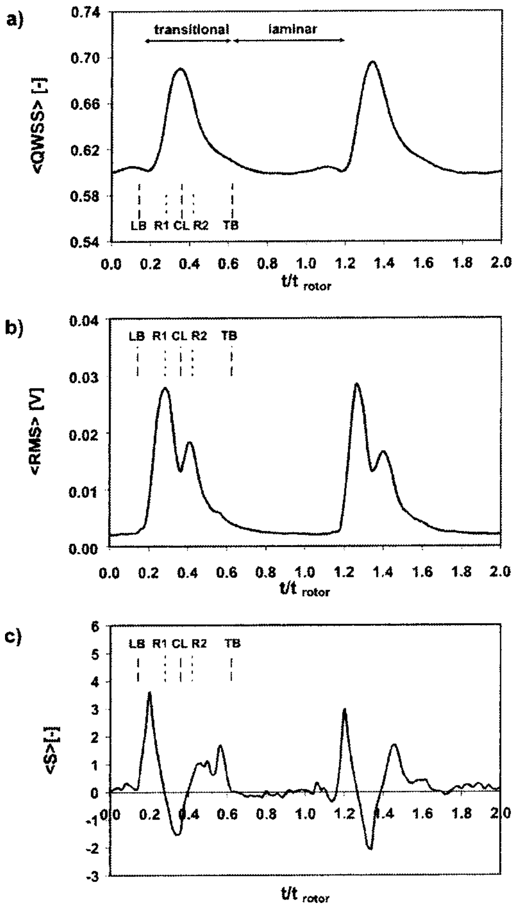

Fig. 5 Parameters of the boundary layer, stator 1, suction side, midspan, 33% of chord length, design point (ξ=1.0)

propagates within the BL with a lower velocity than the wake within the blade passage. This effect is schematically shown in **Fig. 3** and is further discussed in Section 5.2.

If the impact of the wake leading boundary (LB) arrives at the observed position, the laminar BL is disturbed (**Fig. 5**, $t/t_{\text{rotor}} = 0.15$). This is the starting point for the wake-induced transition process. The wall shear stress—respectively the QWSS that is used here—increases due to increasing turbulent portions within the wake. The QWSS reaches a maximum at that point of time, where the center line (CL) of the wake path arrives and the incoming velocity is lowest. Subsequently the wall shear stress decreases asymptotically and returns to the base level at the trailing boundary (TB) of the wake path. Until the next wake arrives the BL is again laminar.

Moreover the wake passing can be recognized by a strong increase of the fluctuations of the wall shear stress between LB and TB of the wake (**Fig. 5(*b*)**). As already visible in the wake structure, also in the BL two maxima of fluctuations appear. These points R1 and R2 within the wake and the wake-induced path in the BL must not be directly related to each other. Generally an increase of turbulent portions within the BL can be observed if the turbulence intensity of the incoming wake increases. This is confirmed by previous investigations of the authors, [21], for different measuring configurations. However, the strongest fluctuations (maximum of RMS) can be observed, when the wall shear stress always switches between the laminar and turbulent level. This is the case for equal portions of laminar and turbulent BL in time. Thus at the points R1 and R2 the intermittency is $\gamma=0.5$. Between R1 and R2 the BL is predominantly turbulent with smaller laminar portions ($0.5<\gamma<1.0$). This is the reason why the RMS value decreases and reaches a local minimum within the wake CL.

These conclusions are confirmed looking at the development of the skewness. In **Fig. 5(*c*)** the skewness is zero between $t/t_{\text{rotor}} = 0-0.15$. Thus the BL is fully laminar.

At the LB of the wake influence the turbulent portions within the predominant laminar BL increases. Between LB and the first turbulence maximum R1 the skewness is positive. Thus the BL is laminar with some turbulent portions ($0<\gamma<0.5$). At R1 the skewness is again zero. With regard to the previous development of the BL it can be concluded, that at this relative position to the rotor blades even portions of laminar and turbulent BL appear in time. The intermittency is $\gamma=0.5$ in this case.

Between R1 and R2 turbulent portions dominate ($0.5<\gamma<1.0$). Because of the decreasing wall shear stress during the short time periods with laminar BL the skewness becomes negative. The maximum intermittency appears at the CL, where the skewness reaches its minimum. However, at the point CL the intermittency γ cannot be determined by means of **Fig. 5(*c*)**. This is discussed later following the path of the CL along the blade.

After passing of the CL the BL is stabilized due to the increasing incoming flow velocity within the SS branch of the wake and the turbulence intensity, which tends to decrease towards the wake TB. As a result of this the turbulent portions within the BL are gradually diminished between CL and TB **(Fig. 5(*c*))**. At R2 the skewness is zero again, the intermittency is $\gamma=0.5$ then. Consecutively the BL becomes predominantly laminar with less turbulent portions between R2 and TB. This can be concluded from the positive values of the skewness. At the TB of the wake-induced transitional path the skewness is zero, which means that the BL is again fully laminar ($\gamma=0$).

The wake-induced region covers around 50% of the passing time of a rotor blade passage at the considered position. Compared to the wake pattern **(Fig. 4)** it is substantially broadened. This is due to the wake mixing out during its propagation between the hot-wire position in middle of the axial gap between the blade rows and the blade leading edge. Furthermore, the wake-induced path diverges during its propagation on the blade surface (Section 5.2).

It can be summarized that the incoming flow field and the response of the wall shear stress are clearly related to each other. A decrease/increase of the incoming flow velocity results in an increase/decrease of the wall shear stress at positions in the front part of the blade. The turbulence structure of the wake and the response of the BL to the wake can be compared.

Eventually the topic "calmed region" will be discussed. In the periodically disturbed BL this region is observed directly after the passing of the wake-induced transitional or turbulent region (e.g., [4,7,8]). The formation of new instabilities is suppressed within this region without turbulent activity. On turbomachine blades the calmed regions has the positive effect that the start of transition point is shifted downstream towards the trailing edge. Possibly separated flow is avoided. Following Halstead et al. [9] the calmed regions are connected with an asymptotically decreasing, but still elevated wall shear stress. For a given position on the blade it starts at the point of time where the maximum of wall shear stress appears due to the wake influence and ends when the wall shear stress returns to a constant low level.

Our investigations do not confirm the appearance of calmed regions due to the passing wakes. In our data the region with asymptotically decreasing wall shear stress can be localized between the centreline CL and trailing boundary TB of the wake-induced transitional region **(Fig. 5)**. Thus the BL is influenced by the fluid stemming from the SS branch of the incoming rotor wake during this time. Therefore it is the wake impact on the BL and not an effect after wake passing. It includes turbulent portions (predominantly turbulent between CL and R2 and predominantly laminar between R2 and TB). Therefore it cannot be a calmed region.

The slowly decreasing wall shear stress between CL and TB of the wake induced path in the BL seems to be determined by the wake structure. The acceleration due to the wake and its discrete vortices, which affects the BL in the considered region, tends to decrease the gradient of the reducing wall shear stress. This is further discussed in Section 6 for the PS.

5.2 Time-Resolved Boundary Layer Development Along the Suction Side Blade Surface

5.2.1 Design Point. After comparing the wake structure with the BL response at a position in the front part of the blade, the time-resolved BL development along the blade chord will be discussed. The results for the design point of the compressor are shown in the space-time diagrams (s-t) in **Figs. 6(*a–c*)**. As already explained by means of **Figs. 4** and **5** several typical points can be observed in the BL response to the wakes (LB,R1,CL,R2,TB). Because of the propagation of the wake influence along the blade chord these typical features can be seen as lines in the s-t diagrams. For better understanding the different zones of the BL which can be distinguished in **Figs. 6(*a–c*)** are labeled in **Fig. 6(*d*)**. These are the following:

A . . .	fully laminar BL ($\gamma=0.0$), between wake paths
A1 . . .	transitional BL, laminar with turbulent spots ($\gamma<0.5$), between wake paths (only for $\xi=0.85$)
B, **C** . . .	transitional BL, laminar with turbulent spots ($\gamma<0.5$), path between LB and R1 (B) and between R2 and TB (C)
D, **E** . . .	transitional BL, turbulent with laminar parts ($0.5<\gamma<1.0$), path between R1 and CL (zone D) and between CL and R2 (zone E)
F . . .	fully turbulent BL ($\gamma=1.0$)

These zones can be classified firstly by analyzing the BL at individual positions and secondly by following the particles in the BL in a Lagrangian frame along the blade surface. The first method was applied for the analysis of the BL at all individual measuring positions, as described for an example in Section 5.1. Using the second method, which is suggested by Liu and Rodi [6], the BL was analyzed for different paths underneath the wake and between the wakes. This is discussed later with **Fig. 7**.

As discussed in Section 5.1 a laminar BL (zone A) can be observed in the front part of the blade, which is disturbed by the incoming wakes. During the development of the laminar BL along the blade surface the wall shear stress decreases (**Fig. 6(*a*)**). The lowest value is achieved at the point, where the BL layer is laminar for the longest distance. This is near that point, where the TB of a wake-induced strip meets the LB of the next one **(Fig. 6(*a*)**, $t/t_{\mathrm{rotor}}=1.4$, $x/l=50\%$). The consecutive wake-induced regions, which are converging during its propagation along the blade, limit the extension of the laminar BL.

The incoming wake-induced regions propagate along the blade surface with a velocity below the velocity of the incoming flow. The mean propagation velocities were calculated between the first sensor at 3% and 45% of chord length. This is the maximum extension of the fully laminar BL in time (design point). The mean propagation velocity of the LB is 95% of the incoming flow velocity, that of the CL is 75%, while the TB of the wake path propagates with only 35%. These values are above the values specified by Halstead et al. [9].

However, our investigations show that an averaging along a certain chordwise distance is inadequate for comparing the data obtained on the blades of different machines. It is already discussed by Mailach and Vogeler [22] that the propagation of the wake-induced path within the BL is not directly coupled to the wake propagation within the passage. Anyway there is a relation between the propagation of the wake-induced path in the BL and the velocity in the passage, [22].

For design point the velocity within the passage near SS of the blade decreases between 20–100% chord (compare to pressure distribution in Part II of the paper, [23]). According to this the velocity of the wake path (CL) also decreases during its propagation along the blade **(Fig. 6)**. However, the propagation velocity within the BL is clearly below that in the passage. This can be explained by the lower mean velocity within the BL.

Because of the strong deceleration of the TB it meets the LB of the next blade wake path (**Fig. 6**: $t/t_{\mathrm{rotor}}=1.3$, $x/l=45\%$). Thus the TB of the wake path and the LB of the next one limits the

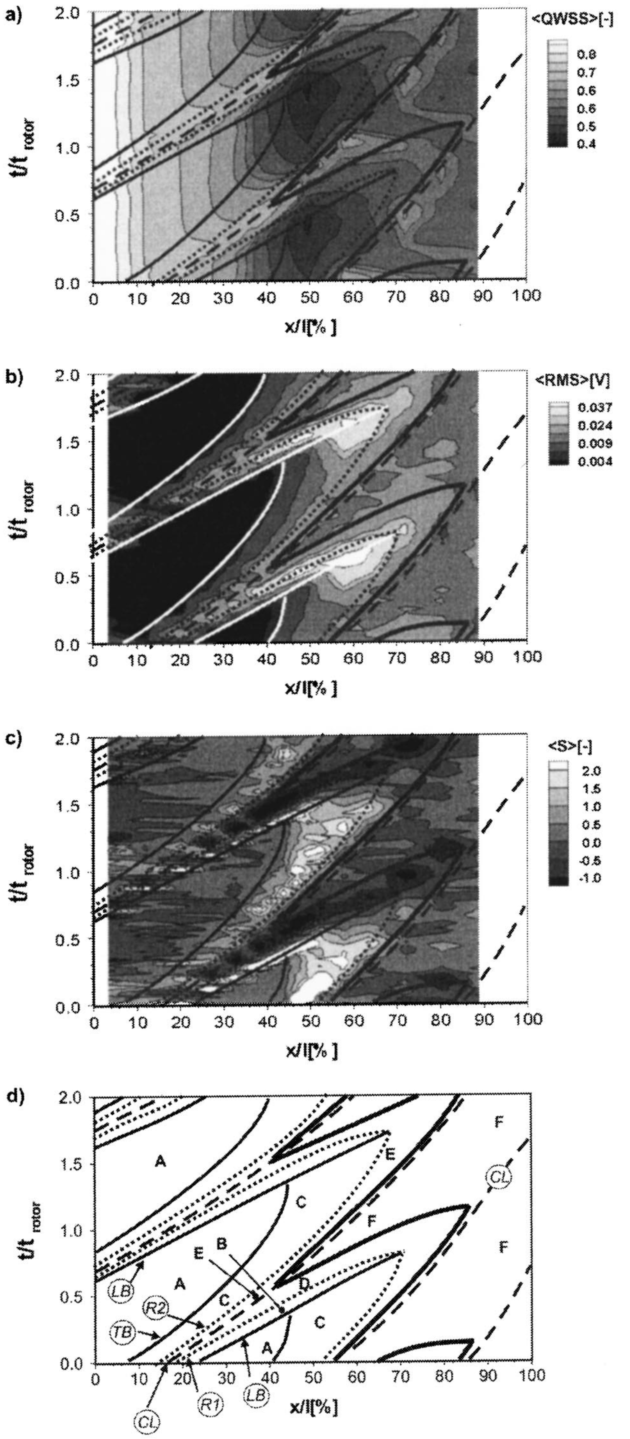

Fig. 6 (***a–c***) **Parameters of BL,** (***d***) **zones of BL** (**from Figs. 6**(***a–c***)), **stator 1, suction side, midspan, design point** (ξ=**1.0**)

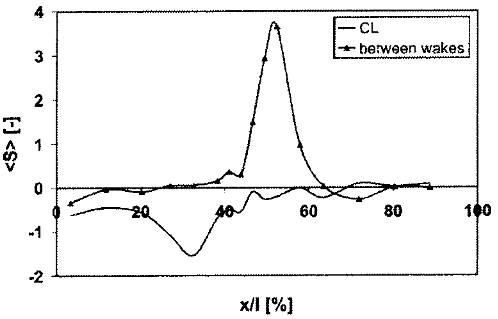

Fig. 7 Skewness along the centerline of wake path (CL) and a path starting between the wakes, stator 1, suction side, midspan, design point (ξ=1.0)

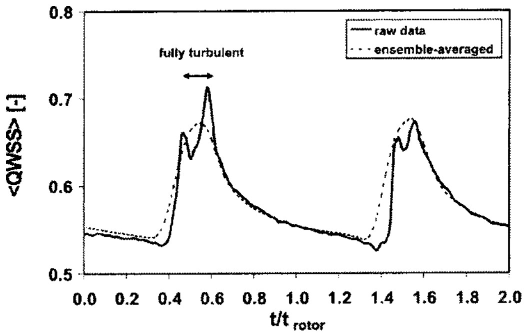

Fig. 8 Comparison of raw data and ensemble-averaged data, stator 1, suction side, midspan, 41% of chord length, design point (ξ=1.0)

region of the laminar flow (zone A). For this chordwise position the flow deceleration is strongest for the design point (Part II of the paper, [23]).

The BL reaction to a passing wake was already explained in detail in the previous section. It can be seen in **Fig. 6** that the BL becomes transitional due to the wake influence between the regions of laminar BL (A). Between LB and R1 (dotted line in **Fig. 6**) the zone B is formed, where the BL is predominantly laminar with turbulent spots ($\gamma<0.5$). Between R1 and the CL (dashed line in **Fig. 6**) the BL is predominantly turbulent (zone D, $0.5<\gamma<1.0$). A maximum of turbulent portions is reached at the CL.

Within the zones E and C the BL is transitional as well. Due to the decreasing turbulence of the incoming wakes after passing of the CL the turbulent parts dominates in zone E and the laminar ones in zone C. After the passing of the TB of the wake-induced path the BL becomes again fully laminar in the front part of the blade.

During its development along the profile generally the turbulent portions within the BL increases. Starting within the CL of the wake-induced transitional strip a region of fully turbulent flow develops (F). The starting point of zone F is at 45% chord for the CL (**Fig. 6**: $t/t_{\mathrm{rotor}}=0.6$). This zone of fully turbulent BL broadens during its propagation along the blade. Finally between about 80% chord and the trailing edge the BL is fully turbulent all the time.

This development can be clarified by looking at the BL parameters along the typical flow paths in a Lagrangian frame **(Fig. 7)**. As an example the skewness is shown for the path of the CL and a path starting within the laminar region A in the middle between the centerlines of two subsequent wake-induced paths.

For the path starting between the wakes the BL is laminar between the leading edge of the blade and about 40% chord (zone A). The skewness between these positions is about zero. At 40% the TB of the wake-induced transitional path is reached (compare **Fig. 6**). The BL within this path becomes transitional with more laminar parts ($S>0$, zone C, 40–65% of chord) and subsequently more turbulent parts ($S<0$, zone E, 65–80% of chord). Between 80% of chord and the trailing edge the BL is fully turbulent ($S=0$, zone F).

For the CL of the wake-induced path the BL is already transitional with dominating turbulent portions near the leading edge ($0.5<\gamma<1.0$). This is indicated by the negative skewness. At 45% of chord the skewness reaches a value close to zero and remains on this level. Thus the BL is fully turbulent between this position and the trailing edge. At 33% chord the skewness reaches a minimum, the intermittency is $\gamma=0.75$ in this case. At 45% chord the skewness becomes approximately zero and remains constant until the trailing edge of the blade. Then the BL is fully turbulent (zone F).

The onset of fully turbulent BL can also be seen in the raw data of the QWSS **(Fig. 8)**. Beginning at about 40% chord two maxima of wall shear stress appears during wake passing. At the first maximum the BL becomes fully turbulent. After that point the wall shear stress reduces within the fully turbulent BL until the CL of the wake influence. After passing of the CL the BL relaxes. At the second peak the BL becomes again transitional. This confirms the observations discussed above by means of the ensemble-averaged data. For the ensemble-averaged data of the QWSS the two peaks are averaged out.

As discussed with **Fig. 6** the wakes substantially influence the BL development. The potential flow field of the downstream rotor blade row is less important for the unsteady BL. On the SS it can only be recognized by means of a wavelike variation of the wall shear stress within the fully turbulent BL (e.g., fluctuation of QWSS between 70–90% chord, **Fig. 6(*a*)**). For the design point this upstream influence is only weak. A more detailed differentiation between the broadened wake influence and the effect of the potential flow field on the BL is not straightforward because of the identical blade number of the up and downstream rotor blade rows.

The time-averaged profile pressure distribution (Part II of the paper, [23]) shows, that the deceleration starts at 25% chord. The strongest deceleration appears between 40–50% chord. This is the region where the BL transition between the wakes starts **(Fig. 7)**. The effect of the unsteady changes of the profile pressure distribution on the BL development is estimated to be small. This is due to the fact that the unsteady profile pressure changes nearly instantaneously in time along the whole chord due to incoming wakes and the potential effect of the downstream blades. This is further discussed in Part II of the paper.

5.2.2 Operating Point Near the Stability Limit. If the stability limit of the compressor is approached, the width as well as the turbulence intensity of the incoming wakes increases (Section 4). On the SS surface of the blade the point where the flow starts to decelerate is shifted towards the leading edge of the blade (Part II of the paper, [23]).

Figure 9 shows the development of the BL for an operating point near the stability limit ($\xi=0.85$). Exemplarily the development of the skewness as well as the resulting zones of the BL are shown. The general response of the BL to the incoming wake is comparable to that for the design point. Because of the broadened wakes the wake-induced regions within the BL are broader as well. Already near the leading edge the wake influences the BL about 50% of the passing time of a blade passage. The propagation velocities of the wake-induced path, which are related to the incoming flow velocity, are comparable to design point (Section 5.2.1)

The transition zone is clearly shifted upstream because of the higher turbulence of the incoming flow and the earlier onset of flow deceleration. Furthermore the TB meets the LB of the next wake earlier because of the broad wakes and the reduced velocity for the operating points with reduced mass flow.

In contrast to the design point the BL between the wakes is in a transitional state already at the leading edge (**Fig. 9**, zone A1).

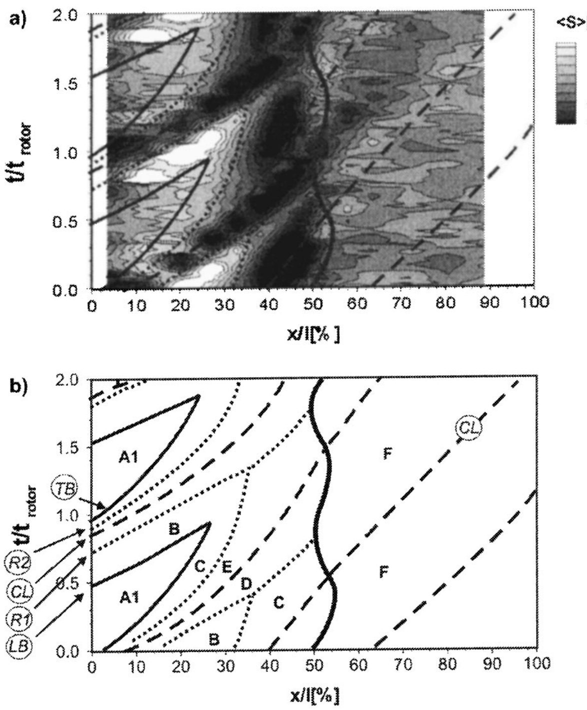

Fig. 9 (*a*) **Boundary layer development** (**skewness**), (*b*) **zones of BL** (**from Fig. 9**(*a*)), **stator 1, suction side, midspan, operating point near the stability limit for design speed** (ξ=**0.85**)

The skewness in this region is positive. This means that laminar parts dominate ($\gamma<0.5$). The region A1 extends for short time periods only up to 30% chord.

Around the CL turbulent portions dominate already at the leading edge ($0.5<\gamma<1.0$). This is comparable to the behavior for the design point. Between 30–50% the BL is turbulent with some laminar portions ($0.5<\gamma<1.0$) all the time. Behind 50% the BL is fully turbulent independent on the relative position to the wake ($\gamma=1.0$).

6 Unsteady Boundary Layer Development on the Pressure Side

Generally the boundary layer on the pressure side is of minor interest, because the losses generated there are much smaller than on the SS. However, for comparison to the behavior on the SS the unsteady BL development on the PS will be discussed for the design point (**Fig. 10**).

Between the leading edge of the blade and 40% chord a strong decrease of the wall shear stress can be observed (**Fig. 10**(*a*)). This is the region where the flow decelerates (profile pressure distribution in Part II of the paper, [23]). Periodic changes of the wall shear stress due to the wakes can be observed there. The wake paths are shown as dashed lines.

Due to the slight flow acceleration in the rear part of the blade the wall shear stress remains on a nearly constant level behind 40% chord. The propagation of the wake-induced path along the surface can also be seen in the rear part of the blade (**Figs. 10**(*b,c*)). However, it has no remarkable influence on the wall shear stress. At these positions periodic changes of the wall shear stress due to the influence of the potential flow field of the downstream rotor blades dominate (**Fig. 10**(*a*)). These periodic changes appear nearly instantaneously in time between 40% chord and trailing edge. (This instantaneous change of the flow properties due to the potential effect of the downstream blades can also be observed for the unsteady changes of the profile pressure distribution, as discussed in Part II, [23]).

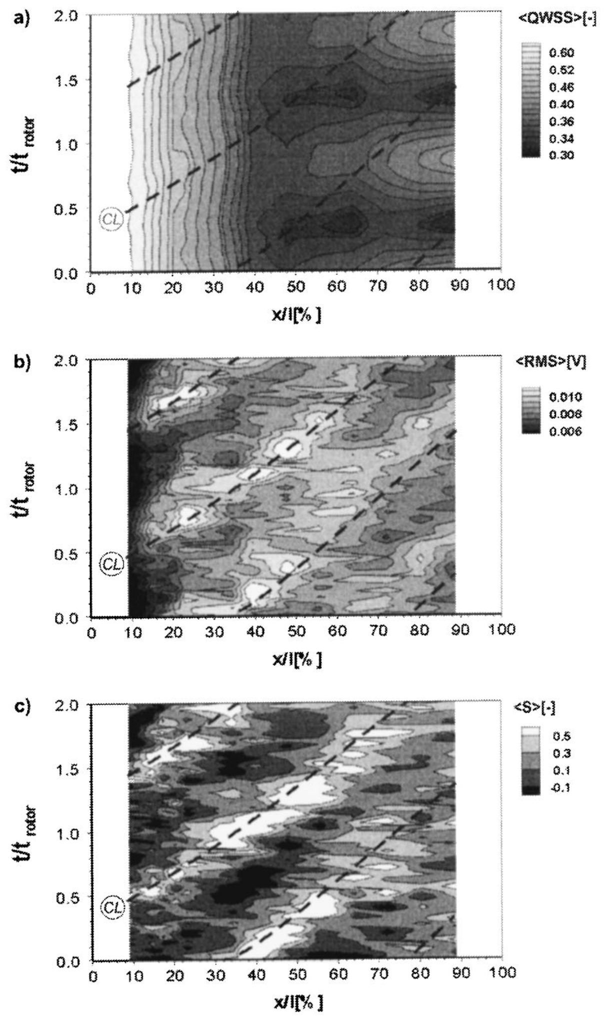

Fig. 10 Parameters of boundary layer, stator 1, pressure side, midspan, design point (ξ=**1.0**)

Generally there are smaller changes of the QWSS due to the rotor wake influence than on the SS. The skewness, which periodically changes between positive and negative values, shows that the BL is in a transitional state along the whole blade chord (**Fig. 10**(*c*)). This confirms the observations of Dong and Cumpsty [24], who found that the BL on the PS can always be transitional.

For operating points towards the stability limit of the compressor no fundamental changes of the BL behavior on the PS appear.

Figure 11 shows the development of the QWSS in time for a position in the front part of the blade. Due to the wake influence

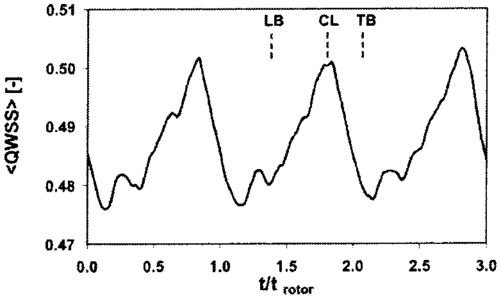

Fig. 11 Boundary layer development, stator 1, pressure side, midspan, 23% of chord length, design point (ξ=**1.0**)

the QWSS slowly increases to a maximum (between LB and CL) and much faster decreases after that point (CL to TB). This is the opposite behavior than observed on the SS (**Fig. 5(*a*)**). This seems to be an effect of the different influences of the wake vortices on PS and SS of the blade, as discussed by means of **Fig. 3**. In contrast to the SS on the PS an acceleration of the flow can be found at the LB and a deceleration at the TB of the wake. Because of this a relative slow increase of the QWSS can be found between LB and CL while it rapidly decreases between CL and TB (**Fig. 11**). It seems to be generally the case that the acceleration due to the wake and its discrete vortices tends to broaden the influence zone within the BL (**Fig. 5**: CL to TB on SS/**Fig. 11**: LB to CL on PS). Within these regions the gradient of the wall shear stress changes is relatively small.

7 Conclusions

In this two-part paper experimental investigations of unsteady aerodynamic blade row interactions in the first stage of the four-stage Dresden low-speed research compressor were presented. Results are shown for design point and an operating point near the stability limit of the compressor. In Part I of the paper the unsteady boundary layer behavior was discussed. Part II is focused on the unsteady profile pressure distribution and provides results on the unsteady blade forces.

The investigations in this part of the paper mainly focus on the behavior on the suction side. The structure of the incoming rotor wakes and the boundary layer response on the stator blade suction side were analyzed in detail. The typical features of the wake can be found again within the boundary layer structure.

Due to the periodic wake influence a region of transitional boundary layer and subsequently fully turbulent boundary layer develops and propagates along the suction side blade surface. The wake-induced transitional regions limit the extension of the laminar boundary layer, which exists between the wakes in the front part of the blades. Within the wake path the transition process starts already at the leading edge. The transition zone periodically extends to maximum 80% of chord for the design point. The propagation velocity of the wake path on the blade surface depends on the flow velocity in the passage outside the boundary layer. Approaching the stability limit of the compressor the wake-induced transition zone is clearly shifted upstream.

On the pressure side the influence of the wakes on the unsteady boundary layer is comparably small. In the rear part of the blade the boundary layer is affected by the potential effect of the downstream rotor blades. However, it remains in a transitional state along the whole blade surface.

The topic ‘‘calmed regions,’’ which can be coupled to the wake passing, is discussed. Furthermore the influence of the induced velocities due to the wake on the wake-induced transition is considered.

Acknowledgments

The work reported in this paper was performed within the project: ‘‘Unsteady Forces and Boundary Layer Behavior on the Blades of a Low-Speed Axial Compressor’’ which is part of the joint project: ‘‘Periodical Unsteady Flow in Turbomachines’’ funded by the DFG (German Research Society). Information on this project can be found at http://www.turboflow.tu-berlin.de. The permission for publication is gratefully acknowledged.

Nomenclature

$\langle\ \rangle$ = ensemble-averaged values
A, C = constant
c = velocity (m/s)
E = anemometer voltage (V)
K = constant
l = chord length (m)
N = number of values
RMS = root mean square value (m/s, V)
S = skewness
t = time (s)
T = temperature (K)
TI = turbulence intensity (%)
x = chordwise position (m)
v = measured value
γ = intermittency, ratio of turbulent parts within the boundary layer in time (fully laminar: $\gamma=0$, fully turbulent: $\gamma=1$)
τ_w = wall shear stress (N/m^2)
ξ = mass flow/design mass flow

Subscripts

0 = reference value, without flow
ax = axial component
i = index for time trace

Abbreviations

BL = boundary layer
CL = center line of wake/wake-induced path
LB = leading boundary of wake/wake-induced path
LSRC = low-speed research compressor
PS = pressure side
R1, R2 = maxima of RMS values within the PS branch and SS branch of wake/wake-induced path
SS = suction side
TB = trailing boundary of wake/wake-induced path
QWSS = quasi wall shear stress

References

[1] Mayle, R. E., 1991, ‘‘The Role of Laminar-Turbulent Transition in Gas Turbine Engines,’’ ASME J. Turbomach., **113**, pp. 509–537.
[2] Schlichting, H., 1979, *Boundary-Layer Theory*, McGraw-Hill, New York.
[3] Pfeil, H., and Herbst, R., 1979, ‘‘Transition Procedure of Instationary Boundary Layers,’’ ASME Paper No. 79-GT-128.
[4] Pfeil, H., Herbst, R., and Schröder, T., 1983, ‘‘Investigation of the Laminar-Turbulent Transition of Boundary Layers Disturbed by Wakes,’’ ASME J. Eng. Gas Turbines Power, **105**, pp. 130–137.
[5] Mayle, R. E., and Dullenkopf, K., 1989, ‘‘A Theory for Wake-Induced Transition,’’ ASME J. Turbomach., **111**, pp. 188–195.
[6] Liu, X., and Rodi, W., 1991, ‘‘Experiments on Transitional Boundary Layers With Wake-Induced Unsteadiness,’’ J. Fluid Mech., **231**, pp. 229–256.
[7] Orth, U., 1993, ‘‘Unsteady Boundary-Layer Transition in Flow Periodically Disturbed by Wakes,’’ ASME J. Turbomach., **115**, pp. 707–713.
[8] Teusch, R., Brunner, S., and Fottner, L., 2000, ‘‘The Influence of Multimode Transition Initiated by Periodic Wakes on the Profile Loss of a Linear Compressor Cascade,’’ ASME Paper No. 2000-GT-271.
[9] Halstead, D. E., Wisler, D. C., Okiishi, T. H., Walker, G. J., Hodson, H. P., and Shin, H. W., 1997, ‘‘Boundary Layer Development in Axial Compressors and Turbines: Parts I–IV,’’ ASME J. Turbomach., **119**, Part 1, pp. 114–127, Part II, pp. 426–444, Part III, pp. 225–237, Part IV, pp. 128–139.
[10] Walker, G. J., Hughes, J. D., and Solomon, W. J., 1999, ‘‘Periodic Transition on an Axial Compressor Stator: Incidence and Clocking Effects: Part I—Experimental Data,’’ ASME J. Turbomach., **121**, pp. 398–407.
[11] Schubauer, G. B., and Klebanoff, P. S., 1956, ‘‘Contributions on the Mechanics of Boundary-Layer Transition,’’ NACA Report No. 1289.
[12] Hodson, H. P., Huntsman, I., and Steele, A. B., 1994, ‘‘An Investigation of Boundary Layer Development in a Multistage LP Turbine,’’ ASME J. Turbomach., **116**, pp. 375–383.
[13] Sauer, H., Bernstein, W., Bernhard, H., Biesinger, T., Boos, P., and Möckel, H., 1996, ‘‘Konstruktion, Fertigung und Aufbau eines Verdichterprüfstandes und Aufnahme des Versuchsbetriebes an einem Niedergeschwindigkeits-Axialverdichter in Dresden,’’ Abschlußbericht zum BMBF-Vorhaben 0326758A, Dresden, Germany.
[14] Müller, R., Mailach, R., and Lehmann, I., 1997, ‘‘The Design and Construction of a Four-Stage Low-Speed Research Compressor,’’ *Proceedings of the IMP ’97 Conference on Modelling and Design in Fluid-Flow Machinery*, J. Badur, Z. Bilicki, J. Mikielewicz, and E. Sliwicki, eds., Nov. 18–21, Gdansk, Poland, pp. 523–530.
[15] Boos, P., Möckel, H., Henne, J. M., and Selmeier, R., 1998, ‘‘Flow Measurement in a Multistage Large Scale Low Speed Axial Flow Research Compressor,’’ ASME 98-GT-432.
[16] Bellhouse, B. J., and Schultz, D. L., 1966, ‘‘Determination of Mean and Dynamic Skin Friction, Separation and Transition in a Low-Speed Flow With a Thin-Film Heated Element,’’ J. Fluid Mech., **24**, pp. 379–400.
[17] Eulitz, F., 2000, ‘‘Numerische Simulation und Modellierung der instationären Strömung in Turbomaschinen,’’ Ph.D. thesis, Ruhr-Universität Bochum, DLR Forschungsbericht 2000-05, ISSN 1434-8454.
[18] Sanders, A. J., Papalia, J., and Fleeter, S., 2001, ‘‘Multi-Blade Row Interac-

tions in a Transonic Axial Compressor, Part I: Stator Particle Image Velocimetry (PIV) Investigations,'' ASME 2001-GT-268.

[19] Lehmann, I., 2003, ''Strömungsuntersuchungen in stehenden und rotierenden Schaufelkanälen mittels Laser-Doppler-Anemometrie,'' Ph.D. thesis, TU Dresden, Fortschritt-Berichte VDI, Reihe 7, Nr. 444, ISBN 3-18-344407-0, VDI-Verlag, Düsseldorf, Germany.

[20] Meyer, R. X., 1958, ''The Effect of Wakes on the Transient Pressure and Velocity Distributions in Turbomachines,'' Trans. ASME, **80**, pp. 1544–1552.

[21] Mailach, R., and Vogeler, K., 2002, ''Experimentelle Untersuchung des instationären Grenzschichtverhaltens auf den Schaufeln eines Niedergeschwindigkeits-Axialverdichters,'' DGLR-JT2002-071, Deutscher Luft-und Raumfahrtkongress, Sept. 23–26, Stuttgart, Germany.

[22] Mailach, R., and Vogeler, K., 2003, ''Wake-Induced Boundary Layer Transition in a Low-Speed Axial Compressor,'' Journal of Flow, Turbulence and Combustion, **69**(3–4), pp. 271–294.

[23] Mailach, R., and Vogeler, K., 2004, ''Aerodynamic Blade Row Interaction in an Axial Compressor, Part II: Unsteady Profile Pressure Distribution and Blade Forces,'' **126**, pp. 45–51.

[24] Dong, Y., and Cumpsty, N. A., 1990, ''Compressor Blade Boundary Layers: Part I—Test Facility and Measurements With No Incident Wakes,'' ASME J. Turbomach., **112**, pp. 222–230.

Aerodynamic Blade Row Interactions in an Axial Compressor—Part II: Unsteady Profile Pressure Distribution and Blade Forces

Ronald Mailach
e-mail: mailach@tus.mw.tu-dresden.de

Konrad Vogeler
e-mail: kvogeler@tus.mw.tu-dresden.de

Dresden University of Technology,
Institute for Fluid Mechanics,
01062 Dresden, Germany

This two-part paper presents experimental investigations of unsteady aerodynamic blade row interactions in the first stage of the four-stage low-speed research compressor of Dresden. Both the unsteady boundary layer development and the unsteady pressure distribution of the stator blades are investigated for several operating points. The measurements were carried out on pressure side and suction side at midspan. In Part II of the paper the investigations of the unsteady pressure distribution on the stator blades are presented. The experiments were carried out using piezoresistive miniature pressure sensors, which are embedded into the pressure and suction side surface of a single blade. The unsteady pressure distribution on the blade is analyzed for the design point and an operating point near the stability limit. The investigations show that it is strongly influenced by both the incoming wakes and the potential flow field of the downstream rotor blade row. If a disturbance arrives the leading edge or the trailing edge of the blade the pressure changes nearly simultaneously along the blade chord. Thus the unsteady profile pressure distribution is independent of the wake propagation within the blade passage. A phase shift of the reaction on pressure and suction side is observed. The unsteady response of the boundary layer and the profile pressure distribution is compared. Based on the unsteady pressure distribution the unsteady pressure forces of the blades are calculated and discussed. [DOI: 10.1115/1.1649742]

1 Introduction

The flow in turbomachines is highly unsteady and turbulent. Due to aerodynamic interactions the pressure distributions on the blades change considerably in time. For this reason unsteady blade forces and moments are generated. Within the whole operating range of turbomachines the rotor and stator blades, moving relative to each other, aerodynamically interact because of the viscous wakes and potential effects of the blades. Other sources stimulating unsteady blade forces are struts and inlet distortions, for instance. Critical blade vibrations are excited if the frequency of the aerodynamic excitation matches the natural frequencies of the blades. This can lead to a reduction of lifetime or even a destruction of the blading. Therefore it is necessary to improve the knowledge of the aerodynamic response of the unsteady profile pressure distributions as well as the excitation mechanism and the expected magnitude of the blade forces.

Early analytical studies into the propagation of wakes through blade rows and the excitation of unsteady blade forces were performed by Kemp and Sears [1], Meyer [2], and Lefcort [3]. Experimental data on unsteady blade forces in cascades are available from Grollius [4]. Within recent years several experimental investigations on the unsteady response of the profile pressure distributions to incoming disturbances are performed in turbomachines. Manwaring and Fleeter [5] analyzed the aerodynamic response of the rotor blades to inlet distortions in an axial research compressor. Pieper [6] investigated the unsteady pressures on the blades of a single-stage compressor with IGV. He showed the upstream influence of the rotor potential flow field on the IGV pressure distribution as well as the rotor wake influence on the downstream stator blades. Sanders and Fleeter [7] considered the unsteady response of the stator blades in a single-stage compressor to incoming wakes. Durali and Kerrebrock [8] investigated the unsteady pressure distribution in a single-stage transonic compressor and provided results on the unsteady blade forces due to the incoming wakes. Computations on the effect of wakes and the potential flow field on the excitation of unsteady blade forces were conducted by Korakianitis [9].

In a previous publication of the authors [10] results on the unsteady blade forces on the rotor and stator blades of the first stage of the Dresden low-speed research compressor (LSRC) for several operating points as well as for rotating stall are discussed. In contrast to the investigations mentioned above in this case the investigated blade rows are surrounded by up and downstream blade rows. The unsteady blade forces are influenced by the wakes as well as the potential effect of the downstream blade row.

This paper presents experimental investigations of the steady and unsteady profile pressure distributions in the four-stage Dresden LSRC. The experiments were performed on the stator blades of the first stage, which are embedded into an up and downstream rotor blade row. Results for the design point and an operating point near the stability limit will be discussed. The resulting pressure forces acting on the blades are calculated. Comparisons of the unsteady response of the surface pressure to that of the boundary layer of the stator blades, which is discussed in Part I of the paper, [11], will be drawn. The aim of the investigations is to improve the understanding of the unsteady blade row interaction process in compressors.

Contributed by the International Gas Turbine Institute and presented at the International Gas Turbine and Aeroengine Congress and Exhibition, Atlanta, GA, June 16–19, 2003. Manuscript received by the IGTI Dec. 2002; final revision Mar. 2003. Paper No. 2003-GT-38766. Review Chair: H. R. Simmons.

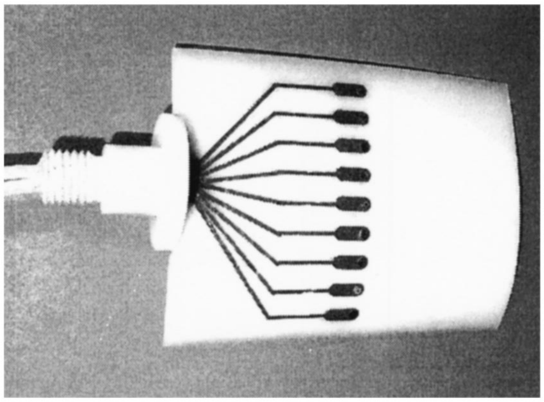

Fig. 1 Stator blade equipped with piezoresistive pressure transducers on SS and PS at midspan

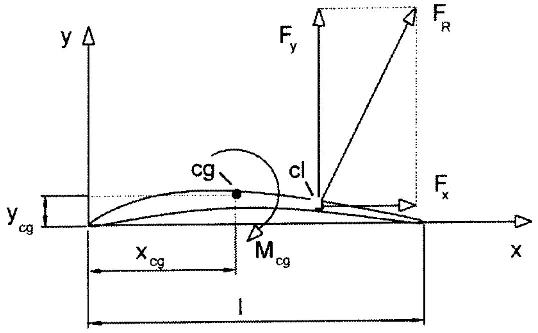

Fig. 2 Forces in blade coordinate system

2 Experimental Setup

The experiments were performed in the four-stage low-speed research compressor of Dresden University of Technology (Dresden LSRC). Information about this compressor is given in Part I of the paper, [11].

The steady and unsteady pressure distribution was investigated on the first stage stator blades at midspan on pressure side (PS) and suction side (SS). Different operating points were investigated for design speed including the design point and an operating point near the stability limit.

The steady pressure distribution on the blades was determined using pressure taps. A *Scanivalve*-system was applied to transform the pneumatic pressures to electrical voltages.

The unsteady pressures on the stator blade were acquired using time-resolving piezoresistive miniature pressure transducers (*Kulite LQ47*). The sensors are equally distributed along midspan as well on the PS and the SS of a single stator blade (**Fig. 1**). They are positioned from 10% to 90% chord with steps of 10% chord. To minimize the influence on the flow they are fitted into the blade surfaces. The positions near the leading edge and the trailing edge could not be equipped with pressure transducers without disturbing the flow noticeably.

The signals from the transducers were amplified 125 times. This was done using a separate miniature amplifier for each sensor. The signals were recorded using a 16-channel *VXI* data acquisition system of *Hewlett Packard*. The sampling rate for the measurements was 51.2 kHz while the blade passing frequency of the rotor blades is 1.05 kHz for design speed.

The considered stator blade was positioned between the wakes of the IGV, which travel through the first-stage rotor blade row. All rotor blade rows of the compressor, moving relative to the considered stator, have identical blade numbers. All rotor blades have the same geometry. They are at the same circumferential positions in each stage. Clocking effects were not investigated.

3 Data Postprocessing and Calculation of Pressure Forces

The zero point drift of the piezoresistive pressure sensors during the experiments is not negligible. To improve the precision of the results the pressure $p(t)$ was determined by adding the time-averaged pressure from the pressure taps $\overline{p}$ and the unsteady part of the pressure $\tilde{p}(t)$, measured with the piezoresistive pressure transducers for each time step.

$$p(t)=\overline{p}+\tilde{p}(t) \tag{1}$$

The time-averaged root mean square value (RMS) includes information about both periodic and stochastic pressure fluctuations

$$\overline{\mathrm{RMS}}_p=\sqrt{\frac{1}{N}\sum_{i=0}^{N-1}(p_i(t)-\overline{p})^2}. \tag{2}$$

For averaging the pressure with respect to the rotor blades the data were ensemble-averaged using a 1/rev signal. Using this method periodic and stochastic fluctuations can be separated. This was done using the equation

$$\langle p(t)\rangle=\frac{1}{K}\sum_{j=0}^{K-1}p_j(t). \tag{3}$$

The parameter $p_j(t)$ is the instantaneous pressure at a given relative position to a point of reference, which is a rotor blade in this case. The value $\langle p(t)\rangle$ is the resulting ensemble-averaged value at this relative position. In our case the number of time traces per ensemble was $K=250$.

The ensemble-averaged RMS value reveals information about the stochastic pressure fluctuations. It is calculated as follows:

$$\langle \mathrm{RMS}_p(t)\rangle=\sqrt{\frac{1}{K}\sum_{j=0}^{K-1}(p_j(t)-\langle p(t)\rangle)^2}. \tag{4}$$

On the basis of the pressure measurements the unsteady blade forces at midspan can be calculated. As in Grollius [4] the force components are referred to the blade coordinate system (**Fig. 2**). The force components are those acting along the blade chord (F_x) and perpendicular to that (F_y). The moment M_{cg} is referred to the center of gravity (cg) of the blade.

If the variation of the pressure distributions along the blade height is neglected, the force acting on the blade can be calculated as follows: The components of the blade forces as well as the moment are calculated by integrating the pressure along pressure and suction side of the blade surface with respect to the blade contour (Eqs. (5)–(7)). The blade height h has to be taken into consideration.

$$\langle F_x(t)\rangle=h\oint\langle p(t,x)\rangle\cdot\frac{dy}{dx}dx \tag{5}$$

$$\langle F_y(t)\rangle=-h\oint\langle p(t,x)\rangle dx \tag{6}$$

$$\langle M_{cg}(t)\rangle=-h\oint\langle p(t,x)\rangle\left((y_{cg}-y)\frac{dy}{dx}+(x_{cg}-x)\right)dx \tag{7}$$

Following Grollius [4] the pressure in the leading edge and the trailing edge region was extrapolated. This is necessary in particular for the calculation of F_x, since the largest portions of this force component in x-direction are induced near the leading edge and the trailing edge. The stagnation points are assumed to be at the leading and the trailing edge, respectively. The algorithm for calculating the pressure forces is described in more detail by Müller [12].

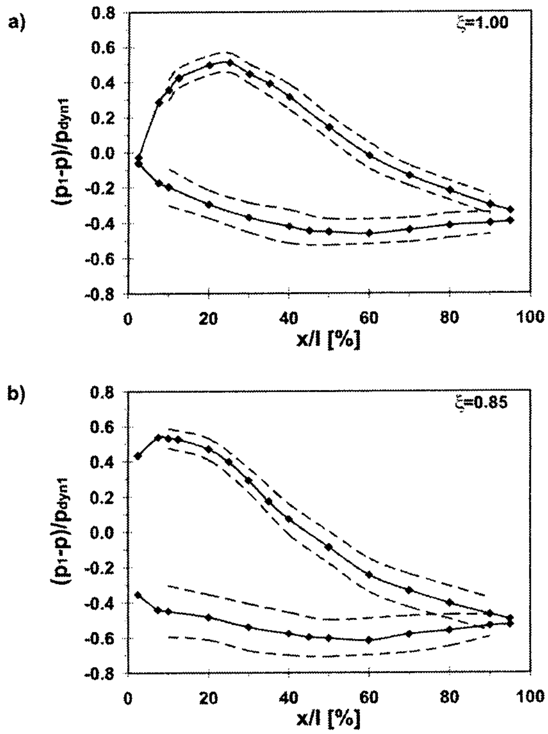

Fig. 3 Pressure distribution on the stator blades of first stage, midspan, design speed; (*a*) design point (ξ=1.00), (*b*) operating point near the stability limit (ξ=0.85)

4 Pressure Distribution on the Blades

4.1 Steady Pressure Distribution. **Figure 3** shows the steady pressure distribution at midspan of the stator blades for the design point ($\xi=1.00$) and an operating point near the stability limit ($\xi=0.85$) for design speed. In addition the statistical fluctuations around the steady distribution are represented (dashed lines). In this case the pressure coefficient is calculated from the time-averaged values $\overline{p}\pm\overline{\mathrm{RMS}}_p$.

For the design point on the SS an acceleration of the flow can be observed between the leading edge and 25% of chord length, where the minimum pressure is reached. After this point the flow is decelerating. The strongest adverse pressure gradient occurs between 40–50% of chord length. After that point the pressure gradient decreases. On the PS of the stator blades the flow decelerates between the leading edge and 60% chord and slightly accelerates between that position and the trailing edge.

Strong fluctuations around the mean values occur. The fluctuations on the PS are larger than on SS. Both on PS and SS maximum fluctuations can be found for strongest deceleration of the flow. This is near the leading edge on PS and around 50% chord on SS.

Approaching the stability limit ($\xi=0.85$) the aerodynamic loading of the blades increase. The point of minimum pressure on the SS is shifted toward the leading edge and can be found at 10% chord. As for the design point the flow on the PS decelerates between the leading edge and 60% chord and slightly accelerates between this position and the trailing edge.

On the SS the fluctuations noticeably increase at the point of the strongest adverse pressure gradient (30–40% chord). Behind that point the fluctuations remain on a high nearly constant level. The fluctuations on the PS increase along the whole blade chord. Maximum values appear in the front part of the blade where the flow decelerates.

For the operating point near the stability limit the level of fluctuations on both sides of the blade is higher than for the design point. This is due to the higher blade loading, responsible for a stronger periodic influence of the wakes and the potential effects.

4.2 Unsteady Pressure Distribution

4.2.1 Design Point. The stator blade row of the first stage is embedded into up and downstream rotor blade rows with identical blade numbers. This is why the unsteady pressure distribution is affected by both the wakes and the potential effect of the upstream blade row and the potential effect of the downstream blade row. Following results on the unsteady pressure distributions on PS and SS of the stator blades for the design point and an operating point near the stability limit will be discussed (**Figs. 4** and **5**).

Figures 4(*a–d*) shows the unsteady response of the stator pressure distribution with respect to the influences of the up and downstream rotor blade rows for the design point. This figure reveals information about the rotor-periodic pressure and the stochastic pressure fluctuations with respect to the relative position of the rotor. The time is related to the blade passing period of the rotor blades t_{rotor}. For comparison the wake propagation in the passage near SS is shown (**Figs. 4(*c,d*)**, dashed line). (On the PS the wake propagation is not visualized, since no interaction between the wake in the passage and the surface pressure could be detected.)

Generally the circulation of a blade changes if the inlet or outlet flow conditions of the blade vary. Thus the circulation as well as the profile pressure distribution of the considered stator blade changes for every passing rotor blade of the up and downstream blade rows.

If a rotor wake impinges on the leading edge of the stator blade the circulation of this blade changes due to the changing incidence angle and velocity. Because of this the wake influence propagates along the blade surface towards the trailing edge with the velocity of sound. Thus the surface pressure is independent of the wake propagation within the stator passages **(Figs. 4(*a,c*))**. This corresponds to the observations of Sanders and Fleeter [7] and Durali and Kerrebrock [8]. The data discussed there were obtained without a downstream blade row.

The potential effect of the downstream rotor blades propagates upstream with the velocity of sound. This is the reason why the pressure along the surface responds to this rotor-periodic influence again nearly instantaneously in time **(Figs. 4(*a,c*))**. As already described in Section 4.1 the highest pressure fluctuations on PS and SS along the blade surface can be observed in the regions with decelerated flow.

Because of the identical blade numbers of the up and downstream rotor blade row and the fast propagation of the pressure fluctuations along the blade surface the influence of the wakes and the potential effect of the downstream blade row can not clearly be distinguished.

In a previous investigation on the rotor blades of the Dresden LSRC the authors showed that both the wakes and the potential effect have a strong influence on the unsteady pressure distribution, [10]. In this case the up and downstream blade rows (IGV and stator 1) had different blade numbers. So the influences of these two blade rows on the unsteady pressure distribution of the rotor could be distinguished. However, the potential effect of the stator blades had a much stronger effect than the IGV wakes, [10].

Several pressure peaks can be observed during one passing period at a given position of the blade **(Figs. 4(*a,c*))**. This becomes more obvious in **Fig. 6**, which explicitly shows the results for the midchord position on PS and SS. The appearance of several peaks within one blade passing period is presumably caused by the phase shift of the arrival of the incoming wakes at the leading edge and the potential flow field at the trailing edge of the considered stator blade. These peaks are reflected as higher harmonics in a frequency spectrum (not shown).

However, it can be seen in the data published by Sanders and Fleeter [7] and Durali and Kerrebrock [8] that more than one peak can appear due to the passing of a wake only. In contrast to that

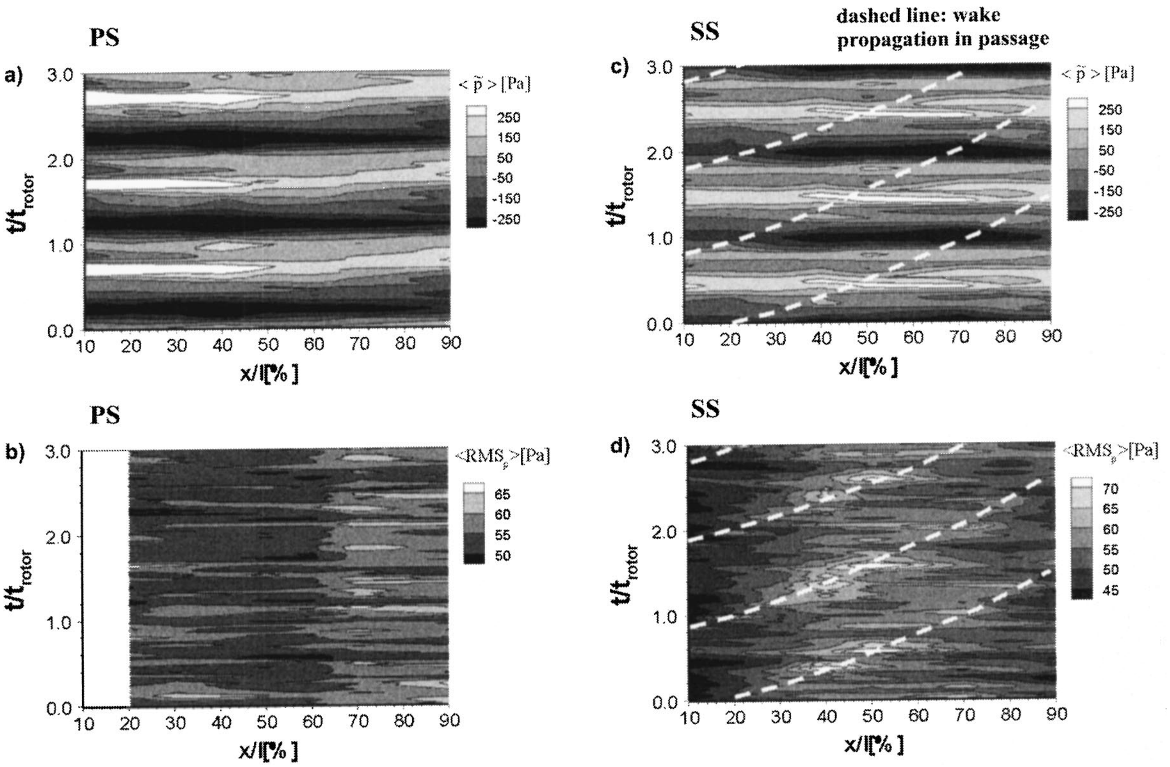

Fig. 4 Unsteady pressure distribution on PS and SS of the stator blades of the first stage, midspan, design point (ξ=1.0)

Stadtmüller and Fottner [13] observed a single wavelike pressure variation on the blade surface as a result of a passing wake.

The shape of the pressure development in time is comparable on both sides of the blade. A phase shift of the unsteady pressure of 90 deg can be observed between PS and SS of the blade (**Figs. 4(*a,c*)** and **Fig. 6**). **Figure 6** clearly shows for the midchord positions, that this phase shift is constant in time. This is because of the same blade numbers of the up and downstream blade rows.

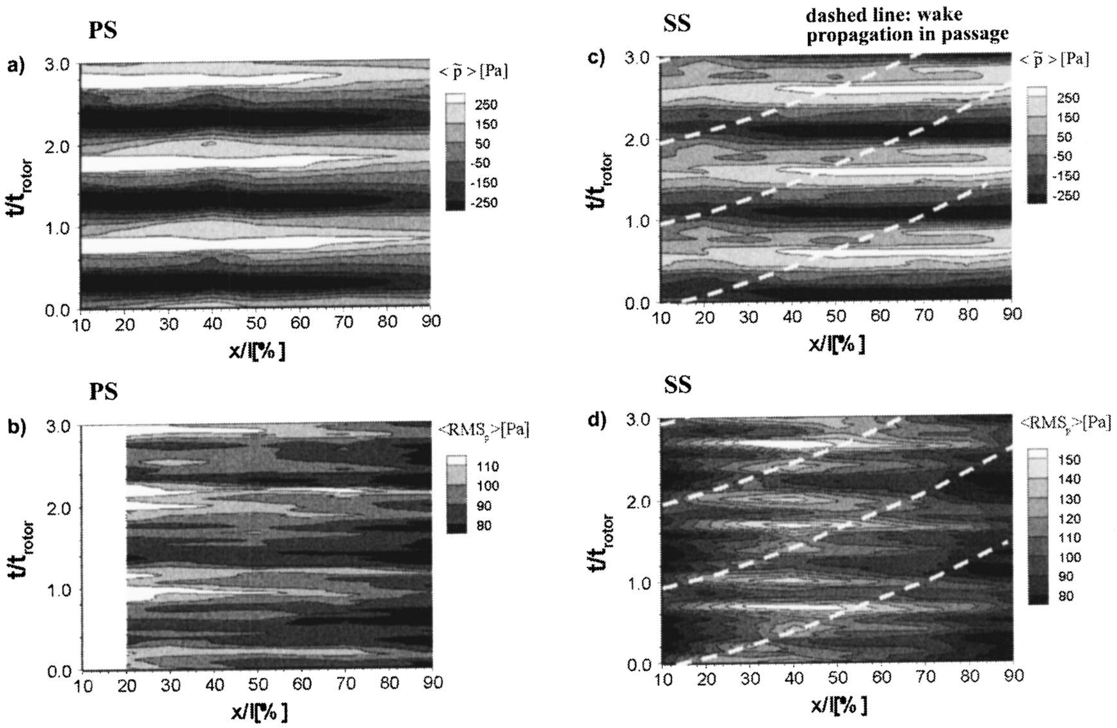

Fig. 5 Unsteady pressure distribution on PS and SS of the stator blades of the first stage, midspan, operating point near the stability limit, design speed (ξ=0.85)

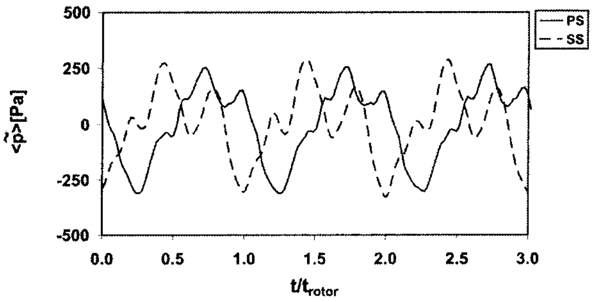

Fig. 6 Unsteady pressure on PS and SS of the stator blade, midspan, 50% chord, design point (ξ=1.0)

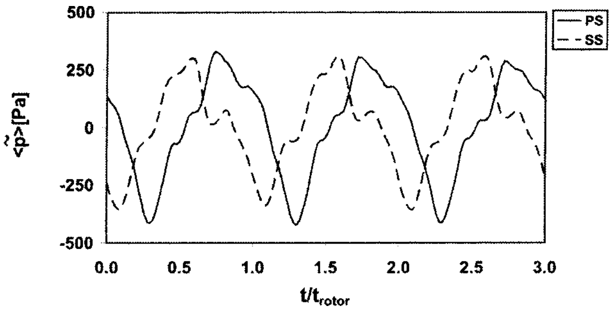

Fig. 7 Unsteady pressure on PS and SS of the stator blade, midspan, 50% chord, operating point near the stability limit (ξ=0.85), design speed

The pressure on the SS reacts earlier on the periodic influences of the wakes and the upstream propagating potential effect.

In contrast to our results Sanders and Fleeter [7] observed a phase shift of 180 deg between PS and SS as a response to incoming wakes. Also in the data published by Durali and Kerrebrock [8] a phase shift between PS and SS on incoming wakes can be seen, but the amount of the phase shift is not specified.

On the first stage rotor blades of the Dresden LSRC a phase shift between PS and SS, varying in time between 90–180 deg, was observed (Mailach et al. [10]). In this case the surface pressure on the rotor blades is influenced by the IGV and the downstream stator blades, moving relative to the observed rotor blade. The IGV and the stator have different blade numbers. Due to that the time difference between the arrival of the IGV wakes at the leading edge and the potential effect of the downstream stator blades at the trailing edge of the rotor blades changes in time. This is the reason why the phase of the pressure on PS and SS of the rotor blade varies in time.

For the design point the stochastic fluctuations on the PS of the stator blade are nearly constant along the chord and without dominating periodic portions **(Fig. 4(*b*))**. The fluctuations are clearly lower than on the SS.

Near the leading edge on the SS, where the flow accelerates, the fluctuations are comparably small **(Fig. 4(*d*))**. Increasing fluctuations can be found around 20% chord, where the flow starts to decelerate. Maximum values can be found at 40–50% chord, where the deceleration is strongest. Near the trailing edge with moderate deceleration the fluctuations decrease.

Furthermore, clear periodic fluctuations can be found on the SS. It can be seen in **Fig. 4(*d*)** that higher fluctuations appear along the path of the wake propagation in the passage (dashed line). The spot-like appearance of the pressure maxima on the wake paths is due to the limited number of measuring positions. So the pressure on the blade surface is not completely independent from the wake propagation in the passage. However, the ensemble-averaged pressure does not provide an indication of the wake propagation **(Fig. 4(*c*))**.

On the PS the wake propagation in the passage is not visible in the ensemble-averaged results of the blade surface pressure.

4.2.2 Operating Point Near the Stability Limit. The pressure development on the blades does not change significantly when approaching the stability limit of the compressor.

As for the design point the pressure reacts nearly instantaneously in time along the blade surface due to the influence of wakes and potential effects of the blades **(Figs. 5(*a–d*))**. The amplitudes are somewhat higher than for the design point. Again several peaks are superimposed on a basically wavelike pressure variation during the blade passing. These several pressure maxima are less significant compared to the design point **(Figs. 5(*a,c*)**, **Fig. 7)**. This may be due to the stronger fluctuations of the flow field near the stability limit of the compressor.

As for the design point comparable pressure traces with a phase shift can be seen for the same chordwise position on PS and SS **(Fig. 7)**. This phase shift is reduced to 70–80 deg (design point: 90 deg). As discussed before the time distance between the arrival of the wake at the leading edge and the potential flow field at the trailing edge seems to be responsible for this effect.

The fluctuations on both sides of the blades are clearly increased compared to the design point, whereby higher values can be recognized on the SS **(Figs. 5(*b,d*))**. Due to the higher loading the stochastic fluctuations on the pressure side increase in the front part of the blade. Both on the PS and the SS a double peak of the fluctuations appears during each blade passing. These fluctuations seem to stem from the potential effect of the downstream rotor blades as they propagate very fast from the trailing edge to the leading edge of the considered stator blade. This is more clearly visible on the SS (**Fig. 5(*d*)**, $t/t_{\text{rotor}}=0.70/1.05$). The reason for the larger influence of the potential flow field is the higher pressure increase over the blade row (respectively, the compressor).

Again fluctuations due to the wake propagation in the passage can only be seen on the SS (**Fig. 5(*d*)**, dashed line). This influence can be tracked to about 50% chord.

5 Unsteady Pressure Forces

The unsteady pressure forces on the stator blades were determined using the algorithm described in Section 3. As a result of this the time traces of the force components and the moment are represented in **Fig. 8**. Typical results are shown for the design point. The values are related to the respective time-mean value in each case. The mean value of F_y is about 10 times the mean value of F_x.

The unsteady pressures and consequently the forces on the stator blades are periodically influenced by the up and downstream passing rotor blades **(Fig. 8)**. Thus the rotor passing period is clearly visible for the force components and the moment. Again several peaks appear during one passing period. The shape of the time traces of the dominating force component and the pressure fluctuation is comparable **(Fig. 8(*a*)**, **Fig. 6)**. This is mainly due to the fact that the pressure changes nearly instantaneously along the blade chord due to the aerodynamic interaction of the blade rows. Certainly the phase shift of the pressure between PS and SS influences the shape of the resulting time-dependent force traces as well.

The maximum fluctuation amplitudes of the force component F_y are about ±30% of its mean value. Those of F_x are somewhat lower. High fluctuation amplitudes can be observed for the moment around the center of gravity of the blade, which is again related to its mean value. This parameter is strongly dependent on the blade profile, especially on the blade curvature.

Comparable amplitudes for the unsteady force fluctuations of 25% are reported by Durali and Kerrebrock [8]. However, these authors showed results for the force component in axial and circumferential directions. For comparison we calculated these force components for our data. The shapes of the time traces of these

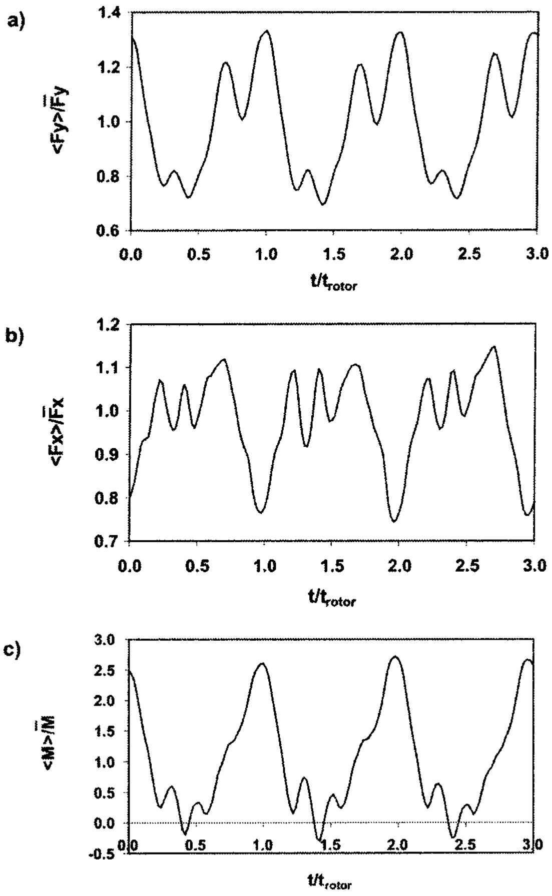

Fig. 8 Unsteady force components and moment on stator blades, design point (ξ=1.0)

force components are comparable to that of F_y in **Fig. 8(*a*)**. The fluctuations are in the same order of magnitude as for the F_y component.

A consideration of the frequency components of the pressure forces is useful for an estimation of the excited blade vibrations and a comparison to the natural frequencies of the blades. In the frequency spectrum the different periodic influences can clearly be separated from each other. As an example this is done for the force component normal to the blade F_y (**Fig. 9**). In accordance to the previous findings the rotor blade passing frequency (BPF) and its higher harmonics dominates the frequency distribution of the stator blade forces. The highest amplitudes occur for the 1. BPF. The periodic forces for the 3. BPF are of stronger influence than the 2. BPF. This is due to the fact that three more or less distinct peaks appear during the passing period of the rotor blades **(Fig. 8)**. Higher frequency components up to the 6. BPF can be observed with small amplitudes. Other discrete frequency components, which are not related to the rotor blade passing, do not appear.

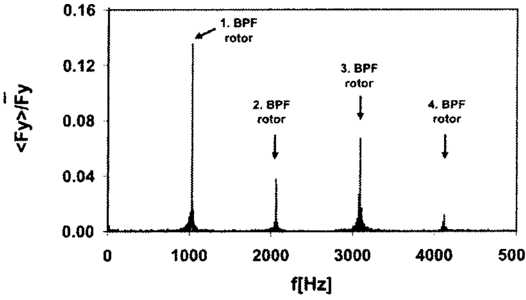

Fig. 9 Frequency spectrum of force component F_y of the stator blade, design point (ξ=1.0)

For the operating point near the stability limit (ξ=0.85) the unsteady forces are of the same order of magnitude as for the design point. The shape of the time-resolved pressure and the phase shift between PS and SS determine the shape of the unsteady force versus time and consequently their frequency content. For ξ=0.85 a slight increase of the amplitudes of the 1. BPF as well as a clear decrease of the 3. BPF of the frequency content of the forces can be observed. This is in accordance to the shape of the time-dependent pressure traces shown before (Section 4.2). More results for different operating points are discussed in [10].

6 Conclusions

In this two-part paper experimental investigations of unsteady aerodynamic blade row interactions in the first stage of the four-stage low-speed research compressor of Dresden are presented. The measurements were carried out on pressure side and suction side of the stator blades at midspan. Two different operating points were observed. In Part I of the paper results on the unsteady boundary layer behavior are discussed. Part II is focused on the unsteady profile pressure distribution and provides results on the unsteady blade forces.

It has been shown that the mechanisms of the unsteady response of the boundary layer and that of the profile pressure distribution to incoming wakes and potential effects of the downstream blade row are basically different.

The boundary layer development is crucially influenced by the incoming wakes. The potential effect of the downstream blade row is less important for the transition process. The propagation of the wake-induced path within the boundary layer is coupled to the wake propagation in the passage, whereby the propagation velocities differ.

In contrast the pressure distribution definitely reacts both to the incoming wakes of the upstream rotor blade row and the potential effects of the downstream rotor blade row. The unsteady circulation of the considered stator blade changes for every passing rotor blade of the up and downstream blade rows. As a result of this the unsteady pressure along the blade chord reacts nearly instantaneously if a wake arrives the leading edge or if the potential flow field of the downstream blade row affects the flow at the trailing edge of the considered stator blade. Thus the changes of the unsteady profile pressure due to the wakes are principally independent from the wake propagation in the blade passage. As discussed, the influences of the wakes and the potential effect cannot clearly be distinguished for the given experimental setup.

Between pressure side and suction side of the blade a phase shift of the response to the disturbances can be observed. The phase shift is 90° for the design point and reduces to 70–80 deg for an operating point near the stability limit. The time lag between the arrival of the wakes and the potential effects at the leading and the trailing edge of the blade seems to be responsible for the shape of the time traces of the pressure. The shapes of the pressure traces are comparable on pressure and suction sides.

Based on the unsteady pressure distributions the blade forces are calculated. The wakes and the potential effects of the surrounding rotor blade rows are responsible for unsteady changes of the blade forces. The amplitudes of the unsteady forces are up to 30% of the mean values. The time traces as well as the frequency content of the unsteady blade forces are discussed.

Acknowledgments

The work reported in this paper was performed within the project: "Unsteady Forces and Boundary Layer Behavior on the Blades of a Low-Speed Axial Compressor" which is part of the joint project: "Periodical Unsteady Flow in Turbomachines" funded by the DFG (German Research Society). Information on this project can be found at http://www.turboflow.tu-berlin.de. The permission for publication is gratefully acknowledged.

Nomenclature

$\langle\ \rangle$ = ensemble-averaged value
$\overline{\ \ }$ = mean value
f = frequency (Hz)
F = force (N)
h = blade height (m)
K = number of time traces
l = chord length (m)
M = moment (Nm)
N = number of time traces per ensemble
p = pressure (Pa)
$\tilde{p}$ = fluctuating part of pressure (Pa)
RMS_p = root mean square of pressure (Pa)
t = time (s)
x = chordwise position (m)
y = position perpendicular to chord (m)
ξ = mass flow/design mass flow

Subscripts

l = measuring plane upstream of the blade row
dyn = dynamic
i,j = indices for time traces
j = index for time trace
x = component in blade chord direction
y = component perpendicular to the blade chord

Abbreviations

BPF = blade passing frequency
cg = center of gravity
cl = center of lift
LSRC = low-speed research compressor
IGV = inlet guide vane
PS = pressure side
SS = suction side

References

[1] Kemp, N. H., and Sears, W. R., 1955, ''The Unsteady Forces Due to Viscous Wakes in Turbomachines,'' J. Aeronaut. Sci., July, pp. 478–483.

[2] Meyer, R. X., 1958, ''The Effect of Wakes on the Transient Pressure and Velocity Distributions in Turbomachines,'' Trans. ASME, **80**, pp. 1544–1552.

[3] Lefcort, M. D., 1965, ''An Investigation Into Unsteady Blade Forces in Turbomachines,'' ASME J. Eng. Gas Turbines Power, **87**, pp. 345–354.

[4] Grollius, H.-W., 1981, ''Experimentelle Untersuchung von Rotor-Nachlaufdellen und deren Auswirkungen auf die dynamische Belastung axialer Verdichter- und Turbinengitter,'' Ph.D. thesis, RWTH Aachen, Germany.

[5] Manwaring, S. R., and Fleeter, S., 1991, ''Forcing Function Effects on Rotor Periodic Aerodynamic Response,'' ASME J. Turbomach., **113**, pp. 312–319.

[6] Pieper, S. J., 1995, ''Erfassung instationärer Strömungsvorgänge in einem hochtourigen invers ausgelegten einstufigen Axialverdichter mit Vorleitrad,'' Ph.D. thesis, RWTH Aachen, Germany.

[7] Sanders, A. J., and Fleeter, S., 2001, ''Multi-Blade Row Interactions in a Transonic Axial Compressor, Part II: Rotor Wake Forcing Function & Stator Unsteady Aerodynamic Response,'' ASME 2001-GT-0269.

[8] Durali, M., and Kerrebrock, J. L., 1998, ''Stator Performance and Unsteady Loading in Transonic Compressor Stages,'' ASME J. Turbomach., **120**, pp. 224–232.

[9] Korakianitis, T., 1993, ''On the Propagation of Viscous Wakes and Potential Flow in Axial-Turbine Cascades,'' ASME J. Turbomach., **115**, pp. 118–127.

[10] Mailach, R., Müller, L., and Vogeler, K, 2003, ''Experimental Investigation of Unsteady Forces on Rotor and Stator Blades of an Axial Compressor,'' *Proceedings of the 5th European Conference on Turbomachinery—Fluid Dynamics and Thermodynamics*, M. Stastny, C. H. Sieverding, and G. Bois, eds., Mar. 18–21, Prague, Czech Republic, pp. 221–233.

[11] Mailach, R., and Vogeler, K., 2003, ''Aerodynamic Blade Row Interaction in an Axial Compressor, Part I: Unsteady Boundary Layer Development,'' ASME-GT2003-38765.

[12] Müller, L., 2002, ''Zeitaufgelöste Bestimmung von Schaufelkräften auf Verdichterschaufeln,'' Diploma thesis, TU Dresden, Germany.

[13] Stadtmüller, P., and Fottner, L., 2000, ''Fast Response Pressure Transducers for the Investigation of Wake-Induced Transition on a Highly Loaded LP Turbine,'' *Proceedings of the XVth Bi-Annual Symposium on Measuring Techniques in Transonic and Supersonic Flows in Cascades and Turbomachines*, Sept. 21–22, Firenze, Italy.

O. G. McGee
Department of Civil and Environmental
Engineering and Geodetic Science,
The Ohio State University,
Columbus, OH 43210

M. B. Graf
Mars and Company,
124 Mason Street,
Greenwich, CT 06830

L. G. Fréchette
Department of Mechanical Engineering,
Columbia University,
New York, NY 10027

Tailored Structural Design and Aeromechanical Control of Axial Compressor Stall—Part I: Development of Models and Metrics

This two-part paper presents general methodologies for the evaluation of passive compressor stabilization strategies using tailored structural design and aeromechanical feedback control (Part I), and quantitatively compares the performance of several aeromechanical stabilization approaches which could potentially be implemented in gas turbine compression systems (Part II). Together, these papers offer a systematic study of the influence of ten aeromechanical feedback controllers to increase the range of stable compressor operation, using static pressure sensing and local structural actuation to postpone modal stall inception. In this part, the stability of aeromechanically compensated compressors was determined from the linearized structural-hydrodynamic equations of stall inception. New metrics were derived, which measure the level of aeromechanical damping, or control authority of aeromechanical feedback stabilization. They indicate that the phase between the pressure disturbances and the actuation is central to assess the impact of aeromechanical interactions on compressors stability.

[DOI: 10.1115/1.1644555]

1 Introduction

The operating range of aeroengine compression systems is limited by two classes of aerodynamic instabilities known as rotating stall and surge (Emmons et al. [1]). *Rotating stall* is a multidimensional instability in which regions of low or reversed mass flow (i.e., stall cells), propagate around the compressor annulus, due to incidence variations on adjacent airfoils (Greitzer [2–4]). *Surge* is a primarily one-dimensional instability of the entire pumping system (compressor, ducts, plenums, and throttle). It is characterized by axial pulsations in annulus-averaged mass flow, including periods of flow reversal through the machine. In low-speed (incompressible) machines, stall and surge may be viewed as distinct aerodynamic instabilities; in high-speed machines, experimental evidence suggests that once rotating stall is initiated, surge is quickly triggered often after a few rotor revolutions (Greitzer [2] and Day [5]). With either instability, the compression system experiences a substantial loss in performance and operability, which may even include mechanical failure.

An experienced-based approach for avoiding this is to operate the compressor at a safe range from the point of instability onset (i.e., with stall margin). This stall margin ensures that the engine can withstand transient operation. However, the margin also reduces the available pressure rise and efficiency of the machine. Addition of dynamic components interacting with the compressor flow path have been shown to inhibit the inception of rotating stall, effectively extending the stable operating range, hence, allowing higher performance operating conditions. Significant stall margin improvements have been realized in single-stage and multistage laboratory compressors, using both *electromechanical* or ‘‘active’’ control and *aeromechanical* feedback control.

Aeromechanical feedback can be loosely defined as the dynamic interaction between flexible structures and fluid dynamics of the compression system, without external electromechanical input. When approaching the stall line, flow perturbations induce local pressures on the structures. When tailored with the appropriate dynamic characteristics, the structure deforms, to counteract flow perturbation disturbances, either directly or by modifying the local unsteady pressure rise of the compressor. Compressor stabilization using aeromechanical feedback control is investigated here as a *passive* means of improving stability so that the compressor can operate safely at lower mass flows. This approach incorporates tailored structural feedback control within the machine that can alter the fluid dynamic behavior, so that the performance of the compressor can be extrapolated to operating ranges outside the empirical database generated by years of experience. In contrast, active control implements this approach through digitally controlled electromechanical actuation. Practical challenges in implementing active flow control, mostly due to cost, weight, and reliability of actuators, have precluded their application in production engines. Although passive approaches could overcome these drawbacks, they have received little attention outside the work of Gysling et al. [6] and Gysling and Greitzer [7].

Fluid-structural interaction effects are not only important in devising compressor stabilization strategies, but they are also useful in establishing constraints on the structural design of compression systems. As lightweight, less rigid structures are incorporated into new designs, the level of fluid-structure interactions is likely to increase and result in reduced stall margin, if the structures are not properly tailored. The practical incentive here is to achieve lightweight, more efficient compressor builds using tailored, less rigid structures, while preventing potential stall margin reductions. There is therefore a need for a broad study evaluating the potential of various passive control schemes in order to better assess the effect of aeromechanical interaction on compressor stability.

Contributed by the International Gas Turbine Institute and presented at the International Gas Turbine and Aeroengine Congress and Exhibition, Atlanta, GA, June 16–19, 2003. Manuscript received by the IGTI Dec. 2002; final revision Mar. 2003. Paper No. 2003-GT-38975. Review Chair: H. R. Simmons.

2 Objectives and Scope of Study

To meet this need, this two-part paper presents a systematic study on tailored structural design and aeromechanical feedback stabilization of rotating stall in axial compressors that employ static pressure sensing and structural actuation for dynamic compensation. The overarching goals of this study are to evaluate the role of flexible structures on compressor stability, and to elucidate that a proper choice of local structural dynamic compensation close-coupled to the compressor affects (either beneficially or detrimentally) the stability of the system. Analytical stability models are developed for ten aeromechanical feedback stabilization strategies. Since discretized numerical analysis of coupled fluid-mechanical unsteady interactions in a multi-stage compressor would be computationally intractable, the low-order modeling approach adopted here was required.

Furthermore, this paper will focus on a class of instabilities referred to as long-wave length, modal stall inception, which consists of flow non-uniformities that extend around the compressor annulus and can grow into a rotating stall cell if the compressor adds energy to these modes. Extensive literature has been developed to mathematically represent the stability of such pre-stall waves (Moore [8], Moore and Greitzer [9], Greitzer and Moore [10], Haynes et al. [11], Longley [12], Bonnaure [13], Hendricks et al. [14], Feulner et al. [15], and Fréchette [16]). This representation has been validated through experiments that postponed the inception of rotation stall using active control (Haynes et al. [11], Paduano et al. [17], Vo [18], and Weigl et al. [19]). This behavior is in contrast with short wave length stall inception noticed in some compressors, typically due to local disturbances in the tip region flows, which induce a rotating stall cell. The development of models predicting this short wavelength phenomenon continues to be an area of research interest (Camp and Day [20] and Hoying [21]), and at present no complete low-order model exists. This study is therefore restricted to long wavelength stall inception, which naturally occurs in any annular compression system, as long as short wavelength stall does not occur at a higher, nominally more stable flow rate.

This first part of the paper outlines the modeling methodology and defines new metric to evaluate the stability of aeromechanically compensated axial compressors. In the following sections, we (i) describe the various aeromechanical stabilization schemes and the relevant assumptions underpinning the modeling development, (ii) derive the structural-hydrodynamic stability conditions, and (iii) formulate the annulus-average unsteady work required for aeromechanically stabilized compression systems. The second part of this two-part paper will use these models and metric to quantify the impact of aeromechanical interaction on compressor stability in order to identify the most promising passive control approaches, as well as potentially destabilizing fluid-structure interactions.

3 Schemes and Modeling Assumptions

The aeromechanical feedback strategies studied are shown in **Fig. 1** and listed in **Table 1**. They are categorized as (i) dynamic fluid injection (with and without exit flow recirculation) to supplement the axial momentum entering the compressor, implemented with a circumferential array of reed valve injectors that react to local static pressure (Gysling and Greitzer [7]) (Schemes #1 to #4); (ii) movable compressor inlet and exit duct walls for flow field impedance control, potentially implemented as flexible wall liners or as a structurally tuned case that resonates with the pre-stall, local static pressure fluctuations (Schemes #5 to #7); (iii) flexible compressor casing wall to provide dynamic control of rotor tip clearance flow processes, implemented through structurally tuned casing or flexible casing treatment (Scheme #8); and (iv) dynamically restaggered inlet guide vanes and rotor blades, possibly implemented through flexible root attachments or structurally tuned blades (Schemes #9 & #10). Pressure fluctuations in the linear, pre-stall regime are typically very small, inducing and requiring only small structural deformations for these schemes. The stabilizing physical mechanisms introduced by these aeromechanical feedback schemes differ in phenomenology and are qualitatively described in the companion paper (Fréchette et al. [22]).

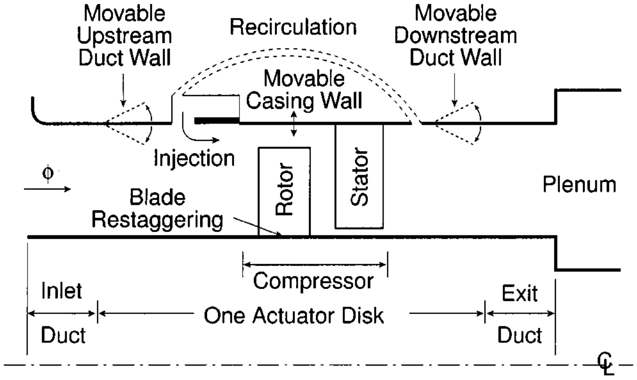

Fig. 1 Illustration of aeromechanical feedback schemes

This broad range of aeromechanical control schemes is considered without limiting the study to the most practical schemes to implement. Doing so provides further insight on the impact of fluid-structure interactions on rotating stall inception, and an indication of which phenomena are most stabilizing or destabilizing. Various combinations of actuation principles and sensing locations (upstream, downstream, average) are therefore investigated here. Further design work would then be required to define a practical configuration that implements the most promising approaches.

A schematic of the system considered is shown in **Fig. 1**. Flow enters through an inlet duct, a compressor then pumps the flow through an exit duct to a plenum, which then exhausts through a throttle (not shown) and an exit nozzle (not shown). The aeromechanical components are integrated at one of the various locations shown.

Modeling of the compressor and ducts is identical to that presented by Longley [12] and described in more detail by McGee et al. [23]. Flow is considered to be incompressible through a constant annulus compressor, allowing the analysis of fundamental pre-stall dynamics only. With regard to the aeromechanical control schemes, the following assumptions were employed. The axial location of the aeromechanical feedback device was assumed to be short and close enough (compared to the circumfer-

Table 1 Aeromechanical feedback schemes

Scheme	Description
#1	Radially mixed-out injection at the compressor face
#2	Tip injection at the rotor leading edge
#3	Radially mixed-out injection at the compressor face with exit flow recirculation
#4	Tip injection at the rotor leading edge with exit flow recirculation
#5	Movable inlet duct wall with inlet static pressure sensing
#6	Movable exit duct wall with inlet static pressure sensing
#7	Movable exit duct wall with exit static pressure sensing
#8	Movable casing wall with front-to-back average static pressure sensing
#9	Dynamically restaggered inlet guide vanes with inlet static pressure sensing
#10	Dynamically restaggered rotor blades with front-to-back average static pressure sensing

ential length scale of the upstream disturbances) that it could be combined with the actuator disk describing the compressor, as shown in **Fig. 1**. Circumferentially, the aeromechanical elements are assumed to be of shorter extent than the flow perturbations considered, suggesting eight or more injectors or flexible wall segments uniformly distributed around the annulus. Also, aeromechanical feedback stabilization employing exit flow recirculation was assumed to alter only mass and momentum conservation, and not temperature upstream and downstream of the compressor, since only low-speed compression systems were considered (incompressible flow). Finally, it was assumed that the unsteady pressure rise across the compressor with aeromechanical feedback did not respond instantaneously to flow variations. Thus, an enhanced actuator disk model including transient lag dynamics (Longley [12] and Haynes et al. [11]) was used, which accounts for: (i) finite reaction time for viscous dissipation to affect the compressor pressure rise response to flow unsteadiness, and (ii) flow turning (deviation) delays in the rotors and stators.

Based on these approximations, the governing differential equations for the system were derived and a stability analysis was performed. The growth or decay of small perturbations superimposed on a uniform, axisymmetric background flow, is determined from an analysis of the linearized version of the governing equations. Mathematically, it is the eigenvalues of these linearized equations that determine the disturbance growth or decay and hence, the stability. The derivation of the compression systems models is given below.

4 Stability Modeling of Compression Systems With Aeromechanical Feedback

To facilitate description and illustrate the modeling process, an enhanced rotating stall model including transient loss dynamics is developed for the dynamic fluid injection aeromechanical stabilization scheme #1. Having provided this example in detail, the equations describing the remaining nine schemes are then provided in the Appendix. First, a few relevant suppositions connected to scheme #1 are given, which will provide a framework to view the problem.

Scheme #1 utilizes an unsteady injection process to dynamically add momentum to flow entering the compressor and damp inlet pre-stall disturbances. The mechanical arrangement would be similar to that tested by Gysling and Greitzer [7] wherein a set of reed valves are distributed around the annulus to provide control of the injected flow. The cantilever reeds sense the unsteady pre-stall pressure perturbations in the inlet duct, and when the perturbation amplitude is sufficiently large, the reed valves are forced (by the perturbations) to open allowing a discrete flow to be injected into the primary gas path from a plenum surrounding the casing. The injected flow enters the upstream duct and is assumed to mix radially before entering the compressor.

The flow through the actuator disk is coupled to the up and downstream flow fields by four matching conditions across the compressor and injection region. The first and second conditions are kinematic and prescribe that the mean axial velocity distribution is constant at axial stations just upstream of the injection region and just downstream of the compressor, and that the flow exits the machine with constant leaving angle through a high solidity blade row. The next two matching conditions are dynamic and are derived using mass and momentum conservation across the injection region and compressor. The general description of the injection process is nonlinear, however, the initial evolution of the pre-stall disturbances can be deduced from the linearized equations governing small unsteady perturbations from the steady, axisymmetric background flow. These perturbations can be expressed as: $\delta\phi = \tilde{\phi}_n e^{(in\theta + s_n\tau)}$, where the harmonic, n, describes the circumferential shape. The temporal behavior is defined by the eigenvalue, $s_n = \sigma + i\omega$, where σ is the growth rate of the perturbation and ω its frequency as it rotates around the annulus. Considering this leads to linearized partial differential equations which relate perturbation variables (i.e., the local axial velocity $\delta\phi$, its derivatives, and the structural controller response $\delta\varepsilon_r$) upstream of the injection region and downstream of the compressor (Gysling and Greitzer [7]). Therefore, conservation of mass across the region gives

$$\delta\phi_u + [\,\cdot\,]_{\text{mass flow, aeromechanical}} = \delta\phi_d\,, \tag{1}$$

where the operator is steady-state injected flow scaled by the normalized response of the structural controller, $\delta\varepsilon_r$,

$$[\,\cdot\,]_{\text{mass flow, aeromechanical}} = \Phi_i\,\delta\varepsilon_r\,. \tag{2}$$

Momentum conservation across the region gives

$$\delta\psi_{ts} = \delta\psi_{s_d} - \delta\psi_{t_u} = \frac{\partial\psi_{\text{ideal}}}{\partial\phi}\,\delta\phi_u - \delta L_{\phi S} - \delta L_{\phi R} - \delta L_{dS} - \delta L_{dR} - \lambda\,\frac{\partial\delta\phi_u}{\partial\theta} - \mu\,\frac{\partial\delta\phi_u}{\partial\tau} + [\,\cdot\,]_{\text{pressure rise, aeromechanical}}\,. \tag{3}$$

This equation shows that the change in total-to-static pressure rise across the compressor, $\delta\psi_{ts}$, depends upon the quasi-steady change in pressure rise with flow, unsteady losses and deviations, the circumferential and temporal variations in flow, and lastly, the pressure changes associated with the aeromechanical control. This last term is given by the operator,

$$[\,\cdot\,]_{\text{pressure rise, aeromechanical}} = \frac{\partial\psi_{ideal}}{\partial\phi}\,\Phi_i\,\delta\varepsilon_r - \lambda\Phi_i\frac{\partial\delta\varepsilon_r}{\partial\theta} - \mu\Phi_i\frac{\partial\delta\varepsilon_r}{\partial\tau} + 2\Phi_i(\Phi_i - \Phi_u)\,\delta\varepsilon_r\,, \tag{4}$$

and the measured inlet total-to-static pressure rise ψ_{ts} is related to the ideal pressure rise ψ_{ideal} by

$$\psi_{ts} = \psi_{\text{ideal}} - L_{\phi S} - L_{\phi R} - L_{dS} - L_{dR}\,, \tag{5}$$

while λ and μ are inertia parameters for the fluid in the compressor blade passages, and Φ_i and Φ_u are the steady-state injected flow and compressor mass flow, respectively. Equation (4) shows that the pressure changes associated with the control, $[\,\cdot\,]_{\text{pressure rise, aeromechanical}}$, depend upon the quasi-steady change in ideal pressure rise with injected flow, the circumferential and temporal variations in injected flow, and the amount of fluid injected relative to the total inlet flow. (The losses due to injection are accounted for in the unsteady loss model given in Section 4.1.) Similar mass flow and pressure rise matching conditions were developed for the nine other aeromechanical feedback schemes, and because the detailed derivations are quite lengthy only the final linearized equations are presented in Appendix. It should be noted that each feedback scheme resulted in a unique compression system model whose dynamics differ primary because of the additional terms incorporated in the operators $[\,\cdot\,]_{\text{mass flow, aeromechanical}}$ and $[\,\cdot\,]_{\text{pressure rise, aeromechanical}}$.

The flow in the duct upstream of the injection region is assumed to be irrotational, and hence the velocity potential for this flow satisfies a two-dimensional Laplace equation with periodic boundary conditions and vanishing potential far upstream. In contrast, the flow field in the downstream duct is rotational, with the static pressure perturbations satisfying a Laplace equation having periodic boundary conditions and constant static pressure far downstream. Considering this, the upstream stagnation and downstream static pressure perturbations, $\delta\psi_{t_u}$ and $\delta\psi_{s_d}$, respectively, may be written in terms of the unsteady flow perturbations, $\delta\phi_u$ and $\delta\phi_d$ (Epstein et al. [24] and Haynes et al. [11]),

$$\delta\psi_{t_u} = \frac{\delta P_{t_u}}{\frac{\rho}{2}U^2} = -\frac{2}{|n|}\,\frac{\partial(\delta\phi_u)}{\partial\tau} \tag{6}$$

$$\delta\psi_{s_d}=\frac{\delta P_{s_d}}{\frac{\rho}{2}U^2}=\frac{2}{|n|}\frac{\partial(\delta\phi_d)}{\partial\tau}. \tag{7}$$

Equations (1) to (7) describe the unsteady fluid dynamics across the injection region, compressor, and ducts. These equation are combined by inserting Eqs. (1), (2), (6), and (7) into (3) and (4), and rearranging with $\delta\phi's$ on the left and $\delta\varepsilon_r's$ on the right. The resulting equation is

$$\begin{aligned}\left(\frac{4}{|n|}+\mu\right)\frac{\partial(\delta\phi_u)}{\partial\tau}-\frac{\partial\psi_{\text{ideal}}}{\partial\phi}\delta\phi_u+\lambda\frac{\partial\delta\phi_u}{\partial\theta}+\delta L_{\phi S}+\delta L_{\phi R}+\delta L_{dS}\\ +\delta L_{dR}=-\left(\frac{2}{|n|}+\mu\right)\Phi_i\frac{\partial(\delta\varepsilon_r)}{\partial\tau}+\frac{\partial\psi_{\text{ideal}}}{\partial\phi}\Phi_i\delta\varepsilon_r\\ -\lambda\Phi_i\frac{\partial\delta\varepsilon_r}{\partial\theta}+2\Phi_i(\Phi_i-\Phi_u)\delta\varepsilon_r.\end{aligned} \tag{8}$$

This equation describing the dynamics is, however, not complete, because it contains terms which can only be empirically derived or obtained by further, more detailed, analysis of the flow within the machine. Specifically, ψ_{ts}, $L_{\phi S}$, $L_{\phi R}$, L_{dS}, L_{dR}, and ε_r are needed. In the model, ψ_{ts} and the loss terms $L_{\phi S}$, $L_{\phi R}$, L_{dS}, and L_{dR} were obtained from measured compressor data for the two machines considered. In addition, the unsteady dynamics associated with loss and deviation are modeled as first-order lags and this is outlined in the next section. To obtain ε_r, the structural deflection of the controller, further modeling of the structural dynamics is required, and this is discussed in Section 4.2.

4.1 Additional Blade Passage Dynamics. To account for the fact that the pressure rise across, or loss and deviation within, a compressor does not respond immediately to variations in flow (or flow coefficient), the following first-order rate equations were utilized (see Nagano et al. [25], Mazzawy [26], Paduano et al. [17], and Haynes et al. [11]). The equations are more generally referred to as unsteady loss and deviation models.

Stator pressure lags:

$$\overline{\tau}\frac{\partial\delta(\cdot)}{\partial\tau}=\frac{\partial\overline{(\cdot)}}{\partial\phi}\delta\phi_u-\delta(\cdot)+[\cdot]_{\text{steady-state stator lag,aeromechanical}}, \tag{9}$$

where the $(\cdot)$ operator could contain either stator pressure loss $L_{\phi S}$ or deviation L_{dS}, variables.

Rotor pressure lags:

$$\begin{aligned}\overline{\tau}\left(\frac{\partial\delta(\cdot)}{\partial\tau}+\frac{\partial\delta(\cdot)}{\partial\theta}\right)=\frac{\partial\overline{(\cdot)}}{\partial\phi}\delta\phi_u-\delta(\cdot)\\ +[\cdot]_{\text{steady-state rotor lag, aeromechanical}},\end{aligned} \tag{10}$$

where the $(\cdot)$ operator could contain either rotor pressure loss $L_{\phi R}$ or deviation L_{dR}, variables. Further, since both of the compressors considered in this study had 75% reaction, it was assumed that 75% of the steady total pressure losses occurred across the rotors, and 25% across the stators.[1] The time constant $\overline{\tau}$, provides a measure of the time needed for the instantaneous loss or deviation to reach steady-state, given a perturbation of the inlet flow and structural controller. Throughout this investigation $\overline{\tau}$ was nominally set to 1.5 times the blade row flow through time. This value was determined based on the best agreement with the experimental data in parametric studies performed by Haynes et al. [11].

Inclusion of the lag dynamics was shown by Longley [12] to be important for accurate modeling, and by Haynes et al. [11] for better matching the dynamic behavior seen in compressor data. The lags tend to have a stabilizing effect on the higher circumferential harmonics, making the lower harmonics go unstable first as the machine is throttled.[2]

In addition to the basic unsteady loss model described above, the aeromechanical feedback devices considered in this study also impact the machines' instantaneous pressure rise by modifying the losses. As an example, consider the compressor inlet flow injection process of scheme #1. The unsteady injection of fluid entering the compressor face generates circumferential variations in flow which impact the local pressure rise through changes in steady and unsteady loss. The additional steady losses are generated by the injection process and would not be present if the injection were turned off ($\delta\varepsilon_r=0$). Stated differently, these are new losses above those occurring in the baseline compressor without injection. Based on this description, the following terms were obtained from the linearized model of a compressor stabilized with mixed-out fluid injection (scheme #1):

$$\begin{aligned}[\cdot]_{\text{steady-state stator lag, aeromech.}}=[\cdot]_{\text{steady-state rotor lag, aeromech.}}\\ =\frac{\partial\overline{(\cdot)}}{\partial\phi}\Phi_i\delta\varepsilon_r,\end{aligned} \tag{11}$$

Therefore, the quasi-steady pressure loss associated with the response of the dynamic feedback has been modeled through an additional term in the basic lag dynamics. As expected, the form of these new terms depends upon the aeromechanical scheme employed, and hence a summary for the nine stabilization schemes examined is given in the Appendix. In this model the compressor is primarily characterized by its pressure rise-mass flow characteristic, additional pressure loss sensitivities (due to for instance, tip blowing, tip clearance, or stagger angle of movable IGVs and rotors), aeromechanical variables (such as effects of casing wall deflections), and parameters related to the inertia of the fluid in the blade rows.

4.2 Structural Controller Dynamics. It is the response of the structural controllers to the local static pressure perturbations in the upstream flow field that provides the feedback to dynamically control the compression system. The structural controllers were modeled as single-degree-of-freedom generalized spring-mass-damper systems driven by static pressure variations. For scheme #1, the nondimensional second-order equation that governs the structural controller dynamics is

$$\frac{\partial^2\delta\varepsilon_r}{\partial\tau^2}+2Q\zeta\frac{\partial\delta\varepsilon_r}{\partial\tau}+Q^2\delta\varepsilon_r=\overline{W}\delta\psi_{s_u}, \tag{12}$$

where ε_r is the normalized response of the reed valve injector, Q is the controller natural frequency normalized by rotor frequency, ζ is the critical damping ratio, $\overline{W}$ is the nondimensional mass parameter, and $\delta\psi_{s_u}$ is the static pressure disturbance in the flow field upstream of the injection region. As stated earlier, the controllers were modeled as axially short compared to the circumferential length scale of the disturbances, and hence the pressure perturbations at the compressor face were assume to act over the controller's entire axial extent. Because of this the static pressure, $\delta\psi_{s_{\text{avg}}}$, driving the movable casing wall controller response, ε_c (schemes #8) and the dynamically restaggered rotor blade controller response, γ_r (scheme #10) were taken to be the average static pressures in the flow fields up and downstream of the compressor. Similarly, the static pressure, $\delta\psi_{s_d}$, driving the exit duct wall controller response, ε_D (scheme #7) was taken as the static pressure in the flow field in the exit duct just upstream of the movable wall region. To determine the sensitivity of the results to this assump-

---

[1] See Haynes [11] for impact of choice of loading distribution.

[2] The lag dynamics will induce a circumferential shift of the pressure rise disturbance induced by a flow disturbance. This offset will correspond to a greater *phase shift* at higher harmonics due to their shorter circumferential wavelength, and postpone their point of neutral stability.

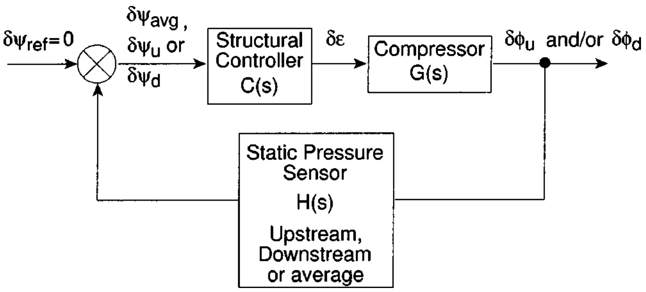

Fig. 2 Block diagram representation of the aeromechanical feedback loop

tion, an assessment of the location of static pressure sensing was conducted for the inlet duct wall controller by considering the static pressure in the inlet duct immediately upstream of the movable wall region (scheme #5), or farther downstream in the exit duct (scheme #6).

5 Control-Theoretic Viewpoint

A control-theoretic formulation is now developed using a frequency domain analysis typical of classical control theory. This viewpoint provides a useful basis for performing compression system analysis, design, and fluid-structural parameter optimization, and for understanding the system's unsteady mechanical energy (Sec. 6).

To facilitate the development, it is helpful to consider the system in terms usually associated with feedback control. The schematic in **Fig. 2** gives a block diagram representation of a compressor with a closed-loop aeromechanical feedback stabilization system. In the present work all of the controllers were assumed to respond to unsteady pressure disturbances in the compressor ($\delta\psi$) by generating structural perturbations (δq) which then modify the flow in the machine ($\delta\phi$) via actuation (e.g., injection, blade motion, etc.). Because the controllers are structural in nature, the relationship between the sensed quantity (static pressure) and the dynamic response is governed by a second-order control law (Eq. (12)). Therefore, given an initial disturbance in static pressure the forward path of the closed-loop control is defined as follows: The structural controller, described by the function, $C(s)$, responds to the (upstream, downstream, or an average) static pressure perturbation, $\delta\psi_u$. This pressure disturbance then drives the structural controller to produce a mechanical actuation with displacements, $\delta\varepsilon$, which then modify the flow perturbations, within the compressor described by $G(s)$. Finally, the modified flow perturbations are detected by "sensors" $H(s)$ which convey the information back to the structure as unsteady pressure perturbations. The structural controller, $C(s)$ pressure "sensors", $H(s)$, together describe the closed-loop dynamics of the system. The transfer functions associated with each element will be discussed in the following subsections.

5.1 Compressor, $G(s)$. Equations (8) through (11) provide relations for the compressor and duct dynamics, but do not prescribe the specific form of the disturbance being considered. The Moore-Greitzer model upon which the current work is based, considers small amplitude pre-stall traveling wave disturbances which can be decomposed and described by Fourier harmonics. Further, because the present work examines the linearized form of the governing equations, the growth or decay of the individual Fourier harmonics can be analyzed separately. Based on this the perturbation variables are assume to be traveling waves of the form $e^{(in\theta+s_n\tau)}$. Inserting these forms into (8) through (11), yields a set of single-input, single-output (SISO) complex-coefficient, complex state, ordinary differential equations (ODEs) in time for each decoupled spatial harmonic n:

$$\dot{\tilde{\phi}}_n=p\tilde{\phi}_n+z_b\tilde{\varepsilon}_n-z_c(\tilde{L}_{\phi R_n}+\tilde{L}_{dR_n})-z_c(\tilde{L}_{\phi S_n}+\tilde{L}_{dS_n})-z_g\dot{\tilde{\varepsilon}}_n \tag{13}$$

along with the first-order lag equations for the unsteady loss and deviation in the blade passages:

$$\overline{\tau}\dot{\tilde{L}}_{\phi S_n}=L_{\phi S_\phi}\tilde{\phi}_n+L_{\phi S_\varepsilon}\tilde{\varepsilon}_n-\tilde{L}_{\phi S_n}, \tag{14}$$

$$\overline{\tau}\dot{\tilde{L}}_{dS_n}=L_{dS_\phi}\tilde{\phi}_n+L_{dS_\varepsilon}\tilde{\varepsilon}_n-\tilde{L}_{dS_n}, \tag{15}$$

$$\overline{\tau}\dot{\tilde{L}}_{\phi R_n}=L_{\phi R_\phi}\tilde{\phi}_n+L_{\phi R_\varepsilon}\tilde{\varepsilon}_n-(1-in\overline{\tau})\tilde{L}_{\phi R_n}, \tag{16}$$

$$\overline{\tau}\dot{\tilde{L}}_{dR_n}=L_{dR_\phi}\tilde{\phi}_n+L_{dR_\varepsilon}\tilde{\varepsilon}_n-(1-in\overline{\tau})\tilde{L}_{dR_n}. \tag{17}$$

The relevant parameters governing the growth of pre-stall disturbances are the eigenvalues, $p=(\sigma_{rs}+i\omega_{rs})$, and zeros, $z_c=c_{r_n}$, and the fluid-structure interaction parameters, $z_b=(b_{r_n}+ib_{i_n})$, and $z_g=(g_{r_n}+ig_{i_n})$. The behavior of each nth spatial harmonic of the system can thus be characterized by the sets $\{\sigma_{rs},\omega_{rs},b_{r_n},b_{i_n},c_{r_n},g_{r_n},g_{i_n}\}$, $\{L_{\phi S_\phi},L_{dS_\phi},L_{\phi R_\phi},L_{dR_\phi}\}$, and $\{L_{\phi S_\varepsilon},L_{dS_\varepsilon},L_{\phi R_\varepsilon},L_{dR_\varepsilon}\}$. Utilizing the definition $\mu_n=[4/|n|+\mu]$, then

$$\sigma_{rs}=\frac{\partial\psi_{\text{ideal}}/\partial\phi}{\mu_n},\quad \omega_{rs}=\frac{-n\lambda}{\mu_n}, \tag{18}$$

which gives parameters for the mixed-out injection, scheme #1, as follows:

$$\begin{gathered}
b_{r_n}=\frac{\Phi_i[\partial\psi_{\text{ideal}}/\partial\phi+2(\Phi_i-\Phi_u)]}{\mu_n},\\
b_{i_n}=\frac{-n\lambda\Phi_i}{\mu_n},\quad g_{i_n}=0,\quad g_{r_n}=\frac{\left(\dfrac{2}{|n|}+\mu\right)\Phi_i}{\mu_n},\quad c_{r_n}=\frac{1}{\mu_n},\\
L_{\phi S_\phi}=\frac{\partial L_{\phi S}}{\partial\phi},\quad L_{\phi S_\varepsilon}=\frac{\partial L_{\phi S}}{\partial\phi}\Phi_i,\\
L_{dS_\phi}=\frac{\partial L_{dS}}{\partial\phi},\quad L_{dS_\varepsilon}=\frac{\partial L_{dS}}{\partial\phi}\Phi_i,\\
L_{\phi R_\phi}=\frac{\partial L_{\phi R}}{\partial\phi},\quad L_{\phi R_\varepsilon}=\frac{\partial L_{\phi R}}{\partial\phi}\Phi_i,\\
L_{dR_\phi}=\frac{\partial L_{dR}}{\partial\phi},\quad L_{dR_\varepsilon}=\frac{\partial L_{dR}}{\partial\phi}\Phi_i.
\end{gathered} \tag{19}$$

Definitions of these parameters for schemes #2 to #10 are given in the Appendix. A frequency s-domain representation of the governing SISO ODEs is obtained by taking the Laplace transform and constructing the transfer function for the compression system:

$$\tilde{\phi}_n(s)=G_n(s)\tilde{\varepsilon}_n(s), \tag{20}$$

where

$$\begin{gathered}
G_n(s)=\frac{G_n(s)_{\text{num}}}{G_n(s)_{\text{den}}},\\
G_n(s)_{\text{num}}=-z_gs+z_b-z_c\frac{L_{\phi R_\varepsilon}+L_{dR_\varepsilon}}{1+\overline{\tau}(s-in)}-z_c\frac{L_{\phi S_\varepsilon}+L_{dS_\varepsilon}}{1+\overline{\tau}s},\\
G_n(s)_{\text{den}}=s-p+z_c\frac{L_{\phi R_\phi}+L_{dR_\phi}}{1+\overline{\tau}(s-in)}+z_c\frac{L_{\phi S_\phi}+L_{dS_\phi}}{1+\overline{\tau}s}.
\end{gathered} \tag{21}$$

The coefficients of $G_n(s)$ are complex and therefore modern techniques for control system design and analysis were applied to analyze the behavior of this system.

5.2 Static Pressure Sensing, $H(s)$. The structural feedback responds to fluctuations in static pressure in the ducts either upstream, downstream, or within the compressor (depending on the scheme). These unsteady pressure perturbations were then used directly or averaged, and served as input to the structural controller. A transfer function for the sensors can be developed utilizing the relationship between the upstream (or downstream) velocity and pressure perturbation. By assuming the flow to be inviscid, and applying a momentum balance in the upstream duct and linearizing the result, we obtain

$$-\frac{2}{|n|}\dot{\tilde{\phi}}_{u_n}=\tilde{\psi}_{su_n}+2\Phi_u\tilde{\phi}_{u_n}, \tag{22}$$

which is for the *n*th spatial harmonic. Similarly in the downstream duct,

$$\frac{2}{|n|}\dot{\tilde{\phi}}_{d_n}=\tilde{\psi}_{sd_n}. \tag{23}$$

In the frequency domain, the sensor transfer functions are then

$$\tilde{\psi}_{su_n}(s)=H_{u_n}(s)\tilde{\phi}_{u_n}(s), \tag{24}$$

$$\tilde{\psi}_{sd_n}(s)=H_{d_n}(s)\tilde{\phi}_{d_n}(s), \tag{25}$$

where

$$H_{u_n}(s)=-2\left(\frac{s}{|n|}+\Phi_u\right), \tag{26}$$

$$H_{d_n}(s)=2\frac{s}{|n|}. \tag{27}$$

It should be noted that the front-to-back static pressure sensing was assumed to be an average of the upstream and downstream pressure disturbances, $\tilde{\psi}_{\mathrm{avg}_n}=1/2[\tilde{\psi}_{su_n}(s)+\tilde{\psi}_{sd_n}(s)]$, and thus the transfer functions were combined in parallel as $H_{\mathrm{avg}_n}(s)=1/2[H_{u_n}(s)+H_{d_n}(s)]$.

5.3 Structural Controller, $C(s)$. The structural response to the local static pressure perturbations in the flow field provides the feedback in the closed-loop compression system. In the frequency domain, the transfer function of the structural feedback is equivalent for upstream, downstream, or front-to-back pressure sensing. For instance from Eq. (12),

$$\tilde{\varepsilon}_n(s)=C_n(s)\tilde{\psi}_{su_n}(s), \tag{28}$$

where

$$C_n(s)=\frac{\overline{W}}{s^2+2Q\zeta s+Q^2}. \tag{29}$$

The parameters which characterize the structural controller dynamics for the *n*th spatial harmonic of the flow field are then defined as the real set, $\{Q,\zeta,\overline{W}\}$.

5.4 Open and Closed-Loop System Stability. The stability of the open-loop system is determine by the eigenvalues of the compressor transfer function $G_n(s)$, shown in **Fig. 2**. Similarly, stability of the closed-loop system was determined from the roots of the closed-loop characteristic equation, which was defined by the denominator of the overall transfer function:

$$\tilde{\phi}_n(s)=F_n(s)\tilde{\psi}_n(s), \tag{30}$$

where

$$F_n(s)=\frac{C_n(s)G_n(s)}{1-C_n(s)G_n(s)H_n(s)}. \tag{31}$$

The system was stable when and only when all roots of the characteristic equation, $1-C_n(s)G_n(s)H_n(s)=0$, had strictly negative real parts. The characteristic equation of the open-loop system was fifth-order, and that of the closed-loop systems was seventh-order (eighth order including the IGV loss dynamics in scheme #9). Hence, the roots of the characteristic equation were determined numerically.

When the real part of the eigenvalue s_n is negative, the disturbance is aeromechanically damped, indicating stable operation of the compression system. Conversely, when the real part of the eigenvalue s_n is positive, there is insufficient aeromechanical damping and the disturbance grows indicating unstable operation. Since the individual spatial harmonics were assumed to be decoupled, the stability can be determined on a harmonic-by-harmonic basis. For the simple baseline compressor (uncontrolled without unsteady losses), the disturbance growth rate can be shown to be directly linked to the slope of the total-to-static pressure rise characteristic, $\partial\psi_{ts}/\partial\phi$ (Gysling and Greitzer [7]). However, for an aeromechanically stabilized compressor, the growth rate is determined by two components: (1) the slope of the total-to-static pressure rise characteristic, and (2) the control authority of the aeromechanical stabilization strategy. The control authority of aeromechanical stabilization and related unsteady aeromechanical work metrics are defined in the following section.

6 Aeromechanical Feedback Stabilization Metrics

6.1 Control Authority of Aeromechanical Stabilization. Let us consider for the sake of simplicity of this discussion the dynamics of a compression system stabilized using scheme #1 (excluding the effects of unsteady dynamics associated with loss and deviation):

$$\begin{aligned}\left(\frac{4}{|n|}+\mu\right)\frac{\partial(\delta\phi_u)}{\partial\tau}-\frac{\partial\psi_{ts}}{\partial\phi}\delta\phi_u+\lambda\frac{\partial\delta\phi_u}{\partial\theta}&\\=-\left(\frac{2}{|n|}+\mu\right)\Phi_i\frac{\partial(\delta\varepsilon_r)}{\partial\tau}+\frac{\partial\psi_{ts}}{\partial\phi}\Phi_i\delta\varepsilon_r-\lambda\Phi_i\frac{\partial\delta\varepsilon_r}{\partial\theta}&\\+2\Phi_i(\Phi_i-\Phi_u)\delta\varepsilon_r.&\end{aligned} \tag{32}$$

At neutral stability, $\sigma_n=0$, so, $s_n=i\omega_n$. Thus,

$$\delta\phi_u=\tilde{\phi}_ne^{i(n\theta+\omega_n\tau)},\quad \delta\varepsilon_r=\tilde{\varepsilon}_ne^{i(n\theta+\omega_n\tau+\beta_n)}, \tag{33}$$

where $\beta_n=\beta_n(i\omega_n)$ denotes a phase shift between the flow perturbation, $\delta\phi_u$, and the structural response, $\delta\varepsilon_r$. Inserting the above into (32), dividing by $e^{i(n\theta+\omega_n\tau)}$, and then collecting terms, one obtains a set of SISO ODEs in time for each decoupled spatial harmonic *n* (similar to Eq. (13)):

$$\dot{\tilde{\phi}}_n-p\tilde{\phi}_n=z_b\tilde{\varepsilon}_ne^{i\beta_n}-z_g\dot{\tilde{\varepsilon}}_ne^{i\beta_n}, \tag{34}$$

whereas like Eq. (13), $p=(\sigma_{rs}+i\omega_{rs})$, $z_b=(b_{r_n}+ib_{i_n})$, and $z_g=(g_{r_n}+ig_{i_n})$. Utilizing the definition $\mu_n=[4/|n|+\mu]$, then

$$\sigma_{rs}=\frac{\partial\psi_{ts}/\partial\phi}{\mu_n},\quad \omega_{rs}=\frac{-n\lambda}{\mu_n}, \tag{35}$$

which gives parameters for the mixed-out injection, scheme #1, as follows:

$$\begin{gathered}b_{r_n}=\frac{\Phi_i[\partial\psi_{ts}/\partial\phi+2(\Phi_i-\Phi_u)]}{\mu_n},\\ b_{i_n}=\frac{-n\lambda\Phi_i}{\mu_n},\quad g_{i_n}=0,\quad g_{r_n}=\frac{\left(\frac{2}{|n|}+\mu\right)\Phi_i}{\mu_n}.\end{gathered} \tag{36}$$

Table 2 Matching flow conditions of stabilized compression systems

	$[\cdot]_{\text{mass flow, aeromechanical}}$	$[\cdot]_{\text{pressure rise, aeromechanical}}$	$[\cdot]_{\text{stator lag, aeromechanical}}$	$[\cdot]_{\text{rotor lag, aeromechanical}}$
#2	0	$\frac{\partial\psi_{\text{ideal}}}{\partial\alpha_i}\left(\frac{\Phi_i}{\Phi_u}\right)^2\delta\varepsilon_r$	0	$-\frac{\partial\overline{(\cdot)}}{\partial\alpha_i}\left(\frac{\Phi_i}{\Phi_u}\right)^2\delta\varepsilon_r$
#3	0	$\frac{\partial\psi_{\text{ideal}}}{\partial\phi}\Phi_i\delta\varepsilon_r-\lambda\Phi_i\frac{\partial\delta\varepsilon_r}{\partial\theta}-\mu\Phi_i\frac{\partial\delta\varepsilon_r}{\partial\tau}+2(\Phi_i)^2\delta\varepsilon_r$	0	$\frac{\partial\overline{(\cdot)}}{\partial\phi}\Phi_i\delta\varepsilon_r$
#4	$-\Phi_i\delta\varepsilon_r$	$\frac{\partial\psi_{\text{ideal}}}{\partial\alpha_i}\left(\frac{\Phi_i}{\Phi_u}\right)^2\delta\varepsilon_r+2\Phi_i\Phi_u\delta\varepsilon_r$	0	$-\frac{\partial\overline{(\cdot)}}{\partial\alpha_i}\left(\frac{\Phi_i}{\Phi_u}\right)^2\delta\varepsilon_r$
#5	$\Phi_u\delta\varepsilon_D$	$\frac{\partial\psi_{\text{ideal}}}{\partial\phi}\Phi_u\delta\varepsilon_D-\lambda\Phi_u\frac{\partial\delta\varepsilon_D}{\partial\theta}-\mu\Phi_u\frac{\partial\delta\varepsilon_D}{\partial\tau}-(\Phi_u)^2\delta\varepsilon_D$	$\frac{\partial\overline{(\cdot)}}{\partial\phi}\Phi_u\delta\varepsilon_D$	$\frac{\partial\overline{(\cdot)}}{\partial\phi}\Phi_u\delta\varepsilon_D$
#6	$\Phi_u\delta\varepsilon_D$	$[\psi_{ts}-2(\Phi_u)^2]\delta\varepsilon_D$	0	0
#7	$\Phi_u\delta\varepsilon_D$	$\left[\psi_{ts}-2(\Phi_u)^2-\frac{\partial\psi_{ts}}{\partial\phi}\Phi_u\right]\delta\varepsilon_D$	0	0
#8	0	$\frac{\partial\psi_{\text{ideal}}}{\partial\varepsilon_c}\delta\varepsilon_c$	0	$-\frac{\partial\overline{(\cdot)}}{\partial\varepsilon_c}\delta\varepsilon_c$
#9	$-\Phi_u\mu_{igv}\frac{\partial\delta\gamma_{igv}}{\partial\theta}$	$-\frac{\partial\psi_{\text{ideal}}}{\partial\phi}\Phi_u\mu_{igv}\frac{\partial\delta\gamma_{igv}}{\partial\theta}+\frac{\partial\psi_{\text{ideal}}}{\partial\gamma}\delta\gamma_{igv}+\lambda\Phi_u\mu_{igv}\frac{\partial^2\delta\gamma_{igv}}{\partial\theta^2}$ $+(\mu+\mu_{igv})\Phi_u\mu_{igv}\frac{\partial^2\delta\gamma_{igv}}{\partial\tau\partial\theta}-\mu_{igv}\frac{\partial}{\partial\tau}\left(\frac{\Phi_u\mu_{igv}}{2}\frac{\partial\delta\gamma_{igv}}{\partial\theta}\right)$	$-\frac{\partial\overline{(\cdot)}}{\partial\phi}\Phi_u\mu_{igv}\frac{\partial\delta\gamma_{igv}}{\partial\theta}$	$-\frac{\partial\overline{(\cdot)}}{\partial\phi}\Phi_u\mu_{igv}\frac{\partial\delta\gamma_{igv}}{\partial\theta}$ $+\frac{\partial\overline{(\cdot)}}{\partial\phi}\delta\gamma_{igv}$
#10	0	$\frac{\partial\psi_{\text{ideal}}}{\partial\gamma}\delta\gamma_R-\lambda(\Phi_u\tan\overline{\gamma_R})\frac{\partial\delta\gamma_R}{\partial\theta}$	0	$\frac{\partial\overline{(\cdot)}}{\partial\gamma}\delta\gamma_R$

Similar definitions of these parameters for schemes #2 to #10 are given in the Appendix (noting that in this instance $\partial\psi_{\text{ideal}}/\partial\phi$ should be replaced with $\partial\psi_{ts}/\partial\phi$, and that all loss and deviation parameters are set to zero).

We can express $\tilde{\varepsilon}_n e^{i\beta_n}$ as a function of $\tilde{\phi}_n$, as follows:

$$\begin{aligned}\tilde{\varepsilon}_n e^{i\beta_n}&=H_{u_n}(i\omega_n)C(i\omega_n)\tilde{\phi}_n\\&=\lvert HC(i\omega_n)\rvert e^{i\beta_n(i\omega_n)}\tilde{\phi}_n\\&=\lvert HC(i\omega_n)\rvert(\cos\beta_n+i\sin\beta_n)\tilde{\phi}_n.\end{aligned}\tag{37}$$

Note that $\beta_n=\beta_n(i\omega_n)$ is also the phasing of the HC transfer function (see Eqs. (24)–(27) and (29)). Substituting the above into Eq. (34) yields

$$\begin{aligned}i\omega_n\tilde{\phi}_n-p\tilde{\phi}_n&=z_b\lvert HC\rvert(\cos\beta_n+i\sin\beta_n)\tilde{\phi}_n\\&\quad+z_g\lvert HC\rvert\omega_n(\sin\beta_n-i\cos\beta_n)\tilde{\phi}_n.\end{aligned}\tag{38}$$

Simplifying $\tilde{\phi}_n$, one determines that the real and imaginary parts of this expression must be zero. That is, the real part is a closed-form definition of the disturbance growth rate, σ_n, at neutral stability of a compression system stabilized using aeromechanical feedback (such as scheme #1, or any one of the other schemes, using the definitions of the feedback control parameters listed in the Appendix),

$$\begin{aligned}\sigma_n=\sigma_{rs}&+\lvert HC\rvert(b_{r_n}\cos\beta_n-b_{i_n}\sin\beta_n)\\&+\lvert HC\rvert\omega_n(g_{r_n}\sin\beta_n+g_{i_n}\cos\beta_n)=0,\end{aligned}\tag{39}$$

and that the imaginary part is a closed-form expression in terms of the disturbance frequency, ω_n, at neutral stability of the system,

$$\begin{aligned}\omega_n=\omega_{rs}&+\lvert HC\rvert(b_{r_n}\sin\beta_n+b_{i_n}\cos\beta_n)\\&-\lvert HC\rvert\omega_n(g_{r_n}\cos\beta_n-g_{i_n}\sin\beta_n).\end{aligned}\tag{40}$$

In their study, Gysling and Greitzer [7] suggested that the temporal displacement of the structural controllers (reed valves used to control flow injection) provided dynamic compensation approximately 180 deg out-of-phase with upstream axial velocity perturbations over a wide range of controller frequencies. Suppose we assume for the moment that the "ideal condition" is to have the upstream flow oscillations, $\delta\phi_u$, completely out-of-phase with the structural controller response, $\delta\varepsilon_r$. Then, $\beta_n=180$ deg, and $\sin\beta_n=0$, and $\cos\beta_n=-1$. Hence, the disturbance growth and frequency expressions simplify to

$$\sigma_{n_{\text{ideal}}}=\sigma_{rs}-\lvert HC\rvert(b_{r_n}+\omega_n g_{i_n})\simeq 0,\tag{41}$$

$$\omega_{n_{\text{ideal}}}=\omega_{rs}-\lvert HC\rvert(b_{i_n}+\omega_n g_{r_n}).\tag{42}$$

The expressions for the disturbance growth, σ_n and $\sigma_{n_{\text{ideal}}}$, offer a new metric interpreted here as the *control authority (C.A.) of aeromechanical stabilization*—defined at neutral stability of the system as

$$\begin{aligned}C.A.=-\sigma_{rs}\mu_n&=\lvert HC\rvert\mu_n(b_{r_n}\cos\beta_n-b_{i_n}\sin\beta_n)\\&\quad+\lvert HC\rvert\omega_n\mu_n(g_{r_n}\sin\beta_n+g_{i_n}\cos\beta_n),\end{aligned}\tag{43}$$

$$C.A._{\text{ideal}}=(\sigma_{n_{\text{ideal}}}-\sigma_{rs})\mu_n=-\mu_n\lvert HC\rvert(b_{r_n}+\omega_n g_{i_n}).\tag{44}$$

Essentially, $\mu_n\sigma_{n_{\text{ideal}}}\neq 0$ represents a loss in control authority of aeromechanical stabilization.

Note again that the expressions for the control authority developed above do not account for unsteady loss and deviation dynamics. However, this new metric which is based on the phasing of the flow disturbances and the structural response should be utilized to provide: (1) a quantitative assessment and estimate of the ability of different aeromechanical control schemes to stabilize a compression system, and (2) a measure of how close to "ideal" a particular scheme's actual performance may be in practice.

Table 3 Definitions of feedback control parameters

	b_{r_n}	b_{i_n}	g_{r_n}	$L_{\phi S_\varepsilon}$	L_{dS_ε}	$L_{\phi R_\varepsilon}$	L_{dR_ε}
#2	$\dfrac{\left(\dfrac{\partial\psi_{\text{ideal}}}{\partial\alpha_i}\right)(\Phi_i/\Phi_u)^2}{\mu_n}$	0	0	0	0	$-\dfrac{\partial L_{\phi R}}{\partial\alpha_i}\left(\dfrac{\Phi_i}{\Phi_u}\right)^2$	$-\dfrac{\partial L_{dR}}{\partial\alpha_i}\left(\dfrac{\Phi_i}{\Phi_u}\right)^2$
#3	$\dfrac{\Phi_i[\partial\psi_{\text{ideal}}/\partial\phi+2\Phi_i]}{\mu_n}$	$\dfrac{-n\lambda\Phi_i}{\mu_n}$	$\dfrac{\left(\dfrac{2}{\lvert n\rvert}+\mu\right)\Phi_i}{\mu_n}$	0	0	$\dfrac{\partial L_{\phi R}}{\partial\phi}\Phi_i$	$\dfrac{\partial L_{dR}}{\partial\phi}\Phi_i$
#4	$\dfrac{\left(\dfrac{\partial\psi_{\text{ideal}}}{\partial\alpha_i}\right)(\Phi_i/\Phi_u)^2+2\Phi_i\Phi_u}{\mu_n}$	0	0	0	0	$-\dfrac{\partial L_{\phi R}}{\partial\alpha_i}\left(\dfrac{\Phi_i}{\Phi_u}\right)^2$	$-\dfrac{\partial L_{dR}}{\partial\alpha_i}\left(\dfrac{\Phi_i}{\Phi_u}\right)^2$
#5	$\dfrac{\Phi_u[(\partial\psi_{\text{ideal}}/\partial\phi)-\Phi_u]}{\mu_n}$	$\dfrac{-n\lambda\Phi_u}{\mu_n}$	$\dfrac{\left(\dfrac{2}{\lvert n\rvert}+\mu\right)\Phi_u}{\mu_n}$	$\dfrac{\partial L_{\phi S}}{\partial\phi}\Phi_u$	$\dfrac{\partial L_{dS}}{\partial\phi}\Phi_u$	$\dfrac{\partial L_{\phi R}}{\partial\phi}\Phi_u$	$\dfrac{\partial L_{dR}}{\partial\phi}\Phi_u$
#6	$\dfrac{[\psi_{ts}-2\Phi_u^2]}{\mu_n}$	0	$\dfrac{\dfrac{2}{\lvert n\rvert}\Phi_u}{\mu_n}$	0	0	0	0
#7	$\dfrac{[\psi_{ts}-2\Phi_u^2-(\partial\psi_{ts}/\partial\phi)\Phi_u]}{\mu_n}$	0	$\dfrac{\left(\dfrac{2}{\lvert n\rvert}+\mu\right)\Phi_u}{\mu_n}$	0	0	0	0
#8	$\dfrac{(\partial\psi_{\text{ideal}}/\partial\varepsilon)}{\mu_n}$	0	0	0	0	$-\dfrac{\partial L_{\phi R}}{\partial\varepsilon_c}$	$-\dfrac{\partial L_{dR}}{\partial\varepsilon_c}$
#9	$\dfrac{\left[\left(\dfrac{\partial\psi_{\text{ideal}}}{\partial\gamma}\right)-\lambda n^2\Phi_u\mu_{igv}\right]}{\tilde{\mu}_n}$	$\dfrac{-n\left(\dfrac{\partial\psi_{\text{ideal}}}{\partial\phi}\right)\Phi_u\mu_{igv}}{\tilde{\mu}_n}$	$\dfrac{n\Phi_u\mu_{igv}\left(\dfrac{1}{\lvert n\rvert}+\dfrac{\mu_{igv}}{2}+\mu\right)}{\tilde{\mu}_n}$	$-\dfrac{\partial L_{\phi S}}{\partial\phi}in\Phi_u\mu_{igv}$	$-\dfrac{\partial L_{dS}}{\partial\phi}in\Phi_u\mu_{igv}$	$\dfrac{\partial L_{\phi R}}{\partial\gamma}$ $-\dfrac{\partial L_{\phi R}}{\partial\phi}in\Phi_u\mu_{igv}$	$\dfrac{\partial L_{dR}}{\partial\gamma}-$ $\dfrac{\partial L_{dR}}{\partial\phi}in\Phi_u\mu_{igv}$
#10	$\dfrac{(\partial\psi_{\text{ideal}}/\partial\gamma)}{\mu_n}$	$\dfrac{-n\lambda\Phi_u\tan\overline{\gamma_b}}{\mu_n}$	0	0	0	$\dfrac{\partial L_{\phi R}}{\partial\gamma}$	$\dfrac{\partial L_{dR}}{\partial\gamma}$

[Note that $g_{i_n}=0$, $L_{\phi S_\phi}=\partial L_{\phi S}/\partial\phi$, $L_{dS_\phi}=\partial L_{dS}/\partial\phi$, $L_{\phi R_\phi}=\partial L_{\phi R}/\partial\phi$, $L_{dR_\phi}=\partial L_{dR}/\partial\phi$, and $c_{r_n}=1/\mu_n$ for all schemes. For scheme #9: $L_{igv_\gamma}=\partial L_{igv}/\partial\gamma$, and if we let $\tilde{\mu}_n=[2/\lvert n\rvert+\mu_{igv}+\mu]$, then $\sigma_{rs}=(\partial\psi_{\text{ideal}}/\partial\phi)/\mu_n$ and $\omega_{rs}=-n\lambda/\tilde{\mu}_n$, $c_{r_n}=1/\tilde{\mu}_n$.]

Next, *control authority* will be shown to directly reflect the aeromechanical work of a closed-loop (fluid-structure) compression system.

6.2 Unsteady Work of Aeromechanical Stabilization. Let us consider a compression system with structural dynamics subjected to a small, unsteady, oscillatory disturbance. If the work associated with the disturbance grows in time, the oscillations will grow and the system will be unstable. However, if this work decreases as a function of time, then the oscillations will be damped and the system will remain stable. The definition of annulus-averaged unsteady aeromechanical work (or time rate of change of unsteady energy) utilized in this study is the product of the total-to-static pressure rise perturbation produced by the compression system, $\delta\psi_{ts}$, and the upstream flow perturbation, $\delta\phi_u$, integrated around the annulus:

$$\overline{\delta E}=\frac{\int_{\text{annulus}}\delta\psi_{ts}\,\delta\phi_u\,dA}{\int_{\text{annulus}}dA}. \tag{45}$$

Justification and detailed discussion of this metric is given elsewhere (Epstein et al. [24], Gysling [27], Gysling and Greitzer [7] and Fréchette [16]). Examination of this expression shows that it is the component of the pressure rise perturbation in-phase with the upstream flow perturbation that contributes to the unsteady work and hence, the stability of the system.

6.2.1 True Aeromechanical Work. In general, a relationship between the perturbation in pressure rise, $\delta\psi_{ts}$, and unsteady flow oscillations, $\delta\phi_u$, across the compressor can be created using the relations derived herein. However, to facilitate discussion of the unsteady work, the relationship for the fluid injection aeromechanical control (scheme #1) will now be derived. Considering the momentum balance Eqs. (3) and (4):

$$\begin{aligned}\delta\psi_{ts}=\delta\psi_{s_d}-\delta\psi_{t_u}=&\left(\frac{\partial\psi_{ts}}{\partial\phi}\right)\delta\phi_u+\left(\frac{\partial\psi_{ts}}{\partial\phi}\right)\Phi_i\,\delta\varepsilon_r-\lambda\,\frac{\partial\delta\phi_u}{\partial\theta}\\&-\lambda\Phi_i\frac{\partial\delta\varepsilon_r}{\partial\theta}-\mu\,\frac{\partial\delta\phi_u}{\partial\tau}-\mu\Phi_i\frac{\partial\delta\varepsilon_r}{\partial\tau}+2\Phi_i(\Phi_i-\Phi_u)\,\delta\varepsilon_r\,.\end{aligned} \tag{46}$$

Substituting Eqs. (33) and (37) into the above and rearranging yields a compression system transfer function:

$$\delta\psi_{ts}(s)=M_c(s)\cdot\delta\phi_u(s), \tag{47}$$

where $M_c(s)=\text{Re}[M_c(s)]+i\,\text{Im}[M_c(s)]$ (a complete expansion can be found in McGee et al. [23]).

The real component of the pressure rise (i.e., the real part of the compression system transfer function, $\text{Re}[M_c(s)]$) working in-phase with the upstream flow perturbation, $\text{Re}[\delta\phi_u]=|\delta\phi_u|$, contributes to the unsteady aeromechanical work, and hence the stability of the system. $\text{Re}[M_c(s)]$ is useful because it provides a link between the feedback controller parameters and the unsteady aeromechanical work (whose growth or decay is indicative of stability). The sign of $\text{Re}[M_c(s)]$ indicates whether the compression system is operating at a condition where aeromechanical energy of the perturbations will grow or dissipate.

Substituting Eqs. (47) into (45) yields an expression for the unsteady aeromechanical work:

$$\overline{\delta E}=\frac{1}{A}\int_{\text{annulus}}\left(\frac{\partial\psi_{ts}}{\partial\phi}(|\delta\phi_u|)^2+\mathcal{E}\right)dA, \tag{48}$$

where

$$\begin{aligned}\mathcal{E}=&\left(\frac{\partial\psi_{ts}}{\partial\phi}\right)\Phi_i|HC|\cos\beta_n(|\delta\phi_u|)^2\\&+2\Phi_i(\Phi_i-\Phi_u)|HC|\cos\beta_n(|\delta\phi_u|)^2\\&+\left(\omega_n\mu+\frac{2\omega_n}{|n|}+n\lambda\right)\Phi_i|HC|\sin\beta_n(|\delta\phi_u|)^2.\end{aligned} \tag{49}$$

If we assume $|\delta\phi_u|=1$, then $\mathcal{E}$ represents the control authority (Eq. (43)) of the mixed-out fluid injection stabilization (scheme #1). This shows us that the role of aeromechanical stabilization is to modify the real part of the compression system transfer function, and thus, the unsteady aeromechanical work through the control authority. Hence, the stability impact of a number of different structural control techniques can be assessed by examining two metrics—the unsteady aeromechanical work and the control authority. At neutral stability, both the unsteady aeromechanical work and effective growth rate (or instantaneous aeromechanical damping) vanish.

6.2.2 Ideal Aeromechanical Work. Suppose again that the "ideal condition" to damp pre-stall disturbances is to have the structural controller response, $\delta\varepsilon_r$, completely out-of-phase with the upstream flow oscillations, $\delta\phi_u$. Then, $\beta_n=180°$, $\sin\beta_n=0$, and $\cos\beta_n=-1$; and $\delta\phi_u=\tilde{\phi}_n e^{(in\theta+s_n\tau)}$, $\delta\varepsilon_r=-|HC|\delta\phi_u$; and $s_n=i\omega_n$ and $\sigma_n=0$. This yields a compression system transfer function for this "ideal" condition:

$$\delta\psi_{ts}(s)=M_{c_{\text{ideal}}}(s)\cdot\delta\phi_u(s). \tag{50}$$

An expression for the ideal annulus-averaged unsteady aeromechanical work is then

$$\overline{\delta E}_{\text{ideal}}=\frac{1}{A}\int_{\text{annulus}}\left(\frac{\partial\psi_{ts}}{\partial\phi}(|\delta\phi_u|)^2+\mathcal{E}_{\text{ideal}}\right)dA, \tag{51}$$

where the ideal control authority, $\mathcal{E}_{\text{ideal}}$, of the mixed-out fluid injection stabilization (scheme #1) is

$$\mathcal{E}_{\text{ideal}}=-\frac{\partial\psi_{ts}}{\partial\phi}\Phi_i|HC|(|\delta\phi_u|)^2-2\Phi_i(\Phi_i-\Phi_u)|HC|(|\delta\phi_u|)^2. \tag{52}$$

If we assume $|\delta\phi_u|=1$, then an "ideal" effective growth rate (or instantaneous aeromechanical damping) is determined by the slope of the steady-state compressor characteristic, $(\partial\psi_{ts}/\partial\phi)$, plus the ideal control authority which is $|HC|[-(\partial\psi_{ts}/\partial\phi)\Phi_i-2\Phi_i(\Phi_i-\Phi_u)]$ for scheme #1. The ideal effective growth rate provides an indication of the compression system range extension possible (via operable slope changes) for a particular control scheme. This metric is a measure of how close to "ideal" a particular scheme's actual performance may be in practice.

7 Summary and Conclusions

This study presented extended versions of the Moore-Greitzer compression system stability model incorporating various aeromechanical feedback control schemes. In total, ten different aeromechanical stabilization methods were modeled for use on low-speed axial compressors. In addition to the aeromechanical controllers, all the models developed were generalized to include time lags associated with unsteady blade row loss and deviation.

New metrics were developed to allow comparison of the effectiveness of different control methods with regard to operating range extension. In complement to the maximum achievable slope, the control authority metric provides a measure of the ability of a scheme to damp disturbances. It represents the change of unsteady work due to the aeromechanical feedback. Comparison of *true* and *ideal* control authorities determines the effectiveness in applying a specific scheme. Calculations using these models and metrics are carried out in a companion paper (Fréchette et al. [22]) using the geometries and measured characteristics for two laboratory compressors.

Based on the present development of models and metrics, the following conclusions may be drawn:

1. The role of an effective aeromechanical stabilization technology is to suppress rotating stall by adding damping to the overall compression system. This can be seen in the models as changing the real part of the system transfer function. However, even with structural control the physical mechanism responsible for stall can still be interpreted as being linked to the compressor feeding unsteady energy into pre-stall disturbances, as the machine is throttled to reduced flow. An ''ideal'' effective growth rate and control authority based on the aeromechanical work was also derived assuming that the structural controller provides dynamic compensation 180 deg out-of-phase with the inlet axial velocity perturbations. This metric allows the maximum achievable benefit for a particular scheme to be quantified and compared against the actual performance obtained based on the true phasing of the fluid-structure perturbations. Together, these new metrics provide the designer or analyst with a number of ways to measure the impact and effectiveness of various aeromechanical stabilization technologies.
2. The present modeling suggests the potential importance of aeromechanical coupling effects on stall inception. If the aeromechanical feedback schemes presented herein are viewed as flexible structures which exist in all aeroengines to some extent, then this work begins to address the stabilizing (or destabilizing) potential of employing such flexible structures as an enabling technology for stall control at the component or subcomponent (fan, compressor, etc.) level. In the future, careful attention may be necessary to tailor the structural parameters of these machines as lighter and less rigid aeroengine structures are developed.

Acknowledgments

This work was accomplished while the authors were at the Gas Turbine Laboratory, Massachusetts Institute of Technology, Cambridge, MA.

This research was supported by the National Aeronautics and Space Administration (NASA) Faculty Award for Research (FAR), Grant No. NAG3-1571 under the technical monitoring of Mr. John Lucero and Dr. George Stefko for the Structural Dynamics Branch at the NASA Lewis Research Center. Additional support was provided by the Army Research Office, Department of Defense Multidisciplinary Research Program of the University Research Initiative (MURI) under the technical monitoring of Dr. David Mann, Associate Director of the Engineering Sciences Division. Portions of this paper were prepared while the first author was the Martin Luther King, Jr. Visiting Associate Professor in the Department of Aeronautics and Astronautics at MIT. Support from the Department is most gratefully acknowledged. Finally, the technical guidance and insights of Profs. E. M. Greitzer and J. D. Paduano, whose valuable suggestions early on influenced the scope of the paper, is also thankfully acknowledged.

Nomenclature

A = annulus area
b_ξ = structural damping constant
b_{r_n}, b_{i_n} = feedback control parameters, nth mode
b_{igv}, b_r, b_s = IGV, rotor, and stator chords
c = staggered chord length of blade
c_{r_n} = feedback control parameters, nth mode
C = transfer function, structural feedback
C_x = axial velocity
g_{r_n}, g_{i_n} = feedback control parameters, nth mode
$G_n(s)$ = transfer function, compression system plant
H_u, H_d, $H_{\rm avg}$ = transfer functions, pressure sensors
L = structural controller modal length
L_ϕ = loss in pressure rise due to viscous dissipation
L_d = loss in pressure rise due to deviation
M = structural modal mass
M_c = compressor transfer function
n = spatial Fourier harmonic number
P = pressure
Q = $\omega_n/(U_R/R)$, frequency ratio
R = compressor annulus mean radius
s_n, p = $(\sigma+i\omega)R/U_R$, complex poles
t = time
U_R = mean line rotor speed
W = $\rho\overline{L}R^2/M$ mass ratio
z = $\partial\varepsilon/\partial\tau$, time rate of structural response

Greek Symbols

ε = structural response
ε_D = duct wall deflection/duct height, normalized duct wall deflection
ε_r = fluid injector valve deflection/annulus height, normalized injector valve deflection
ε_c = casing wall deflection/tip clearance, normalized casing wall deflection
$\tilde{\varepsilon}_n$ = nth spatial Fourier coefficient of $\delta\varepsilon$
ζ = $b_\xi/2M\omega_n$ critical damping ratio
ϕ = C_x/U_R mean axial flow coefficient
Φ_i = C_{x_i}/U_R, injection parameter
Φ_u = C_{x_u}/U_R steady state upstream axial flow
γ = stagger angle
λ = rotor fluid inertia $(2\times\Sigma_{\rm rotors}c_x/R\cos^2\gamma)$
μ = compressor fluid inertia $(2\times\Sigma_{\rm all\ rows}c_x/R\cos^2\gamma)$
μ_{igv} = inlet guide vane fluid inertia $(c_x/R\cos^2\gamma)_{igv}$
ρ = fluid density
σ = disturbance growth rate
θ = circumferential position, rad
τ = tU_R/R, nondimensional time
$\overline{\tau}_{r,s}$ = $\tau_{r,s}U_R/R$ nondimensional total pressure loss characteristic time
ω = disturbance rotational frequency
ω_n = natural frequency of structural controller
ψ = $P/\frac{1}{2}\rho U_R^2$, nondimensional pressure
$\psi_{\rm ideal}$ = ideal stagnation pressure rise
$\psi_{\rm isen}$ = isentropic stagnation pressure rise
ψ_{ts} = $(P_{\rm exit}-P_{\rm inlet})\frac{1}{2}\rho U_R^2$, steady total-to-exit-static pressure rise

Subscripts

d = downstream flow field, deviation
n = nth spatial harmonic mode
r, s, igv = rotor, stator, inlet guide vanes
s = static pressure
t = total pressure
u = upstream flow field

Operators

$\delta(\ )$ = perturbation quantity
$\overline{(\ )}$ = steady state quantity
$\tilde{(\ )}_n$ = nth spatial Fourier coefficient of $\delta(\ )$
$\dot{(\ )}$ = $\partial(\ )/\partial\tau$

Appendix

Tables 2 and **3** summarize the matching flow conditions and the feedback control parameters for all the schemes. Note that for scheme #9: $\psi_{\rm ideal}=\psi_{ts}+L_{\phi S}+L_{\phi R}+L_{dS}+L_{dR}+L_{igv}$ and the IGV pressure lag: $\tau_r(\partial(\delta L_{igv})/\partial\tau+\partial(\delta L_{igv})/\partial\theta)=(\partial L_{igv}/\partial\gamma)\delta\gamma_{igv}-\delta L_{igv}$. Also, for scheme #10, the fluid inertias are: $\lambda=\lambda(\overline{\gamma_R})=2b_x/R\cos^2\overline{\gamma_R}$ and $\mu=\mu(\overline{\gamma_R})=2b_x/U\cos^2\overline{\gamma_R}$. All perturbation variables are of the form $e^{(in\theta+s_n\tau)}$.

References

[1] Emmons, H. W., Pearson, C. E., and Grant, H. P., 1955, ‘‘Compressor Surge and Stall Propagation,’’ Trans. ASME, **77**, pp. 455–469.

[2] Greitzer, E. M., 1976, ‘‘Surge and Rotating Stall in Axial Flow Compressors, Part I & II,’’ ASME J. Eng. Power, **99**, pp. 190–217.

[3] Greitzer, E. M., 1980, ‘‘Review: Axial Compressor Stall Phenomenon,’’ ASME J. Fluids Eng., **102**, pp. 134–151.

[4] Greitzer, E. M., 1981, ‘‘The Stability of Pumping Systems, The 1980 Freeman Scholar Lecture,’’ ASME J. Fluids Eng., **103**, pp. 193–242.

[5] Day, I. J., 1993, ‘‘Stall Inception in Axial Flow Compressors,’’ ASME J. Turbomach., **115**, pp. 1–9.

[6] Gysling, D. L. et al., 1991, ‘‘Dynamic Control of Centrifugal Compressor Surge Using Tailored Structures,’’ ASME J. Turbomach., **113**, pp. 710–722.

[7] Gysling, D. L., and Greitzer, E. M., 1995, ‘‘Dynamic Control of Rotating Stall in Axial Flow Compressors Using Aeromechanical Feedback,’’ ASME J. Turbomach., **117**, pp. 307–319.

[8] Moore, F. K., 1984, ‘‘A Theory of Rotating Stall of Multistage Compressors—Parts I–II–III,’’ ASME J. Eng. Gas Turbines Power, **106**, pp. 313–336.

[9] Moore, F. K., and Greitzer, E. M., 1986, ‘‘A Theory of Post Stall Transients in Axial Compression Systems: Part I—Development of Equations,’’ ASME J. Eng. Gas Turbines Power, **108**, pp. 68–76.

[10] Greitzer, E. M., and Moore, F. K., 1986, ‘‘A Theory of Post-Stall Transients in Axial Compression Systems: Part II—Application,’’ ASME J. Eng. Gas Turbines Power, **108**, pp. 231–239.

[11] Haynes, J. M., Hendricks, G. J., and Epstein, A. H., 1994, ‘‘Active Stabilization of Rotating Stall in a Three-Stage Axial Compressor,’’ ASME J. Turbomach., **116**, pp. 226–239.

[12] Longley, J. P., 1994, ‘‘A Review of Non-Steady Flow Models for Compressor Stability,’’ ASME J. Turbomach., **116**, pp. 202–215.

[13] Bonnaure, L. P., 1991, ‘‘Modeling High Speed Multistage Compressor Stability,’’ M.S. thesis, Department of Aeronautics and Astronautics, M.I.T., Cambridge, MA.

[14] Hendricks, G. J., et al., 1993, ‘‘Analysis of Rotating Stall Onset in High-Speed Axial Flow Compressors,’’ AIAA Paper No. 93-2233.

[15] Feulner, M. R., Hendricks, G. J., and Paduano, J. D., 1994, ‘‘Modeling for Control of Rotating Stall in High-Speed Multistage Axial Compressors,’’ ASME Paper No. 94-GT-200.

[16] Fréchette, L. G., 1997, ‘‘Implications of Stability Modeling for High Speed Axial Compressor Design,’’ Master thesis, Department of Aeronautics and Astronautics, M.I.T., Cambridge, MA.

[17] Paduano, J. D. et al., 1993, ‘‘Active Control of Rotating Stall in a Low Speed Compressor,’’ ASME J. Turbomach., **115**, pp. 48–56.

[18] Vo, H. D., 1997, ‘‘Active Control of Rotating Stall in a Three-Stage Axial Compressor With Jet Actuators,’’ M.S. thesis, Department of Aeronautics and Astronautics, M.I.T., Cambridge, MA.

[19] Weigl, H. J., Paduano, J. D., Fréchette, L. G., Epstein, A. H., Greitzer, E. M., Bright, M. M., and Strazisar, A. J., 1998, ‘‘Active Stabilization of Rotating Stall and Surge in a Transonic Single Stage Axial Compressor,’’ ASME J. Turbomach., **120**, pp. 625–636.

[20] Camp, T. R., and Day, I. J., 1997, ‘‘A Study of Spike and Modal Stall Phenomena in a Low-Speed Axial Compressor,’’ ASME Paper 97-GT-526.

[21] Hoying, D. A., 1996, ‘‘Blade Passage Flow Structure Effects on Axial Compressor Rotating Stall Inception,’’ Ph.D. thesis, MIT Department of Aeronautics and Astronautics, M.I.T., Cambridge, MA.

[22] Fréchette, L. G., McGee, O. G., and Graf, M. B., 2004, ‘‘Tailored Structural Design and Aeromechanical Control of Axial Compressor Stall—Part II: Evaluations of Approaches,’’ ASME J. Turbomach. **126**, pp. 63–72.

[23] McGee, O. G., Graf, M. B., and Fréchette, L. G., 2003, ‘‘Tailored Structural Design and Aeromechanical Feedback Control of Axial Compressor Stall,’’ Civil Engineering Report, Ohio State University, to appear.

[24] Epstein, A. H., Ffowcs-Williams, J. E., and Greitzer, E. M., 1989, ‘‘Active Suppression of Compressor Instabilities,’’ Am. J. Hum. Genet., **5**, pp. 204–211.

[25] Nagano, S., Machida, Y., and Takata, H., 1971, ‘‘Dynamic Performance of Stalled Blade Rows,’’ JSME Paper No. 11, Tokyo Joint Int’l Gas Turbine Conf., Tokyo, Japan, Oct.

[26] Mazzawy, R. S., 1977, ‘‘Multiple Segment Parallel Compressor Model for Circumferential Flow Distorsion,’’ ASME J. Eng. Gas Turbines Power, **99**.

[27] Gysling, D. L., 1993, ‘‘Dynamic Control of Rotating Stall in Axial Flow Compressors Using Aeromechanical Feedback,’’ Ph.D. thesis, Department of Aeronautics and Astronautics, M.I.T., Cambridge, MA.

L. G. Fréchette
Department of Mechanical Engineering,
Columbia University,
New York, NY 10027

O. G. McGee
Department of Civil, Environmental
Engineering, and Geodetic Science,
The Ohio State University,
Columbus, OH 43210

M. B. Graf
Mars and Company,
124 Mason Street,
Greenwich, CT 06830

Tailored Structural Design and Aeromechanical Control of Axial Compressor Stall—Part II: Evaluation of Approaches

A theoretical evaluation was conducted delineating how aeromechanical feedback control can be utilized to stabilize the inception of rotating stall in axial compressors. Ten aeromechanical control methodologies were quantitatively examined based on the analytical formulations presented in the first part of this paper. The maximum operating range for each scheme is determined for optimized structural parameters, and the various schemes are compared. The present study shows that the most promising aeromechanical designs and controls for a class of low-speed axial compressors were the use of dynamic fluid injection. Aeromechanically incorporating variable duct geometries and dynamically restaggered IGV and rotor blades were predicted to yield less controllability. The aeromechanical interaction of a flexible casing wall was predicted to be destabilizing, and thus should be avoided by designing sufficiently rigid structures to prevent casing ovalization or other structurally induced variations in tip clearance. Control authority, a metric developed in the first part of this paper, provided a useful interpretation of the aeromechanical damping of the coupled system. The model predictions also show that higher spatial modes can become limiting with aeromechanical feedback, both in control of rotating stall as well as in considering the effects of lighter, less rigid structural aeroengine designs on compressor stability. [DOI: 10.1115/1.1644556]

1 Introduction

This paper presents a systematic evaluation of the models developed in a companion paper, [1], on tailored structural design and aeromechanical feedback stabilization of rotating stall in axial compressors. The focus of this work is to evaluate aeromechanical feedback stabilization strategies of long wave length, modal stall that employ static pressure sensing and structural actuation for dynamic compensation. Ten aeromechanical feedback stabilization strategies are considered. To quantify the effectiveness of the various schemes, the analysis is applied to two low-speed compressors for which the modeling inputs have been previously determined: (i) the MIT single-stage compressor (Gysling and Greitzer [2]) and (ii) the MIT three-stage compressor (Haynes et al. [3]). The level of effectiveness of the various schemes is compared using new metrics proposed in a companion paper (McGee et al. [1]), illustrating the relative control authority of the aeromechanical feedback strategies.

In the following sections, we (i) describe the various aeromechanical stabilization schemes, (ii) discuss the fluid-structural dynamics of the coupled systems, and (iii) compare of the aeromechanical stabilization systems using metrics related to compressor operability. Finally, the paper concludes by listing the most promising schemes, the main physical phenomena as described by the metrics, and summary remarks on the utility of these findings.

2 Description of Aeromechanical Feedback Stabilization Schemes

Various possible types of aeromechanical feedback strategies can be envisioned. Those considered herein are shown in **Fig. 1** and **Table 1**. They are categorized as (i) dynamic fluid injection at the compressor face, with and without exit flow recirculation (schemes #1 to #4), (ii) movable compressor inlet and exit duct walls for impedance control (schemes #5 to #7), (iii) flexible compressor casing wall to provide dynamic control of tip clearance flows (scheme #8), and (iv) dynamically restaggered inlet guide vanes and rotor blades (schemes #9 and #10).

The stabilizing physical mechanisms introduced by the proposed aeromechanical control schemes represent new approaches to problems that seriously limit propulsion technology. The schemes, however, differ in phenomenology and engineering concept, which are qualitatively understood as follows. Consider a small arbitrary disturbance to an initially steady, axisymmetric flow, which causes a small decrease in axial velocity in a local region of the compressor annulus. This velocity non-uniformity is associated with a local increase in static pressure in the duct upstream of the compressor.

For the dynamic fluid injection schemes #1 to #4, this pressure increase causes a local force on a reed valve structure, which triggers injection of flow upstream of the compressor (Gysling and Greitzer [2]). Dynamic injection which varies circumferentially thus produces an unsteady modulation of the local mass flow and pressure rise across the compressor. In schemes #1 and #3, the jet is assumed to radially mix-out before reaching the first blade row. This has an effect of changing the local flow coefficient and the momentum at the compressor face. In schemes #2 and #4, however, the injected flow is assumed to be localized to the tip clearance region, not affecting the core flow. This type of injection affects the pressure rise of the compressor by modifying the tip region losses, hence the compressor characteristic directly. The mass flow and incoming momentum are not directly affected. The injected flow is taken from an external plenum (schemes #1

Contributed by the International Gas Turbine Institute and presented at the International Gas Turbine and Aeroengine Congress and Exhibition, Atlanta, GA, June 16–19, 2003. Manuscript received by the IGTI December 2002; final revision March 2003. Paper No. 2003-GT-38976. Review Chair: H. R. Simmons.

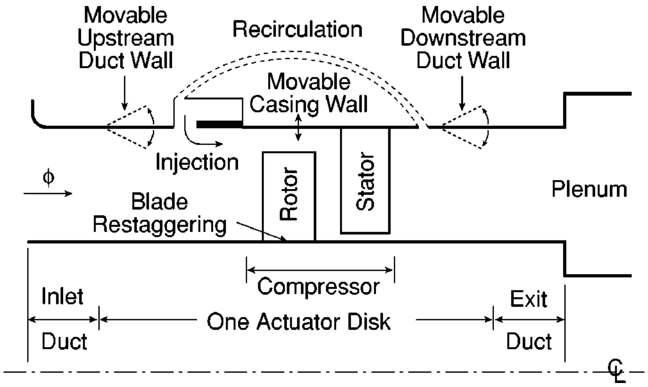

Fig. 1 Illustration of aeromechanical feedback schemes

Table 1 Aeromechanical feedback schemes

Scheme	Description
#1	Radially mixed-out injection at the compressor face
#2	Tip injection at the rotor leading edge
#3	Radially mixed-out injection at the compressor face with exit flow recirculation
#4	Tip injection at the rotor leading edge with exit flow recirculation
#5	Movable inlet duct wall with inlet static pressure sensing
#6	Movable exit duct wall with inlet static pressure sensing
#7	Movable exit duct wall with exit static pressure sensing
#8	Movable casing wall with front-to-back average static pressure sensing
#9	Dynamically restaggered inlet guide vanes with inlet static pressure sensing
#10	Dynamically restaggered rotor blades with front-to-back average static pressure sensing

and#2) or recirculated from the compressor exit (schemes #3 and #4).[1]

The movable inlet/exit duct walls (schemes #5 to #7) are also driven by static pressure disturbances in the flow field, resulting in a dynamic deflections outward that allows a deceleration in flow velocity to be locally produced (like an attached diffuser); whereas, an inward deflection increases the flow velocity (like an attached nozzle). The movable duct walls can be conceived as flexible inner duct liners or a structurally tuned case. Instead of designing the case structure to prevent mechanical resonances, it is tuned to interact with the pre-stall fluid modes, acting as flow impedance control in the ducts.

The flexible compressor casing wall (scheme #8) is driven by an average of the front-to-back static pressure perturbations in the machine. It would consists of a tuned casing or flexible casing treatment designed such that a local deflection outward increases the tip clearance flow (causing a decrease in compressor pressure rise locally), and a deflection inward decreases the tip clearance flow (causing an increase in the local pressure rise across the compressor).

Finally, the IGV and rotor blade restaggering (schemes #9 and #10) is represented by the flow and momentum change as the restaggering of adjacent blades creates diffusing or contracting blade passages. Through structurally tailored oscillating inlet guide vanes and rotor blades, driven by disturbances in static pressure, counter-disturbances may be aeromechanically launched to evolve a compressor's nonsymmetric flow distribution to an axisymmetric one. This is similar to the work of Paduano et al. [5] who utilized digitally controlled variable-stagger inlet guide vanes to control rotating stall inception in their research compressor. In the aeromechanical implementation, the IGV and rotor blades are assumed to be driven by upstream and front-to-back average static pressures, respectively.

These aeromechanical feedback strategies are implemented as *components* which can stabilize (or destabilize) the pre-stall flow field through three basic actuation mechanisms. First, these components can directly reduce (damp) the pre-stall flow perturbations. For example, the mixed-out injection schemes (#1 and #3) inject high-momentum fluid in local regions of velocity deficit, which effectively reduces the magnitude of the perturbation. Another mechanism consists of changing the operating conditions seen by the compressor. The inlet movable duct wall (scheme #5), for example, will change the local flow coefficient and the corresponding operating point on the pressure rise characteristic. Locally, the slope of the characteristic will be different such that the compressor provides a different level of damping. Here, the aeromechanical component does not directly damp out the perturbations, but impacts the amount of damping provided by the compressor. The third mechanism also relies on the compressor as a damper, but actuates by locally modifying the compressor characteristic as opposed to changing the operating point. For example, the tip injection and movable casing wall schemes (#2, #4, and #8) affect the losses due to tip clearance flows, hence modifying the shape of the compressor characteristic and the related damping provided by the compressor.

3 Modeling Parameters

3.1 Compressor Characteristics. To enable numerical evaluation of the models considered, well known compressor characteristics were used. **Figure 2** shows characteristic curves and pressure loss buckets for the MIT single-stage compressor (Gysling and Greitzer [2]) and for the MIT three-stage compressor (including the characteristic sensitivity to inlet guide vane restaggering γ, cf. Haynes et al. [3]) used for this study (detailed polynomial representations are found in McGee et al. [6]).

The pressure loss due to deviation was estimated from the difference between the ideal pressure rise characteristic (ψ_{ideal}) and the isentropic characteristic (ψ_{isen}). Although the isentropic characteristic was inferred from measurements for the three-stage compressor, it was estimated (via the Euler turbine equation) for the single-stage machine. The pressure loss due to viscous dissipation was estimated from the difference between the isentropic pressure rise (ψ_{isen}) and the measured one (ψ_{ts}). Polynomial fits to these pressure loss buckets **(Fig. 2)** were subsequently used to calculate the slopes of the rotor and stator loss curves, $\partial L_{\phi R}/\partial\phi$, $\partial L_{\phi S}/\partial\phi$, $\partial L_{dR}/\partial\phi$, $\partial L_{dS}/\partial\phi$. In **Fig. 2**, the loss buckets attributed to dissipation ($\psi_{ts}-\psi_{\text{isen}}$) show increases with decreasing flow coefficient over the desired range (to the left of the peak of the measured characteristic). The loss buckets due to deviation ($\psi_{\text{ideal}}-\psi_{\text{isen}}$) are, however, relatively flat over the desired flow range. Thus, the effect of dissipation appears to be greater than that of deviation at reduced flow coefficient, although both were included in the present analysis.

The blade row response time constant for loss and deviation, $\overline{\tau}$, was set equal to 1.5 times the blade passage convection times. This value has been commonly used in stability analyses since its experimental determination by Haynes et al. [3].

3.2 Aeromechanical Stabilization Parameters. The proposed aeromechanical stabilization schemes **(Table 1** and **Fig. 1)** are a function of some key nondimensional control parameters

---

[1] In the present study, which is focused on low-speed machines, the effect of inlet temperature distribution due to exit recirculation is neglected. Variable density or fully compressible flow modeling would be required (Fréchette [4]).

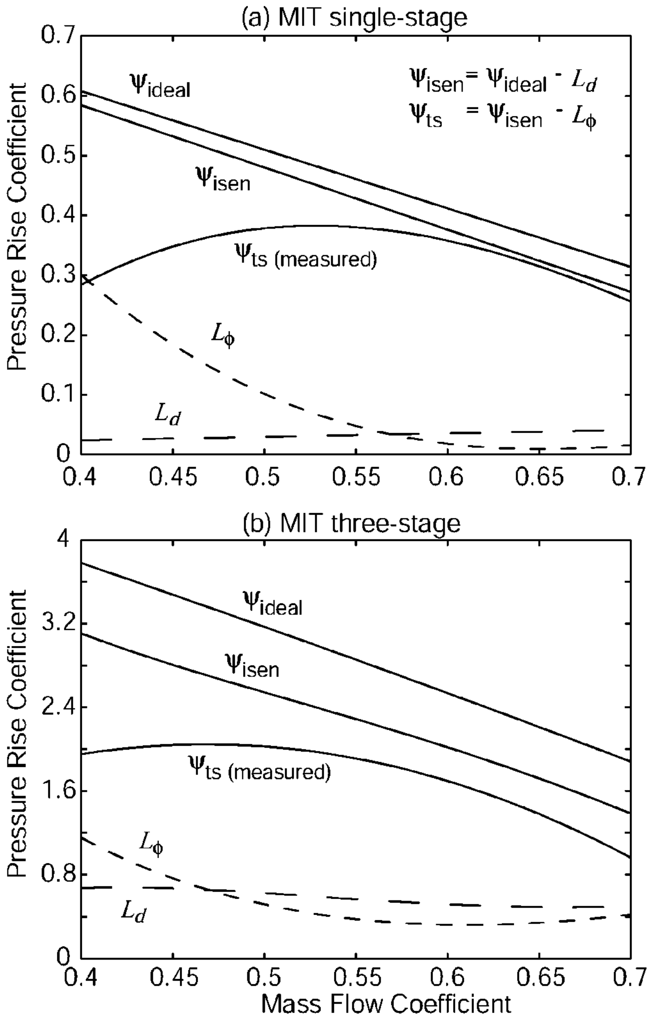

Fig. 2 Compressor characteristics used in this study: (*a*) MIT single stage (Gysling and Greitzer [2]), (*b*) MIT three-stage (Haynes et al. [3])

which determine the interaction between the structural controllers and the flow field. Based on our use of the generalized mass-spring-damper structural model described in the companion paper (McGee et al. [1]), these parameters typically include the structural frequency $Q=\omega_n/(U_R/R)$, critical damping ratio $\zeta = b_\xi/2M\omega_n$, mass ratio $W=\rho LR^2/M$, and injection coefficient $\Phi_i=C_{x_i}/U_R$ (used for schemes #1 and #3 only).

A number of sensitivity coefficients identified in the companion paper (McGee et al. [1]) are also needed as additional modeling inputs. Definitions and estimates of these aeromechanical parameters are now given. For schemes #2 and #4, the sensitivities of the ideal characteristic to tip injection, $\partial\psi_{\text{ideal}}/\partial\alpha_i$ was zero, however, the stagnation pressure loss sensitivity to tip injection, $\partial L_{\phi R}/\partial\alpha_i$ was estimated by fitting unpublished experimental data from a variety of compressors and fans, and found to be approximately 0.64. For scheme #8, the sensitivity of the ideal characteristic to tip clearance, $\partial\psi_{\text{ideal}}/\partial\varepsilon_c$ was zero, however the sensitivity of the actual characteristic was considered nonzero. Using a simple channel diffuser analogy (cf. Kerrebrock [7]), one finds that the local static pressure loss at stall is proportional to the ratio of clearance (casing wall deflection, Δ_c, to blade chord, c), that is, $\delta\psi=-\sigma^2(\Delta_c/c)=-\sigma^2\varepsilon_c$. The proportionality constant is the square of the effective stage solidity σ, which is defined as the ratio of blade chord to average staggered blade spacing. For a typical low-speed compressor, the solidity $\sigma=2$, and this argument predicts that the stalling pressure rise coefficient should decrease by about four times the ratio of clearance to blade chord. This is close to what was experimentally observed by Smith [8], and later confirmed by Koch [9]. Their data showed that for a range of compressors, the sensitivity to tip clearance, $\partial L_{\phi R}/\partial\varepsilon_c$ is approximately -4.6% in pressure for each 1% increase in clearance to chord. Hence, a value of $\partial L_{\phi R}/\partial\varepsilon_c=-4.6$ was used as a model input to scheme #8. For all relevant schemes, the sensitivities of the rotor pressure loss to deviation with respect to tip injection and tip clearance, $\partial L_{dR}/\partial\alpha_i$ and $\partial L_{dR}/\partial\varepsilon_c$, respectively, were assumed negligible since the deviation buckets shown in Fig. 2 are relatively flat over the flow range considered. Finally, the stagnation pressure loss and deviation sensitivities in the rotors, $\partial L_{\phi R}/\partial\gamma$ and $\partial L_{dR}/\partial\gamma$, associated with dynamically restaggered IGVs (scheme #9), were estimated as $\partial L_{\phi R}/\partial\gamma = \partial\psi_{\text{isen}}/\partial\gamma - \partial\psi_{ts}/\partial\gamma$ (via., Eqs. (9) and (10)) and $\partial L_{dR}/\partial\gamma = \partial\psi_{\text{ideal}}/\partial\gamma - \partial\psi_{ts}/\partial\gamma$ (via., Eqs. (9) and (11)).

4 Pre-Stall Dynamics With Aeromechanical Feedback

Using the model described in the first part of this paper (McGee et al. [1]) and chosen values for the parameters listed above, the growth rate and rotational frequency of modal waves in the compression system can be calculated, establishing if fluid perturbations will grow or decay, hence leading to the inception of rotation stall, or not. To describe the inception dynamics, scheme #1 (mixed-out injection) will be considered.

The effect of aeromechanical feedback on a baseline compression system can be illustrated by a root locus plot, which shows the rotation and growth rates of the pre-stall modes as a function of flow coefficient. **Figure 3** shows a collection of root locus plots: with and without lags, with and without aeromechanical feedback (i.e., closed or open-loop) for both machines considered. In each plot, the eigenvalues of the first two spatial harmonics are plotted for flow coefficient values decreasing from 0.6 to 0.3 by increments of 0.03. The pre-stall modes are stable if their growth rate is negative (i.e., on the left side of the origin). The stalling flow is determined as the lowest flow coefficient at which the growth rate of all the modes is less than or equal to zero. The eigenvalues at stall are identified in the root locus plots by "+." The eigenvalues shown correspond to the fundamental fluid mode (Moore-Greitzer) and to the fluid-structure modes introduced by the structural dynamics. Those mostly associated with the lag dynamics (located at frequencies of approximately 0 and 1) are highly stable (i.e., negative damping greater than -1), and thus, are out of the plotting range in **Figs. 3**(*c*), (***d***), (***g***) and (***h***). It should be noted that the open-loop (fluid only) dynamics calculated for the three-stage machine using the present models (McGee et al. [1]) were shown to be the same as obtained previously by Haynes et al. [3]. Also, the open and closed-loop dynamics for the single stage machine modeled without lags were shown to be the same as modeled by Gysling and Greitzer [2].

Figure 3(***a***), which was calculated using the Moore-Greitzer model, shows that the disturbance frequencies are constant for each spatial harmonic over all flow coefficients, and that each spatial harmonic is unstable at the same flow coefficient, corresponding to the peak of the total-to-static pressure rise characteristic. As the flow coefficient decreases below Φ_{peak} (passing over the peak of the characteristics), the aerodynamic damping decreased negatively.

The prediction of aerodynamic damping and disturbance frequencies which include the effects of loss and deviation dynamics are shown in Fig. 3(*c*). In this case each spatial harmonic is not neutrally stable at the same flow coefficient, but instead the higher harmonic is more stable. This stabilizing effect of unsteady losses has been previously modeled and experimentally observed on an actively controlled research compressor (Haynes et al., [3]).

Comparing **Fig. 3**(***a***) with **3**(***b***), and **Fig. 3**(***c***) with **3**(***d***) shows that closing the aeromechanical loop introduces additional fluid-structure modes and also modifies the damping and frequency of

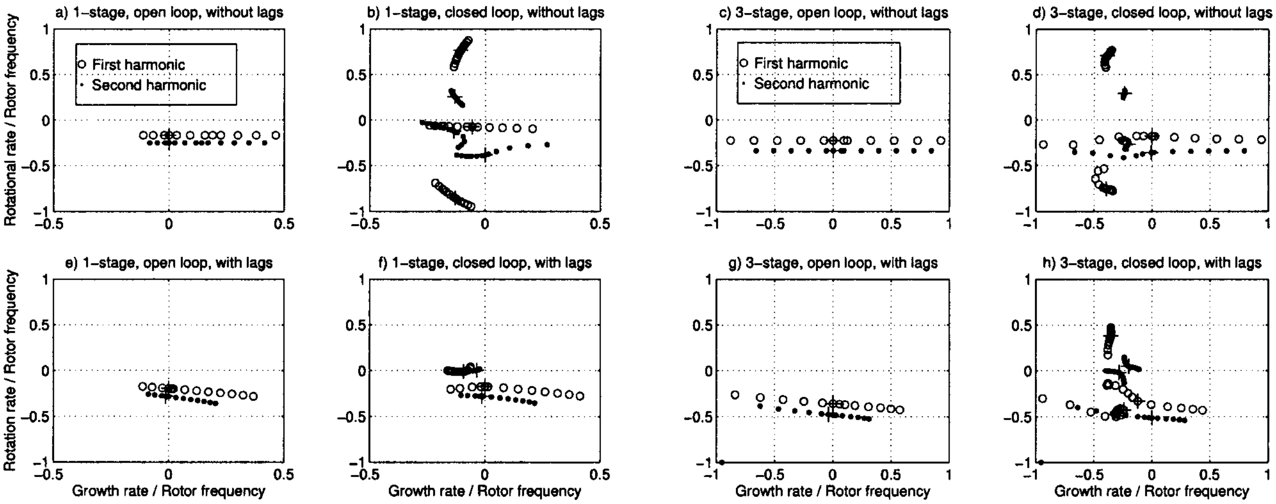

Fig. 3 Root locus plots showing the growth rates and rotation rates of the first and second harmonic modes in the MIT 1-stage and 3-stage compressors. Results are shown for cases with and without aeromechanical feedback scheme #1, using the models with and without aerodynamic lags. Flow coefficient values decrease from 0.6 to 0.3 by increments of 0.03, with the eigenvalues at the stalling flow coefficient identified by the plus sign.

the fundamental fluid mode. In the case of an aeromechanically controlled system, both harmonics do not have the same level of aeromechanical damping. For example, the single-stage compressor with mixed-out injection is limited by the second harmonic when modeled without lags (**Fig. 3(*b*)**), or by the first harmonic when modeled with lags (**Fig. 3(*d*)**). It should be noted that the limiting harmonic modes are different for the three-stage compressor (**Fig. 3(*f*)** and **3(*h*)**). As will be discussed later, the lowest harmonic is not necessarily the limiting mode in aeromechanically compensated compression systems. Overall, the most unstable modes are associated with predominately fluid rather than structural dynamic instabilities, since the modes that existed before closing the loop are found to be limiting.

To simplify the presentation of later results, only the dynamics at stall will be presented, determined by the lowest mass flow achievable until one of the modes becomes neutrally stable.

5 Comparison of Aeromechanical Stabilization Strategies

This section presents the stall inception modeling results for the ten aeromechanical schemes studied. First, optimal controller design parameters are determined in order to maximize the potential of each scheme. Then, the stall inception predictions for all schemes are described.

5.1 Structural Controller Optimization. Using the linearized stability models developed in McGee et al. [1], a parameter optimization was performed to determine the controller frequency ratio, Q, and damping ratio, ζ, that minimized the growth rate (or maximize the instantaneous aeromechanical damping) of the two lowest spatial harmonics of the compression system. The optimized configuration allowed the compression system to reach a maximum achievable characteristic slope and to achieve an extended flow range beyond that of the baseline compressor (without aeromechanical stabilization). Optimizing the dynamics of the spatial harmonics higher than $n=2$ was not considered, since the pressure field acting on the structural controllers became increasingly nonuniform in the higher harmonics. Consequently, the uniform pressure assumption adopted in the modeling (McGee et al. [1]) becomes increasingly invalid.

As proposed by Gysling and Greitzer [2], high values of the injection coefficient and mass ratio were utilized for properly tuned structural controllers. Injection pressure was restricted to the order of the dynamic pressure based on the mean wheel speed of these compressors. The mass and frequency parameters of the structural controllers used in the optimization study were restricted to constructible sizes for these low-speed compressor builds using readily obtainable materials. These constraints restricted the injection coefficient to $\Phi_i=1$, the mass ratio to $\overline{W}=0.583$, the structural controller frequency ratio within $0.3\leqslant Q\leqslant 2.9$, and the controller damping ratio within $0.3\leqslant\zeta\leqslant 2.9$ (Gysling and Greitzer [2]). Although the actual limits for the various schemes may indeed differ, the above ranges of values for Φ_i, $\overline{W}$, Q, and ζ were chosen for all schemes to maximize stability.

The values of Q and ζ resulting from an optimization study of the closed-loop dynamics are compared for all schemes in **Fig. 4** (solid line). Only feedback schemes #1 to #8 were modeled for the single-stage compressor, since no data were available regarding the compressor's sensitivity to IGV and rotor blade restaggering (used in schemes #9 and #10). All ten schemes were modeled for the three-stage machine.

The inlet duct wall schemes #5 and #6, the movable casing wall scheme #8, and the IGV restaggering scheme #9 produced tailored controller designs which were nonoptimal, i.e., on the maximum constraint boundaries of Q and ζ. Choice of different parameters and limits would affect some results, which will be discussed later.

An additional parameter optimization was performed to determine a second set of design values of Q and ζ (shown dashed in **Fig. 4**) that optimized the stability of the two lowest spatial harmonics when unsteady losses and deviation dynamics were neglected. The latter reduced the present model to one involving only three states per nth harmonic, one fluid—the flow perturbation $\tilde{\phi}_n$, and two structural ones—the controller displacement $\tilde{\varepsilon}_n$, and its velocity $\tilde{z}_n$. The influence of unsteady losses and deviation dynamics on the tailored design of the structural controllers is not very significant. The exceptions to this observation are the inlet duct wall scheme #5 and the rotor blade restaggering scheme #10 for the three-stage machine. Here, the parameter optimization yielded tailored controllers with significantly lighter damping than that obtained when unsteady losses and deviation was neglected (see **Fig. 4**).

5.2 Compressor Operability Predictions. The stall point was determined for all aeromechanical feedback strategies using the models developed in McGee et al. [1], with optimum structural control parameters (**Fig. 4**) and a blade row time constant, $\overline{\tau}=1.5$. **Figure 5** shows compressor characteristics and slope

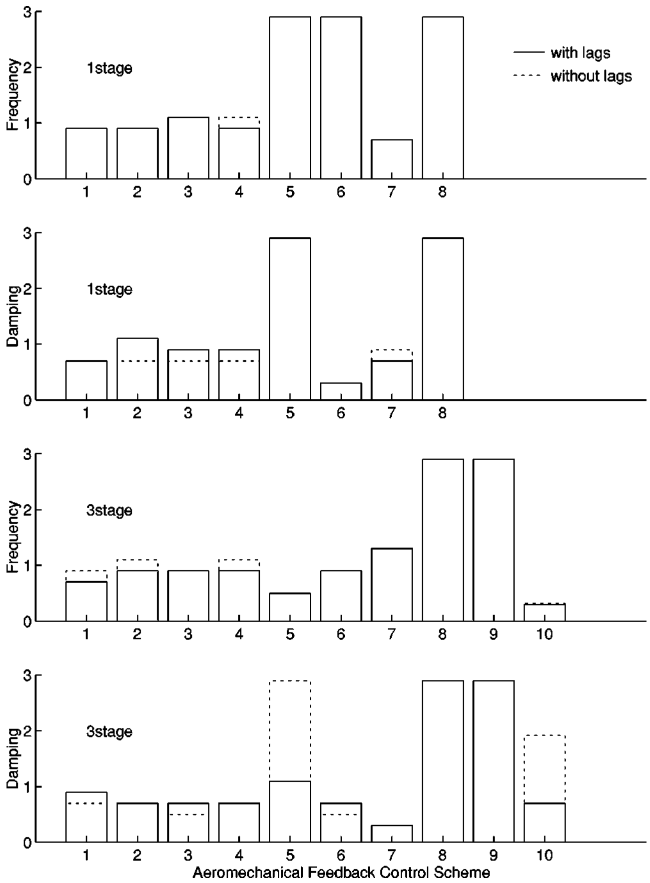

Fig. 4 Structural control parameters for maximum stable range extension. Optimal structural frequency, Q, and damping ratio, ζ are shown for the various aeromechanical schemes. Results are presented for the MIT 1-stage and 3-stage compressors, modeling the aerodynamic blade row response with and without time lags for loss and deviation (solid and dashed lines respectively).

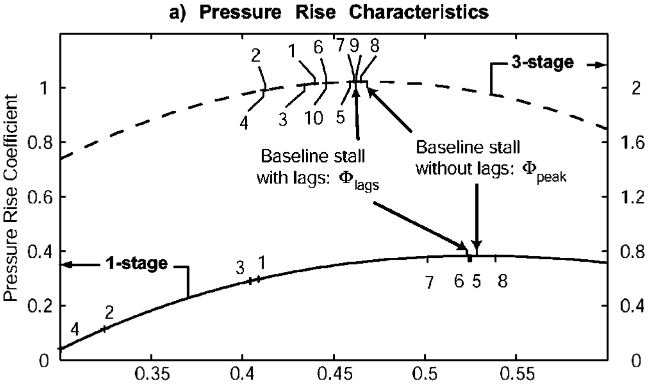
a) Pressure Rise Characteristics

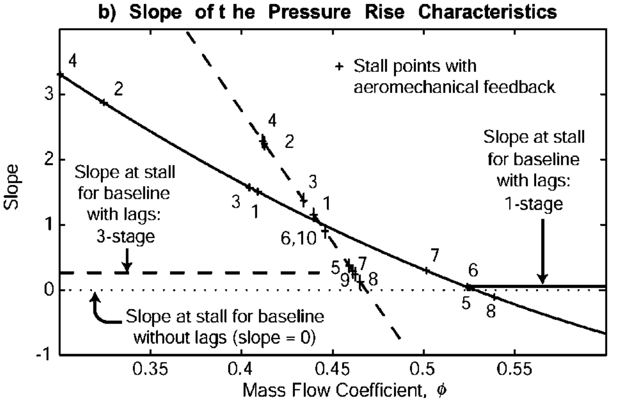
b) Slope of t he Pressure Rise Characteristics

Fig. 5 Pressure rise characteristics and slope for the MIT 1-stage and 3-stage compressors. Stall points with the various aeromechanical feedback schemes are identified, as well as the stall points for the baseline compressors with and without loss and deviation lag dynamics.

curves for the MIT single-stage machine (shown solid) and three-stage machine (shown dashed). The absissca in **Fig. 5**(***a***), (***b***) is mass flow coefficient ϕ, and it is calculated as the mass flow through the combined compressor and feedback actuator disks. The ordinate in **Fig. 5**(***a***) is inlet total-to-exit-static pressure rise coefficient ψ_{ts}, based on the difference in pressures upstream and downstream of the compressor.

The stalling flow for each of the baseline compressors without control nor lags are at the peak of the characteristic, indicated in **Fig. 5**. The stalling flow with lags, $\Phi_{\rm lags}$, is also identified in Fig. 5 for each of the baseline compressors. Comparing these stalling flows illustrates the stabilizing effect of blade passage response lags, as discussed previously. The stall points, $\Phi_{\rm stall}$, obtained by using the optimum design configurations of the various stabilization schemes (**Fig. 4**) including lag dynamics are denoted as 1,2,3,... etc. The flow in the compression system is unstable when operating at $\phi < \Phi_{\rm stall}$, and stable for $\phi > \Phi_{\rm stall}$. The flow range extension can be defined as the difference between the stalling flow of the baseline compressor and that with aeromechanical feedback. In other words, the flow range extension is defined as $(\Phi_{\rm lags} - \Phi_{\rm stall})$ for the case with lag dynamics and as $(\Phi_{\rm peak} - \Phi_{\rm stall})$ for the case without lags. **Figure 5**(***b***) shows the slope of the pressure rise characteristic as a function of ϕ. The stall points are indicated, highlighting that larger flow range corresponds to higher achievable slope. The level of maximum achievable stable slope is therefore a measure of goodness of the stabilization schemes at their design configurations.

These results for flow range and maximum achievable slope are recast as bar charts in **Fig. 6**, for all schemes and both machines studied. In addition to the results using the aeromechanical model with loss and deviation lags (solid line), results for the same model without lags are overlaid (dotted line).

Figures 6(***a***) and **6**(***c***) compare the flow range extension achieved before stall inception, limited by either of the lowest two spatial harmonics. Positive values of flow range indicate an increase in stabilized operating range due to aeromechanical feedback, whereas negative values of flow range indicate reduced operating range. Ideally, with positive flow range, the operating point could be moved to lower ϕ (hence possibly higher pressure rise and compressor efficiency) for the same effective stall margin. Note that the flow range extension achieved for feedback scheme #1 (excluding loss and deviation lag dynamics, **Fig. 6**(***c***)) was consistent with that modeled previously by Gysling and Greitzer [2]. Therefore, this flow range extension serves as a benchmark for comparison with those ranges achieved using schemes #2 to #8 modeled in the single-stage compressor.

The maximum achievable stabilized characteristic slopes, $\partial\psi_{ts}/\partial\phi$, are shown in **Figs. 6**(***b***) and **6**(***d***), for both machines and all schemes considered. This slope was determined at the analytically computed stall point with optimized controller parameters, and it serves as another figure of merit for the stabilization schemes. Also shown are the slopes at stall for the baseline compressors with and without lags, represented by the solid and dashed horizontal lines, respectively. Values of slope larger than the baseline value indicate those schemes predicted to yield increase operability (i.e., flow range), whereas values of slope lower than the baseline indicate those schemes which exhibited decreased operability.

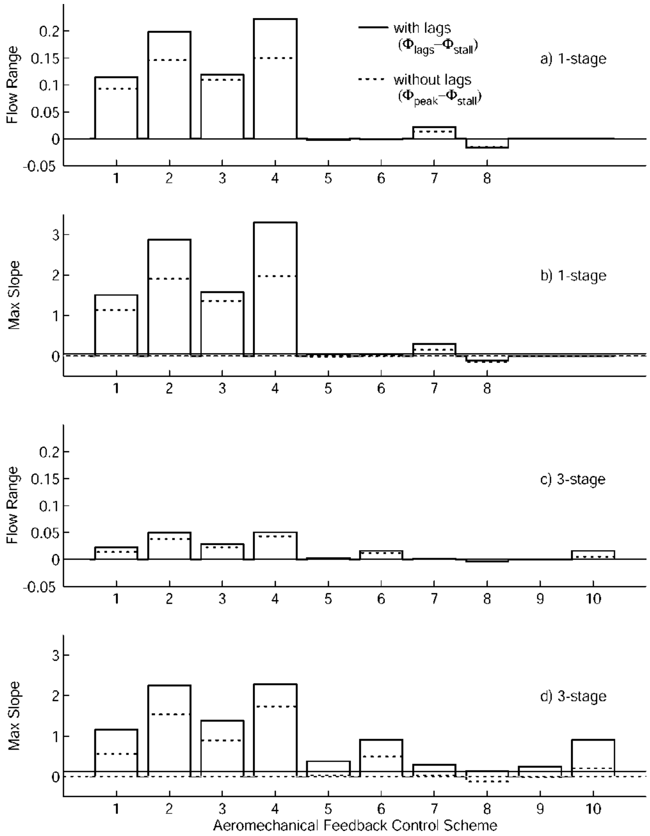

Fig. 6 Flow range extension and the corresponding maximum achievable slope for the MIT 1-stage and 3-stage compressors with the various aeromechanical feedback schemes (flow range is defined as the difference in stalling flow coefficient between the aeromechanical (close-loop) and baseline (open-loop) compression systems

Overall, the results shown in **Figs. 5** and **6** indicate that dynamic fluid injection schemes exhibit more potential for stabilization than the other types of schemes. Some of the movable casing and duct wall schemes have low potential and are even shown to be destabilizing. It can also be seen that the single-stage and multistage machines modeled with aeromechanical feedback exhibited similar maximum achievable slopes, but that the multistage benefited from less range extension due to its steeper characteristic. Furthermore, the inclusion of loss and deviation lags increases the achievable slope, which is consistent with other studies without aeromechanical feedback (Longley [10]). These additional dynamics do not drastically modify the relative effectiveness of the various schemes. The remainder of this section will describe these aspects for the ten aeromechanical schemes in more detail.

Dynamic fluid injection stabilization, in particular, was especially enabling to operability of both machines, regardless of whether or not unsteady loss and deviation lag dynamics were included in the modeling. The tip injection schemes #2 and #4 produced the largest increase in flow range and maximum achievable slope, $\partial\psi_{ts}/\partial\phi$. The mixed-out fluid injection schemes #1 and #3 were the next most effective at increasing the operability of both machines. This suggests that dynamic fluid injection stabilization should be confined to the casing region upstream of the compressor for maximum benefit to stability and operability when aeromechanically controlling the evolution of stall.

On the whole, impedance control achieved aeromechanically through variable duct geometries (i.e., movable duct walls schemes #5, #6, #7) yielded considerably smaller gains (or even loss) in operating performance, regardless of whether or not loss and deviation dynamics were included. Depending on the pressure sensing mechanism employed, the effectiveness of variable duct geometry varies. For instance, modeling a movable exit duct wall (incorporating downstream pressure sensing—scheme #7) produced the largest quantifiable increased in operability of the single-stage machine (**Figs. 5** and **6**). Whereas, modeling a movable inlet duct wall (incorporating downstream pressure sensing—scheme #6) yielded the largest gain in operability of the three-stage machine.

Modeling a movable casing wall (scheme #8) to dynamically control the tip clearance flows is predicted to destabilize both compressors. The compressor's stall margin was reduced, whether or not lag dynamics were neglected. However, when lag dynamics were included in the modeling of scheme #8, the predicted operability of both machines was slightly improved, following the trend for all other schemes. These results suggest that little dynamic compensation or stabilization can be quantifiably achieved through structurally tailored casing deformation which affects the tip clearance flow processes. From a structural design point of view, this dynamic interaction should be avoided to prevent detrimental reduction in stall margin.

In the present analysis, only the three-stage machine was analyzed with dynamically restaggered inlet guide vanes (scheme #9) and rotor blades (scheme #10). While the inlet guide vanes had a negligible effect, the rotor blades were shown to be more beneficial to stability. Not modeling the lag dynamics significantly reduced the flow range extension for the restaggered rotor blade scheme (#10). Before discussing the significance of these results any further, they will be described in further detail in the following sections.

5.3 Damping Predictions.

Figure 7 summarizes the growth rates of the first and second harmonic main fluid modes at stall, for both compressors and all schemes. The solid and dashed bar charts represent aeromechanical damping, for the fluid-structure (close-loop) system at neutral stability, when modeled with and without lag dynamics, respectively. All results were calculated based on the optimum design configurations (**Fig. 3**). At stall, either the first or second harmonic mode is neutrally stable (vanishing growth rate), while the other harmonic is stable (negative growth rate, representing *positive* aeromechanical damping). The limiting harmonic is not the same for all schemes and may be different when modeled with and without lags. Although the lowest harmonic is stability limiting for the baseline system modeled with lag dynamics, no generality can be drawn for systems with aeromechanical feedback.

5.4 Aeromechanical Energy Predictions.

As the operating point shifts to lower mass flows, the compressor approaches stall, and the level of damping is sufficient such that flow perturbations decay. Consequently, the unsteady energy associated with the pre-stall perturbations diminishes. Beyond the stall point, the compression system exhibits a lower damping and even increases unsteady energy in the flow, such that perturbations will grow until they eventually lead to the inception of a rotating stall cell. In the baseline compression system, the increase in total-to-static characteristic slope is the source of this destabilization. Such an energy-based point of view has been used by others (Epstein et al., [11], Gysling and Greitzer [2], and Fréchette [4]) and will be useful here to describe the relative impacts of the aeromechanical feedback strategies.

A stabilizing aeromechanical scheme is one for which the combined actuator disk (compressor with aeromechanical feedback) provides higher damping of the unsteady perturbation energy in the flow, compared to the baseline compressor. A metric for judging the impact of an aeromechanical scheme can therefore be based on the unsteady work of a combined fluid-structure system. In a companion paper (McGee et al. [1]) *Control Authority* is defined as such a figure of merit. It is derived from the analytical formulations of the combined aeromechanical actuator disk, for each scheme analyzed herein. The *true* control authority uses the

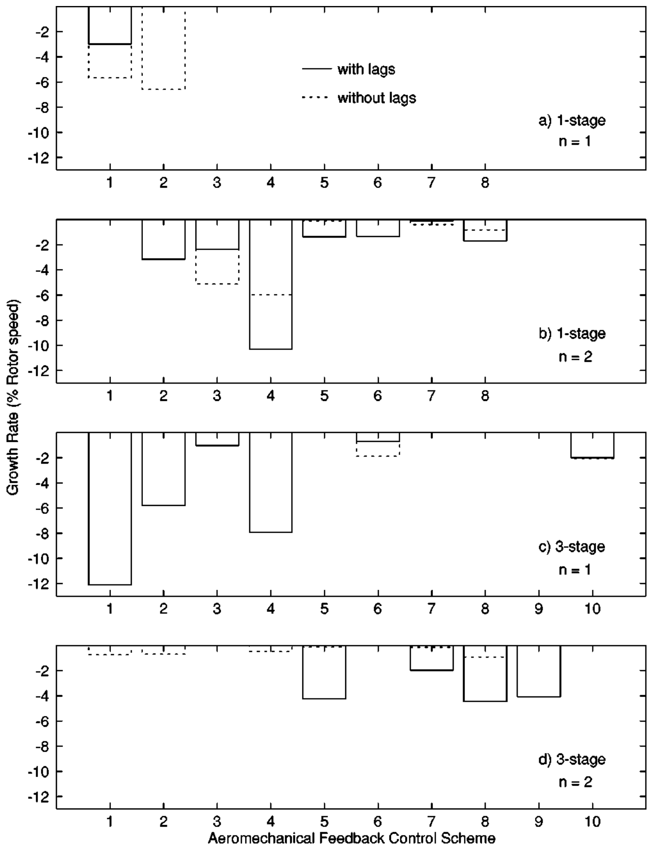

Fig. 7 Aeromechanical modal damping represented by the closed-loop growth rates of the first and second harmonic main fluid modes in the MIT 1-stage and 3-stage compressors. Results shown at the stall point for each optimized aeromechanical scheme using the present models with and without aerodynamic lags.

predicted phasing between the the velocity perturbations and the structural response, while the *ideal* control authority assumes a phasing of 180 deg.[2] Since static pressure and velocity perturbations are nominally 180 deg out-of-phase, the ideal metric corresponds to a structural response *in-phase* with the pressure perturbations.

Figures 8 and **9** compare for all schemes the true and ideal control authorities respectively, at the point of stall inception of both the single-stage and three-stage compressors. Shown solid and dashed in **Figs. 8** and **9** are the control authorities when the aeromechanical feedback system is modeled with and without unsteady blade passage lag dynamics, respectively. All results were calculated for the least stable mode, using the optimum design configurations (**Fig. 4**). The small quantifiable difference between the ideal and true control authorities suggests that the structural controllers ideally provided dynamic compensation roughly 180 deg out-of-phase with the upstream velocity disturbance in the compressors. The structural design parameters used are therefore confirmed as optimum.

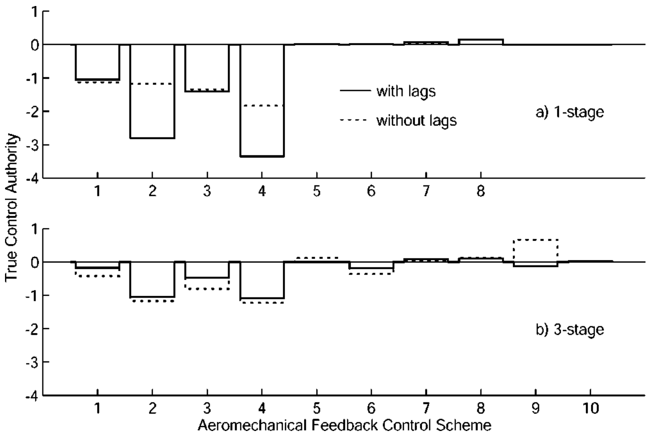

Fig. 8 True control authority of the various aeromechanical schemes, based on the limiting harmonic at the neutral stability for each optimized aeromechanical scheme

In **Fig. 8**, positive values of control authority are interpreted as aeromechanical energy being fed into stalling disturbances due to the fluid-structure coupling. This induced the physical mechanism of rotating stall in the dynamically compensated compressors. Negative values of control authority can be viewed as unsteady energy being aeromechanically dissipated from stalling disturbances. Let us suppose for the moment that the control authority is equivalent to exactly the amount of additional damping provided. Then, the control authority would be equal and opposite to the amount of unsteady energy produced—that is, the slope of the compressor characteristic at stall. Comparing the control authorities to the maximum achievable slopes in **Figs. 6*(b)*** and **6*(d)***, we notice that they are mostly equal and opposite. Most trends and magnitudes are captured, although not replicated exactly. The simple formulation of the control authority metric, which neglects the phasing due to loss and deviation lag dynamics (McGee et al. [1]) is the source of this difference. The metric, however, leads to the justification of the relative effectiveness of the schemes, as discussed in the next section.

6 Discussion

At the heart of control authority is unsteady aeromechanical work, which is derived from the annulus averaged product of the compressor pressure rise and axial flow perturbations (McGee et al. [1])

$$\overline{\delta E} = \frac{1}{A}\int_{\text{Annulus}} \delta\psi_{ts}\delta\phi dA. \tag{1}$$

In general, a negative upstream flow perturbation $\delta\phi$ will be locally associated with a positive pressure perturbation. In the tip injection schemes (#2 and #4), this higher pressure will open the valve, locally injecting flow in the tip region, and increasing the

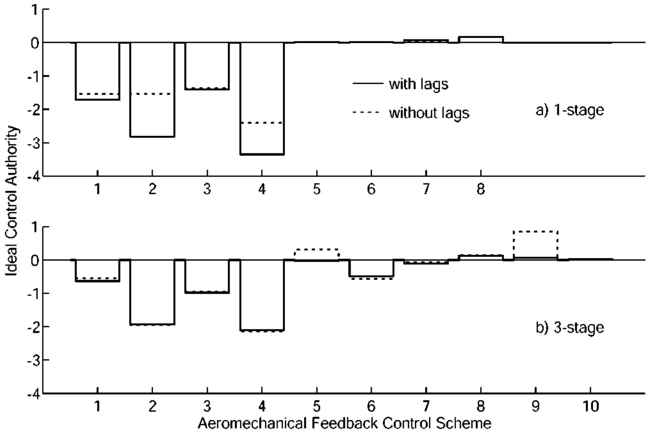

Fig. 9 Ideal control authority of the various aeromechanical schemes, based on the limiting harmonic at the neutral stability for each optimized aeromechanical scheme

---

[2] Experimental evidence shows that the greatest range extension is achieved when the structural response is approximately 180° out-of-phase with the velocity perturbations (Gysling and Greitzer [2]).

local pressure rise. The product of this positive pressure rise with the negative flow perturbation is negative, hence unsteady energy is dissipated from the flow and the perturbations are damped. In comparison to this stabilizing scheme, let us consider the movable casing wall, which generally was shown to be destabilizing. In this case, the effect of the pressure perturbation is to open the tip clearance and degrade the local pressure rise. The unsteady aeromechanical work is the product of the negative pressure rise and negative flow perturbations, resulting in positive unsteady work and amplification of the disturbances. Fundamentally, the intrinsic phasing of these two aeromechanical compensation schemes are opposite to each other, leading to opposite impacts on stability. The mixed-out injection schemes (#1 and #3) also have a favorable intrinsic phasing (as shown by the results in **Figs. 8** and **9**). Due to the actuation mechanisms in play for mixed-out injection, movable duct walls, and restaggered blade rows, the physical description of the unsteady aeromechanical work is more complex than that described above. We should, however, note that the control authority is a direct function of the pressure rise sensitivities (Sections 3.1 and 3.2), which determine the impact of the structural controllers on the pre-stall flow field. Although the values used for these sensitivities in the calculations herein are fully justifiable, they may vary for different compressors. The actual relative merit of various schemes may vary, but not the major trends, since they are guided by the intrinsic phasing of the feedback strategy.[3]

Implementation of the movable casing wall scheme through active control would enable one to *close* the tip clearance under a *positive* local pressure perturbation. Electromechanical feedback can therefore allow one to invert the sensitivities of destabilizing schemes such that they become beneficial. Another aspect that distinguishes aeromechanical from electromechanical feedback implementations is the additional versatility provided by the latter. For example, active control allows for more flexibility by applying a control law adapted to each harmonic, such as experimentally shown by many researchers (Paduano et al. [5], Haynes et al. [3], and Weigl et al. [12]). In the case of aeromechanical feedback interaction, a single feedback control law is seen by all harmonics—the control law transfer functions being determined by a set of tailored structural design parameters. The stability limiting harmonics presented herein were a function of these structural design parameters, which were determined using a nonlinear optimization procedure. This procedure varied the feedback design parameters to maximize the operating range, regardless of which harmonic (that is, the first or second) became stability limiting.

Passive aeromechanical controllers can extend the operating range by stabilizing multiple harmonics, although not equally. When modeling with lag dynamics, the pressure rise disturbance from the compressor is circumferentially offset with the flow perturbation that induced it. This offset will correspond to a greater *phase shift* for higher harmonics due to their shorter circumferential wavelength. As stated in Eq. (1), this phasing directly affects the unsteady work, or damping, of the perturbations, and typically leads to more stable higher harmonics. As illustrated in the root locus plots in **Fig. 3** and in the aeromechanical modal damping charts in **Fig. 7**, higher harmonics can become limiting with aeromechanical feedback. The constraints of a common controller for fluid-structure interactions can therefore override the stabilizing effect of lag dynamics on the higher harmonics.

Optimized Structural Design Parameters. As in any optimization procedure, special attention must be paid to parameters pushed to the design space boundaries. The optimized structural design parameters were found to be minimized or maximized for certain schemes, as illustrated by values of 0.3 or 2.9 of the damping ratios and natural frequencies in **Fig. 4**. In particular, the movable inlet duct wall, casing wall, and inlet guide vane schemes (#5, 6, 8, and 9) show maximized frequency for either or both compressors. These schemes are also characterized by low (or even negative) range extension (**Figs. 5** and **6**), as well as unfavorable fluid-structure phasing (Section 5.4). It can be suggested that the frequency was maximized to increase the stiffness and hence, reduce the magnitude of the structural response and the aeromechanical coupling.

Loss and Deviation Time Lag Sensitivity. The loss and deviation lag time constant, $\overline{\tau}$, was set to a nominal value of 1.5 times the flow through time, which is an appropriate scale associated with viscous flow processes (Haynes et al. [3]). This time constant was varied in the range $0 \leqslant \overline{\tau} \leqslant 2\tau$, with reoptimized controller parameters, to find that the ranking of the schemes was conserved, although stronger increase in damping with $\overline{\tau}$ was seen for the injection schemes.

7 Summary and Conclusions

The study presented here and in the companion paper (McGee et al. [1]) has focused on providing an analysis of the impact of structural dynamics and the use of tailored structural controllers on the aerodynamic stability of axial flow compression systems. Since the inception of this work, a central theme has been to provide the turbomachinery community with simple, yet useful, physics-based models that allow basic comparisons and systematic trends to be deduced for aeromechanical stabilization of a class of axial compressors. The multidisciplinary nature and scope of this study has called for the authors to draw upon and combine analytical approaches from several different fields—fluid dynamics, structural dynamics, classical and modern control theory, and nonlinear optimization theory. Only by utilizing and combining tools from these various disciplines could the current study have been completed.

In McGee et al. [1], we presented a methodology to compare the merits of different implementations of aeromechanical feedback stabilization of compression systems. This paper quantifies the impact of ten aeromechanical feedback schemes categorized as: (i) dynamic fluid injection at the compressor face, (ii) dynamic adjustment of movable inlet and exit duct walls, (iii) dynamic variation of the compressor tip clearance via a flexible casing wall, and (iv) local circumferential redistribution of blade row stagger angles. Operating principles and potential implementation approaches were presented in Section 2. Each of the feedback schemes evaluated in this study was assumed to be closely coupled to the compressor. Thus, they created a dynamically compensated compression system having altered operating range.

To evaluate the aeromechanical feedback strategies, numerical calculations were carried out using the geometries and measured characteristics of two MIT laboratory low-speed compressors to design tailored structures and to render open and closed-loop stabilization assessments. The tailored structural design was a performance optimization aimed at improving the stability of the compressor, within structural limits. Pre-stall dynamics were investigated showing coupled fluid-structural interaction effects on compression systems, using the stability models developed in McGee et al. [1], both with and without blade passage lag dynamics. The metrics used to evaluate the impact of the aeromechanical stabilization strategies were the stabilized flow range extension, maximum achievable characteristic slope, and unsteady aeromechanical energy (or control authority). However, the calculations presented herein have yet to be verified experimentally.

Based on this, the following conclusions may be drawn:

1. Predictions have shown that dynamic fluid injection provided the largest gains in compression system stability compared to the other types of schemes explored. This result is consistent with experimental findings from other researchers who have suc-

---

[3] It should be emphasized that when using the present models one should incorporate the correct algebraic sign of the pressure rise sensitivities (see Sections 3.1 and 3.2). This is requisite for one to distinguish which feedback strategies are stabilizing or destabilizing.

cessfully demonstrated active control with flow injection (Day [13], Behnken et al. [14], Freeman et al. [15], and Weigl et al. [12]). Maximum benefit to stability was achieved when the injection was confined to the casing region such as to directly modify the characteristic through tip clearance losses, as also seen with steady-state injection (Lee and Greitzer [16], Suder et al. 2001 [17]). To first order, the impact of flow recirculation from exit to upstream injection was minimal on stability.[4] Depending on the pressure sensing mechanism employed, the predicted effectiveness of incorporating aeromechanically variable duct geometry for impedance control was varied, and the use of such technology suggested considerably smaller gains in operating performance than dynamic injection. Small gains on stability were also obtained with dynamically restaggered blades rows, more so for rotor blades then inlet guide vanes.

2. Modeling a movable casing wall to dynamically control the tip clearance flow phenomena was predicted to noticeably destabilize both compressors. Such an aeromechanical interaction should therefore be avoided by designing sufficiently rigid structures to prevent casing ovalization or similar sources of variations in tip clearance.

3. Using energy-based calculations, a physical argument was given for the role of the structural controllers in aeromechanical stabilization technology. The *control authority* metric was found to effectively distinguish between potentially stabilizing and destabilizing aeromechanical interactions, since it captured the intrinsic phasing between the flow perturbation and the structural response of the aeromechanical technology. A stabilizing scheme couples with the compressor to damp out unsteady energy of the flow perturbations, allowing the compression system to operate at a lower mass flow.

4. Although the present multidisciplinary study combines structural dynamics with fluid dynamics, the latter prevailed in importance. The main fluid (rotating stall) modes were stability limiting in all cases, even though structural dynamics greatly impacted the behavior of these modes. Closing the system loop using aeromechanical feedback alleviated the widely held view that the higher harmonic modes are more stable than the lower ones, when loss and deviation lag dynamics are included in stability modeling. Hence, the order of the stability limiting harmonic was dependent on the aeromechanical feedback technology utilized.

5. The present study also confirms the necessity for a better understanding of the complex flow processes in turbomachinery. Specifically, the quasi-steady and unsteady effects of injection in the tip region and of varying the tip clearance need to be further investigated, as well as the loss and deviation lag dynamics, in order to predict the stability enhancements from enabling control technologies with improved confidence.

Acknowledgments

This work was accomplished while the authors were at the Gas Turbine Laboratory, Massachusetts Institute of Technology, Cambridge, MA.

This research was supported by the National Aeronautics and Space Administration (NASA) Faculty Award for Research (FAR), Grant No. NAG3-1571 under the technical monitoring of Mr. John Lucero and Dr. George Stefko for the Structural Dynamics Branch at the NASA Lewis Research Center. Additional support was provided by the Army Research Office, Department of Defense Multidisciplinary Research Program of the University Research Initiative (MURI) under the technical monitoring of Dr. David Mann, Associate Director of the Engineering Sciences Division. A portion of this paper was prepared whilst the second author was a Martin Luther King, Jr., Visiting Associate Professor in the Department of Civil and Environmental Engineering at MIT. Support from the Department is most gratefully acknowledged.

Nomenclature

b_ξ = structural damping constant
c = staggered chord length of blade
C_x = axial velocity
$\overline{L}$ = structural controller modal length
L_ϕ = loss in pressure rise due to viscous dissipation
L_d = loss in pressure rise due to deviation
M = structural modal mass
n = spatial Fourier harmonic number
P = pressure
Q = $\omega_n/(U_R/R)$, frequency ratio
R = compressor annulus mean radius
s_n = $(\sigma + i\omega)R/U_R$, complex poles
t = time
U_R = mean line rotor speed
$\overline{W}$ = $\rho \overline{L} R^2/M$ mass ratio structural response

Greek Symbols

ε = structural response
ε_D = duct wall deflection/duct height, normalized duct wall deflection
ε_r = fluid injector valve deflection/annulus height, normalized injector valve deflection
ε_c = casing wall deflection/tip clearance, normalized casing wall deflection
ζ = $b_\xi/2M\omega_n$ critical damping ratio
ϕ = (C_x/U_R) mean axial flow coefficient
Φ_i = C_{x_i}/U_R, injection parameter
Φ_{peak} = stalling flow of baseline system without lags
Φ_{lags} = stalling flow of baseline system with lags
Φ_{stall} = stalling flow of aeromechanical system with lags
γ = stagger angle
ρ = fluid density
σ = disturbance growth rate
θ = circumferential position, rad
τ = tU_R/R, nondimensional time
$\overline{\tau}_{r,s}$ = $\tau_{r,s}U_R/R$ nondimensional total pressure loss characteristic time
ω = disturbance rotational frequency
ω_n = natural frequency of structural controller
ψ = $P/\frac{1}{2}\rho U_R^2$, nondimensional pressure
ψ_{ideal} = ideal stagnation pressure rise
ψ_{isen} = isentropic stagnation pressure rise
ψ_{ts} = $(P_{\text{exit}} - P_{\text{inlet}})/\frac{1}{2}\rho U_R^2$, steady total-to-exit-static pressure rise

Operators

$\delta(\ )$ = perturbation quantity
$\overline{(\ )}$ = steady-state quantity
$\tilde{(\ )}_n$ = nth spatial Fourier coefficient of $\delta(\ )$

References

[1] McGee, O. G., Graf, M. B., and Fréchette, L. G., 2003, ''Tailored Structural Design and Aeromechanical Feedback Control of Axial Compressor Stall—Part I: Development of Models and Metrics,'' ASME J. Turbomach., 126, pp.
[2] Gysling, D. L., and Greitzer, E. M., 1995, ''Dynamic Control of Rotating Stall in Axial Flow Compressors Using Aeromechanical Feedback,'' ASME J. Turbomach., **117**, pp. 307–319.
[3] Haynes, J. M., Hendricks, G. J., and Epstein, A. H., 1994, ''Active Stabilization of Rotating Stall in a Three-Stage Axial Compressor,'' ASME J. Turbomach., **116**, pp. 226–239.
[4] Fréchette, L. G., 1997, ''Implications of Stability Modeling for High Speed Axial Compressor Design,'' Master thesis, Department of Aeronautics and Astronautics, M.I.T., Cambridge, MA.
[5] Paduano, J. D., et al., 1993, ''Active Control of Rotating Stall in a Low Speed Compressor,'' ASME J. Turbomach., **115**, pp. 48–56.
[6] McGee, O. G., Graf, M. B., and Fréchette, L. G., 2003, ''Tailored Structural

---

[4] Assessment of the impact of inlet temperature distribution due to exit recirculation would require a variable density or compressible model, beyond the scope of this work.

Design and Aeromechanical Feedback Control of Axial Compressor Stall,'' Civil Engineering Report, Ohio State University, to appear.

[7] Kerrebrock, J. L., 1992, *Aircraft Engines and Gas Turbines*, 2nd Ed., The MIT Press, Cambridge, MA.

[8] Smith, L. H., Jr., 1958, ''The Effect of Tip Clearance on the Peak Pressure Rise of Axial-Flow Fans and Compressors,'' Proceedings of the ASME Symposium on Stall, ASME Fluid Mechanics Committee, Hydraulic Div., Dec. 4–5, New York.

[9] Koch, C. C., 1981, ''Stalling Pressure Capability of Axial Flow Compressor Stages,'' ASME J. Eng. Power, **103**, pp. 645–656.

[10] Longley, J. P., 1994, ''A Review of Non-Steady Flow Models for Compressor Stability,'' ASME J. Turbomach., **116**, pp. 202–215.

[11] Epstein, A. H., Ffowcs-Williams, J. E., and Greitzer, E. M., 1989, ''Active Suppression of Compressor Instabilities,'' J. Propul. Power, **5**, pp. 204–211.

[12] Weigl, H. J., Paduano, J. D., Fréchette, L. G., Epstein, A. H., Greitzer, E. M., Bright, M. M., and Strazisar, A. J., 1998, ''Active Stabilization of Rotating Stall and Surge in a Transonic Single Stage Axial Compressor,'' ASME J. Turbomach., **120**, pp. 625–636.

[13] Day, I. J., 1993, ''Active Suppression of Rotating Stall and Surge in Axial Compressor,'' ASME J. Turbomach., **115**, pp. 40–47.

[14] Behnken, R. L., D'Andrea, R., and Murray, R. M., 1995, ''Control of Rotating Stall in a Low-Speed Axial Flow Compressor Using Pulsed Air Injection: Modeling, Simulations, and Experimental Validation,'' 34th IEEE Conference on Decision and Control, New Orleans, Dec. 13–15.

[15] Freeman, C., Wilson, A. G., Day, I. J., and Swinbanks, M. A., 1998, ''Experiments in Active Control of Stall on an Aeroengine Gas Turbine,'' ASME J. Turbomach., **120**, pp. 637–647.

[16] Lee, N. K. W., and Greitzer, E. M., 1990, ''Effects of Endwall Suction and Blowing on Compressor Stability Enhancement,'' ASME J. Turbomach., **112**, pp. 133–144.

[17] Suder, K. L., Hathaway, M. D., Thorp, S. A., Strazisar, A. J., Bright, M. B., ''Compressor Stability Enhancement Using Discrete Tip Injection,'' ASME J. Turbomach., **123**, pp. 14–23.

M. Zangeneh
Department of the Mechanical Engineering,
University College London,
London, UK

M. Schleer
Turbomachinery Laboratory,
Swiss Federal Institute of Technology,
Zurich, Switzerland

F. Pløger
HV Turbo,
Helsingør, Denmark

S. S. Hong[1]
Turbomachinery Laboratory,
Swiss Federal Institute of Technology,
Zurich, Switzerland

C. Roduner
ABB Turbo Systems,
Baden, Switzerland

B. Ribi
MAN turbomaschinen AG,
Hardstrasse 319,
Ch 8005 Zurich, Switzerland

R. S. Abhari
Turbomachinery Laboratory,
Swiss Federal Institute of Technology,
Zurich, Switzerland

Investigation of an Inversely Designed Centrifugal Compressor Stage—Part I: Design and Numerical Verification

In this paper the three-dimensional inverse design code TURBOdesign-1 is applied to the design of the blade geometry of a centrifugal compressor impeller with splitter blades. In the design of conventional impellers the splitter blades normally have the same geometry as the full blades and are placed at mid-pitch location between the two full blades, which can usually result in a mismatch between the flow angle and blade angles at the splitter leading edge. In the inverse design method the splitter and full blade geometry is computed independently for a specified distribution of blade loading on the splitter and full blades. In this paper the basic design methodology is outlined and then the flow in the conventional and inverse designed impeller is compared in detail by using computational fluid dynamics (CFD) code TASCflow. The CFD results confirm that the inverse design impeller has a more uniform exit flow, better control of tip leakage flow and higher efficiency than the conventional impeller. The results also show that the shape of the trailing edge geometry has a very appreciable effect on the impeller Euler head and this must be accurately modeled in all CFD computations to ensure closer match between CFD and experimental results. Detailed measurements are presented in part II of the paper. [DOI: 10.1115/1.1645868]

Introduction

In the design of high-pressure centrifugal compressors it is essential to use splitter blades in order to ensure a good aerodynamic performance without compromising the flow range. The overall impeller performance not only depends on the meridional location of the splitter blade leading edge but also on its blade geometry. In conventional design practice, it is customary to use the same blade profile on the splitter blade as on the main blades with splitter camber line being placed at mid-pitch between the two main blades. There is, however, considerable evidence that this practice leads to poor performance of splitter blade as a result of the mismatch between the splitter leading edge blade angle and the local flow angles. In recent years there has been some attempt by designers to modify the splitter leading edge slightly to improve the matching of the splitter to the local flow. An example of this is the work of Drtina et al. [1] who showed that by modifying the pitchwise location of the leading edge of a splitter blade they could improve the pressure recovery of a vaned diffuser.

The optimization of the splitter vane geometry by using conventional methods can be quite time-consuming, especially if the vane geometry is to be optimized three-dimensionally. In this two-parts paper, the application and numerical and experimental validation of the three-dimensional inverse design method TURBOdesign-1 to the design of a centrifugal compressor impeller with splitter is described. In this inverse design method the blade geometry is computed for a specified distribution of blade loading $(\partial r\overline{V}_\theta/\partial m)$, which is the meridional derivative of the tangentially mean swirl velocity and is directly related to the blade bound circulation $2\pi r\overline{V}_\theta$. In this method, in addition to the blade loading the normal thickness distribution is specified. The basic theory behind this approach is presented in Zangeneh [2] and its extension to design of blades with splitters is presented in Zangeneh [3]. The method has already been applied to the design of industrial centrifugal compressor impellers, where simple design guide-lines have been developed for suppression of secondary flows and the resulting jet/wake flow effects at the impeller exit (see Zangeneh et al. [4,5]). This method has also been applied to the design of compact high performance vaned diffusers for centrifugal compressors (see Zangeneh et al. [6]).

In Part I of the paper, the input specification used in the inverse design code TURBOdesign-1 for the design of the new impeller is described. This is then followed by detailed comparison of the geometry of the new impeller with that of the conventional impeller. Finally the flow field in the conventional and inverse designed impellers are compared by using three-dimensional computational fluid dynamics (CFD) computations. In Part II of the paper (see Schleer et al. [7]) detailed experimental comparison of the flow field at the exit of the two impellers will be made.

Design Objectives and Inverse Design of the Impeller

The study is based on the single stage centrifugal compressor test rig at the Swiss Federal Institute of Technology (ETH-Zurich). The test stand used for this study has been described in detail by Hunziker and Gyarmathy [8]. It is a closed loop test rig with an impeller diameter of 280 mm. The baseline impeller has 11 full blades and 11 splitters with 30° backsweep and design shaft speed of 21218 RPM. The exit axial width of the impeller is 16.8 mm. The stage had been the subject of intensive experimen-

---

[1] Currently at Turbopump Department, Korea Aerospace Institute, Yusung, Daejeon, Korea.

Contributed by the International Gas Turbine Institute and presented at the International Gas Turbine and Aeroengine Congress and Exhibition, Atlanta, GA, June 16–19, 2003. Manuscript received by the IGTI December 2002; final revision March 2003. Paper No. 2003-GT-38531. Review Chair: H. R. Simmons.

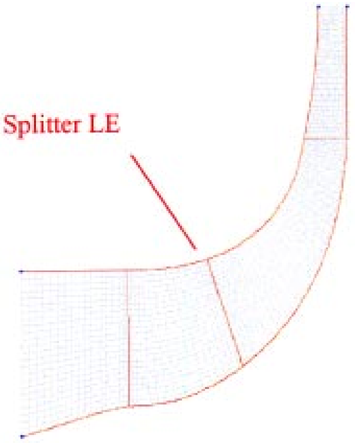

Fig. 1 The meridional mesh used for inverse design of the inverse designed impeller

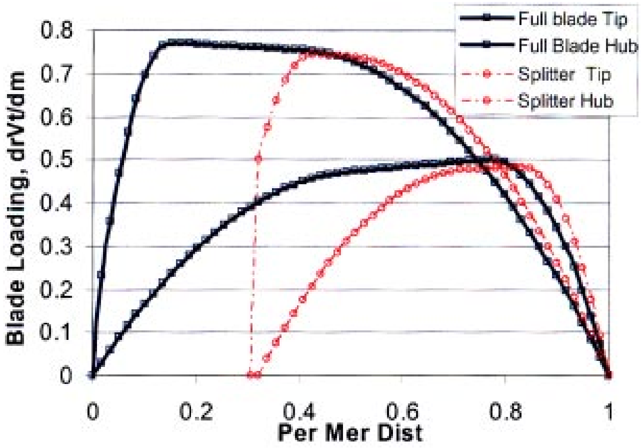

Fig. 2 Specified blade loading (or $\partial r\bar{V}_\theta/\partial m$) distribution

tal and numerical studies at ETH-Zurich. Examples of previous work on this stage include Dalbert et al. [9], Roduner et al. [10], and Zangeneh et al. [6].

The inverse design method TURBOdesign-1 allows the designer to design the blade geometry on the full and splitter blades subject to a specified distribution of blade loading. The main objective of the design was to see whether it is possible to obtain a more uniform exit flow from the impeller. This is to be achieved by better matching of the flow at the splitter leading edge and also by better control of the secondary flows on the impeller's suction surface as has already been done for industrial compressors, see Zangeneh et al. [4,5].

In the re-design of the new impeller no attempt is made to re-design the meridional geometry and the same meridional geometry as the conventional impeller is used in the design. The meridional geometry used is shown in **Fig. 1**.

The splitter leading edge location is typical of low-speed applications where the splitter is placed at almost the same location in terms of percentage of meridional distance at the hub and tip. In fact in high-speed application a more cut back leading edge is used, in which the leading edge of the splitter is almost radial. Also shown in **Fig. 1** is the meridional mesh used in TURBOdesign-1 for the design of the impeller. This mesh consists of 97 quasi-orthogonals and 25 quasi-streamlines. Since the method represents all the blade-blade variations in flow quantities by a Fourier series no computational mesh is used in the blade-blade directions. The computations were performed with 11 Fourier harmonics.

Once the meridional geometry is fixed, the main choice of design parameter in TURBOdesign-1 which controls the flow field in the impeller is the blade loading distribution. In this design the blade loading distribution shown in **Fig. 2** was used. In this case a fore-loaded distribution is used at the shroud and aft-loaded distribution at the hub of full blade. This type of distribution is used since previous work has shown that this can help to minimize meridional secondary flows on the suction surface (see Zangeneh et al. [4]) and can lead to a more uniform exit flow from the impeller. It must be emphasized, however, that this type of loading distribution is only effective in this case since the impeller has a relatively low pressure ratio and the inlet Mach number is subsonic. In cases, where the inlet Mach number is transonic a fore-loaded distribution at the shroud may result in a strong shock and so a slightly aft-loaded distribution is normally preferred in these cases. The loading distribution on the splitter blades is also similarly fore-loaded at the shroud and aft-loaded at the hub. An important input specification in TURBOdesign-1 is the $r\bar{V}_\theta ratio$ which is defined as

$$r\bar{V}_\theta ratio = (\Delta r\bar{V}_\theta)^{splitter}/(\Delta r\bar{V}_\theta)^{total}$$

where $(\Delta r\bar{V}_\theta)^{splitter}$ is the change in specific work on the splitter blade and $(\Delta r\bar{V}_\theta)^{total}$ is the change in specific work in the overall impeller. Normally the $r\bar{V}_\theta ratio$ is based on the ratio of the meridional length of splitter (at the shroud) over the overall meridional length. This type of definition of $r\bar{V}_\theta ratio$ will essentially ensure similar levels of maximum loading between the full and splitter blades. However, it is equally possible to unload the splitter at the expense of full blades or vice versa. This provides additional flexibility in the design of impellers with splitter blades. In this case the $r\bar{V}_\theta ratio$ was fixed at 0.39, which is almost the same as that given by the meridional geometry ratio. The pitchwise location of the splitter leading edge is dependent on the choice of the loading distribution and $r\bar{V}_\theta ratio$. By keeping the loading distribution on the splitter blades to be similar to that on the full blades away from the leading edge it is possible to ensure that the splitter leading edge is within $\pm 5\%$ of the mid-pitch location.

The final important input specification in TURBOdesign-1 is the stacking condition, where the spanwise variation of wrap angles at one quasi-orthogonal are specified. TURBOdesign-1 uses the wrap angles specified on the stacking quasi-orthogonal as the initial condition of the hyperbolic partial differential equation used to compute the blade wrap angles. In this case the blades were stacked at the trailing edge plane with a wrap angle stacked in such a way as the hub leads the shroud in the direction of rotation. This type of stacking condition as described by Zangeneh et al. [4] can help to reduce spanwise secondary flows in the impeller.

The New Blade Geometry. The resulting blade geometry is three-dimensional. A solid model of the impeller geometry is presented in **Fig. 3**. The inverse designed blade was designed with a uniform thickness distribution with elliptic leading and trailing edges. The elliptic trailing edge was used for ease of CFD computations, since the early CFD computations were performed by Dawes code, see Dawes [11], which can not deal with blunt trailing edges. The conventional impeller had a profile thickness distribution. and has a positive lean angle of 20° at the TE plane while the inverse impeller has a negative lean angle of 30° at the trailing edge, due to the type of stacking specified. Also the full blade throat area is quite similar in the two cases, which results in a similar choke flow rate for the new design.

The main difference in the blade geometry can be observed by comparing the blade angles for the conventional and inverse designed impellers at the hub and shroud. This is presented in Fig. 4. For the inverse impeller the blade angles on both the main and

Fig. 3 Solid model of T

splitter blades are shown, while for the conventional impeller the blade angles on the splitter blades are the same as those on the main blade and therefore no data for splitter blade is presented. As far as the comparison of the main blades are concerned the blade angle at the hub are quite similar which confirms that conventional impeller is also aft-loaded at the hub. However, at the shroud the blade angles for the conventional impeller indicate an aft-loaded design, while the inverse impeller is fore-loaded, as shown in **Fig. 2**. Also there is very little difference between the blade angles of the full and splitter blades of the inverse designed impeller at the hub leading edge, while a difference of about 5° exists at the shroud leading edge. The blade angle difference is quite small in this case because of the meridional location of the splitter (see **Fig. 1**). In more typical high speed applications, where the splitter is cut back, more significant difference in blade angles between the main and splitter blades will be obtained if the inverse design method is used to design the impeller geometry. The inlet blade angle at the hub and shroud of the full blades are quite similar. However, at the trailing edge the exit blade angle is about 10° higher at the hub and shroud of the inverse design impeller as compared to the conventional. On purely one-dimensional considerations the higher exit angles may imply a lower Euler head but in fact the three-dimensional CFD predictions, to be presented later, indicated similar Euler head for the inverse designed impeller despite the lower exit blade angles.

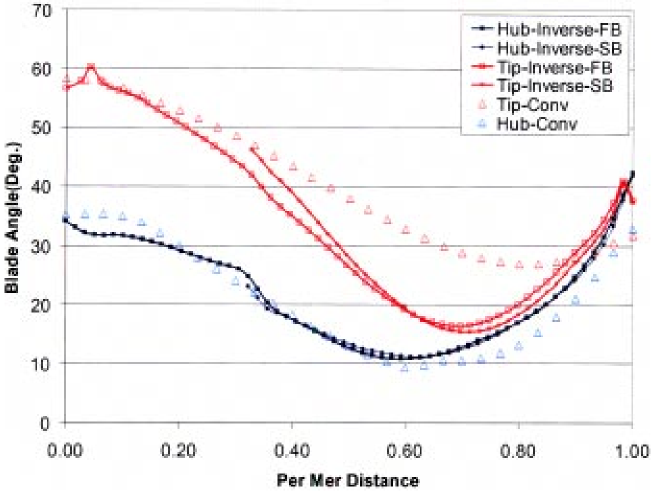

Fig. 4 Comparison of blade angles (measured from radial)

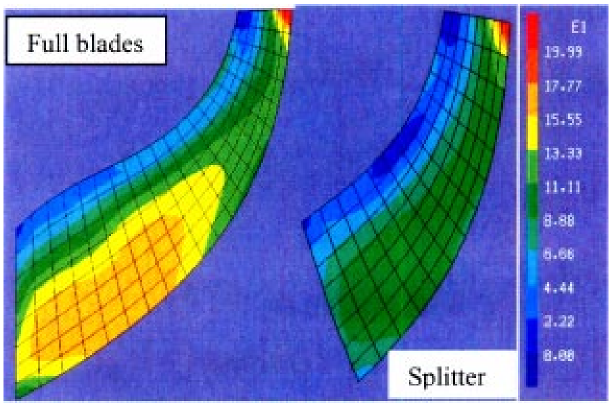

Fig. 5 Predicted von Mises stresses on the inverse impeller

A. Structural Analysis of the New Design. The stresses and deflections in the inverse designed impeller, which has a three-dimensional dimension geometry, was computed by using a finite element structural analysis method. The resulting Von Mises stresses on the full and splitter blades are shown in **Fig. 5**. From **Fig. 5** it is clear that the maximum stress of about 17.7 N/mm^2 occurs in the inducer region. The stacking condition used in the design, which helps to suppress the secondary flows on the suction surface, results in a maximum stress of 19.9 N/mm^2 there both on the splitter and full blades, near the trailing edge plane. The high blade lean angle near the leading edge of the inverse impeller results in relatively high radial displacement of the blade under the centrifugal stresses as compared to that of the conventional impeller. It is clear that the deflections of the blade tips could be a problem both regarding the possible mechanical interference with the housing and when comparing performance with the original E7X impeller. This was confirmed by the calculations which showed large deflections at the blade tips. It was therefore decided to cut back the blade tips so that the tip gap of full blades would match that of the original E7X impeller as closely as possible when running at maximum speed. In order to achieve this cut back the inverse impeller blade tips were machined in a turning operation resulting in the full blade having the same tip gap as the original impeller at maximum speed conditions. However, as a consequence of the turning operation the gap at the splitter blade will not be identical to that of the original impeller. The change in the splitter blade tip gap under maximum speed conditions are shown in **Fig. 6**, where a positive value indicates a reduction in the gap and a negative value an increase. It must be noted that this approach to match the tip gap at maximum speed will mean that the tip gap at part speed conditions in the inverse impeller will be higher than that of the conventional impeller.

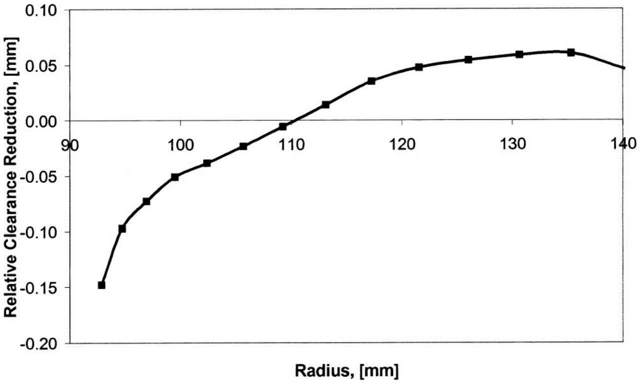

Fig. 6 Predicted relative tip gap of the splitter blade

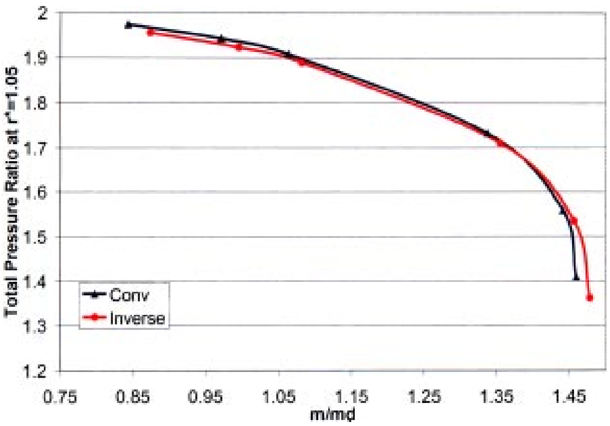

Fig. 7 Comparison of predicted total pressure ratio at $r^*=1.05$-Mu2=0.9

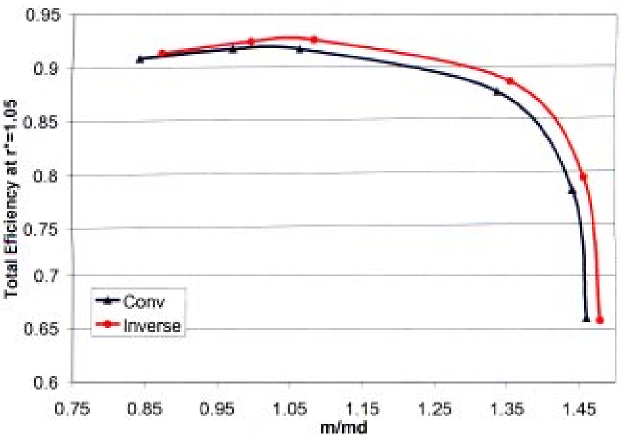

Fig. 8 Comparison of predicted total efficiency at $r^*=1.05$-Mu2=0.9

CFD Predictions at the Design Point

In order to investigate the effect of the new blade design on the flow field in the impeller, conventional impeller and the inverse design impeller were analyzed by using the commercial Reynold's-averaged Navier-Stokes code TASCflow [12]. The code uses strongly conservative pressure correction technique together with a finite volume formulation for the solution of the NS equations. A standard k-ε turbulence model was used for the calculation. The same mesh topology was used for the computation of the flow through the inverse and conventional impellers. In all the computations to be presented at the design speed both the conventional and inverse designed impellers have a sharp trailing edge. As explained earlier, sharp trailing edges were used in the design process for ease of computations by Dawes Code. The effect of the trailing edge shape on the flow field in the inverse impeller will be investigated later in this paper. The mesh used consists of 105 streamwise, 62 blade-blade and 30 spanwise mesh points, i.e., a total of 195,000 mesh points. In all computations nominal tip clearance of 0.5 mm was modeled by using 3 points in the clearance area. This mesh topology was used after a comprehensive mesh independency study using both coarser (of the order 90,000 nodes) and finer meshes of the order 381,000 nodes (FG). The different solutions were analyzed by using the detailed computational results for the conventional impeller as well as the maximum values of $Y+$ in the solution. With the current grid the maximum values of $Y+$ were in most region of the order 10–20 and only near the leading edge regions they reached a maximum value of about 50.

For each computation the stagnation temperature, stagnation pressure and flow angle were fixed upstream of the impeller. The static pressure was fixed downstream of the vaneless diffuser. In order to obtain different points on the operating characteristic the exit static pressure was varied. In this section computations performed for the nominal design speed corresponding to impeller tip Mach number (M_{u2}) of 0.9 will be presented. In **Figs. 7** and **8**, the overall predicted performance characteristic of the conventional and inverse impeller is compared. Overall the predicted total pressure ratio of the inverse impeller at impeller exit radius ratio of 1.05 is similar to that of the conventional impeller (Conv). *This is despite the fact that the exit blade angle of the inverse impeller was about 10 deg higher than the conventional impeller*. The predicted efficiency of the inverse impeller at impeller exit radius ratio of 1.05 is between 1–1.5 points higher than the conventional impeller over most of the predicted flow range.

The main reason for the improvement in efficiency of the inverse impeller can be seen by comparing the predicted exit flow distribution from the inverse impeller with that of the conventional impeller. In **Fig. 9**, the predicted relative Mach number contours at the trailing edge of the conventional and inverse impellers are compared. **Figure 9(*a*)** presents the predicted exit Mach number distribution for the conventional impeller for the case without tip clearance, while the computation with nominal tip clearance of 0.5 mm are presented in **Fig. 9(*b*)**. In the case with no tip clearance more low momentum fluids are accumulated in the blade channel between the suction surface of the full blade (F) and pressure surface of the splitter (S). The reason for this accumulation of low momentum fluid is the strong secondary flows on suction surface of the full blade. The predictions also indicate spanwise secondary flows on the suction surface of the splitter. However, since the splitter blade is shorter than the full blade less low momentum fluid is generated on the splitter blade and hence less low momentum fluid is accumulated in the blade channel between the suction surface of the splitter and pressure surface of the full blade. The predictions for the conventional blade with nominal tip clearance, however, indicate a larger region of very low momentum fluid in the blade channel between the suction surface of the splitter and the pressure surface of the full blade. This result, which is confirmed by the experimental measurements (see Fig. 17 of Schleer et al. [7]), seems puzzling in the first instance. However, closer inspection of the predicted velocity vectors in the clearance region presented in **Fig. 10(*a*)**, indicates that the clearance vortex separates from the leading edge of the full blade and then ends up in the passage between the suction surface of the splitter blade and pressure surface of the full blade. It is this low momentum fluid in the clearance vortex which results in the increase in exit flow nonuniformity of this passage when tip clearance is modeled. The predicted exit Mach number distribution for the inverse designed impeller is presented in **Fig. 9(*c*)**. The predictions indicate a reduction in the exit flow nonuniformity in the blade channel between the suction surface of the full blade and the pressure surface of the splitter. This is mainly due to the better suppression of secondary flows on the suction surface of the full blade in the inverse impeller.

However, the predictions also indicate a reduction of the exit flow nonuniformity in the blade channel between the splitter SS and full blade PS. By considering the predicted velocity vectors in the clearance region (one mesh away from the shroud wall) of the inverse impeller (see Fig. **10(*b*)**) it is possible to see the different structure of the clearance vortex in the inverse designed impeller, which seems to split the clearance vortex between the two channels. Furthermore, there is a marked reduction in the strength of clearance flow in the mid section of the full blade in the inverse impeller. *The combination of better control of the secondary flows on the suction surface and a reduction in the strength of the clearance flow seems to help to produce a more uniform flow at the exit from the inverse designed impeller*. An important feature of the

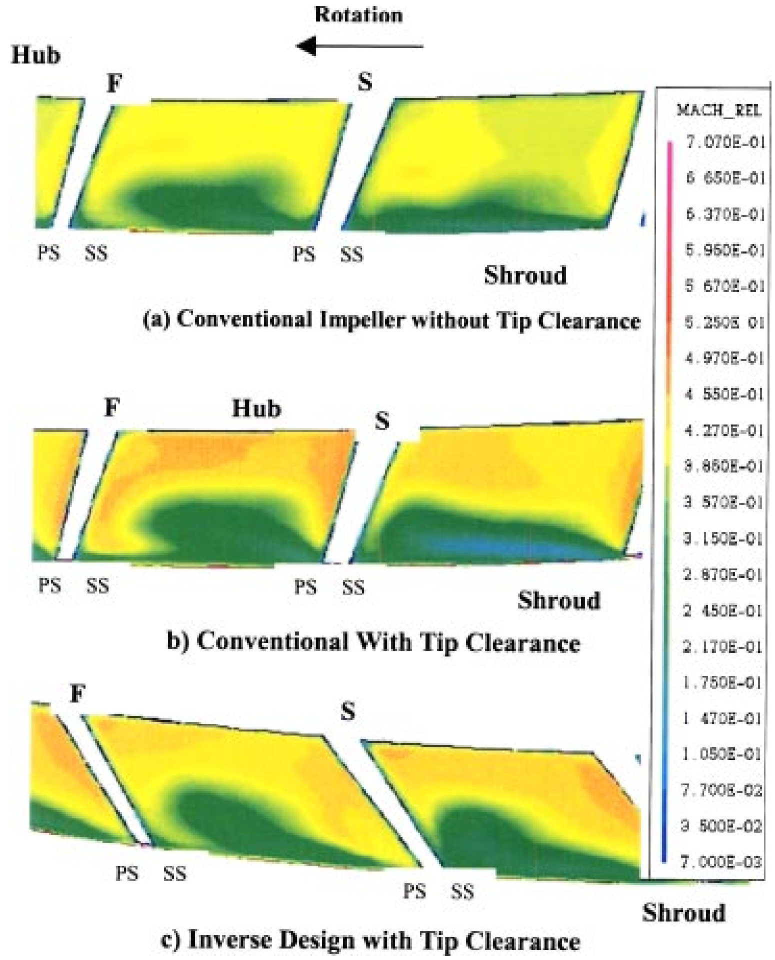

(a) Conventional Impeller without Tip Clearance

b) Conventional With Tip Clearance

c) Inverse Design with Tip Clearance

Fig. 9 **Comparison of predicted relative Mach number near the trailing edge plane—Mu2 = 0.9**

exit flow from the inverse impeller is the similar flow patterns in the two blade channels (i.e., between SS of full blade and PS of Splitter and SS of splitter ad PS of full blade), which should help to reduce the circumferential mixing losses at the exit from the impeller leading to higher overall stage performance.

Effect of Trailing Edge Shape on Impeller Performance

The comparison of the overall measured performance indicated that the total pressure at the exit from the inverse designed stage (impeller and vaneless diffuser) is in fact about 2.9% lower than that of the conventional impeller, see Part II of the paper, Schleer et al. [7]. In addition the detailed traverse results indicated a 7% reduction in Euler head of the inverse designed impeller. Since this result was in contradiction to the earlier CFD predictions (see **Fig. 7**). An investigation was undertaken to find any possible discrepancy in blade geometry of the manufactured impeller and the impeller geometry used for CFD computations. No significant difference in blade geometry were found apart from the trailing edge shape. In the CFD computations a sharp trailing edge was used while the impeller was manufactured with a cut-off trailing edge. The difference between the two blade geometries is shown in **Fig. 11**.

In order to investigate the effect of the trailing edge geometry on the impeller performance the flow through both conventional and inverse designed impellers were computed again by TASCflow using a blunt trailing edge as was used in the final manufactured impeller. All the computations with blunt trailing edges were performed at impeller speed corresponding to Mu2 = 0.75, where most of the detailed measurements were made, see Schleer et al. [7]. A summary of these CFD computations at near the experimentally measured design flow rate are shown in **Table 1**. Five cases are indicated in **Table 1**. The first four cases (labeled OG) were computed by using the normal 195,000 computational grid. However, the last case, corresponds to computation for a finer mesh of about 380,000 nodes with 129 streamwise, 82 blade-blade, and 36 spanwise nodes. According to these predictions, with the OG mesh, the use of blunt trailing edge results in a 3.1% drop in the inverse impeller's exit stagnation pressure and 6% drop in its Euler head. The corresponding figures for the conventional impeller are only −1% and −1.4%, respectively. The significant drop in stagnation pressure and Euler head for the inverse impeller as a result of using a blunt trailing edge are quite comparable with the level of drop in performance found in the experimental measurements, i.e., 2.9% and 7.7% for stagnation pressure and Euler head, respectively, see Schleer et al. [7].

These results are further confirmed by the detailed spanwise variation of these flow quantities at the $r^* = 1.05$, which is presented in **Figs. 12–14**. In these figures $z/b = 0$ corresponds to the hub and $z/b = 1.0$ corresponds to the shroud wall. In **Fig. 12** the comparison of the meridional velocity for the inverse impeller is presented. The results indicate very little sensitivity of the meridional velocity to the trailing edge shape. Also the predicted meridional velocity is generally in good agreement with the measurements. **Figure 13**, however, confirms the considerable effect of the trailing edge shape on the impeller exit tangential velocity. The comparison of the tangential velocity between the fine grid (FG) and ordinary grid solution confirms that apart from the region close to the endwalls the solution has reached mesh indepen-

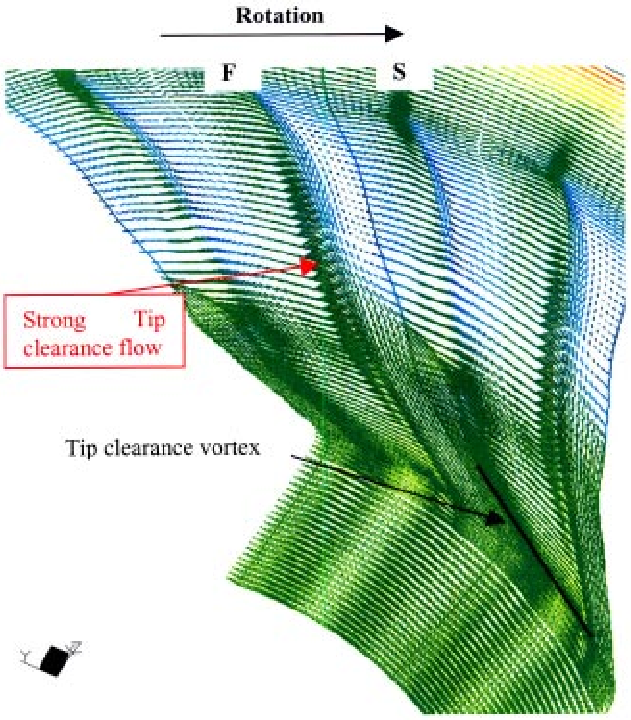

(a) Conventional Impeller with nominal tip clearance

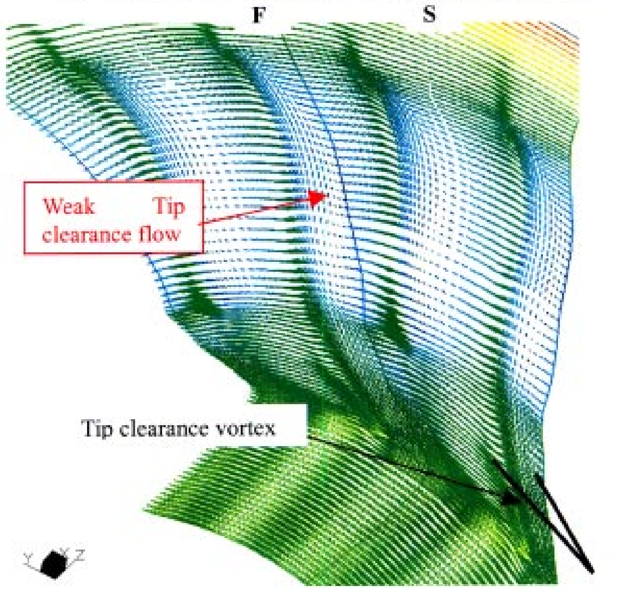

(b) Inverse Designed Impeller with nominal tip clearance

Fig. 10 Predicted velocity vectors in the tip clearance region

dency as far as the tangential velocity and therefore Euler head is concerned. Similar results can be seen in **Fig. 14** for the exit stagnation pressure. However, the more significant discrepancy between the stagnation pressures predicted by the two different meshes perhaps confirms that the loss predictions have not reached mesh independency. Furthermore, from **Figs. 13** and **14**, it is clear that the CFD computations are over-predicting the Euler head and underpredicting the impeller efficiency.

The CFD predictions confirm that the main reason for the lower Euler head and therefore lower exit stagnation pressure at the exit from the manufactured inverse impeller is the use of blunt trailing edge in the manufactured impeller while all the CFD computations during the design process were performed with sharp trailing edge. Further investigation is required in order to understand why the inverse impeller is more sensitive to the trailing edge thickness.

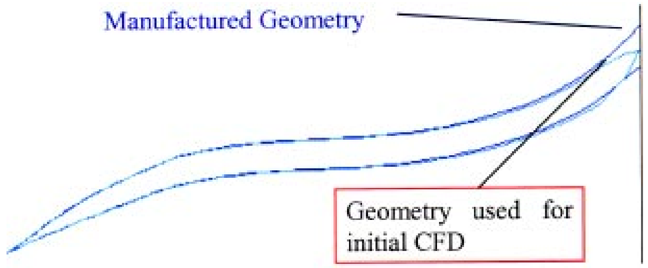

Fig. 11 Comparison of manufactured geometry and initial geometry

Detailed Comparison at Mu=0.75

Most of the detailed experimental measurements of the inverse impeller were made at Mu2=0.75, see Schleer et al. [7]. So in this part of the paper detailed CFD results will be presented for this operating speed for comparison with detailed FRAP measurements presented in Part II of the paper, see Schleer et al. [7]. In **Fig. 15**, the contours of exit stagnation pressure at $r^*=1.05$ are compared. Comparisons of **Figs. 15**(***a***) and **15**(***c***) confirms the considerable reduction in the low stagnation pressure area near the shroud in the inverse designed impeller. Also comparisons of

Table 1 Summary of CFD computations at Mu=0.75

	PS-Exit (PA)	Mass flow (KG/S)	P0(Pa) at $r^*=1.05$	η at 1.05	RVT @1.05 M^2/S
Conv-OG Sharp TE	141000	1.75	160000	0.919	−24.5
Conv.-OG Blunt TE	139000	1.79	158752 (−1%)	0.917	−24.16 (−1.4%)
Inv3D-OG Sharp TE	141000	1.79	158441	0.926	−23.73
Inv3D-OG Blunt TE	138000	1.785	153507 (−3.1%)	0.915	−22.3 (−6%)
Inv3D-FG Sharp TE	142000	1.755	159658	0.956	−24.15

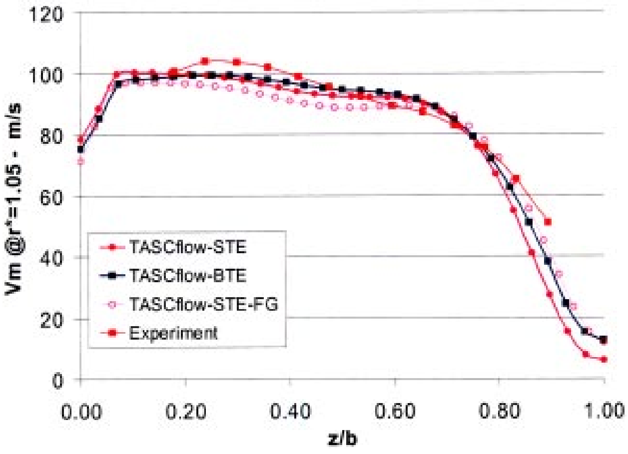

Fig. 12 Comparison of measured and predicted meridional velocity for the inverse impeller at $r^*=1.05$ at Mu2=0.75

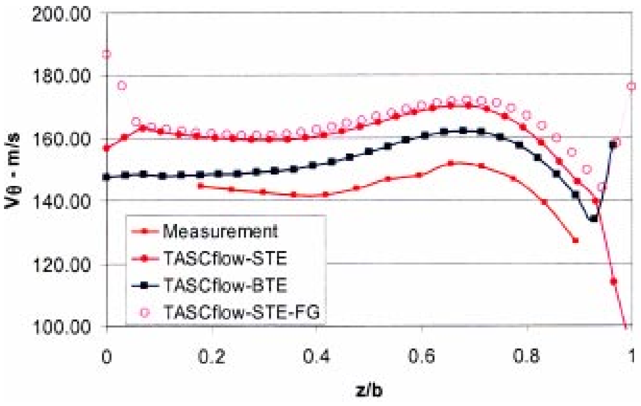

Fig. 13 Comparison of measured and predicted tangential velocity for the inverse impeller at $r^*=1.05$ at Mu2=0.75

Figs. 15(*b*) and **15(*c*)** confirms that the change in trailing edge shape has resulted in the formation of a low total pressure region in the blade wake near the hub. This flow feature is also observed in the detailed experimental measurements presented in Part II of the paper (see Fig. 8(*a*) of Schleer et al. [7]). The corresponding data for the tangential velocity is presented in **Fig. 16**. These contours for the conventional impeller indicate significant differences in flow distribution between the two channels of the impeller, as indicated earlier. However, the flow in the inverse designed impeller is quite similar in the two blade channels. In **Fig. 16**(*c*) one can observe a region of low Vθ in the blade wake at the hub. This flow feature is confirmed by the experimental measurements (see Fig. 11 of Schleer et al. [7]).

This flow feature is not present in the inverse impeller with sharp trailing edge. The exact reason for the formation of this region of low absolute tangential velocity near the hub as a result of using a blunt trailing edge is not currently well understood.

Implications for Application of Inverse Design to High-Speed Compressor Impellers With Splitters

Increasingly inverse design methods are being considered by the turbomachinery industry as an efficient means of designing centrifugal compressor components. Inverse design methods can not only shorten development time considerably but they can also help designers achieve breakthrough designs. The previous application of inverse design to suppression of secondary flows in centrifugal impellers (see Zangeneh [4]) and suppression of corner separation in vaned diffusers (see Zangeneh et al. [6] and Goto and Zangeneh [13]) have shown the potential of inverse design in achieving breakthrough designs. The work reported in this paper and the companion (see Schleer et al. [7]) confirms that by using the three-dimensional inverse design method it is possible to design high-speed impellers with splitters with more uniform exit flow which results in higher impeller and overall stage efficiency. However, in applying the method in high speed applications a number of practical issues need to be addressed.

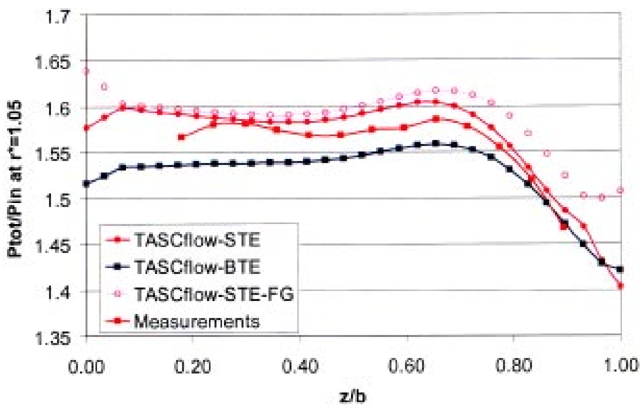

Fig. 14 Comparison of measured and predicted total pressure for the inverse impeller at $r^*=1.05$ at Mu2=0.75

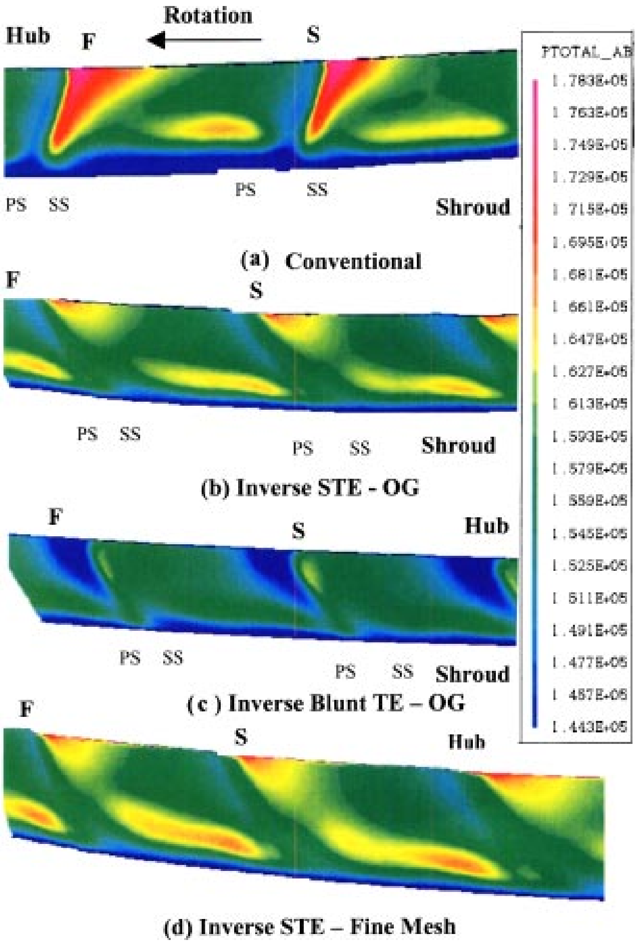

Fig. 15 Comparison of predicted total pressure at $r^*=1.05$

(i) Structural Issues. The impeller geometry designed by the inverse method has a three-dimensional geometry with bowed and leant blade profiles. The structural analysis of the impeller indicated that the main problem is the large lean angles at the leading edge of the impeller which results in substantial bending stresses and high radial deflections. Studies carried out subsequently has shown that it is possible to control the leading edge lean angle by slight adjustments to the hub loading distribution, These small adjustments can enable one to design the impeller with zero leading edge lean angles but with slight bowing.

(ii) Manufacturing Issues. The three-dimensional blade geometry of the inverse impeller had to be manufactured by point milling rather than flank milling, which is commonly used for conventional impellers with straight blade filaments. The inverse impeller was manufactured by ABB Turbo System who found that the additional cost of using point milling over flank milling is only of the order of 25% and not the 100% that is commonly believed, Roduner [14].

(iii) Design Condition Issues. The inverse design method can normally design the impeller geometry with the specified pressure rise and Euler head. However, in this case the designed

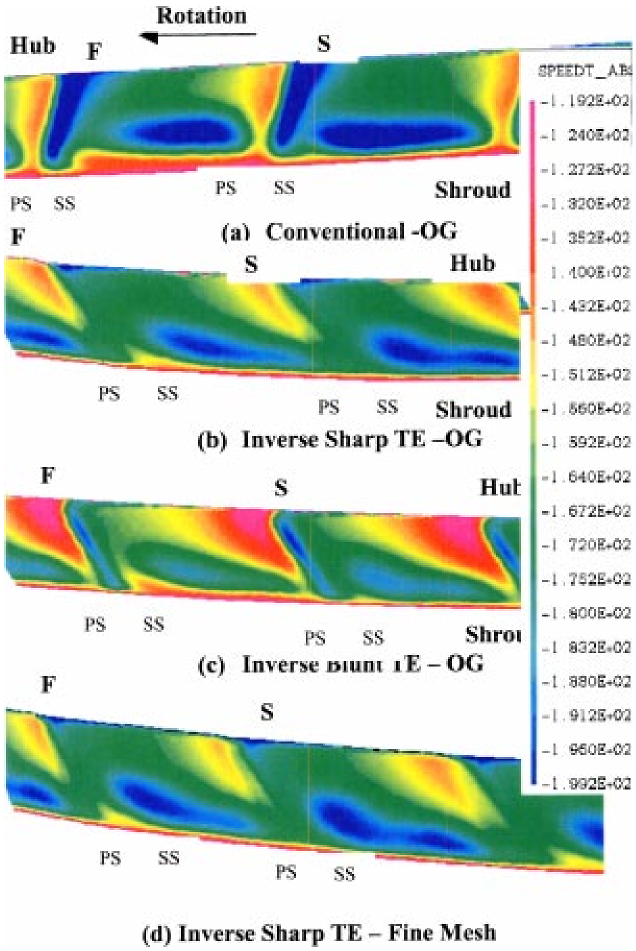

(a) Conventional -OG

(b) Inverse Sharp TE –OG

(c) Inverse Blunt TE – OG

(d) Inverse Sharp TE – Fine Mesh

Fig. 16 Comparison of predicted tangential velocity—$r^*=1.05$

impeller was found to have a lower pressure rise and Euler head as compared to the originally predicted values. This was due to the fact the original CFD computations were performed with sharp trailing edges, as a result of limitation of the CFD code used, while the manufactured impellers had blunt trailing edges. The detailed computational study of the effect of the trailing edge shape on impeller performance indicated a relatively small drop of the order of 1% in Euler head for the conventional impeller but significant drops of about 6% for the inverse impeller. Further investigation is required to understand the reason for the sensitivity of the inverse impeller to the trailing edge shape but similar sensitivities have been found in the past for some conventional impellers (Ribi [15]) and this may depend on the impeller exit blade angle and lean angles.

(iv) Higher Backsweep. The inverse impeller's blade angles were found to be about 40° (measured from radial direction) as opposed to 30° used in the conventional impeller. Despite the higher levels of backsweep in the inverse impeller the CFD predictions, with sharp trailing edges indicated the same level of pressure rise and Euler head in the inverse impeller. This is partly due to the fact that the inverse impeller is more efficient and also the better control of secondary flows and less accumulation of low momentum fluids on the shroud suction surface has helped to reduce slip. To confirm this fact the inverse impeller was *redesigned*, subsequent to the completion of the testing, using the same loading distribution, normal thickness and meridional geometry *but with 6% higher specified Euler head*. The *redesigned* impeller was found to have an exit blade angle of about 38°, rather than 40° for the original inverse impeller. The flow through the *redesigned* impeller was computed by using the same mesh as the OG configuration described in **Table 1** and using *blunt trailing edges* by using TASCflow. The stagnation pressure at the exit of the *redesigned* impeller was found to be very close to that of the conventional with an exit angle of 38° rather than 30° used in the conventional impeller. Furthermore the exit flow distribution was found to be as uniform as the original inverse impeller. This is shown in Fig. 17, where the predicted stagnation pressure for the redesigned impeller is shown at impeller exit radius ratio of 1.05.

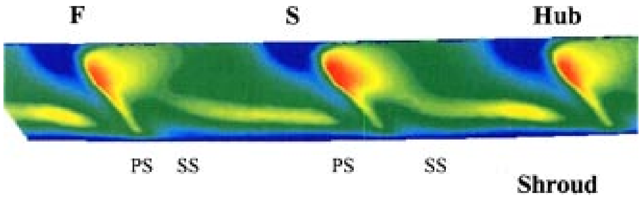

Fig. 17 Stagnation pressure at $r^*=1.05$ for redesigned inverse impeller—Mu2=0.75 (same contour intervals as Fig. 15)

Conclusions

The impeller geometry of a subsonic centrifugal compressor with splitter blades was redesigned by using the three-dimensional inverse design method TURBOdesign-1. The inverse method allows the designer to design the impeller geometry for a specified distribution of loading distribution for the splitter and full blades together with the thickness distribution. In this way the method automatically adjusts the splitter leading edge geometry to match the local flow field. In this case the impeller was designed by using identical meridional geometry as the conventional impeller and a design criteria that had already been developed for reduction of impeller exit flow nonuniformity. Detailed CFD computations confirmed that the exit flow from the impeller is more uniform than the conventional impeller. Furthermore, while the conventional impeller shows different degrees of flow nonuniformity in the two different blade channels (i.e., between PS of splitter and SS of full blade and PS of full blade and SS of splitter) which results in further circumferential flow nonuniformity no such nonuniformity can be observed in the inverse designed impeller. Another important feature of the inverse designed impeller, which is fore-loaded at the shroud, is a reduction in tip clearance effects. Also the CFD predictions, which used a sharp trailing edge model of the impeller, indicated that the inverse impeller produces the same level of pressure rise as the conventional impeller even through the impeller exit blade angle is about 10° higher than that of the conventional impeller, as measured from meridional direction.

The inverse impeller's performance was adversely, and more significantly than the conventional impeller, affected by the use of blunt trailing edges. It is recommended that in all future CFD computations of high speed impellers the shape of the trailing edge geometry should be properly modeled. An investigation will start shortly to consider in details the effect of trailing edge geometry on impeller performance for impellers with different exit blade angles and leans angles.

Acknowledgments

The work reported in this paper is part of the EUREKA COMPDESIGN project with financial support from Swiss government, UK Department of Trade and Industry, Danish government, ABB Turbo Ltd (Switzerland), Sulzer Turbo Ltd (Switzerland) and HV TURBO (Denmark). The authors would like to thank Prof. G. Gyarmathy of ETH and Dr. P. Dalbert of Sulzer Innotec and Dr. Thiele of ABB Turbo System for their comments during the course this project. Moreover, we would like to thank I. Tristanto for his help on the mesh topology used in the CFD computations and H. Watanabe of Advanced Design Technology Ltd for his helpful comments and support of the design process.

Nomenclature

B = impeller exit width
m = meridional distance
m_d = design flow rate
Mu2 = Mach number based on impeller tip speed
p = static pressure
P0 = stagnation pressure
r = radius
r^* = radius normalized by impeller tip radius
V_θ = tangential velocity
Z = axial coordinate

Subscripts

2 = impeller trailing edge
3 = diffuser trailing edge

Superscript

$-$ = circumferential averaging

References

[1] Drtina, P., Dalbert, P., Rutti, K., and Schachenmann, A., 1993, ''Optimization of a Diffuser With Splitter by Numerical Simulation,'' ASME Paper 93-GT-110.
[2] Zangeneh, M., 1991, ''A Compressible Three Dimensional Blade Design Method for Radial and Mixed Flow Turbomachinery Blades,'' Int. J. Numer. Methods Fluids, **13**, pp. 599–624.
[3] Zangeneh, M., 1998, ''On 3D Inverse Design of Centrifugal Compressor Impellers With Splitter Blades,'' ASME Paper 98-GT-507.
[4] Zangeneh, M., Goto, A., and Harada, H., 1998, ''On the Design Criteria for Suppression of Secondary Flows in Centrifugal and Mixed Flow Impellers,'' ASME J. Turbomach., **120**, pp. 723–735.
[5] Zangeneh, M., Goto, A., and Harada, H., 1999, ''On the Role of Three-Dimensional Inverse Design Methods in Turbomachinery Shape Optimization,'' Proc. IMECHE Part C, J. Mech. Eng. Sci., **213**(C1), pp. 27–42.
[6] Zangeneh, M., Vogt, D., and Roduner, C., 2002, ''Improving a Vaned Diffuser for a Given Centrifugal Impeller by 3D Inverse Design,'' ASME Paper GT-2002-30621.
[7] Schleer, M., Hong, S., Zangeneh, M., Roduner, C., Ribi, B, Ploger, F., and Abhari, R. S. 2004, ''Investigation of an Inversely Designed Centrifugal Compressor Stage–Part II: Experimental Investigations,'' ASME J. Turbomach., **126**, pp. 82–90.
[8] Hunziker, R., and Gyarmathy, G., 1993, ''The Operational Stability of a Centrifugal Compressor and Its Dependence on the Characteristics of the Sub-Components,'' ASME Paper 93-GT-284.
[9] Dalbert, P., Gyarmathy, G., and Sebestyen, A., 1993, ''Flow Phenomena in Vaned Diffuser of a Centrifugal Stage,'' ASME Paper 93-GT-53.
[10] Roduner, C., Koppel, P., Kupferschmied, P., and Gyarmathy, G., 1998, ''Comparison of Measurement Data at the Impeller Exit of Centrifugal Compressor Measured With Both Pneumatic and Fast Response Probes,'' ASME Paper 98-GT-241.
[11] Dawes, W. N., 1988, ''The Development of a 3D Navier-Stokes Solver for Application to all Types of Turbomachinery,'' ASME Paper 88-GT-70.
[12] TASCflow, 1999, Version 2.10 documentation, AEA Technology Ltd., London.
[13] Goto, A., and Zangeneh, M., 2002, ''Hydrodynamic Design of Pump Diffuser Using Inverse Design Method and CFD,'' ASME J. Fluids Eng., **124**, pp. 319–328.
[14] Roduner, C., 2002, private communications.
[15] Ribi, B, 2002, private communications.

M. Schleer

S. S. Hong[1]

Swiss Federal Institute of Technology,
Turbomachinery Laboratory,
Sonneggstrasse 3,
CH-8092 Zurich, Switzerland

M. Zangeneh
Department of Mechanical Engineering,
University College London,
Torrington Place
London WCIE 7JE, UK

C. Roduner
ABB Turbo Systems,
Bruggerstrasse 71A,
5401 Baden, Switzerland

B. Ribi
MAN Turbomaschinen AG,
Hardstrasse 319,
CH8005 Zurich, Switzerland

F. Pløger
HV Turbo A/S,
Allegade 2,
DK-3000 Helsingør, Denmark

R. S. Abhari
Swiss Federal Institute of Technology,
Turbomachinery Laboratory,
Sonneggstrasse 3,
CH-8092 Zurich, Switzerland

Investigation of an Inversely Designed Centrifugal Compressor Stage—Part II: Experimental Investigations

This paper presents an experimental investigation of two centrifugal compressor stage configurations. The baseline configuration has been designed using conventional design engineering tools. The second configuration was designed using advanced inverse design rules as described in Part I. It is designed to match the choke flow as well as the best point of the conventionally designed stage. The experimental investigation is conducted in the industry-scale centrifugal compressor facility at the Turbomachinery Laboratory of the Swiss Federal Institute of Technology. Performance maps for both configurations at several speed lines are presented. These plots show the overall behavior of the stages designed using the different design approaches and their operating range. Time-resolved measurements show details of the unsteady flow field within the diffuser close to the impeller exit. The time-resolved data have been analyzed to assist the explanation of changes in the characteristics and associated efficiency penalties and gains. The processed data show the benefits of the new inverse design method with respect to an improvement of the compressor efficiency and the operating range. It is seen that the application of an inverse design method results in a more uniform flow into the diffuser. [DOI: 10.1115/1.1625690]

Introduction

Centrifugal compressors are widely used in industry, gas turbines, engines, or diesel turbocharging because of their high stage pressure ratio and their robust and compact design. But for high specific speed applications they suffer from a lower optimum efficiency compared to an axial machine with the same pressure head and volume flow rate. The lower performance is a result of complex three-dimensional viscous effects that cannot be properly assessed with the ‘‘conventional’’ design methodology. Furthermore, the traditional manufacturing processes provide only limited freedom in the design of centrifugal compressors. Especially the flank milling of the impellers restricted their design to the use of ruled surfaces. In the 1980’s improvements of the milling and computer technology allowed a free definition of three-dimensional blading and manufacturing by point milling. New design procedures, such as the inverse design methods considered in this publication, became feasible.

Inverse design methods offer a more systematic approach to the design whereby the geometric shape of crucial parts of fluid machinery is defined using a given distribution of the aerodynamic loading over the elements surface. The inverse design method computes the blade shape for the user-specified distribution of bound circulation. The approach has already been successfully applied in the design of a radial diffuser [1] and the compact design of radial impellers with suppressed meridional secondary flows [2,3].

In a companion paper by Zangeneh et al. [4] the three-dimensional inverse design code TURBOdesign^{-1} [3,5] is applied to the re-design of the impeller of the compressor ‘‘Rigi.’’ This compressor has been the subject of very detailed measurement over a number of years (e.g., [6–10]) and provides the baseline for the re-design.

The objective of the present paper is to experimentally investigate the details of the flow and the performance of a conventional and inverse impeller design. A fast response probe is used to obtain detailed time-resolved flow field measurements at the impeller exit. In addition, the overall efficiency and the stage behavior are examined. These measurements quantify the flow structures improvements achieved by the inversely designed impeller.

---

[1] Currently at Turbopump Department, Korea Aerospace Research Institute, Yusung, Daejeon, Korea.

Contributed by the International Gas Turbine Institute and presented at the International Gas Turbine and Aeroengine Congress and Exhibition, Atlanta, GA, June 16–19, 2003. Manuscript received by the IGTI Dec. 2002; final revision Mar. 2003. Paper No. 2003-GT-38127. Review Chair: H. R. Simmons.

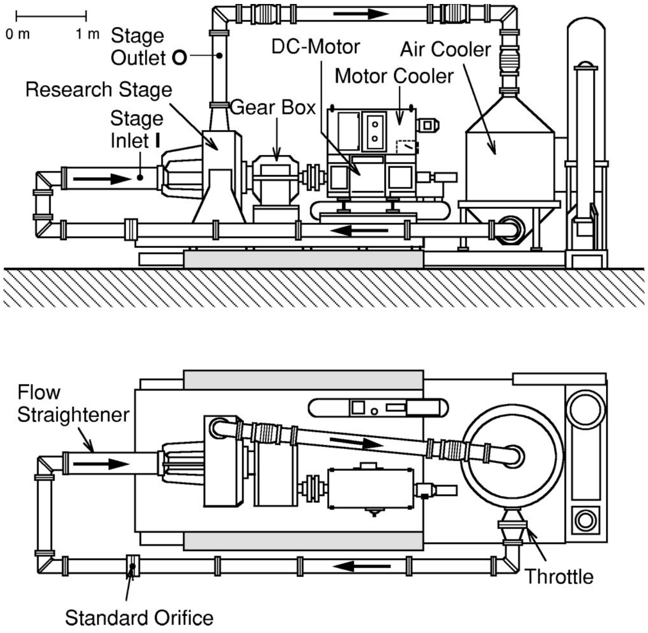

Fig. 1 System layout compressor facility "Rigi"

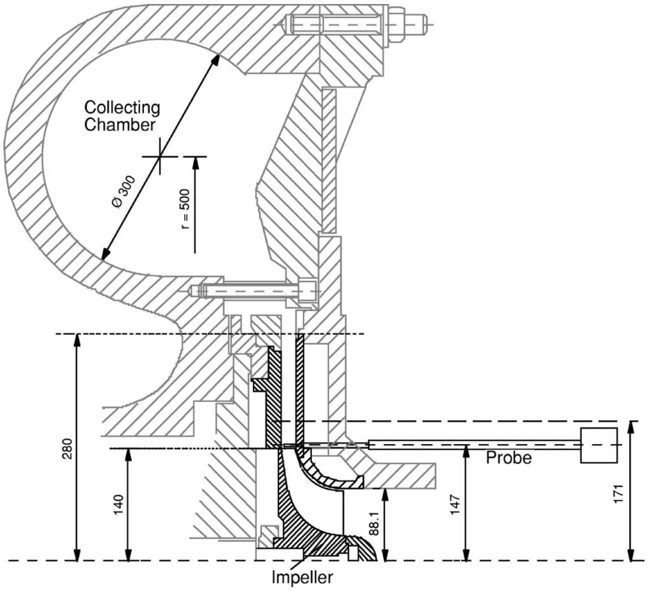

Fig. 2 Cross-sectional view of the compressor with probe location

The Research Facility

Layout of the Research Facility. All the experiments were carried out in the research facility "Rigi" at the Swiss Federal Institute of Technology Zürich (ETH Zürich). This facility consists of a single stage, industrial centrifugal compressor system operating in a closed loop as shown in Fig. 1. A flow straightener mounted in the suction pipe ensures axial flow at the stage inlet. A 440 kW DC motor coupled to a two-stage gearbox drives the facility.

The inlet pressure can be set by an automatic control system between 250 and 1250 mbar. However, for the present experiments it is set constant at 980 mbar. The inlet temperature is controlled and fixed to 24°C. The flow rate is controlled by a throttle and is measured by a standard orifice according to DIN 1952. The mass flow measurement is estimated to be accurate within 1%. The overall stage performance was measured using conventional wall pressure taps and temperature probes in the suction and outlet ducts. The present detailed flow measurements were taken at 17720 rpm, which is in the high subsonic regime and corresponds to the circumferential speed $U_2 = 260\,\mathrm{m/s}$ or an impeller tip Mach number of $\mathrm{Mu} = 0.75$.

The vaneless diffuser configuration consists of two parallel walls. The inlet and outlet diameter of the diffuser are 280 mm and 560 mm, respectively. A large-diameter toroidal collecting chamber follows the radial diffuser (Fig. 2). This arrangement ensures a virtually uniform circumferential pressure distribution at the impeller exit under all through-flow conditions [6].

Investigated Impeller. In the course of the present work two impellers were manufactured and studied in detail. Both impellers are unshrouded and have an inlet tip diameter of $D_1 = 175\,\mathrm{mm}$ and an exit diameter of $D_2 = 280\,\mathrm{mm}$. Their splitter design with 11 full and 11 splitter blades results in a total of 22 blades. The diffuser width at impeller exit is $b_2 = 16.8\,\mathrm{mm}$.

The baseline impeller, called E7X, has been designed using conventional design engineering tools as described by Casey and Roth [11] and Casey [12]. The blades are swept 30° back from the radial direction at impeller exit.

Inverse design principals [3] have been applied to produce the second centrifugal impeller, which is called INV. Its design was intended to match the choke flow as well as the best point of the conventionally designed stage. For the inversely designed impeller the blades are swept 40° back from the radial direction at the impeller exit. A more detailed description of the design process and methods for this impeller is given in part 1 of this paper [4]. A picture of both impellers is shown in Fig. 3.

During the performance tests it was revealed that the designs do not match as intended. The computational fluid dynamics (CFD) predictions used during the design process underpredicted the losses at the blade trailing edge and thus the exit blade angles have been designed with a too large backsweep. This results in a mismatch of the Euler work and thus a lower stage pressure ratio. The lower stage pressure ratio could not have been compensated by the reduction in loss generation that was predicted for the inverse design.

A stress calculation for the inversely designed impeller revealed a strong radial deflection and high bending stresses in the root of the blades. The strongly bowed blading of the inversely designed impeller is the reason for this radial deflection. These increased deflections demanded an increase in the nonrunning tip clearance of 0.4 mm in order to avoid rubbing. The tip clearances at the design running condition are, however, similar to the conventional design due to the deflection of the blades under the centrifugal forces. At part speed the tip gap is slightly larger for the inverse design than that for the baseline design.

Compressor Performance. For both impellers the stage performances have been measured at different operating lines defined by the impeller tip Mach number ($\mathrm{Mu} = 0.60$, $\mathrm{Mu} = 0.75$, and Mu

Fig. 3 Investigated impeller. Left: conventional E7X design. Right: inverse INV design.

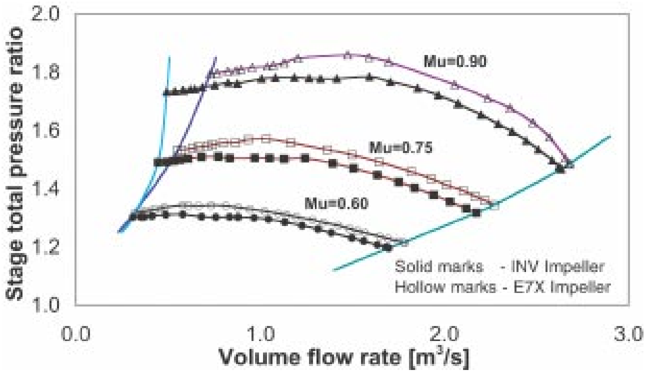

Fig. 4 (Color online) **Performance map for E7X and INV stage**

=0.90). In Fig. 4 the performance map of stage total pressure ratio against inlet volume flow rate is shown. On the left side of the map the performance curve is limited by the surge of the system. Surge was determined by evaluating the frequency content of a wall pressure signal taken within the diffuser.

For all three rotational speeds the total pressure ratio of the INV impeller is lower than that of the E7X impeller. However the INV impeller surge limit is extended to lower flow rates compared to the E7X impeller for the three rotational speeds. The extension increases with increasing Mach numbers. The right-hand end of the curve is the intersection of the performance curve and the system resistance curve. It does not represent the choke limit of the impeller itself.

Measurement Setup

All probe traverses were performed with a single-sensor fast response aerodynamic probe (FRAP). Figure 5 shows a picture of the probe used. For steady and periodically unsteady flows this probe provides two-dimensional velocities as well as total and static pressures. Thus, the periodic fluctuation of the flow caused by blade passing can be resolved.

The probe traversing system was mounted on the front wall of the diffuser at a radius of 105% of the impeller exit radius as shown in Fig. 2. The passage width of the diffuser is $b=16.8$ mm. The probe is axially traversed by an automated system to 13 positions that span the diffuser width. However, the position of the pressure tap limited the spatial extent of the measurements in close proximity to the diffuser walls. Ensemble-averaged sets of measurements are shown for a probe traverse from axial position $z=3.0$ to 15.0 mm by 1 mm intervals. A z/b value of unity corresponds to measurements at the shroud.

The probe was operated at every traverse position in a pseudo-three-sensor mode. The fluctuating flow was measured in a time-resolved manner at three angular positions of the probe shaft. The center angle position was set to the time-averaged flow direction as known from earlier traverses [7,8]. For the other two angle positions the probe was rotated in yaw by 43 deg clockwise and counterclockwise, respectively. In each yaw position the sensor signal was measured and stored. The position of the impeller was determined from a trigger on the impeller shaft that provided a once per revolution trigger signal. This signal was stored together with the flow data. The data chains obtained for the three yaw positions simulate the signals that would be delivered by a three-sensor probe with sensors at the same yaw positions.

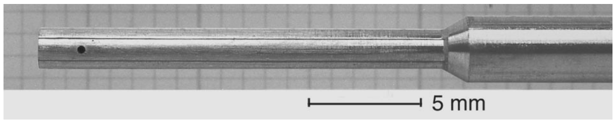

Fig. 5 Tip of the single-sensor FRAP probe

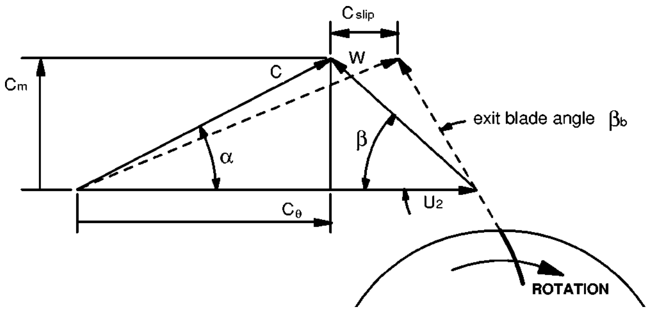

Fig. 6 Velocity triangle at impeller exit

The mean level of the signal represents the overall pressure level and provides information on the flow direction. The fluctuating part of the signal is composed of deterministic (rotor position determined) and stochastic (e.g., turbulence-induced) pressure fluctuations. Phase-locked sampling based on the rotor position and ensemble-averaging techniques statistically eliminate all stochastic fluctuations. Thus the deterministic fluctuations can be obtained for one rotation of the impeller.

In order to achieve a statistically significant number of events the sampling rate of the data acquisition system was set to 200 kHz. With a rotation speed of 17,720 rpm (295 Hz) and a data collection time of 1.0 sec at each yaw position, 295 revolutions are measured and averaged. Doing so a resolution of 678 data points per revolution was achieved. This results in an angular resolution better than 0.5 deg. Kupferschmied et al. [13] give a more detailed description of the FRAP probe measurement system and the data reduction methods.

Gizzi et al. [10] compares flow measurements using the FRAP probe and an optical laser Doppler velocimetry (LDV) system. They obtained similar results of the flow structure within the diffuser passage for both measurement systems. Extensive three-component LDV measurements within this research facility by Stahlecker and Gyarmathy [9] show that the axial component of the velocity vector is at least one order of magnitude smaller than the other two components. Therefore the diffuser flow can be assumed to be two-dimensional.

The accuracy of the probe measurements was checked with a mass balance. The calculated mass flow from the probe traverses was compared to the standard orifice measurements. The difference of the two mass flows was less than 3% for a linear extrapolation at the diffuser walls.

Experimental Investigations

Flow measurement with the FRAP technique was carried out for each impeller at an impeller tip Mach number of Mu=0.75. All results are given corresponding to the angle definitions illustrated in the velocity triangle of a centrifugal impeller exit (Fig. 6). The absolute and relative flow angles are measured with respect to the tangential direction.

The pressure rise versus flow coefficient for both impellers is shown in Fig. 7. The symbols indicate the operating conditions at which the measurements are obtained. The inversely designed compressor achieves a total pressure ratio of $\pi=1.46$ while the baseline stage delivers a pressure ratio of $\pi=1.5$ at a specific flow rate 1.55 m^3/s. This corresponds to a 2.7% reduction in the stage exit total pressure for the inverse design at the same specific flow rate. In order to account for the changed impeller work an additional set of measurements were taken in the conventionally designed impeller operated at an increased volume flow rate but at the same stage pressure ratio. Thus time-mean and time-resolved

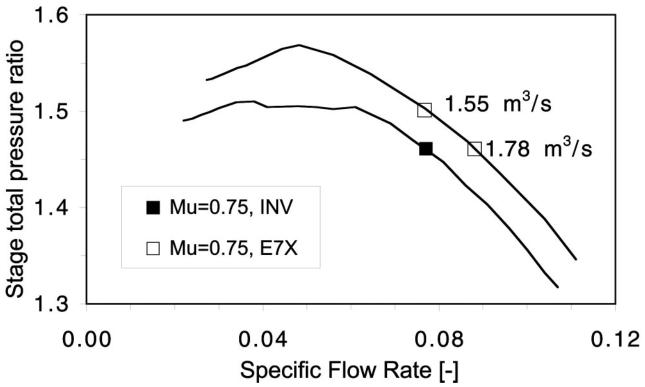

Fig. 7 Operating points for flow measurements

flow measurements in the two impellers were obtained for a constant flow rate of $\dot{V}=1.55\,\mathrm{m}^3/\mathrm{s}$ and for a constant total pressure ratio of $\pi=1.46$.

Time-Resolved Flow Measurements

Total Pressure Ratio. Figure 8 shows the total pressure ratio distribution. At the same volume flow rate the inversely designed impeller has a lower total pressure ratio [Figs. 8(*a*) and 8(*b*)]. At the same pressure ratio—but for an increased mass flow for the conventional design—the mean levels are similar to each other [Figs. 8(*a*) and 8(*c*)]. For both comparisons it is seen that stage total pressure ratio is more uniform for the inverse design.

Close to the shroud a wake region, [14], is seen for both impellers. For the inversely designed stage the wake region was pushed towards the shroud. The channel is occupied by the wake in the E7X case up to a height of approximately $z/b=0.75$ while for the INV impeller the channel was only occupied up to a height of $z/b=0.85$. This is especially remarkable as the inverse design is operated at a slightly increased nominal tip gap at the part speed condition investigated.

Meridional Velocity. The meridional velocity is presented in Fig. 9. A flow deficit can be seen near the shroud. This low meridional velocity channel wake is a typical feature of centrifugal impellers and is seen at blade channels behind the full blades as well as behind the splitter blades. A region of high meridional velocity (jet) is seen on the suction side of the blade close to the hub. This secondary flow distribution in the channel is associated with the jet-wake structure as observed by Eckardt [14], Johnson and Moore [15], Inoue and Cumpsty [16], and Zangeneh [3]. The wake can also be seen in the total pressure distribution (Fig. 8). The deficit in the meridional velocity results in a nonuniform mass flow distribution over the diffuser width and across the impeller exit.

Another clearly visible feature is the existence of a blade wake. The blade wake structure is parallel to the blade trailing edges and has a different shape for the full blade (F) and the splitter blades (S) in the conventional design [Fig. 9(*b*)]. The full blade causes a sharp and very narrow wake across the full width of the diffuser span. The blade wake caused by the splitter blades is merged with the channel wake.

The meridional velocity of the inverse design in Fig. 9(*a*) is generally found to be more uniform than that for the conventional impeller. The flow patterns behind main and splitter blades show the same fundamental behavior. The blade wake is weaker and the velocity deficit is smaller compared to the conventional impeller. The jet-wake structures in the blade channel are less pronounced. The meridional velocity is a measure for the losses and blockage inside the impeller. Generally more uniform flows indicate lower losses. Especially the higher flow velocities near the shroud for the inverse design indicate lower losses in the tip gap and wake

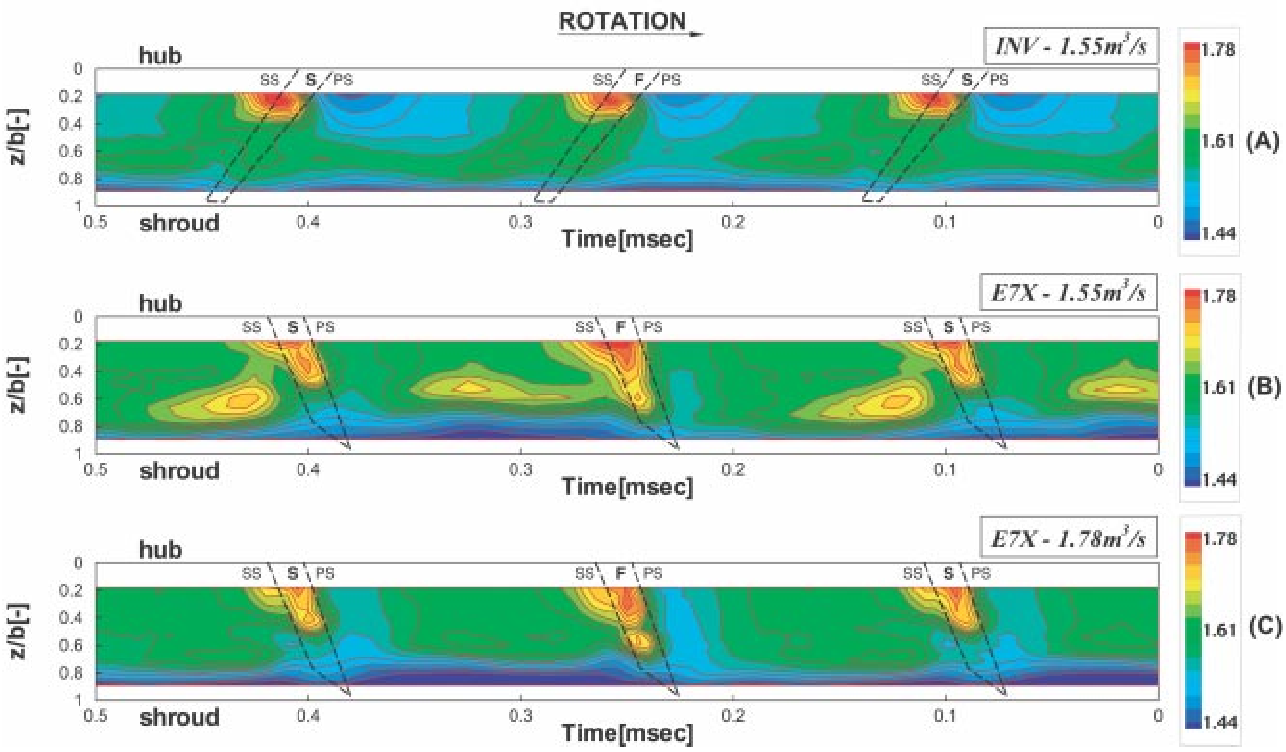

Fig. 8 (Color online) Total pressure ratio versus time across the diffuser passage at 105% radius location. (*A*) Inverse design. (*B*) E7X, nominal flow rate. (*C*) E7X, nominal pressure rise.

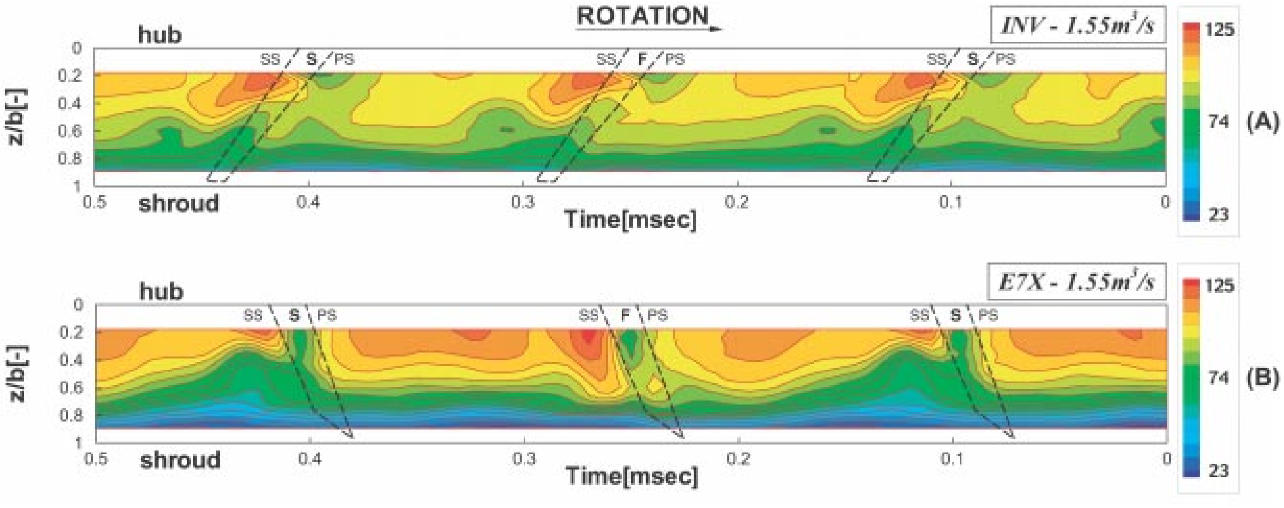

Fig. 9 (Color online) Meridional velocity versus time across the diffuser passage at 105% radius location. (*A*) Inverse design. (*B*) E7X, nominal flow rate.

region. The development of secondary flows is suppressed by the inverse design despite the slightly larger tip gap at the investigated operating condition.

The time-averaged meridional flow velocity (see Fig. 10), shows that there is an increased flow velocity near the shroud wall in the inverse design impeller. This more uniform span wise distribution of the meridional velocity indicates a more uniform mass flow distribution.

Tangential Velocity. For a negligible tangential velocity at the impeller inlet the Euler work is given by the equation:

$$h_{00}-h_{02}=\omega(r_2c_{\theta 2}). \quad (1)$$

Therefore the tangential velocity shown in Fig. 11 is a measure for the Euler work. The comparison of the three cases investigated shows that the tangential velocity of the inversely designed case is lower due to the change in blade exit angle. This is particularly noticeable at midpassage and near the hub where very low absolute tangential velocities are seen. This low absolute tangential velocity region strongly affects the overall Euler work because also the highest mass flows occur in this region. It is seen that the wake area close to the shroud is reduced. The jet-wake structure that is observed for the conventional cases near the shroud is nearly absent in the inverse case.

The time-averaged tangential velocity shown in Fig. 12 illustrates the reduction in velocity more clearly. The time-averaged tangential velocity at midspan and towards the hub is for the inverse case only 145 m/s. For the conventional case at the same pressure head a velocity of 156 m/s is obtained. Using the definition of the Euler head [Eq. (1)] this results in a reduction of the specific work input of 7% for the same pressure head. Close to the shroud wall the absolute tangential velocity drops for all cases down to 110 m/s.

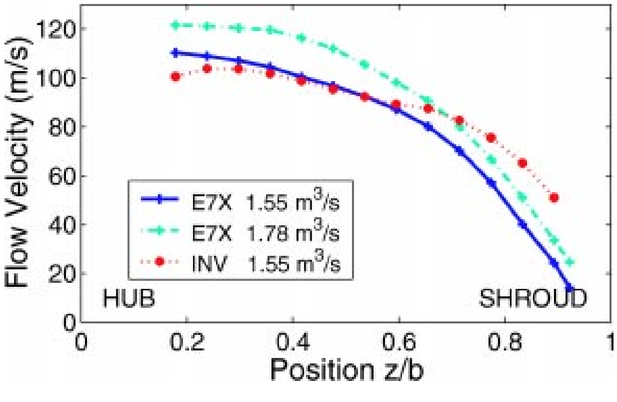

Fig. 10 (Color online) Time-averaged meridional velocity

Absolute Flow Angle. Figure 13 illustrates the absolute flow angle for the inverse and the conventional design at the same corrected flow rate. As a consequence of the more uniformly distributed mass flow, the absolute flow angles are also more uniform for the INV case. Especially the flow angle near the shroud for the inverse case is increased compared to the conventional design.

Steeper flow angles for the inverse design at the shroud can be seen very clearly in the averaged plot of the absolute flow angles (Fig. 14). The absolute flow angles are distributed more uniformly over the diffuser width, which results in an improvement of the flow at the diffuser inlet. It can also be seen that for the same volume flow rate the overall absolute flow angles are increased by 5 deg. This change in the absolute flow angle at an unchanged overall volume flow comes together with a reduced tangential velocity and a reduction in the Euler work. This effect explains the lower pressure rise for the inversely designed impeller that is seen in the overall performance maps (see Fig. 4).

The comparison of the two designs at the same pressure rise shows that the change in absolute flow angle from hub to shroud is much larger for the conventional design (E7X-1, 78 m^3/s). The average absolute flow angle is, however, the same and therefore a similar Euler head and pressure rise is obtained.

Relative Flow Angles. A comparison of the time-averaged relative flow angles is shown in Fig. 15. The plot shows very clearly that there is an overall reduction of the relative flow angles with the inverse design. This is the result of the changed impeller blade exit angle.

A remarkable effect is that the relative flow angle drops down from 48.5° near the hub down to 21 deg near shroud for the E7X impeller. The INV impeller shows only a drop of 20 deg from hub to shroud. This is greatly changing the velocity triangles at the hub and shroud (see also Fig. 20). The difference in the time-averaged relative flow angle near the hub is lower than the difference in the blade angle. This suggests that the flow is able to follow the blades better in the inverse design.

Relative Velocity. In Fig. 16 the relative velocity at impeller exit is plotted for both comparisons. It shows that there is a reduction of secondary flows inside the impeller for the inversely designed case. The blade wakes are clearly seen for both cases as

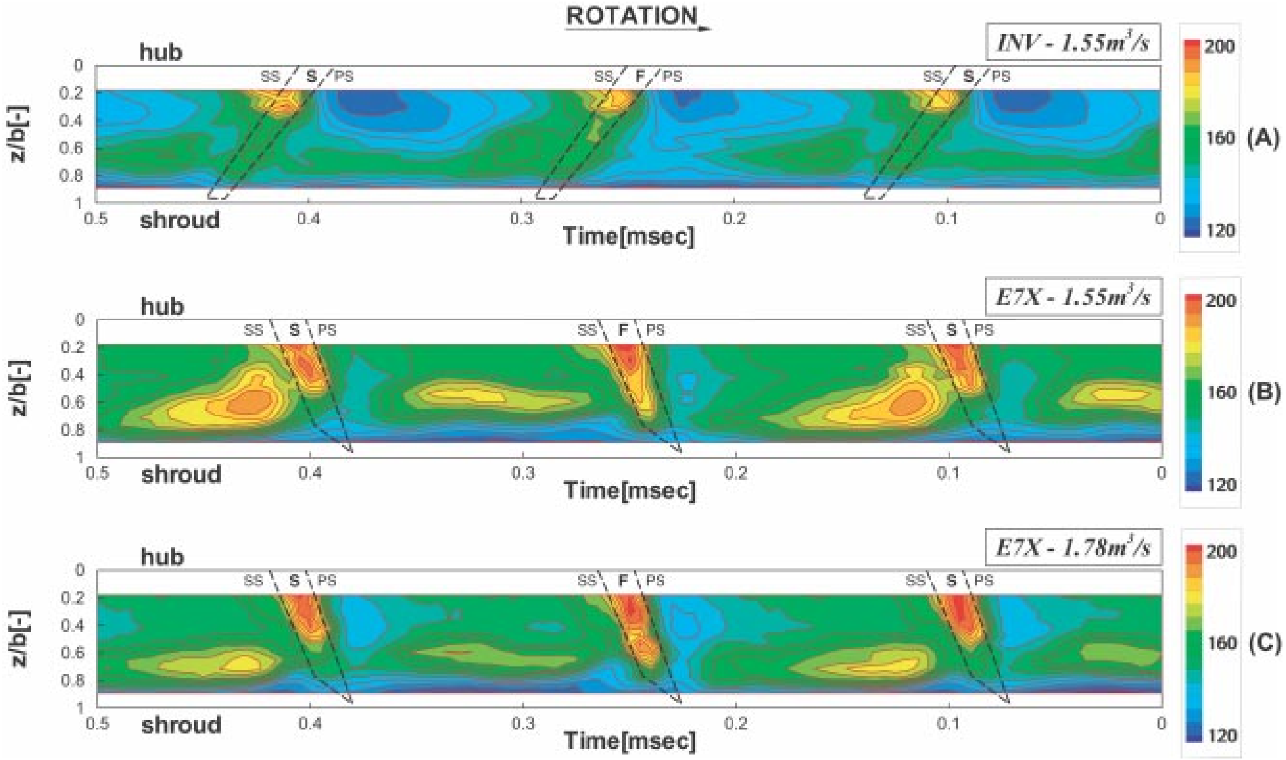

Fig. 11 (Color online) Absolute tangential velocity versus time across the diffuser passage at 105% radius location. (*A*) Inverse design. (*B*) E7X, nominal flow rate. (*C*) E7X, nominal pressure rise.

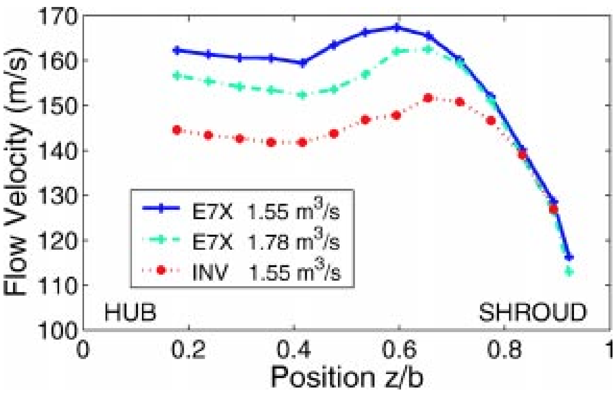

Fig. 12 (Color online) Time-averaged absolute tangential velocity

the pronounced deficits in the relative velocity at the blade locations. It can also be seen that the wakes of the blades for the inverse design lean back while for the conventional design the wake structure points forwards. This corresponds to the impeller design, where the INV impeller is designed with a backward lean while the E7X impeller has forward-leaning blades.

For the conventional E7X impeller the channel type wakes at the splitter blade suction side appear as a dominant flow feature. In the case of the inverse impeller the channel flow is more evenly distributed.

In Fig. 17 the time-averaged relative velocity is shown. In order to compare the two designs correctly the operating conditions for the same pressure rise have to be compared. It can be very clearly seen that the flow is leaving the impeller with a more uniform velocity distribution from hub to shroud in the inverse design case. For the E7X case at a flow rate of 1.78 m^3/s the difference between the highest and the lowest relative flow velocity is 37 m/s

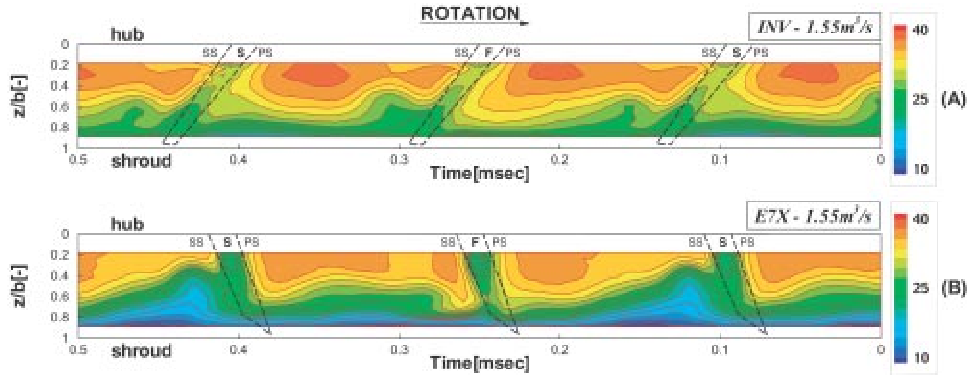

Fig. 13 (Color online) Absolute flow angle versus time across the diffuser passage at 105% radius location. (*A*) Inverse design. (*B*) E7X, nominal flow rate.

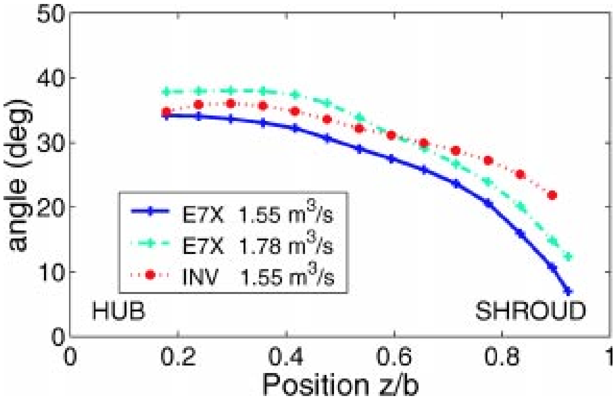

Fig. 14 (Color online) Time-averaged absolute flow angle

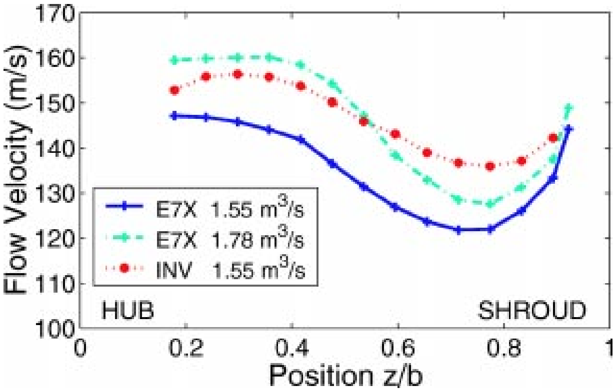

Fig. 17 (Color online) Time-averaged relative velocity

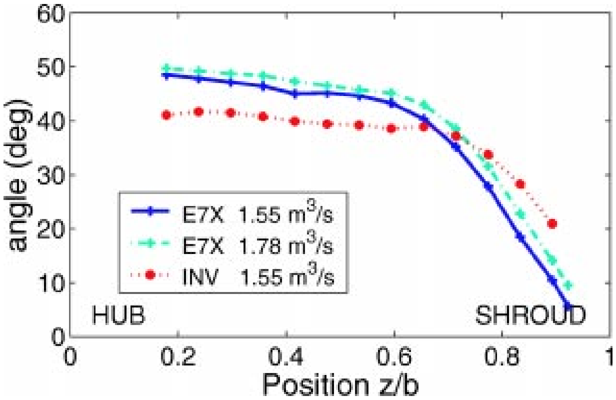

Fig. 15 (Color online) Time-averaged relative flow angle

while the INV case shows only a difference of 20 m/s. This lower velocity difference causes lower mixing losses in the diffuser.

Slip Factor. The capability of the flow to follow the blading is defined by the slip factor. It is defined as the ratio of the actual tangential velocity over the idealized tangential velocity [Eq. (2)]. The slip factor can also be written as a function of the slip velocity and the rotational speed where the slip velocity is defined as the difference in actual and ideal tangential velocity (see velocity triangles in Fig. 6):

$$\sigma=\frac{c_{\theta 2}}{c_{\theta 2\ \text{ideal}}}=1-\frac{c_{\text{slip}}}{U_2}. \tag{2}$$

High values of the local slip factor indicate that the time-averaged flow is better able to follow the blading. In Fig. 18 the slip factor over the diffuser width is illustrated for both designs. In the region close to the shroud generally lower slip factors are found. This is a consequence of the flow deficit caused by the

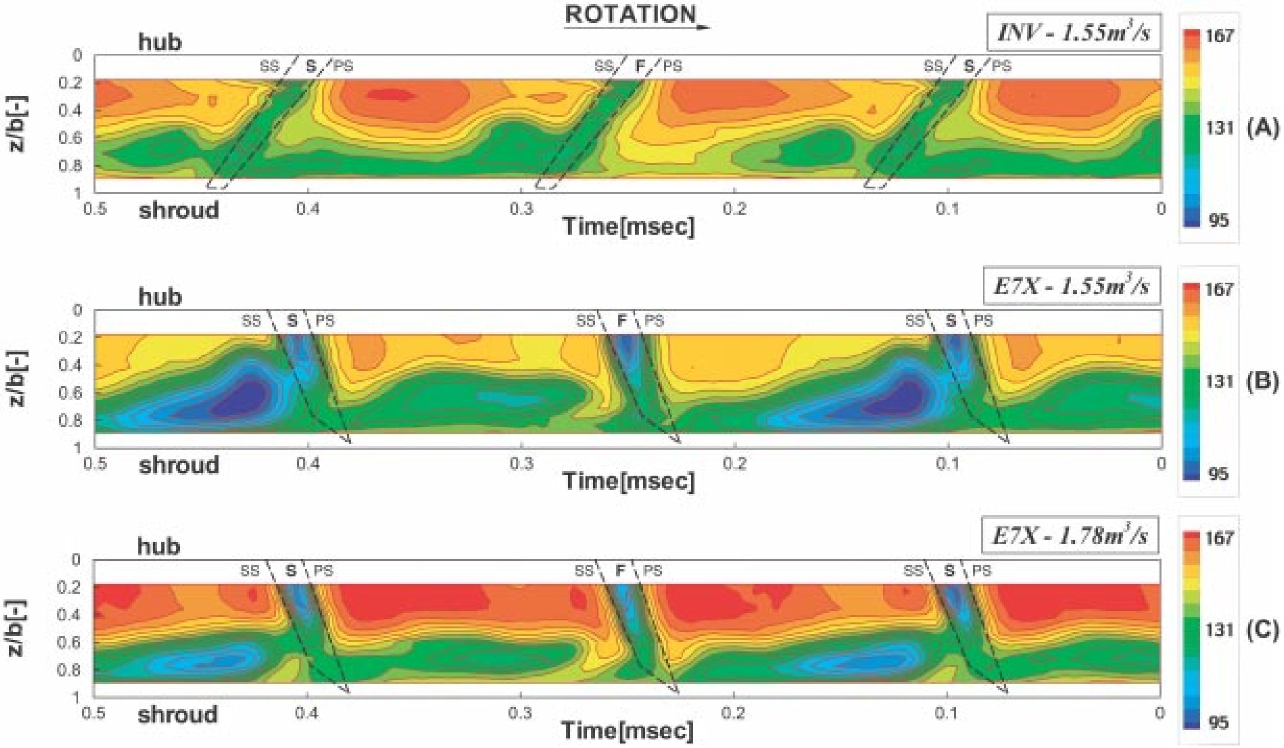

Fig. 16 (Color online) Relative velocity versus time across the diffuser passage at 105% radius location. (*A*) Inverse design. (*B*) E7X, nominal flow rate. (*C*) E7X, nominal pressure rise.

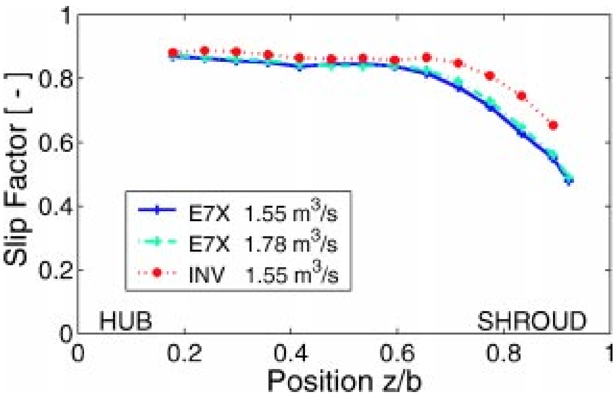

Fig. 18 (**Color online**) **Slip factor**

channel jet-wake structure (see Figs. 9 and 11 above). Especially close to the shroud, the slip factor is substantially lower for the conventional design. This indicates that the slip could have been reduced by the inverse design approach due to the suppression and mixing of the jet-wake structure near the shroud wall.

Impeller Efficiency. The isentropic total-to-total efficiency of the stage is defined by the stage pressure ratio and the temperature ratio across the stage:

$$\eta_{tt}=\frac{T_{0\ \mathrm{in}}\left(\left[\frac{P_{0\ \mathrm{out}}}{P_{0\ \mathrm{in}}}\right]^{(\kappa-1)/\kappa}-1\right)}{(T_{0\ \mathrm{out}}-T_{0\ \mathrm{in}})}. \tag{3}$$

In addition to the unsteady pressure data, the FRAP measurement technique provides the time-averaged flow temperature. Thus the impeller efficiency can be calculated using a similar equation as that for the stage efficiency. The isentropic efficiency of the stage and the impeller are plotted in Fig. 19. All measurements are mass averaged and taken under thermal equilibrium conditions. For the flow rate of 1.55 m^3/s the impeller efficiencies are 94.5% for the E7X impeller and 97.5% for the INV impeller. The measured overall stage efficiency is 86.5% for the inverse and 80.3% for the conventional design, respectively.

These performance measures are similar to previous observations. Rodgers [17] shows that for unshrouded impellers with inducer, isentropic efficiencies of 94% are attainable. With backswept impellers he found about 2% higher efficiencies than for radial blades. Krain [18] described a centrifugal impeller with a vaneless diffuser and showed an impeller efficiency of 95% and a total-to-total stage efficiency of about 84%.

A comparison of the two impeller designs reveals that the stage efficiency for the inverse design is improved. The inverse impeller also shows higher impeller efficiency. That improvement in the impeller efficiency is a consequence of the more uniform flow distribution at the impeller exit. Lower mixing losses occur in the diffuser and also the diffuser efficiency is improved.

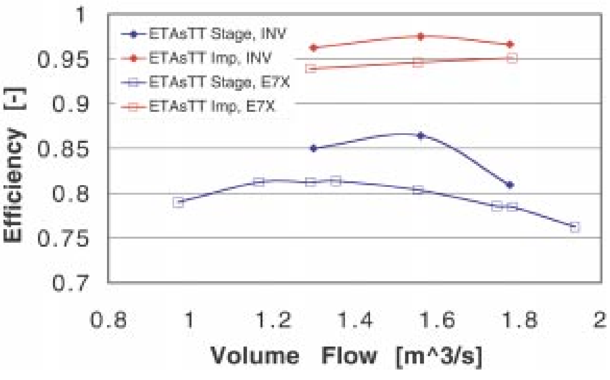

Fig. 19 (**Color online**) **Impeller efficiency**

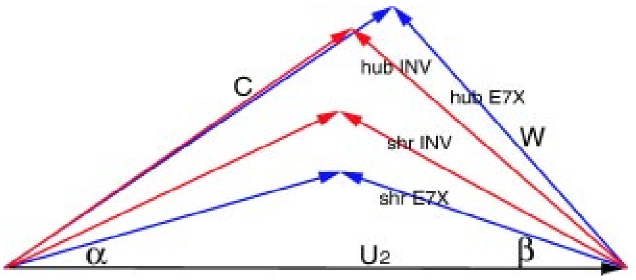

Fig. 20 (**Color online**) **Velocity triangles at impeller exit near hub and shroud for both designs**

Discussion

In general the flow for the inverse design is more uniform in the spanwise direction as well as in the blade-to-blade direction. This is shown clearly in Figs. 9, 11, 13, and 16 above. Therefore, the design specification that was presented in part 1 [4] of a more uniform flow at the impeller exit was obtained. As expected in the inverse design the specified blade loading distribution and the resultant blade shape suppress the formation of the secondary flow jet-wake structures. In particular the wake region at the shroud wall is reduced and the formation of the jet at the hub suction side corner is suppressed. The slip velocity of the inverse impeller is also reduced. This results in a reduced loss and a higher efficiency within the impeller at the investigated operating points.

In Fig. 20 velocity triangles at the impeller exit are drawn for both stages. The velocity triangles are composed out of the averaged data shown above for a cut close to the hub ($z/b=0.18$) and shroud ($z/b=0.83$). The figure shows that especially for the baseline design E7X close to the shroud the average flow angles and velocities differ strongly from the values close to the hub. This is caused by the channel-type jet-wake structure near the shroud. Again it is seen that the flow is distributed more uniformly from hub to shroud for the inverse case. This increased uniformity helps to avoid mixing losses in the following diffuser.

It is also seen that close to the hub there is a region with comparably high total pressure while close to the blades near the shroud low total pressures are found (Fig. 8). In the region close to the hub in a blade-to-blade cut very high gradients of meridional and tangential velocities (Figs. 9 and 11) and a strongly fluctuating flow angle (Fig. 13) is also observed. These flow features are detected in both impellers, but with much higher gradients for the inverse case.

The absolute flow velocities (Figs. 9 and 11) show a severe velocity difference between the hub suction and pressure side corner. This suggests a highly vortical flow in the corner at the hub suction side. The vortical structure is visible in both designs but is substantially larger for the conventional design where the velocity gradient is found up to midpassage of the diffuser. The CFD [4] shows the same vortical structure for the calculation of impeller with a blunt trailing edge.

There is an effect of the increased backsweep on the secondary flow structure and efficiency off the impeller [19]. But in the present case the improved efficiency and flow uniformity within the impeller passage of the inverse design is caused mainly due to the loading distribution. The wake region near the shroud is less severely developed than that for the baseline design.

Out of the given data no conclusion could be drawn if the stabilization of the compressor stage and the extension of the surge limit towards lower mass flows were caused by the more uniform flow pattern or due to the increased backsweep of the impeller.

Summary and Conclusions

The impeller of a centrifugal compressor has been designed using an inverse design method. The stage performance and detailed flow measurement at the impeller exit have been obtained and compared to those of a conventionally designed impeller. The detailed flow measurements at the impeller exit are obtained with very high spatial and temporal resolution using a fast response aerodynamic probe (FRAP).

It is found that the flow field is more uniform for the inverse design than for the conventional design. The inverse impeller generates lower losses, which are seen in the time-resolved flow distribution plots. The jet-wake phenomenon is much less developed in the inversely designed case compared to the conventional design. The inverse design has a higher efficiency than the conventional design, as results of the more uniform blade-to-blade and hub-to-shroud flow fields at the impeller exit.

This work has shown a high capability of the inverse design method for the improvement of centrifugal compressors. It is shown that it is feasible to use inverse design tools to improve the performance of a centrifugal impeller. It is further shown that the development of secondary flows could be suppressed by the blade design and the inverse design provides a more uniform flow into the diffuser.

Acknowledgments

This project was funded by the Swiss Commission for Technology and Innovation (KTI) and the European EUREKA program. The authors would like to thank the Swiss Federal Institute of Technology as well as our industrial partners ABB Turbo Systems Ltd., MAN Turbomaschinen AG, and HV Turbo A/S for their financial and scientific support. And last, but not least, the authors would like to thank the technical staff of the laboratory, Mr. Reshef, Mr. Lehner, Mr. Künzle, and Mr. Suter, for their invaluable support.

Nomenclature

E7X = Conventionally designed stage
INV = Inversely designed stage
b = Diffuser width (axial)
c = Absolute velocity
D = Diameter
h = Enthalpy
p = Pressure
r = Radius
t = Time
T = Temperature
U = Circumferential speed
V = Volume flow rate
w = Relative velocity
z = Axial coordinate
α = Absolute flow angle
β = Relative flow angle
η = Efficiency
κ = Ratio of specific heats
σ = Slip factor
π = Stage pressure ratio (total-static)
ω = Rotational speed
ϕ = Specific flow coefficient $=V_0/(D_2^2 U_2)$
ψ = Specific work coefficient $=\Delta h_{ts}/U_2^2$
Mu = Mach number at impeller tip $=U_2/\sqrt{\kappa R T_{t,\mathrm{in}}}$

Subscripts

1 = Impeller inlet
2 = Impeller outlet
0, in = Stage inlet
out = Stage outlet
m = meridional
r = radial
θ = tangential
t = total

References

[1] Zangeneh, M., Vogt, D., and Roduner, C., 2002, ‘‘Improving a Vaned Diffuser for a Given Centrifugal Impeller by 3D Inverse Design,’’ ASME paper no. GT-2002-30621.

[2] Goto, A., Ashihara, K, Sakurai, T., and Saito, S., 1999, ‘‘Compact Design of Diffuser Pump Using 3D Inverse Design Method,’’ ASME Fluids Engineering Summer Meeting, Paper No. FEDSM99-6847.

[3] Zangeneh, M., Goto, A., and Harada, H., 1998, ‘‘On the Design Criteria for Suppression of Secondary Flows in Centrifugal and Mixed Flow Impellers,’’ ASME J. Turbomach., **120**, pp. 723–735.

[4] Zangeneh, M., Schleer, M., Pløger F., Hong, S. S., Roduner, C., Ribi, B., and Abhari, R., 2004, ‘‘Investigation of an Inversely Designed Centrifugal Compressor Stage—Part 1: Design and Computational Investigations,’’ ASME J. Turbomach., **126,** pp. 73–81.

[5] Zangeneh, M., 1991, ‘‘A Compressible Three Dimensional Blade Design Method for Radial and Mixed Flow Turbomachinery Blades,’’ Int. J. Numer. Methods Fluids, **13**, pp. 599–624.

[6] Hunziker, R., and Gyarmathy, G., 1993, ‘‘The Operational Stability of a Centrifugal Compressor and its Dependence on the Characteristics of the Sub-Components,’’ ASME paper no. 93-GT-284.

[7] Roduner, C., Köppel, P., Kupferschmied, P., and Gyarmathy, G., 1999, ‘‘Comparison of Measurement Data at the Impeller Exit of Centrifugal Compressor Measured With Both Pneumatic and Fast Response Probes,’’ ASME J. Turbomach., **121**, pp. 609–619.

[8] Roduner, C., Kupferschmied, P., Köppel, P., and Gyarmathy, G., 2000, ‘‘On the Development and Application of the Fastresponse Aerodynamic Probe System in Turbomachines—Part 2: Flow, Surge, and Stall in a Centrifugal Compressor,’’ ASME J. Turbomach., **122**, pp. 517–526.

[9] Stahlecker, D., and Gyarmathy, G. 1998, ‘‘Investigations of Turbulent Flow in a Centrifugal Comprerssor Vaned Diffuser by 3-Component Laser Velocimetry,’’ ASME paper no. 98-GT-300.

[10] Gizzi, W., Roduner, C., Stahlecker, D., Köppel, P., and Gyarmathy, G., 1999, ‘‘Time Resolved Measurements With Fast Response Probes and Laser Doppler Velocimetry at the Impeller Exit of a Centrifugal Compressor—A Comparison of two Measurement Techniques,’’ 3rd European Conference on Turbomachinery, London.

[11] Casey, M. V., and Roth, P., 1984, ‘‘A Streamline Curvature Throughflow Method for Radial Turbocompressors,’’ I Mech E Conf. Publ., **C57/34**, pp. 9–18.

[12] Casey, M. V., 1985, ‘‘Aerodynamische Auslegung von Hochleistungsradialverdichtern für Industrielle Turboverdichter,’’ VDI-Berichte 72.1, Strömungsmaschinen, pp. 167–181.

[13] Kupferschmied, P., Köppel, P., Roduner, C., and Gyarmathy, G., 2000, ‘‘On the Development and Application of the Fast-Response Aerodynamic Probe System in Turbomachines—Part 1: The Measurement System,’’ ASME J. Turbomach., **122**, pp. 505–516.

[14] Eckardt, D., 1976, ‘‘Detailed Flow Investigations Within a High-Speed Centrifugal Compressor Impeller,’’ ASME J. Fluids Eng., pp. 390–402.

[15] Johnson, M. W., and Moore, J., 1980, ‘‘The Development of Wake Flow in a Centrifugal Impeller,’’ J. Eng. Power, **102**, pp. 382–389.

[16] Inoue, M., and Cumpsty, N. A., 1984, ‘‘Experimental Study of Centrifugal Impeller Discharge Flow in Vaneless and Vaned Diffusers,’’ ASME J. Eng. Gas Turbines Power, **106**, pp. 455–467.

[17] Rodgers, C., 1980, ‘‘Efficiency of Centrifugal Compressor Impellers,’’ Paper 22 of AGARD Conference Proceedings No. 282, Centrifugal Compressors, Flow Phenomena and Performance, Brussels, 1980.

[18] Krain, H., 1987, ‘‘Swirling Impeller Flow,’’ 32nd ASME Gas Turbine Conference and Exhibit, Anaheim, California, ASME paper no. 87-GT-19.

[19] Farge, T., and Johnson, M., 1990, ‘‘The Effect of Backswept Blading on the Flow in a Centrifugal Compressor Impeller,’’ Brussels, ASME paper no. 90-GT-231.

Stéphane Burguburu
ONERA–Applied Aerodynamics Department,
29, avenue de la division Leclerc,
BP 72,
92 322 Châtillon, France
e-mail: stephane.burguburu@onera.fr

Clement Toussaint
ONERA–Systems and Flight Dynamics
Department,
2, avenue E. Belin,
31 055 Toulouse, France
e-mail: clement.toussaint@onera.fr

Christophe Bonhomme
CNES–Propulsion Division,
Rond Point de l'Espace,
91003 Evry Cedex, France
e-mail: christophe.bonhomie@cnes.fr

Gilles Leroy
TURBOMECA–Aerothermodynamic Department,
64511 Bordes Cedex,
France
e-mail: gilles.Leroy@turbomeca.fr

Numerical Optimization of Turbomachinery Bladings

An optimization process is used to design bladings in turbomachinery. A gradient-based method is coupled to Navier-Stokes solvers and is applied to three different bladings. A new rotor blade of a transonic compressor is designed by using a quasi three-dimensional approach, with a significant efficiency improvement at the design point. The off-design behavior of this new compressor is also checked afterwards. The same quasi three-dimensional approach is used on a stator blade of a turbine, but the whole stage is computed in this case. The losses are locally reduced, proving the good sensitivity of the solver. Finally, a new three-dimensional rotor blade of a compressor is designed by applying deformation functions on the initial shape. The efficiency is improved over a wide range of mass flow. The whole results indicate that the optimization process can find improved design and can be integrated in a design procedure. [DOI: 10.1115/1.1645869]

Introduction

Engine manufacturers are steadily asking for higher performance in terms of efficiency, pressure ratio or mass flow of the different components of the engine (rows, stages . . .). This leads to the use of computational fluid dynamics (CFD) in an intensive way for turbomachinery blade design, [1], but this higher performance must be achieved within shorter design cycles and at lower cost. Traditionally, CFD has been used in an analysis mode for cut-and-try approaches to design, in which the design process is guided by the designer's expertise, with eventually a large scattering of the results. The recent progress of the CFD code performance in terms of accuracy, sensitivity and efficiency, enables to reduce the design cycle by coupling CFD codes with optimization tools. This can be applied with a quasi three-dimensional and more recently with a fully three-dimensional approach, with various optimization and blade deformation techniques.

This paper describes three optimization cases carried out by coupling a standard gradient optimizer to Navier-Stokes solvers.

The first test case concerns the efficiency improvement of a transonic compressor with a quasi three-dimensional approach. The suction side of the blade is modified by applying a deformation function defined by a Bézier curve. One of the goals is to reduce the losses generated by the normal shock upstream of the leading edge. The other objective is to keep the choked mass flow as constant as possible during the optimization process. Finally, the good behavior of the compressor at off-design is also checked.

The second optimization deals with the design modification of a stator of turbine. The steady quasi three-dimensional computation is carried out on the whole stage, i.e., including the rotor blade. The camberline of the stator is firstly modified, and the suction side is deformed in a second step, still with a Bézier curve. The challenge here is to find a more efficient stator shape while preserving the operating point.

The last case presented concerns the fully three-dimensional optimization of a transonic compressor. The three-dimensional Navier-Stokes calculation is carried out including the tip clearance in order to take into account the end wall vortex (and losses) in this region. The suction side of the blade is modified by a Bézier surface deformation, applied from hub to tip and from leading edge to trailing edge. The performance of the new shape is compared to the initial at the design point as well as at off-design points.

Optimization Procedure

As shown on **Fig. 1**, the optimization strategy is composed of four main parts. The optimization algorithm supplies a set of design variables to the grid deformation tool which propagates deformations and generates a new mesh. The aerodynamic field is updated by calling a steady Navier-stokes code quasi three-dimensional or three-dimensional. The objective function and constraints are then deduced from the flow results by integration of the flow solution downstream of the blading.

Numerical Optimization. The gradient-based method used here is CONMIN [2,3]. The aim is to define a vector of design variables $\mathbf{y}=(y_1, y_2, \ldots y_{nv})$ which minimizes a scalar objective function $F_{\rm obj}(\mathbf{y})$ with constraints $\mathbf{G}(\mathbf{y})=(g_1, g_2 \ldots g_{nc})$. The constraints are violated if $\mathbf{G}(\mathbf{y})>0$. In the present methodology, all gradients are determined by finite differences at each optimization iteration. For the first iteration, the gradient is taken as

$$\mathbf{S}_q=-\boldsymbol{\nabla} F_{\rm obj}(\mathbf{y}). \tag{1}$$

For the following iterations, the gradient depends on the constraints. If the constraints are violated, $\mathbf{S}_q$ is given by the feasible direction method of Zoutendijk. Else, $\mathbf{S}_q$ is calculated by the Fletcher and Reeves conjugate gradient method. In the iterative process, the design variables vector is given in function of the one from the previous calculation by the relation $\mathbf{y}^{n+1}=\mathbf{y}^n+\lambda\cdot\mathbf{S}_q$ where λ is the displacement modulus to be applied in the $\mathbf{S}_q$ direction. This λ modulus is evaluated by a polynomial approximation. At each iteration, three steps are performed to search for the objective function minimum and to respect the constraints. In summary, for $-nv-$design variables, the$-n-$iteration optimization process requires at least $1+n(nv+3)$ calls to the solver.

Contributed by the International Gas Turbine Institute and presented at the International Gas Turbine and Aeroengine Congress and Exhibition, Atlanta, GA, June 16–19, 2003. Manuscript received by the IGTI December 2002; final revision March 2003. Paper No. 2003-GT-38310. Review Chair: H. R. Simmons.

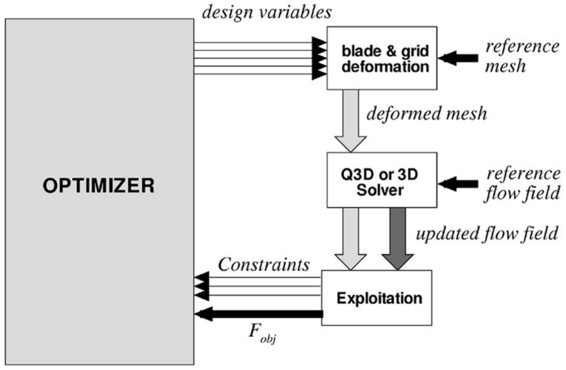

Fig. 1 Optimization flow chart

Grid Deformation. As mentioned in the Introduction, this optimization procedure is used to reduce the blade design cycle. A mesh operator applies a deformation function on the blade and this deformation is propagated all over the mesh. This technique allows to dissociate the design variables (used during the optimization) and the blade definition variables (used to define the blade shape). This principle, extended to multidisciplinary applications (the "MASSOUD" process), is described by J.A. Samareh [4]. The deformation function are Bézier curves and surfaces, [5,6], and are used for both quasi three-dimensional and three-dimensional applications. These parametric functions are well suited to aerodynamic applications because of their tangential and curvature properties. In both cases, the control points are more or less driven by the design variables.

Various operators can be used to propagate the deformation into the entire grid (linear or Laplacian for example). In the presented applications, a linear operator is applied in all directions.

In quasi three-dimensions the grid deformation tool can treat various topologies and the deformation functions can modify the suction side, the pressure side and the camber line, [7]. For the three-dimensional applications, a sweep and a lean effect can be introduced. The hub and casing shape can also be modified but the most interesting case concerns the modification of a local zone of the blade by applying a surfacic deformation function.

Flow Solvers. Two flow solvers are used in the present analysis: COLIBRI [8] for quasi three-dimensional and CANARI [9] for three-dimensions. Both codes solve the time-averaged Navier-Stokes equations on multiblock structured grids. A space-centered Jameson scheme cell-vertex approach is used with artificial viscosity (second and fourth order). Numerical time integration is ensured by a standard four-step Runge-Kutta algorithm; an implicit residual smoothing phase is added in order to get high CFL number values. Boundary treatment is ensured by characteristic relations. In the present optimization cases, constant total pressure, total temperature and absolute flow angle are fixed at the inlet. At the outlet a constant static pressure is imposed.

For reducing the computation time, turbulence is modeled by an algebraic mixing length turbulence model (Michel, Quemart, and Durand [10]). In addition, wall functions can be used for increasing the local time-step and decreasing the node number.

Post-Processing. The flow results are computed by averaging the typical flow quantities downstream: total mass flow, pressure ratio, temperature ratio, efficiency. In quasi three-dimensions, convergence is reached when losses remain constant during a fixed iteration number. In three-dimensions, the CPU time is to be well controlled and a fixed iteration number is used. This number is adjusted after calibration on a deformed mesh.

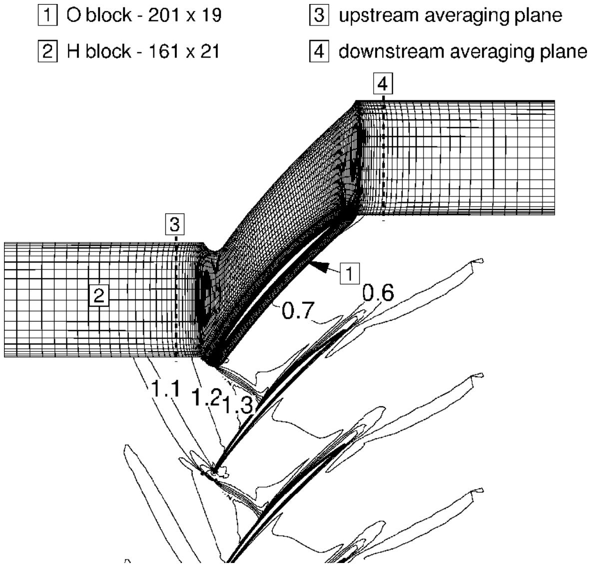

Fig. 2 Mesh grids and relative Mach number iso-lines

Quasi Three-Dimensional Compressor Optimization

The quasi three-dimensional optimizations are useful in the design process because of the short computation time which allows a large number of cycles to reach the best performance at a given span. Such optimizations are described in a previous work, [7] and by J. Chung et al. [11] with an important efficiency improvement, but the choked mass flow may vary during the optimization process and a manual override is required. The method proposed here maintains the choked mass flow constant without applying any constraints for a better efficiency improvement.

Description of the Case. This chapter describes the quasi three-dimensional optimization of a transonic compressor blade section. The stream surface is supposed to be far away from the hub and the casing to avoid three-dimensional effects. The Navier-Stokes calculation is performed with a OH-type grid (**Fig. 2**).

The nodes are exactly matching on the O-H boundary and on the periodic boundaries. An adiabatic wall condition is applied on the blade and the first cell size is suited to a low Reynolds model of the boundary layer.

In this transonic case, the operating point is chosen at the maximum of efficiency. The strong shock upstream of the leading edge (**Fig. 2**) highly slows down the relative velocity and generates a large part of the losses in the compressor. The challenge is to reduce the shock intensity while keeping constant the pressure ratio and the choked mass flow.

Design Variables, Objective Function and Constraints. The suction side curve is extracted from the mesh without taking into account the leading edge and the trailing edge (**Fig. 3**, the ξ coordinate represents the reduced abscissa).

The deformation function is defined by a Bézier curve whose control points are defined by the reduced abscissa ξ_i [0;1] and the design variables y_i. The deformation curve to be applied is then given by the following equation:

$$\mathbf{R}=\sum_{k=0}^{n}\mathbf{P}_k\cdot B_k^n(u) \tag{2}$$

with $\mathbf{R}\left\{\begin{matrix}\xi(u)\\ \delta(u)\end{matrix}\right\}$, $\mathbf{P}_i\left\{\begin{matrix}\xi_i\\ y_i\end{matrix}\right\}$ and B_k^n the Bernstein polynom:

$$B_k^n(u)=C_k^n\cdot u^k(1-u)^{n-k}. \tag{3}$$

The δ deformation is then calculated by an interpolation at the ξ abscissa. This deformation is projected on the suction side by

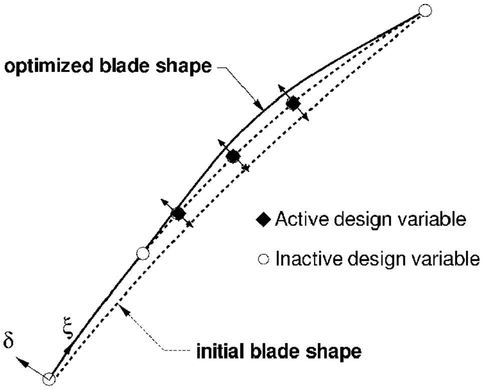

Fig. 3 Blade deformation

translating each point of this curve over a distance δ along the current normal to the reference blade. It should be added that the design variables y_i and displacement δ are normalized by the current thickness of the blade.

For the present application, six design variables (i.e., Bézier curve of fifth degree) are distributed along the suction side of the blade. The active ones are respectively located at 40%, 55%, and 70% of the blade chord as plotted on **Fig. 4**.

The active status means that this control point is driven by a design variable. Conversely, an inactive status means that this control point is only used for the Bézier curve definition. The design variable located at $\xi_2 = 30\%$ is in an inactive state in order to keep unchanged the inlet part of the suction side. By this way, the choked mass flow remains constant following the principle of the unique incidence. The other locations have been fixed after few trials.

The objective function and constraints are evaluated with the upstream and downstream flow characteristics. They are calculated by a momentum average on a line located at -30% and $+30\%$, respectively, of the axial chord. In two dimensions, this kind of average is defined by

$$\left| \begin{array}{l|l} \overline{\rho V_n}=\frac{1}{s}\sum \rho V_n ds & \overline{p+\rho V_n^2}=\frac{1}{s}\sum (p+\rho V_n^2)ds \\ \overline{\rho V_n V_{t1}}=\frac{1}{s}\sum \rho V_n V_{t1}ds & \overline{\rho V_n H_i}=\frac{1}{s}\sum \rho V_n H_i ds \end{array} \right. . \qquad (4)$$

In order to improve the overall efficiency, the objective function is given by the relation

$$F_{\mathrm{obj}} = 100\cdot(1-\eta_{\mathrm{isentropic}}) \qquad (5)$$

with

$$\eta_{\mathrm{isentropic}} = \frac{1-\pi^{\gamma-1/\gamma}}{1-Rt_i}. \qquad (6)$$

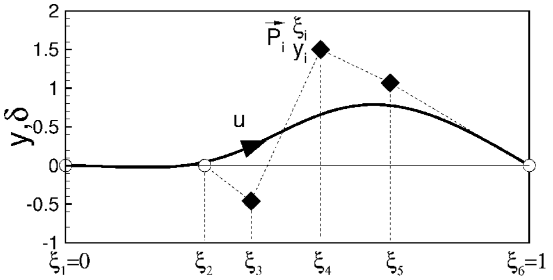

Fig. 4 Deformation function

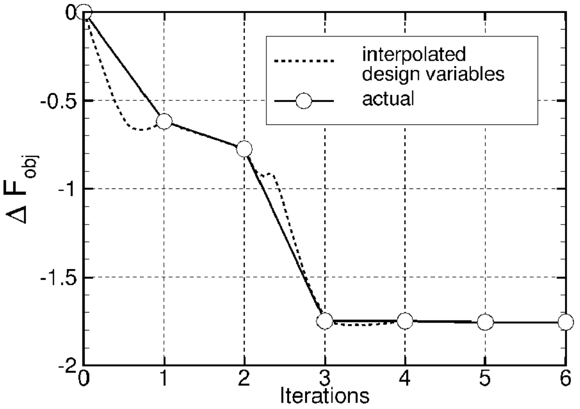

Fig. 5 Objective function history

The total-to-total pressure ratio is maintained between a lower and an upper boundary by applying the constraint

$$0.99\cdot\pi_{\mathrm{reference}} \leqslant \pi \leqslant 1.07\cdot\pi_{i_{\mathrm{reference}}}. \qquad (7)$$

In addition, the axial chord is maintained constant during the optimization process by applying geometrical transformations.

Optimization. The optimization process converges in six iterations which required 35 calls to the quasi three-dimensional solver. The total CPU time is 700s on NEC SX5. The average run time for each Navier-Stokes computation is about 20s; this performance is reached through the high vectorization degree of the COLIBRI solver.

The objective function history on **Fig. 5** shows a reduction of the objective function (-1.75 points). Actually, only three iterations of optimization are necessary to reach this level, the three last ones being performed to enforce the convergence of the process.

Compared to the reference, the optimized blade presents a bulge in its rear part (see **Figs. 3** and **4**). The maximum thickness, previously located at 70% of the reduced chord, is increased by 50%. Between 30% and 50% of the reduced chord, one can observe a negative curvature. Conversely, there is a positive curvature from 50% to 80% of the chord. The inlet part of the blade located between the leading edge and 30% presents a very low modification (**Fig. 4**), as expected and following the remarks on the unique incidence. By a mechanical point of view, the blade section area is increased after optimization and a mechanical stress calculation on the whole blade would be useful. The variation of the overall performance is given in **Table 1.**

The increase of mass flow is a consequence of the losses reduction, and this can be easily adjusted with the downstream pressure. The downstream relative and absolute flow angles does not present a large variation, which is encouraging for the off-design behavior of the new blading.

On **Fig. 5**, the objective function between two consecutive iterations is also plotted (red curve). This is obtained by interpolating the design variables and by computing the updated geometry. One can observe the good behavior of the optimizer CONMIN which is able to avoid a local minimum.

The relative Mach number flow field on **Fig. 6** shows that no modification of the inlet flowfield occurred after optimization, as expected. On the other hand, the flowfield structure in the duct is

Table 1 Variation of the overall performance

ΔF_{obj}	$\Delta\eta_{ig}$	$\Delta\dot{m}$	$\Delta\pi$	ΔRt_i	$\Delta\alpha$	$\Delta\beta$
Δ%	Δ%	%	%	%	deg	deg
−1.75	+1.75	+0.68	−0.40	−0.40	+0.73	+0.58

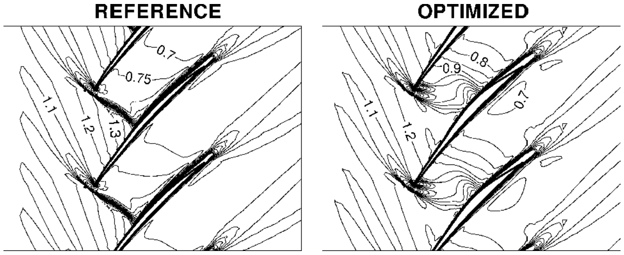

Fig. 6 Relative Mach number contours before and after optimization

different: The negative curvature of the blade upstream of the shock leads to the reduction of the upstream relative Mach number ($M=1.4\rightarrow M=1.2$).

With this combination of curvature changes, the velocity slowdown is better driven. Instead of creating a normal shock, the new shape creates two low-intensity shocks as shown on the normalized density gradient on **Fig. 7**, with a subsonic diffusion downstream. On the pressure side, one observes a higher relative Mach number after optimization (see isentropic Mach number evolution on **Fig. 8**), and leads to a smooth velocity slowdown.

The off-design behavior of the blade is illustrated on **Fig. 9**. The isentropic efficiency and the total-to-total pressure ratio π are plotted as a function of the reduced mass flow. One observes that a large part of the efficiency improvement at the design point is remained at off-design points. As expected, the choking mass flow is also well conserved by keeping the inlet part of the blade constant. Moreover, the 1.75% of efficiency improvement claimed by the optimizer is actually close to 2% if the mass flow is adjusted. Finally, the pressure ratio has been increased by 2% that gives a margin to reach the whole stage performance.

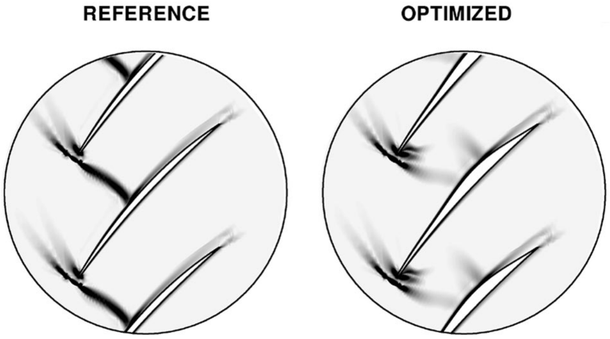

Fig. 7 $|\nabla\rho|/\rho$ contours before and after optimization

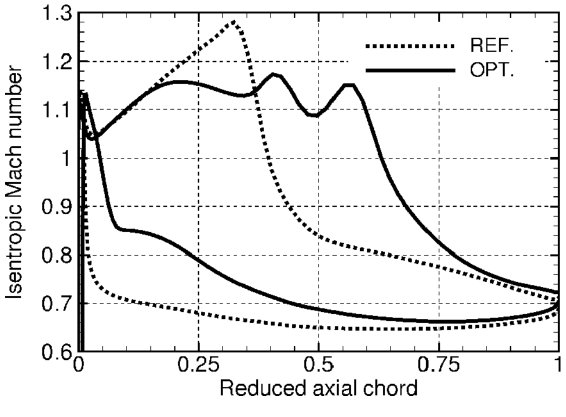

Fig. 8 Isentropic Mach number

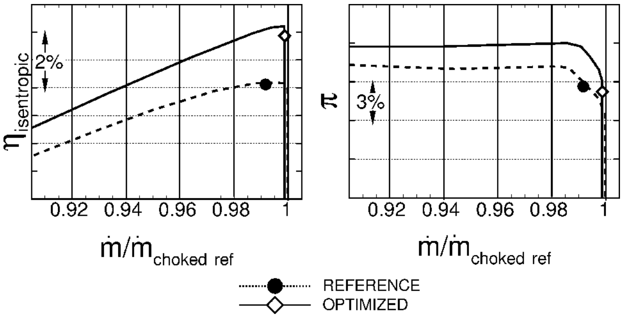

Fig. 9 Off-design performance before and after optimization

The off-design flow pattern of the relative Mach number at 0.94% of the choked mass flow is represented on **Fig. 10**. The behavior of the optimized shape is the same as the optimization point. On the optimized shape, the Mach number upstream of the shock is reduced and the diffusion downstream of the shock is better controlled.

Quasi Three-Dimensional Turbine Optimization

Description of the Case. The optimization presented here concerns the shape modification of the stator of a turbine stage. The objective is to improve the efficiency only by modifying the stator, but taking into account the rotor bladings. So this optimization is carried out by computing the whole stage.

The mesh, represented on **Fig. 11**, is made of four blocks per row, with a O3H topology for each of them. One can notice the large number of nodes around the stator blade. A particular attention has been paid to keep the mesh as homogeneous as possible, especially at the interface of the wheels.

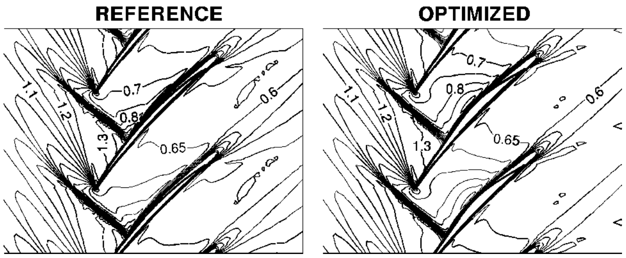

Fig. 10 Off-design relative Mach number contours before and after optimization

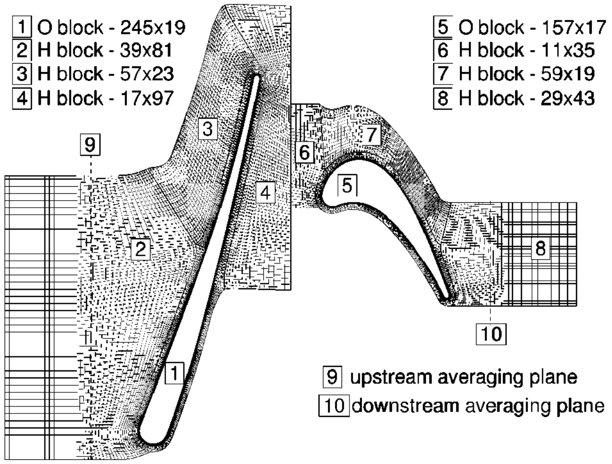

Fig. 11 Structured grids of the stage

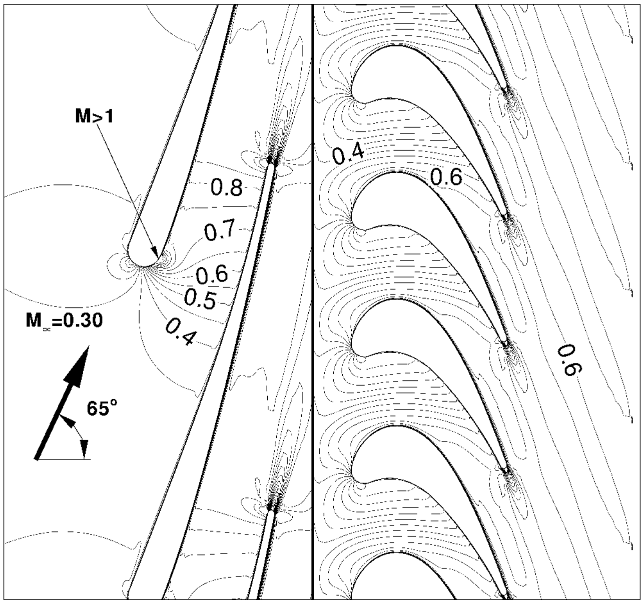

Fig. 12 Relative Mach number contours

As illustrated in **Fig. 12**, the inlet absolute flow angle is close to the stator exit absolute flow angle. The deviation is rather small ($<20°$) compared to the standard stator turbine blade where the deviation can be greater than 70°. The relative Mach number flow field plotted on **Fig. 12** shows a subsonic flow in the major part of the stage. Only a supersonic zone at the suction side of the stator can be observed downstream of the leading edge. In the rotor, the relative Mach number remains lower than 0.7.

Design Variables, Objective Function, and Constraints. For the present application, the optimization is carried out in two steps: The camber line is modified at first, and the suction side is then deformed.

The deformation function (**Fig. 13**) applied on the camber line is a Bézier curve whose control points are placed along the blade by their reduced abscissa ξ_i [0;1]. The control points $\mathbf{P}_i$ are positioned by the relation

$$\mathbf{P}_i \left| \begin{array}{l} \xi_i \\ \psi_i = \psi_{i-1} + (\xi_i - \xi_{i-1}) \tan y_i \, . \end{array} \right. \tag{8}$$

One can observe that the first design variable y_0 must necessarily be set to zero. In this case, the Bézier curve is defined by Eq. (2) with

$$\mathbf{R}\left\{ \begin{array}{c} \xi(u) \\ \delta(u) \end{array} \right\} \text{ and } \mathbf{P}_i\left\{ \begin{array}{c} \xi_i \\ \psi_i \end{array} \right\}.$$

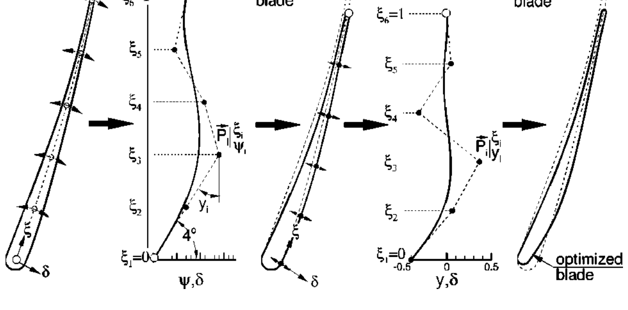

Fig. 13 Deformation function and optimized bladings

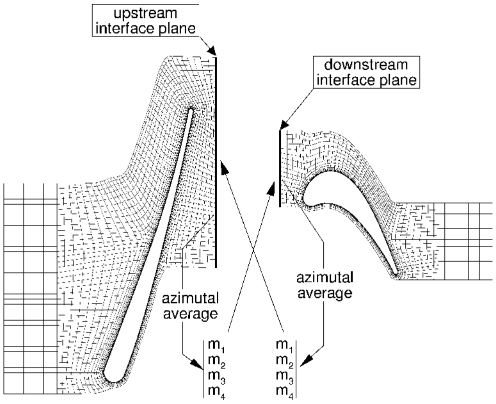

Fig. 14 Interface boundary condition

The δ displacement is applied on the camber line and the new shape is defined by keeping unchanged the old thickness function from leading to trailing edge.

The deformation function applied on the suction side of the blade is more simply given by Eq. (2) with

$$\mathbf{R}\left\{ \begin{array}{c} \xi(u) \\ \delta(u) \end{array} \right\} \text{ and } \mathbf{P}_i\left\{ \begin{array}{c} \xi_i \\ y_i \end{array} \right\}.$$

In this optimization, five active design variables are distributed along the camber line of the stator. In the second step, five active design variables are distributed on the suction side, excluding the trailing edge (inactive design variable), but including the leading edge thickness. In both cases, the Bézier curve that defines the deformation function is of seventh order.

The objective function and constraints are evaluated by averaging the aerodynamic flowfield with a momentum average. The averaging planes are located upstream of the stator and downstream of the rotor (see planes #9 & #10 on **Fig. 11**).

As the goal is to improve the performance of the stage, the objective function is taken as the opposite of the "gas power" of the stage

$$F_{\mathrm{obj}} = -\dot{m} \cdot C_p \cdot (T_{i_2} - T_{i_1}). \tag{9}$$

Of course, the mass $\dot{m}$ flow must be maintained to its initial value with the relation

$$\dot{m} \leqslant \dot{m}_{\mathrm{initial}} \, . \tag{10}$$

One also notice that the improvement of the gas power is linked to the improvement of the efficiency because the total-to-total pressure ratio remains constant during the optimization. This is a result of the constraint on the mass flow and the same downstream static pressure for all the calculations.

Different constraints are applied for technological reasons and in order to improve the robustness of the optimizer. The stator axial chord remains constant when applying a deformation and the design variables are restricted to "reasonable" values (i.e., leads to feasible bladings). For example, the camber line is not allowed to be curved by more than 4° and the blade thickness can only vary among ±50% of the initial thickness.

Eventually, a special treatment has been realized at the interface of the wheels. This mixing plane boundary condition is detailed in **Fig. 14**.

An azimutal average is computed on both upstream and downstream blocks. These four values are then applied at the opposite face with a nonreflective boundary condition. As the interface plane is close to the bladings, the kind of average is important because of the nonuniform flow at this station. The Riemann invariant average is usually used (Eq. (11)), but leads to an unrealistic solution of optimization. As the goal is to reduce the losses,

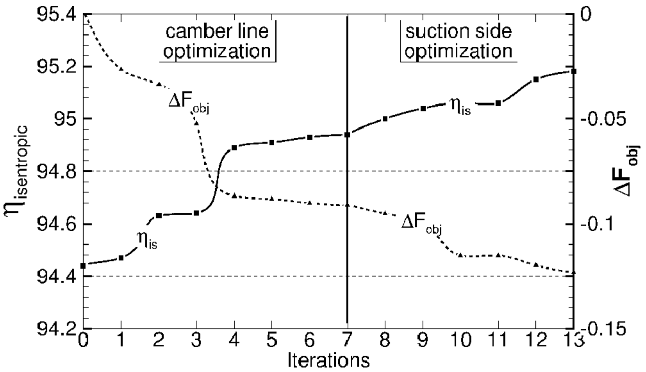

Fig. 15 Objective function and isentropic efficiency history

one solution is to choose an average which conserves the losses through the interface, such as the momentum average

$$\text{Riemann invariant average}\quad\left|\begin{aligned} m_1&=\frac{1}{s}\sum (p-\rho a V_n)ds\\ m_2&=\frac{1}{s}\sum \frac{p}{\rho^{\gamma}}ds\\ m_3&=\frac{1}{s}\sum V_{t_1}ds\\ m_4&=\frac{1}{s}\sum (p+\rho a V_n)ds\\ s&=\sum ds\end{aligned}\right. \tag{11}$$

$$\text{momentum average}\quad\left|\begin{aligned} m_1&=\frac{1}{s}\sum \rho V_n ds\\ m_2&=\frac{1}{s}\sum (p+\rho V_n^2)ds\\ m_3&=\frac{1}{s}\sum \rho V_n V_{t_1}ds \quad .\\ m_4&=\frac{1}{s}\sum \rho V_n H_i ds\\ s&=\sum ds\end{aligned}\right. \tag{12}$$

Optimization. The optimization of the camber line requires seven iterations, and six iterations are needed for the optimization of for the suction side. With this number of active design variables, a total of 102 calls to the quasi three-dimensional Navier-Stokes solver COLIBRI are required. The total CPU time on NEC SX5 is lower than 4000s (~1,1 hour). As the "gas power" of such a stream surface can not be linked to reference values, the isentropic efficiency has been plotted to describe the optimization history in **Fig. 15**. One can observe an efficiency improvement of about 0.8 point, 70% of which is provided by the modification of the camber line.

As indicated in the **Table 2** above, the variations of the overall performance show that there is no need to apply a constraint on the total-to-total pressure ratio.

The optimized shape shown in **Fig. 14** indicates a rotation of 4° of the blade at the leading edge and a large reduction of the leading edge thickness. This indicates that the losses are mainly produced by the supersonic zone downstream of the leading edge. The relative Mach number contours represented in **Fig. 16** confirm this analysis; the peak velocity downstream of the leading edge has disappeared after optimization and the acceleration in the guided part is better controlled.

Table 2 Variation of the overall performance

ΔF_{obj}	$\Delta\,\eta_{ig}$	$\Delta\dot{m}$	$\Delta\pi$	$\Delta(1-Rt_i)$
Δ	Δ%	%	%	%
−0.12	+0.82	−0.08	0.00	+0.87

The normalized density gradient contours plotted in **Fig. 17** allow to be more precise in the analysis. One can not only observe a large reduction of the gradients downstream of the leading edge, but also a reduction of the gradient at the trailing edge, on the pressure side. Moreover, the boundary layer on the suction side is thinner on the optimized blade.

The isentropic Mach number distribution on the blade (**Fig. 18**) indicates that the incidence is close to zero after optimization: The Mach number is almost the same on both sides of the leading edge. Moreover, the maximum Mach number at the leading edge is clearly reduced (M=1.2→M=0.7) at the suction side. More globally, the load is reduced in the first quarter of the blade, and increased in the last one.

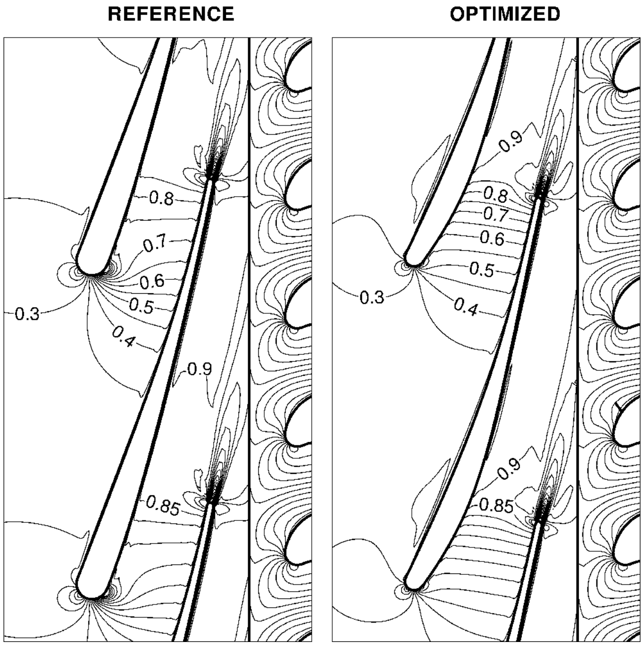

Fig. 16 Relative Mach number contours before and after optimization

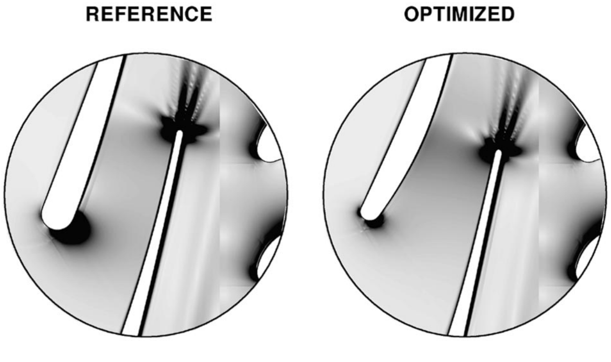

Fig. 17 $|\nabla\rho|/\rho$ contours before and after optimization

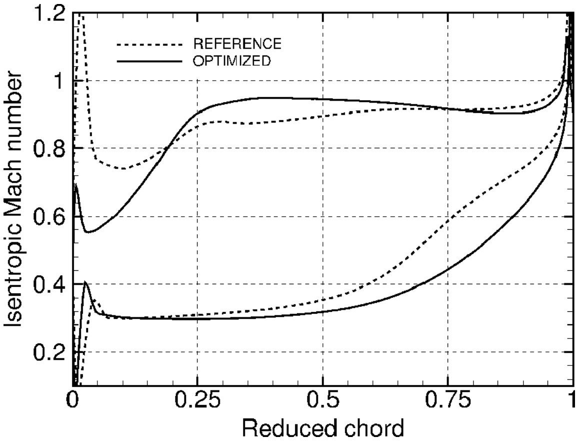

Fig. 18 Isentropic Mach number before and after optimization

Three-Dimensional Compressor Optimization

The first step for a three-dimensional optimization consists in introducing sweep and dihedral to control three-dimensional flows, [12]. This method is efficient for static bladings, [7,13], but is not well suited to rotating bladings due to mechanical constraints. A three-dimensional rotating blade optimization can be done with a quasi three-dimensional approach at different span, [14], but the three-dimensional effects are not taken into account. With the reduction of the CPU time consumption, it is now possible to carry out a fully three-dimensional optimization.

Description of the Case. A three-dimensional blade of a transonic compressor is optimized in this chapter. The CFD calculation is carried out on the isolated rotor with account of the tip clearance.

The grid is made up of three blocks (H-O-H topology) in the main duct (**Fig. 19**) and of two blocks (O-H topology) in the tip clearance zone. The node distribution in the different blocks is given in **Table 3:**

On the periodic boundaries, the nodes are not coincident, but lie on the same surface for an accurate interpolation. An adiabatic wall boundary condition is applied in the rotating frame at the hub and on the blade. A fixed wall boundary condition is applied at the casing. The grid is suited for computations using wall functions (in order to reduce the CPU time).

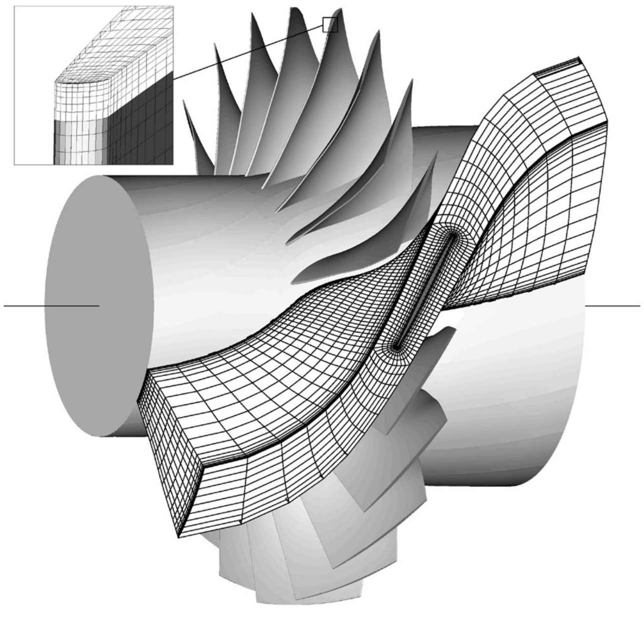

Fig. 19 Three-dimensional view of the rotor and mesh topology

Table 3 Three-dimensional grid characteristics

	Type	n_i	n_l	n_k	Total
Main duct	H	21	21	47	20,727
	O	181	17	47	144,619
	H	21	21	47	20,727
Tip clearance	O	181	5	7	6335
	H	85	7	7	4165
					196,573

The operating point is in a transonic state: the relative Mach number at the tip of the blade is about 1.2 but the compressor is not choked in these conditions.

Design Variables and Objective Function. The same principle as described with the quasi three-dimensional approach is extended to three-dimensions. The blade surface is extracted from the grid, and a deformation zone is defined on this surface by its indices. A current point in this zone is defined by the reduced coordinate (ξ, η) in the chord and in the span direction, respectively, (**Fig. 20**).

In the present application, the zone where geometrical modifications are applied covers the suction side, from the leading edge to the trailing edge and from hub to casing. The deformation surface is defined by a Bézier surface whose control points are located by their coordinate $(\xi_{i,j}, \eta_{i,j}, y_{i,j})$. The Bézier surface is defined by the parameters with the relation

$$\mathbf{R}=\sum_{k=0}^{n}\left\{\sum_{l=0}^{m}P_{k,l}\cdot B_l^m(v)\right\}\cdot B_k^n(u) \tag{13}$$

$$\text{with } \mathbf{R}\left\{\begin{matrix}\xi(u,v)\\ \eta(u,v)\\ \delta(u,v)\end{matrix}\right\} \quad \text{and } \mathbf{P}_{i,j}\left\{\begin{matrix}\xi_{i,j}\\ \eta_{i,j}\\ y_{i,j}\end{matrix}\right\}$$

where B_k^n is the Bernstein polynom—see Eq. (2).

The δ displacement is applied to the reference blade by translating each point along the local normal to the blade.

For this three-dimensional application, a (6th×3th) Bézier surface is defined by seven control points in the ξ direction and by four control points in the η direction (**Fig. 21**).

Only nine parameters are activated, i.e., modified during the optimization. The control points located at the abscissa ξ_1, ξ_2,

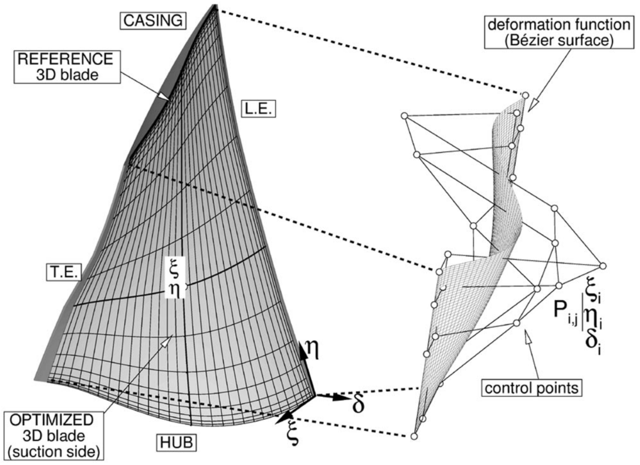

Fig. 20 Three-dimensional blade deformation function

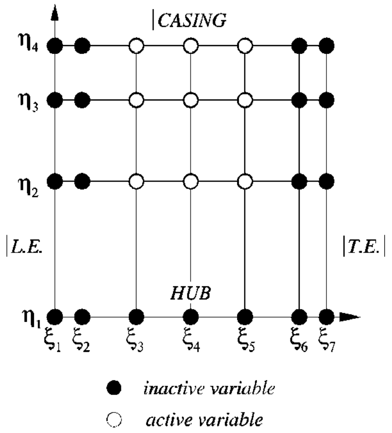

Fig. 21 Three-dimensional design variables

ξ_6, and ξ_7 are not activated in order to ensure a tangential continuity at the leading edge and at the trailing edge. At hub (η_1), the control points are also deactivated to avoid mechanical constraints problems after optimization.

The deformations of the suction side are propagated through the grid and a particular attention is paid to maintain the tip clearance constant.

The overall performances are calculated by a momentum average on planes normal to the rotation axis located at one axial chord upstream and one axial chord downstream of the blade. In three-dimensions, this average is defined by

$$\left|\begin{array}{l|l} \overline{\rho V_n}=\frac{1}{s}\sum \rho V_n ds & \overline{\rho V_n V_{t1}}=\frac{1}{s}\sum \rho V_n V_{t1} ds \\ \overline{p+\rho V_n^2}=\frac{1}{s}\sum (p+\rho V_n^2) ds & \overline{\rho V_n V_{t2}}=\frac{1}{s}\sum \rho V_n V_{t2} ds. \\ \overline{\rho V_n H_i}=\frac{1}{s}\sum \rho V_n H_i ds & s=\sum ds \end{array}\right. \tag{14}$$

As in quasi three-dimensions, the objective function is defined by $F_{\text{obj}}=100\cdot(1-\eta_{\text{isentropic}})$ and no constraints are applied in the present application.

Optimization. For this three-dimensional case, only three iterations of optimization are performed (see **Fig. 22**). This optimization requires 41 calls to the CANARI solver for a total calculation time of 41,000 seconds (~11 hours) on NEC SX5.

As in the quasi three-dimensional optimization, the convergence rate is high: The objective function is reduced by more than one point for three iterations of optimization (see **Table 4.**)

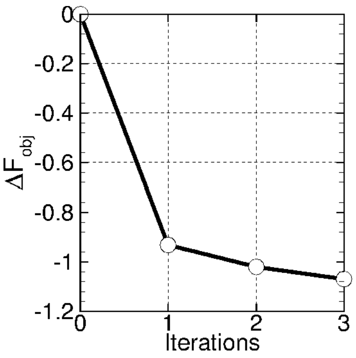

Fig. 22 Objective function history

Table 4 Variation of the overall performance

ΔF_{obj}	$\Delta\eta_{ig}$	$\Delta\dot{m}$	$\Delta\pi$	ΔRt_i
Δ	Δ%	%	%	%
−1.07	+1.07	+1.2	−0.1	−0.2

One can notice a low variation of the mass flow (but larger than in the quasi three-dimensional application); the total-to-total pressure and temperature ratio remains almost constant.

The deformations of the blade are plotted on **Fig. 23** with an amplification factor of 10. As we can see on the optimized blade, the new shape at 80% and at 50% of the reduced span follows the same trend as observed in quasi three-dimensions. The thickness is increased in the rear part of the blade and a curvature change is applied at 30% of the chord. At 80% of the span, the blade thickness is reduced downstream of the leading edge. A mechanical constraint should be applied in this part of the blade to avoid any vibration problems. At 20% of the span, the blade thickness is increased from the leading edge to the trailing edge with a maximum located at 60% of the chord.

The radial distribution of aerodynamic characteristics at one axial chord downstream of the blade are plotted on **Fig. 24**. The most significant result is indicated by the radial evolution of the efficiency difference between the optimized and the reference blade: the efficiency improvement is larger than 5 points at 95% of the span, close to the tip clearance. Most of the efficiency improvement is located between 50% of the blade span and casing although the blade has changed in the lower part of the blade. The evolution of the other quantities does not present large modification as compared to the reference: The increment of mass flow from 70% of the span to casing is balanced by a 2% reduction in the lower part. The total-to-total pressure ratio evolution is not modified after the optimization except in the tip clearance region. Some differences occur on the flow angle (more than 1° from 80% of the span to casing) but they stay low in the major part of the duct; only the tip clearance presents some variations larger than 2°.

The entropy flow field on a plane located at one chord downstream of the rotor (**Fig. 25**) confirms the efficiency improvement. The losses are largely reduced from 50% of the span to casing by reducing the rotor wake thickness and the tip clearance effects.

The relative Mach number flow field at 90% of the blade span is represented on **Fig. 26**. As in the quasi three-dimensional application, the relative Mach number upstream of the shock is reduced ($M=1.5\rightarrow M=1.3$) and a subsonic diffusion downstream enables a "reduced losses" compression. As in the quasi three-dimensional computation, the major part of the efficiency im-

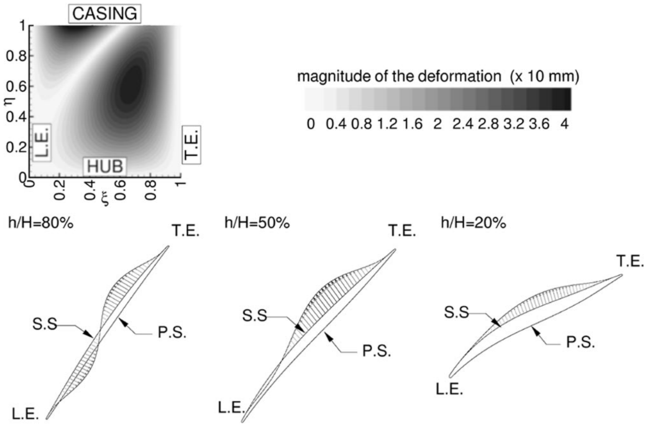

Fig. 23 Blade deformation at 80%, 50%, and 20% of the reduced blade span

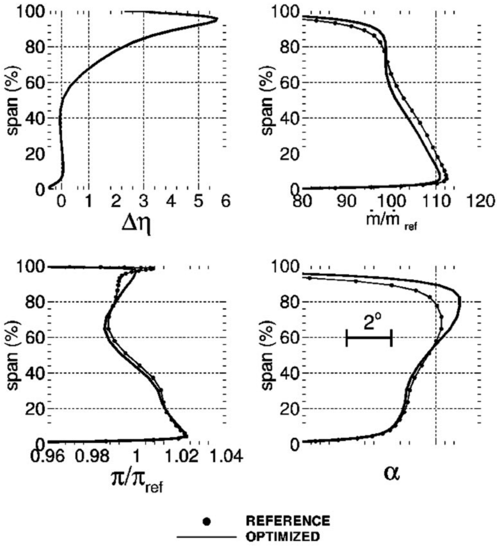

Fig. 24 Reference and optimized radial profiles

provement is done by the reduction of the normal shock intensity, as shown on the reduced density gradient contours on **Fig. 27**.

The characteristic of the compressor is plotted on **Fig. 28**. The variation of choked mass flow is lower than 1% although it has not been controlled during the optimization process. The method to keep this mass flow constant, described in the first part of this paper, should be extended and applied to this three-dimensional optimization.

Conclusion

A transonic compressor and a turbine stator are optimized by using a steady quasi three-dimensional Navier-Stokes calculation coupled to a gradient optimizer. The suction side of the compressor blading is modified by a Bézier curve. The new blading has its efficiency increased by 1.75 points and the choked mass flow is kept constant during the optimization. The good behavior of the optimized blading is checked by computing other operating points over a wide range of mass flows.

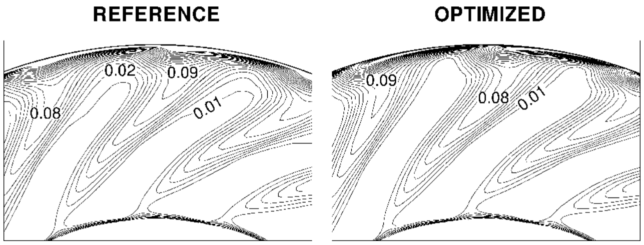

Fig. 25 Downstream entropy iso-lines before and after optimization

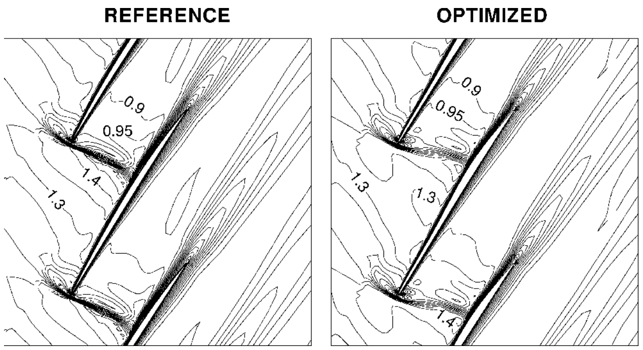

Fig. 26 Relative Mach number iso-lines at 90% of the reduced span

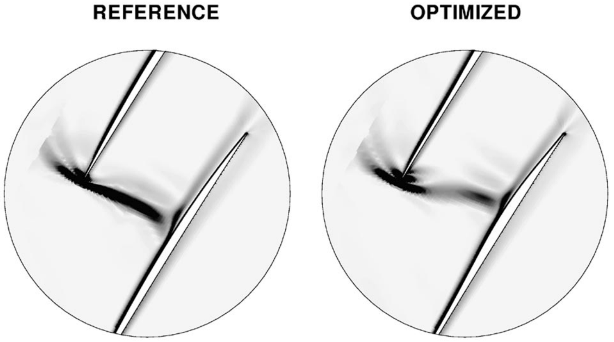

Fig. 27 $|\nabla\rho|/\rho$ contours before and after optimization

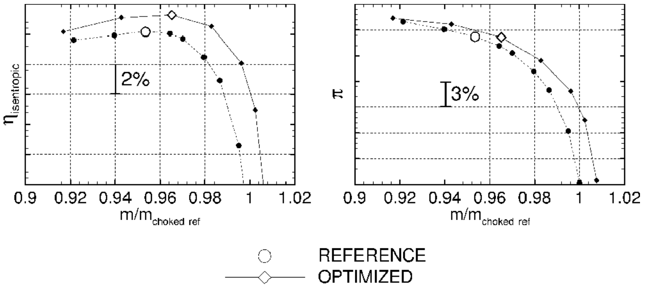

Fig. 28 Off-design performance of the compressor

The stator of a turbine is optimized by taking into account the whole stage, i.e., including the rotor during the calculation. In a first step, the camber line of the stator is modified. The suction side is then deformed and the new stator blading leads to an efficiency improvement of the stage by 0.8 points. This losses reduction is obtained by reducing the leading edge peak velocity and by reducing the incidence of the blade.

The same principle is extended to a three-dimensional blade. A steady Navier-Stokes code is coupled to a gradient-based optimizer. The blade is modified by applying a deformation function defined by a Bézier surface. The optimization, carried out with account of the tip clearance, improves the efficiency by more than 1 point with only low variations of the operating point. The fully three-dimensional aerodynamic optimization presented here shows that such a process can be included in a design cycle, as new blading can be defined in about 10 CPU hours.

The next step concerns the introduction of additional geometrical constraints, and the opening to multidisciplinary approach such as mechanics and thermal transfers in the optimization process.

Acknowledgments

The authors thank the engine manufacturer TURBOMECA (SNECMA group) and the CNES for their contribution to the paper. The French Ministry of Defense is also acknowledged for partial funding of the study.

Nomenclature

y_i, $y_{i,j}$ = design variables
ξ_i, $\xi_{i,j}$ = position of design variables (% chord)
$\eta_{i,j}$ = position of design variables (% span)
nv = number of design variables
nc = number of constraints

$\mathbf{G}$ = constraints vector
F_{obj} = objective function
u, v = Bézier curve parameter
ξ = reduced chord
η = reduced span
δ = local deformation
B_k^n = Bernstein polynom
n = degree of the Bézier curve in the u-direction
m = degree of the Bézier curve in the v-direction
$\mathbf{P}_i$, $\mathbf{P}_{i,j}$ = control point
$\eta_{\text{isentropic}}$ = isentropic efficiency
$\dot{m}$ = mass flow (kg/s)
π = total pressure ratio
Rt_i = total temperature ratio
α = absolute flow angle (deg)
β = relative flow angle (deg)
V_n, V_{t1}, V_{t2} = norm. and tangt. velocities (m/s)
p = static pressure (Pa)
ρ = density (kg/m^3)
a = speed of sound (m/s)
H_i = total enthalpy (J/kg)
ds = local surface (m^2)

References

[1] Joubert, H., and Quiniou, H., 2000, "Turbomachinery Design Used Intensive CFD 22nd ICAS," Sept., Harrogate, UK.

[2] Vanderplaats, G. N., 1973, "CONMIN—a Fortran Program for Constrained Function Minimisation," NASA TMX 62282.

[3] Vanderplaats, G. N., 1984, *Numerical Optimization Techniques for Engineering Design With Applications*, McGraw-Hill, New York.

[4] Samareh, Jamshid A., 2000, "Multidisciplinary Aerodynamic-Structural Shape Optimization Using Deformation (MASSOUD)," 8th AIAA/NASA/USAF/ISSMO Symposium on Multidisciplinary Analysis and Optimization, Sept. 6–8, Long Beach, CA.

[5] Bézier, P., 1977, "Essais de définition numérique des courbes et surfaces expérimentales," thèse de doctorat d'état, Feb.

[6] Quinhuan, W., and Xiaoyan, H., 1988, "The Use of Bézier Polynomial Patches to Define Geometrical Shape of the Flow Channels of Compressors," ASME Paper 88-GT-60.

[7] Burguburu, S., Toussaint, C., and Leroy, G., 2001, "Numerical Optimization for Turbomachinery Blades Aerodynamic Design Using a Gradient Method Coupled With a Navier-Stokes Solver 15th ISABE," ISABE2001-1117, Sept. 2–7, Bangalore.

[8] Le Madec, I., 1993, "Modélisation des écoulements transitionnels et turbulents dans les grilles d'aubes de turbomachines suivant l'orientation turbines," PhD thesis, Rennes University.

[9] Couailler, V., 1999, "Numerical Simulation of Separated Turbulent Flows Based on the Solution of a RANS/Low Reynolds Two-Equations Model," 37th AIAA/ASME, Reno NV.

[10] Michel, R., Quémard, C., and Durand, R., 1969, "Application d'un schéma de longueur de mélange *à* l'étude des couches limites turbulentes d'équilibre," Technical Note 154, Office National d'Etudes et Recherches Aérospatiales.

[11] Chung, J., and Lee, K. D., 2000, "Shape Optimization of Transonic Compressor Blades Using Quasi-3D Flow Physics," ASME Paper 2000-GT-0489.

[12] Gummer, V., Wenger, U., and Kau, H. P., 2000, "Using Sweep and Dihedral to Control Three-Dimensional Flow in Transonic Stator of Axial Compressor," ASME Paper 2000-GT-0491.

[13] Shaphar, S., 2001, "Three-Dimensional Design and Optimization of Turbomachinery Blades Using the Navier-Stokes Equations," 15th ISABE, ISABE2001-1053, Sept. 2–7, Bangalore.

[14] Chung, J., Shim, J., and Lee, K. D., 2001, "3D Design of Transonic Axial Compressor Blades With 3D Navier-Stokes Physics," AIAA Paper 2001-3305.

Heat-Transfer Measurements and Predictions for the Vane and Blade of a Rotating High-Pressure Turbine Stage

Charles W. Haldeman

Michael G. Dunn

Gas Turbine Laboratory,
The Ohio State University,
Columbus, OH 43235

This paper describes heat-transfer measurements and predictions obtained for the vane and blade of a rotating high-pressure turbine stage. The measurements were obtained with the stage operating at design corrected conditions. A previous paper described the aerodynamics and the blade midspan location heat-transfer data and compared these experimental results with predictions. The intent of the current paper is to concentrate on the measurements and predictions for the 20%, 50%, and 80% span locations on the vane, the vane inner and outer endwall, the 20% and 96% span location on the blade, the blade tip (flat tip), and the stationary blade shroud. Heat-transfer data obtained at midspan for three different thermal-barrier-coated vanes (fine, medium, and coarse) are also presented. Boundary-layer heat-transfer predictions at the off-midspan locations are compared with the measurements for both the vane and the blade. The results of a STAR-CD *(a commercial code) three-dimensional prediction are compared with the 20% and 96% span results for the blade surface. Predictions are not available for comparison with the tip and shroud experimental results.* [DOI: 10.1115/1.1626132]

Introduction

Heat transfer is an important design consideration for all the parts of a modern gas turbine, especially the combustor, turbine, and exhaust nozzle. Modern high-pressure turbines are coming on line with significantly increased turbine inlet temperatures and stage pressure ratios. It is well known that the maximum allowable turbine inlet temperature strongly affects the efficiency of these engines and substantial performance increases can be achieved via this parameter. The current industry trend is to push the turbine inlet temperature closer to the fuel stoichiometric temperature, especially for military engines. There is no reason to believe that the strong interest within the design community for increasing turbine inlet temperature will subside in the near future. There are numerous ongoing research activities designed to improve calculations of the hot section heat loads ranging from the basic to applied orientations. The designer, the ultimate customer of this activity, is under extreme pressures of time, affordability, durability, and reliability. The suggestions derived from these research efforts must not be so complicated and/or expensive to implement that the older, more familiar procedures for doing business continue to be used and the new information ignored.

Describing the dynamic condition of the gas exiting the combustor and entering the high-pressure turbine (HPT) vane row is a difficult task. The flow field at the HPT inlet includes nonuniform radial and circumferential temperature profiles (hot streaks) and free-stream turbulence of some unknown intensity and scale. Several research efforts have attempted to measure turbulence intensity and scale of actual engine combustors at the combustor exit, but with limited success.

One of the more complicated flow environments associated with any practical machine occurs in the hot section of a turbine. The flow is always unsteady, it may be transonic, it is three dimensional, and it is subjected to strong body forces. In the pursuit of achieving higher efficiency, the turbine inlet temperature continues to be pushed to higher levels, requiring advances in cooling schemes and improved materials. Due to the ingenuity and intelligence of numerous dedicated design engineers, satisfactory and ever improving designs have been achieved over the past 40 to 50 years. The past several years have seen a refinement in understanding of the underlying fluid and heat-transfer mechanics that govern the basic physics occurring within the turbine. In addition, there have been several advances in materials and manufacturing processes over this same time. Most of this was accomplished due to refinements in approximations used by earlier designers. These approximations maintained a level of detail sufficient to reveal important physical effects while still allowing solutions using available analytical/numerical methods.

The boundary-layer prediction presented here represents a common design tool in use by many engine companies. These types of codes have the advantage that they are easy to run and do not require excessive amounts of processor time. In addition, each individual engine company generally has modified the prediction codes to account for the secondary effects that are deemed most critical to obtaining a robust design. The STAR-CD (a commercial Navier-Stokes CFD code) prediction represents a more advanced diagnostic level code that is being used in industry for design application. There are many advanced codes in use in the industry; however, despite their promise many of them have yet to be integrated into the design system on a regular basis because of the huge amount of processor time and the complexities in obtaining a solution. The predictions presented in this paper are not intended to represent what the industry is capable of, but rather what the industry does on a daily basis. The data set presented here is relatively old (late 1980s), but remains one of the most complete data sets available and is useful because it provides a good comparison of heat-flux data in the vane, blade, shroud, and endwall areas as a function of Reynolds number, as well as data regarding surface roughness. The paper also includes several predictions that have been done over a period of several years using different techniques, illustrating how the design code prediction capability has changed with time. A review of related work published by many authors regarding convective heat transfer and aerodynam-

---

Contributed by the International Gas Turbine Institute and presented at the International Gas Turbine and Aeroengine Congress and Exhibition, Atlanta, GA, June 16–19, 2003. Manuscript received by the IGTI Dec. 2002; final revision Mar. 2003. Paper No. 2003-GT-38726. Review Chair: H. R. Simmons.

ics in axial flow turbines that has been alluded to in the previous paragraphs and is relevant to the discussion presented here is given by Dunn [1].

Experimental Facility and Turbine Stage

The experimental apparatus used to obtain the measurements reported here consists of a large shock-tunnel facility (then currently located at Calspan Corporation in Buffalo, New York and now located at the OSU GTL), a full-stage rotating turbine housed in a rig, surface-pressure instrumentation installed along the flowpath, total-pressure and total-temperature rakes ahead of the vane inlet and downstream of the rotor exit, and surface-pressure and heat-flux instrumentation installed on the vane and blade surfaces. The experimental facility has been described in detail by Dunn et al. [2], and has been used extensively in past work of this nature and will not be described in detail here. In the interest of brevity, only the instrumentation specific to this measurement program will be described.

Stage Instrumentation. The turbine stage used in this work was designed and constructed by General Electric Aircraft Engine Group (GEAE) and consists of 32 vanes and 44 blades. With the exception of three thermal-barrier-coated (TBC) vanes, the remainder had a surface finish that was considered hydraulically smooth. The TBC surfaces were classified as smooth [125 μin. centerline average (CLA) or 3.18 μm], medium (250 μin. CLA or 6.35 μm), and coarse (450 μin. CLA or 11.45 μm). The rotor was operated at the design corrected speed, the stage design total to static pressure ratio was duplicated, and the design stage flow function was duplicated. Rotor speed was measured continuously using a shaft encoder (720 pulses/revolution).

The surfaces of the vanes and blades were instrumented with thin-film heat-flux gauges and with miniature-pressure transducers. The pressure instrumentation was confined to the midspan portion of the vanes and blades. The strip insert heat-flux instrumentation was located at midspan and button-type heat-flux gauges were located at several different spanwise locations on both the vane and blade, on the vane inner and outer endwall, on the blade platform and tip, and on the stationary shroud.

Heat-Flux Instrumentation. Both button-type heat-flux gauges and contoured leading-edge inserts were used on this stage. The specific buttons used were 0.040 in. (1 mm) in diameter by 0.031 in. (0.8 mm) thick and made of Pyrex 7740. Thin-film heat-flux gauges were installed in the hydraulically smooth airfoil at 20%, 50%, and 80% span and in the inner and outer endwalls. At each of these spanwise locations, there are nine button-type heat-flux gauges on the suction surface and eight on the pressure surface. The vane also contained a contoured leading-edge insert located at midspan with five heat-flux gauges on the suction surface and five on the pressure surface. For some of the experiments, additional inserts were installed at midspan on both the pressure and suction surfaces. These inserts extended from near the stagnation region to the trailing edge with 13 gauges on the suction surface and 12 gauges on the pressure surface. The inner band of the vane contains 10 button-type heat-flux gauges distributed near the leading edge of the vane, at midchord, and at the trailing edge of the vane. The outer band also has 10 gauges distributed in a similar pattern. Each of the TBC vanes contained 20 button-type heat-flux gauges, with 10 on the suction surface and 10 on the pressure surface. All of the gauges are located at the midspan location.

Heat-flux gauges were installed on the pressure and suction surfaces of the blade at 20%, 50%, and 96% span. At each of the 20%, 50%, and 96% spanwise locations, there are eight button-type heat-flux gauges on the suction surface and eight on the pressure surface. The two blades containing the button-type gauges were instrumented with internal heaters along the stacking axis of the blades and in the dovetail region of the blades so that for selected experiments the blades could be heated in order to estimate the adiabatic wall temperature. The heaters were supplied power through the slip ring. A contoured leading-edge insert containing five heat-flux gauges on the suction surface and five on the pressure surface was located at the 50% span location on the blade. The insert blade did not have a heater element installed, so that measurements at different wall temperature are not available for the insert heat-flux data. Data were obtained from six tip gauges and four platform gauges. Data were also obtained from five gauges in the stationary shroud, but the shroud was not heated.

Surface-Pressure Instrumentation. Both the hydraulically smooth vane and the blade of this turbine were instrumented with miniature flush-diaphragm Kulite pressure transducers. The pressure measurements obtained as part of this measurement program were compared with predictions in an earlier paper by Bergholz et al. [3] and will not be presented here.

Flowpath Instrumentation. Ten surface static pressure measurements were obtained along the flowpath: two in the channel upstream of the contraction to the vane row, one in the contraction immediately ahead of the vane row, two in the vane passage, two at the interstage location on the tip endwall, two downstream of the stage on the hub endwall, and one downstream of the stage on the tip endwall. Rakes of transducers to measure total pressure were located within the flowpath ahead of the nozzle guide vane (NGV) inlet and downstream of the rotor exit. Corresponding rakes of fast-response miniature thermocouples were located in the flowpath to obtain an indication of total temperature ahead of the NGV inlet and downstream of the rotor exit. The flowpath measurements just noted were also described in Bergholz et al. [3] and will not be repeated here.

Experimental Conditions

Table 1 presents the experimental conditions for which the measurements were performed. It was noted earlier that for two of the experiments, the blade containing the button-type heat-flux gauges was heated to a known temperature. By presenting the results in the form of a Stanton number, these data can be appropriately normalized and compared with the unheated blade data.

The turbulence intensity and length scale for the fluid entering the NGV was not measured for these particular experiments, but turbulence intensity was measured for a similar experimental configuration in the same facility by Rivir et al. [4]. Two different techniques were used to measure the free-stream turbulence intensity and the results indicated a value on the order of 5.5% to 6%. The turbulence length scale was not measured.

Table 2 presents the midspan dimensions for both the vane and the blade. The Stanton number results are presented as a function of the local wetted distance on the airfoil divided by the surface length at the appropriate spanwise location.

Heat-Transfer Results

The intent of the current paper is to concentrate on the results obtained for the 20%, 50%, and 80% span locations on the vane, the vane inner and outer end wall, the 20% and 96% span location on the blade, the blade tip (flat tip), the stationary blade shroud, and data obtained at midspan for three different TBC vanes. Boundary-layer predictions are presented for the vane and the blade spanwise locations, but are not available for the endwall, TBC airfoils, blade tip, or shroud results. The results of a STAR-CD 3D prediction are compared with the 20% and 96% span results for the blade surface. A previous paper [3] described the aerodynamics and the blade midspan location heat-transfer data and compared these experimental results with predictions for the blade only. In addition, Dunn et al. [5] presented a comparison between heat-flux measurements obtained using button-type gauges versus strip inserts for the vane used in the measurements discussed herein. However, only midspan data and no comparisons with prediction were presented in Ref. [5]. For reference, the surface

Table 1 Run conditions

Run	P_{Total} inlet, psi (kPa) ($\pm$3.8%, typ.)	T_{Total} inlet, R (K) ($\pm$ 1.8% typ.)	T_{wall} (initial) R (K) ($\pm$ 0.5% typ.)	Re/unit length at NGV inlet, 1/in. (l/m)	Comments
6	95.2 (656)	1039 (577)	533 (296)	2.07×10^{-5} (81.5×10^{-5})	Nominal design pt.
8	97.4 (672)	1040 (578)	533 (296)	2.11×10^{-5} (83.2×10^{-5})	Nominal design pt
9	95.1 (655.7)	1084 (602)	533 (296)	1.97×10^{-5} (77.4×10^{-5})	Heated blade
11	92.8 (640)	1085 (603)	533 (296)	1.92×10^{-5} (75.4×10^{-5})	Heated blade
14	51.19 (353)	1064 (591)	533 (296)	1.08×10^{-5} (42.6×10^{-5})	Low Reynolds
15	52.89 (364.7)	1076 (598)	533 (296)	1.10×10^{-5} (4.34×10^{-5})	Low Reynolds
16	49.21 (339)	1063 (591)	533 (296)	1.05×10^{-5} (41.4×10^{-5})	Low Reynolds
18	61.2 (422)	1077 (598)	533 (296)	1.31×10^{-5} (51.5×10^{-5})	Medium Reynolds

pressure distributions for the high-pressure vane and high-pressure blade at 50% span are given in the Appendix.

Since both button-type and insert-type heat-flux gauges were used in the measurement program, it is appropriate to address the issue of heat-island correction to the button-gauge data early in the discussion. Several authors have described the correction for the "heat-island effect" in the literature e.g., Dunn et al. [5], Zilles and Abhari [6], Bergholz et al. [3], Mukerji et al. [7,8], and Kim et al. [9]. The magnitude of the correction factor depends upon the specific flow conditions, with high-pressure and high-total-temperature vane inlet conditions requiring a larger correction than lower values of the corresponding parameters. Thus, for any turbine stage, the corrections applied to the vane data (in particular, near the trailing edge of the pressure and suction surfaces) will be larger than the correction factors for the remainder of the blade surface. The button-gauge data presented in this paper have been corrected using a combination of the technique described in Ref. [6] and the experimental data for these experiments reported in Ref. [5]. The results of the correction were found to be consistent with those results presented in Ref. [3]. The basic correction follows the form used by Zilles and Abhari [6],

$$\text{Corr}=\frac{1-\Theta}{1-\Theta F}, \quad \Theta=\frac{T_{\text{button}}-T_{\text{wall}}}{T_{\text{total}}-T_{\text{wall}}},$$

$$F=\left[1-\left(1-\frac{D}{2x}\right)^{0.9}\right]^{-(1/9)},$$

where D is the diameter of the gauge and x is the distance from the leading edge.

Figures 1 and 2 present the uncorrected and the corrected data for the midspan location on the HPT vane and the HPT blade for the design Reynolds number ($\text{Re}=7.94\times10^{6}$) condition. Included on Figs. 1 and 2 are the measurements from the leading-edge inserts that do not require correction. Figures 1 and 2 also include a prediction of the Stanton number distribution obtained by Suo and Lounsbury [10] using the KEP boundary-layer technique. This prediction will be discussed in much more detail later in the paper when measurements at other vane and blade spanwise locations are presented.

Figure 1 illustrates that the effect of the heat-island correction on the vane is to increase the measured Stanton number results at the 90% to 95% wetted distance locations on the pressure and suction surfaces by approximately 20% for the vane. With the exception of the data point at 30% wetted distance on the suction surface, the correction at wetted distances less than 50% is much smaller. Figure 2 presents a similar comparison for the blade and demonstrates that for the blade the correction is much smaller than was shown for the vane. Also included on Fig. 2 are three predictions of the Stanton number distribution. These predictions will also be discussed in detail in a later section of the paper. The correction shown in Fig. 1 is by far the largest correction for any of the data presented herein. At the lower Reynolds numbers and for wetted distances smaller than 8 to 10 cm, the correction is much smaller. For the remainder of the measurements presented in this paper, the correction for heat-island effect has been done and

Table 2 Vane and blade midspan dimensions

	Pressure side	Suction side
Vane (32)	2.93 in. (74.42 mm)	3.90 in. (99.06 mm)
Blade (44)	2.29 in. (58.17 mm)	2.98 in. (75.69 mm)

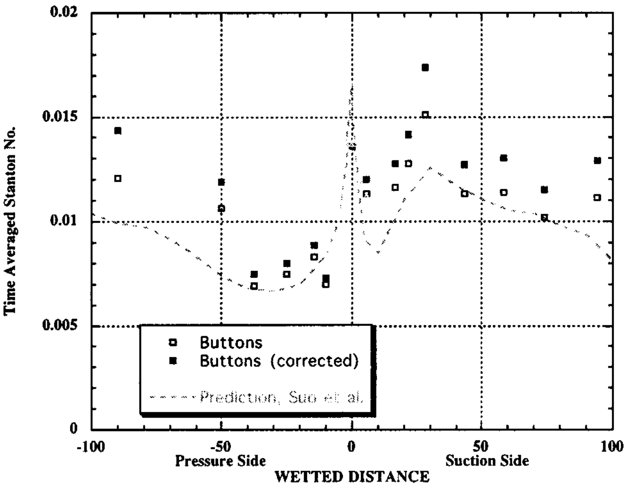

Fig. 1 Vane Stanton number at 50% span; Reynolds number $=7.94\times10^{6}$ (runs 6, 8, 9, and 11)

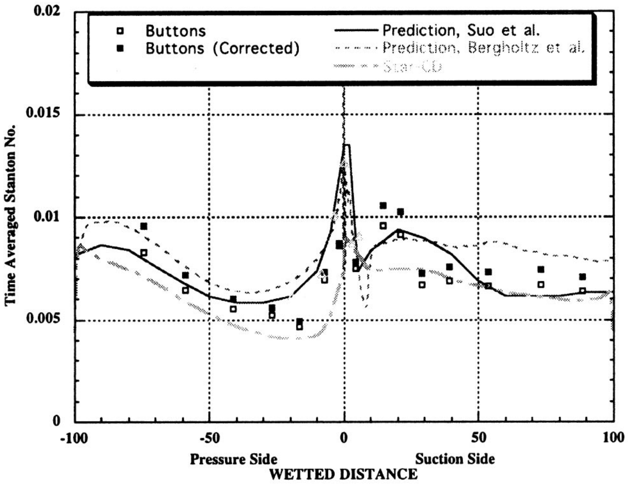

Fig. 2 Rotor Stanton number at 50% span; Reynolds number $=7.94\times10^6$

only the corrected data will be shown. The exceptions to this are the insert data, where no corrections are needed, and the data on the shroud and tip, where the corrections are extremely small due to the small running length of the boundary layer (see discussion). It is important to note that for the blade, the heat-island corrections fall within the band predicted by the various codes. For the vane, the heat-island corrections pull the data further from the predictions.

Influence of Reynolds Number on Vane and Blade Stanton Number Distribution. Measurements were performed at four values of the vane inlet Reynolds number, 8.24×10^6, 7.64×10^6, 5.16×10^6, and 4.25×10^6. Figure 3 presents the time-averaged Stanton number measurements for the vane as a function of wetted distance for the 50% span location as a function of inlet Reynolds number. The bars represent the range of the measurements at the individual locations. Examining the variation in Stanton number as a function of Reynolds number, for a flat plate one would expect the Stanton number to decrease slightly with Reynolds number. For turbulent flow this decrease would be proportional to the Reynolds number raised to the -0.2 power, and for laminar flow it would be raised to the -0.5 power. From Fig. 3, however, one can see that the Stanton number increases substantially with Reynolds number.

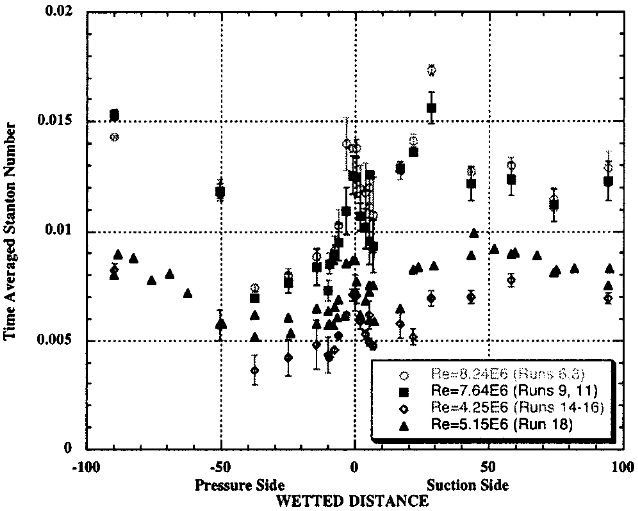

Fig. 3 Influence of Reynolds number on vane Stanton number at 50% span

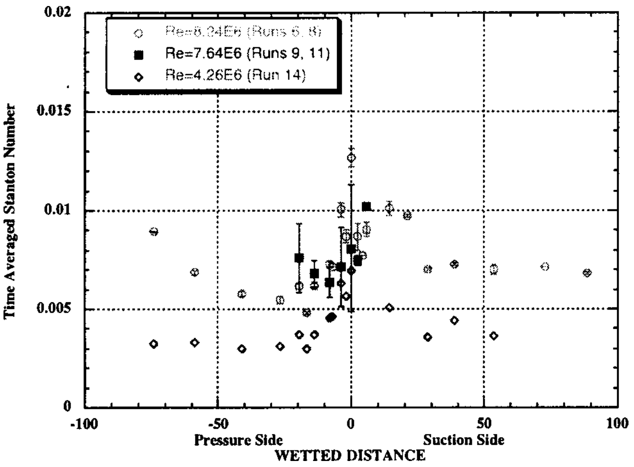

Fig. 4 Influence of Reynolds number on blade Stanton number at 50% span

This behavior suggests that the boundary-layer transitions from some mixed state at the lower Reynolds number is fully turbulent at the higher Reynolds number condition. Assuming that the low-Reynolds-number condition was laminar, one would expect an increase of close to a factor of 4 in the Stanton number if the boundary layer were turbulent at that same Reynolds number at the trailing edge. Then there would be a decrease in Stanton number moving to the higher-Reynolds-number condition. This is indeed the case, but the resulting scaling does not suggest flat plat behavior.

The influence of Reynolds number on the Stanton number results for the blade is demonstrated in Fig. 4 for vane inlet Reynolds numbers of 8.24×10^6, 7.64×10^6, 5.15×10^6, and 4.25×10^6. Limited data are available for the Reynolds number of 7.64×10^6 on the blade because it was for these runs that the blade was heated. Thus, the only blade data available for the purpose of this presentation comes from the leading-edge insert that was located on an unheated blade. The Stanton number variation with Reynolds number shows a similar pattern as the vane, with a possible transitional flow at the low-Reynolds-number condition.

For the comparisons with predictions, the results obtained at Reynolds numbers of 8.24×10^6 and 7.64×10^6 will be combined into a single data set labeled Reynolds number 7.94×10^6.

Comparison of Vane and Blade Data With Prediction for the Design Reynolds Number. Figure 1 presented the Stanton number distribution for the HPT vane at 50% span and Fig. 2 presented the corresponding results for the blade at 50% span for the design Reynolds number of $(7.94\pm0.3)\times10^6$. Figures 5 and 6 present the vane results for 20% and 80% span and Figs. 7 and 8 present the blade results for 20% and 96% span. The results from four different experiments are averaged to construct the vane plots shown in Figs. 1, 5, and 6 and two of the four experiments are used to construct the blade plots (recall that the blade was heated in two of the experiments) shown in Figs. 2, 7, and 8. Also presented in Figs. 1, 2, and 5–8 is a 1990 post-test prediction obtained by Suo and Lounsbury [11] using the KEP boundary-layer code. Figures 1, 7, and 8 also contain a more recent KEP prediction and a prediction obtained using the commercial code STAR-CD and reported by Bergholz et al. [3]. The KEP code used for these predictions is used within the engine community for engineering design estimates. The code is based on a version of the initial STAN5 code by Crawford et al. [12] that was modified by Rodi and Scheuerer [13] to include the Lam and Bremhorst [14] low-

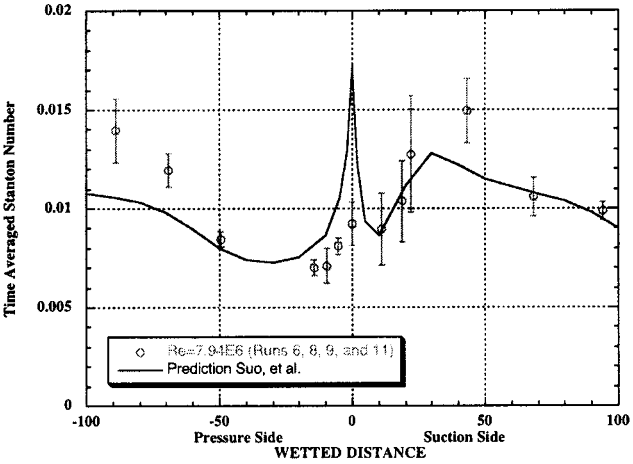

Fig. 5 Comparison of measured and predicted Stanton number for HPT vane at 20% span

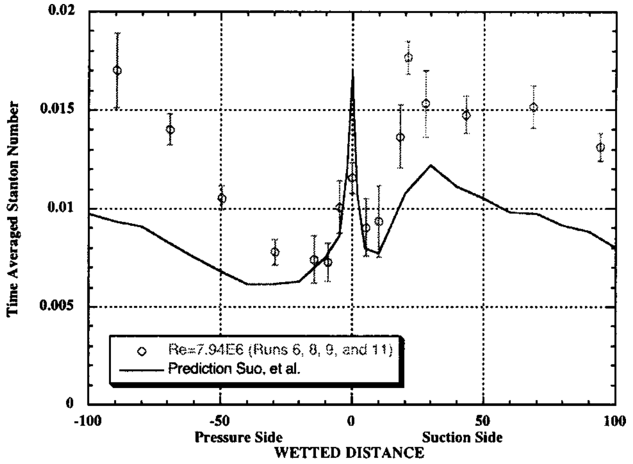

Fig. 6 Comparison of measured and predicted Stanton number for HPT vane at 80% span

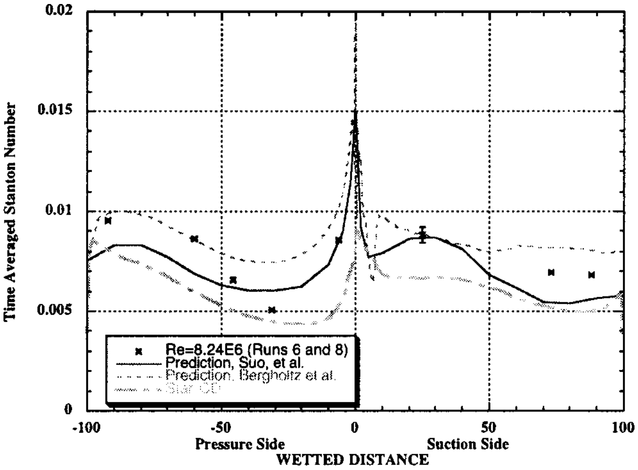

Fig. 7 Comparison of measured and predicted Stanton number for HPT blade at 20% span

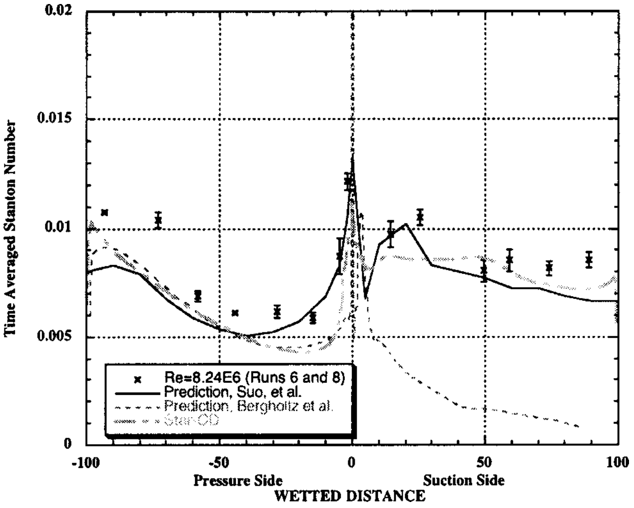

Fig. 8 Comparison of measured and predicted Stanton number for HPT blade at 96% span

Reynolds-number version of the k-ε turbulent flow model and included the capability of providing as an input parameter the desired value of free-stream turbulence. The version of the code used to obtain the predictions presented here is described by Zerkle and Lounsbury [15].

The post-test prediction [11] presented in Figs. 1, 5, and 6 significantly underestimates the experimental result when the correction for heat-island effect is applied to the data. However, if one were to ignore the correction for the moment, the prediction is in reasonable agreement with the experimental results at the 20% span location. The prediction significantly underestimates the single data point at 50% wetted distance on the pressure surface for the 50% span location (even worse with the correction), and significantly underestimates the experimental results for both the pressure and suction surfaces for the 90% spanwise location. In defense of the predictions, it is important to emphasize that time did not permit incorporation into these predictions of the measured surface pressure distribution. Also, because of time constraints, the predictions were performed using the design geometry and not the measured vane throats and associated geometry, which are known to vary from design. Thus, the predictions presented do not represent what would have been possible with significantly more time available for analysis.

The 1990 post-test prediction [11] along with a much more current KEP and STAR-CD prediction [3] is included in the blade data plots presented in Figs. 2 and 6–8 for the 20%, 50%, and 96% span locations. It was previously noted that for the blade the correction for heat-island effect is much smaller than it is for the vane, and this is illustrated in Fig. 2. At the 20% location (Fig. 7), the STAR-CD underestimates the experimental results and the more recent KEP prediction overestimates the experimental results for both the suction and pressure surfaces while the older KEP prediction does a good job of predicting the experimental results. At the 50% span location (Fig. 2), the STAR-CD and older KEP predictions bound the experimental results while the more recent KEP prediction generally overpredicts the experimental results. The overprediction of the recent KEP results on the pressure surface is not significant, but on the suction surface the overprediction is on the order of 20%. The experimental results shown for the 50% span location are made up of both insert data and button gauge data. As indicated on Fig. 2, the agreement between the two measurements is reasonable. The more recent KEP prediction for the suction surface of the blade encountered some difficulty and failed to converge, as shown on the figure. For the suction surface at 96% span (Fig. 8), both the STAR-CD and the older KEP prediction were in

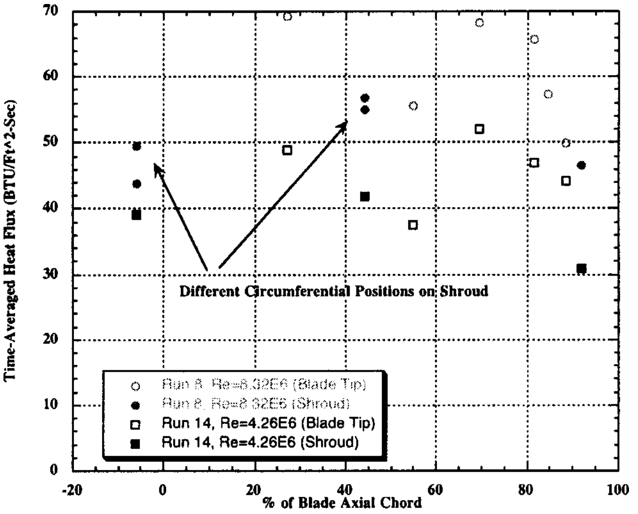

Fig. 9 HPT blade tip and HPT blade shroud measured heat flux as a function of Reynolds number

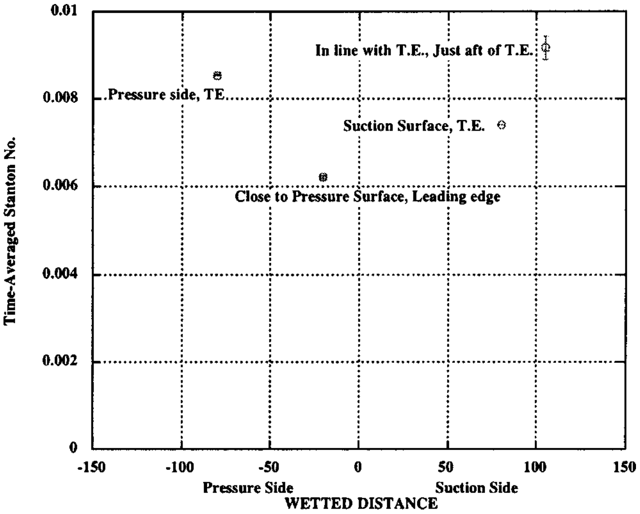

Fig. 11 HPT blade platform Stanton number at Re=8.24×10^6 (average runs 6 and 8)

good agreement with the experimental results. The agreement on the pressure surface was not as good as for the suction surface, but was still reasonably good.

Blade Tip and Blade Outer Air Seal Results. Heat transfer to blade tips and the outer air seal or shroud has attracted a great deal of attention in recent years. Bunker [16] recently provided an excellent review of blade tip heat transfer and Ameri and Bunker [17] report the results of a combined experimental and computational study designed to investigate the heat transfer to the first-stage blade tip of a power generation gas turbine. The experiment utilized a three blade linear cascade with no outer shroud motion. Using liquid crystals in the tip region, the authors were able to obtain a rather detailed distribution of heat transfer. The computational phase of the effort used to support the experiments utilized the code reported in Rigby et al. [18] and Ameri et al. [19]. The authors showed good comparison between experiment and computation.

Several previous experimental/computational analyses of flow in the tip region for a flat tip blade have been reported, i.e., Metzger et al. [20], Ameri and Steinthorsson [21], and Polanka [22]. The computational sophistication varied among these three studies, but all tended to provide information regarding the complicated flow behavior in the tip region. For Ref. [20], time-resolved heat-transfer measurements obtained on the blade tip and simultaneously obtained time-resolved heat transfer and surface pressure measured on the adjoining stationary shroud for the full-stage Garrett TFE-731-2 turbine were compared with the results of a computational fluid dynamics (CFD) analysis. The authors in Ref. [21] reported the results of time-averaged heat-transfer calculations compared to the data of Dunn et al. [23] for the Garrett TFE-731 turbine and a similar comparison for the data of Dunn et al. [24] obtained on the first blade of a full two-stage Space Shuttle main engine hydrogen side turbopump. The predictions of Refs. [20] and [21] both demonstrated good agreement with the experimental results. In Ref. [22] the authors used a rather simple analysis technique, but provided significant information regarding the influence of Reynolds number, stage pressure ratio, and gas to metal temperature ratio.

Tip and shroud measurements were obtained for the turbine stage described in this paper using a tip clearance at speed on the order of 1.25% of blade height. A flat blade tip configuration was used in these measurements. The difficulty of knowing how to nondimensionalize the heat-transfer data was discussed in some detail in Ref. [22] and will not be repeated here. However, to

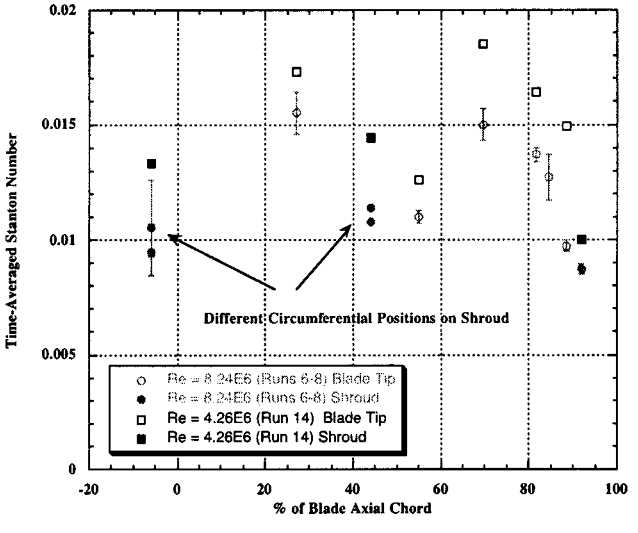

Fig. 10 HPT blade tip and HPT blade shroud measured Stanton number as a function of Reynolds number

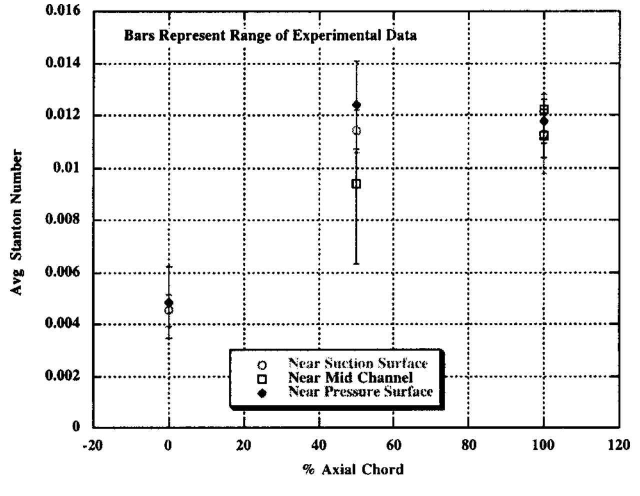

Fig. 12 HPV inner wall Stanton number as a function of axial chord at Re=7.94×10^6 (average runs 6, 8, 9, and 11)

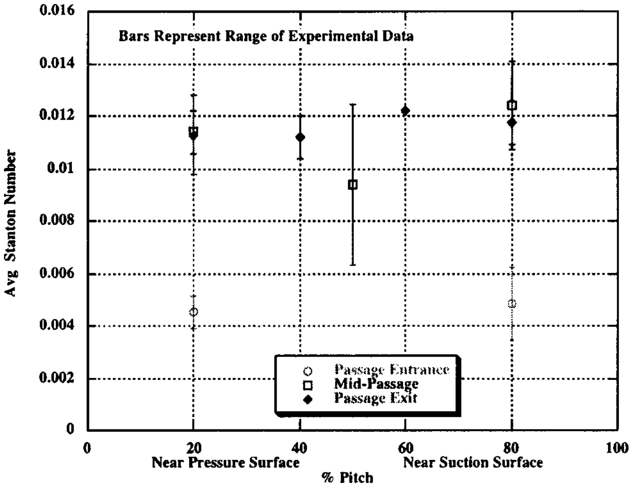

Fig. 13 HPV inner wall Stanton number as a function of pitch at Re=7.94×10^6 (average runs 6, 8, 9, and 11)

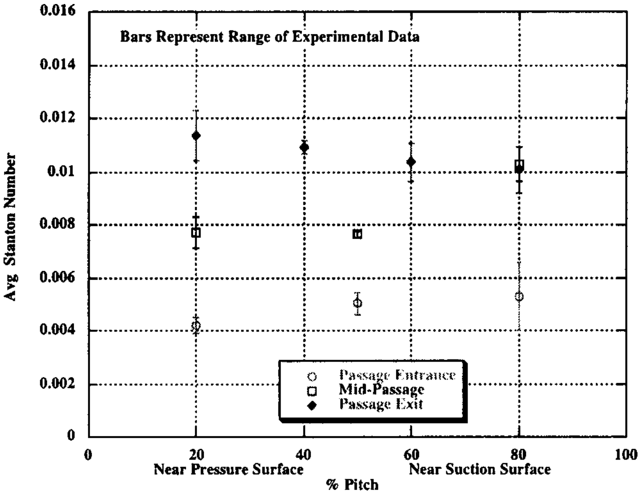

Fig. 15 HPT vane outer wall Stanton number as a function of % pitch at Re=7.94×10^6 (average runs 6, 8, 9, and 11)

illustrate some of the difficulty in nondimensionalizing the data, the measurements will be presented both as measured heat flux and as Stanton number in Figs. 9 and 10, respectively. Tip and shroud data were obtained for two values of the Reynolds number, 8.32×10^6 and 4.26×10^6. Stationary shroud instrumentation extended from approximately 5% ahead of the blade leading edge to approximately 95% of blade axial chord. The shroud heat flux gauges were located at different circumferential locations that were not in the same physical location relative to the vane trailing edge so they should not be expected to read exactly the same heat flux. Figure 9 presents the heat-flux data for both values of Reynolds number and the trend of the results are shown to be consistent for both cases. The heat-flux data obtained for the higher Reynolds number are shown to be significantly greater than those at the low Reynolds number. This plot also illustrates that the blade tip heat flux is significantly greater than the shroud heat flux at the locations over the blade tip and that both the tip and shroud values decrease rapidly after about 60% of blade axial chord. This result is consistent with the results previously shown in Refs. [25], [26], [20], [22], and [24]. Though a direct comparison is not included herein, the maximum heat-flux value measured for the tip was about 15% greater than that measured for the blade stagnation point. Also shown in Fig. 9 is a significant dip in the tip heat flux at about 58% axial chord. The time history of heat flux at this location and at a corresponding location at 96% span on the suction surface indicates a significant unsteadiness in the heat-flux time history at this particular location. Figure 10 presents the same experimental results, but with time-averaged Stanton number on the ordinate instead of measured heat flux. The same general trends in the data are illustrated with the exception that by nondimensionalizing the data to obtain Stanton number, the low-Reynolds-number data suggest greater values of the Stanton number than do the high-Reynolds-number data. This result once again illustrates the difficulty associated with knowing how to properly normalize the tip and shroud data to obtain Stanton number or Nusselt number plots. The heat-island corrections are not necessary for the blade tip and shroud gauges shown in Figs. 9 and 10 because the boundary-layer running length on the blade tip is very small.

Heat-flux measurements were also obtained for the blade platform and are shown in Fig. 11. Measurements were obtained close to the pressure surface at the leading edge of the airfoil, near the pressure surface at the trailing edge and near the suction surface near the trailing edge, and in line with the trailing edge just aft of the airfoil. Comparison of the results presented in Fig. 11 with the

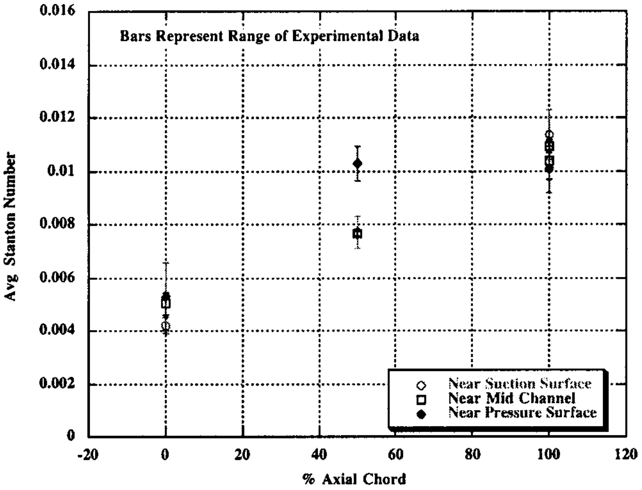

Fig. 14 HPT vane outer wall Stanton number as a function of axial chord at Re=7.94×10^6 (average runs 6, 8, 9, and 11)

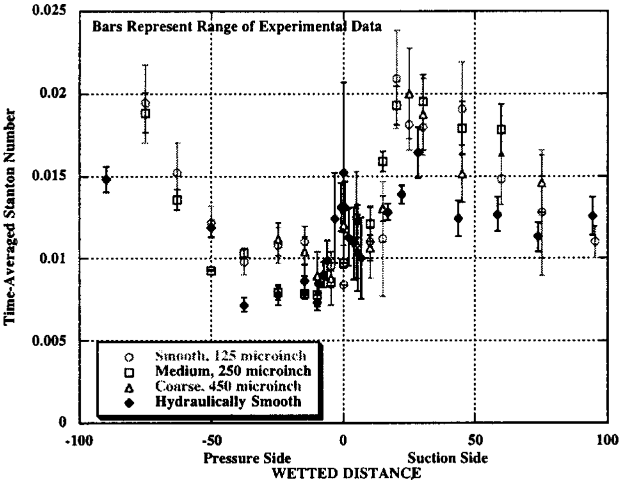

Fig. 16 Vane thermal-barrier-coating (VBC) effects on Stanton number at vane 50% span Re=7.94×10^6 (average runs 6, 8, 9, and 11)

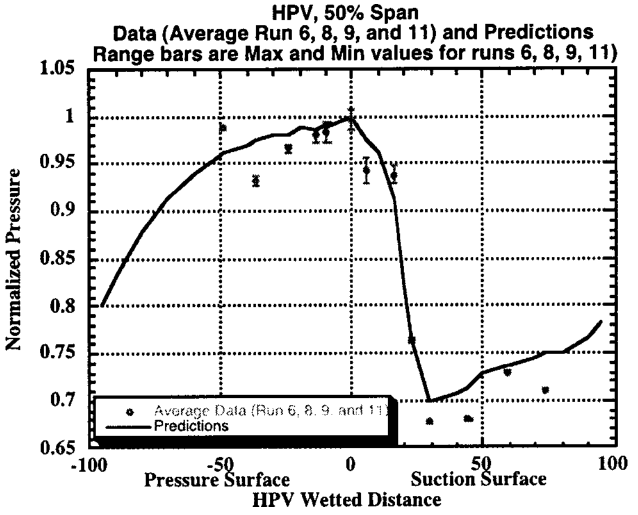

Fig. 17 HPV pressure distribution with predictions, 50% span

airfoil midspan results presented in Fig. 2 illustrates that the platform Stanton numbers are of the same relative value as the blade suctions surface Stanton numbers with the largest platform values occurring near the trailing edge.

Vane Inner and Outer Wall Stanton Number Distribution. Heat-flux measurements were made on both the inner and outer vane endwall and the results are presented in Figs. 12 and 13 for the vane inner wall. The results for the inner wall are shown in Fig. 12 as a function of the percent axial chord with measurements obtained near the suction surface, near midchannel, and near the pressure surface. The Stanton number increases significantly as the axial chord increases with the magnitude of the Stanton number being generally larger for the location nearest the pressure and suction surfaces and at the passage exit. Figure 13 presents the same data displayed as percent pitch of the passage. As illustrated by this figure, the coverage at the exit plane of the vane was a bit more detailed than at midpassage, but the results illustrate that both the midpassage and exit values of the Stanton number are comparable to the vane airfoil values presented in Fig. 1.

Similar results are presented in Figs. 14 and 15 for the vane outer wall. Figure 14 illustrates that for the outer wall, the Stanton number at midaxial chord near the pressure surface was significantly greater than the value at the passage entrance and comparable to the value at the vane exit. Figure 15 illustrates that the exit plane Stanton number values as a function of percent pitch are comparable across the exit and are of about the same magnitude as for the inner wall. Once again, the values at the exit plane are significantly greater than at the passage entrance.

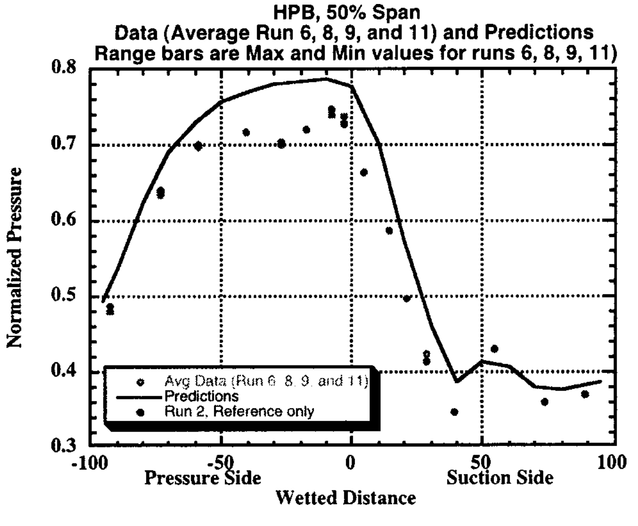

Fig. 18 HPB pressure distribution with predictions, 50% span

Influence of Surface Roughness (Thermal Barrier Coating) on Vane Stanton Number. It is well known that surface roughness can have a profound influence on surface heat transfer, e.g., Blair and Anderson [27], Boyle and Civinskas [28], Taylor et al. [29], Blair [30], Boynton et al. [31], and Dunn et al. [24]. In Ref. [24] results were presented for a blade that to the eye appeared to be very rough. However, when the roughness density was accounted for, the analysis showed only a small increase in blade surface heat transfer due to the surface roughness. The analysis illustrates that the effect of surface roughness is strongly dependent on Reynolds number. For the surface roughness and the Reynolds numbers used in this measurement program, it will be shown that the roughness used was sufficient to cause a significant increase in the local heat-flux values.

Three of the vanes used in these experiments were coated with TBC creating a smooth, medium, and coarse surface for comparison with the hydraulically smooth surface. The TBC vanes were instrumented at midspan with thin-film button-type heat-flux gauges. These gauges were installed under a microscope so that the top of the button was flush with the top of the roughness. Figure 16 presents the results obtained for the TBC vanes and compares these results with those of the hydraulically smooth vane. These results suggest that in general the Stanton number results for the TBC vanes were significantly greater than the comparable smooth vane results. However, the results do not show that the Stanton number distribution for the coarse surface is consistently greater than the corresponding distribution for the medium surface. In fact, at some airfoil locations, the results for the smooth, medium, and coarse surfaces are comparable with each other, all being well above the hydraulically smooth vane result.

Conclusions and Summary Remarks

The experimental results of a detailed heat-transfer measurement program for a modern high-pressure turbine stage have been presented. For the blade airfoil surface, the results of standard prediction techniques resulted in reasonable comparison with the experimental data for the 20%, 50%, and 96% spanwise locations. In the case of the vane, only a boundary layer prediction was available and the results of that prediction were not particularly good at any of the spanwise locations for which comparisons were made. The influence of the Reynolds number on the vane and blade Stanton number distribution was demonstrated for three spanwise locations on both the vane and the blade. In general, the Stanton number scaled approximately with the Reynolds number to the power 0.8; however, the scaling for the vane and the rotor appear to differ slightly. This would imply that there is an interaction between the rotation effects (which were kept constant over these runs) and the Reynolds number changes (although it is small). Experimental results are also presented for the vane inner and outer endwall, vanes with three different thermal barrier coatings, the blade tip and the adjacent stationary shroud, and the blade platform. Predictions were not available for comparison with the experimental results for any of these stage locations. For the vane endwalls it is important to note that the Stanton numbers are close to the same values as obtained on the vane airfoil itself, indicating the heat transfer to these areas is just as high as to the airfoil. For the Reynolds numbers and roughness associated with the vane thermal barrier coatings used in these experiments, the surface heat-transfer increased significantly in going from hydraulic smooth surfaces to coarser surfaces. Variations in the degree of coarseness were found to be relatively unimportant.

Overall this data set shows a more complete picture of heat transfer in a large turbine than is usually shown. The variation on the blade and vanes as a function of span shows the three-dimensional characteristics of the flow at even the modest span differences of 20%, 50%, and 80% on the vane. The results obtained at different Reynolds numbers illustrate the range of heat-transfer rates that could be experienced during different engine operating conditions.

Acknowledgments

The experimental portion of the effort reported herein was supported under General Electric Aircraft Engines Subcontract No. 200-14-14G25986 in support of Air Force Contract to GEAE No. F33615-84-C-2484. The measurements were performed while the OSU authors were employed by Calspan Corporation in Buffalo, New York. Permission to publish the data associated with this measurement program was obtained under Public Release Approval No. ASC-99-2326. The technical monitor for the Calspan work was Dr. Mikio Suo of GEAE. The authors would like to thank Dr. William Troha, Dr. Charles MacArthur, and Charles Stevens of the Aeropropulsion Laboratory of Wright Laboratories for their interest and support. The authors would like to express their appreciation to Dr. Robert Bergholz of GEAE for many constructive conversations during the course of this work.

Nomenclature

Re = Reynolds number/unit length
Re = $(\dot{m}/A)(1/\mu) = $(mass flow rate/area)(1/viscosity)
Re_x = Reynolds number based on wetted distance along airfoil
Re_x = $\mathrm{Re}(X/D)$
= Reynolds number at inlet×wetted distance
St = Stanton number
St = $\dot{q}$(evaluated at $T_{\mathrm{gauge}})/(\dot{m}/A)(C_{p_{T_{\mathrm{ref}}}}T_{\mathrm{ref}} - C_{p_{T_{\mathrm{gauge}}}}T_{\mathrm{gauge}})$
measured heat flux at gauge/(mass flow rate/area) (change in enthalpy)
T_{ref} = inlet total temperature

Appendix

The pressure distributions for the high-pressure vane (HPV) and high-pressure blade (HPB) at 50% span locations are shown in Figs. 17 and 18, respectively. These are provided as a reference for the heat-flux distributions provided in this paper. The predictions are from Bergholz [3]. The data shown are the average for runs 6, 8, 9, and 11. For the HPB, there was a failure of one blade with the suction surface instrumentation for these later runs, which reduced the number of data samples. To provide a comparison to the predictions, the data from run 2 (which has not been used in this paper) has been plotted for the HPB. One can see that the normalized pressure distribution does not vary much between run 2 and the average for the pressure surface.

References

[1] Dunn, M. G., 2001, ''Convective Heat Transfer and Aerodynamics in Axial Flow Turbines,'' ASME J. Turbomach., **123**, pp. 637–686.
[2] Dunn, M. G., Moller, J. C., and Steele, R. C., 1989, ''Operating Point Verification Data for a Large Shock Tunnel Test Facility,'' WRDC Tech. Rep. No. WRDC-TR-89-2027.
[3] Bergholz, R. F., Dunn, M. G., and Steuber, G. D., 2000, ''Rotor/Stator Heat Transfer Measurements and CFD Predictions for Short-Duration Turbine Rig Tests,'' ASME paper No. 2000-GT-208.
[4] Rivir, R. B., Elrod, W. C., and Dunn, M. G., 1985, ''Two Spot Laser Velocimeter Measurements of Velocity and Turbulence Intensity in Shock Tube Driven Turbine Flows,'' AGARD Heat Transfer and Cooling in Gas Turbines, Conf. Proc. No. 390, pp. 33-1 to 33-12, Bergen, Norway.
[5] Dunn, M. G., Kim, J., and Rae, W. J., 1997, ''Investigation of the Heat-Island Effect for Heat-Flux Measurements in Short-Duration Facilities,'' ASME J. Turbomach., **119**, pp. 753–759.
[6] Zilles, D. A., and Abhari, R. S., 1999, ''Influence of Non-Isothermal Button Gage Surface Temperature in Heat Flux Measurement Applications,'' Proc. IMECE99, Nashville, TN.
[7] Mukerji, D., Eaton, J. K., and Moffat, R. J., 1998, ''A New Correlation for Temperature Rise Correction of Heat Flux Gages,'' Proceedings of ASME HTD, Vol. 361-5, pp. 631–636.
[8] Mukerji, D., Eaton, J. K., Moffat, R. J., and Elkins, C. J., 1999, ''A 2-D Numerical Study of the Heat-Island Effect for Button-Type Heat Flux Gages,'' Paper AJTE 99/6186, Proc. 5th ASME/JSME Joint Thermal Engineering Conference.
[9] Kim, J., Sakamoto, H., and Dunn, M. G., 2000, ''A Two-Dimensional Numerical Investigation of Transient Heat Flux Gage Performance in Short-Duration Facilities,'' ASME J. Turbomach., **122**, pp. 184–187.
[10] Suo, M., and Lounsbury, R., 1990, General Electric Aircraft Engines Co., private communication.
[11] Suo, M., and Lounsbury, R., 1990, General Electric Aircraft Engines Co., private communication.
[12] Crawford, M. E., and Kays, W. M., 1976, ''STAN5—A Program for Numerical Computation of Two-Dimensional Internal and External Boundary Layer Flows,'' NASA Report No. CR-2742.
[13] Rodi, W., and Scheuerer, G., 1985, ''Calculation of Heat Transfer to Convection-Cooled Gas Turbine Blades,'' ASME J. Eng. Gas Turbines Power, **107**, pp. 621–627.
[14] Lam, C. K. S., and Bremhorst, K., 1981, ''A Modified Form of the k-ε Model for Predicting Wall Turbulence,'' ASME J. Fluids Eng., **103**, pp. 456–460.
[15] Zerkle, R. D., and Lounsbury, R. J., 1987, ''The Influence of Freestream Turbulence and Pressure Gradient on Heat Transfer to Gas Turbine Airfoils,'' AIAA paper no. AIAA-87-1917, AIAA/SAE/ASME/ASEE 23rd Joint Propulsion Conference, San Diego, CA.
[16] Bunker, 2000, ''A Review of Turbine Blade Tip Heat Transfer,'' presented at the Turbine 2000 International Symposium on Heat Transfer in Gas Turbine Systems, Izmir, Turkey.
[17] Ameri, A. A., and Bunker, R. S., 1999, ''Heat Transfer and Flow on the First Stage Blade Tip of a Power Generation Gas Turbine Part 2: Simulation Results,'' IGTI paper no. 99-GT-283.
[18] Rigby, D. L., Ameri, A. A., and Steinthorsson, E., 1996, ''Internal Passage Heat Transfer Prediction Using Multiblock Grids and k-ω Turbulence Model,'' ASME paper no. 96-GT-188.
[19] Ameri, A. A., Steinthorsson, E., and Rigby, D. L., 1998, ''Effect of Squealer Tip on Rotor Heat Transfer and Efficiency,'' ASME J. Turbomach., **120**, pp. 753–759.
[20] Metzger, D. E., Dunn, M. G., and Hah, C., 1991, ''Turbine Tip and Shroud Heat Transfer,'' ASME J. Turbomach., **113**, pp. 502–507.
[21] Ameri, A. A., and Steinthorsson, E., 1996, ''Analysis of Unshrouded Rotor Blade Tip and Shroud Heat Transfer,'' ASME paper no. 96-GT-189.
[22] Polanka, M. D., Hoying, D. A., Meininger, M., and MacArthur, C. D., 2002, ''Turbine Tip and Shroud Heat Transfer and Loading Part A: Parameter Effects Including Reynolds Number, Pressure Ratio, and Gas to Metal Temperature Ratio,'' ASME paper no. GT-2002-30186.
[23] Dunn, M. G., Rae, W. J., and Holt, J. L., 1984, ''Measurement and Analysis of Heat Flux Data in a Turbine Stage: Part II—Discussion of Results and Comparisons With Predictions,'' ASME J. Eng. Gas Turbines Power, **106**, pp. 234–240.
[24] Dunn, M. G., Kim, J., Civinskas, K. C., and Boyle, R. J., 1994, ''Time-Averaged Heat Transfer and Pressure Measurements and Comparison With Prediction for a Two-Stage Turbine,'' ASME J. Turbomach., **116**, pp. 14–22.
[25] Dunn, M. G., and Hause, A., 1982, ''Measurement of Heat Flux and Pressure in a Turbine Stage,'' ASME J. Eng. Power, **104**, pp. 215–223.
[26] Epstein, A. H., Guenette, G. R., Norton, R. J. G., and Yuzhang, C., 1985, ''Time Resolved Measurements of a Turbine Rotor Stationary Tip Casing Pressure and Heat Transfer Field,'' AIAA paper no. 85-1220.
[27] Blair, M. F., and Anderson, O. L., 1989, ''The Effect of Reynolds Number, Rotor Incidence Angle and Surface Roughness on the Heat Transfer Distribution in Large-Scale Turbine Rotor Passage,'' United Technologies Research Center Report No. UTRC-R89-957852-24.
[28] Boyle, R. J., and Civinskas, K. C., 1991, ''Two-Dimensional Navier-Stokes Heat Transfer Analysis for Rough Turbine Blades,'' AIAA paper no. AIAA-91-2129.
[29] Taylor, R. P., Taylor, J. K., Hosni, M. H., and Coleman, H. W., 1991, ''Heat Transfer in the Turbulent Boundary Layer With a Step Change in Surface Roughness,'' ASME paper no. 91-GT-266.
[30] Blair, M. F., 1994, ''An Experimental Study of Heat Transfer in a Large-Scale Turbine Rotor Passage,'' ASME J. Turbomach., **116**, pp. 1–13.
[31] Boynton, J. L., Tabibzadeh, R., and Hudson, S. T., 1993, ''Investigation of Rotor Blade Roughness Effects on Turbine Performance,'' ASME J. Turbomach., **115**, pp. 614–620.

Measurements and Predictions of Heat Transfer on Rotor Blades in a Transonic Turbine Cascade

Paul W. Giel
OSS Group, Inc.,
NASA Glenn Research Center,
Cleveland, OH 44135
e-mail: Paul.W.Giel@grc.nasa.gov

Robert J. Boyle
NASA Glenn Research Center,
Cleveland, OH 44135
e-mail: Robert.J.Boyle@grc.nasa.gov

Ronald S. Bunker
General Electric Company,
Global Research Center,
Schenectady, NY 12301
e-mail: bunker@crd.ge.com

Detailed heat transfer measurements and predictions are given for a power generation turbine rotor with 127 deg of nominal turning and an axial chord of 130 mm. Data were obtained for a set of four exit Reynolds numbers comprised of the facility maximum point of 2.50×10^6*, as well as conditions which represent 50%, 25%, and 15% of this maximum condition. Three ideal exit pressure ratios were examined including the design point of 1.443, as well as conditions which represent* -25% *and* $+20\%$ *of the design value. Three inlet flow angles were examined including the design point and* ±5 *deg off-design angles. Measurements were made in a linear cascade with highly three-dimensional blade passage flows that resulted from the high flow turning and thick inlet boundary layers. Inlet turbulence was generated with a blown square bar grid. The purpose of the work is the extension of three-dimensional predictive modeling capability for airfoil external heat transfer to engine specific conditions including blade shape, Reynolds numbers, and Mach numbers. Data were obtained by a steady-state technique using a thin-foil heater wrapped around a low thermal conductivity blade. Surface temperatures were measured using calibrated liquid crystals. The results show the effects of strong secondary vortical flows, laminar-to-turbulent transition, and also show good detail in the stagnation region.* [DOI: 10.1115/1.1643383]

Introduction

Turbine blade aerodynamics is generally given a high degree of analysis prior to commitment for fabrication. This attention to detail is carried through to the manufacturing specifications and quality inspections in the form of dimensional accuracies demanded of both the airfoils and the rotor disks. While a substantial amount of data exists concerning the effects of blade incidence angle, Reynolds number, and pressure ratio (loading) on aerodynamics, less information is available on the associated airfoil heat transfer distributions for off-design conditions. Computational fluid dynamics (CFD) is increasingly being relied upon in the design and analysis of gas turbine components. The need to predict heat transfer along with aerodynamics during the design of turbine blades greatly complicates these analyses. Thus, the heat transfer predictive capability of CFD currently lags that of aerodynamics. Heat transfer data are therefore needed both to assess the effects of various flow parameters and to improve CFD analyses so that these effects can be accurately predicted.

Arts et al. [1] studied incidence, Reynolds number, and exit Mach number effects on heat transfer, but with midspan thermocouples only. Incidence was varied over a range of -14 deg to $+11$ deg. Camci and Arts [2] also examined incidence effects on a film-cooled heat transfer test blade, but again only at midspan. The three-dimensional nature of the flow and heat transfer indicates that a full-blade understanding is needed, not just a two-dimensional understanding at midspan. Previous studies have shown that rotor geometries in linear cascades provide good midspan data as compared to their rotating equivalents. See, for example, Baughn et al. [3] or Guenette et al. [4]. Also, Graziani et al. [5] studied the effects of thick and thin endwall boundary layers on rotor heat transfer in a low speed linear cascade. Blair [6] measured heat transfer in a low speed facility on a rotating blade that had the same midspan section as the blade of Graziani et al. [5]. Similar three-dimensional heat transfer patterns were observed at and below midspan of those two tests, validating the use of linear cascades for these types of heat transfer studies. Dunn et al. [7] measured rotor heat transfer at discrete chordwise and spanwise locations in a shock tube facility at engine-typical gas-to-wall temperature ratios and Mach numbers. These measurements were on engine-size hardware using heat flux gauges. Consequently, the resolution was less than for the large scale facility measurements.

Detailed heat transfer data at conditions approximating those in actual engines are needed to assess flow parameter effects and to verify CFD predictive analyses over a wide range of operating conditions. Variations in flow parameters often have an impact on secondary flows and thus on the three-dimensional nature of the heat transfer distribution. Data are therefore needed all over the blade surface, not just at midspan.

The blade geometry of the present study is representative of a first stage turbine blade for a new GE heavy frame power turbine machine design. The present design is a heavily loaded blade using highly effective internal cooling with limited film cooling. The blade aerodynamic section is relatively thick in conjunction with a low solidity blade row design, and contains a large leading edge diameter. Knowledge of the external convective heat transfer distribution is desired for both validation and for the improvement of predictive methods. The turbine blade is for a machine operating in the 1370°C (2500°F) class. The full-power design point isentropic pressure ratio of the current blade section is 1.443. The inlet Mach number is 0.399 and the exit isentropic Mach number is 0.743. The inlet angle of attack is 59.1 deg while the exit angle is 67.9 deg, producing an aggressive total turning of 127 deg. The airfoil Reynolds number is 2.68×10^6 based upon axial chord length and exit conditions. The test facility inlet plenum pressure cannot exceed 162 kPa (23.5 psia), which limits the exit Reynolds number to 2.50×10^6. For the purposes of this report therefore, this later value will be referred to as the design Reynolds number. The blade geometry is shown in **Fig. 1** along with geometric details. Surface distance coordinates are also shown on the blade.

Tests have been conducted covering a range of blade pressure ratios from -25% to $+20\%$ of the design nominal condition, spanning the full spectrum from well subsonic ($M_{ex,is}=0.33$) to

---

Contributed by the International Gas Turbine Institute and presented at the International Gas Turbine and Aeroengine Congress and Exhibition, Atlanta, GA, June 16–19, 2003. Manuscript received by the IGTI December 2002; final revision March 2003. Paper No. 2003-GT-38839. Review Chair: H. R. Simmons.

Parameter	Value
axial chord	129.8 mm (5.110 in.)
pitch	130.0 mm (5.119 in.)
span	152.4 mm (6.000 in.)
d, leading edge	18.4 mm (0.726 in.)
turbulence grid	25.4 mm square bar
blade passages	11

(d = 2 × minimum radius of curvature)

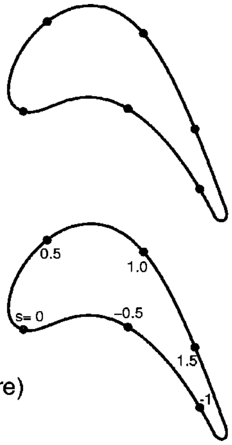

Fig. 1 Test blade geometry

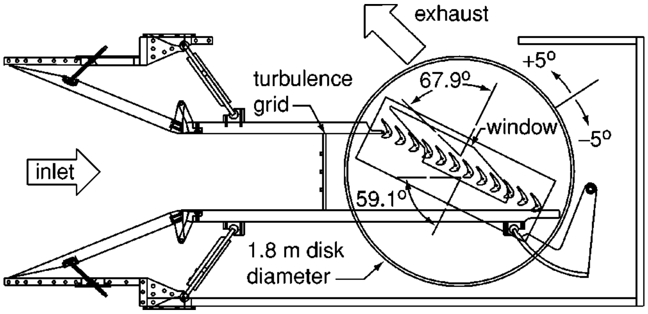

Fig. 2 Transonic turbine blade cascade facility

transonic ($M_{ex,is}=0.92$). Reynolds numbers as low as 15% of the design point allow the evaluation of heat transfer distributions over conditions from turning crank to first fire to full power. In addition, inlet attack angle variations of $+5$ deg and -5 deg have been investigated. All of these test conditions serve to map out a large performance space with significant alterations in pressure and heat transfer distributions, and consequent challenges for numerical predictive techniques.

The set of data produced in this study serves as a test of CFD predictive capability for an actual airfoil design space. The primary objective of this research is the continued extension of three-dimensional predictive modeling techniques for airfoil external heat transfer through the acquisition of full-surface blade data. Previous blade heat transfer studies in this facility include those of Giel et al. [8,9]. The airfoil shape of the current study is distinctly different than those previously tested in the same facility, thus providing a new CFD test case for previously validated predictive techniques. The CFD comparisons are challenged further by the wider variations of incidence angle, pressure ratio, and Reynolds number. The CFD predictions, when compared to the measurements, point out areas where modeling improvements are needed. Liquid crystal surface temperature measurement techniques are capable of obtaining detailed data over an entire surface and were therefore chosen for the present study.

Description of Facility

Cascade Description. The NASA Glenn Research Center Transonic Turbine Blade Cascade provides heat transfer and aerodynamic data to verify CFD analyses. The facility can and has been used to test over wide, independent ranges of Reynolds number and Mach number. High pressure, ambient temperature air can be throttled to an inlet pressure that can be varied from the exit pressure to 162 kPa (23.5 psia). The exhaust pressure can be varied independently from the inlet pressure down to 13.8 kPa (2.0 psia). The facility operates in a continuous mode with mass flow rates for the current study ranging from 3.2 kg/s (7.1 $\mathrm{lb_m/s}$) to 26.3 kg/s (58.0 $\mathrm{lb_m/s}$). A two-dimensional view of the facility is shown in **Fig. 2**. Heat transfer measurements were made on the sixth of 12 blades counting from left to right. The pressure measurement blades were the fifth and sixth. The flowpath width of the portion of the facility shown in **Fig. 2** is uniform and matches the blade span.

While the blade and cascade geometries are two-dimensional, the blade passage flows are highly three-dimensional due to the aggressive turning, the thick boundary layers developed on the long cascade inlet, and the low aspect ratio blades ($\mathrm{span}/C_x=1.17$). The thickness of each endwall boundary layer varied from 28% to 37% of the half-span depending on the inlet Reynolds number, as estimated from measurements approximately one axial chord upstream of the blade row. The thick boundary layers and high flow turning resulted in spanwise flow variations as large as those seen in rotating turbines. See, for example, Joslyn and Dring [10] or Thulin et al. [11]. These variations result from secondary flows, and accurately predicting them is a significant test of a three-dimensional analysis.

Inlet turbulence was produced using a square bar, bidirectional grid upstream of the blade row. The grid was made of 25.4 mm (1 in.) square hollow bars with 75 uniformly spaced 3.2 mm (1/8 in.) diameter holes blowing air in the upstream direction. One bar extended between the inlet boards at midspan and three bars spaced six bar dimensions apart were placed spanwise as shown in **Fig. 2**. The total mass flow from the grid was 0.68 kg/s (1.5 $\mathrm{lb_m/s}$) for all cases, corresponding to 2.6% of the cascade mass flow at the design exit Reynolds number. The open area of the grid was 74% and it was located 1.10 m (43 in.) upstream of the heat transfer measurement blade. It was positioned normal to the inlet flow as shown in **Fig. 2**. An aerodynamic probe measurement slot was located an axial distance of 127 mm in front of the cascade face. Results of the inlet turbulence measurements can be found in a previous study by Giel et al. [8]. The blades of the current study have the same pitch and are located at the same distance from the grid as those of the previous study. The inlet turbulence level measured there was approximately 9% at an inlet Mach number of 0.39. The longitudinal, integral turbulence length scale was measured to be $\Lambda_x=26$ mm. Pitchwise and spanwise surveys of mean velocity, Tu, and length scale were made in the probe slot over several blade passages.

Boyle et al. [12] found that there could be a substantial increase in apparent turbulence intensity at the design inlet Mach number when a correction is made to account for Knudsen number effects on small diameter wires. The inlet turbulence intensity was measured as 9%, but the Knudsen number effect was not accounted for. Accounting for the Knudsen number effect increased Tu_{in} from 9% to 13%. Additional measurements showed that as the Mach number decreased, the uncorrected turbulence level increased. The corrected turbulence level of 13% was found to be nearly the same for all inlet Mach numbers. Subsequent remeasurements of length scale showed Lu to be 58mm (2.28 in.).

Figure 2 shows the test section mounted on a large rotatable disk. The disk can be rotated $+15$ deg to -30 deg to accommodate blades with different inlet flow angles as well as to vary the incidence angle. Upstream inlet boards were used, but the facility uses no exit tailboards. Endwall static pressure measurements and other flow field aerodynamic probe measurements all showed excellent periodicity in at least the center three blade passages (see Giel et al. [13]). The flow conditions of two previous blade heat transfer studies are shown in **Fig. 3** along with those of the current study. The conditions are shown as unit exit Reynolds number versus exit isentropic Mach number or pressure ratio. The operating envelope of the facility is also shown in the figure with limits imposed by minimum exhaust pressure, maximum mass flow, and maximum inlet pressure.

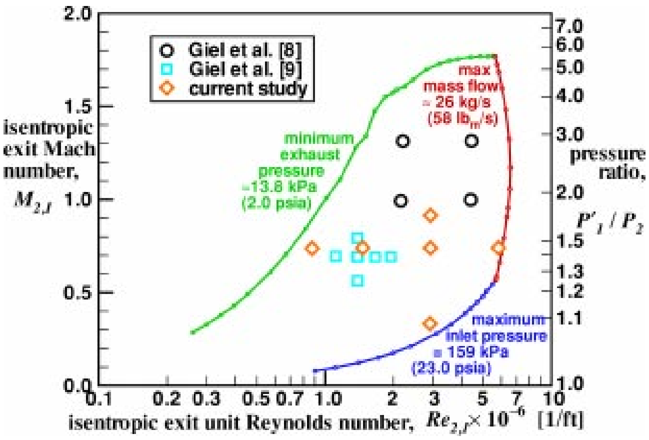

Fig. 3 Facility operating parameters

Pressure Measurement Blade Description. The two blades forming passage 5 were instrumented for pressure measurements. Blade 5 had 18 static pressure taps at 10% span and 20 more at 25% span. Blade 6 had 38 taps at midspan. The tap diameters were 0.5 mm (0.020 in.).

Heat Transfer Measurement Blade Description. The blade in position 6 was fabricated from low conductivity foam ($k=0.2$ W/m·K) for heat transfer measurements. The undersized foam core was placed in a mold and gelcoat epoxy was cast around it. The outer epoxy shape was itself undersized by 152 μm (0.006 in.) to accommodate a 25 μm (0.001 in.) Inconel thin foil heater and a 127 μm (0.005 in.) double-faced adhesive layer. The single sheet heater covered the entire blade except on the trailing edge circle. Two thin-film thermocouples were glued to the heater sheet at $z=0.25$, one on the pressure surface at $s=-0.21$ and one on the suction surface at $s=1.81$. These were used for overheat control and for liquid crystal temperature verification. Flat black paint was sprayed over the outer surface and a 25×25 mm (1×1 in.) grid of white dots was painted on for location reference. Finally, chiral nematic, micro-encapsulated liquid crystals were sprayed onto the outer heater surface. A temperature calibration plate, instrumented with a thermocouple, and a roughness measurement plate were sprayed at the same time. The liquid crystal yellow-line temperature was calibrated with the calibration plate and verified during data acquisition with the two blade surface-mounted thermocouples. Both ends of the blade were made of 12.7 mm (0.50 in.) thick nickel-plated copper, cut out in the shape of the blade, and were used as buss bars to supply DC electrical power to the heater. The heater foil extended over the copper ends and was tack welded to them. Hollow studs extended from the copper, through the acrylic windows, and were used for mounting and for electrical connections. They were also connected through vacuum tubing to the exhaust section of the facility to approximately equalize the pressure inside and outside of the blade, preventing damage to the surface when the test section pressure was changed. Both endwalls were 63.5 mm (2.50 in.) thick clear acrylic for optical access. An outline of the window is shown in **Fig. 2**.

A profilometer was used to measure several 5-mm traces on the roughness measurement plate after the liquid crystals were applied. The arithmetic mean roughness was 3.7 μm and the r.m.s. roughness was 4.7 μm. The average peak-to-peak distance was 62 μm. Estimates of the equivalent roughness height ranged between 3.7 μm and 23 μm. The maximum equivalent height corresponds to an estimated maximum k^+ of 13.6. Blade surface heat transfer could have been influenced by roughness at the higher Reynolds numbers. Even if the average roughness value was the same as that of an in-service blade, the roughness distribution is likely to be different.

Measurement Techniques

Blade Static Pressure Measurements. Surface static pressures were measured independently from the heat transfer measurements using a separate blade set. The two blades forming passage 5 were instrumented with 76 static pressure taps. The pressure taps were scanned at a rate of once per second with an electronically scanned measurement system. Fifteen scans were averaged. The inlet total pressure was measured as the average of three midspan Kiel probes upstream of passages 4, 7, and 8. The probes were located an axial distance of 127 mm (5.0 in.) ahead of the cascade face. More details of the blade static pressure measurement techniques are given by Giel et al. [13].

Heat Transfer Measurements. The selections of liquid crystal yellow line temperatures and color band widths were made subject to several constraints. The crystal temperature was chosen to be as high as possible to minimize uncertainty without exceeding the 80°C (175°F) material limit of the double-faced adhesive. This limit was approached in regions of minimum heat transfer when the heater power was increased to make measurements in regions of maximum heat transfer. A crystal temperature 16°C (29°F) above the inlet total temperature typically met both criteria. The measured yellow line crystal temperature was 37.3°C (99.1°F) and the inlet air varied between 5.1°C (41.2°F) and 22.3°C (72.2°F). Narrower bandwidth crystals provide better resolution in regions of very low gradients but the yellow line could become too thin to be clearly visible in high gradient regions. Crystals with full-color bandwidths of ±2°C were found to be a good compromise for the current measurements.

The following procedure was used to obtain the heat transfer data: Flow conditions were established and the heater power was increased until the first yellow isotherm was visible. When steady-state conditions were achieved, typically within ten minutes, data recording of voltage, current, and flow conditions was initiated. The blade surface was simultaneously photographed with four 35 mm still cameras using color slide film. Each camera photographed a subset of the blade surface, with some overlap between views. Moffat [14] showed that micro-encapsulated crystals are less sensitive to illuminating and viewing angles than non-encapsulated crystals. High speed photographic strobes were used to prevent radiative heating of the liquid crystals. The strobes were mounted as close as possible to the camera lens to minimize differences between viewing and illumination angles. No differences in isotherm location were detected between overlapping photographs. Heater power was then increased to move the isotherms and the process was repeated until the entire blade surface was mapped. 24 power levels were typically used for each flow condition.

The following procedure was used to reduce the heat transfer data. The photographic slide images were projected onto paper and the reference dot pattern and the isotherms were sketched. The slide image dot pattern was aligned for subsequent isotherms. Separate sketches were made for each camera view. These composite isotherm sketches were then digitized, with between 4000 to 8000 digitized points for each flow condition. A grid having five times the resolution of the blade dot pattern was laid over the blades and photographed. Every fifth point on the grid photograph was aligned with the dots in the data photographs. The finer resolution coordinates were then used to interpolate each digitized point to (s,z) unwrapped blade coordinates. This procedure corrected for distortions due to blade curvature and viewing angles.

The local surface heat flux, q'', was determined from the heater voltage, V [volts], and current, I [amps], then corrected for radiative heat loss:

$$q'' = \frac{V \cdot I}{A} - \varepsilon \sigma (T_{lc}^4 - T_{aw}^4).$$

With the emissivity, ε, assumed to be 0.98, radiative losses were at most 8.8% of the net heat flux at the lowest Reynolds number and declined rapidly with increasing Reynolds number to a local maximum of only 1.3% at the highest Reynolds number. Here, σ is the Stefan-Boltzmann constant. The heat transfer coefficient and the Nusselt number were defined as follows:

$$h = \frac{q''}{T_{lc} - T_{aw}} \quad \text{and} \quad \text{Nu} = \frac{h \cdot C_x}{k(T'_{in})}. \tag{1}$$

The local adiabatic wall temperature, T_{aw}, is

$$\frac{T_{aw}}{T'_{in}} = r + \frac{1 - r}{1 + 0.5(\gamma - 1) M_{is}^2}$$

with the specific heat ratio, $\gamma = 1.4$. The choice of T_{aw} as the convective driving temperature ensures that h and Nu are reasonably independent of the thermal boundary condition, specifically, independent of the particular choice of liquid crystal temperature. The inlet total temperature, T'_{in}, was determined by a mass weighted average of the main flow and the turbulence grid flow. Two additional total temperature probes were located an axial distance of 127mm (5.0 in.) ahead of the cascade face and agreed with the mass weighted average to within the measurement uncertainty. The local adiabatic wall temperature was needed at each digitized point in order to calculate the heat transfer coefficient. This information was interpolated from CFD calculations of blade surface static pressure which will be shown to agree well with measured values. The calculated values provided significantly better spatial resolution than was available from the experimental data. The isentropic Mach number, M_{is}, was determined from CFD calculations, and a recovery factor of $r = \text{Pr}^{1/3}$ was used everywhere. The data were triangulated for contour plotting and interpolated onto constant span lines of 15%, 25%, and 50% for line plotting.

Uncertainty Analysis. An uncertainty analysis was performed using the method of Kline and McClintock [15]. The major sources of uncertainty in Eq. (1) are the adiabatic wall temperature, $\delta T_{aw} = \pm 1.0°\text{C}(\pm 1.8°\text{F})$ and the liquid crystal temperature, $\delta T_{lc} = \pm 0.5°\text{C}(\pm 0.9°\text{F})$. At the temperature differences and the relatively low Mach numbers of the current study, the uncertainty in pressure measurements, the differences between measured and calculated pressures, and the interpolations are minor contributors to the overall uncertainty of T_{aw} as compared to the uncertainty in T'_{in}. The uncertainty in T_{aw} for the same reason assumes no uncertainty in the recovery factor, r, although it is not precisely known as shown by Schlichting [16]. Other less dominant sources of uncertainty such as the heater voltage and current, $\delta V/V = \delta I/I = 1\%$, and the heater length and width, $\delta L/L = 2\%$ and $\delta W/W = 1\%$, were included in the analysis. The overall uncertainty in Nu was determined to be less than 8.2% for all cases and was typically less. Because the uncertainty varied with specific conditions, maximum values for each case will be presented with the results.

CFD Analysis

To illustrate where analysis improvements are needed, baseline CFD results were done using the three-dimensional Navier-Stokes analysis code, $RVC3D$ described by Chima and Yokota [17] and by Chima [18]. C-type grids were generated using the method of Arnone et al. [19]. Further details of the computational approach are found in Giel et al. [9]. Predictions were made using a $313 \times 49 \times 65$ grid. The grid size was based on previous work, (Boyle and Giel [20]). Even though the Reynolds number, and therefore y_1^+ varied by more than a factor of six, all comparisons were made using the same grid. A uniform blade temperature of $1.15 \times T'_{in}$ was specified. The temperature of the unheated endwall was set equal to the inlet total temperature. Midspan symmetry was assumed.

A two-layer algebraic turbulence model, described by Chima et al. [21], was used. Transition start was specified using Mayle's [22] model. The start of transition is a function of the local momentum thickness and turbulence intensity. The freestream turbulence level for the start of transition was calculated using the relationship given by Steelant and Dick [23]. The measurements of Boyle et al. [12] showed that this relationship predicted the change in midpassage turbulence in a turbine vane cascade. The transition length model of Boyle and Simon [24] was used. This model is an extension of the one by Solomon et al. [25] to include Mach number effects.

The analysis incorporated a model to account for the effects of freestream turbulence on eddy viscosity. This model was based on the Smith and Kuethe [26] model for the effects of turbulence in the leading edge region. The Smith and Kuethe model gives

$$\mu_t = C_{SK} l \rho Tu_{in} U_{in}.$$

Augmentation of the viscosity due to freestream turbulence effects is needed, not only in the leading edge region, but whenever the flow is laminar. Otherwise, the laminar surface heat transfer is often underpredicted. Dullenkopf and Mayle [27] suggested that the velocity gradient is the important parameter for use in augmenting laminar heat transfer. In the leading edge region $dU/ds = a_1 U/d$. To first order $a_1 = 4$. For a variable velocity gradient, μ_t is calculated from

$$\mu_t = C_{DM} C_{SK} l \rho Tu_{in} U_{fs} \sqrt{d \left(\frac{dU_{fs}}{ds} \right) \left(\frac{1}{U_{fs}} \right)}.$$

The square root is used because, in the Dullenkopf and Mayle [27] model Tu is also a function of $\sqrt{dU/ds}$.

$C_{SK} = 0.00164$,Tu in percent. $C_{DM} = 0.5$. Both equations for μ_t are independent of length scale. Experiments, (Ames and Moffat [28] and Van Fossen et al. [29]) showed that increasing the scale of turbulence decreases heat transfer. From a computational standpoint there are disagreements in the literature. According to Dullenkopf and Mayle [27], there is a peak in Frossling number at a specific normalized length scale. Length scales greater or less than this value result in lower Frossling numbers. Also, the equation for μ_t uses the leading edge diameter. This may not be appropriate for modeling turbulence intensity effects on the pressure surface away from the leading edge. The analyses were done assuming that Tu_{in} is 13%.

Blade Static Pressure Results

Figure 4 shows sample measured and calculated aerodynamic parameters on an unwrapped blade surface. **Figure 4(*a*)** shows calculated contours of M_{is} for the design flow case. The horizontal and vertical axes of this and all subsequent surface contour plots are scaled such that the physical blade surface distance/blade span aspect ratio is preserved. **Figure 4(*b*)** shows the corresponding comparison with data. In this case and for all other cases not presented here, the comparison with data is very good. The surface contour plot shows the strong three-dimensionality of the flow, as evidenced by the distorted suction surface contours caused by the horseshoe/passage vortices. No decelerating flow regions are seen on the suction surface until near the geometric throat at $s \approx 1.07$ where very slight deceleration occurs on the uncovered portion of the blade. Deceleration is also seen on the pressure surface just downstream of the leading edge, extending to $s \approx -0.35$. Three-dimensional distortions caused by secondary vortical flows are also seen on the pressure surface. These regions are noted because of their potential implications on flow transition and thus on heat transfer. The calculated values of M_{is} were used for heat transfer data reduction because they provided significantly better spatial resolution than was available from the experimental data.

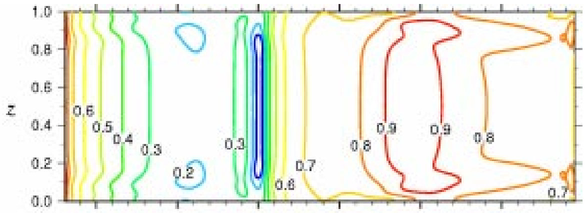

(a) calculated M_{is} contours at design conditions

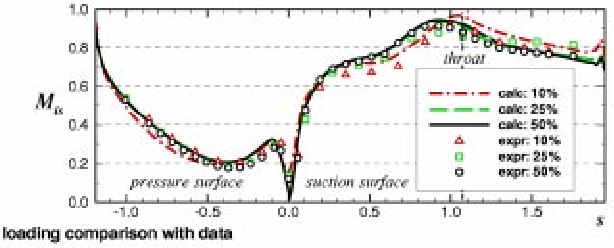

(b) loading comparison with data

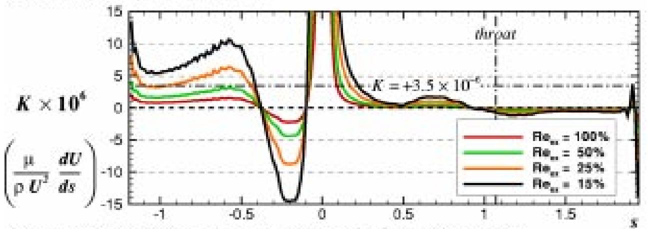

(c) pressure gradient parameter variations with Reynolds number

Fig. 4 Measured and calculated blade loadings

Figure 4(*c*) shows the calculated pressure gradient parameter, K, at midspan for varying Reynolds numbers, all at the design pressure ratio and inlet flow angle. Again note the decelerating flow region $(K<0)$ on the pressure surface just downstream of the stagnation region. The flow then accelerates for the remainder of the pressure surface. Because K is inversely proportional to the Reynolds number, only the two lowest Reynolds number cases have pressure gradient parameters that exceed 3.5×10^{-6}. Relaminarization was predicted when K exceeded this value.

Experimental Heat Transfer Results

Data and CFD calculations will be presented as Nusselt number contours on the unwrapped blade surface and as line plots at 15%, 25%, and 50% span. Discussion of the experimental data will be presented first, followed by a discussion of the calculated results. Gray areas on the data contour plots indicate regions where data were not available. The copper buss bars are also evident in the data plots as regions near the endwalls where no data were available. The CFD calculations were made with a uniform temperature specified on the entire blade and did not model the buss bar thermal boundary condition. Lines showing their locations are included in the contour plots for reference. It should be noted that no midspan symmetry was assumed in presenting the experimental data; measured symmetry is typically good, but minor differences can be seen.

The measured flow conditions for the eight heat transfer cases are listed in **Table 1**. Data at other combinations of flow parameters were obtained but will not be presented here. The first case to be presented will be the baseline case, obtained at the design flow conditions. Subsequent cases are grouped to examine the effects of Reynolds number, pressure ratio, and incidence angle. Variations in Reynolds number of 50%, 25%, and 15% (Cases 2–4) will be examined with the pressure ratio and the incidence angle held at their design values. Variations in pressure ratio of -25% and $+20\%$ (Cases 5–6) will be examined with the exit Reynolds number at 50% of its design value and the incidence angle at its design value. Pressure ratios less than the design value could not be examined at the design Reynolds number because of facility limitations (see **Fig. 3**). Finally, variations in incidence of ±5 deg (Cases 7–8) will be examined with the exit Reynolds number at 50% of its design value and the pressure ratio at its design value. Repeatability of Re_{ex} was within 1.2% for all cases and repeatability of PR was within 0.8%. As mentioned earlier, Nu uncertainty depended primarily on the difference between the air temperature and the liquid crystal temperature. The variations in uncertainty shown in *Table* 1 resulted primarily from day-to-day variations in inlet air temperature. $\mathrm{Re}_{d,in}$ is included in the table for discussion of the stagnation point heat transfer. An inlet Reynolds number based on axial chord can be calculated from this by multiplying by $C_x/d=7.04$.

Baseline Case. **Figure 5** shows the measured and predicted Nusselt number distribution at the nominal design flow condition of $\mathrm{Re}_{ex}=2.5\times10^6$, $PR=1.443$, and $\alpha=0$ deg. The rear portion of the pressure side data shows increasing values of Nu characteristic of turbulent flow. **Figure 4(*b*)** shows a favorable pressure gradient in this region, but **Fig. 4(*c*)** shows that the pressure gradient parameter, K, for this Reynolds number is at most 1.6×10^{-6} which is too low to expect flow relaminarization. **Figure 4(*b*)** also shows an adverse pressure gradient region downstream of $s\approx-0.1$. A local peak in Nu is seen corresponding to this region which may indicate incipient flow separation. The peak stagnation line heat transfer at $s=0.043$ is almost indistinguishable because of the strong effects of the very rapid transition at the beginning of the suction surface. Stagnation point heat transfer values will be examined in more detail after discussing the effects of Reynolds number.

On the suction surface, for $s>0.2$, downstream of the transition peak, Nu decreases as expected for fully turbulent flow. Midspan values of Nu decrease up to the geometric throat at $s=1.07$. Nu increases slightly after this in the uncovered turning region. The effect of the secondary flow is seen in **Fig. 5(*c*)** as departures of the 15% and 25% data from midspan data beyond $s\approx0.8$. Many of these effects can be attributed to the vortex structures described by Langston [30]. The passage vortex and the pressure-side leg of the horseshoe vortex approach the suction surface. Heat transfer is enhanced by the relatively cool secondary flow fluid impinging on

Table 1 Description of blade heat transfer cases

Case	$\mathrm{Re}_{C_x,ex}$	PR	α_{in}	$\mathrm{Re}_{d,in}$	$\frac{\delta_{in}}{0.5\cdot\text{span}}$	$M_{ex,is}$	Max Nu uncert
1	2,488,000	1.442	0.0°	213,822	0.283	0.742	4.5%
2	1,239,000	1.435	0.0°	105,448	0.313	0.738	4.4%
3	621,900	1.446	0.0°	53,761	0.347	0.745	5.5%
4	374,700	1.445	0.0°	33,160	0.370	0.745	5.0%
5	1,237,000	1.080	0.0°	114,938	0.310	0.333	4.8%
6	1,246,000	1.735	0.0°	100,859	0.317	0.923	4.7%
7	1,238,000	1.430	−5.0°	97,150	0.317	0.734	8.2%
8	1,241,000	1.441	+5.0°	123,789	0.307	0.741	7.6%

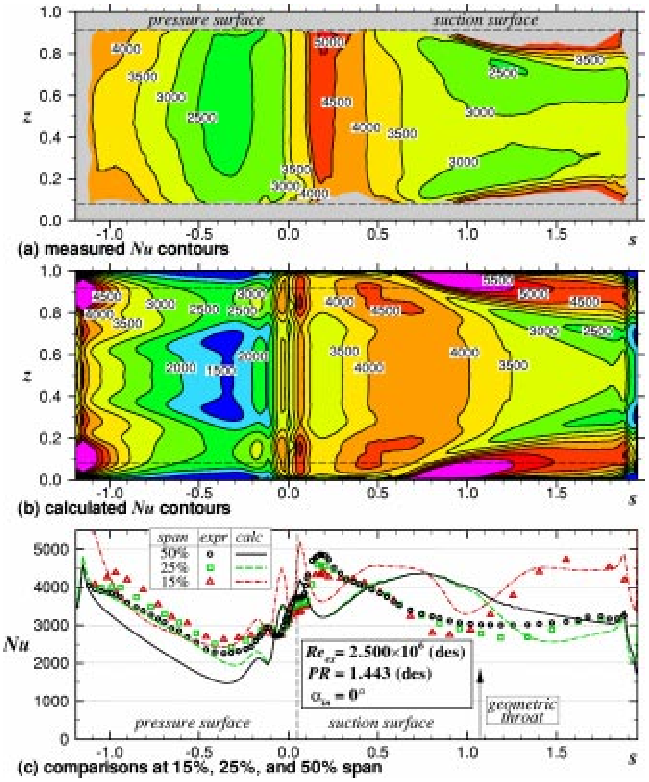

Fig. 5 Heat transfer distributions—Case 1

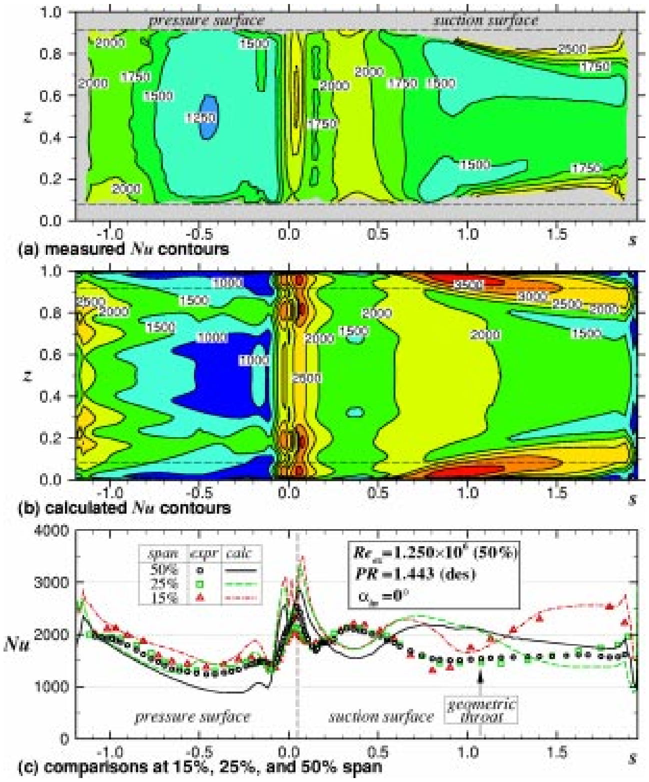

Fig. 6 Heat transfer distributions—Case 2

the endwall regions of the blade suction surface. The passage vortex and the pressure-side leg of the horseshoe vortex approach the suction surface. Heat transfer is enhanced by the relatively cool secondary flow fluid impinging on the endwall regions of the blade suction surface.

Effects of Reynolds Number. Data were obtained at exit Reynolds numbers that were nominally 50%, 25%, and 15% of the design value. Analysis of the data, particularly on the pressure surface, is aided by examination of the midspan pressure gradient parameter, K shown in **Fig. 4(*c*).**

Figure 6 shows the data obtained at 50% of the design Reynolds number and at the design pressure ratio and incidence angle. As expected, the rear half of the pressure surface appears to again be fully turbulent. The local peak just on the pressure surface side of the stagnation region is not as severe as it was for Case 1. The stagnation line near $s=0$ is much more evident for this case because the lower Reynolds number has caused the suction surface transition to move away from the stagnation region, appearing to begin at $s\approx 0.15$. Suction surface heat transfer rates decrease after the fully turbulent point at $s\approx 0.3$ again until reaching the throat at $s=1.07$. Values of Nu away from midspan are then seen to increase for the remainder of the suction surface. This increase can again be attributed to the secondary flows that are evident in **Fig. 6(*a*)**.

Data obtained at 25% of the design Reynolds number but again at the design pressure ratio and incidence angle are shown in **Fig. 7**. Recall that the maximum estimate of k^+ was 13.6. Because k^+ varies nearly linearly with Reynolds number, for $\mathrm{Re}\leqslant 25\%$ of the maximum value, the blade is expected to be hydraulically smooth everywhere. In contrast to the first two cases, the heat transfer distribution on the pressure surface now appears to be quite uniform. This is probably due to flow relaminarization because the pressure gradient parameter shown in **Fig. 4(*c*)** significantly exceeds 3.5×10^{-6}. Relaminarization at low Reynolds number was noted in a previous study (Giel et al. [9]) with some slightly

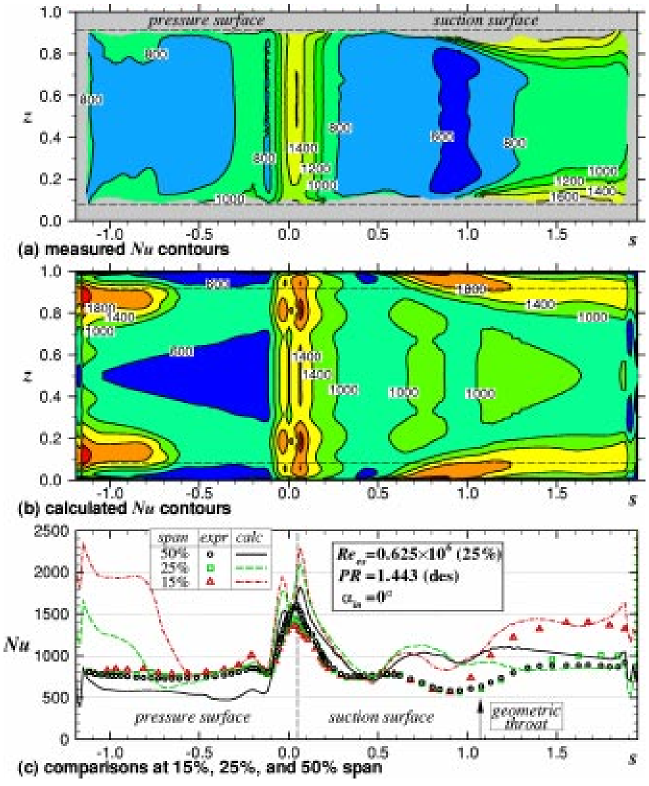

Fig. 7 Heat transfer distributions—Case 3

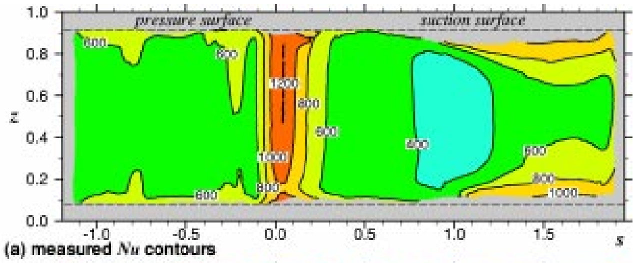

(a) measured *Nu* contours

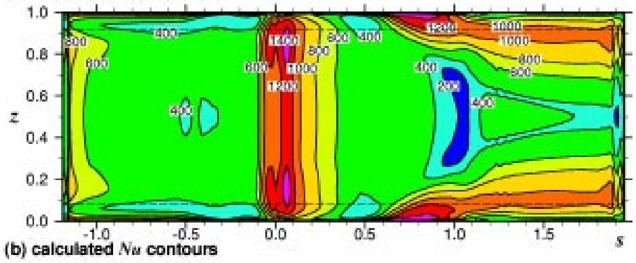

(b) calculated *Nu* contours

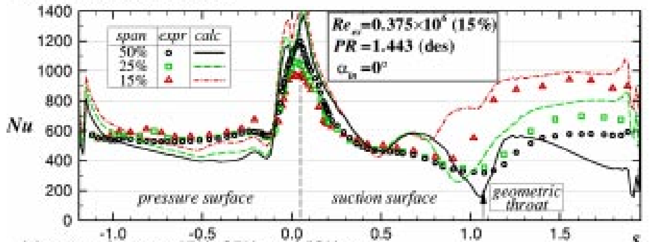

(c) comparisons at 15%, 25%, and 50% span

Fig. 8 Heat transfer distributions—Case 4

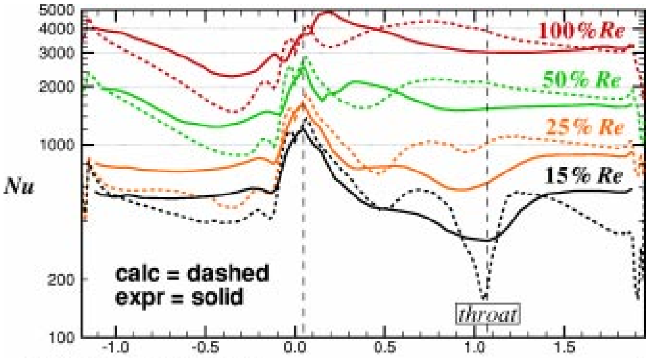

(a) 50% span comparisons

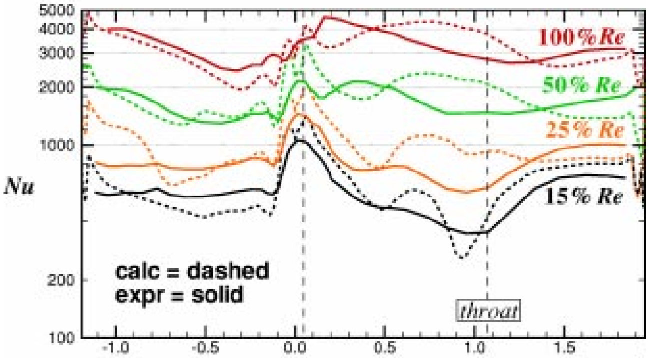

(b) 25% span comparisons

Fig. 9 Effects of Reynolds number on heat transfer

higher Reynolds number cases undergoing a second transition near the pressure surface trailing edge. This second transition does not seem to be evident in the present study. The local peak caused by the decelerating flow just downstream of the stagnation region is again less severe than for the higher Reynolds number cases. The stagnation line is very evident near $s \approx 0.04$. Despite the high inlet turbulence, the lower Reynolds number forces the suction surface transition to be delayed all the way to the point where the flow decelerates just upstream of the geometric throat. Transition then causes Nu values to increase and then level off for $s > 1.5$.

The final case showing the effects of variations in Reynolds number is shown in **Fig. 8**. The Reynolds number for this case is only 15% of the nominal design value. As for the 25% $Re_{Cx,ex}$ case, the heat transfer distribution on the pressure surface is quite uniform, again indicating relaminarization with no second transition. The local peak just downstream of the stagnation line is barely evident, and the stagnation line is clearly evident. Transition at midspan is delayed even further than for the 25% Re case with transition starting at the geometric throat location, $s = 1.07$. The overall contour plot in **Fig. 8(*a*)** and the 15% span data in **Fig. 8(*c*)** both show that the secondary flow effects are most significant for this case, presumably because the inlet boundary layer is 30% thicker than the design case as listed in Table 1.

The liquid crystal measurement technique is very helpful in obtaining full-surface contour plots. The data can be interpolated to obtain spatially detailed data for line plots through a subdomain as was done with the 15%, 25%, and 50% span data above. These line plots are very useful in comparing results at different flow conditions as is done in **Fig. 9** for variations in Reynolds number. Comparisons are made separately in the figure at 50% and 25% of span. Many of the comments made in the previous discussions are brought out here, particularly the pressure surface relaminarization effects for the 15% and 25% Re cases, the differences in the local peak heat transfer near $s \approx -0.1$, the stagnation point heat transfer, and the variations in suction surface transition location.

The data at the midspan stagnation points can be further analyzed by comparing the measured values to established data. Van Fossen et al. [29] studied stagnation region heat transfer on isolated elliptical leading edges. They developed the following correlation for a stagnation point turbulent augmentation factor:

$$\frac{Fr_{Tu}}{Fr_{lam}} = 0.00792\sqrt{Tu\, Re_d^{0.8}\left(\frac{\Lambda_x}{d}\right)^{-0.574}} + 1.0. \qquad (2)$$

The value of the constant in Eq. (2) was originally given by Van Fossen et al. [29] as 0.00851. Subsequently, Van Fossen [31] determined that the constant should be decreased to 0.00792. The lower value arose from a revision of the measured length scales. The leading edge of the blade corresponds to an ellipse with an aspect ratio of 1.5. Van Fossen et al. [29] gave a laminar Frossling number of 0.870 for this aspect ratio. The stagnation point data of

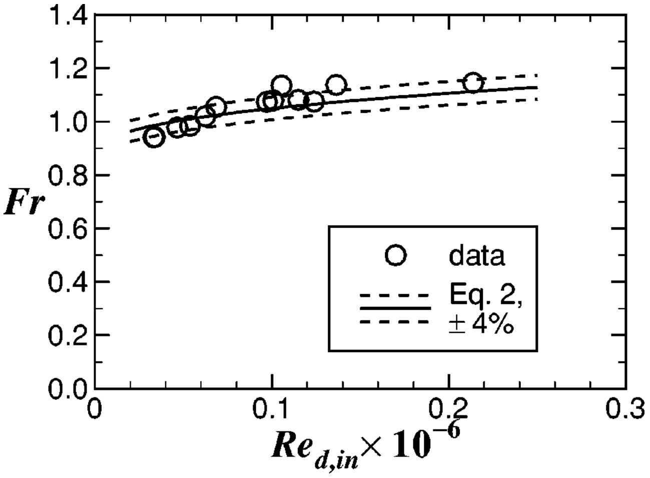

Fig. 10 Stagnation point heat transfer data and correlation

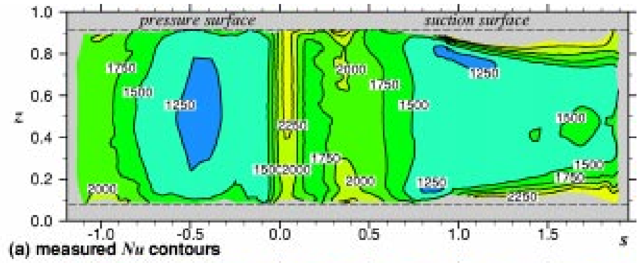

(a) measured Nu contours

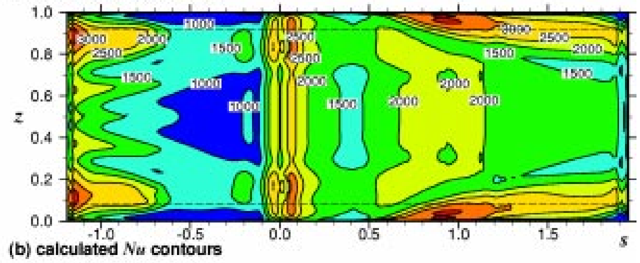

(b) calculated Nu contours

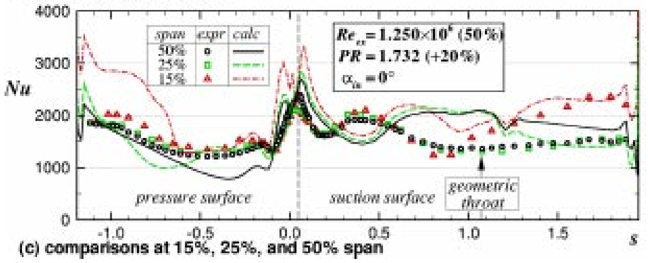

(c) comparisons at 15%, 25%, and 50% span

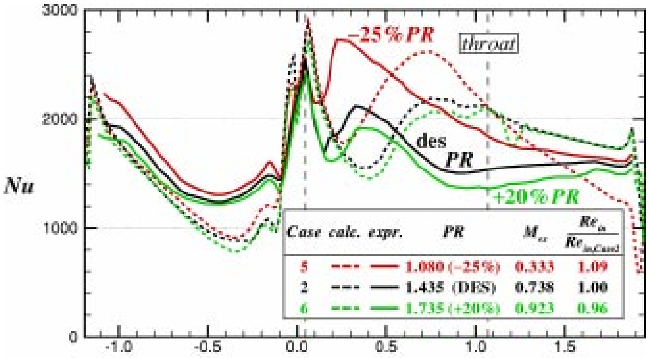

(a) 50% span comparisons

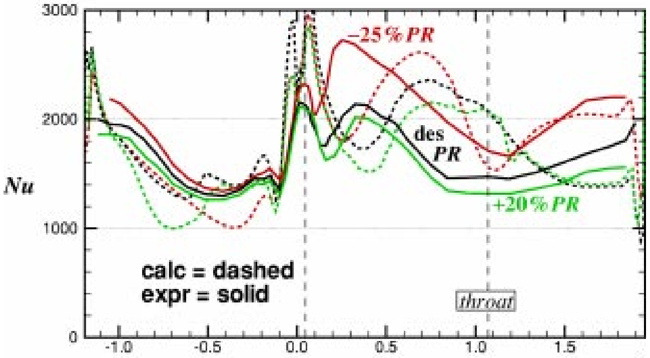

(b) 25% span comparisons

Fig. 11 Heat transfer distributions—Case 6

Fig. 12 Effects of pressure ratio on heat transfer

the current study are shown in **Fig. 10** along with Eq. (2) with $Tu = 0.13$ and $\Lambda_x/d = 3.14$. It was assumed that Λ_x was equal to Lu. Lines that are ±4% off of the correlation are also shown in the figure as was done in the original reference. Data from all cases obtained for this blade are shown in the figure, including some that are not described in detail in this report. **Figure 10** shows that the agreement with the correlation is good. Only a slight increase in inlet turbulence, or a decrease in length scale would improve the agreement even more.

Effects of Pressure Ratio. The isentropic exit pressure ratio was varied from −25% to +20% of the nominal design value of 1.443. The exit Reynolds number was held at 50% of the design value for these measurements because facility limits prevented lower pressure ratios at the 100% Re condition (see **Fig. 3**). The independent inlet and exhaust control of the facility allowed the nominal exit Reynolds number to be held fixed while varying the cascade pressure ratio. Because of compressibility effects, changes in the inlet Reynolds number were found to be small but not insignificant. Relative to the nominally fixed exit Reynolds number, Re_{in} changed +9.2% for a −25% change in PR and changed −4.9% for a +20% change in PR.

The results for Case 6 are shown in **Fig. 11**. Comparing this to Case 2 in **Fig. 6** shows the effects of an exit isentropic pressure ratio increase of 20%. On the fully turbulent pressure surface, those effects are relatively minor and are representative of the 4% decreases that are expected from Re_{in} changes of −5%. Differences on the suction surface are more significant because of the effect that the lower inlet Reynolds number has on transition near the stagnation point. This effect is seen most clearly in the midspan data comparison shown in **Fig. 12**. Transition is moved back on the suction surface and heat transfer levels are lower on the remainder of the blade. The midspan data of Case 5 at −25% PR are also shown in **Fig. 12**. Here again, the Nusselt number differences on the fully turbulent pressure surface of ≈+7% are consistent with the 9% increase in inlet Reynolds number. The suction surface transition start has moved correspondingly closer to the leading edge as expected. Note that the reduced pressure ratio has caused the peak heat transfer rate following transition to exceed that of the stagnation point. The midspan stagnation point data for all three of these cases are included in **Fig. 10**.

Effects of Incidence Angle. The primary effects of incidence angle variation are two-dimensional in nature, so full-span contour plots will not be shown for these cases. **Figure 13** compares the data obtained with +5 and −5 deg of incidence to those of design inlet flow angle, all at 50% of the nominal exit Reynolds number and at the nominal pressure ratio. In terms of surface distance, the total change in stagnation point location for inlet angle variations of ±5 deg is $\Delta s < 0.02$. The changes in heat transfer brought about by changes in inlet Reynolds number are again apparent. As seen in *Table* 1, relative changes in Re_{in} are significant; −7.7% for the −5 deg case and +17.2% for the +5 deg case. These changes affect the stagnation point heat transfer (also see **Fig. 10**). The pressure surface region just downstream of the stagnation region is affected directly by the change in inlet flow angle. Also on the pressure surface, the local heat transfer peak caused by the adverse pressure gradient region downstream of $s \approx -0.1$ is enhanced for the −5 deg case and almost eliminated for the +5 deg case. Near the pressure surface trailing edge, the measured Nu differences from the design data again tend to approach the differences expected for fully turbulent flow, i.e., about −6% for the −5 deg case and about +13% for the +5 deg case.

Differences in Nu on the suction surface again appear to be driven primarily by differences in Re_{in}. The higher inlet Reynolds number for the +5 deg case drives the transition location closer to the stagnation point while the lower inlet Reynolds number for the −5 deg case drives the transition location farther aft on the blade.

Computational Heat Transfer Results

The heat transfer predictions are discussed, first for the pressure surface, then for the leading edge region, and finally for the suction surface.

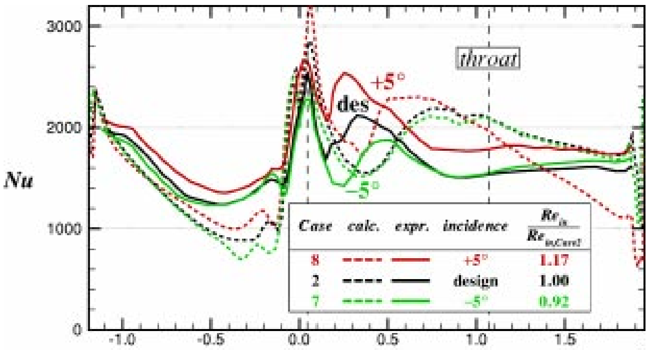

(a) 50% span comparisons

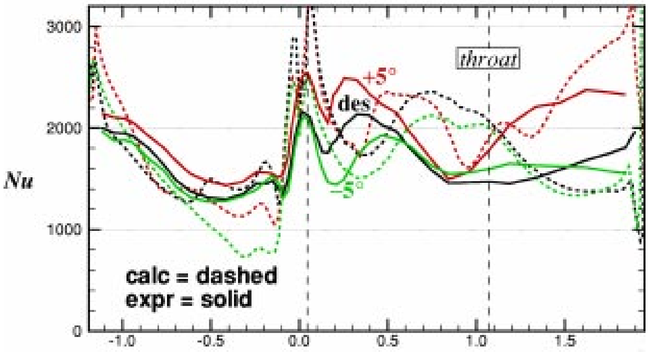

(b) 25% span comparisons

Fig. 13 Effects of inlet flow angle on heat transfer

Pressure Surface. At the highest Reynolds number, **Fig. 5** shows that pressure surface is turbulent almost everywhere. At mid and quarter span towards the rear of the pressure surface, data and analysis show higher Nusselt numbers than towards the rear of the suction surface. **Figure 5(*c*)** shows that the analysis agrees with the pressure surface data at 15% and 25% of span. At midspan the analysis underpredicts the pressure surface heat transfer. Since secondary flows near the blade pressure surface move towards the endwalls, the analysis appears to be overpredicting the pressure surface boundary layer thickness.

Figure 6 shows that the agreement with the data at 50% of design Reynolds number is somewhat better than the agreement shown in **Fig. 5**.

The data in **Fig. 7** show a very flat pressure surface heat transfer distribution. This is characteristic of laminar flow. **Figure 4(*c*)** shows that relaminarization was predicted at this Reynolds number. At midspan the analysis is somewhat lower than the data. It would be considerably lower if augmentation due to freestream turbulence was neglected. At midspan Nu would be less than 340 over much of the pressure surface. The underprediction near $s = -0.3$ illustrates a difficulty with the augmentation model. Along the pressure surface the pressure gradient is first favorable, then adverse, and then favorable again. The velocity gradient augmentation model gives μ_t augmentation only for favorable pressure gradients. Calculations were done where d in the equation for μ_t was replaced by the surface distance. Agreement with data was not improved, and the shape of the Nusselt number distribution was no longer flat. Because μ_t increased with distance, the Nusselt number distribution was similar in shape to those seen in **Figs. 5** and **6**. At the other two spanwise locations shown in **Fig. 7(*c*)** the agreement is good for the forward half of the pressure surface and poor for the rear portion of this surface. The data in **Fig.** 7(***a***) show increased heat transfer near the rear corners of the pressure surface. The analysis shows the same trend, but with a much higher increase in Nu. The reason for this behavior is not well understood. Here transition is not the cause of the high heat transfer. Relaminarization was predicted near $s = -0.5$ at mid and quarter span, although it was delayed until $s = -0.8$ near 15% of span. Variations in the relaminarization location would not account for the differences between mid and quarter span. They could be responsible for some of the differences between the 15% and 25% of span results. Augmentation due to freestream turbulence was not the cause of the high corner region heat transfer. Calculations done without augmentation showed similar heat transfer distributions.

Figure 8 shows that at the lowest Reynolds number, where K is well above the critical value, the pressure surface heat transfer is reasonably well predicted. Without augmentation, the predicted pressure surface heat transfer is less than 300 for $-0.8 < s < -0.45$.

Overall, while the augmentation model improves agreement with data, pressure surface heat transfer is underpredicted near adverse pressure gradient regions. But here the model is turned off. **Figures 5** and **6** show good agreement when the pressure surface boundary layer is mostly turbulent.

Figures 12 and **13** show only small variations in experimental pressure surface heat transfer resulting from variations in either pressure ratio or flow angle. At midspan, the predicted variations are close to what is expected from the Reynolds number variations. At the -5 deg flow angle the adverse pressure gradient is reduced, and computationally, the laminar region is extended. At 25% of span the analysis agrees with the data at the design condition. At off-design conditions the analysis is more likely to underpredict the data.

Leading Edge Region. The leading edge region is the region between $-0.01 < s < 0.03$. The predictions often show a double peak in the stagnation region. The double peak is the result of using U_{fs} instead of U_{in} to calculate μ_t. Near stagnation U_{fs} is much less than U_{in}. Because of the double peak, line plots with closely spaced peaks are less able than contour plots to illustrate differences between measurements and predictions. The contour plots show a single color for a range of Nu values, (500 in **Fig. 5**). Peaks and valleys will be in different bands if they differ by more than the range. The peak predicted heat transfer is higher than the data. The degree of agreement between the analysis and data is similar for all cases in the leading edge region. Calculations done using just the Smith and Kuethe [26] model gave leading edge region Nusselt numbers as high as the higher of the two peaks seen in the figures. This is not surprising in light of the results shown in **Fig. 10**, where the increase in the Frossling number is less than 30%. As discussed by Van Fossen et al. [29], correlations which are independent of length scale give augmentations in excess of 50% for the conditions seen in this experiment. Dullenkopf and Mayle [27] show that variations in the scale of turbulence can vary the turbulence augmentation by nearly a factor of three. These results indicate the necessity of including the scale of turbulence in models to predict the effects of turbulence on laminar heat transfer. Calculations with no augmentation due to turbulence underpredicted leading edge region almost as much as the Smith and Kuethe model for μ_t overpredicted the data.

Figures 9, **12**, and **13** show that at midspan the analysis agrees reasonably well with the data. The predictions are somewhat higher, but not excessively so. At 25% of span the analysis shows higher heat transfer than at midspan. The data show no significant spanwise variation. The analysis shows even higher heat transfer close to the endwalls. This is not seen in the data. However, the unheated region on the blade close to the endwalls could account for the absence of high heat transfer near the endwall. Overall, the analysis is higher than the data in this region. Assuming that the model for predicting leading edge turbulence effects is accurate, leads to the conclusion that the analysis should have been done with a lower inlet turbulence intensity. Alternatively, a model accounting for turbulence scale, might have given improved data agreement.

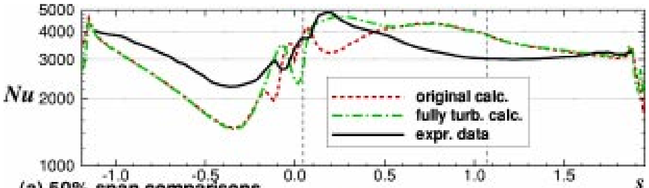

(a) 50% span comparisons

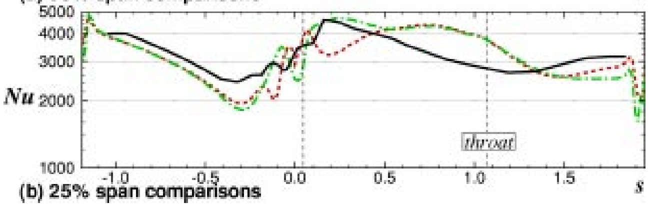

(b) 25% span comparisons

Fig. 14 Comparison with fully turbulent calculations—Case 1

Suction Surface. The data in **Fig. 5(*a*)** show high heat transfer just outside the leading edge region. Here, the highest heat transfer is seen at midspan. The midspan prediction shows a dip in the heat transfer, followed by a rise that exceeds the experimental data. This is followed by a decrease to the experimental values near the trailing edge. Transition is not complete in the analysis until $s \approx 0.4$. The resulting thin boundary layer gives higher heat transfer over much of the remaining part of the suction surface. The data are consistent with an abrupt suction surface heat transfer transition. Even though the measured arithmetic surface roughness of 6.5 μm is low, the Reynolds number is high. Boyle and Senyitko [32] investigated the effects of surface roughness on loss. They and Pinson and Wang [33] found that transition was initiated by low k^+ values. Boyle and Senyitko showed that the roughness transition length was short with respect to losses. They proposed a correlation to account for roughness transition, and a recommendation to determine the equivalent roughness height from the roughness measurement. Measurements indicated that the roughness transition could have occurred at the two highest Reynolds numbers. Transition would be fairly close to the leading edge, and much sooner than would be predicted using Mayle's smooth surface transition model. Although the roughness criterion was not incorporated into the three-dimensional heat transfer analysis, fully turbulent calculations were made. **Figure 14** compares data and calculations using the fully turbulent assumption. At this high Reynolds number there are very little history effects, and the predicted heat transfer in the turbulent region does not change. For $0 < s < 0.4$ the fully turbulent assumption gives better data agreement.

Figure 5(*c*) shows good agreement between predictions and data at 15% of span. As **Fig. 5(*b*)** shows, this is a region of both high heat transfer rates, and high heat transfer gradients. This region, mostly downstream of the throat, sees upwash from endwall flows. The good agreement in this region validates the basic three-dimensional Navier-Stokes approach. The flows are turbulent, so that modeling issues associated with transition and buffeted laminar flows do not influence the results.

Table 1 shows that, at $\mathrm{Re}_{ex} = 1.2 \times 10^6$, there are a range of inlet Reynolds numbers. The 17% increase in Re_{in} between Cases 2 and 8 represents about the same percentage increase in k^+. **Figure 15** compares data and fully turbulent predictions for Cases 2, 5, and 8. At the highest Re_{in} shown in **Fig. 15** an assumption of fully turbulent flow is appropriate. But, reducing the Reynolds number by 17% shows the smooth surface transition prediction to be more appropriate. As the Reynolds number, and thus k^+, is decreased, smooth surface transition is more appropriate.

Interestingly, the results in **Fig. 7** at 25% of the design Reynolds number imply that the start of transition occurred prematurely in the prediction. However, the augmentation model also influences the results. Without augmentation a minimum Nu of 600 is reached near $s = 0.35$, and rises to 1000 near $s = 1$. Transition occurred for $0.35 < s < 1.0$. Augmentation decreased linearly with increased intermittency. But here a linear relationship was not appropriate. **Figures 8(*b*)** and **8(*c*)** show accurate heat transfer predictions at the lowest Reynolds number. Here the behavior in the transition region is well predicted. The midspan predicted heat transfer over the last third of the suction surface is lower than the data. But, by 25% of span, the analysis slightly overpredicted the suction surface heat transfer.

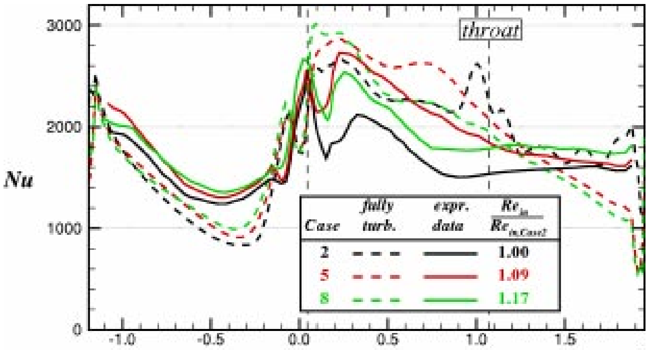

(a) 50% span comparisons

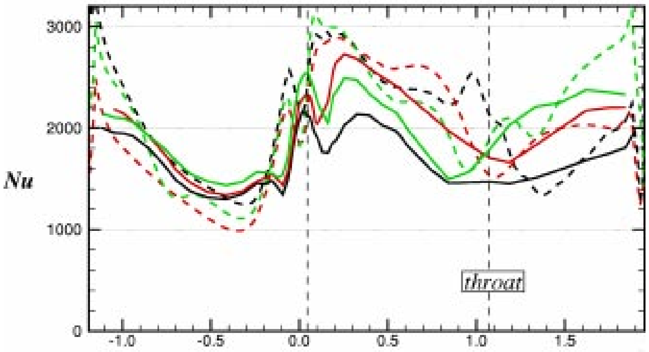

(b) 25% span comparisons

Fig. 15 Comparison with fully turbulent calculations—Cases 2, 5, and 8

For all Reynolds numbers the predicted and measured full span heat transfer show high Nu values near the endwalls for the rear half of the suction surface. In this region the agreement with data is very good.

Figures 14 and **15** show that, after the likelihood of tripping the boundary layer at the higher Reynolds numbers is accounted for, the analysis is in reasonably good agreement with the data. The change in heat transfer with changes in flow conditions is well predicted. **Figure 13(*b*)** shows a large increase in quarter span suction surface heat transfer at the higher inlet flow angle. This behavior is predicted by the analysis.

Summary and Conclusions

Detailed aerodynamic and heat transfer measurements and predictions were given for a power generation turbine rotor under engine specific conditions. The effects of variations in Reynolds number, exit pressure ratio, and incidence angle were quantified. The primary effect of Reynolds number variations in the range of 15% to 100% of the design value was to move the location of the laminar-to-turbulent transition on the suction surface and to drive relaminarization on the pressure surface at the lower Reynolds numbers. Variations in isentropic exit pressure ratio over a range of -25% to $+20\%$ were found to have little direct effect on the blade heat transfer, but an indirect effect was seen through the differences in inlet Reynolds number. Inlet flow angle variations of ± 5 deg affected a small adverse pressure gradient region downstream of the stagnation point and also affected the inlet Reynolds number which had an impact on the suction surface transition location. The data appeared to agree well with appropriate scaling laws and showed good agreement with a stagnation point heat transfer correlation.

The good spatial resolution due to the large scale and the liquid crystal measurement technique allowed the secondary flow effects to be clearly quantified. These secondary flows significantly increased suction surface heat transfer rates near the endwalls. The data also quantified the three-dimensional impact of laminar-to-turbulent transition on blade heat transfer. Good midspan symmetry was observed for all cases.

A goal of a CFD heat transfer prediction is to predict the data to within the uncertainty of the measurements. While these predictions showed most of the trends in the data, this goal was not met. At the two highest Reynolds numbers, suction surface transition start and length were not accurately predicted. Roughness measurements indicated that roughness could have caused the abrupt transition. Roughness should be considered in predicting heat transfer, especially at high Reynolds numbers. At the two lowest Reynolds numbers, suction surface transition was reasonably well predicted. The approach used to predict the effects of turbulence on laminar heat transfer tended to overpredict the heat transfer in the leading edge region and and to underpredict it on the pressure surface. Most likely this resulted from not including a turbulence scale effect in the augmentation modeling. Near midspan the analysis underpredicted the pressure surface heat transfer. Away from midspan the analysis was more likely to overpredict the heat transfer.

Acknowledgments

This work was conducted under Space Act Agreement FA-147 between NASA and the General Electric Corporation. It was supported by the NASA Glenn Research Center under contract NAS3-00145 with QSS Group, Inc. The assistance of Mr. Kevin Radil of the U.S. Army Vehicle Propulsion Directorate in measuring the surface roughness is gratefully acknowledged as is the support of Mr. Jason Morey of Syracuse University in digitizing the heat transfer data.

Nomenclature

A = heater area (m^2)
C_x = blade axial chord (mm)
d = leading edge diameter (mm)
Fr = Frossling number, $\mathrm{Fr} = \mathrm{Nu} \cdot (d/C_x)/\sqrt{\mathrm{Re}_{d,in}}$
h = heat transfer coefficient (W/m$^2 \cdot$K)
K = pressure gradient parameter, $K = (\mu/\rho U^2)(dU/ds)$
k = thermal conductivity (W/m$\cdot$K)
k^+ = normalized roughness height
Lu = turbulence energy length scale (mm)
M = Mach number
Nu = Nusselt number, $\mathrm{Nu} = h \cdot C_x/k$
P = pressure (Pa)
Pr = Prandtl number
PR = exit pressure ratio, $PR = P'_{in}/P_{ex}$
q'' = heat flux (W/m^2)
r = recovery factor, $r = \mathrm{Pr}^{1/3}$
Re_{ex} = Reynolds number, $\mathrm{Re}_{ex} = \rho U_{ex} C_x/\mu$
s = blade surface coordinate, normalized by C_x
T = temperature (K)
Tu = turbulence intensity
U = total velocity (m/s)
y^+ = equivalent normal distance
z = spanwise coordinate, normalized by blade span
α = relative incidence angle (degrees)
δ = 99% boundary layer thickness (mm)
Λ_x = longitudinal integral turbulence length scale (mm)
μ = dynamic viscosity (kg/s$\cdot$m)
μ_t = turbulent eddy viscosity (kg/s$\cdot$m)
ρ = density (kg/m^3)

Subscripts

aw = adiabatic wall temperature
fs = freestream inviscid value
lc = liquid crystal
ex = exit isentropic value
in = inlet freestream value
is = isentropic value

Superscripts

$'$ = total conditions

References

[1] Arts, T., Duboue, J.-M., and Roolin, G., 1998, "Aerothermal Performance Measurements and Analysis of a Two-Dimensional High Turning Rotor Blade," ASME J. Turbomach., **120**(3), pp. 494–499.
[2] Camci, C., and Arts, T., 1991, "Effect of Incidence on Wall Heating Rates and Aerodynamics on a Film Cooled Transonic Turbine Blade," ASME J. Turbomach., **113**(3), pp. 493–513.
[3] Baughn, J. W., Butler, R. J., Byerley, A. R., and Rivir, R. B., 1995, "An Experimental Investigation of Heat Transfer, Transition and Separation on Turbine Blades at Low Reynolds Number and High Turbulence Intensity," ASME Paper 95-WA/HT-25.
[4] Guenette, G. R., Epstein, A. H., Giles, M. B., Haimes, R., and Norton, R. J. G., 1989, "Fully Scaled Transonic Turbine Rotor Heat Transfer Measurements," ASME J. Turbomach., **111**, pp. 1–7.
[5] Graziani, R. A., Blair, M. F., Taylor, R. J., and Mayle, R. E., 1980, "An Experimental Study of Endwall and Airfoil Surface Heat Transfer in a Large Scale Turbine Blade Cascade," ASME J. Eng. Power, **102**, pp. 1–11.
[6] Blair, M. F., 1994, "An Experimental Study of Heat Transfer in a Large-Scale Turbine Rotor Passage," ASME J. Turbomach., **116**, pp. 1–13.
[7] Dunn, M. G., Kim, J., Civinskas, K. C., and Boyle, R. J., 1994, "Time-Averaged Heat Transfer and Pressure Measurements and Comparison With Predictions for a Two-Stage Turbine," ASME J. Turbomach., **116**, pp. 14–23.
[8] Giel, P. W., Van Fossen, G. J., Boyle, R. J., Thurman, D. R., and Civinskas, K. C., 1999, "Blade Heat Transfer Measurements and Predictions in a Transonic Turbine Cascade," ASME Paper 99-GT-125.
[9] Giel, P. W., Bunker, R. S., Van Fossen, G. J., and Boyle, R. J., 2000, "Heat Transfer Measurements and Predictions on a Power Generation Gas Turbine Blade," ASME Paper 2000-GT-0209.
[10] Joslyn, D., and Dring, R., 1992, "Three-Dimensional Flow in an Axial Turbine: Part 1—Aerodynamic Mechanisms," ASME J. Turbomach., **114**, pp. 61–70.
[11] Thulin, R. D., Howe, D. C., and Singer, I. D., 1982, "Energy Efficient Engine—High-Pressure Turbine Detailed Design Report," NASA CR-165608.
[12] Boyle, R. J., Lucci, B. L., and Senyitko, R. G., 2002, "Aerodynamic Performance and Turbulence Measurements in a Turbine Vane Cascade," ASME Paper GT-2002-30434.
[13] Giel, P. W., Thurman, D. R., Lopez, I., Boyle, R. J., Van Fossen, G. J., Jett, T. J., Camperchioli, W. P., and La, H., 1996, "Three-Dimensional Flow Field Measurements in a Transonic Turbine Cascade," ASME Paper 96-GT-113.
[14] Moffat, R. J., 1990, "Experimental Heat Transfer," *Proc. of the Ninth Int'l Heat Transfer Conf.*, Hemisphere, Washington, DC, **1**, pp. 187–205.
[15] Kline, S. J., and McClintock, F. A., 1953, "Describing Uncertainty in Single-Sample Experiments," Mech. Eng. (Am. Soc. Mech. Eng.), **75**(Jan), pp. 3–8.
[16] Schlichting, H., 1979, *Boundary-Layer Theory*, Seventh Ed., McGraw-Hill, New York, p. 714.
[17] Chima, R. V., and Yokota, J. W., 1990, "Numerical Analysis of Three-Dimensional Viscous Internal Flows," AIAA J., **28**(5), pp. 798–806.
[18] Chima, R. V., 1991, "Viscous Three-Dimensional Calculations of Transonic Fan Performance," AGARD Propulsion and Energetics Symposium on Computational Fluid Mechanics for Propulsion, San Antonio, Texas, May 27–31.
[19] Arnone, A., Liou, M.-S., and Povinelli, L. A., 1992, "Navier-Stokes Solution of Transonic Cascade Flows Using Non-Periodic C-Type Grids," J. Propul. Power, **8**(2), pp. 410–417.
[20] Boyle, R. J., and Giel, P. W., 1995, "Three Dimensional Navier-Stokes Heat Transfer Predictions for Turbine Blade Rows," J. Propul. Power, **11**(6), pp. 1179–1186.
[21] Chima, R. V., Giel, P. W., and Boyle, R. J., 1993, "An Algebraic Turbulence Model for Three-Dimensional Viscous Flows," AIAA Paper 93-0083 (NASA TM-105931).
[22] Mayle, R. E., 1991, "The Role of Laminar-Turbulent Transition in Gas Turbine Engines," ASME J. Turbomach., **113**, pp. 509–537.
[23] Steelant, J., and Dick, E., 1999, "Prediction of By-Pass Transition by Means of a Turbulence Weighing Factor—Part I: Theory and Validation," ASME Paper 99-GT-29.
[24] Boyle, R. J., and Simon, F. F., 1999, "Mach Number Effects on Turbine Blade Transition Length Prediction," ASME J. Turbomach., **121**, pp. 694–702.
[25] Solomon, W. J., Walker, G. J., and Gostelow, J. P., 1995, "Transition Length Prediction For Flows With Rapidly Changing Pressure Gradients," ASME Paper 95-GT-241.

[26] Smith, M. C., and Kuethe, A. M., 1966, ''Effects of Turbulence on Laminar Skin Friction and Heat Transfer,'' Phys. Fluids, **9**(12), pp. 2337–2344.
[27] Dullenkopf, K., and Mayle, R. E., 1995, ''An Account of Free-Stream, Turbulence Length Scale on Laminar Heat Transfer,'' ASME J. Turbomach., **117**, pp. 401–406.
[28] Ames, F. E., and Moffat, R. J., 1990, ''Heat Transfer with High Intensity, Large Scale Turbulence: The Flat Plate Turbulent Boundary Layer and the Cylindrical Stagnation Point,'' Department of Mechanical Engineering Report No. HMT-44, Stanford University, Stanford, CA.
[29] Van Fossen, G. J., Simoneau, R. J., and Ching, C. Y., 1995, ''Influence of Turbulence Parameters, Reynolds Number, and Body Shape on Stagnation-Region Heat Transfer,'' ASME J. Heat Transfer, **117**, pp. 597–603.
[30] Langston, L. S., 1980, ''Crossflows in a Turbine Cascade Passage,'' ASME J. Eng. Power, **102**, pp. 866–874.
[31] Van Fossen, G. J., 2003, personal communication.
[32] Boyle, R. J., and Senyitko, R. G., 2003, ''Measurements and Predictions of Surface Roughness Effects on Turbine Vane Aerodynamics,'' ASME Paper GT-2003-38580.
[33] Pinson, M. W., and Wang, T., 2000, ''Effect of Two-Scale Roughness on Boundary Layer Transition Over a Heated Flat Plate: Part 1—Surface Heat Transfer,'' ASME J. Turbomach., **122**, pp. 301–307.

Flow Field Computations of Combustor-Turbine Interactions Relevant to a Gas Turbine Engine

Sarah Stitzel[1]
Karen A. Thole

Mechanical Engineering Department,
Virginia Tech,
Blacksburg, VA 24061

The current demands for high-performance gas turbine engines can be reached by raising combustion temperatures to increase power output. High combustion temperatures create a harsh environment that leads to the consideration of the durability of the combustor and turbine sections. This paper presents a computational study of a flow field that is representative of what occurs in a combustor and how that flow field convects through the first downstream stator vane. The results of this study indicate that the development of the secondary flow field in the turbine is highly dependent on the incoming total pressure profile. The endwall heat transfer is also found to depend strongly on the secondary flow field. [DOI: 10.1115/1.1625691]

Introduction

The major contributions to the advances in gas turbine engine performance have been improvements in power output, reliability, and fuel efficiency. The current demands for increasingly higher performance while maintaining affordability and engine durability can be reached through the achievement of hotter combustion temperatures and better cooling schemes. To improve these cooling schemes for both the combustor and the turbine sections, an understanding of the flow field is needed. In particular, an understanding is needed as to how the combustor flow field impacts the heat transfer in the downstream turbine.

Secondary flows that develop in the turbine vane passage lead to detrimental heat transfer on the endwall. These secondary flows are dependent on the incoming radial pressure gradient along the vane span and on the inherent pitchwise pressure gradient between two adjacent airfoils. While past studies have assumed that the spanwise pressure gradient results from a simple turbulent boundary layer along the combustor liner, that assumption is not necessarily correct given the complexity of most combustor designs. The purpose of this research was twofold: to computationally model a nonreacting combustor in order to predict the resulting flow fields, and to determine the effect of these flow fields on the development of the secondary flows in the downstream turbine passage. In particular, one aspect that was investigated was the influence of a backward-facing slot relative to a flush interface between the combustor and turbine section. The uniqueness of this study exists in the fact that combustors and turbines have typically been treated as two independent systems.

Past Studies

For the idealistic case of a flat velocity profile with a simple isothermal turbulent boundary layer along the upstream platform, Langston [1] proposed an accurate representation of the secondary flows that develop in a turbine. A horseshoe vortex is formed by a downward turning of the flow as it approaches the vane leading edge. The pressure side leg of the horseshoe vortex turns into the passage vortex while the suction side leg of the horseshoe vortex is suppressed by the passage vortex as it convects through the passage.

The first studies to have simulated total pressure variations using those variations as the vane inlet conditions were by Schwab et al. [2] and Stabe et al. [3]. These two studies used a combustor exit radial temperature simulator (CERTS), which included circumferential cooling slots with no dilution holes. It was clearly identified from this study that changes occurred in the total pressure profile when using the CERTS as compared to not using the CERTS. Details are not available, however, for comparing any effects that the two different total pressure profiles had on the secondary flow field in the vane section.

Butler et al. [4] showed that the secondary flows within the first vane remained unaffected when the total pressure of the incoming flow was held constant between the cases having and not having a temperature distortion. This is consistent with the theoretical results of Munk and Prim [5], which showed that a constant total pressure leads to no changes in the streamline pattern. Shang and Epstein [6] and Hermanson and Thole [7] both showed computational verification that temperature gradients do not affect the secondary flow patterns in the stator vane section unless the total pressure field is altered.

A few studies have measured endwall heat transfer as a result of injection from a two-dimensional, flush slot just upstream of the vane. Early studies by Blair [8] and Granser and Schulenberg [9] reported measured adiabatic effectiveness levels for a range of blowing ratios. One of the key findings was that the endwall adiabatic effectiveness distributions showed extreme variations across the vane pitch with much of the coolant being swept across the slot toward the suction side corner, resulting in reduced coolant near the pressure side. Measured heat transfer coefficients by Blair [8] were similar between no slot and slot injection cases.

A series of experiments were reported for various injection schemes upstream of a nozzle guide vane with a contoured endwall by Burd and Simon [10], Burd et al. [11], Oke et al. [12], and Oke et al. [13]. In these studies coolant was injected from an interrupted, flush slot that was inclined at 45 deg just upstream of their vane. Similar to others, they found that most of the slot coolant was directed toward the suction side at low slot flow conditions. They also found that a two-dimensional slot was more effective at cooling the downstream vane platform than two rows of discrete film-cooling holes [13].

Kost and Nicklas [14] and Nicklas [15] combined an upstream slot with film-cooling holes in the downstream vane passage to examine the effects of each on the secondary flow field and platform heat transfer at transonic conditions. One of the most interesting results from this study was that they found for the slot flow alone, which was 1.3 percent of the core flow, the horseshoe vortex became more intense. They attributed the strengthening of the

---

[1] Present address: Techsburg, Inc., 2901 Prosperity Road, Blacksburg, VA 24060.

Contributed by the International Gas Turbine Institute and presented at the International Gas Turbine and Aeroengine Congress and Exhibition, Atlanta, GA, June 16–19, 2003. Manuscript received by the IGTI December 2002; final revision March 2003. Paper No. 2003-GT-38253. Review Chair: H. R. Simmons.

horseshoe vortex to the fact that for the no slot injection the boundary layer was separated with fluid being turned away from the endwall at the injection location.

The only studies involving a slot that was not flush with the endwall surface were the experimental studies reported by Colban et al. [16,17]. They combined the effects of upstream combustor film-cooling holes and slot flow from a backward-facing step. Their results indicated that as the liner film-cooling flow was increased, much of the coolant was transported up the vane surface and resulted in no additional benefit to the downstream turbine endwall.

Computational Methodology

For this study all of the computational fluid dynamics (CFD) simulations were done using a commercial code by Fluent, Inc. (1998). This software package utilizes pressure based flow solvers to model the mass, momentum, and energy conservation equations using either structured or unstructured meshes. All of the solutions were achieved with second-order discretization of the conservation equations. The pressure and velocity were coupled using the semi-implicit method for pressure-linked equations (SIMPLE) algorithm.

Fluent provides the capability of choosing between several turbulence models. Previous studies by Hermanson and Thole [7] of the same geometry used in this research provided a comprehensive turbulence benchmarking study employing the standard k-ε model (Launder and Spalding [18]), the renormalization group (RNG) k-ε model (Yakhot and Orszag [19]), and the Reynolds stress model (RSM) (Launder et al. [20]). Reasonable comparisons between predictions and experiments of the passage secondary flows were achieved using the RNG k-ε model with wall functions. Good agreement was also achieved with the RSM predictions, but the added computational expense was not warranted. Based on these findings and the fact that film cooling and secondary flow development were the primary interest for the study, the RNG k-ε model with nonequilibrium wall functions was used for these computations.

The computational models were all created using primarily tetrahedral mesh elements, with some hexahedral, pyramidal, and wedge elements. The quality of the meshes was determined by the cell skewness. The skewness gives a measure of how far a triangular or quadrilateral (two-dimensional) or tetrahedron (three-dimensional) is from its perfect form, where perfect form is defined as equilateral. A skew of zero is perfect and one is poor. For this model the mesh surface skew was kept below 0.75, with an average value of 0.3. The interior volumetric skew was kept below 0.85 with an average value of 0.4. For all the cases studied grid adaptions were based on three main quantities; velocity gradient, wall unit, and turbulent kinetic energy. Grid independence of a given case was judged based on two main parameters: the total pressure loss at several locations through the combustor and downstream, and adiabatic effectiveness values, η, on the combustor liner. For the combustor model containing a quarter sector (half turbine vane pitch) the change in the total pressure loss was less than 8.5 percent between a grid size of 8×10^5 as compared to 1.1×10^6 cells. The change in the average effectiveness levels just downstream of the dilution holes was less than 1.2 percent between the grids having 8×10^5 and 1.1×10^6 cells. A 9×10^5 cell mesh was considered grid independent for these studies. The final mesh on the vane portion of the domain was created using the grid from Hermanson and Thole [7]. The final mesh sizes, summarized in Table 1, are a combination of the vane grid size plus a full turbine vane pitch.

For all cases computed, the convergence criteria was set such that the residuals decreased by four orders of magnitude for all equations except energy in which the residuals decreased by seven orders of magnitude. Each computation was continued 50–100 iterations beyond convergence to ensure that the residuals continued to decrease steadily and that the solution was actually converged. The vane no-slot case required approximately 950 iterations to reach convergence and took approximately 95 hours (four days) running on four processors. The slot cases required approximately 200–300 more iterations than the no-slot cases to reach convergence. The computations were made on either an SGI Origin 2000 or an SGI Origin 2100 on four parallel processors to increase the speed per iteration.

Table 1 Flow conditions for the three cases studied

Case	1	2	3
Cooling hole geometry	Axial	Axial	Compound
Cells	2.3 million	2.5 million	2.5 million
Domain	1 pitch	1 pitch	1 pitch
	Exit Mass Flow (%)		
Inlet	55		53.6
Dilution 1 top/bottom	8.75/8.75		8.75/8.75
Dilution 2 top/bottom	8.75/8.75		8.75/8.75
Panels 1, 4	1.5/1.5		1.5/1.5
Panels 2, 3	3.5/3.5		3.5/3.5
Exit slot	0/0		0.7/0.7

Boundary Conditions and Test Cases

Three different test cases were modeled in an attempt to understand the effects of the important characteristics of the combustor geometry on the exit flow field and on the endwall secondary flow field. These cases, along with the particular flow conditions, are summarized in Table 1 with the geometrical features indicated in Figs. 1(*a*) and 1(*b*). The computational domain for the vane and

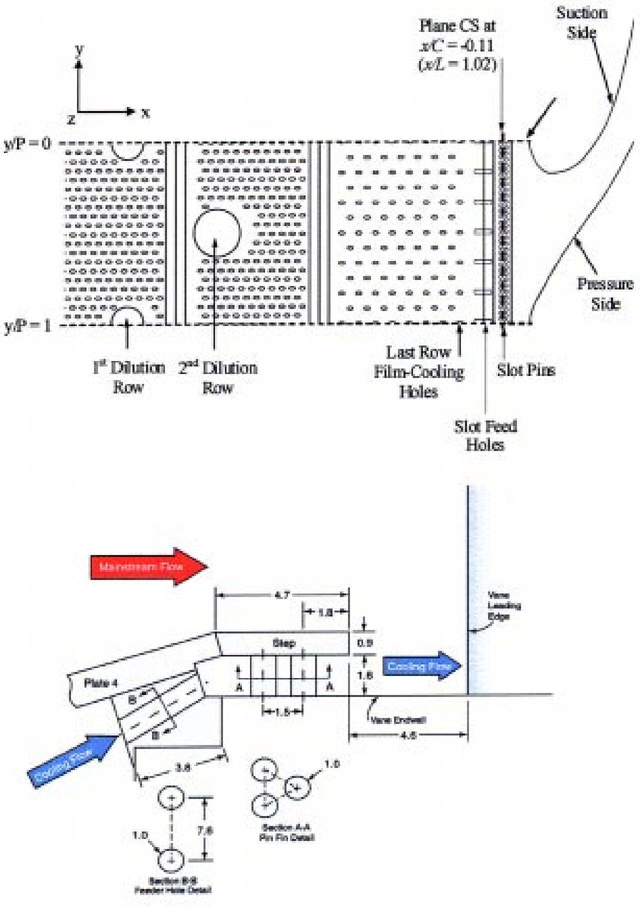

Fig. 1 (**Color online**) **Illustration showing layout for the film-cooling holes and dilution holes relative to the vane location**

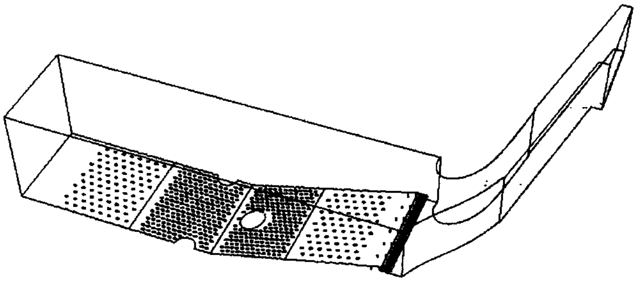

Fig. 2 Schematic of computational domain for a full pitch combustor model for Case 2 with the slot

combustor are shown in Fig. 2. These cases differed from each other only in the geometry of the combustor cooling scheme. The baseline case (Case 1) included film cooling and dilution jets. Case 2 contained film cooling and dilution with an exit slot at the combustor-vane interface. Case 3 included film cooling, dilution, and the exit slot, but with film-cooling holes that were oriented with a 45 deg compound angle in addition to the 30 deg inclination. This compound angle was such that the coolant flow is injected in the same direction as that of the turbine vane. Note that Case 2 had a slightly lower contraction angle (15.5 deg) in the combustor section relative to the baseline case (contraction angle of 17.2 deg). This higher contraction angle was necessary to account for the height of the step. The computational models of the slot cases (Cases 2 and 3) included seven slot feed holes and 52 slot pin fins. The vane stagnation was located 3.6 slot step heights downstream of the trailing edge of the last combustor liner panel.

The inlet boundary conditions to the combustor were set to the proper constant velocity to ensure the correct mass flow rate through the turbine vane giving an exit vane $\mathrm{Re}=1\times10^6$. An outflow boundary condition was used at 1.5 chord lengths downstream of the vane trailing edge. An additional 0.1 chord length was added to the boundary in the streamwise direction to avoid highly skewed cells at the outflow. Symmetry conditions were applied at the midspan while side boundaries were periodic. All surfaces were assumed to have adiabatic boundary conditions. To reduce the mesh size, a velocity boundary condition was applied at the exit of the film-cooling holes. This boundary condition was determined by simulating a single film-cooling hole and plenum with the same momentum flux ratio. The resulting velocity field computed at the inlet of the single hole simulation was applied to all of the film-cooling holes in the liner panels having that same momentum flux ratio (note that the mass flow was conserved through each hole). Each cooling hole contained 144 cells across the surface, giving 1700 cells in the entire hole. A constant mass flow was applied across the inlets for the dilution jets and slot feed holes.

Comparison of Predictions and Measurements

The computations presented in this paper were made for comparison purposes to large-scale experiments using a nonreacting combustor simulator as described by Barringer et al. [21] and Colban et al. [16,17]. Complete measurements of the near wall flows exiting an actual combustor are nearly impossible to obtain in an operating engine. For this purpose, a facility was designed to simulate the geometry and flow conditions of an early design of a prototypical aeroengine combustor with these values being provided by industry (Soechting and Cheung [22]). The purpose of making this facility large scale (9×) was to allow for good spatial measurement resolution. The stator geometry that was placed in a linear cascade has been described in numerous previous studies (Kang and Thole [23]; and Radomsky and Thole [24,25]). The vane was also scaled up by a factor of 9.

As a first step in the computational study, benchmarking of the CFD results against experimental data was done for Case 2, including axial film cooling slots, dilution jets, and exit slot. Comparisons will be made to the measured endwall surface temperatures as described by Colban [16,17]. Endwall surface temperature measurements were taken with an infrared camera and presented as adiabatic effectiveness values.

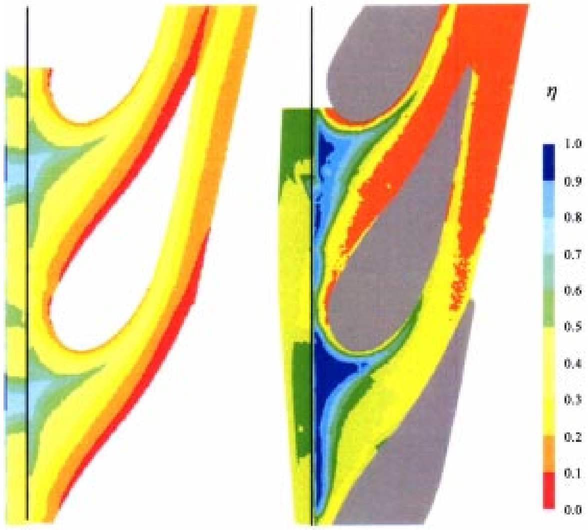

Fig. 3 (Color online) **Comparisons of surface adiabatic effectiveness contours for Case 2 with the slot (*a*) predicted using CFD and (*b*) experimentally measured (Colban and Thole [16])**

The surface temperature measurements in Fig. 3 show that CFD predicts slightly higher temperatures as compared with the experimental results near the suction surface. The overall results, however, show reasonable agreement, particularly in the critical regions at the leading edge with a warm ring around the vane. The laterally averaged adiabatic effectiveness values through the passage are shown in Fig. 4 where $X/C=0$ is located on the downstream slot edge. The largest differences between the experimental and computational results are seen upstream of the vane where cooler temperatures were measured relative to those predicted. Through the passage the difference between the computational and experimental results is less than 5 percent, which we found to be reasonable agreement.

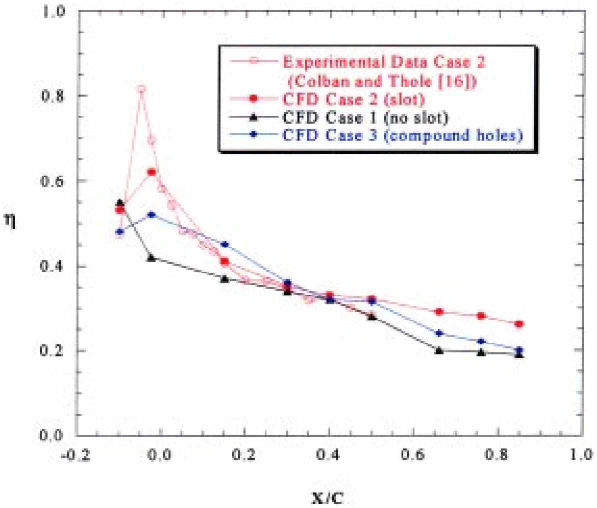

Fig. 4 (Color online) **Comparisons of laterally averaged adiabatic effectiveness through the vane passage computationally predicted and experimentally measured**

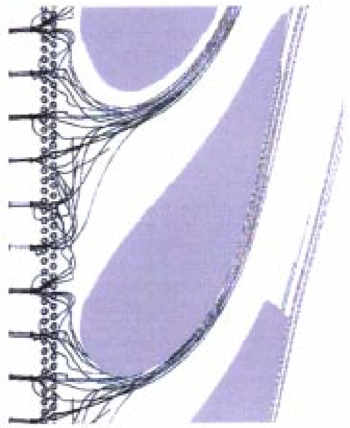

Fig. 5 (Color online) Streamlines released from slot feed holes around vane for Case 2 with a slot

Effects of Exit Slot on Flow Fields

This section will present a discussion of the effects of the slot flow on the combustor exit profile and downstream effectiveness for the no-slot injection (Case 1) and the slot injection (Case 2). Although the coolant available has increased due to the slot for Case 2 relative to Case 1, it is still valuable to compare the effects that the stepped slot has on the overall flow field as well as cooling performance. In addition, comparisons will be made to previous computational results published by Hermanson and Thole [7] for a turbulent boundary layer along the platform approaching the same vane geometry.

Prior to making the secondary flow comparisons, it is important to recognize the dynamics of the slot flow. Figure 5 shows path lines of the flow exiting the slot. Many of these streamlines indicate a flow reversal into the slot. This flow reversal for the slotted juncture is caused by the fact that there is a much lower total pressure in the slot flow as compared with the flow above the step. The blowing ratio for the slot is quite low at $M=0.24$. Ingestion of the mainstream gas into the slot greatly reduces the effect that the slot could have had on the endwall effectiveness. The endwall streamlines show that all of the flow from the slot was either drawn back under the slot or drawn towards the suction side of the vane.

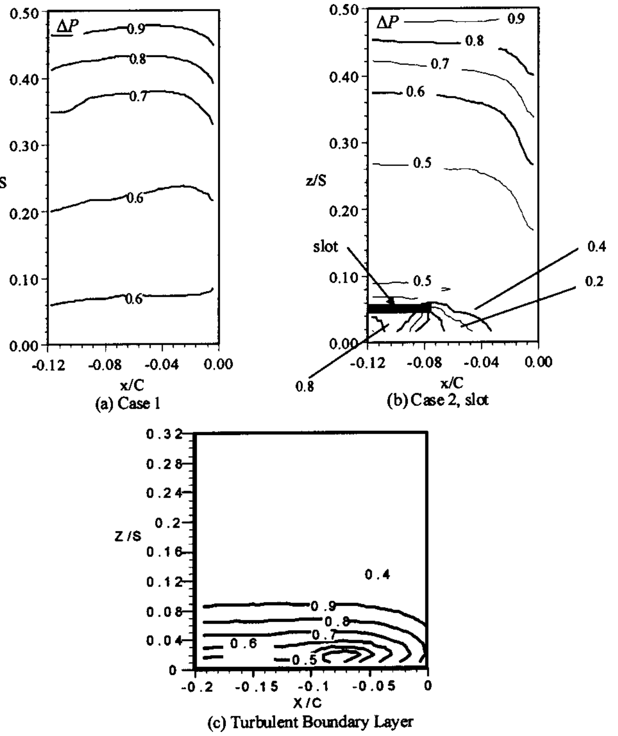

(a) Case 1

(b) Case 2, slot

(c) Turbulent Boundary Layer

Fig. 6 Total pressure contours in plane SP for (*a*) Case 1, (*b*) Case 2 with the slot and (*c*) an approaching turbulent boundary layer along the endwall [7]

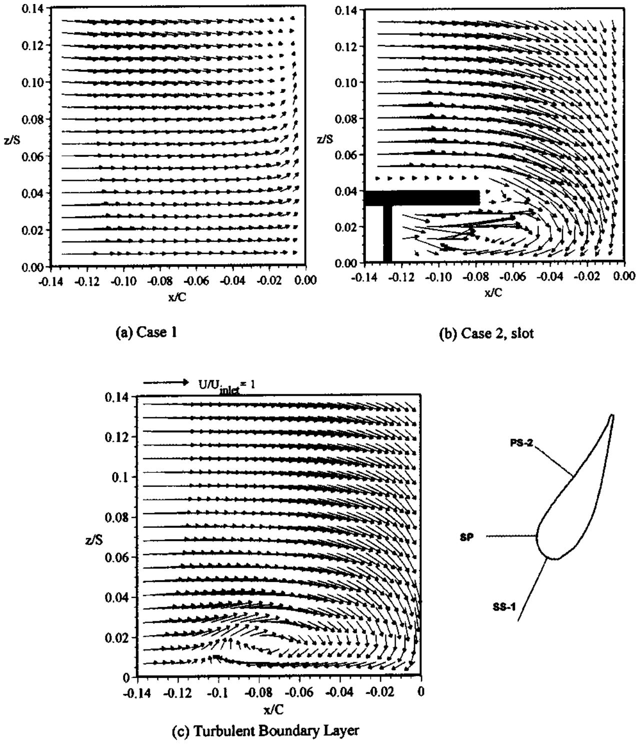

(a) Case 1

(b) Case 2, slot

(c) Turbulent Boundary Layer

Fig. 7 Velocity vectors in SP for (*a*) Case 1, (*b*) Case 2, and (*c*) turbulent boundary layer [7]

This flow ingestion can be explained by considering a comparison of total pressure profiles along the vane span in the stagnation plane for the no slot (Case 1) and slot case (Case 2) as compared to an approaching turbulent boundary layer along the platform [7]. These comparisons are shown in Figs. 6(*a*)–6(*c*). The maximum total pressure is located for all of the cases at the vane midspan decreasing towards the endwall. The differences between these cases are in the near endwall region. Case 1 shows an increase in the near-wall region due to the film approaching the vane. This pressure profile and its development as it moves through the vane passage had a distinct effect on the passage secondary flows. Case 2 with the slot shows this same peak due to the film-cooling flow just above the slot, but also shows a significant reduction in the total pressure under the slot. It is this lower total pressure that drives the flow from above the slot into the slot mixing out the slot coolant with a higher temperature gas.

Figures 7(*a*)–7(*c*) show the in-plane flow vectors in a plane that is aligned with the inlet flow direction at the vane stagnation location (plane SP) for the slot and no-slot cases as well as for an approaching turbulent boundary layer. For the turbulent boundary layer case, the leading edge vortex is centered at $x/C=-0.07$ and $z/S=0.015$. For the slot case this vortex was present at approximately the same location. For the no-slot case, however, there was no leading edge vortex that formed. The reason for no leading edge vortex is the fact that the approaching boundary layer has been energized such that there is a relatively flat total pressure profile approaching the vane. These patterns are consistent with what would be expected from the total pressure profiles in the stagnation plane, as shown in Figs. 6(*a*)–6(*c*).

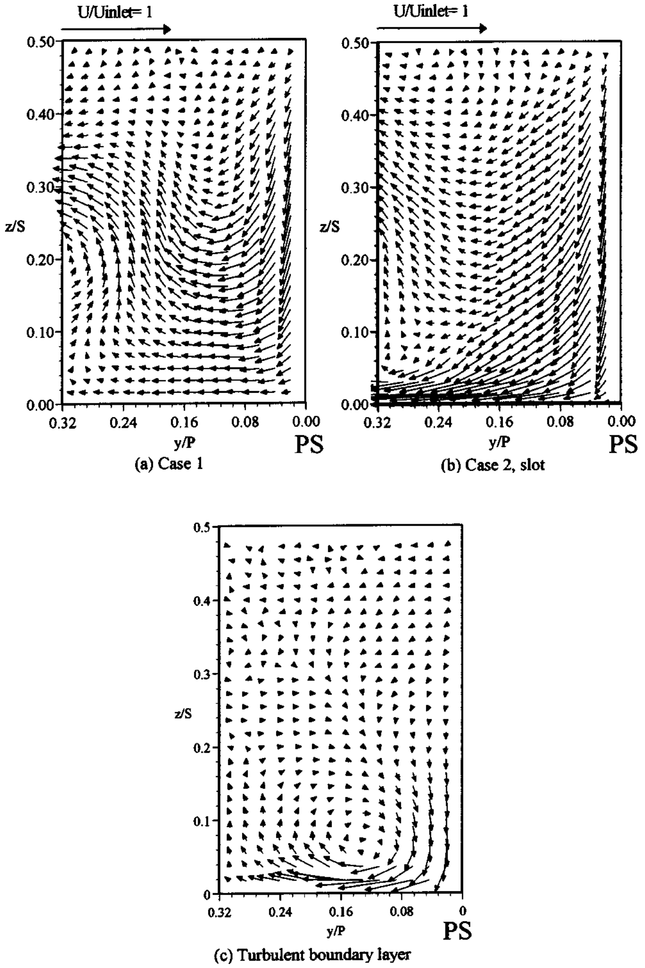

(a) Case 1

(b) Case 2, slot

(c) Turbulent boundary layer

Fig. 8 Secondary flow fields in PS-2 for (*a*) Case 1, (*b*) Case 2, and (*c*) an approaching turbulent boundary layer [7]

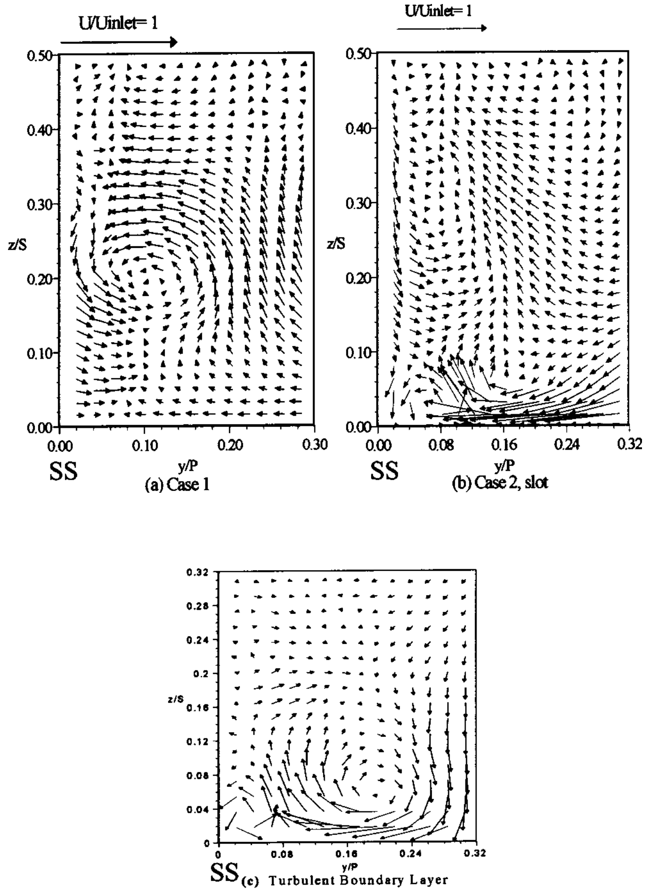

(a) Case 1

(b) Case 2, slot

(c) Turbulent Boundary Layer

Fig. 9 Secondary flow fields in SS-1 (*a*) Case 1, (*b*) Case 2 with the slot, and (*c*) an approaching turbulent boundary layer along the endwall [7]

Figures 8(*a*)–8(*c*) show a comparison of the secondary flows produced in a plane orthogonal to the pressure side of the vane (PS-2, as illustrated in Fig. 7). The case with the approaching turbulent boundary layer along the endwall produces a clear passage vortex centered at $z/S=0.06$ and $y/P=0.12$. In comparison with the turbulent boundary layer, Case 1 shown in Fig. 8(*a*) indicates a secondary flow pattern that is much different with two vortical patterns near $z/S=0.2$. These vortical patterns can be explained by the change in sign of the total pressure profile at the vane inlet [Fig. 6(*a*)]. There is a minimum in the total pressure near this same span location for Case 1, whereby the secondary flow pattern indicates flow towards this minimum total pressure region. For Case 2 with the slot, however, no complete passage vortex is present in plane PS-2. While similar spanwise motion occurs for both Cases 1 and 2 with downward flows along the suction surface, there is a much stronger velocity across the pitch for Case 2.

Figures 9(*a*)–9(*c*) show a comparison of the secondary flows produced in plane SS-1 for Cases 1 and 2 along with that for a case with the approaching turbulent boundary layer. Again, the secondary flow patterns for these three cases are significantly different. For the case with an approaching turbulent boundary layer, the remnants of the suction side leg of the horseshoe vortex are present as well as the passage vortex from the adjacent vane (this is in good agreement with the model by Langston [1]). For Case 1 with film cooling and no slot, there is a vortex with the same orientation as the suction side leg of the horseshoe vortex, but it is much removed from the endwall being located at $z/S=0.2$. There is no evidence of a vortex having the same orientation as the passage vortex for Case 1. Again this can be explained by the approaching endwall boundary layer being energized. For Case 2, the suction side leg of the horseshoe vortex was clearly visible at $y/P=0.05$, $z/S=0.03$ in plane SS-1 with downward motion along the suction surface. No distinct passage vortex was seen but a weak vortex at $z/S=0.28$ rotating in the opposite direction of a passage vortex was seen similar to Case 1.

The development of the flow through the passage in the near-wall region can be clearly visualized by looking at streamlines released upstream of stagnation at $x/C=-0.05$, as shown in Figs. 10(*a*) and 10(*b*) for Case 1 and Fig. 10(*c*) for Case 2 with the slot. For Case 1 the streamlines showed no secondary vortex development below 13 percent span and showed a slight downward motion along both the pressure and suction surfaces. Figure 10(*b*) shows streamlines released from 15–20 percent of the span for the no slot case at $x/C=-0.05$. The vortical motion centered at approximately 18 percent of the span that was seen in the vector plot in Fig. 9(*a*) can be seen here, whereas no secondary motion was seen in the near-wall streamlines. For Case 2 the path of the suction side horseshoe vortex in Fig. 10(*c*) could be clearly seen, with the streamlines colored by the spanwise velocity component. The flow traveled downward on the pressure side with no clear vortical motion consistent with the secondary flow vector plots. The strong cross-passage flows are clearly seen in the streamlines moving towards the adjacent vane near the endwall.

Effects of Film-Cooling Geometry

Film-cooling hole configurations for the liner of a combustor varies among the different combustor designs. The variation of the

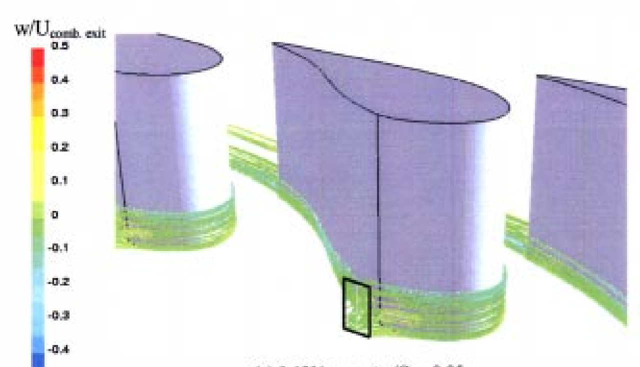

(a) 0-13% span at $x/C = -0.05$

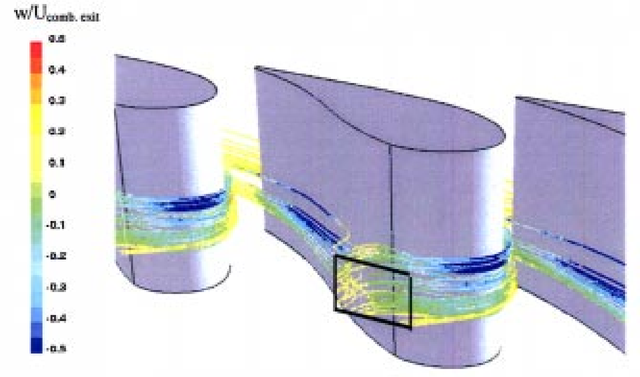

(b) 15-20% span at $x/C = -0.05$

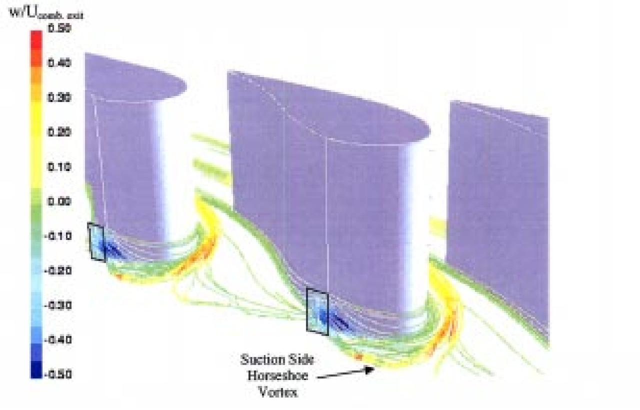

Fig. 10 (Color online) **Streamlines released for Case 1 (no slot) colored by $w/U_{\text{comb,exit}}$ from (*a*) 0–13 percent span and (*b*) 15–20 percent span. (*c*). Streamlines released at stagnation from 0 to 13 percent of the span at $x/C = -0.05$ for Case 2 with the slot colored by $w/U_{\text{comb,exit}}$.**

flow field as a result of having a compound angle on the film-cooling hole was predicted computationally for this study (Case 3). The effect of having a compound angle on the resulting, pitchwise-averaged total pressure profile exiting the combustor is shown in Fig. 11 in the stagnation plane. Figure 11 can be compared directly to the axial hole case in Fig. 6(*b*). The general pattern was the same with high pressure at the midspan and a low-pressure region under the slot. For Case 2 with the axial cooling holes, $\Delta P = 0.4$ occurred directly above the slot, while for the compound hole case the value on top of the slot increased to $\Delta P = 0.6$. The difference in ΔP in this region resulted from the film exiting the cooling holes. This larger total pressure for the compound holes is consistent with the fact that the flow exiting from a hole at a compound angle sees a larger resistance than flow exiting an axial hole and will therefore require a larger total pressure for injection at the same momentum flux ratio. In comparing the compound angle with that of the axial hole for the single hole computations under the same flow conditions, a 22 percent higher total pressure difference between the coolant and mainstream was required for the compound angle hole relative to the axial hole (note that this is relative to the freestream dynamic head). This caused a higher total pressure for the compound hole case above the step. The compound angle film cooling also had an impact on the secondary flow field since it changed the total pressure profile approaching the vane. Figures 12(*a*) and 12(*b*) show the secondary flow field for the compound angle case in planes PS-2 and SS-1, which can be directly compared with Case 2 results shown in Figs. 8(*b*) and 9(*b*). PS-2 flow fields were quite similar with strong motion downward along the vane surface and away from the vane along the endwall. One difference for the compound angled case is an upward motion at $y/P = 0.3$ that is not seen for the axial hole case.

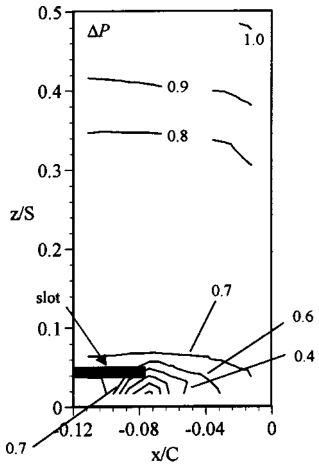

Fig. 11 Total pressure contours in plane SP for Case 3 with a slot and compound angle film-cooling holes

More noticeable differences were detected in the secondary flow fields along the suction side of the vane. The secondary flow field indicates that the suction side leg of the horseshoe vortex was clearly visible for both cases with the compound angle case showing a stronger vortex. The compound angle case also showed a distinct passage vortex located at $y/P = 0.12$ and $z/S = 0.2$ while the axial case did not. The axial case showed additional vortical

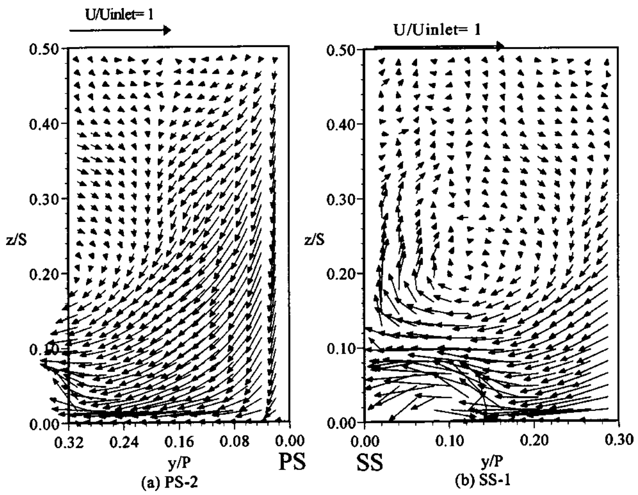

(a) PS-2 (b) SS-1

Fig. 12 Secondary flow fields for Case 3 with compound angle film-cooling and slot (*a*) plane PS-2 and (*b*) plane SS-1.

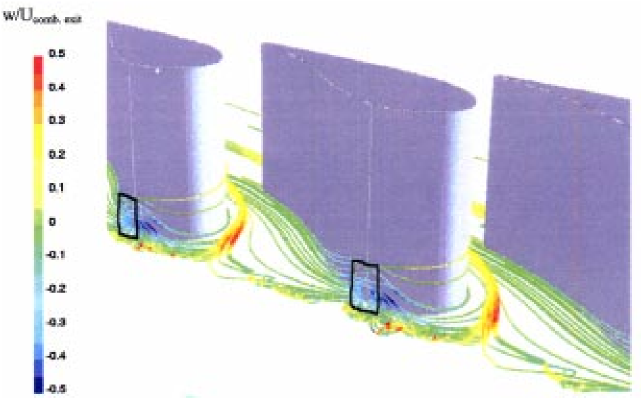

Fig. 13 (Color online) Streamlines released from 0–13 percent span at $x/C=-0.05$ for Case 3 colored by $w/U_{\text{comb,exit}}$.

motion in the opposite direction of the passage vortex at $y/P=0.08$ and $z/S=0.28$, which was not present for the compound angle case.

Streamlines released from 0–13 percent of the span at $x/C=-0.05$ are shown in Fig. 13 for Case 3, the compound angle case. The suction side horseshoe vortex is visible as well as the upward motion of the streamlines along the suction surface. The pressure side shows no vortical motion in the near-wall region and downward motion along the surface. These results indicate that in general the effect of the compound angle hole orientation on the secondary flow field was to create stronger vortical motion, particularly on the suction side. This could be attributed to the total pressure profile, which showed a larger pressure gradient in the near-wall region for the compound angle than for the axial cooling hole case.

Comparisons of Adiabatic Effectiveness Levels

The effects of these flow fields on the endwall effectiveness can be seen by looking at the effectiveness contours shown in Figs. 14(*a*)–14(*c*). The laterally averaged adiabatic effectiveness on the endwall for these cases was indicated in Fig. 4. Note that these effectiveness levels use the mass-averaged temperature as the reference temperature for the freestream. Using the mass-averaged temperatures (defined at the exit of the slot), which includes both the dilution and coolant flows, allows direct comparisons to be made between the cases.

For all of the cases, hot spots developed at the leading edge and along the pressure surface towards the trailing edge. For Case 2 with the slot, lower levels of effectiveness occurred at the leading edge and along the pressure side despite the additional coolant as compared with Case 1. Since Case 2 with the slot gave low total pressures near the endwall, the hot mainstream flow was convected downwards onto the endwall. Figure 4 indicates that the laterally averaged values for Case 2 showed increased effectiveness directly after the addition of the slot flow; however through the passage the average effectiveness for Cases 1 and 2 were nearly equal. The decrease in adiabatic effectiveness on the endwall for the compound angle (Case 3) is attributed to the increased secondary flow.

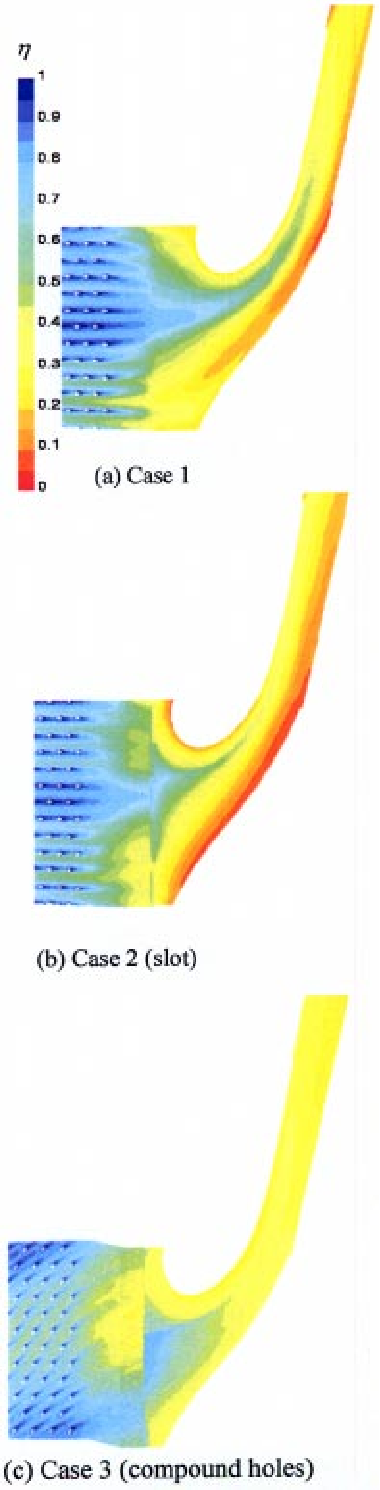

(a) Case 1

(b) Case 2 (slot)

(c) Case 3 (compound holes)

Fig. 14 (Color online) Endwall effectiveness contours for (*a*) Case 1 with no slot, (*b*) Case 2 with slot, and (*c*) Case 3 compound angled film-cooling holes and slot

Conclusions

The combustor-turbine junction has an important effect on the inlet profile for the turbine, particularly in the near-endwall region, which is often difficult to measure. Comparisons were made in this paper for cases with upstream film cooling on the liner panel of the combustor, with the same film cooling and the addition of a slot at the combustor-turbine juncture, and with compound angled film-cooling holes. These cases were compared with the typical assumption of having a two-dimensional, turbulent boundary on the approaching endwall. With the exit slot present the mainstream flow field remained the same as without the exit slot; however, significant changes in the near-wall region occurred. The slot flow produced a significantly low total pressure region from 0 to 5 percent of the span due to the deceleration of the slot flow as it exited the feed holes and pin fin arrangement. In addition, ingestion of mainstream fluid into the slot was predicted.

While the slot introduced additional coolant along the wall, thereby increasing the average adiabatic effectiveness just downstream of the combustor exit, an overall reduction in endwall temperatures further downstream along the endwall were not predicted. This reduction in endwall temperatures was not present due to the secondary flow fields that were predicted to be much stronger for the case with the slot than for the no-slot case.

Changing the orientation of the film-cooling holes from an axial to a compound angle with the turning in the same direction as the vane had a smaller impact on the combustor exit profile than the effect of the slot. The flow exiting the compound angle holes had a higher total pressure than the flow exiting the axial holes. This led to a total pressure profile at the combustor exit for the compound angle case with a higher total pressure over the entire span as compared to the axial case. The compound holes showed a slightly decreased adiabatic effectiveness along the vane endwall due to the stronger secondary flows relative to the axial cooling hole case.

These results all lead to the conclusion that it is a poor assumption to conduct turbine vane flow field studies with a two-dimensional turbulent boundary layer as the incoming condition. A realistic combustor, such as the one studied here, will exhibit a three-dimensional exit flow field with nonuniformities in temperature, pressure, and velocity in both the radial and circumferential directions. Making small changes in the cooling scheme and geometry affect the combustor exit profiles, thereby affecting the vane secondary flow pattern.

Acknowledgment

The authors would like to acknowledge Pratt & Whitney for their support.

Nomenclature

C = true chord of stator vane
D = film cooling hole or slot feed hole diameter
L = combustor length
M = mass flux ratio $= \rho_{\text{jet}} V_{\text{jet}} / \rho_\infty V_\infty$
Ma = Mach number
p_0 = total pressure
P = pitch
Re = Reynolds number $= C U_{\text{exit}} / \nu$
S = span
T, T_{aw} = static and adiabatic temperatures
T_{jet} = coolant temperature
U, V, W = absolute velocity components
u, v, w = local flow plane, transformed velocity components
x, y, z = local coordinate system
X, Y, Z = global, stationary coordinate system
η = adiabatic effectiveness $= (T_{\text{aw}} - T_{\text{ave}})/(T_{\text{jet}} - T_{\text{ave}})$
ΔP = normalized total pressure $= 1 - (p_{0,\max} - p_0)/(p_{0,\max} - p_{s,\min})$

Subscripts

ave = mass-averaged value
exit = exit value at midspan
inlet = inlet value at midspan
0 = stagnation value
∞ = freestream value

References

[1] Langston, L. S., 1980, ''Crossflows in a Turbine Cascade Passage,'' J. Eng. Power, **102**, pp. 866–874.
[2] Schwab, J. R., Stabe, R. G., and Whitney, W. J., 1983, ''Analytical and Experimental Study of Flow through and Axial Turbine Stage with a Nonuniform Inlet Radial Temperature Profile,'' AIAA paper no. 83-1175.
[3] Stabe, R. G., Whitney, W. J., and Moffitt, T. P., 1984, ''Performance of High-Work Low-Aspect Ratio Turbine Tested with a Realistic Inlet Radial Temperature Profile,'' AIAA paper no. 84-1161.
[4] Butler, T. L., Sharma, O. P., Joslyn, H. D., and Dring, R. P., 1989, ''Redistribution of an Inlet Temperature Distortion in an Axial Flow Turbine Stage,'' J. Propul. Power, **5**, pp. 64–71.
[5] Munk, M., and Prim, R. C., 1947, ''On the Multiplicity of Steady Gas Flows Having the Same Streamline Pattern,'' Proc. Natl. Acad. Sci. U.S.A., **33**, pp. 137–141.
[6] Shang, T., and Epstein, A. H., 1997, ''Analysis of Hot Streak Effects on Turbine Rotor Heat Load,'' J. Turbomach., **119**, pp. 544–553.
[7] Hermanson, K. S., and Thole, K. A., 2000, ''Effect of Inlet Conditions on Endwall Secondary Flows,'' J. Propul. Power, **16**, pp. 286–296.
[8] Blair, M. F., 1974, ''An Experimental Study of Heat Transfer and Film Cooling on Large-Scale Turbine Endwalls,'' J. Heat Transfer, pp. 524–529.
[9] Granser, D., and Schulenberg, T., 1990, ''Prediction and Measurement of Film Cooling Effectiveness for a First-Stage Turbine Vane Shroud,'' ASME paper no. 90-GT-95.
[10] Burd, S. W., and Simon, T. W., ''Effects of Slot Bleed Injection over a Contoured Endwall on Nozzle Guide Vane Cooling Performance: Part I: Flow Field Measurements,'' ASME paper no. 2000-GT-199.
[11] Burd, S. W., Satterness, C. J., and Simon, T. W., 2000, ''Effects of Slot Bleed Injection over a Contoured Endwall on Nozzle Guide Vane Cooling Performance: Part II Thermal Measurements,'' ASME paper no. 2000-GT-200.
[12] Oke, R., Simon, T., Burd, S. W., and Vahlberg, R., 2000, ''Measurements in a Turbine Cascade Over a Contoured Endwall: Discrete Hole Injection of Bleed Flow,'' ASME paper no. 2000-GT-214.
[13] Oke, R., Simon, T., Shih, T. Zhu, B., Lin, Y. L., and Chyu, M., 2001, ''Measurements Over a Film-Cooled, Contoured Endwall with Various Coolant Injection Rates,'' ASME paper no. 2001-GT-140.
[14] Kost, F., and Nicklas, M., 2001, ''Film-Cooled Turbine Endwall in a Transonic Flow Field: Part I—Aerodynamic Measurements,'' ASME paper no. 2001-GT-0145.
[15] Nicklas, M., 2001, ''Film-Cooled Turbine Endwall in a Transonic Flow Field: Part II—Heat Transfer and Film-Cooling Effectiveness Measurements,'' ASME paper no. 2001-GT-0146.
[16] Colban, W. F., Thole, K. A., and Zess, G., 2002, ''Combustor-Turbine Interface Studies: Part 1: Endwall Measurements,'' ASME paper no. 2002-GT-30526.
[17] Colban, W. F., Lethander, A., T., Thole, K. A., and Zess, G., 2002, ''Combustor-Turbine Interface Studies: Part 2: Flow and Thermal Field Measurements,'' ASME paper no. 2002-GT-30527.
[18] Launder, B. E., and Spalding, D. B., 1974, ''The Numerical Computation of Turbulent Flows,'' Comput. Methods Appl. Mech. Eng., **3**, pp. 269–289.
[19] Yakhot, V., and Orszag, S., 1986, ''Renormalization Group Analysis of Turbulence: I. Basic Theory,'' J. Sci. Comput., **1**, pp. 1–51.
[20] Launder, B. E., Reece, G. J., and Rodi, W., 1975, ''Progress in the Development of a Reynolds-Stress Turbulence Closure,'' J. Fluid Mech., **68**, pp. 537–566.
[21] Barringer, M. D., Richard, O. T., Walter, J. P., Stitzel, S. M., and Thole, K. A., 2002, ''Flow Field Simulations of a Gas Turbine Combustor,'' J. Turbomach., **124**, pp. 508–516.
[22] Soechting, F. O., and Cheung, A., 1999, private communication.
[23] Kang, M., and Thole, K. A., 2000, ''Flowfield Measurements in the Endwall Region of a Stator Vane,'' J. Turbomach., **122**, pp. 458–466.
[24] Radomsky, R. W., and Thole, K. A., 2000, ''Flowfield Measurements for a Highly Turbulent Flow in a Stator Vane Passage,'' J. Turbomach., **122**, pp. 255–262.
[25] Radomsky, R., and Thole, K. A., 2000, ''High Freestream Turbulence Effects in the Endwall Leading Edge Region,'' J. Turbomach., **122**, pp. 699–708.

Effect of Blade Tip Geometry on Tip Flow and Heat Transfer for a Blade in a Low-Speed Cascade

Vikrant Saxena

Hasan Nasir

Srinath V. Ekkad[1]
Assistant Professor,
Mem. ASME
e-mail: ekkad@me.lsu.edu

Mechanical Engineering Department,
Louisiana State University,
Baton Rouge, LA 70803

A comprehensive investigation of the effect of various tip sealing geometries is presented on the blade tip leakage flow and associated heat transfer of a scaled up HPT turbine blade in a low-speed wind tunnel facility. The linear cascade is made of four blades with the two corner blades acting as guides. The tip section of a HPT first stage rotor blade is used to fabricate the two-dimensional blade. The wind tunnel accommodates an 116 deg turn for the blade cascade. The mainstream Reynolds number based on the axial chord length at cascade exit is 4.83×10^5. The upstream wake effect is simulated with a spoked wheel wake generator placed upstream of the cascade. A turbulence grid placed even farther upstream generates the required freestream turbulence of 4.8%. The center blade has a tip clearance gap of 1.5625% with respect to the blade span. Static pressure measurements are obtained on the blade surface and the shroud. The effect of crosswise trip strips to reduce leakage flow and associated heat transfer is investigated with strips placed along the leakage flow direction, against the leakage flow and along the chord. Cylindrical pin fins and pitch variation of strips over the tip surface are also investigated. Detailed heat transfer measurements are obtained using a steady-state HSI-based liquid crystal technique. The effect of periodic unsteady wake effect is also investigated by varying the wake Strouhal number from 0. to 0.2, and to 0.4. Results show that the trip strips placed against the leakage flow produce the lowest heat transfer on the tips compared to all the other cases with a reduction between 10–15% compared to the plain tip. Results also show that the pitch of the strips has a small effect on the overall reduction. Cylindrical pins fins and strips along the leakage flow direction do not decrease the heat transfer coefficients and in some cases enhance the heat transfer coefficients by as much as 20%.

[DOI: 10.1115/1.1643385]

Introduction

Turbine blade tip heat transfer has been a strong focus of ongoing studies recently. Turbine tips are exposed to a pressure driven leakage flow across the tip from the pressure side to the suction side of the blade. The leakage flow, although undesirable, cannot be eliminated. The leakage flow causes high heat load to the tip region and leads to oxidation and cracking resulting in blade failure and leading to significant losses in power and efficiency. However, it is impossible to eliminate the tip leakage flow between the blade and the stationary shroud, effort is focused on designing the blade tip region to reduce leakage flow and thus reduce overall heat load and delay failure initiation processes. Most of the effort is now focused on designing tip geometries that will reduce the leakage flow and heat transfer to the tip.

Bindon [1] and Morphis and Bindon [2] studied tip clearance loss, using a linear cascade under low-speed conditions, and concluded that the losses varied linearly with gap size. Using static pressure measurements and flow visualization, Bindon observed a separation bubble on the blade pressure edge that mixes with a high-speed leakage jet induced at midchord. The leakage flow was defined as sink-like on the pressure side and source-like on the suction side of the blade. Yaras et al. [3] also observed the presence of a separation bubble away from the leading edge and concluded that flow towards the leading edge had little effect on overall losses. In Yaras' study, a high-speed test rig was used.

Yamamoto [4] also found that leakage vortices were sensitive to incident angle and the blade tip gap height. Kaiser and Bindon [5] investigated various effects on tip leakage flow and associated losses in a rotating turbine rig.

Mayle and Metzger [6] investigated heat transfer on a two-dimensional rectangular tip with rotating and stationary shroud. They established that the effects of relative motion between a blade model and the shroud have negligible effects on heat transfer data. Metzger et al. [7] and Chyu et al. [8] investigated the effects of varying the recess depth on the tip heat transfer of a blade tip model. It was determined that tip heat transfer was reduced under the presence of a cavity. The cavity simulated the squealer tip geometry. Leakage flow was reduced until the depth reached $D/W=0.2$.

Metzger et al. [9] measured tip heat flux on a rotating turbine rig using multiple heat flux sensors. Yang and Diller [10] made discrete point measurements on the tip of a blade in a linear cascade under blowdown conditions using a single heat flux gage. Bunker et al. [11] published the first study with detailed blade tip heat transfer measurements on actual blade tips. The measurements were made for a first stage power generation blade using a steady-state liquid crystal technique. They varied the curvature of the blade tip edges (rounded and sharp). They found that the blade with a tip edge radius had greater leakage flow and higher heat transfer coefficients. Bunker et al. [11] also reported that an increase in free stream turbulence intensity increased the heat transfer coefficient. The authors observed an area of low heat transfer toward the blade leading edge, referred to as the sweet spot. Ameri and Bunker [12] used computational fluid dynamics (CFD) simulations to reproduce the results for the same blade geometry shown by Bunker et al. [11]. They concluded that the assumption of periodic flow was invalid for tip heat transfer calculations be-

---

[1] To whom correspondence should be addressed.

Contributed by the International Gas Turbine Institute and presented at the International Gas Turbine and Aeroengine Congress and Exhibition, Atlanta, GA, June 16–19, 2003. Manuscript received by the IGTI December 2002; final revision March 2003. Paper No. 2003-GT-38176. Review Chair: H. R. Simmons.

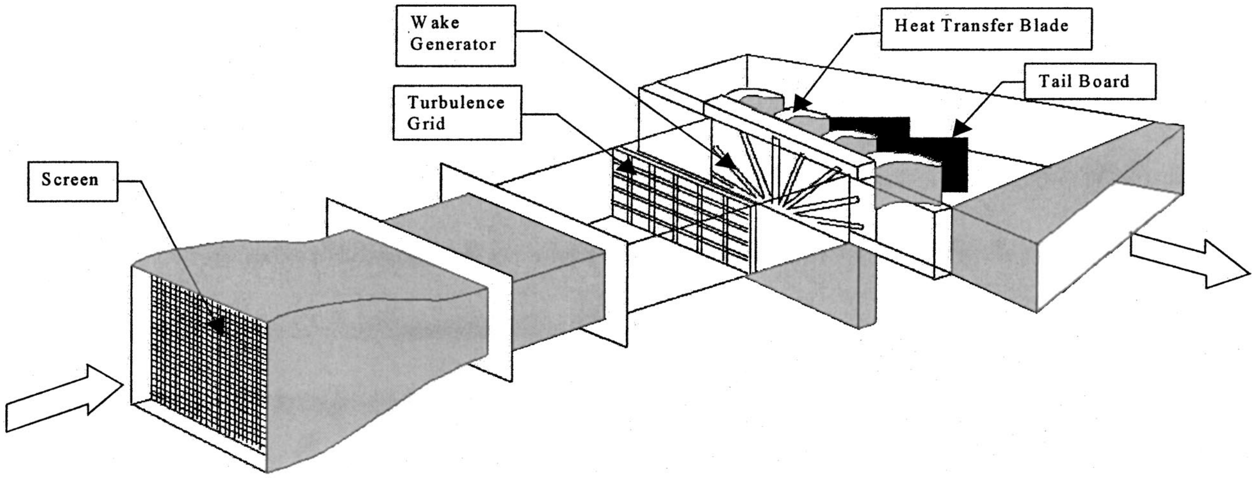

Fig. 1 Illustration of the low-speed cascade

cause the entire passage had to be modeled. Their numerical results for the radiused edge showed better agreement with the experimental data than that of the sharp edge.

Azad et al. [13] performed heat transfer investigation on blade tips in which three different tip clearance gaps ($C/H = 1,1.5,2.5\%$) were used. They used a GE-E^3 engine blade and a pressure ratio of 1.2 in a five-blade cascade. They measured heat transfer coefficients using the transient liquid crystal technique. The results of this experiment showed that a larger gap causes higher heat transfer coefficient on the tip. A second study by Azad et al. [14] investigated the effects of a recessed tip ($D/H = 3.77\%$) on the heat transfer coefficient. It was determined that the squealer tip produced a lower overall heat transfer coefficient compared to the plain tip. The squealer redirected the airflow over the tip forcing the flow to move from the leading edge pressure side to the trailing edge suction side.

Bunker and Bailey [15] investigated the effectiveness of chordwise sealing strips to reduce leakage flow and heat transfer. Sealing strips increased resistance to leakage flow. Sealing strips also reduced flow when the gap between the strip and shroud was the same as that between the plain tip and shroud. The strip location affected the tip heat load distribution. The present study is partly based on this study by Bunker and Bailey [15]. Bunker and Bailey [16] continued the study with more complicated strip geometries: circumferential rub strips, 45 deg angled rub strips. The experiments showed that circumferential and angled strips increase heat loads by 20–25% and 10–15%, respectively.

Bunker and Bailey [17] and Azad et al. [18] examined the different squealer geometries for reducing tip leakage flow and associated heat transfer, including single and double squealers. They found several squealer geometries reduce overall heat transfer to the tip compared to the plain tip. The midchord squealer produced the best leakage reduction. Recently, Dunn and Haldeman [19] presented time-averaged heat flux measurements on a recessed tip, the lip of the recess of a rotating blade in a full-scale rotating stage at transonic vane exit conditions.

There have been several studies that have focused on the effect of periodic unsteady wakes on linear cascades. Wittig et al. [20] and Han et al. [21] focused on the blade surface heat transfer under the effect of periodic unsteady wakes. These early studies simulated rotor-stator interactions with an upstream rotating rod wake generator. This technique has been accepted as a solution to simulating upstream unsteady wake effects on blades in low-speed cascades. Teng et al. [22] presented detailed heat transfer coefficient distributions on a large-scale blade tip with different tip gaps. The effect of unsteady wake on tip heat transfer was investigated. They concluded that a reduced tip clearance gap produces lesser effect of the upstream unsteady wake thereby producing lower heat transfer coefficients. However, they did not investigate the effects of various tip geometries under unsteady wake effects. Also, they used the midspan section of the blade to simulate the leakage flow and not the tip section. This can produce nontypical leakage flow over the tip compared to the tip section.

The present study focuses on using trip strips in different orientations and other leakage reduction techniques such as pin fins to reduce leakage flow and heat transfer. Detailed heat transfer measurements are obtained using the steady-state liquid crystal technique. The HSI-based technique is described in detail by Camci et al. [23]. A typical high-pressure turbine blade was used in a four-blade linear cascade. Heat transfer measurements are presented for different tip geometries for one tip gap clearance of 1.5625% of the blade span (20.32 cm). The effect of unsteady wake and freestream turbulence is also investigated for each of the proposed tip geometry, which is the novel contribution of this work.

Experimental Setup

A schematic of the experimental setup is shown in Fig. 1. The test setup consists of a suction type blower, a low-speed wind tunnel with an inlet-nozzle. Three screens are inserted at the inlet and exit of the nozzle section to help reduce and breakdown the large-scale turbulence entering the wind tunnel. The wind tunnel is designed to accommodate the turning angle of the blade cascade. The flow turning angle for the cascade is 116 deg. The flow passes through a rectangular section where a turbulence grid can be inserted to increase the freestream turbulence approaching the four-blade linear cascade. The turbulence grid is placed 46.67 cm upstream of the cascade leading edge. The grid is made of 6.35 mm thick circular rods arranged in a crossbar fashion with a spacing of 25.4 mm between the rods in both directions. A spoked-wheel wake generator similar to previous studies, [20–22], is used to generate the periodic unsteady flow simulating rotor-stator interaction on the cascade and is 17.15 cm upstream of the blade cascade. The wake generator has 32 rods, each 0.63 cm in diameter simulating the upstream trailing edge of the guide vane. The wake Strouhal number can be adjusted by adjusting the rotating speed of the rods using a frequency controller. The cascade inlet velocity can be varied using a frequency controller for the blower to adjust the required inlet velocity for different inlet flow conditions.

The cascade has four blades with an axial chord length of 12 cm, span of 20.32 cm, and blade spacing of 19.06 cm at cascade inlet. The two end blades form the outer edge of the cascade guide

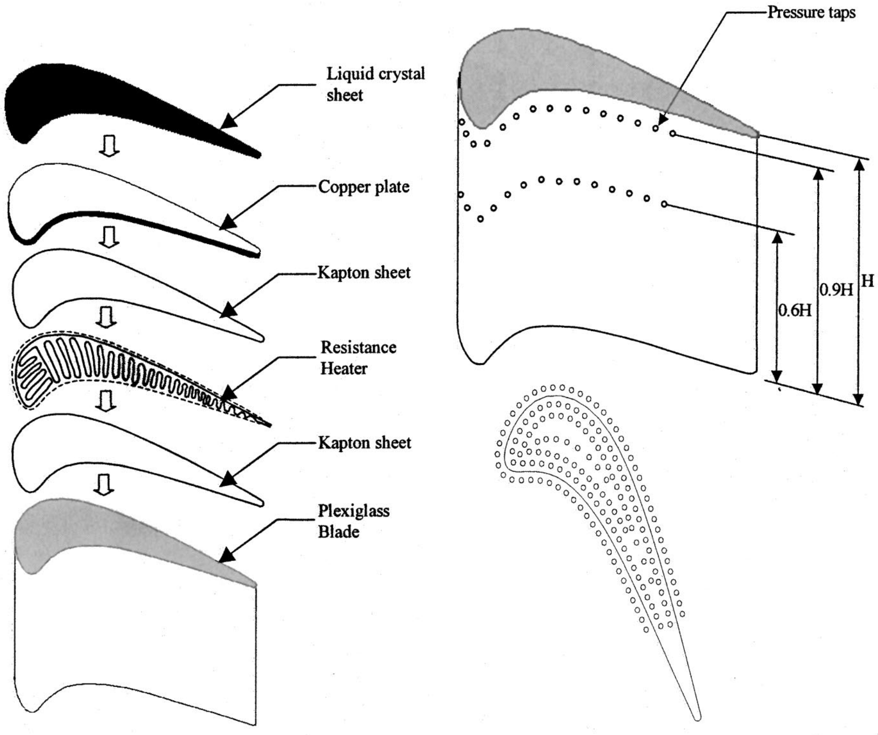

(a) (b)

Fig. 2 (*a*) Heat transfer blade, (*b*) pressure blade and shroud taps

the flow through the middle three passages. One of the middle blades serves as the test blade location. The blade can be interchanged to obtain pressure or heat transfer measurements. The test blade is the only blade that has a tip gap clearance. All the blades are machined out of plexiglass. The blade shapes were cut out of 5.04 cm thick plexiglass sheet and four cuts were stacked up and glued together to obtain one blade for the cascade. Figure 2 shows the heat transfer blade. The heat transfer blade is first instrumented with a Kapton sheet, a resistance wire of known length was designed with a certain distribution and is attached to the underneath of a thin copper plate (0.79 mm) using another Kapton sheet. The liquid crystal sheet of known color range (R30C5W) with red beginning at 30°C and a bandwidth of 5°C was then glued to the top of the copper plate. The heater system provided an almost uniform heat flux on the blade tip. The regions along the blade edges may produce some nonuniformities although they are not visible during the tests.

Figure 2 also shows the test blade with surface pressure taps. Pressure taps were placed on the blade surface at 60% span and 90% span to measure the static pressure distributions on the blade surface at different span locations. Static pressure taps were also placed on the shroud of the blade with a tip clearance as shown in Fig. 2. The shroud pressure distributions were obtained to characterize the leakage flows with different tip sealing geometries. Each static pressure tap was connected to a 32-channel NetScanner system from Pressure Systems, Inc.

Figure 3 presents the six tip geometry cases studied. Case 1 is the plain tip case with the tip clearance at 1.5625%. For the tip sealing geometries, the ribs or trip strips were arranged at different angles to the leakage flow direction over the tip. The leakage flow angles were determined from the shroud pressure distributions for the plain tip case. Case 2 is for trip strips placed 25.4 mm apart with the trip strips orthogonal to the leakage flow direction. Case 3 is for the trip strips at 102 deg angle to the mainstream flow and slightly turned away from the leakage flow with a reduced spaced of 18.7 mm. Case 4 is for the trip strips placed at +9 deg to the mainstream flow such that the strips are organized 25.4 cm apart to be along the leakage flow direction. Case 5 is for the trip strips placed at −9 deg to the mainstream flow such that the trip strips are tilted against the flow slightly with a spacing of 25.4 cm. Case 6 is for the tip with cylindrical pin fins attached to the tip surface only. All the trip strips are 3.17 mm square in cross section. The pin fins are 6.35 cm in diameter and 6.35 cm tall with a spacing of 25.4 mm. The pins are arranged in a staggered configuration on the tip. The first pin is placed at the leading edge of blade tip. The tip gap above the trip strips and pin fins is maintained at 1.5625% of the blade span.

A high-resolution RGB camera is placed right above the tip surface of the heat transfer blade location. Lights are mounted on the frame that holds the camera in position. The RGB camera is connected to a 24-bit color frame grabber board inside a PC. An image processing software is used to capture and analyze the liquid crystal color images on the blade tips.

Procedure and Data Reduction

Liquid Crystal Calibration. The first step in the experimental procedure is to calibrate the liquid crystal color to temperatures. The calibration was done in-situ with a thermocouple placed on the liquid crystal sheet. The camera was focused on the region around the thermocouple. The liquid crystal sheet was heated by turning on the heater underneath the sheet. The heater temperature was slowly increased by about 0.2°C and allowed to come to steady state. The hue of the color was recorded by the image processing unit and the temperature was measured using a temperature recorder. The hue of the color was plotted against the temperature to obtain the calibration curve. Camci et al. [23] provide a detailed description of hue-based liquid crystal measure-

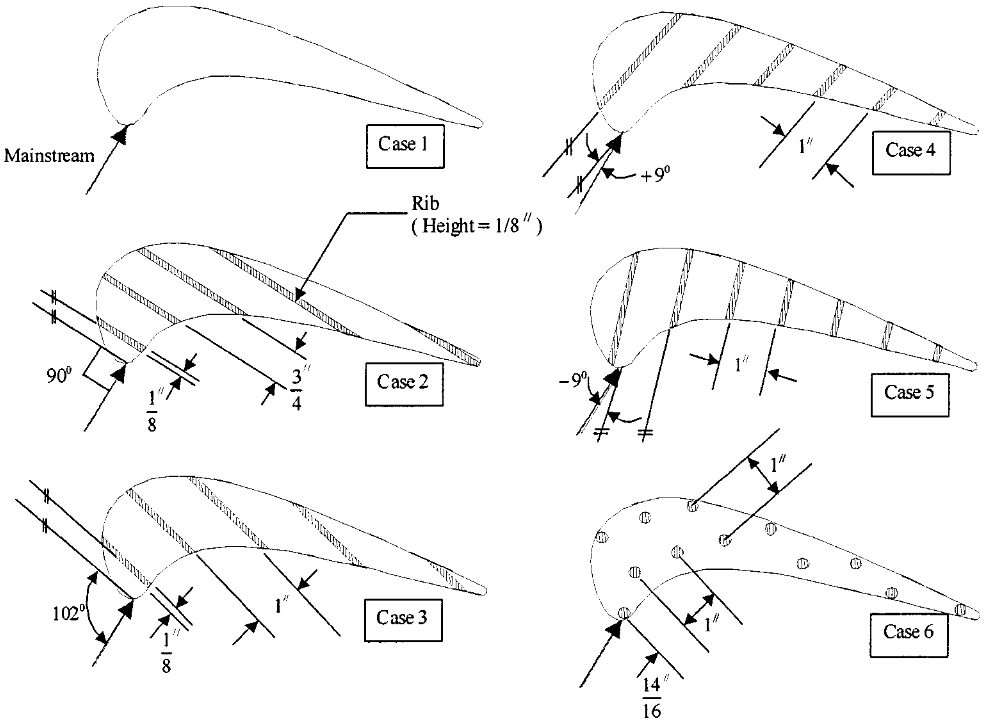

Fig. 3 Blade tip configurations tested

ment technique. A hue-temperature relationship is obtained from the curve. Figure 4 shows the temperature versus hue curve. This relationship for the present setup is given as

$$\text{Temperature} = 0.047 * \text{Hue} + 28.619.$$

Heat Transfer Experiment. The camera is focused on the test surface. The suction blower is turned on to start the mainstream flow through the cascade. Once the flow is steady, the heater is turned on using an electrical supply and a variac. The variac is used to control the current and voltage into the heating wire. The wire heats up the copper plate and the copper plate heats up the liquid crystal layer. The heat flux is increased till most of the blade is either green or red. The hue calibration is not very reliable in the blue color range as the curve tends to plateau with increasing temperature. To avoid this, color changes are limited to red and green. Once the surface is mostly green, the heat flux is maintained constant till the test surface achieves steady state. This typically takes about 30–45 minutes. The image is then captured and the local hue values are obtained at every pixel on the blade tip surface. The Hue is then converted to the local surface temperature using the above hue-temperature relation. The wall surface heat flux is calculated from the known voltage and current and the blade tip surface area. The local heat transfer coefficient is calculated from the relation:

$$h = \frac{q''_{\text{elec}} - q''_{\text{loss}}}{(T_w - T_\infty)},$$

where q''_{elec} is the applied electrical power per unit area, and q''_{loss} is the losses due to conduction, natural convection, and radiation. This was estimated to be about 6% of the applied heat flux over the entire tip surface. The local wall temperature T_w is calculated from the local hue measurement and T_∞ is the oncoming freestream temperature measured upstream of the cascade.

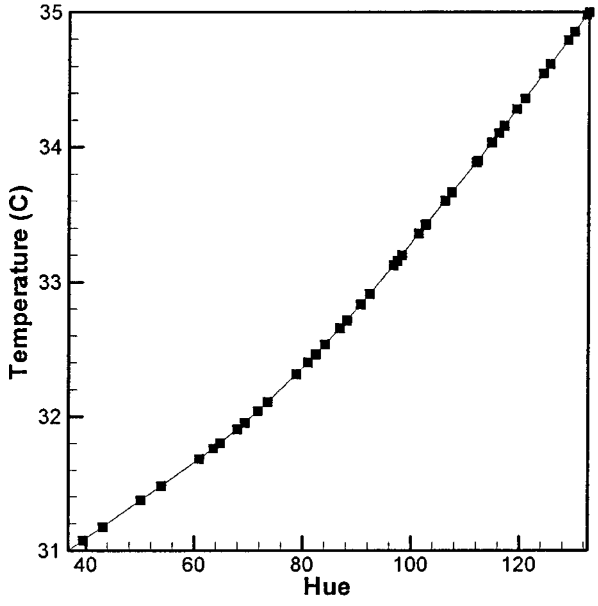

Fig. 4 Hue versus temperature curve for liquid crystal sheet

The average experimental uncertainty in the local heat transfer coefficient measurement, based on Kline and McClintock [24] is about ±7.8%. The heat transfer coefficient measurement is affected by the uncertainty in hue measurement, the hue-temperature relation, freestream temperature measurement, and heat flux input, and loss estimation.

Results and Discussion

Flow Measurements. The freestream velocity at cascade inlet is 23 m/s and 58 m/s at the cascade exit. The cascade Reynolds number based on axial chord length is 4.83×10^5. Four different flow conditions were studied for each tip geometry. The no grid, no wake case has a baseline turbulence intensity of around 1.4% and the upstream grid produces a turbulence intensity of 4.9% upstream of the cascade. Two different wake generator rotational speeds produce wake Strouhal numbers of 0.2 and 0.4. Figure 5

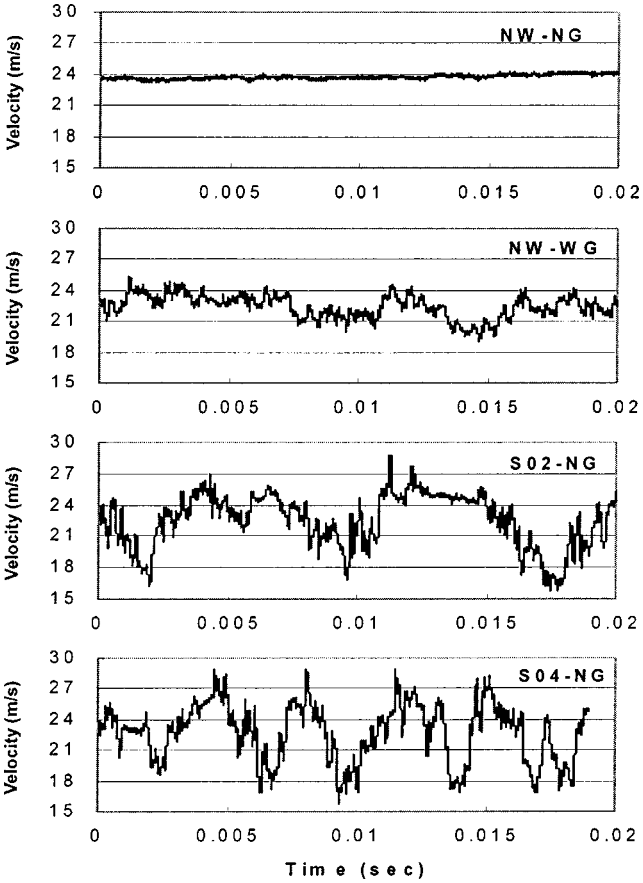

Fig. 5 Velocity signature for the four flow conditions

shows the velocity signature from four flow conditions. A TSI hot wire system was used with a probe model 1260A-T15 for the velocity and turbulence measurements. The baseline case with no wake and no grid (NW-NG) produced a turbulence intensity of 1.4%. The turbulence intensity with the no wake and turbulence grid (NW-WG) was 4.8%. With the unsteady wake superimposed on the grid, the periodicity of the wake passing is clearly evident. For the case with Strouhal number of 0.2, the wake passing period is 0.007 seconds. The case for the Strouhal number of 0.4 produces half the wake passing period of $S=0.2$ as expected. The periodicity for the passing wake is clearly evident from the velocity signatures. Table 1 summarizes the flow conditions and the associated turbulence intensity for each case.

Pressure Measurements. The flow in all the three blade passages was equalized by repositioning the tailboards behind the cascade. The tailboards were adjusted till the leading edge velocities were uniform for all the three passages. Figure 6 presents the surface pressure distributions $\{(P_t-P_s)/P_t\}$ for the test blade at 60% and 90% span locations. The static pressure measurements were obtained for four different flow conditions. Results show that the upstream flow condition, whether wake or grid, does not affect the static pressure distributions on the blade surface significantly. This is true at both span locations. The pressure side shows almost uniform pressure over the entire surface. The lowest pressure occurs around 0.45*C* on the suction surface. The flow accelerates from the leading edge to 0.45*C* on the suction surface and then decelerates towards the trailing edge. Figure 7 shows the comparison of the pressure distributions at the two different span locations. The pressure side pressures are identical but at a span of 90%, the acceleration on the suction surface is slower than for 60% span location. This may be due to the tendency for the flow to migrate towards the tip at larger span locations.

Table 1 List of flow conditions

Flow Condition	Rods	Grid	Turbulence Intensity	Wake Strouhal No. (S)
NW-NG	No	No	1.4%	0
NW-WG	No	Yes	4.8%	0
S02-NG	Yes	No	1.4%	0.2
S04-NG	Yes	No	1.4%	0.4
S04-WG	Yes	Yes	4.8%	0.4

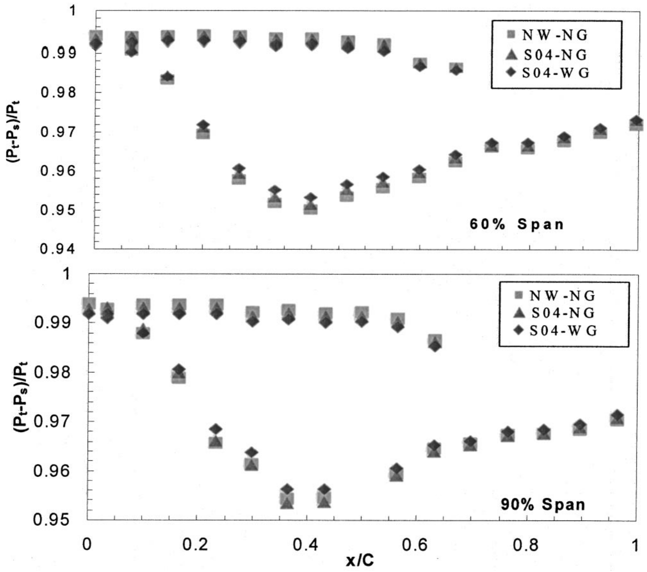

Fig. 6 Surface pressure distributions on the test blade at different span locations

Figure 8 presents the static pressure distributions $\{(P_t-P_s)/P_t\}$ on the shroud for the plain tip with four different flow conditions. The presence of wake appears to show little effect on the shroud pressure distributions comparing case 1 and case 3. However, the presence of grid-generated turbulence appears to reduce the low pressure region in the middle of the blade. Figure 9 presents the shroud pressure distributions for various tip geometries. The pressure distributions clearly show that the least pressure drop is obtained for the geometry with trip strips placed 18 cm apart against the flow. All the other cases show a large low-pressure zone in the middle of the tip surface. For the last three cases, this zone is more spread out due to breakdown of flow by the presence of trip strips and pin fins on the tip surface.

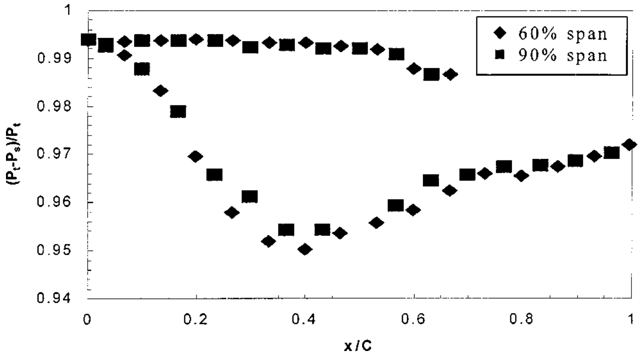

Fig. 7 Comparison of surface pressure distributions for two different span locations

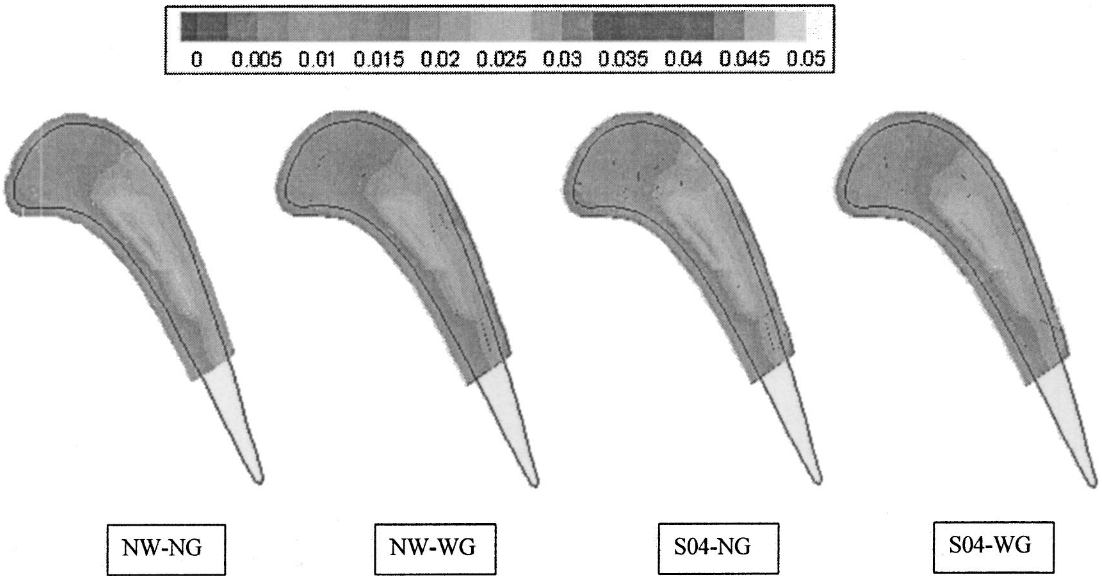

Fig. 8 Static pressure distributions $\{(P_t-P_s)/P_t\}$ on the shroud for the plain tip under different flow conditions

Heat Transfer Measurements. Figure 10 presents detailed heat transfer distributions for the plain tip under different upstream flow conditions. The baseline case is the no wake, no grid case with a low turbulence intensity of 1.4%. For this condition, heat transfer coefficient is highest along the blade tip trailing edge region. The lowest heat transfer coefficients are obtained in the middle of the leading edge region. This region of low heat transfer was observed by previous studies. Bunker and Bailey [15] referred to it as the ''sweet spot.'' From the pressure distributions on the shroud, it is clear that bulk of the leakage flow will follow the line along the strongest pressure gradient across the tip which is downstream of the leading edge region around $X/C=0.4-0.5$. Further downstream, the heat transfer coefficient is higher due to highly accelerated flow over the tip. With a change in mainstream flow condition, the high heat transfer region seems to be unaffected. However, the sweet spot region sees higher heat transfer coefficients. It can be summarized that the increase in free-stream turbulence enhances heat transfer closer to the leading edge.

Figure 11 compares the heat transfer coefficient distributions on the tip for all the different tip geometry configurations for the baseline flow condition of no wake, no grid. For the tip sealing geometries, there are no measurements on the trip strips and pins. It is expected that the heat transfer coefficients on the strip and the pin itself will be significantly higher than the tip surface. This may cause the overall average heat transfer over the tip surface including the trip strip/pin surface area to be higher than measured. However, the increase in surface area and reduced leakage flow can reduce the enhancement due to the presence of trip strips/pins. Also, these trip strips/pins can be expendable pieces that can be brazed on the surface after several hours of operating and thus protecting the actual tip from loss of material.

Comparing case 2 with the baseline plain tip case, the trip strips placed against the flow with a spacing of 18 mm appear to reduce the trailing edge heat transfer coefficients significantly. As can be seen from the pressure distributions, this configuration produces

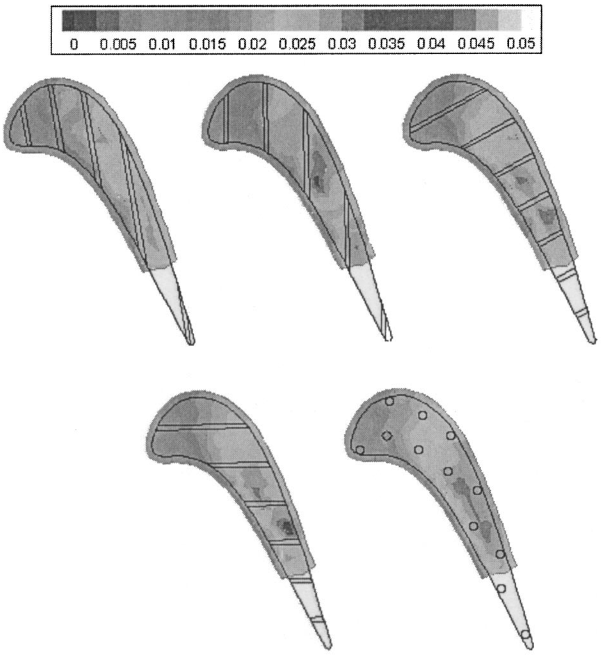

Fig. 9 Static pressure distributions $\{(P_t-P_s)/P_t\}$ on the shroud for the different tip configurations

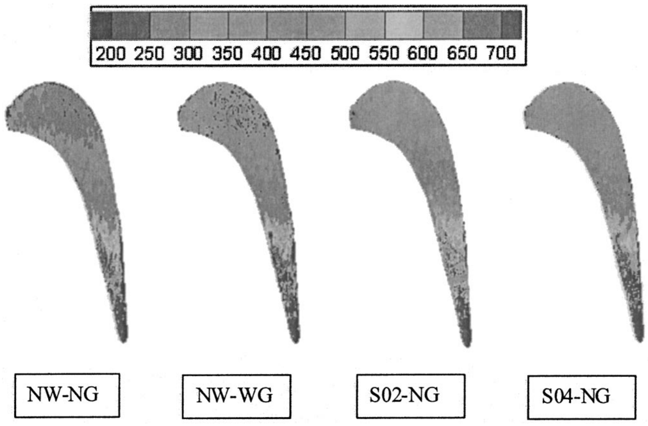

Fig. 10 Detailed heat transfer coefficient distributions on plain tips

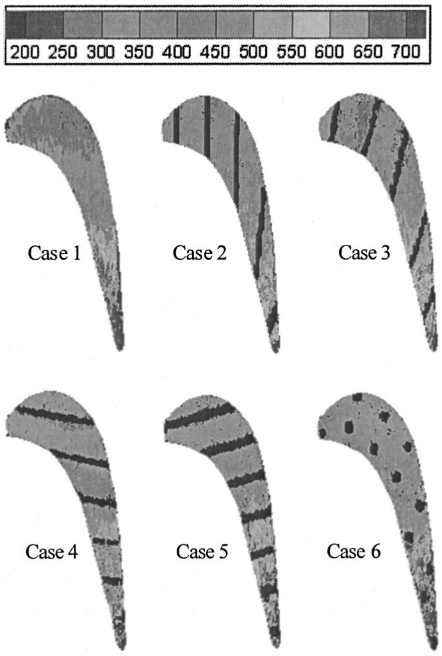

Fig. 11 Detailed heat transfer coefficient distributions for different tip sealing geometries

the least pressure differential across the tip gap. The trip strips appear to provide some form of blockage to the leakage flow resulting in lower heat transfer coefficients over most of the tip surface. In the leading edge regions, the heat transfer coefficients are similar if not slightly higher than the plain tip.

Comparing case 3 with the baseline plain tip case, the leading edge region heat transfer coefficient appears to be reduced but the trailing edge region appears to produce similar levels as the plain tip. The leakage flow direction may be moving from the midchord towards the trailing edge for this case resulting in more flow in the rear end of the tip.

Comparing case 4 with the baseline plain tip case, this case produces slightly higher heat transfer coefficients in the leading edge region and slightly lower values near the trailing edge. The trip strips are aligned against the leakage flow direction. The leakage flow appears to accelerate between the regions between the trip strips enhancing heat transfer coefficients. The trailing edge region has lower values due to the reason that bulk of the leakage flow moves over the blade tip before it reaches the trailing edge.

Comparing case 5 with the baseline plain tip case, the heat transfer values are similar to that of case 4. In this case, the trip strips are aligned parallel to the leakage flow. In this case also, the leakage flow accelerates between the trip strips and there appears to be no blockage effect by the trip strips to reduce the leakage flow. Comparing case 6 with the baseline plain tip case, this case produces higher or similar levels of heat transfer coefficients over the entire tip surface as the plain tip. The pin fins do not appear to be increasing blockage or reducing leakage flow. This case increased acceleration of the leakage flow between the pin fins and thus producing similar levels of heat transfer coefficient as the plain tip. Overall, it appears that case 2 and case 3 produce the largest reduction in heat transfer coefficients over the tip surface compared to the plain tip.

Figure 12 compares the camberline heat transfer coefficients on the tip for different geometries with the baseline flow condition (no wake-no grid). Comparing case 2 versus the baseline condition in Fig. 12(*a*), It can be seen that the leading edge region has similar levels of heat transfer coefficient for both cases around 300 W/m^2-K. The two lines diverge near the trailing edge with case 2 providing lower heat transfer coefficients. However, this may be offset by increased heat transfer coefficients on the top of the trip strips, which is not measured in the present study. The trip strip locations show no values (dips) in the plots. Figures 12(*b*–*d*) compares case 4–6 with the baseline case. It seems cases 4 and 5 produce similar levels of heat transfer coefficient over the entire camberline compared to the baseline case. However, case 6 with pins produces higher heat transfer coefficients than the baseline, which is detrimental. Bunker and Bailey [15] indicated that the trip strips either enhance heat transfer depending on the alignment to leakage flow or in the limiting case, do not produce any enhancement. The results are consistent with the findings of the earlier study for all the cases except case 2 where we find that there is some reduction on tip surface heat transfer coefficients. Also, the pin fins are not a viable option to reduce the heat transfer to the tips. Figure 12(*e*) compares the effect of trip strip spacing by comparing cases 2 and 3. It appears that the effect of trip strip spacing has very little effect on heat transfer coefficient over most of the tip except in the trailing edge where a shorter spacing (case 2) produces lower heat transfer coefficients.

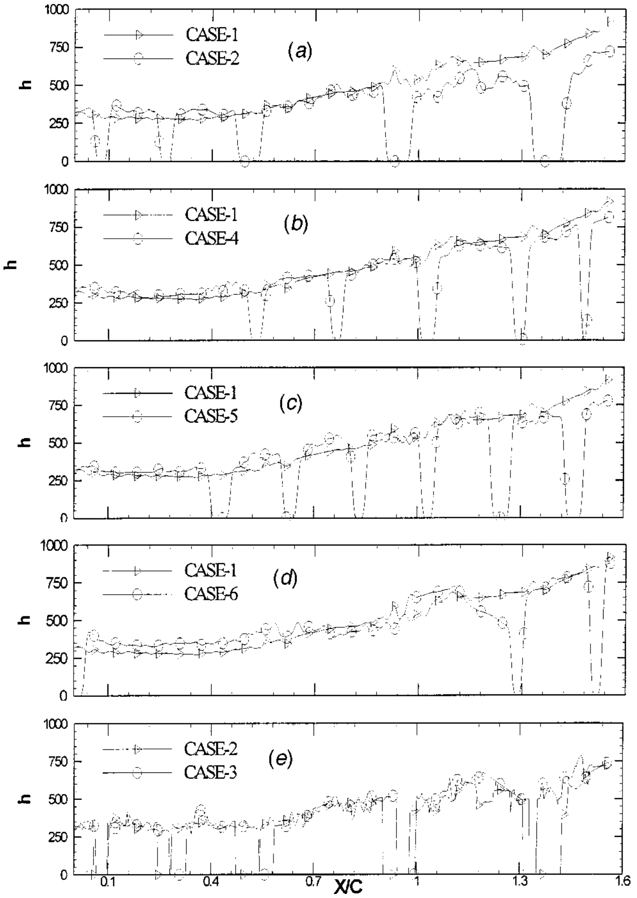

Fig. 12 Camberline heat transfer coefficient distributions: top (*a*) to bottom (*e*)

It appears that most of the tested sealing geometries do not significantly reduce the tip heat transfer coefficients with the clear reduction in leakage flow shown from pressure distributions. This may be mainly because the trip strips enhance local heat transfer due to constant tripping of the leakage flow through the gap resulting in higher heat transfer coefficients for reduced leakage flow. In some cases, such as cases 4–6 wherein the heat transfer coefficients are enhanced and the leakage flow is not reduced significantly. Aerodynamically, cases 2, 3, and 4 may reduce the downstream aerodynamic losses as the leakage flow is reduced and thus may produce smaller leakage vortices downstream along the suction surface of the blades. However, detailed flow measure-

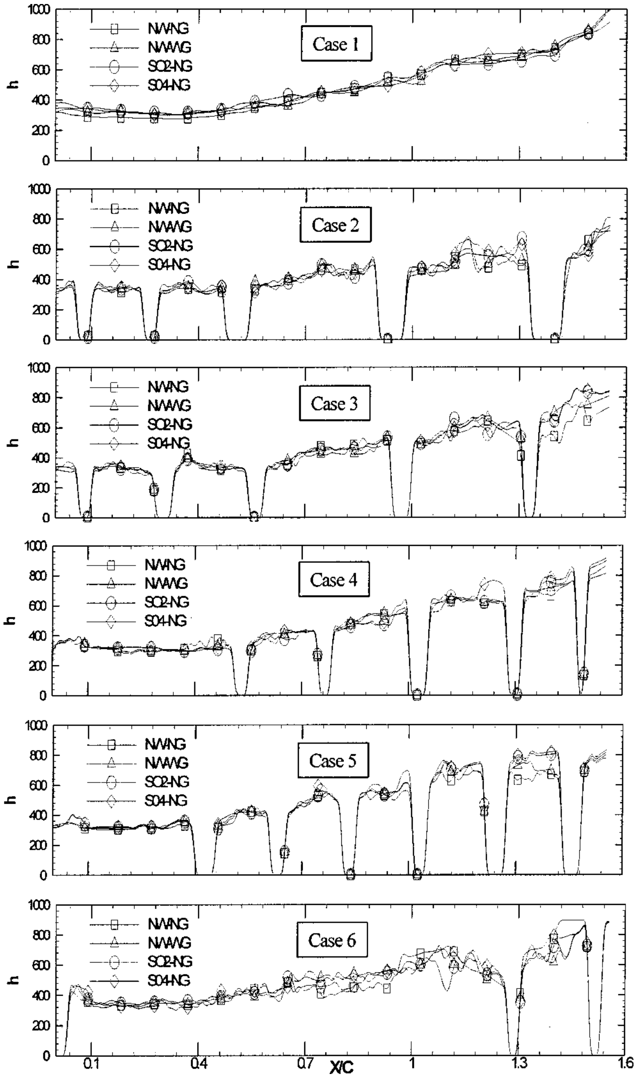

Fig. 13 Effect of upstream flow condition on tip camberline heat transfer coefficient

ments are required to determine the effect of these tip geometries on leakage flow associated vortices and aerodynamic losses. The circumferential or tangential losses can only be estimated based on detailed flowfield measurements in the cascade, which are not presented in this study.

Figure 13 presents the effect of upstream flow conditions on heat transfer coefficient for each of the tip geometries. For case 1, the effect is strongly evident with increasing wake and addition of grid producing higher heat transfer coefficients. However for the other cases, where the tip has trip strips and pin fins, the effect of upstream flow condition is diminished. The effect of grid and wake is local with some regions higher and some are similar to the baseline case.

Conclusions

A systematic investigation of various tip leakage flow sealing methods on flow and heat transfer over a turbine blade tip in a low-speed cascade was performed. A hue-based steady-state liquid crystal technique was used to make detailed heat transfer coefficient measurements. Several configurations of trip strips and pin fins placed on the tip to reduce leakage flow and associated heat transfer were tested. Results show that the trip strips placed in a direction orthogonal to the leakage flow direction produces the lowest leakage flow and heat transfer coefficient over the tip. The other configurations produce similar levels to the plain tip or are higher than the plain tip.

The effect of upstream flow condition with the presence of a grid to generate freestream turbulence of 4.8% and to simulate passing wake due to upstream NGV trailing edge was also investigated. The presence of the wake and freestream turbulence produced higher heat transfer coefficients on the plain tip. However, the other tip geometries show little effect of upstream flow condition. Overall, the usage of trip strips and pin fins as tip sealing mechanisms do not provide desirable results in significant reduction of tip surface heat transfer coefficients. The effect of trip strip alignment appears to have strong effect on leakage flow and but a lesser effect on associated heat transfer. However, aerodynamically the effect of trip strips on tips can produce circumferential losses, which have not been measured in the study. These losses can be exacerbated by a larger leakage vortex on the suction side of the blade. Also the effect of rotation can be an issue although these trip strips face the same forces as the squealer rims that have been industry standard for many years.

Acknowledgments

This work was supported partly through a grant from NSF under the GOALI program and through a grant from NASA EPSCoR—LaSPACE. Acknowledgements are due to the program managers Drs. A. Emery, S. Thynell, and R. Smith from NSF and to Dr. John Wefel of LaSPACE consortium. Acknowledgments are also due to Dr. R. S. Bunker from General Electric Global R&D center, for sharing his technical expertise. Acknowledgments are also due to Dr. S. Acharya, Mr. G. Pamula, Mr. L. Bonadona, Mr. J. Watkins, and Ms. S. Dupree for their help with the cascade facility.

Nomenclature

C_X = blade axial chord length (12 cm)
d = wake rod diameter (cm)
h = local heat transfer coefficient (W/m^2-K)
HSI = hue saturation intensity
n = number of rods on wake generator
N = speed of rotating rods (rpm)
P_s = local static pressure
P_t = total pressure at inlet (atmospheric pressure)
q'' = surface heat flux (W/m^2)
Re = freestream Reynolds number $(V_2 C_X/\nu)$
RGB = red green blue
S = wake Strouhal number, $2\pi N d n/(60 V_1)$
T_m = mainstream temperature
T_w = local wall temperature
Tu = freestream mean turbulence intensity at cascade inlet
V_1 = cascade inlet velocity (m/s)
V_2 = cascade exit velocity (m/s)
X = streamwise distance from leading edge to trailing edge
ν = kinematic viscosity of inlet air

References

[1] Bindon, J. P., 1989, "The Measurement and Formation of Tip Clearance Loss," ASME Journal of Turbomach., , **111**, pp. 257–263.
[2] Morphis, G., and Bindon, J. P., 1988, "The Effect of Relative Motion, Blade Edge Radius and Gap Size on the Blade Tip Pressure Distribution in an Annular Turbine Cascade With Clearance," AMSE Paper 88-GT-256.
[3] Yaras, M., Yingkang, Z., and Sjolander, S. A., 1989, "Flow Field in the Tip Gap of a Planar Cascade of Turbine Blades," ASME Journal of Turbomach., **111**, pp. 276–283.
[4] Yamamoto, A., 1989, "Endwall Flow/Loss Mechanisms in a Linear Turbine Cascade With Blade Tip Clearance," ASEM Journal of Turbomach., **111**, pp. 264–275.
[5] Kaiser, I., and Bindon, J. P., 1997, "The Effect of Tip Clearance on the Development of Loss Behind a Rotor and a Subsequent Nozzle," ASME Paper 97-GT-53.
[6] Mayle, R. E., and Metzger, D. E., 1982, "Heat Transfer at the Tip of an

Unshrouded Turbine Blade,'' *Proceedings of the 7th International Heat Transfer Conference*, **3**, pp. 87–92.
[7] Metzger, D. E., Bunker, R. S., and Chyu, M. K., 1989, ''Cavity Heat Transfer on a Transverse Grooved Wall in a Narrow Flow Channel,'' J. Heat Transfer, **111**, pp. 73–79.
[8] Chyu, M. K., Moon, H. K., and Metzger, D. E., 1989, ''Heat Transfer in the Tip Region of Grooved Turbine Blades,'' ASME Journal of Turbomach., **111**, pp. 131–138.
[9] Metzger, D. E., Dunn, M. G., and Hah, C., 1990, ''Turbine Tip and Shroud Heat Transfer,'' ASME Paper 90-GT-333.
[10] Yang, T. T., and Diller, T. E., 1995, ''Heat Transfer and Flow for a Grooved Turbine Blade Tip in a Transonic Cascade,'' ASME Paper 95-WA/HT-29.
[11] Bunker, R. S., Bailey, J. C., and Ameri, A. A., 1999, ''Heat Transfer and Flow on the First Stage Blade Tip of a Power Generation Gas Turbine: Part I—Experimental Results,'' ASME Journal of Turbomach. **122**, pp. 263–271.
[12] Ameri, A. A., and Bunker, R. S., 1999, ''Heat Transfer and Flow on the First Stage Blade Tip of a Power Generation Gas Turbine: Part II—Simulation Results,'' ASME Journal of Turbomach., **122**, pp. 272–277.
[13] Azad, Gm. S., Han, J. C., and Teng, S., 2000, ''Heat Transfer and Pressure Distributions on a Gas Turbine Blade Tip,'' ASME Paper 2000-GT-194.
[14] Azad, G. S., Han, J. C., and Boyle, R. J., 2000, ''Heat Transfer and Flow on the Squealer Tip of a Gas Turbine Blade,'' ASME Paper 2000-GT-195.
[15] Bunker, R. S., and Bailey, J. C., 2000, ''An Experimental Study of Heat Transfer and Flow on a Gas Turbine Blade Tip With Various Tip Leakage Sealing Methods,'' *Proceedings of the 4th HMT/ASME Heat and Mass Transfer Conference*, Paper No. HMT2000-055, ASME, New York, pp. 411–416.
[16] Bunker, R. S., and Bailey, J. C., 2000, ''Blade Tip heat Transfer and Flow with Chordwise Sealing Strips,'' *International Symposium on Transport Phenomena and Dynamics of Rotating Machinery (ISROMAC)*, Honolulu, HI, pp. 548–555.
[17] Bunker, R. S., and Bailey, J. C., 2001, ''Effect of Squealer Cavity Depth and Oxidation on Turbine Blade Tip Heat Transfer,'' *International Gas Turbine and Aeroengine Congress and Exposition*, New Orleans, LA, June.
[18] Azad, G. S., Han, J. C., Bunker, R. S., and Lee, C. P., 2001, ''Effect of Squealer Geometry Arrangement on Gas Turbine Blade Tip Heat Transfer,'' ASME Paper IMECE2001/HTD-2431.
[19] Dunn, M. G., and Haldeman, C. W., 2000, ''Time-Averaged Heat Flux for a Recessed Tip, Lip and Platform of a Transonic Turbine Blade,'' ASME Paper 2000-GT-0197.
[20] Wittig, S., Schulz, A., Dullenkopf, K., and Fairbank, J., 1988, ''Effects of Free-Stream Turbulence and Wake Characteristics on the Heat Transfer Along a Cooled Gas Turbine Blade,'' ASME Paper 88-GT-179.
[21] Han, J. C., Zhang, L., and Ou, S., 1993, ''Influence of Unsteady Wake on Heat Transfer Coefficient From a Gas Turbine Blade,'' J. Heat Transfer, **115**, pp. 904–911.
[22] Teng, S., Han, J. C., and Azad, Gm. S., 2001, ''Detailed Heat Transfer Coefficient Distributions on a Large Scale Gas Turbine Blade Tip,'' ASME J. Heat Transfer, **123**.
[23] Camci, C., Kim, K., and Hippensteele, S. A., 1991, ''A New Hue Capturing Technique for Quantitative Interpretation of Liquid Crystal Images Used in Convective Heat Transfer Studies,'' ASME Paper 91-GT-277.
[24] Kline, S. J., and McClintock, F. A., 1953, ''Describing Uncertainties in Single Sample Experiments,'' Mechanical Engineering, **75**, pp. 3–8.

Measurement and Prediction of Heat Transfer Distributions on an Aft-Loaded Vane Subjected to the Influence of Catalytic and Dry Low NO_x Combustor Turbulence

F. E. Ames

M. Argenziano

C. Wang

Mechanical Engineering,
University of North Dakota,
UPII, Room 266,
Grand Forks, ND 58202-8359

Aft-loaded vane designs can have an impact on surface heat transfer distributions by accelerating boundary layers for a greater portion of the suction surface. New combustion systems developed for low emissions have produced substantial changes to the characteristics of inlet turbulence entering nozzle guide vanes. This paper documents heat transfer rates on an aft-loaded vane subject to turbulence generated by mock combustion configurations representative of recently developed catalytic and dry low NO_x *(DLN) combustors. Four different inlet turbulence conditions with levels ranging up to 21% are documented in this study and vane heat transfer rates are acquired at vane exit chord Reynolds numbers ranging from 500,000 to 2,000,000. Heat transfer distributions show the influence of the turbulence conditions on heat transfer augmentation and transition. Cascade aerodynamics are well documented and match pressure distributions predicted by a commercial computational fluid dynamics (CFD) code for this large-scale low-speed facility. The aft-loaded vane pressure distribution exhibits a minimum value at about 50% arc on the suction surface. This comprehensive vane heat transfer data set is expected to represent an excellent test case for vane heat transfer predictive methods. Predictive comparisons are shown based on a two-dimensional boundary layer code using an algebraic turbulence model for augmentation as well as a transition model.*

[DOI: 10.1115/1.1645867]

Introduction

Current approaches to achieving a low level of thermal NO_x generation in gas turbine engines include both DLN and catalytic combustion systems. These strategies burn lean mixtures of fuel and air to limit combustion temperatures and the associated thermal NO_x generation. DLN combustors—similar to aero-derivative combustors—generate high turbulence levels in order to promote efficient combustion. The resulting turbulence causes dramatic increases in heat transfer distributions on first vanes. Catalytic combustion systems promote the stable combustion of lean fuel/air mixtures using a catalytic surface reaction, which is dependent on the transport of fuel and air to the surface. Consequently, catalytic combustion systems need a substantial surface area to enable the high combustion densities needed in gas turbine systems. The resulting tiny passages comprising catalytic combustion systems generate a small-scale turbulence, which dissipates rapidly. This small-scale turbulence has only a modest affect on vane surface heat transfer distributions.

The burning of lean fuel/air mixtures in low NO_x combustion systems results in flatter temperature profiles entering the turbine nozzle. These flatter profiles tend to produce higher temperatures near the endwall surface causing more difficulty in cooling the endwall region. Many systems use endwall film cooling to reduce the effective gas to endwall temperature difference. Secondary flows on the endwall surface tend to sweep away a good portion of the cooling film before it can reduce the high heat transfer levels in the high velocity regions of the passage. Designers have found that endwall contouring can reduce the impact of secondary flows on endwall surfaces by reducing the strength of the leading edge vortex.

The overall objective of the current research has been to investigate the characteristics of turbulence generated by new low NO_x combustion systems and to document the resulting endwall and vane surface heat transfer distributions. This database includes three different mock turbulence generator configurations in addition to a low turbulence baseline condition acquired across a four-to-one range in Reynolds numbers in two cascade test sections. The initial cascade test section was configured in a four-vane arrangement with flat endwalls and a fully loaded vane design. The current cascade uses an aft loaded vane and incorporates a strong inlet contraction through the leading edge of the vane. The contracting endwall cascade is used to reduce the impact of the horseshoe vortex system and the aft loaded vane was selected to take advantage of the low turbulence levels produced by the catalytic combustion system by affecting transition on the suction surface of the vane. In the present paper, inlet turbulence characteristics for the contracting inlet cascade have been documented and vane midline heat transfer distributions taken with three mock combustor configurations are presented over a four-to-one range in Reynolds numbers. These mock combustor configurations represent aeroderivative (AC), dry low NO_x (DLN), and catalytic combustion (CC) systems. These data are expected to provide a comprehensive test case to ground heat transfer predictive capabilities. Vane heat transfer distributions for the fully loaded vane cascade were presented in [1] and endwall heat transfer distributions have been documented in [2] and [3].

Contributed by the International Gas Turbine Institute and presented at the International Gas Turbine and Aeroengine Congress and Exhibition, Atlanta, GA, June16–19, 2003. Manuscript received by the IGTI December 2002; final revision March 2003. Paper No. 2003-GT-38509. Review Chair: H. R. Simmons.

Background

Flow over a pressure surface of a first vane typically accelerates over the whole surface and diverges slightly toward the endwall. Flow over a suction surface tends to contract slightly due to the influence of the pressure gradient across the passage from the pressure to suction surface, which tends to sweep low momentum fluid across and up onto the suction surface. However, at relevant Reynolds numbers for moderate sized gas turbines secondary flows typically affect less than 20% of the suction surface by the trailing edge. Consequently, boundary layer development on first vanes is predominately two-dimensional.

In addition to the velocity distribution along a vane, the inlet turbulence characteristics have a predominant influence on surface heat transfer distributions. However, simply quoting a turbulence intensity can be deceptive as its value is often more a function of the convective velocity than the turbulent kinetic energy, which drives turbulent transport in an absolute sense. However, turbulence is responsible for significant levels of heat transfer augmentation in the stagnation region and the laminar portion of the pressure surface and is the primary driver for transition in regions of zero and accelerating pressure gradient.

Combustor Turbulence. Ames, Wang, and Barbot [1] reviewed literature on turbulence levels produced by combustion systems and found values ranging from 7% leaving the combustor of a small helicopter gas turbine, [4], to nearly 30% leaving a DLN combustor configuration, [5]. The exit turbulence levels are dependent on the combustor core flow to vane inlet contraction ratio and the residence time (L/D) of the flow in the combustor. While the measurement of turbulent scale is not typically reported, Ames [6] and Ames, Wang, and Barbot [1] have reported energy scales, Lu, ranging from about 25% to 50% of the inlet span. In all cases a two to one liner to inlet contraction ratio was used. While most of these values have been reported without combustion, Moss and Oldfield [7] found that the wave number spectrum was not significantly affected by the combustion process in their tests at low pressures.

Stagnation Region Heat Transfer Augmentation. Stagnation regions often have the highest heat transfer rates on a turbine airfoil. Relatively high values of stagnation region heat transfer are seen at lower Reynolds numbers and on downstream airfoils where the relative inlet to exit velocity ratios tend to be higher. Turbulence can significantly augment stagnation region heat transfer above low turbulence levels and increases of more than 50% have been reported for first vanes subjected to simulated combustor turbulence. Ames and Moffat [8] found stagnation heat transfer levels were dependent on turbulence intensity, Reynolds number and scale and developed a correlating parameter, TRL based on these variables. The development of this parameter was based on Hunt's, [9], analysis of turbulence near a cylindrical stagnation region and Britter, Hunt, and Mumford's, [10], corroboration of this analysis. Van Fossen, Simoneau, and Ching [11] also developed a correlating parameter, which included turbulence intensity, Reynolds number, and scale but had an empirical basis.

Heat Transfer Augmentation to Accelerating Laminar Boundary Layers. Boundary layers developing on the pressure surface of vanes typically experience a steady acceleration, which keeps boundary layers thin and inhibits transition in spite of very high local levels of turbulence intensity. However, enhanced mixing rates due to external turbulence produce high levels of heat transfer augmentation. For example, Arts et al. [12] measured heat transfer increases of 100% on the laminar portion of a vane in a compressible cascade due to 6% grid generated turbulence. Ames [6] found that augmentation of heat transfer rates through laminar boundary layers developing on the pressure surface of a vane scales on turbulence intensity, chord to length-scale ratio to the third power, and Reynolds number to the third power. However, Ames's range of Reynolds numbers was limited and more recently Ames, Wang, and Barbot [1] found that the same scaling held well over a four-to-one range in Reynolds number.

Transition. Mayle [13] has presented a comprehensive review of transition on turbine airfoils. He suggests that onset of transition largely correlates on momentum thickness Reynolds number and turbulence intensity. He also indicates that turbulent scale may have an impact as well. Recently, Ames, Wang, and Barbot [1] found that smaller scale grid turbulence produced a slightly earlier transition than larger scale combustor turbulence with a slightly higher turbulence intensity. Zhang and Han [14] studied the influence of grid turbulence on heat transfer augmentation and transition on a turbine blade. Their results showed that at roughly equivalent turbulence levels, their finer grid turbulence produced an early transition. In addition, Mayle suggests that transition is suppressed when acceleration rates produce an acceleration parameter K, which is above 3E-6. However, Ames, Wang, and Barbot found initial indications of transition in regions where K was above 3E-6 suggesting that this criteria is more a rule of thumb than a physical limit.

Turbulent Boundary Layer Augmentation. Heat transfer augmentation to turbulent boundary layers has been found to correlate on turbulence intensity, Reynolds number, and boundary layer thickness to scale ratio, [8,15]. Consequently, at moderate Reynolds numbers, the relatively thin turbulent boundary layers found on first stage vanes are not strongly influenced by the large-scale turbulence generated by combustion systems.

Experimental Approach

The present heat transfer investigation has been conducted in the contoured endwall cascade in the University of North Dakota's large-scale low-speed wind tunnel cascade facility. The contoured endwall cascade facility is shown schematically in **Fig. 1**. The wind tunnel consists of a large inlet filter, a 45 kW blower, a two-stage multivane diffuser, a heat exchanger, a screen box and a two-dimensional nozzle. The blower is capable of moving 6.6 m^3/s of air with a static pressure rise of 5000 Pa. This allows the facility to achieve a relatively high chord Reynolds number in spite of the high-pressure drop across the turbulence generators. The heat exchanger recirculation system allows the facility to achieve a controllable steady-state inlet temperature. The four-section screen box in combination with the 3.6:1 area ratio two-dimensional nozzle allows the development of a low turbulence baseline condition for the facility.

The contoured inlet cascade test section used in this study has a specially designed aft-loaded vane. The aft loaded vane shown schematically in **Fig. 2** is compared to the fully loaded vane, which was used in the linear cascade test section, [1]. The fully loaded vane was a midspan incompressible representation of an 11-times scale first vane for a medium sized industrial gas turbine. The aft-loaded vane was designed to accelerate the flow to about mid arc on the suction surface in order to help suppress transition. The cascade, shown in **Fig. 1**, incorporated the aft loaded vane in a four-vane three full passage configuration. The cascade has been designed to accurately develop the two-dimensional aerodynamics represented by the blade profile using the inlet bleed adjustments and exit tailboards. The inlet bleed adjustments were designed around two-dimensional streamlines calculated using FLUENT, [16]. The adjustments are used to help set up a uniformly distributed inlet flow based on the row of inlet static pressure taps, which are placed one-fifth of an axial chord upstream from the vane leading edge plane. The tailboards are used to develop the proper periodicity at the exit of the cascade with the help of a row of exit static pressure taps placed one-quarter axial chord downstream from the vane trailing edge.

The inlet to the cascade has a 30-deg contraction into the leading edge plane of the vanes as shown schematically in **Fig. 3**. This schematic shows a cross-sectional view of the mock turbulence

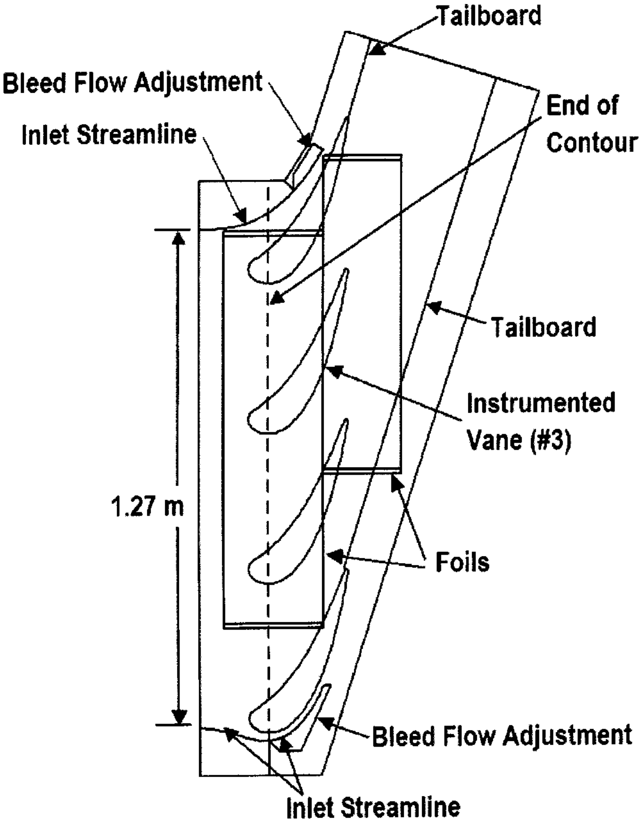

Fig. 1 Schematic of contoured endwall cascade test section with aft-loaded vane

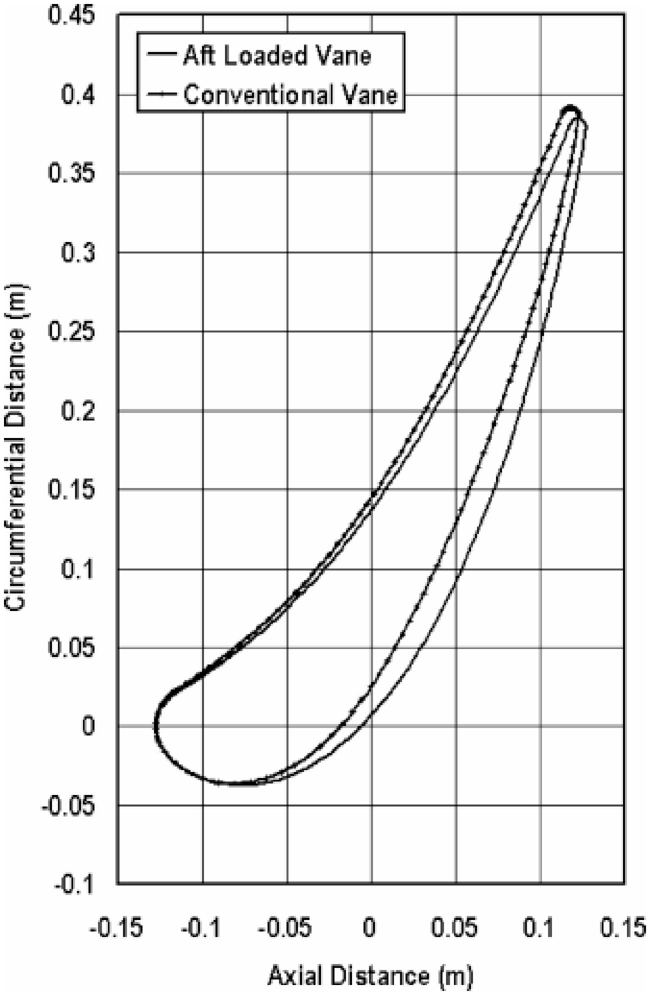

Fig. 2 Cross-sectional view of large-scale aft-loaded vane used in the present study compared with conventionally loaded vane used in the previous study

generator along with its connection with the contoured endwall cascade. At the leading edge plane of the vane, the inlet transitions from a 30-deg contraction on both sides to parallel endwalls using a 10.16 cm radius. This inlet configuration results in the maximum acceleration at the leading edge plane of the vane in order to inhibit the formation of a horseshoe vortex.

The aft-loaded vane has a true chord of 47.35 cm and an axial chord of 25.4 cm. The diameter of the leading edge is 5.34 cm and the diameter of the trailing edge is 0.98 cm. The span of the vanes are 25.4 cm in the parallel endwall section and the circumferential vane spacing is 38.4 cm. The aft loaded vane has a stagger angle of 56.8 deg and a computed air exit angle of 74.4 deg.

The cascade was run at exit chord Reynolds numbers of 500,000, 1,000,000, and 2,000,000. The exit velocity was based on the inlet total to average exit static pressure ratio and the exit static temperature. The average exit static pressure was based on the average static pressure over the ten exit static taps spanning the exit passages downstream from the instrumented vane. The range of Reynolds numbers investigated during this investigation is consistent with chord exit Reynolds numbers in medium sized industrial gas turbines and turbofan engines.

Turbulence Generators. The objective of this portion of the study was to develop inlet turbulence characteristics, which are representative of dry low NO_x and catalytic combustion systems. In order to provide a range of known conditions, both a low turbulence and an aero-derivative gas turbine combustor condition were generated. The mock combustor geometries used to develop these inlet conditions were previously documented in [1], except for the inlet contraction into the test section. The mock combustor liner used for this study is shown schematically in **Fig. 3**. In this schematic the mock combustor is configured in the aero-derivative geometry consisting of a back panel with slots to generate wall jets and side panels with two rows of holes to mimic primary and dilution jets. The liner then begins the two to one contraction into the test section. However, unlike the old liner, which completed the contraction prior to connecting to the cascade test section, the new liner connects along a 30-deg contracting wall. As a consequence, the majority of the contraction takes place within the contoured endwall cascade test section. This effectively moves the leading edge plane of the vanes 31.8 cm forward toward the mock combustor compared to the geometry used in the linear cascade study. For the mock low NO_x combustor geometries, the side panels with holes are replaced with blank panels and the back panel is replaced with either the dry low NO_x (DLN) swirler panel or the catalytic combustor panel. In addition, the area between the sidewalls and casing of the mock combustor are blocked. Photos of the swirler panel used for the DLN configuration and the catalytic panel used for the catalytic combustor configurations are shown in **Figs. 4** and **5**.

The mock DLN combustor configuration consists of a back panel with ten swirlers. Each of the swirlers is comprised of 20.3 cm schedule 40 pipe with a 5.1 cm centerbody. Each swirler has 12 vanes, which are placed at an angle of 45 deg. The design of this DLN configuration is a compromise between the dry low NO_x combustor configuration documented by Van Fossen and Bunker [5] and a green thumb DLN combustor designed for Rolls Royce industrial engines, [17].

The mock catalytic combustor panel was developed from a geometry provided by Catalytica Energy Systems. Catalytica pro-

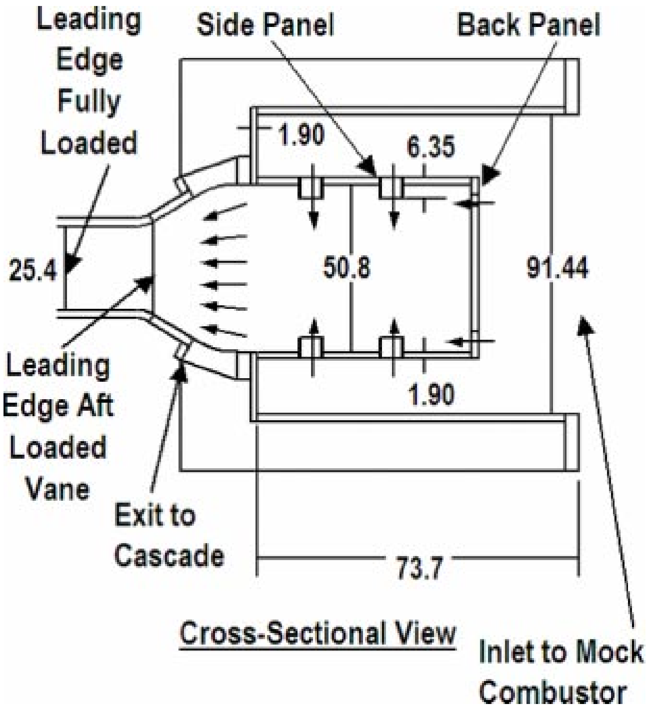

Fig. 3 Schematic of mock combustor turbulence generator in aero-derivative configuration showing interface with cascade

vided a sample foil with serpentine grooves spaced at 2.2 mm. In a catalytic combustor these serpentine grooves cross back and forth to promote mixing. An evaporative cooling panel was found that had a similar crossing groove pattern but was 12 times larger. Considering the cascade is scaled at 11 times the actual vane geometry, this 12-times scale evaporative cooling panel is believed to be a good match to the geometry of the catalytic surface.

Vane Pressure Distribution Comparison. Midline pressure distributions were acquired at chord exit Reynolds numbers of 500,000, 1,000,000, and 2,000,000 using an epoxy vane with integral pressure tubing. The third vane from the bottom can be inserted through a machined opening in the side of the cascade to accommodate either a vane capable of acquiring a pressure distribution or the heat transfer vane. The pressure vane was fabricated by casting 40 1.6 mm diameter brass pressure tubes spanwise along the surface of an epoxy vane at approximately 2.54 cm intervals. Static pressure taps were then formed by drilling through the epoxy surface into the vane with a small (<1 mm) diameter drill bit. The resulting pressure distribution is shown in **Fig. 6** compared to a three-dimensional FLUENT prediction. The three-dimensional FLUENT prediction was needed to account for the contraction at the entrance of the cascade. Also shown in the figure are the experimental pressure distribution for the fully loaded vane and the corresponding two-dimensional FLUENT prediction. In this figure the pressure distribution is shown as local static pressure divided by the inlet total as a function of surface arc. Zero surface arc indicates the stagnation point of the airfoil. Positive surface arc is measured from the stagnation point along the suction surface of the vane and negative surface arc is measured from the stagnation point along the pressure surface of the vane. The aft-loaded vane design provides acceleration along the suction surface to approximately mid arc where the diffusion process begins to slowly proceed. The experimental pressure distribution for the aft loaded vane is a good match for the three-dimensional FLUENT prediction. The fully loaded vane pressure distribution is also shown. Clearly the acceleration up to the point of maximum velocity (minimum Ps/Pt) is very rapid and the vane shows a relatively quick change from favorable to mildly adverse pressure gradient. With the addition of high turbulence levels, this minimum pressure point is often the location of the start of transition. The aft-loaded vane is designed to accelerate well past this point to inhibit transition. However, the design results in more diffusion in the aft region of the suction surface. Overall the comparison between the experimental pressure distribution on the aft-loaded vane and the three-dimensional prediction is quite consistent and provides confidence in the quality of the midspan aerodynamics produced by the cascade. This accurate reproduction of midspan aerodynamics enhances the usefulness of the database for grounding computational models.

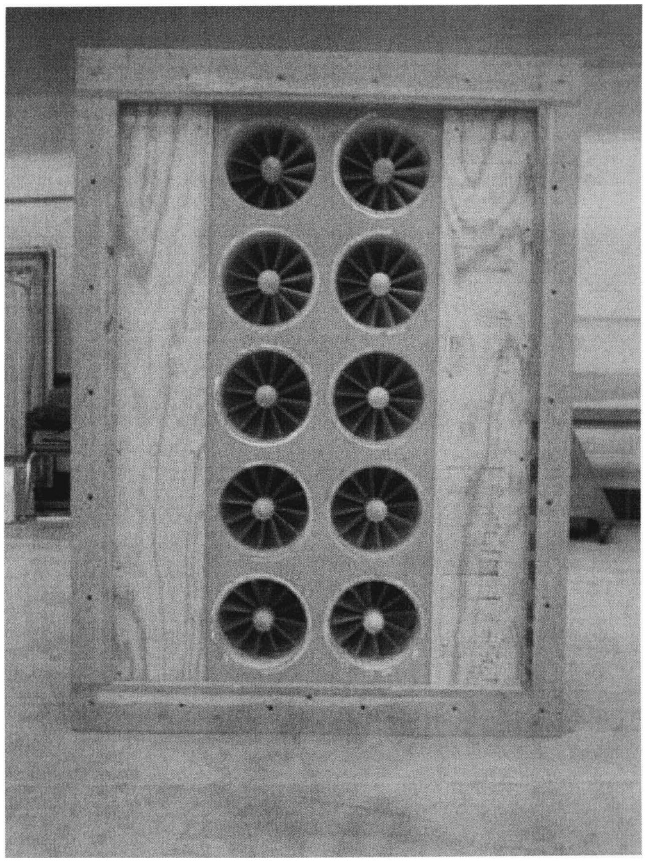

Fig. 4 Digital photo of dry low NO$_x$ swirlers installed in mock combustor liner

Heat Transfer Vane and Baselining. Midline heat transfer distributions were acquired using a vane fabricated from a polyisocyanurate foam core with a 1.6 mm thick cast epoxy outer shell. Temperature along the surface was determined using 52 fine wire type K thermocouples, which were cast into the surface at the midspan of the vane. A constant heat flux was generated on the surface of the vane using a 0.023 mm thick Inconel foil heater backed by a 0.127 mm thick Kapton film and bonded to the vane using 0.05 mm of high temperature acrylic adhesive. Power was delivered to the foil using two 6.35 mm by 0.5 mm copper bus bars, which were soft soldered to the ends of the Inconel foil. The foil was powered by a large DC current, which was measured using a high-current precision shunt resistor. The voltage drop across the heater was also monitored to complete the measurement of power dissipation. The vane surface resulting from adhering the foil onto the epoxy vane was aerodynamically smooth and visually attractive.

Midline heat transfer distributions at the low turbulence condition were acquired and compared to finite difference boundary layer calculations to provide confidence in the experimental method. Surface Stanton number distributions were acquired at

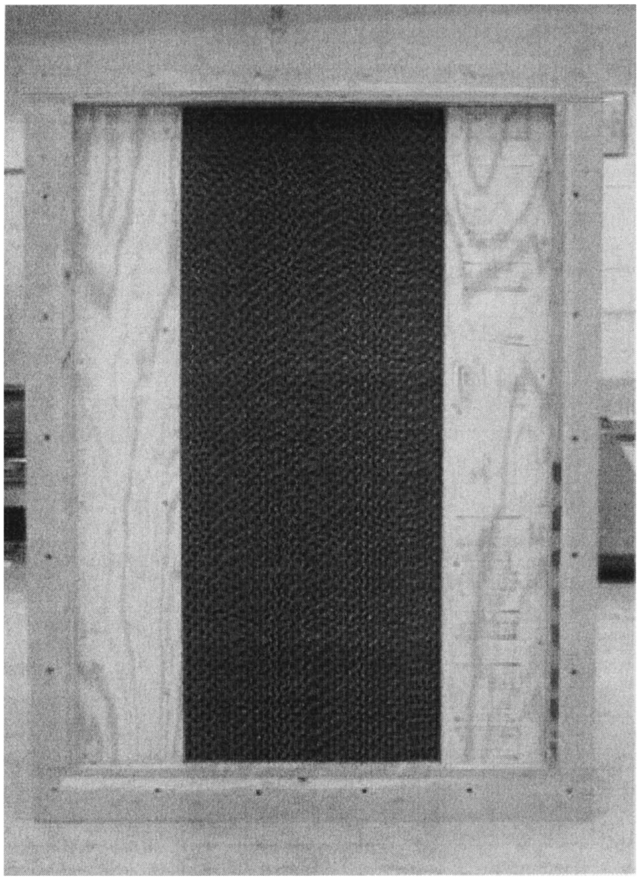

Fig. 5 Digital photo of catalytic combustor surface installed in mock combustor liner

three Reynolds numbers ranging from exit chord Reynolds numbers of 500,000 through 2,000,000. Initially, the tunnel was run without heating the vane and the surface recovery temperatures were acquired. Subsequently, the temperature distribution was acquired at the applied surface heat flux condition. The net surface heat flux was calculated as the measured heat flux of the foil less the radiative loss. Radiative losses were calculated using the local surface temperature assuming the foil with an emissivity of 0.21 was emitting to a black body at inlet total temperature. Conduction losses through the relatively thick isocyanurate foam vane were assumed negligible as was conduction along the surface of the foil. As a consistency check a heat transfer distribution was acquired at half power and full power resulting in an rms variation of less than 0.9% with a maximum variation of 1.3%.

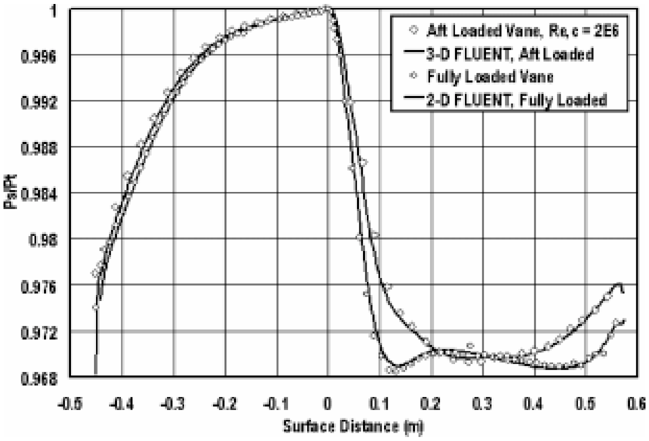

Fig. 6 Comparison between measured and predicted vane midspan pressure distributions for aft and fully loaded vanes

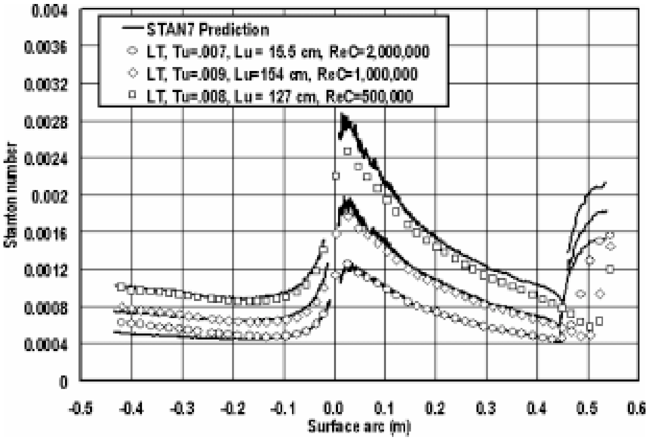

Fig. 7 Low turbulence vane Stanton number distributions with STAN7 predictions

A comparison between the low turbulence condition midline Stanton number distribution and a STAN7, [18], finite difference boundary layer prediction is shown in **Fig. 7**. The reported Stanton numbers are based on properties taken at exit conditions and are plotted at exit chord Reynolds numbers of 500,000, 1,000,000, and 2,000,000 as a function of surface distance. Positive surface distance is determined from the stagnation point along the suction surface, while negative distance is reported along the pressure surface. Generally, experimental values agree with predictions to within 10%, except at the end of the pressure surface at the high Reynolds number condition, and provide confidence in the experimental technique.

Data Acquisition. The PC-based data acquisition system, which was used to acquire the thermocouple emf's, pressure transmitter voltages, and shunt and heater voltages, relies on an HP 3497A data acquisition unit. The HP 3497A has an integral voltmeter with 1 μV resolution and was interfaced with the computer using an IEEE-488 interface bus. Pressures were monitored using two Rosemount Smart Pressure Transmitters scaled to ranges of 250 Pa and 5000 Pa with reported accuracy of 0.1% of full scale. The pressures were scanned with a homemade pressure multiplexer built from miniature solenoid valves. The thermocouples were connected through a passive constant temperature junction box, which was referenced to an ice bath. Hot wires were powered, low pass filtered, bucked and gained using a two-channel TSI ISA 300 hot wire anemometry bridge. Voltage signals from the hot wire system were read using a high-speed 12-bit data acquisition card. Velocity time records acquired for spectral analysis were acquired in 40 sets of 8192 samples and post processed.

Data Uncertainties. Uncertainties in heat transfer, pressure, velocity, and turbulence quantities were estimated using the root sum square method described by Moffat [19]. Based on this method, the uncertainty in the reported Stanton number ranged up to $+/-6\%$ at a 95% confidence interval. The uncertainty for run to run comparisons is estimated to be $+/-3\%$. Uncertainties in local pressure measurements are estimated to be no more than $+/-2.5\%$ of the local dynamic pressure. The uncertainty in the exit Reynolds number was estimated to be $+/-2\%$. The error in the turbulent scale was estimated at $+/-15\%$. All these uncertainty estimates were provided at a confidence interval of 95%.

Inlet Turbulence Characteristics. The three mock combustor configurations used in the present investigation were the same

Table 1 Characteristics of inlet velocities, turbulence level and scale, and dissipation for various turbulence generators

	Reynolds	Tu	U (m/s)	Lx (cm)	Lu (cm)	$\varepsilon(\mathrm{m}^2/\mathrm{s}^3)$
Low turbulence	500000	0.0081	4.22	8.12	127.0	0.0001
(LT)	1000000	0.0089	8.86	5.02	154.5	0.0004
	2000000	0.0071	15.90	3.58	15.45	0.0144
Catalytic	500000	0.0142	4.30	4.74	5.43	0.0065
Combustor	1000000	0.0142	8.35	3.63	3.21	0.0909
(CC)	2000000	0.0126	15.99	1.57	1.58	0.8693
Aeroderivative	500000	0.2049	4.17	4.95	5.61	16.60
Combustor	1000000	0.2091	8.39	4.56	6.01	134.60
(AC)	2000000	0.2097	16.83	4.57	6.35	1036.2
Dry low NO_x	500000	0.1373	4.26	3.90	5.21	5.78
(DLN)	1000000	0.1487	7.74	3.66	5.27	43.56
	2000000	0.1543	15.22	3.91	6.27	310.42

as those used in the fully loaded vane linear cascade study, [1]. However, due to the contoured inlet the cascade was effectively 31.8 cm closer to the turbulence generator. Additionally, since the inlet of the cascade contracts at a 30-deg angle on both sides, the inlet velocities were lower and as a consequence the turbulence measurements were reacquired. Turbulence measurements were taken for all four conditions at the three Reynolds numbers. Velocity and turbulence data were acquired at three spanwise positions at three circumferential (up and down) positions across one passage, 5 cm upstream from the leading edge plane of the vanes. At each location, 40 velocity time records of 8192 points were taken and processed. Based on these records, the turbulence level (Tu), average midspan velocity (U), integral scale (Lx), energy scale (Lu), and dissipation (ε) were determined for each condition and are reported in **Table 1**. The integral scale was determined from the product of the autocorrelation time scale with the local convective velocity. The autocorrelation in time was calculated from the averaged energy spectrum using an inverse FFT. The dissipation was determined from the spectrum function in the inertial subrange. More details concerning the procedure for determining these values are given in [1]. An example of a typical one-dimensional energy spectrum for u' is given in **Fig. 8** for the aero-combustor at the highest Reynolds number.

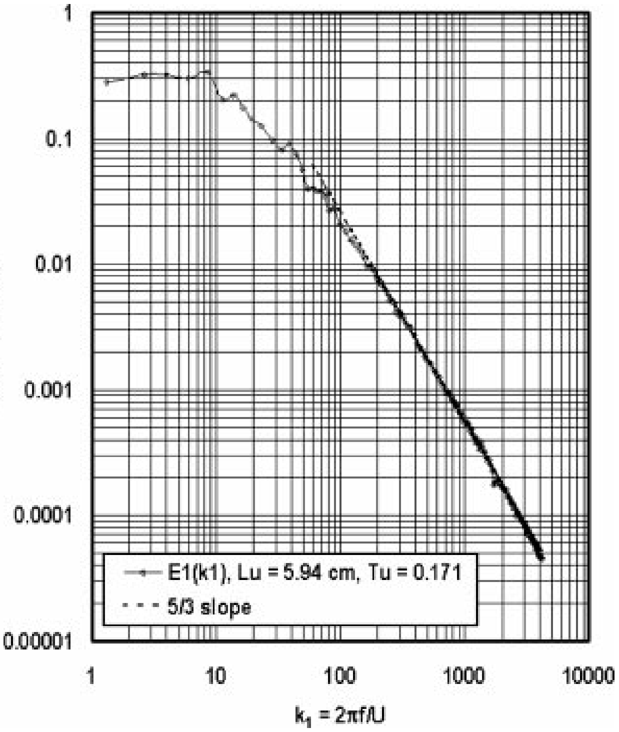

Fig. 8 One-dimensional energy spectra of u' for aero-derivative combustor

The uniformity of the streamwise fluctuation velocity, $|u'|$, and dissipation were reasonably good in the circumferential direction at the inlet of the cascade for the two high turbulence conditions. The dissipation level and $|u'|$ varied by no more than 10% for the aero-derivative combustor and 12% for the mock DLN combustor.

Heat Transfer Results

Turbulence level, scale, and Reynolds number have been found to have a substantial influence on heat transfer augmentation in laminar regions and the onset and length of transition. This section examines the influence of turbulence characteristics and Reynolds number on the heat transfer distributions acquired in the present study in both a qualitative and quantitative manner. Initially, the raw Stanton number distributions will be examined for the three Reynolds number cases. Next, the data will be presented in terms of Stanton number augmentation, which often gives a better picture of the relative influence of turbulence on both augmentation and the location of the onset of transition. Laminar heat transfer augmentation in the stagnation region and pressure surface is examined in terms of turbulence level, scale, and Reynolds number. Finally, heat transfer is predicted using a finite difference boundary layer code, [18], the algebraic turbulence model of Ames, Kwon, and Moffat [20], and the transition model of Mayle [13].

Stanton Number Distributions. Vane heat transfer distributions for exit Reynolds numbers of 500,000, 1,000,000, and 2,000,000 are presented in **Figs. 9**, **10**, and **11** in terms of Stanton number for the four inlet conditions developed for this study. The figures present Stanton number based on exit conditions as a function of surface distance. The turbulence intensities shown in the figures have been adjusted to account for decay assuming $Tu(x) = 1/[1/Tu(0)+x/(2\,Lu)]$.

Midline Stanton number distributions, acquired at a chord Reynolds number of 500,000, are presented in **Fig. 9** for the four inlet conditions developed for this investigation. The low turbulence (LT) case shows laminar behavior over the entire surface except for a short region near the trailing edge of the suction surface where transition appears to begin in this adverse pressure gradient region. The catalytic combustor (CC) produces an inlet turbulence intensity of 1.3% with an energy scale of 1.6 cm and produces the same laminar behavior seen in the low turbulence case. Assuming catalytic combustion systems are of similar geometry to the current mock combustor, the laminar behavior produced by this condition indicates the use of these systems could result in a significant reduction in heat load to the nozzle guide vane. The aero-combustor condition produces significant levels of augmentation on both the laminar pressure surface and in the stagnation region

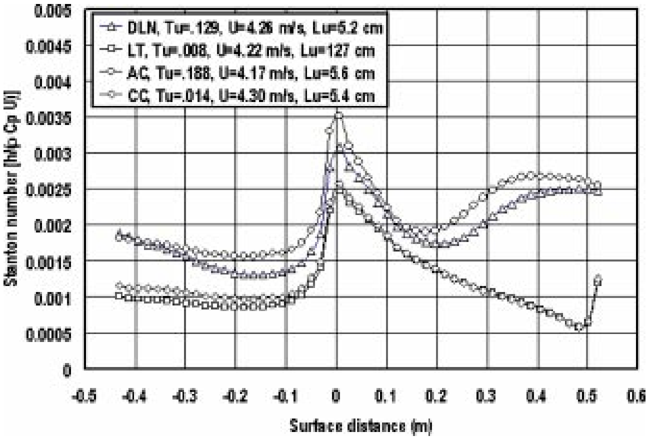

Fig. 9 Effects of mock combustor turbulence on vane Stanton number distributions, Re_C=500,000

and causes transition to begin at about 30% surface arc on the suction surface. Generally, the dry low NO_x (DLN) combustor has similar behavior to the aero-combustor. However, corresponding to its lower turbulence intensity, lower augmentation levels are seen in the laminar regions on the pressure and stagnation region and transition begins a bit later on the suction surface. One peculiar aspect of this distribution is the rise in heat transfer augmentation seen about mid arc on the pressure surface. This somewhat surprising result may be due to the significant vorticity, which is generated by the mock DLN combustor.

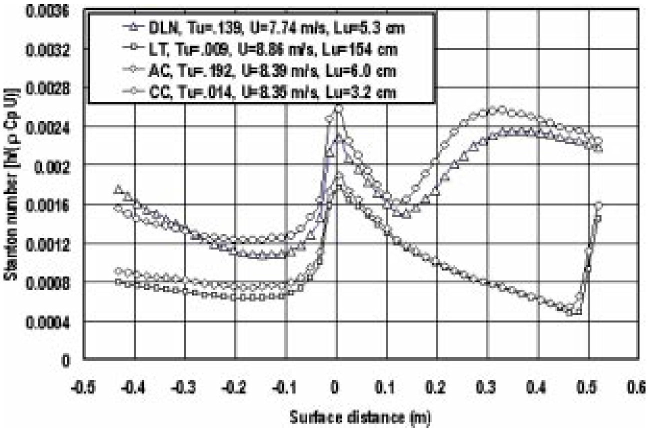

Fig. 10 Effects of mock combustor turbulence on vane Stanton number distributions, Re_C=1,000,000

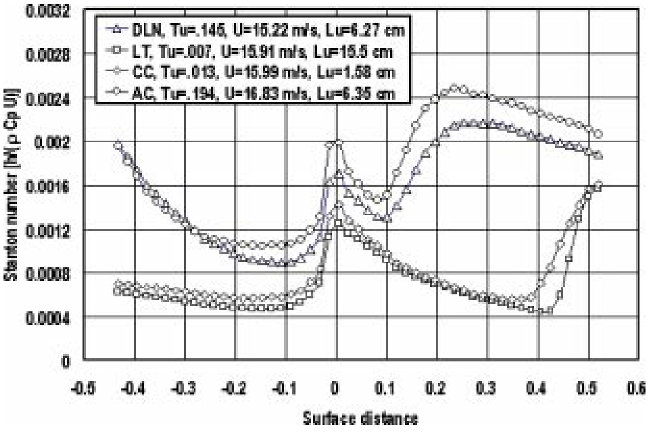

Fig. 11 Effects of mock combustor turbulence on vane Stanton number distributions, Re_C=2,000,000

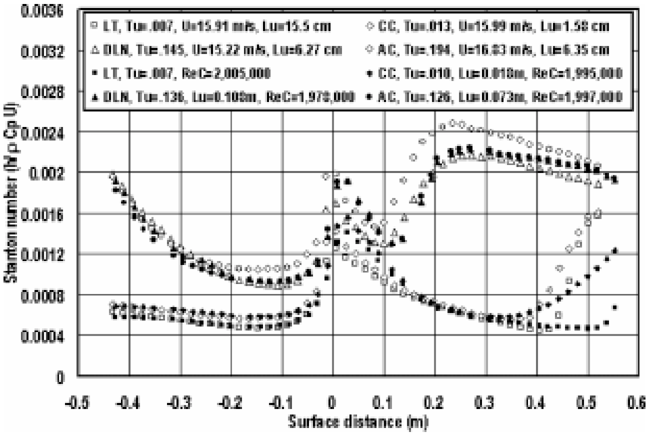

Fig. 12 Comparison between conventional and aft loaded vane heat transfer distributions, Re_C=2,000,000, Catalytic and DLN combustor

Stanton number distributions, acquired at a chord Reynolds number of 1,000,000, are shown in **Fig. 10** for the four inlet conditions. Trends for this case are similar to the lower Reynolds number comparison. Again, both the low turbulence (LT) case and the catalytic combustor (CC) case show predominately laminar behavior over the same surface. Near the trailing edge of the suction surface transition begins in the adverse pressure gradient region. Both the aero-combustor (AC) condition and the dry low NO_x (DLN) case show significant levels of augmentation on the pressure surface and stagnation region as well as a relatively early transition on the suction surface. Again, the same unexpected transitional behavior is seen in the pressure surface DLN profile. **Figure 11** presents Stanton number distributions for a chord Reynolds number of 2,000,000 for the four inlet turbulence conditions. Trends for this condition are similar with the lower Reynolds number cases. However, as expected at the higher Reynolds number laminar augmentation has increased for the DLN and aero-combustor cases and transition occurs earlier on the suction surface for both the two higher and two lower turbulence cases. Also, similar to the two lower Reynolds number cases transition appears to occur early on the pressure surface for the DLN case. However, at this Reynolds number this behavior would not be unexpected.

The present vane has an aft loaded pressure distribution on the suction surface to contrast the fully loaded distribution reported by Ames, Wang, and Barbot [1]. **Figure 12** compares the Stanton number distributions for the aft and fully loaded vanes for the four inlet configurations used in the present investigation. Qualitatively the trends of the heat transfer distributions on the two vanes are quite similar. Due to the contracting inlet on the present cascade the leading edge plane has been pulled forward toward the turbulence generator resulting in a higher level of turbulence. The present distributions show a higher heat transfer level for the aero-combustor case. However, generally the heat transfer in the stagnation region has been reduced due to the contracting inlet, which has the effect of lowering the approach velocity. The aft-loading does not have a significant influence on transition at either the very high or very low turbulence level reported in this investigation.

Laminar Heat Transfer Augmentation and Transition Heat transfer augmentation levels are presented in terms of St/St0 versus surface distance in **Figs. 13–15** for the three Reynolds numbers. Augmentation levels for the 500,000 Reynolds number case are shown in **Fig. 13**. On the pressure surface the augmentation shows a steady rise from the stagnation region until a surface

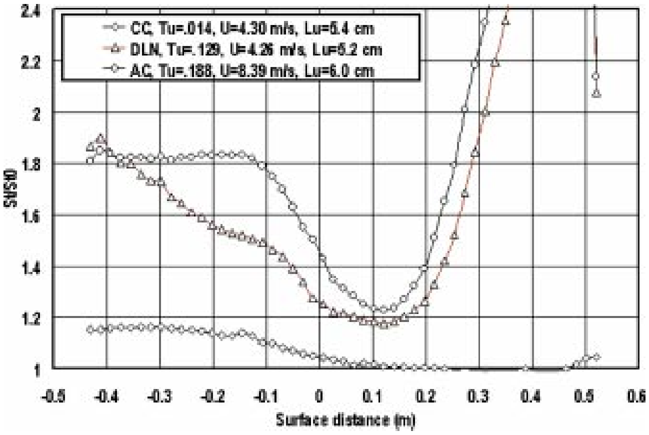

Fig. 13 Effects of mock combustor turbulence on Stanton number augmentation and location of transition, Re_C=500,000

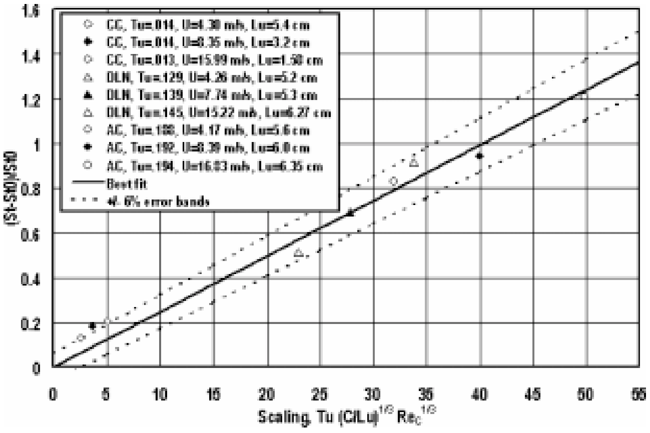

Fig. 16 Correlation of pressure surface Stanton number augmentation with turbulence intensity, energy scale, and chord Reynolds number.

arc of about 0.1 m where values flatten out at 83% for the aero-combustor case. This constant augmentation indicates laminar augmentation due to turbulence. However, augmentation levels for the DLN case first appear to flatten out at about 50% but then start to rise as if transition is occurring. The catalytic combustor case shows an average of 13% augmentation on the pressure surface. The figure also shows significant levels of augmentation in the stagnation region and provides a good indication of the location of transition. Augmentation levels determined for the 1,000,000 Reynolds number case are shown in **Fig. 14**. Qualitatively the behavior is similar to the 500,000 Reynolds number case with the aero-combustor augmentation rising to 94% after -0.1 m and staying relatively constant. The DLN data appear to start to flatten at about 65% but then start to increase indicating transition. The catalytic combustor case shows an augmentation level of around 18% over most of the pressure surface. **Figure 15** shows augmentation levels for Stanton number for the 2,000,000 Reynolds number case. Qualitatively the behavior for this condition is similar to the two lower Reynolds numbers cases. However, one new feature is the indication of transition on the pressure surface occurring for the aero-combustor case at a surface distance of around -0.28.

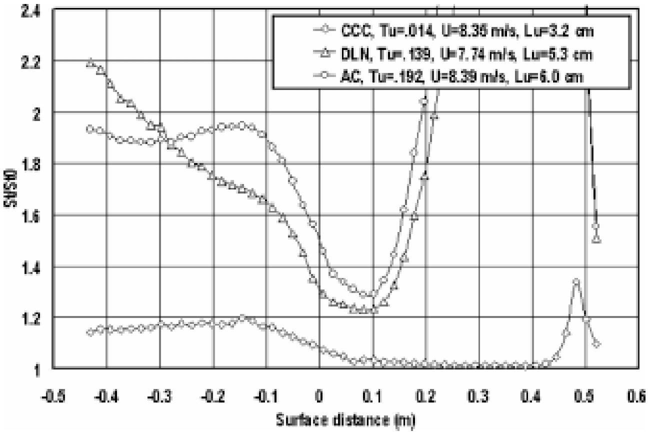

Fig. 14 Effects of mock combustor turbulence on Stanton number augmentation and location of transition, Re_C =1,000,000

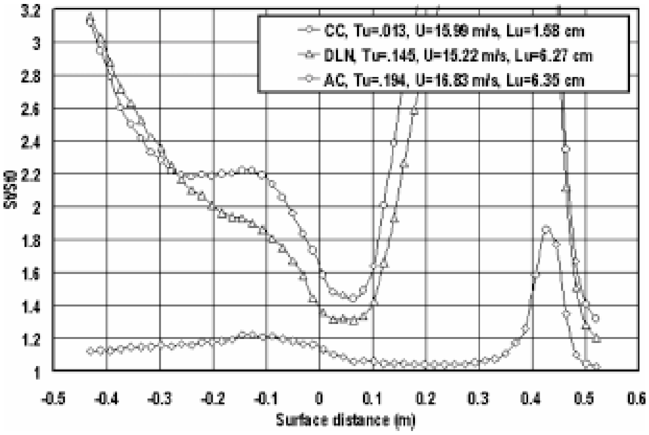

Fig. 15 Effects of mock combustor turbulence on Stanton number augmentation and location of transition, Re_C =2,000,000

According to Ames [6] heat transfer augmentation to the laminar boundary layer should scale on turbulence intensity (Tu), Reynolds number to the one-third power, and energy scale (Lu) to the one−third power. Accordingly, (St-St0)/St0 $\propto Tu\ \mathrm{Re}_C^{1/3}\ (C/Lu)^{1/3}$. This scaling is related to the response of the normal component of turbulence to the presence of a wall, which blocks relatively large eddies from contributing to the mixing process. Ames [6] looked at the influence of Reynolds number over a relatively narrow range but concluded a one-third power dependency. Ames, Wang, and Barbot [1] were able to extend the range of Reynolds numbers from 500,000 to 2,000,000 finding their results supported Ames's conclusion. The present data are plotted in terms of the mean (St-St0)/St0 over the augmentation plateau on the pressure surface versus the $Tu\ \mathrm{Re}_C^{1/3}\ (C/Lu)^{1/3}$ parameter in **Fig. 16**. The augmentation values for the aero-combustor condition were clear and taken to be 83, 94, and 121% augmentation, respectively. The augmentation values for the DLN conditions were averaged over surface arcs from -0.108 m to -0.184 m and were found to be 51, 69, and 82 percent for increasing Reynolds number. The heat transfer data from the aero-combustor and DLN conditions scale well on this parameter falling within the $+/-6\%$ error bands shown in the figure. Generally, the Stanton number augmentation data support the correlating parameter and the physical model, which the variable dependence represents.

Stagnation Region Augmentation. At lower chord Reynolds numbers or in passages where the inlet velocity is relatively high, heat transfer at the stagnation region of a turbine airfoil can often be the highest on the surface. These high heat transfer rates can present difficulties for designers. Consequently, developing methods to predict heat transfer augmentation in this region is important for the design of satisfactory cooling schemes. Ames and

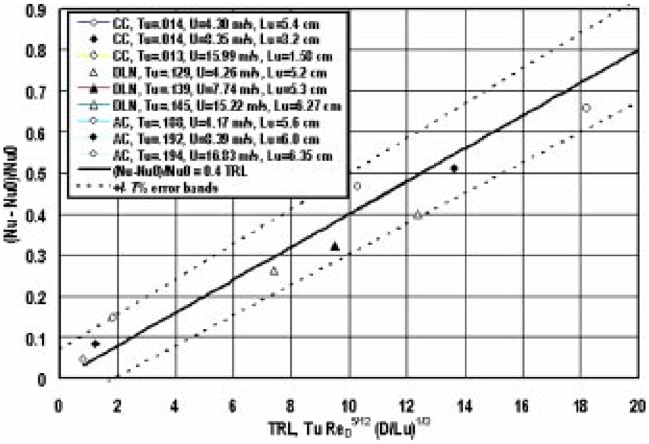

Fig. 17 Correlation of stagnation region Nusselt number augmentation with TRL parameter

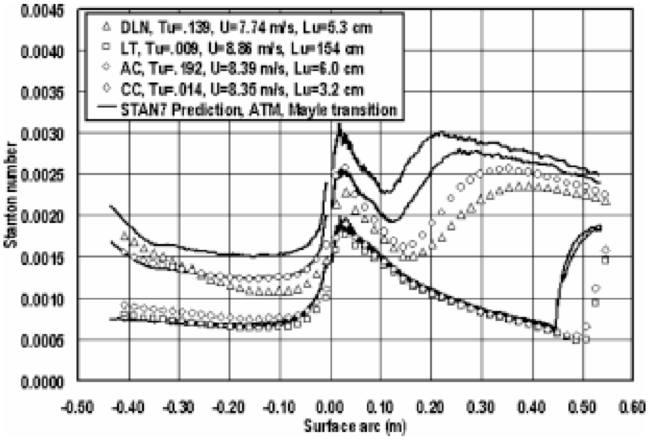

Fig. 19 Prediction of turbulence effects on vane Stanton number distributions using STAN7 with ATM and Mayle [13], $Re_C = 1{,}000{,}000$

Moffat [8] proposed a correlating parameter for stagnation region heat transfer augmentation, which depends on turbulence intensity, diameter Reynolds number, and diameter-to-energy-scale ratio. Ames [6] suggested a good engineering approximation for the increase in Nusselt number was $(\mathrm{Nu}\text{-}\mathrm{Nu0})/\mathrm{Nu0} = 0.04\, Tu\, \mathrm{Re\, D}^{5/12}\ (D/Lu)^{1/3}$. **Figure 17** presents the Nusselt number augmentation for the present data as a function of the TRL parameter of Ames and Moffat. The stagnation region augmentation is based on the average of the two heat transfer data points on either side of 0.0 surface arc normalized on the low turbulence case values. All the data correlate within the +/−7% error bands shown and tend to support the usefulness of the correlating parameter and the physical model it represents. In spite of augmentation levels of 66%, the data show no sign of an approaching plateau suggesting higher turbulence intensities at higher Reynolds numbers will produce even higher augmentation levels.

Finite Difference Boundary Layer Predictions. Designers often use two-dimensional boundary layer codes to predict initial heat loads on turbine airfoils in regions expected to be two-dimensional. The use of this well-established tool in contrast to modern three-dimensional RANS codes available to designers is due to the accuracy of the method and ease of use of these tools. In spite of the long history of boundary layer predictive methods, the development of accurate turbulence models is still a critical research area. The present data represent an excellent test case for boundary layer predictive methods due to the relevant turbulence conditions, the range of Reynolds numbers and the relevant vane geometry. Two-dimensional boundary layer predictions were made for the current database using STAN7, [18], a finite difference boundary layer code, the algebraic turbulence model (ATM) of Ames, Kwon, and Moffat [20] and the transition model of Mayle [13]. Ames, Wang, and Barbot [1] proposed a method to enhance the ATM by accounting for the effect of stagnation region strain rates on turbulent mixing.

Stanton number predictions for the present data are shown in **Figs. 18–20**. In **Fig. 18**, the 500,000 Reynolds number case predictions overestimate Stanton number on the pressure surface by up to 18% for the aero-combustor case and 16% for the DLN case. In general predictions match the predominately laminar flow of the lower turbulence cases well. In the stagnation region the calculations predict the actual data within about 5%. However, on the suction surface the Mayle model is conservative indicating onset and completion of transition well upstream of the data. Trends for the 1,000,000 chord Reynolds number predictions are similar to the lower Reynolds number case. Here calculations overpredict heat transfer on the pressure surface by as much as 22% and in the stagnation region by as much as 13%. Again the prediction of transition of the suction surface is conservative. Predictions for the 2,000,000 Reynolds number case are somewhat

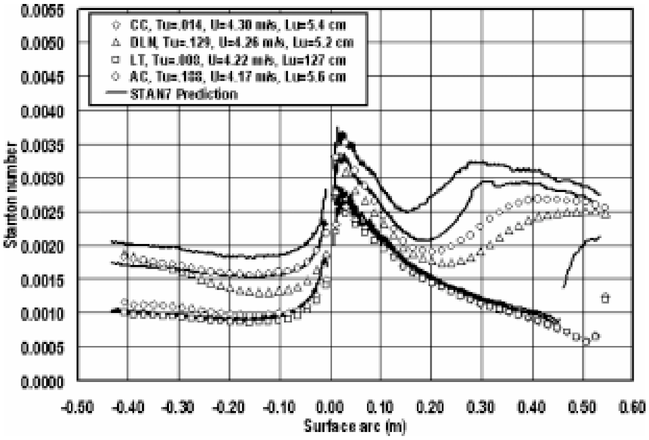

Fig. 18 Prediction of turbulence effects on vane Stanton number distributions using STAN7 with ATM and Mayle [13], $Re_C = 500{,}000$

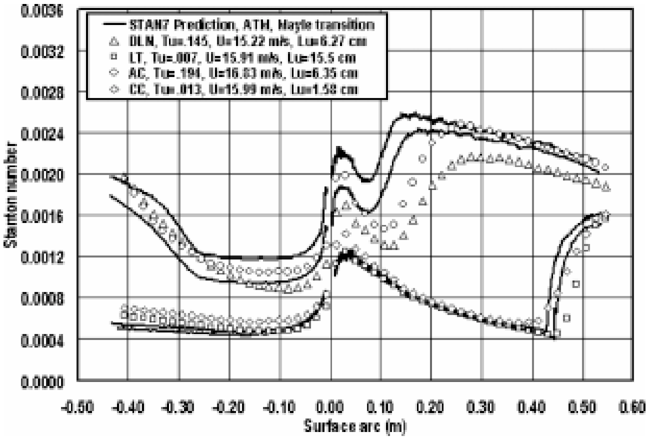

Fig. 20 Prediction of turbulence effects on vane Stanton number distributions using STAN7 with ATM and Mayle [13], $Re_C = 2{,}000{,}000$

closer with predictions matching data to within 12% on the pressure surface and within 10% in the stagnation region. Again, prediction of transition on the suction surface is conservative. Generally, the predictions are conservative and match the data reasonably well suggesting the turbulence model has potential to provide accurate predictions for design calculations.

Summary and Conclusions

The present paper documents the influence of mock DLN, catalytic, and aeroderivative combustor turbulence on heat transfer distributions on an aft loaded vane. These results extend the vane heat transfer database began by Ames, Wang, and Barbot [1]. Together these heat transfer test cases represent a wide range of conditions covering a four-to-one range in Reynolds numbers for two vane geometries tested over six well-documented inlet conditions. Additionally, these data provide information, which help document turbulence conditions likely to be produced by new low NO_x combustion systems. Further, they document the resulting response of vane surface heat transfer to these conditions on relevant geometries arming designers with a useful database.

The present study was conducted in a new cascade test section with strong inlet acceleration and an aft loaded vane geometry. Pressure distributions demonstrated that pushing the vane forward into the inlet contraction reduced the approach velocity and resulting velocity gradient at the vane leading edge. The lower stagnation velocity gradient resulted in a moderate reduction in heat transfer at the leading edge. At the very high and low turbulence levels developed in the present investigation over the Reynolds number range, the aft loaded vane had little noticeable influence on the location of transition. At more moderate turbulence levels and higher Reynolds numbers this may not have been the case.

The present data correlated well with both the stagnation region parameter, TRL, of Ames and Moffat [8] and the pressure surface augmentation parameterization of Ames [6]. These results tend to support the physical model of how the normal component of turbulence responds near a wall and in the presence of the strain field of a stagnation region. Augmentation levels of 66% were found in the stagnation region and 121% on the pressure surface. No augmentation plateau was observed in the data. Consequently, these data suggest at higher Reynolds numbers and more aggressive turbulence situations, higher augmentation levels should be expected.

Comparative predictions were made using the finite difference boundary layer code STAN7, [18], with the ATM model of Ames, Kwon, and Moffat [20] and the transition model of Mayle [13]. Generally, augmentation levels were captured well in the stagnation region and slightly overpredicted on the pressure surface. The location of transition was captured well on the pressure surface but was conservative on the suction surface. The present heat transfer data, together with the results of Ames, Wang, and Barbot [1], are expected to provide a useful database for the grounding of vane heat transfer predictive models.

Acknowledgments

The authors gratefully acknowledge the support from the Advanced Gas Turbine System Research (AGTSR) consortium, which is administrated by the South Carolina Institute for Energy Studies and largely funded through DOE's National Energy Technology Laboratory. The authors would also like to acknowledge the help of Rolls Royce of Indianapolis for working with UND in the development of the aft loaded vane geometry used in this study. Additionally, the facility used in this project was funded through a seed grant from the North Dakota EPSCoR Program. In addition, the authors are indebted to the University of North Dakota for providing additional support and laboratory space. Finally, the authors would like to acknowledge the work of Rob Coughlin, Jennifer Endicott, Ryan Frederick, and David Motter who helped design and fabricate the original test section as a senior design project and to Troy Lassle, Dominik Steinhauer, and Jeff Scully who worked as summer research assistants on this project.

Nomenclature

C = vane true chord length, m
Cp = specific heat at constant pressure, J/(kg K)
D = vane leading edge diameter or effective diameter based on $D = 3.62\,U_\infty/(dU_\infty/dx)$
$E_1(f)$ = one-dimensional spectrum as a function of frequency, f, of the streamwise fluctuation velocity, u', $\mathrm{m^2/s}$
$E_1(k_1)$ = one-dimensional energy spectrum function, $E_1(k_1) = U\,E_1(f)/2/\pi$, $\mathrm{m^3/s^2}$
f = frequency, 1/s
h = heat transfer coefficient, $\mathrm{W/m^2/K}$, based on T_r and T_w
k = thermal conductivity, W/m/K
K = freestream acceleration parameter, $K = \nu/U_\infty^2 \cdot (dU_\infty/dx)$
k_1 = wave number, $k_1 = 2\pi f/U$, $\mathrm{m^{-1}}$
Lu = energy scale, $Lu = 1.5\,|u'|^3/\varepsilon$, m
Lx = longitudinal integral scale of u' fluctuation, m
Nu = Nusselt number, hD/k
P = Pressure, Pa
Re_C = true chord Reynolds number, based on exit conditions
St = Stanton number, $\mathrm{St} = h/(\rho Cp U_\infty)$
Tu = turbulence level, $Tu = |u'|/U_\infty$
TRL = turbulence, Reynolds number, length scale parameter for correlating stagnation region heat transfer, $\mathrm{TRL} = Tu \cdot \mathrm{Re}_D^{5/12} \cdot (D/Lu)^{1/3}$
u' = streamwise fluctuation velocity, m/s
$|u'|$ = rms streamwise fluctuation velocity, m/s

Greek Letter Symbols

ε = turbulent dissipation rate, $\mathrm{m^2/s^3}$
ν = kinematic viscosity, $\mathrm{m^2/s}$
ρ = fluid density, mass per unit of volume, $\mathrm{kg/m^3}$

Subscripts

0 = refers to value at same position for low turbulence condition
s = refers to static condition
t = refers to total or stagnation condition
∞ = evaluated in the freestream

References

[1] Ames, F. E., Wang, C., and Barbot, P. A., 2002, "Measurement and Prediction of the Influence of Catalytic and Dry Low NO_x Combustor Turbulence on Vane Surface Heat Transfer," ASME J. Turbomach, **125**, pp. 221–231.

[2] Ames, F. E., Barbot, P. A., Wang, C., 2002, "Effects of Aeroderivative Combustor Turbulence on Endwall Heat Transfer Distributions Acquired in a Linear Vane Cascade," ASME J. Turbomach., **125**, pp. 210–220.

[3] Ames, F. E., Barbot, P. A., and Wang, C., "Effects of Catalytic and Dry Low NO_x Combustor Turbulence on Endwall Heat Transfer Distributions," Abstract No. GT-2003-38507.

[4] Zimmerman, D. R., 1979, "Laser Anemometer Measurements at the Exit of a T63-C20 Combustor," NASA CR-159623.

[5] Van Fossen, G. J., and Bunker, R. S., "Augmentation of Stagnation Heat Transfer due to Turbulence From a DLN Can Combustor," ASME Paper No. 2000-GT-215.

[6] Ames, F. E., 1997, "The Influence of Large-Scale High-Intensity Turbulence on Vane Heat Transfer," ASME J. Turbomach., **119**, pp. 23–30.

[7] Moss, R. W., and Oldfield, M. L. G., 1991, "Measurements of Hot Combustor Turbulence Spectra," ASME Paper No. 91-GT-351.

[8] Ames, F. E., and Moffat, R. J., 1990, "Heat Transfer With High Intensity, Large Scale Turbulence: The Flat Plate Turbulent Boundary Layer and the Cylindrical Stagnation Point," Report No. HMT-44, Thermosciences Division of Mechanical Engineering, Stanford University, Stanford, CA.

[9] Hunt, J. C. R., 1973, "A Theory of Turbulent Flow Round Two-Dimensional Bluff Bodies," J. Fluid Mech., **61**, Part 4, p. 625.

[10] Britter, R. E., Hunt, J. C. R., and Mumford, J. C., 1979, "The Distortion of Turbulence by a Circular Cylinder," J. Fluid Mech., **92**.

[11] Van Fossen, G. J., Simoneau, R. J., and Ching, C. Y., 1995, "The Influence of

Turbulence Parameters, Reynolds Number, and Body Shape on Stagnation Region Heat Transfer,'' ASME J. Heat Transfer, **117**, pp. 597–603.

[12] Arts, T., Lambert de Rouvroit, M., and Rutherford, A. W., 1990, ''Aerothermal Investigation of a Highly Loaded Transonic Linear Turbine Guide Vane Cascade,'' Technical Note 174, von Karman Institute for Fluid Dynamics, Belgium.

[13] Mayle, R. E., 1991, ''The Role of Laminar-Turbulent Transition in Gas Turbine Engines,'' ASME J. Turbomach., **113**, pp. 509–537.

[14] Zhang, L., and Han, J.-C., 1994, ''Influence of Mainstream Turbulence on Heat Transfer Coefficients From a Gas Turbine Blade,'' ASME J. Heat Transfer, **116**, pp. 896–903.

[15] Thole, K. A., and Bogard, D. G., 1995, ''Enhanced Heat Transfer and Skin Friction due to High Freestream Turbulence,'' ASME J. Turbomach., **117**, p. 418.

[16] FLUENT 5.3, 1999, FLUENT 5.3 User's Guide, Fluent, Inc., Lebanon, NH.

[17] Smith, D., 2000, private communication, Rolls-Royce, Indianapolis, IN.

[18] Kays, W. M., 1987, ''STAN7, a Finite Difference Boundary Layer Code.''

[19] Moffat, R. J., 1988, ''Describing the Uncertainties in Experimental Results,'' Exp. Therm. Fluid Sci. **1**, pp. 3–17.

[20] Ames, F. E., Kwon, K., and Moffat, R. J., 1999, ''An Algebraic Model for High Intensity Large Scale Turbulence,'' ASME Paper No. 99-GT-160.

Mistuning Identification of Bladed Disks Using a Fundamental Mistuning Model—Part I: Theory

D. M. Feiner

J. H. Griffin

Department of Mechanical Engineering,
Carnegie Mellon University,
5000 Forbes Avenue,
Pittsburgh, PA 15213

This paper is the first in a two-part study of identifying mistuning in bladed disks. It develops a new method of mistuning identification based on measurements of the vibratory response of the system as a whole. As a system-based method, this approach is particularly suited to integrally bladed rotors, whose blades cannot be removed for individual measurements. The method is based on a recently developed reduced order model of mistuning called the fundamental mistuning model (FMM) and is applicable to isolated families of modes. Two versions of FMM system identification are presented: a basic version that requires some prior knowledge of the system's properties, and a somewhat more complex version that determines the mistuning completely from experimental data. [DOI: 10.1115/1.1643913]

1 Introduction

Bladed disks used in turbine engines are nominally designed to be cyclically symmetric. If this were the case, then all blades would respond with the same amplitude when excited by a traveling wave. However, in practice, the resonant amplitudes of the blades are very sensitive to small changes in their properties. Therefore, the small variations that result from the manufacturing process and wear cause some blades to have a significantly higher response and may cause them to fail from high cycle fatigue. This phenomenon is referred to as the mistuning problem, and has been studied extensively. Srinivasan provides a thorough review of this topic in [1].

To address the mistuning problem, researchers have developed reduced-order models (ROMs) of the bladed disk. These ROMs have the structural fidelity of a finite element model of the full rotor, while incurring computational costs that are comparable to that of a mass-spring model, [2–5]. In numerical simulations, most published ROMs have correlated extremely well with numerical benchmarks. However, some models have at times had difficulty correlating with experimental data, [6]. These results suggest that the source of the error may lie in our inability to determine the correct input parameters to the ROMs.

The standard method of measuring mistuning in rotors with attachable blades is to mount each blade in a broach block and measure its natural frequency. The difference of each blade's natural frequency from the mean value is then taken as a measure of the mistuning. However, the mistuning measured through this method may be significantly different from the mistuning present once the blades are mounted on the disk. This variation in mistuning can arise because each blade's frequency is dependent on the contact conditions at the attachment. Not only may the blade-broach contact differ from the blade-disk contact, but the contact conditions can also vary from slot-to-slot around the wheel. Therefore, in order to accurately measure mistuning, we must develop methods that can make measurements of the blade-disk assembly as a whole.

Such holistic measurement techniques are particularly important for integrally bladed rotors, since their blades cannot be removed for individual measurement. In this paper, we present a new method of identifying mistuning in bladed disks that is based on the vibration characteristics of the whole system. The key concept is that system modes are highly sensitive to small variations in mistuning. Consequently, the modes themselves provide a sensitive and accurate basis for identifying mistuning in the system.

Our method of system identification is based on a recently developed reduced order model called the fundamental mistuning model (FMM), [5], that accurately represents the vibratory response of an isolated family of modes. FMM is a highly reduced-order model that can completely describe a mistuned rotor using only its tuned system frequencies and the frequency mistuning of each blade/disk sector. As a result, when the FMM based identification method (FMM ID) is applicable, it is very easy to use and requires very little analytical information about the system, e.g., no finite element mass or stiffness matrices. We have developed two forms of FMM ID: a basic version of FMM ID that requires some information about the system properties, and a somewhat more advanced version that is completely experimentally based. The basic FMM ID requires the frequencies of the tuned system[1] as input. Then, given measurements of a limited number of mistuned modes and frequencies,[2] FMM ID solves for the mistuned frequency of each sector. The advanced form of FMM ID uses measurements of some mistuned modes and frequencies to determine all of the parameters in FMM, i.e., the frequencies that the system would have if it were tuned as well as the mistuned frequency of each sector. Thus, the tuned system frequencies determined from the second method can also be used to validate finite element models of the nominal system.

Judge and Pierre have developed an approach for determining mistuning in IBRs, [7], that also uses mistuned modes and frequencies to infer the rotor's mistuning. However, it is based on a more complicated reduced-order model that results in a more complex methodology, and requires significantly more analytically generated input data to implement. However, it is not inherently limited to an isolated family of modes as is FMM ID. Mignolet and Rivas-Guerra have also studied mistuning identification, [8,9]. Their focus, however, was on discerning the difference between mass and stiffness mistuning in an isolated blade.

This paper is Part I of a two part investigation and develops the

---

Contributed by the International Gas Turbine Institute and presented at the International Gas Turbine and Aeroengine Congress and Exhibition, Atlanta, GA, June 16—19, 2003. Manuscript received by the IGTI Dec. 2002; final revision Mar. 2003. Paper No. 2003-GT-38952. Review Chair: H. R. Simmons.

[1] The frequencies of the tuned system are typically calculated using a finite element analysis of a single blade/disk sector with cyclic symmetric boundary conditions applied to the disk.

[2] The modes required in FMM ID are the circumferential modes that correspond to the tip displacement of each blade around the wheel.

theory of the FMM ID methods, then confirms their applicability with numerical test cases. The second paper, Part II, examines the application of the methods to actual hardware.

This paper is organized as follows. Section 2 presents the basic FMM ID theory, and provides numerical test cases of the method. In Section 3, we present the completely experimental version of FMM ID that also identifies the tuned system frequencies. Section 4 discusses an extrapolation method that allows mistuning measured at rest to be used to predict the response of a rotor at speed. Lastly, the key attributes of the method are summarized in Conclusions.

2 Basic FMM ID

This section presents the basic FMM ID method. The basic method uses tuned system frequencies along with measurements of the mistuned rotor's system modes and frequencies to infer mistuning.

2.1 Theory. The FMM ID method is derived from the fundamental mistuning model (FMM). The first part of this section describes the FMM method. Then we invert the equations to obtain a formulation that can be used for system identification.

2.1.1 FMM Method. FMM is a highly simplified reduced-order model that can accurately predict the vibratory response of realistic bladed disks in an isolated family of modes, [5]. FMM requires only two sets of input parameters to calculate the modes and natural frequencies of the mistuned system: the tuned system frequencies of one isolated family of modes, and the frequency deviation of each blade-disk sector. In Appendix A, we derived a more general form of the FMM modal equation than was given in [5] that is applicable to systems with more flexible disks. The more general modal equation is

$$(\boldsymbol{\Omega}^{\circ 2}+2\boldsymbol{\Omega}^{\circ}\bar{\boldsymbol{\Omega}}\boldsymbol{\Omega}^{\circ})\vec{\beta}_j=\omega_j^2\vec{\beta}_j\,. \tag{1}$$

The eigenvector of this equation, $\vec{\beta}_j$, contains weighting factors that describe the jth mistuned mode as a sum of tuned modes, i.e.,

$$\vec{\phi}_j=\sum_{m=0}^{N-1}\beta_{jm}\vec{\phi}_m^{\circ} \tag{2}$$

where $\vec{\phi}_m^{\circ}$ is the mth tuned mode of the family of interest. The corresponding eigenvalue, ω_j^2, is the jth mode's natural frequency squared.

The matrix of the eigenvalue problem contains two terms, $\boldsymbol{\Omega}^{\circ}$ and $\boldsymbol{\Omega}$. $\boldsymbol{\Omega}^{\circ}$ is a diagonal matrix of the tuned system frequencies, ordered by ascending inter-blade phase angle of their corresponding mode. The notation $\boldsymbol{\Omega}^{\circ 2}$ is shorthand for $\boldsymbol{\Omega}^{\circ T}\boldsymbol{\Omega}^{\circ}$, which results in a diagonal matrix of the tuned system frequencies squared. The matrix $\boldsymbol{\Omega}$ contains the discrete Fourier transforms (DFT) of the sector frequency deviations. $\boldsymbol{\Omega}$ has the form

$$\bar{\boldsymbol{\Omega}}=\begin{bmatrix}\bar{\omega}_0 & \bar{\omega}_1 & \cdots & \bar{\omega}_{N-1}\\ \bar{\omega}_{N-1} & \bar{\omega}_0 & \cdots & \bar{\omega}_{N-2}\\ \vdots & \vdots & & \vdots\\ \bar{\omega}_1 & \bar{\omega}_2 & \cdots & \bar{\omega}_0\end{bmatrix} \tag{3}$$

where $\bar{\omega}_p$ is the pth DFT of the sector frequency deviations. Note that $\boldsymbol{\Omega}$ is a circulant matrix, in which each column is equal to the previous column rotated down a row. Therefore, for an N bladed disk, it has only N distinct values.

One of the key changes in the generalized FMM is that it uses a new quantity called a "sector frequency deviation" as a measure of the mistuning for each blade-disk sector. In the original FMM formulation, mistuning was measured by blade frequency deviations. The advantage of the new mistuning measure is that it not only accounts for mistuning in the blade, but also captures mistuning in the disk as well as variations in the way the blades are attached to the disk. The definition of a sector frequency deviation is provided in Appendix A.

FMM treats the rotor's mistuning as a known quantity that it uses to determine the system's mistuned modes and frequencies. However, if we were to treat the mistuned modes and frequencies as known, we could solve the inverse problem to determine the rotor's mistuning. This is the basis of FMM ID.

2.1.2 Inversion of FMM Equation. This section manipulates the FMM equation of motion to solve for the mistuning in the rotor. Consider Eq. (1). All quantities are treated as known except $\boldsymbol{\Omega}$, which describes the system's mistuning. Subtracting the $\boldsymbol{\Omega}^{\circ 2}$ term from both sides of (1) and regrouping terms yields

$$2\boldsymbol{\Omega}^{\circ}\bar{\boldsymbol{\Omega}}[\boldsymbol{\Omega}^{\circ}\vec{\beta}_j]=(\omega_j^2\mathbf{I}-\boldsymbol{\Omega}^{\circ 2})\vec{\beta}_j\,. \tag{4}$$

The bracketed quantity on the left-hand side of (4) contains a known vector, which will be denoted as $\vec{\gamma}_j$,

$$\vec{\gamma}_j=\boldsymbol{\Omega}^{\circ}\vec{\beta}_j\,. \tag{5}$$

Thus, $\vec{\gamma}_j$ simply contains the modal weighting factors, $\vec{\beta}_j$, scaled on an element-by-element basis by their corresponding natural frequencies. Substituting $\vec{\gamma}_j$ into (4) yields

$$2\boldsymbol{\Omega}^{\circ}[\bar{\boldsymbol{\Omega}}\vec{\gamma}_j]=(\omega_j^2\mathbf{I}-\boldsymbol{\Omega}^{\circ 2})\vec{\beta}_j\,. \tag{6}$$

Consider the bracketed term of this expression. After some algebra, it can be shown that this product may be rewritten in the form

$$\bar{\boldsymbol{\Omega}}\vec{\gamma}_j=\boldsymbol{\Gamma}_j\vec{\bar{\omega}} \tag{7}$$

where the vector $\vec{\bar{\omega}}$ equals $[\bar{\omega}_0,\bar{\omega}_1\ldots\bar{\omega}_{N-1}]^T$. The matrix $\boldsymbol{\Gamma}_j$ is composed from the elements in $\vec{\gamma}_j$ and has the form

$$\boldsymbol{\Gamma}_j=\begin{bmatrix}\bar{\gamma}_{j0} & \bar{\gamma}_{j1} & \cdots & \bar{\gamma}_{j(N-1)}\\ \bar{\gamma}_{j1} & \bar{\gamma}_{j2} & \cdots & \bar{\gamma}_{j0}\\ \vdots & \vdots & & \vdots\\ \bar{\gamma}_{j(N-1)} & \bar{\gamma}_{j0} & \cdots & \bar{\gamma}_{j(N-2)}\end{bmatrix} \tag{8}$$

where γ_{jn} denotes the nth element of the vector $\vec{\gamma}_j$; the $\vec{\gamma}_j$ elements are numbered from 0 to N-1.

Substituting (7) into (6) produces an expression in which the matrix of mistuning parameters, $\boldsymbol{\Omega}$, has been replaced by a vector of mistuning parameters, $\vec{\bar{\omega}}$

$$2\boldsymbol{\Omega}^{\circ}\boldsymbol{\Gamma}_j\vec{\bar{\omega}}=(\omega_j^2\mathbf{I}-\boldsymbol{\Omega}^{\circ 2})\vec{\beta}_j\,. \tag{9}$$

Observe that pre-multiplying (9) by $(2\boldsymbol{\Omega}^{\circ}\boldsymbol{\Gamma}_j)^{-1}$ would solve this expression for the DFT of the rotor's mistuning. Furthermore, the vector $\vec{\bar{\omega}}$ can then be related to the physical sector mistuning through an inverse discrete Fourier transform. However, (9) only contains data from one measured mode and frequency. Therefore, error in the mode's measurement may result in significant error in the predicted mistuning.

To minimize the effects of measurement error, we will incorporate multiple mode measurements into our solution for the mistuning. We construct (9) for each of the M measured modes, and combine them into the single matrix expression,

$$\begin{bmatrix}2\boldsymbol{\Omega}^{\circ}\boldsymbol{\Gamma}_1\\ 2\boldsymbol{\Omega}^{\circ}\boldsymbol{\Gamma}_2\\ \vdots\\ 2\boldsymbol{\Omega}^{\circ}\boldsymbol{\Gamma}_m\end{bmatrix}\vec{\bar{\omega}}=\begin{bmatrix}(\omega_1^2\mathbf{I}-\boldsymbol{\Omega}^{\circ 2})\vec{\beta}_1\\ (\omega_1^2\mathbf{I}-\boldsymbol{\Omega}^{\circ 2})\vec{\beta}_2\\ \vdots\\ (\omega_1^2\mathbf{I}-\boldsymbol{\Omega}^{\circ 2})\vec{\beta}_m\end{bmatrix}. \tag{10}$$

For brevity, we rewrite (10) as

$$\tilde{\mathbf{L}}\vec{\bar{\omega}}=\tilde{\vec{r}} \tag{11}$$

where $\tilde{\mathbf{L}}$ is the matrix on the left-hand side of the expression, and $\tilde{\vec{r}}$ is the vector on the right-hand side. The "~" is used to indicate that these quantities are composed by vertically stacking a set of submatrices or vectors.

Note that expression (11) is an over determined set of equations. Therefore, we can no longer solve for $\vec{\overline{\omega}}$ by direct inverse. However, we can obtain a least squares fit to the mistuning, i.e.,

$$\vec{\overline{\omega}} = Lsq\{\tilde{\mathbf{L}}, \tilde{\vec{r}}\}. \tag{12}$$

Equation (12) produces the vector $\vec{\overline{\omega}}$ that best fits all the measured data. Therefore, the error in each measurement is compensated for by the balance of the data. The vector $\vec{\overline{\omega}}$ can then be related to the physical sector mistuning through the inverse transform,

$$\Delta\omega_{\psi}^{(s)} = \sum_{p=0}^{N-1} e^{-isp2\pi/N}\overline{\omega_p} \tag{13}$$

where $\Delta\omega_{\psi}^{(s)}$ is the sector frequency deviation of the sth sector. The following section describes how Eqs. (12) and (13) can be applied to determine a rotor's mistuning.

2.1.3 Experimental Application. In order to solve Eqs. (12) and (13) for the sector mistuning, we must first construct $\tilde{\mathbf{L}}$ and $\tilde{\vec{r}}$ from the tuned system frequencies and the mistuned modes and frequencies. The tuned system frequencies can be calculated through finite element analysis of a tuned, cyclic symmetric, single blade/disk sector model. However, the mistuned modes and frequencies must be obtained experimentally.

The modes used by FMM ID are circumferential modes, corresponding to the tip displacement of each blade on the rotor. Since FMM ID is designed for isolated families of modes, it is sufficient to measure the displacement of only one point per blade. In practice, modes and frequencies are obtained by first measuring a complete set of frequency response functions (FRFs). Then, the modes and frequencies are extracted from the FRFs using modal curve fitting software.

The mistuned frequencies obtained from the measurements appear explicitly in the FMM ID equations as ω_j. However, the mistuned modes enter into the equations indirectly through the modal weighting factors $\vec{\beta}_j$. As described by Feiner and Griffin [5], each vector $\vec{\beta}_j$ is obtained by taking the inverse discrete Fourier transform of the corresponding single point-per-blade mode, i.e.,

$$\beta_{jn} = \sum_{m=0}^{N-1} \phi_{jm} e^{-imn2\pi/N}. \tag{14}$$

These quantities may then be used with the tuned system frequencies to construct $\tilde{\mathbf{L}}$ and $\tilde{\vec{r}}$ as outlined in earlier portions of this section. Finally, (12) and (13) may be solved for the sector mistuning.

This process is demonstrated through the two examples in the following section.

2.2 Numerical Examples. This section presents two numerical examples of the basic FMM ID method. In the first example, we consider an integrally bladed compressor whose blades are geometrically mistuned. The sector frequency deviations identified by FMM ID are verified by comparing them with values directly determined by finite element analyses. The second test case highlights FMM ID's ability to detect mistuning caused by variations at the blade-disk interface.

2.2.1 Geometric Blade Mistuning. Consider the finite element model of the twenty blade compressor shown in **Fig. 1.** Although the airfoils on this model are simply flat plates, the rotor design reflects the key dynamic behaviors of a modern, integrally bladed compressor. We mistuned the rotor through a combination of geometric and material property changes. Approximately one-third of the blades were mistuned through length variations, one-third through thickness variations, and one-third through elastic modulus variations. The magnitudes of the variations were chosen so that each form of mistuning would contribute equally to a 1.5% standard deviation in the sector frequencies.

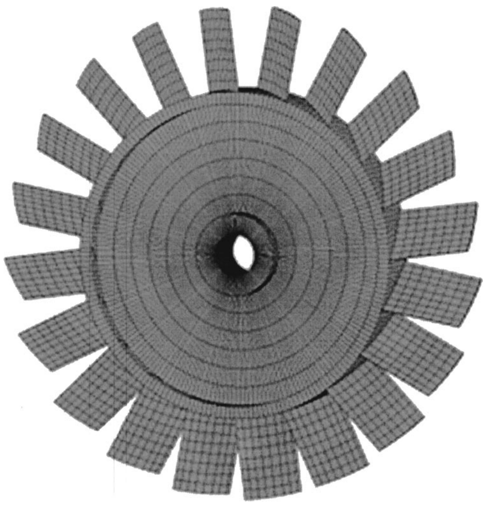

Fig. 1 Finite element model used to represent compressor

We first performed a finite element analysis of the tuned rotor, and generated its nodal diameter map, **Fig. 2.** Observe that the lowest frequency family of first bending modes is isolated, and is therefore a good candidate for FMM ID. The sector mistuning of this rotor was then determined through two different methods: finite element analyses of the mistuned sectors using the commercially available ANSYS finite element code, and FMM ID.

The finite element calculations serve as a benchmark to assess the accuracy of the FMM ID method. In the benchmark, a finite element model was made for each mistuned blade. In the model the blade is attached to a single disk sector. The frequency change in the mistuned blade/disk sector was then calculated with various cyclic symmetric boundary conditions applied to the disk. It was found that the phase angle of the cyclic symmetric constraint had little effect on the frequency change caused by blade mistuning. The values quoted in this paper are for a disk phase constraint of 90 deg, i.e., for the five nodal diameter mode.

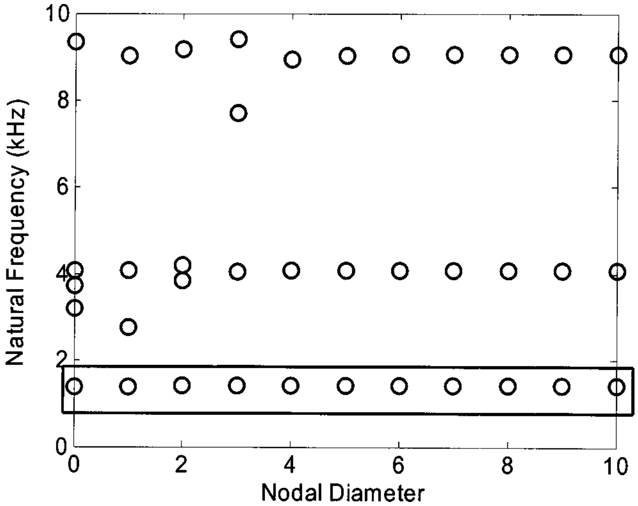

Fig. 2 Natural frequencies of the compressor with no mistuning

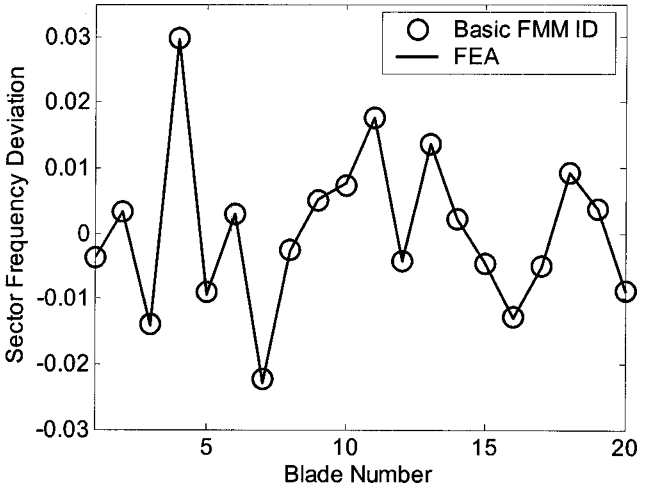

Fig. 3 Comparison of mistuning from FMM ID with FEM benchmark

A finite element model of the full, mistuned bladed disk was also constructed and used to compute its mistuned modes and natural frequencies. The modes and frequencies were used as input data for FMM ID. In an actual experiment, the mistuned modes and frequencies would be obtained through a modal fit of the rotor's frequency response functions. Typically, the measurements will not detect modes that have a node point at the excitation source. To reflect this phenomenon in our numerical test case, we eliminated all mistuned modes that had a small response at blade one. This left 16 modes and natural frequencies to apply to FMM ID.

The mistuned modes and frequencies were combined with the tuned system frequencies of the fundamental mode family to construct the basic FMM ID equations, (10). These equations were solved using a least-squares fit. The solution was then converted to the physical sector frequency deviations through the inverse transform given in (13).

Figure 3 shows the comparison between the sector mistuning calculated directly by finite element simulations of each mistuned blade/sector and the mistuning identified by FMM ID. The two results are in good agreement.

2.2.2 Stagger Angle Mistuning. One of the key differences between FMM ID and other mistuning identification methods is its measure of mistuning. FMM ID uses a frequency quantity that characterizes the mistuning of an entire blade-disk sector. Other methods in the literature consider mistuning to be confined to the blades, [7]. The advantage of the sector frequency approach used by FMM is that it not only identifies the mistuning in the blades, but it also captures the mistuning in the disk and the blade-disk interface. To highlight this capability, the following example considers a rotor in which the blades are identical except they are mounted on the disk with slightly different stagger angles. **Figure 4** schematically illustrates a rotor with exaggerated stagger angle variations as viewed from above.

Consider the compressor shown in **Fig. 1.** To mistune this rotor, we randomly altered the stagger angle of each blade with a maximum variation of ±4 deg. Otherwise the blades are identical. The modes of the system were then calculated using the ANSYS finite element code. **Figure 5** shows a representative mode. Observe that the mode is localized, indicating that varying the stagger angles does indeed mistune the system.

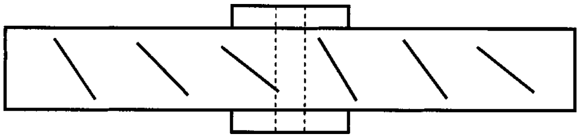

Fig. 4 Illustration of a rotor with exaggerated stagger angle mistuning

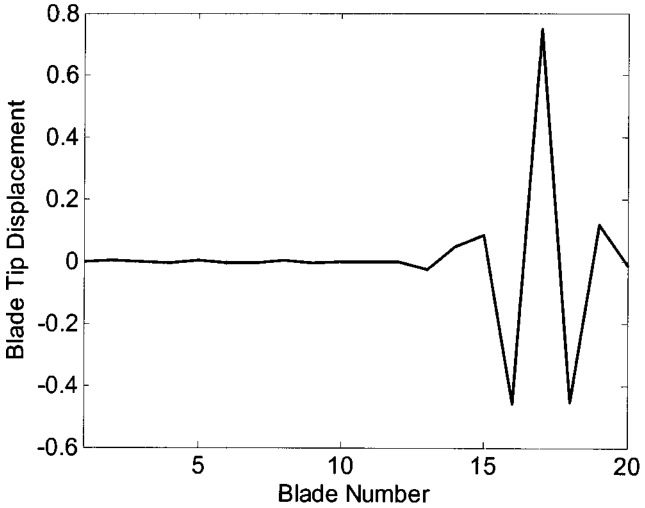

Fig. 5 Representative mistuned mode caused by stagger angle mistuning

We then used the mistuned modes and frequencies calculated by ANSYS to perform an FMM ID analysis of the mistuning. The resulting sector frequency deviations are plotted as the solid line in **Fig. 6.** The squares correspond to the stagger angle variations applied to each blade. The vertical axes have been scaled so that the maximum frequency and angle variation data points (blade 14) are coincident. This was done to highlight the fact that the stagger angle variations are proportional to the sector frequency deviations detected by FMM ID. Thus, not only can FMM ID accurately detect mistuning in the blades, as illustrated in the previous example, but it can also accurately detect other forms of mistuning such as variation in the blade stagger angle.

3 A Completely Experimental Method of Identification

The basic FMM ID method presented in Section 2 provides an effective means of determining the mistuning in an IBR. This

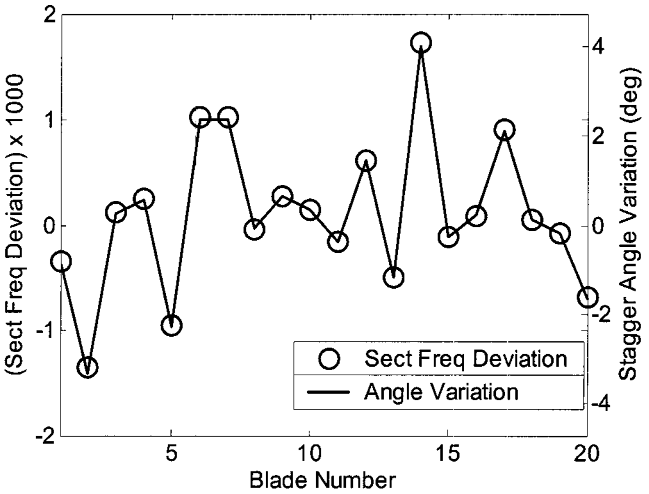

Fig. 6 Comparison of mistuning from FMM ID and the variations in the stagger angles

technique requires a set of simple vibration measurements and the natural frequencies of the tuned system. However, at times neither the tuned system frequencies nor a finite element model from which to obtain them are available to researchers interested in determining an IBR's mistuning. Furthermore, even if a finite element model is available, there is often concern as to how accurately the model represents the actual rotor. Therefore, we have developed an alternative FMM ID method that does not require any analytical data. The approach requires only a limited number of mistuned modes and frequency measurements to determine a bladed disk's mistuning. Furthermore, the method also identifies the bladed disk's tuned system frequencies. Thus, it not only serves as a method of identifying mistuning the system, but can also provide a method of corroborating the finite element model of the tuned system.

3.1 Theory. This version of FMM ID is derived from the basic FMM ID equations. Recall that an important step in the development of the basic FMM ID theory was to transform the mistuning matrix $\underline{\boldsymbol{\Omega}}$ into a vector form. Once we expressed the mistuning as a vector, it could then be calculated using standard methods from linear algebra. A similar approach is used in the current development to solve for the tuned system frequencies. However, the resulting equations are nonlinear, and require a more sophisticated solution approach.

3.1.1 Development of Nonlinear Equations. Consider the basic FMM ID equation given in (9). Moving the $\underline{\boldsymbol{\Omega}}^{\circ 2}$ term to the left-hand side, the expression becomes

$$\underline{\boldsymbol{\Omega}}^{\circ 2}\vec{\beta}_j+2\underline{\boldsymbol{\Omega}}^{\circ}\boldsymbol{\Gamma}_j\overline{\vec{\omega}}=\omega_j^2\vec{\beta}_j\,. \tag{15}$$

We assume that from measurement of the mistuned modes and frequencies, $\vec{\beta}_j$ and ω_j are known. All other quantities are unknown. Note that although $\boldsymbol{\Gamma}_j$ is not known, the matrix contains elements from $\vec{\beta}_j$. Therefore, we do have some knowledge of the matrix.

After some algebra, one can show that the term $\underline{\boldsymbol{\Omega}}^{\circ 2}\vec{\beta}_j$ may be re-expressed as

$$\underline{\boldsymbol{\Omega}}^{\circ 2}\vec{\beta}_j=\mathbf{B}_j\vec{\lambda}^{\circ} \tag{16}$$

where $\vec{\lambda}^{\circ}$ is a vector of the tuned frequencies squared, and $\mathbf{B}_j$ is a matrix composed from the elements of $\vec{\beta}_j$. If we define η to be the maximum number of nodal diameters on the rotor, i.e., η=N/2 if N is even or (N-1)/2 if N is odd, then $\vec{\lambda}^{\circ}$ is given by

$$\vec{\lambda}^{\circ}=\begin{bmatrix}\omega_{0ND}^{\circ 2}\\ \omega_{1ND}^{\circ 2}\\ \vdots\\ \omega_{\eta ND}^{\circ 2}\end{bmatrix}. \tag{17}$$

For N even, the matrix $\mathbf{B}_j$ has the form

$$\mathbf{B}_j=\begin{bmatrix}\beta_{j0} &&&&&\\ & \beta_{j1} &&&&\\ && \beta_{j2} &&&\\ &&& \ddots &&\\ &&&& \beta_{j\eta} &\\ &&& \iddots &&\\ && \beta_{j2} &&&\\ & \beta_{j1} &&&&\end{bmatrix}. \tag{18}$$

A similar expression can be derived for N odd.

Substituting (16) into (15) and regrouping the left-hand side results in a matrix equation for the tuned frequencies squared and the sector mistuning,

$$[\mathbf{B}_j\;\;2\underline{\boldsymbol{\Omega}}^{\circ}\boldsymbol{\Gamma}_j]\begin{bmatrix}\vec{\lambda}\\ \overline{\vec{\omega}}\end{bmatrix}=\omega_j^2\vec{\beta}_j\,. \tag{19}$$

Equation (19) contains information from only one of the M measured modes and frequencies. However, (19) can be constructed for each measured mode, and combined into the single matrix expression

$$\begin{bmatrix}\mathbf{B}_1 & 2\underline{\boldsymbol{\Omega}}^{\circ}\boldsymbol{\Gamma}_1\\ \mathbf{B}_2 & 2\underline{\boldsymbol{\Omega}}^{\circ}\boldsymbol{\Gamma}_2\\ \vdots & \vdots\\ \mathbf{B}_M & 2\underline{\boldsymbol{\Omega}}^{\circ}\boldsymbol{\Gamma}_M\end{bmatrix}\begin{bmatrix}\vec{\lambda}\\ \overline{\vec{\omega}}\end{bmatrix}=\begin{bmatrix}\omega_1^2\vec{\beta}_1\\ \omega_2^2\vec{\beta}_2\\ \vdots\\ \omega_M^2\vec{\beta}_M\end{bmatrix}. \tag{20}$$

Thus we have formed a single expression that incorporates all of the measured data. For brevity, (20) is rewritten as

$$[\tilde{\mathbf{B}}\;\;2\widetilde{(\underline{\boldsymbol{\Omega}}^{\circ}\boldsymbol{\Gamma})}]\begin{bmatrix}\vec{\lambda}\\ \overline{\vec{\omega}}\end{bmatrix}=\tilde{\vec{r}}\,' \tag{21}$$

where $\tilde{\mathbf{B}}$ is the stacked matrix of $\mathbf{B}_j$, the term $\widetilde{(\underline{\boldsymbol{\Omega}}^{\circ}\boldsymbol{\Gamma})}$ is the stacked matrix of $\underline{\boldsymbol{\Omega}}^{\circ}\boldsymbol{\Gamma}_j$, and $\tilde{\vec{r}}\,'$ is the right-hand side of (20).

To complete our formulation, we must introduce an additional constraint equation. It is required because the Eqs. (21) are underdetermined. To understand the cause of this indeterminacy, consider a rotor in which each sector is mistuned the same amount. Due to the symmetry of the mistuning, the rotor's mode shapes will still look tuned, but its frequencies will be shifted. If one has no prior knowledge of the tuned system frequencies, there is no way to determine that the rotor has in fact been mistuned. The same difficulty arises in solving (21) since there is no way to distinguish between a mean shift in the mistuning and a corresponding shift in the tuned system frequencies. To eliminate this ambiguity, we will define mistuning so that it has a mean value of zero.

Mathematically, a zero mean in the mistuning translates to prescribing the first element of $\overline{\vec{\omega}}$ to be zero. With the addition of this constraint, (21) takes the form

$$\begin{bmatrix}\tilde{\mathbf{B}} & 2\widetilde{(\underline{\boldsymbol{\Omega}}^{\circ}\boldsymbol{\Gamma})}\\ 0 & \vec{c}\end{bmatrix}\begin{bmatrix}\vec{\lambda}^{\circ}\\ \overline{\vec{\omega}}\end{bmatrix}=\begin{bmatrix}\tilde{\vec{r}}\\ 0\end{bmatrix} \tag{22}$$

where $\vec{c}$ is a row vector whose first element is 1 and whose remaining elements are zero.

3.1.2 Iterative Solution Method. Consider Eq. (22). If the term $\widetilde{(\underline{\boldsymbol{\Omega}}^{\circ}\boldsymbol{\Gamma})}$ were known, then we could obtain a least-squares solution for the tuned eigenvalues $\vec{\lambda}^{\circ}$ and the DFT of the sector mistuning $\overline{\vec{\omega}}$. However, since $\widetilde{(\underline{\boldsymbol{\Omega}}^{\circ}\boldsymbol{\Gamma})}$ is based in part on the unknown quantities $\vec{\lambda}^{\circ}$, the equations are nonlinear. Therefore, we must use an alternative solution method. This section describes how these equations may be solved using an iterative approach.

In iterative form, the least squares solution to (22) can be written as

$$\begin{bmatrix}\vec{\lambda}^{\circ}\\ \overline{\vec{\omega}}\end{bmatrix}_{(k)}=Lsq\left\{\begin{bmatrix}\tilde{\mathbf{B}} & 2\widetilde{(\underline{\boldsymbol{\Omega}}^{\circ}\boldsymbol{\Gamma})}_{(k-1)}\\ 0 & \vec{c}\end{bmatrix},\begin{bmatrix}\tilde{\vec{r}}\\ 0\end{bmatrix}\right\} \tag{23}$$

where the subscripts indicate the iteration number. For each iteration, we then construct a new matrix $\widetilde{(\underline{\boldsymbol{\Omega}}^{\circ}\boldsymbol{\Gamma})}$ based on the previous iteration's solution for $\vec{\lambda}^{\circ}$. This process is repeated until we obtain a converged solution. With a good initial guess, this method typically converges within a few iterations. Appendix B describes an effective approach for obtaining a good initial guess.

3.2 Numerical Test Case. This section presents a numerical example of the FMM ID method that identifies the tuned system frequencies as well as the mistuning. This example uses the geometrically mistuned compressor model presented in Section 2.

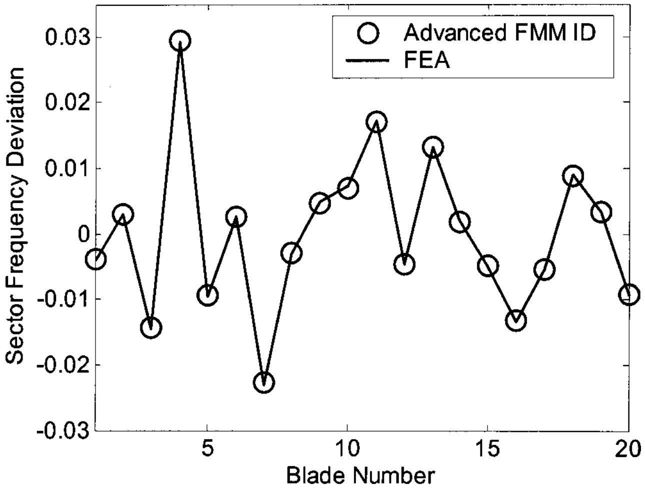

Fig. 7 Comparison of mistuning from FMM ID with FEM benchmark

The tuned system frequencies and sector mistuning identified by FMM ID are then compared with finite element results.

We calculated the modes and natural frequencies of the mistuned bladed disk using a finite element model of the mistuned system. We then converted the physical modes to vectors of modal weighting factors, $\vec{\beta}_j$, through (14). The weighting factors were used to form the elements of Eq. (48) in Appendix B which was solved to obtain an initial estimate of the tuned system frequencies. This was used as an initial guess to iteratively solve Eq. (23). The solution vector contains two parts: a vector of the tuned system frequencies squared, and a vector of the DFT of the sector frequency deviations. The sector mistuning was converted to the physical domain using the inverse transform (13).

The resulting sector frequency deviations are compared with the benchmark finite element values in **Fig. 7** using the same procedure as in Section 2.2. A comparison of the tuned frequencies identified by FMM ID and those computed directly with the finite element model is shown in **Fig. 8.** In each case the agreement is good.

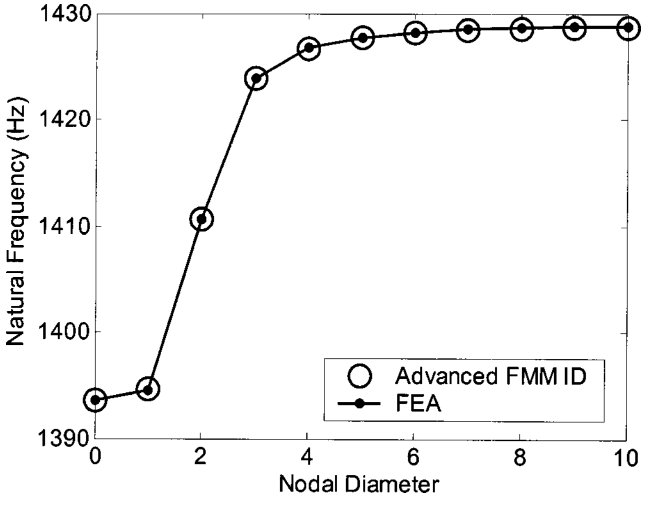

Fig. 8 Comparison of the tuned system frequencies from FMM ID and FEM

4 Response Prediction at Speed

The FMM ID methods presented in Sections 2 and 3 determine the mistuning in bladed disks while they are stationary. However, once the rotor is spinning, centrifugal forces can alter the effective mistuning in the rotor. Section 4.1 presents a method for approximately calculating the effect of rotational speed on mistuning. Then, in Section 4.2, we present a numerical example that applies this technique and then uses FMM to predict its forced response at speed. The accuracy of the method is assessed by comparing the results with a numerical benchmark.

4.1 Mistuning Extrapolation. Centrifugal effects cause the sector frequency deviations to change when the disk is rotating. This section gives a simple method for approximating the effect of rotational speed on mistuning. Details of the derivation are provided by Feiner [10]. Here we summarize the result.

To investigate centrifugal stiffening in [10] the blade is modeled as a pendulum, constrained to a rigid disk by a torsion spring. While the disk is at rest, the blade's frequency is perturbed (mistuned). Then, the model is used to determine the corresponding change in the blade's frequency when the disk is rotating. To first order one finds that

$$\Delta\omega(S)^{(s)} \approx \Delta\omega(0)^{(s)}\left[\frac{\mathring{\omega}_{\alpha ND}(0)^2}{\mathring{\omega}_{\alpha ND}(S)^2}\right] \tag{24}$$

where S is the rotation speed of the disk, $\Delta\omega(S)^{(s)}$ is the sector mistuning ratio of the sth sector and $\mathring{\omega}_{\alpha ND}(S)$ is the frequency of a representative tuned system mode. For example, in the case reported in 4.2, $\mathring{\omega}_{\alpha ND}(S)$ is the frequency of the system mode with a 90 deg interblade phase angle. A key result from (24) is that mistuning is larger at rest than at speed, and that this reduction in mistuning can be estimated by calculating how the tuned system frequencies change with speed. It has been confirmed that (24) works reasonably well for realistic geometric mistuning in real compressor blades, [10]. This will be also be demonstrated by the next example.

4.2 Numerical Test Case. This section uses a numerical test case that shows how FMM ID, Eq. (24), and the FMM forced response code can be combined to predict the response of a bladed disk under rotating conditions. Consider the geometrically mistuned rotor studied in Section 2.2.1, and illustrated in **Fig. 1.** This compressor has a 6th engine order crossing with the first bending modes at a rotational speed of 20,000 rpm. However, to create a more severe test case, we will proceed as if the crossing occurred at 40,000 rpm.

In order to use FMM to predict the rotor's forced response at this speed, we must provide the FMM prediction code, [5], with the bladed disk's tuned system frequencies and the sector frequency deviations that are present at 40,000 rpm. In Section 2.2.1 we determined these two sets of parameters at rest using ANSYS and Basic FMM ID, respectively. However, since both of these properties change with rotation speed, they must first be adjusted to reflect their values at 40,000 rpm.

To adjust the tuned system frequencies, we recalculated them in ANSYS using the centrifugal load option to simulate rotational effects. The centrifugal stiffening caused the tuned system frequencies to increase by about 30%. Then we used the change in the five nodal diameter, tuned system frequency and (24) to analytically extrapolate the sector frequency deviations to 40,000 rpm. In this case, the centrifugal loading reduces the mistuning ratios by about 40%.

Finally, the adjusted parameters were used with the FMM forced response code to calculate the rotor's response to a 6E excitation using the method described in [5]. As a benchmark, the forced response was also calculated directly in ANSYS using a full 360 deg mistuned finite element model. Tracking plots of the FMM and ANSYS results are shown in Fig. 9. For clarity, we

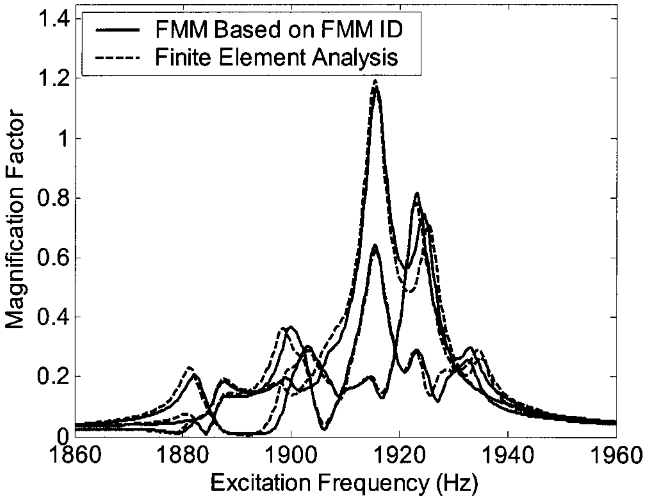

Fig. 9 Frequency response of blades to a six engine order excitation

have shown the response of only three blades: the high responding blade, the median responding blade, and the low responding blade. Observe that each blade's peak amplitude and the shape of its overall response as predicted by FMM agree well with the benchmark results. Thus, by combining FMM ID, the mistuning extrapolation equation, and FMM, we were able to identify the mistuning of a rotor at rest, and use it to accurately predict the system's forced response under rotating conditions.

5 Conclusions

A new method of identifying mistuning in bladed disks is developed. This approach is called FMM ID because it is based on the fundamental mistuning model (FMM). FMM and the methods presented in this paper are applicable to isolated families of modes. Often the frequencies of the first bending and first torsion families of modes satisfy this requirement. Identifying mistuning in these modes is important not only for predicting forced response, but also for predicting flutter. Since mistuning tends to stabilize flutter, the issue is how to relate a particular flutter test to the fleet as a whole. We are pursuing the application of FMM ID to the flutter problem in a joint research effort with Honeywell research engineers.

FMM ID uses measurements of the system mode shapes and natural frequencies to infer the rotor's mistuning. The key concept behind FMM ID is that the high sensitivity of system modes to small variations in mistuning, causes measurements of those modes themselves to be an accurate basis for mistuning identification. Since FMM ID does not require individual blade measurements, it is particularly suited to integrally bladed rotors. We have developed two forms of FMM ID: Basic FMM ID and a version that also identifies the frequencies of the tuned system.

Basic FMM ID uses tuned system frequencies from finite element analysis and measurements of the mistuned system modes and frequencies to determine a rotor's mistuning. The mistuned mode shape and frequencies can be measured with standard modal analysis techniques.

Since Basic FMM ID is derived from FMM, it requires very little analytical information. Specifically, it needs only the tuned system frequencies of the mode family of interest. Thus, for an N bladed disk, we only need approximately $N/2$ pieces of analytical data. These frequencies can be obtained from finite element analysis of a single-sector model using cyclic symmetric boundary conditions. The alternate form of FMM ID requires no analytical data. It relies solely on experimental measurements of the mistuned modes and frequencies. Thus, the second form of FMM ID can be used to identify mistuning even if a finite element model of the bladed disk is not available. Furthermore, this approach not only identifies the mistuning in a rotor, but it also infers its tuned system frequencies. Identifying the tuned system frequencies may be particularly useful for assessing the validity of a finite element model of the nominal system.

A number of numerical test cases are analyzed to demonstrate the applicability of the methods. One of these involve introducing mistuning by varying the stagger angle of each blade in what was otherwise a perfectly tuned system. FMM ID accurately detects the pattern of the stagger angle mistuning. This example is important because it illustrates the fact that mistuning in the bladed disk can be caused by sources that cannot be measured simply in terms of blade frequencies.

FMM ID can be used to identify the mistuning in a bladed disk when it is tested in the laboratory. A method has been demonstrated for approximating how centrifugal loading will change the mistuning when it is rotating in the engine. Other factors may also be present in the engine that can affect the mistuned response. These may include: temperature effects, gas bending stresses, how the disk is constrained in the engine, and how the teeth in the attachment change their contact if the blades are conventionally attached to the disk. Except for the constraints on the disk, these additional effects may be relatively unimportant in integrally bladed compressor stages. The disk constraints can be taken into account by performing the system ID on the IBR after the full rotor is assembled. Consequently, it seems feasible that the methodology presented in this paper can be used to predict the vibratory response of actual compressor stages. U.S. Air Force engineers have agreed to try this approach in forthcoming tests in the Compressor Research Facility (CRF) at Wright Patterson Air Force Base in Dayton, Ohio. If the approach proves successful, then the plan is to use the methodology to select which blades will be instrumented, interpret test data, and relate the vibratory response measured in the CRF to the vibration that will occur in the fleet as a whole.

Acknowledgments

The authors would like to acknowledge that this research was supported in part by the U.S. Air Force, contract number F33615-01-C-2186, under the direction of Dr. Charles Cross and by the GUIde Consortium.

The authors would also like to thank Prof. David J. Ewins of Imperial College, London, for stimulating discussions that helped lead to some of the concepts presented in this paper. Specifically, the idea of stagger angle mistuning used in this paper grew out of an observation by Professor Ewins that he had seen significant levels of mistuning in systems that had had the individual blades carefully tuned. It also lead us to broaden our concept of mistuning from simple blade mistuning used in [5] to the more general concept of sector mistuning as discussed in Appendix A.

Appendix A

A More General Form of FMM. This appendix presents the derivation of a more general form of the modal equation for the fundamental mistuning model (FMM) that is applicable to rotors with more flexible disks. The generalized FMM formulation differs from the original in two ways. First, it no longer approximates the tuned system frequencies by their average value. This allows for a much larger variation among the tuned frequencies. Second, rather than using the blade-alone mode as an approximation of the various nodal diameter sector modes, we now use a representative mode of a single blade-disk sector. Consequently, the approach now includes the disk portion of the mode shape, and thus allows for more strain energy in the disk.

The changes in the formulation also modify our measure of mistuning. In the original FMM form, we measured mistuning as a percent deviation in the blade-alone frequency. However, mistuning is now measured as a percent deviation the frequency of each blade-disk sector. The advantage is that the sector frequency deviations not only capture mistuning in the blade, but can also capture mistuning in the disk as well as variations in the ways the blades are attached to the disk.

Section 1 of this appendix describes how the SNM approach, 11, is used to reduce the order of the mistuned free-response equations and formulates the problem in terms of reduced-order sector matrices. Section 2 relates the sector matrices to mistuned sector frequencies. Section 3 simplifies the resulting mathematical expressions.

1 Reduction of Order. Consider a mistuned, bladed disk in the absence of an excitation. The order of its equation of motion is reduced through a subset of nominal modes approach. The resulting reduced-order equation can be written as, 11:

$$[(\mathbf{\Omega}^{\circ 2}+\Delta\hat{\mathbf{K}})-\omega_j^2(\mathbf{I}+\Delta\hat{\mathbf{M}})]\vec{\beta}_j=0 \tag{25}$$

$\mathbf{\Omega}^{\circ 2}$ is a diagonal matrix of the tuned system eigenvalues,[3] and $\mathbf{I}$ is the identity matrix. $\Delta\hat{\mathbf{K}}$ and $\Delta\hat{\mathbf{M}}$ are the variations in the modal stiffness and modal mass matrices caused by stiffness and mass mistuning. The vector $\vec{\beta}_j$ contains weighting factors that describe the jth mistuned mode as a limited sum of tuned modes, i.e.,

$$\vec{\phi}_j=\mathbf{\Phi}^\circ\vec{\beta}_j \tag{26}$$

where $\mathbf{\Phi}^\circ$ is a matrix whose columns are a limited number of the tuned system modes.

Note that to first order, $(\mathbf{I}+\Delta\hat{\mathbf{M}})^{-1}\approx(\mathbf{I}-\Delta\hat{\mathbf{M}})$. Thus, by pre-multiplying (25) by $(\mathbf{I}+\Delta\hat{\mathbf{M}})^{-1}$ and keeping only first-order terms, the expression becomes

$$(\mathbf{\Omega}^{\circ 2}+\hat{\mathbf{A}})\vec{\beta}_j=\omega_j^2\vec{\beta}_j \tag{27}$$

where

$$\hat{\mathbf{A}}=\Delta\hat{\mathbf{K}}-\Delta\hat{\mathbf{M}}\mathbf{\Omega}^{\circ 2}. \tag{28}$$

Next, we will relate the matrix $\hat{\mathbf{A}}$ to the frequency deviations of the mistuned sectors.

2 Relating Mistuning to Sector Frequency Deviations. Relating $\hat{\mathbf{A}}$ to frequency deviations is a three-step process. First, the mistuning matrix is expressed in terms of the system mode shapes of an individual sector. Then, the system sector modes are related to the corresponding mode of a single, isolated sector. Finally, the resulting sector-mode terms in $\hat{\mathbf{A}}$ are expressed in terms of the frequency deviations of the sectors.

2.1 Relating mistuning to system sector modes. Consider the mistuning matrix, $\hat{\mathbf{A}}$, in (28). This matrix can be expressed as a sum of the contributions from each mistuned sector.

$$\hat{\mathbf{A}}=\sum_{s=0}^{N-1}\hat{\mathbf{A}}^{(s)} \tag{29}$$

where the superscript denotes that the mistuning corresponds to the sth sector. The expression for a single element of $\hat{\mathbf{A}}^{(s)}$ is

$$\hat{\mathbf{A}}_{mn}^{(s)}=\vec{\phi}_m^{\circ(s)^H}(\Delta\mathbf{K}^{(s)}-\omega_n^{\circ 2}\Delta\mathbf{M}^{(s)})\vec{\phi}_n^{\circ(s)} \tag{30}$$

where $\Delta\mathbf{K}^{(s)}$ and $\Delta\mathbf{M}^{(s)}$ are the physical stiffness and mass perturbations of the sth sector. The modes $\vec{\phi}_m^{\circ(s)}$ and $\vec{\phi}_n^{\circ(s)}$ are the portions of the mth and nth columns of $\mathbf{\Phi}^\circ$ which describe the sth sector's motion. The term $\omega_n^{\circ 2}$ is the nth diagonal element of $\mathbf{\Omega}^{\circ 2}$.

Equation (30) relates the mistuning to the system sector modes. In the next section, these modes are related to the mode of a single isolated blade-disk sector.

2.2 Relating system sector modes to an average sector mode

The tuned modes in (30) are expressed in complex traveling wave form. Thus, the motion of the sth sector can be related to the motion of the 0th sector by a phase shift. This allows us to restate (30) as

$$\hat{\mathbf{A}}_{mn}^{(s)}=e^{is(n-m)2\pi/N}\vec{\phi}_m^{\circ(0)^H}(\Delta\mathbf{K}^{(s)}-\omega_n^{\circ 2}\Delta\mathbf{M}^{(s)})\vec{\phi}_n^{\circ(0)}. \tag{31}$$

Because the tuned modes used in the SNM formulation are an isolated family of modes, the sector modes of all nodal diameters look nearly identical. Therefore, we can approximate the various sector modes by an average sector mode. Applying the average sector mode approximation for the system sector modes in (31), $\hat{\mathbf{A}}_{mn}^{(s)}$ can be written as

$$\hat{\mathbf{A}}_{mn}^{(s)}=\left(\frac{\omega_m^\circ\omega_n^\circ}{\omega_\psi^{\circ 2}}\right)e^{is(n-m)2\pi/N}[\vec{\psi}^{\circ(0)^H}(\Delta\mathbf{K}^{(s)}-\omega_n^{\circ 2}\Delta\mathbf{M}^{(s)})\vec{\psi}^{\circ(0)}] \tag{32}$$

where $\vec{\psi}^{\circ(0)}$ is the average tuned system sector mode, and ω_ψ° is its natural frequency. In practice, $\vec{\psi}^{\circ(0)}$ can be taken to be the median modal diameter mode. The factor $(\omega_m^\circ\omega_n^\circ)/(\omega_\psi^{\circ 2})$ scales the average sector mode terms so that they have the approximately the same strain energy as the sector modes they replace.

2.3 Introduction of sector frequency deviation. This version of FMM uses the deviation in a sector frequency quantity to measure mistuning. To understand this concept, consider an imaginary "test" rotor. In the test rotor every sector is mistuned in the same fashion, so as to match the mistuning in our sector of interest. Since our test rotor's mistuning is cyclically symmetric, its mode shapes are virtually identical to those of the tuned system. However, there will be a shift in the tuned system frequencies. For small levels of mistuning, the frequency shift is nearly the same in all of the tuned system modes and can be approximated by the fractional change in the frequency of the median nodal diameter mode.[4] Thus, the fractional shift in the median nodal diameter's frequency is taken as our measure of mistuning and is defined as the sector frequency deviation.

The bracketed terms of (32) are related to these frequency deviations in the following manner. Consider a bladed disk that is mistuned in a cyclic symmetric fashion, i.e., each sector undergoes the same mistuning. Its free-response equation of motion is given by the expression

$$[(\mathbf{K}^\circ+\Delta\mathbf{K})-\omega_n^2(\mathbf{M}^\circ+\Delta\mathbf{M})]\vec{\phi}_n=0. \tag{33}$$

Take the mode $\vec{\phi}_n$ to be the mistuned version of the tuned median nodal diameter mode, $\vec{\psi}^\circ$. $\vec{\psi}^\circ$ is the full system mode counterpart of the average sector mode $\vec{\psi}^{\circ(0)}$. Since mistuning is symmetric, the tuned and mistuned versions of the mode are nearly identical. Substituting $\vec{\psi}^\circ$ for $\vec{\phi}_n$ and pre-multiplying by $\vec{\psi}^{\circ H}$ yields

$$(\omega_\psi^{\circ 2}+\vec{\psi}^{\circ H}\Delta\mathbf{K}\vec{\psi}^\circ)-\omega_n^2(1+\vec{\psi}^{\circ H}\Delta\mathbf{M}\vec{\psi}^\circ)=0. \tag{34}$$

These terms may be rearranged to isolate the frequency terms

$$\vec{\psi}^{\circ H}(\Delta\mathbf{K}-\omega_n^2\Delta\mathbf{M})\vec{\psi}^\circ=\omega_j^2-\omega_\psi^{\circ 2}. \tag{35}$$

Since the mistuning is symmetric, each sector contributes equally to (35). Thus, the contribution from the 0th sector is

$$\vec{\psi}^{\circ(0)H}(\Delta\mathbf{K}-\omega_n^2\Delta\mathbf{M})\vec{\psi}^{\circ(0)}=\frac{1}{N}(\omega_j^2-\omega_\psi^{\circ 2}). \tag{36}$$

By factoring the frequency terms on the right-hand side of (36), it can be shown that

---

[3] An eigenvalue is equal to the square of the natural frequency of a mode.

[4] This is the case for an isolated family of modes in which the strain energy is primarily in the blades. If there is a significant amount of strain energy in the disk then the frequency of the modes change significantly as a function of nodal diameter and the modes are not isolated, i.e., they cover such a broad frequency range that they interact with other families of modes.

$$\vec{\psi}^{\circ(0)^H}(\Delta\mathbf{K}-\omega_n^2\Delta\mathbf{M})\vec{\psi}^{\circ(0)}\approx\frac{2\omega_\psi^{\circ 2}\Delta\omega_\psi}{N} \tag{37}$$

where $\Delta\omega_\psi$ is the fractional change in $\vec{\psi}$'s natural frequency due to mistuning, given by $\Delta\omega_\psi=(\omega_\psi-\omega^\circ_\psi)/\omega^\circ_\psi$. Note that by definition $\Delta\omega_\psi$ is a sector frequency deviation. Equation (37) can be substituted for the bracketed terms of (32), resulting in an expression that relates the elements of the sector *s* mistuning matrix to that sector's frequency deviation

$$\hat{\mathbf{A}}^{(s)}_{mn}=\frac{2\omega^\circ_m\omega^\circ_n}{N}e^{is(n-m)2\pi/N}\Delta\omega_\psi^{(s)} \tag{38}$$

where the superscript on $\Delta\omega_\psi$ is introduced to indicate that the frequency deviation corresponds to the *s*th sector. These sector contributions may be summed to obtain the elements of the mistuning matrix

$$\hat{\mathbf{A}}_{mn}=2\omega^\circ_m\omega^\circ_n\left[\frac{1}{N}\sum_{s=0}^{N-1}e^{is(n-m)2\pi/N}\Delta\omega_\psi^{(s)}\right]. \tag{39}$$

3 The Simplified Form of the Fundamental Mistuning Model Modal Equation. The bracketed term in (39) is the discrete Fourier transform (DFT) of the sector frequency deviations. If we use the dummy variable *p* to replace the quantity $(n-m)$ in (39), then the *p*th DFT of the sector frequency deviations is given by

$$\overline{\omega_p}=\left[\frac{1}{N}\sum_{s=0}^{N-1}e^{isp2\pi/N}\Delta\omega_\psi^{(s)}\right] \tag{40}$$

where $\overline{\omega_p}$ denotes the *p*th DFT. By substituting (40) into (39), $\hat{\mathbf{A}}$ may be expressed in the simplified matrix form

$$\hat{\mathbf{A}}=2\mathbf{\Omega}^\circ\overline{\mathbf{\Omega}}\mathbf{\Omega}^\circ \tag{41}$$

where

$$\overline{\mathbf{\Omega}}=\begin{bmatrix}\overline{\omega_0} & \overline{\omega_1} & \cdots & \overline{\omega_{N-1}}\\ \overline{\omega_{N-1}} & \overline{\omega_0} & \cdots & \overline{\omega_{N-2}}\\ \vdots & \vdots & & \vdots\\ \overline{\omega_1} & \overline{\omega_2} & \cdots & \overline{\omega_0}\end{bmatrix}. \tag{42}$$

$\overline{\mathbf{\Omega}}$ is a matrix which contains the discrete Fourier transforms of the sector frequency deviations. Note that $\overline{\mathbf{\Omega}}$ has a circulant form, and thus contains only *N* distinct elements. $\mathbf{\Omega}^\circ$ is a diagonal matrix of the tuned system frequencies.

Substituting (41) into (27) produces the most basic form of the eigenvalue problem that may be solved to determine the modes and natural frequencies of the mistuned system.

$$(\mathbf{\Omega}^{\circ 2}+2\mathbf{\Omega}^\circ\overline{\mathbf{\Omega}}\mathbf{\Omega}^\circ)\vec{\beta}_j=\omega_j^2\vec{\beta}_j \tag{43}$$

Appendix B

Estimating the Tuned System Frequencies. This appendix presents an effective method of obtaining a good initial guess of the tuned system frequencies for use in the iterative solution process described in Section 3.1.2. The approach is to obtain the initial guess by solving a companion problem.

To identify a good initial guess, recall that FMM ID requires that we analyze an isolated family of modes. In general, the frequencies of isolated mode families tend to span a fairly small range. Therefore, they may be reasonably well approximated by their mean value, i.e.,

$$\vec{\lambda}^\circ_{(0)}=\omega^{\circ 2}_{\text{avg}} \tag{44}$$

However, the value of $\omega^\circ_{\text{avg}}$ is not known and therefore cannot be directly applied to (23). Consequently, we will formulate a slightly modified form of (22), which incorporates the initial guess defined by (44). Consider Eq. (22). If we take the tuned frequencies to be equal to $\omega^\circ_{\text{avg}}$, then the term $(\widetilde{\mathbf{\Omega}^\circ\mathbf{\Gamma}})$ may be expressed as

$$(\widetilde{\mathbf{\Omega}^\circ\mathbf{\Gamma}})=\omega^\circ_{\text{avg}}\tilde{\mathbf{\Gamma}} \tag{45}$$

where $\tilde{\mathbf{\Gamma}}$ is the matrix formed by vertically stacking the M $\mathbf{\Gamma}_j$ matrices.

The matrix $\mathbf{\Gamma}_j$ is also related to the tuned frequencies. As a result, the elements of each matrix $\mathbf{\Gamma}_j$ simplify to the form $\omega^\circ_{\text{avg}}\beta_{jn}$. This allows us to rewrite $\mathbf{\Gamma}_j$ as

$$\mathbf{\Gamma}_j=\omega^\circ_{\text{avg}}\mathbf{Z}_j \tag{46}$$

where $\mathbf{Z}_j$ is composed of the elements β_{jn} arranged in the same pattern as the γ_{jn} elements shown in (8). Thus, consolidating all $\omega^\circ_{\text{avg}}$ terms, (45) can be written as

$$(\widetilde{\mathbf{\Omega}^\circ\mathbf{\Gamma}})=\omega^{\circ 2}_{\text{avg}}\tilde{\mathbf{Z}} \tag{47}$$

where $\tilde{\mathbf{Z}}$ is the stacked form of the $\mathbf{Z}_j$ matrices.

Substituting (47) into (22) and regrouping terms results in the expression

$$\begin{bmatrix}\tilde{\mathbf{B}} & 2\tilde{\mathbf{Z}}\\ 0 & \vec{c}\end{bmatrix}\begin{bmatrix}\vec{\lambda}^\circ\\ \omega^{\circ 2}_{\text{avg}}\overline{\vec{\omega}}\end{bmatrix}=\begin{bmatrix}\tilde{\vec{r}}\\ 0\end{bmatrix}. \tag{48}$$

Note that the $\omega^{\circ 2}_{\text{avg}}$ term was grouped with the vector $\overline{\vec{\omega}}$. Thus, all the unknown expressions are consolidated into the single vector on the left-hand side of (48). These quantities can be solved through a least squares fit of the equations. This represents the 0th iteration of the solution process. The $\vec{\lambda}^\circ$ terms of the solution may then be used as an initial guess for the first iteration of (23).

References

[1] Srinivasan, A. V., 1997, "Flutter and Resonant Vibration Characteristics of Engine Blades," ASME J. Eng. Gas Turbines Power, **119**, pp. 742–775.

[2] Castanier, M. P., Ottarsson, G., and Pierre, C., 1997, "A Reduced Order Modeling Technique for Mistuned Bladed Disks," ASME J. Vibr. Acoust., **119**, pp. 439–447.

[3] Yang, M.-T., and Griffin, J. H., 2001, "A Reduced Order Model of Mistuning Using a Subset of Nominal Modes," ASME J. Eng. Gas Turbines Power, **123**, pp. 893–900.

[4] Petrov, E., Sanliturk, K., Ewins, D., and Elliott, R., 2000, "Quantitative Prediction of the Effects of Mistuning Arrangement on Resonant Response of a Practical Turbine Bladed Disk," 5th National Turbine Engine High Cycle Fatigue Conference, Chandler, AZ.

[5] Feiner, D. M., and Griffin, J. H., 2002, "A Fundamental Model of Mistuning for a Single Family of Modes," ASME J. Turbomach., **124**, 597–604.

[6] Seinturier, E., Lombard, J. P., Berthillier, M., and Sgarzi, O., 2002, "Turbine Mistuned Forced Response Prediction: Comparison With Experimental Results," ASME Paper 2002-GT-30424.

[7] Judge, J. A., Pierre, C., and Ceccio, S. L., 2002, "Mistuning Identification in Bladed Disks," *Proceedings of the International Conference on Structural Dynamics Modeling*, Madeira Island, Portugal.

[8] Mignolet, M. P., Rivas-Guerra, A. J., and Delor, J. P., 2001, "Identification of Mistuning Characteristics of Bladed Disks From Free Response Data—Part I," ASME J. Eng. Gas Turbines Power, **123**, pp. 395–403.

[9] Rivas-Guerra, A. J., Mignolet, M. P., and Delor, J. P., 2001, "Identification of Mistuning Characteristics of Bladed Disks From Free Response Data—Part II," ASME J. Eng. Gas Turbines Power, **123**, pp. 404–411.

[10] Feiner, D. M., 2002, "A Fundamental Model of Mistuning for Forced Response Prediction and System Identification," Ph.D. dissertation, Carnegie Mellon University, Pittsburgh, PA.

Mistuning Identification of Bladed Disks Using a Fundamental Mistuning Model—Part II: Application

D. M. Feiner

J. H. Griffin

Department of Mechanical Engineering,
Carnegie Mellon University,
5000 Forbes Avenue,
Pittsburgh, PA 15213

This paper is the second in a two-part study of identifying mistuning in bladed disks. It presents experimental validation of a new method of mistuning identification based on measurements of the vibratory response of the system as a whole. As a system-based method, this approach is particularly suited to integrally bladed rotors, whose blades cannot be removed for individual measurements. The method is based on a recently developed reduced-order model of mistuning called the fundamental mistuning model (FMM) and is applicable to isolated families of modes. Two versions of FMM system identification are applied to the experimental data: a basic version that requires some prior knowledge of the system's properties, and a somewhat more complex version that determines the mistuning completely from experimental data. [DOI: 10.1115/1.1643914]

1 Introduction

This is the second of two papers on identifying mistuning in bladed disks. The first paper [1] reviews the literature, derives a new theory of identifying mistuning, and illustrates its applicability using numerical examples. Since the method is based on measurements of the system as a whole, it is particularly suited to integrally bladed rotors (IBRs). Two versions of system identification were derived in the first paper: a basic version that requires some prior knowledge of the system's properties, and a somewhat more complex version that determines the mistuning completely from experimental data. The second method not only determines the mistuning in the IBR but also determines the natural frequencies that it would have had if all the blade and disk sectors were identical, i.e., the "tuned" system frequencies. In this second paper, we apply the new methods to a modern compressor stage, identify the mistuning and the tuned system frequencies, and show that the results correlate well with the experimental data and also with independent measurements and calculations made by engineers at Pratt & Whitney Aircraft.

The literature in mistuning is extensive, [2], and the current research is put in context in Part I, [1]. However, it should be emphasized that Judge et al. introduced the concept of using the system modes and frequencies to determine the mistuning in IBRs, [3], and also did extensive comparisons with experimental data. The key differences between their approach and that reported here are: the relative simplicity of FMM ID and the consequence that the mistuning in the system can be determined completely from experimental data; that FMM ID uses a blade/disk sector measure of mistuning; and the fact that their method is not inherently limited to an isolated family of modes as is FMM ID.

The system identification methods presented here will be applied to two IBRs of the same design. The IBRs used in this study were designed by Prof. S. Fleeter at Purdue University in cooperation with Pratt & Whitney Aircraft to reflect the aerodynamic and structural properties of a modern compressor. The work reported in this paper is part of a major research initiative on mistuning, friction damping, and forced response that is sponsored by the U.S. Air Force, the U.S. Navy, NASA, and the industrial members of the GUIde Consortium. Consequently, the vibratory response of the compressor stages discussed in this paper will be the focus of mistuning and forced response studies for some time to come.

This paper is organized as follows. Section 2 describes the two test rotors and the testing procedure. Then, in Section 3, we present the FMM ID results. The determined values of mistuning are used as input with the standard FMM prediction code, [4], to predict the rotor's vibratory response to a traveling wave excitation and the results compared with experimental data in Section 4. An interesting result from Section 3 is that the mistuning patterns in both IBRs are very similar. The implications of this result are discussed in Section 5. Finally, the key attributes of the method are summarized in Conclusions.

2 Test Rotors and Procedures

2.1 Test Rotors. To investigate how well FMM ID works with real experimental data from actual hardware, we applied the methods in Part 1, [1], to a pair of transonic compressors, **Fig. 1.** The two rotors are designated as SN-1 and SN-3.

Our industrial partner on this project, Pratt & Whitney, provided a single blade/disk sector finite element model of the tuned compressor. By solving this model with free boundary conditions at the hub and various cyclic symmetric boundary conditions on the radial boundaries of the disk, we generated a nodal diameter map of the tuned rotor, **Fig. 2.** The free boundary conditions at the hub represented the boundary conditions in our experiment: an IBR supported by a soft foam pad and is otherwise unconstrained. Note in the figure that each of the first two families of modes have isolated frequencies. These correspond to first bending and first torsion modes, respectively. Since FMM ID is applicable for isolated families of modes, both the first bending and first torsion modes are suitable candidates for our identification method.

2.2 Experimental Procedures. FMM ID requires measurements of the mistuned rotor's system modes and natural frequencies. By system mode, we mean the tip displacement of each blade as a function of angular position. These modes were obtained using a standard modal analysis approach: measure the bladed disk's transfer functions, and then curve-fit the transfer functions to obtain the modes and natural frequencies.

Our industrial partners performed standard transfer function measurements. The rotor was placed on a foam pad to approxi-

---

Contributed by the International Gas Turbine Institute and presented at the International Gas Turbine and Aeroengine Congress and Exhibition, Atlanta, GA, June 16–19, 2003. Manuscript received by the IGTI December 2002; final revision March 2003. Paper No. 2003-GT-38953. Review Chair: H. R. Simmons.

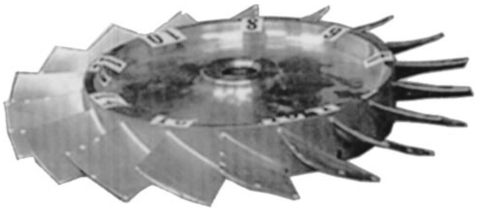

Fig. 1 One of two nominally identical test compressors

mate a free boundary condition. Then, they excited one of the blades over the frequency range of interest, measured the response of each blade with a laser vibrometer, and determined the transfer functions using a spectrum analyzer. A typical transfer function is shown in **Fig. 3.** Note that due to the high modal density, it was necessary to measure the response with a very high frequency resolution. This process was repeated for both compressors over two frequency bands in order to capture the response of both the first bending and first torsion modes.

We then used the commercially available MODENT modal analysis package to curve-fit the transfer functions. This resulted in measurements of the mistuned first bending and torsion modes of each rotor, along with their natural frequencies. Because the blade that was excited was at a low response point in some modes, we were not able to measure two or three of the modes in each family. In the following section, we use these measured mistuned modes and natural frequencies to demonstrate the applicability of FMM ID to actual hardware.

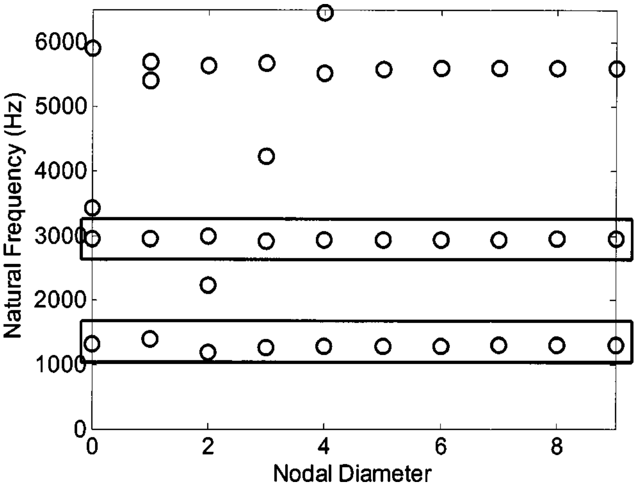

Fig. 2 Natural frequencies of compressor with no mistuning

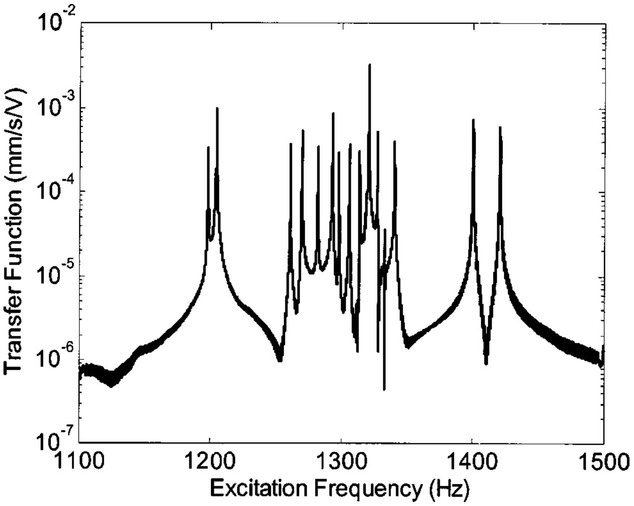

Fig. 3 Representative transfer function from compressor SN-1

3 FMM ID Results

The measured modes and frequencies were used to test both forms of the FMM ID method: Basic FMM ID and the completely experimental Advanced FMM ID. The method was applied to each rotor, for both the first bending and torsion families of modes. The tuned frequencies required by basic FMM ID were the same as those depicted in **Fig. 2.**

In order to assess the accuracy of FMM ID, the results were compared to benchmark data. In Section 3.1, we discuss a method for obtaining a benchmark measure of mistuning. Then, in Sections 3.2 and 3.3 we present the results of FMM ID for the first bending and first torsion modes, respectively.

3.1 Benchmark Measure of Mistuning. In order to assess the accuracy of the FMM ID method, the results must be compared to benchmark data. However, since the test rotors are integrally bladed, their mistuning could not be measured directly. Therefore, an indirect approach was used to obtain the benchmark mistuning. Our industrial partners carefully measured the geometry of each blade on the two rotors. From the geometries, they constructed finite element models for each blade and calculated the frequencies that it would have if it were clamped at its root. Since each blade had a slightly different geometry it also had slightly different frequencies. Thus, the variations in the blade frequencies caused by geometric variations were determined. This data was provided to CMU and we put it in a form that could be compared with the values identified by FMM ID. First, we calculated the frequency variations as a fraction of the mean so that we knew the deviation in the blade frequencies. These in turn had to be related to the sector frequency deviations determined by FMM ID. For modes with most of their strain energy in the blade, sector frequency deviations can be obtained from blade frequency mistuning by simple scaling, i.e.,

$$\Delta\omega_{\psi}=a(\Delta\omega_{b}) \tag{1}$$

where a is the fraction of strain energy in the blade for the average nodal diameter mode.

Section 3.2 presents the results for the family of bending modes, and Section 3.3 presents the results from the torsion modes.

3.2 FMM ID Results for Bending Modes

3.2.1 SN-1 Results. The measured mistuned modes and natural frequencies for the compressor SN-1 were used as input to both versions of FMM ID, as described in [1]. In the case of basic FMM ID, the tuned system frequencies of the first bending family from Fig. 2 were also used as input.

Figure 4 shows the sector frequency deviations identified by each FMM ID method along with the benchmark results. In both cases, the agreement is good. This implies that the mistuning is predominantly caused by geometric variations and that the variations are, in fact, accurately captured by Pratt & Whitney's process.

In order to make these comparisons easier, we plotted all mistuning in **Fig. 4** as the variation from a zero mean. However, it should be noted that this rotor had a mean frequency 1.3% higher than that of the tuned finite element model. This DC shift was detected by Basic FMM ID as a constant amount of mistuning added to each blade's frequency. However, since the Advanced FMM ID formulation does not incorporate the tuned finite ele

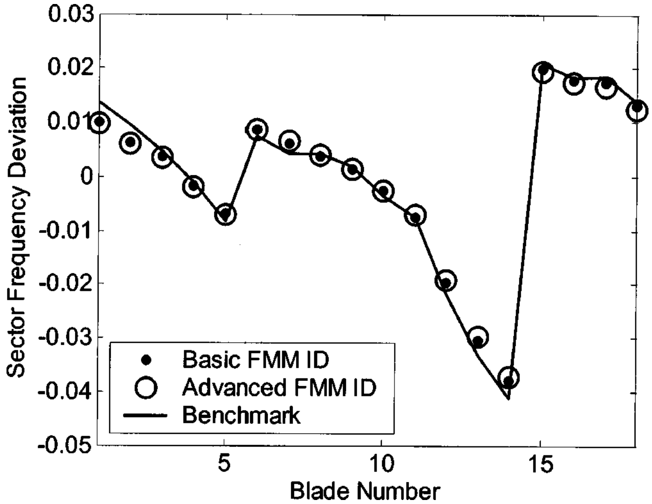

Fig. 4 Comparison of mistuning from FMM ID with benchmark results for SN-1

ment frequencies, it has no way to distinguish between a mean shift in the mistuning and a corresponding shift in the tuned system frequencies. Therefore, in Advanced FMM ID we define mistuning to have a zero mean, and then infer a corresponding set of tuned frequencies.

The tuned frequencies identified by Advanced FMM ID are compared with the finite element values in **Fig. 5.** Notice that the FMM ID frequencies are approximately 17 Hz higher than the finite element values. This corresponds to a 1.3% shift in the mean of the tuned system frequencies that compensates for fact that the blade mistuning now has a zero mean. To facilitate the comparison of the finite element and FMM ID results, we have subtracted off the mean shift, and then plotted the results as circles on **Fig. 5.** Once this adjustment is made, it can be seen that the distribution of the tuned frequencies determined by FMM ID agree quite well with the values calculated from the finite element model. Clearly, the finite element model captures the same variations in the tuned system frequencies as identified by Advanced FMM ID. However, advanced FMM ID identifies the fact that SN-1 had slightly higher average frequencies than the FEM model—a fact that could be important in establishing frequency margins for the stage.

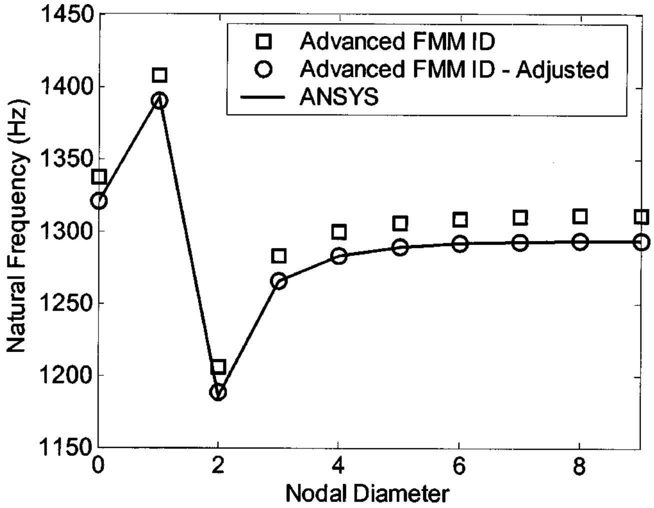

Fig. 5 Comparison of tuned system frequencies from FMM ID and FEM for SN-1

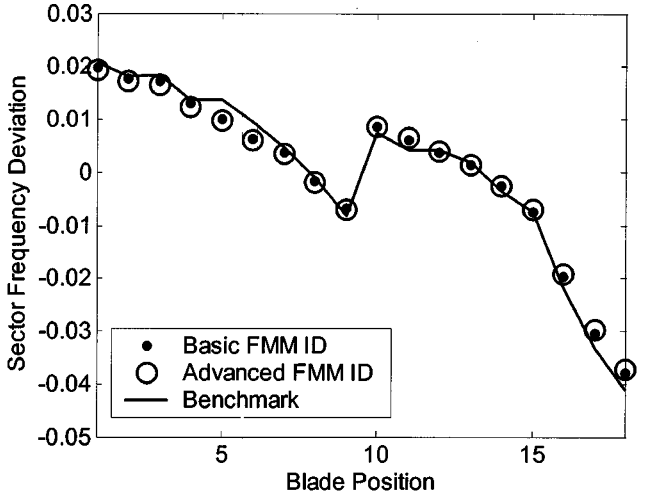

Fig. 6 Comparison of mistuning from FMM ID with benchmark results for SN-1

Consider the sector frequency deviations of SN-1 shown in **Fig. 4.** Notice that the mistuning varies from blade-to-blade in a regular pattern. To highlight this pattern, we will reassign the blade numbering so that blade position 1 corresponds to the high frequency blade, **Fig. 6.** Notice that when plotted in the new numbering scheme, the mistuning pattern has a predominantly decreasing trend, with a jump at position 9. This trend suggests that the mistuning might have been caused by tool wear during the machining process and that an adjustment in the process was made after half of the 18 blades were manufactured. This hypothesis will be reexamined after reviewing the results for SN-3.

3.2.2 SN-3 Results. The Basic and Advanced FMM ID methods were then applied in a similar manner to rotor SN-3's family of first bending modes. The identified mistuning and tuned system frequencies are shown in **Figs. 7** and **8.** For comparison purposes, we have again plotted the mistuning with a zero mean, and subtracted a corresponding mean shift from the predicted tuned system frequencies. The agreement is also good for rotor SN-3.

In **Fig. 7,** we numbered the blades so that blade 1 corresponds to the high frequency sector. Since we used a similar numbering scheme in SN-1, we can more easily compare the mistuning in

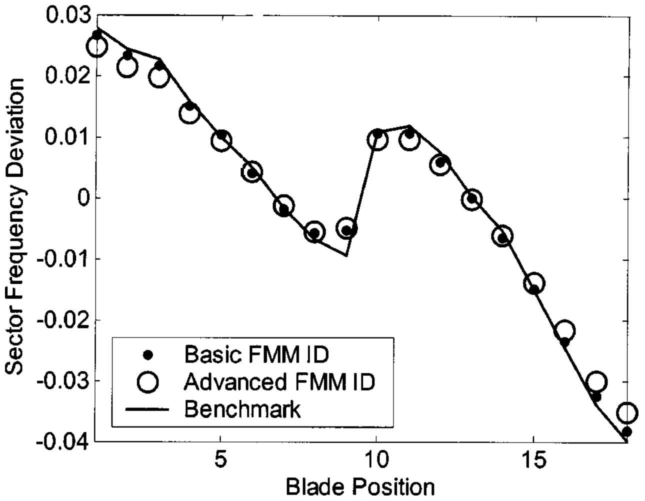

Fig. 7 Comparison of mistuning from FMM ID with benchmark results for SN-3

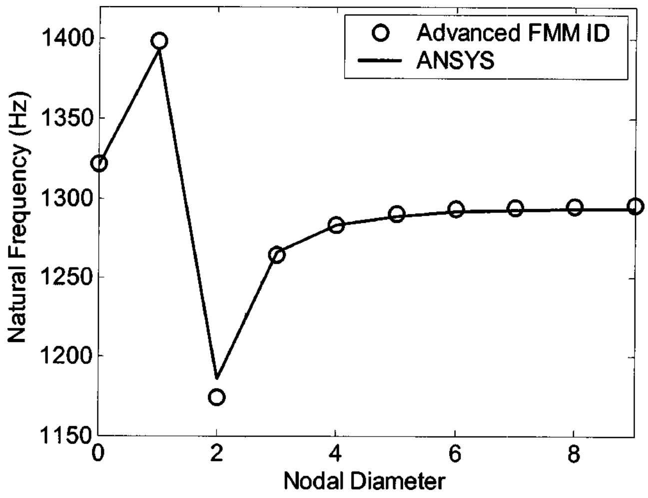

Fig. 8 Comparison of tuned system frequencies from FMM ID and FEM for SN-3

both rotors. It is interesting to note that the mistuning pattern in **Fig. 7** for SN-3 is quite similar to that of **Fig. 6** for SN-1. This result proves that in IBRs mistuning is not always a random phenomenon. The implication of this fact on the predictability of the vibratory response is discussed in Section 5.

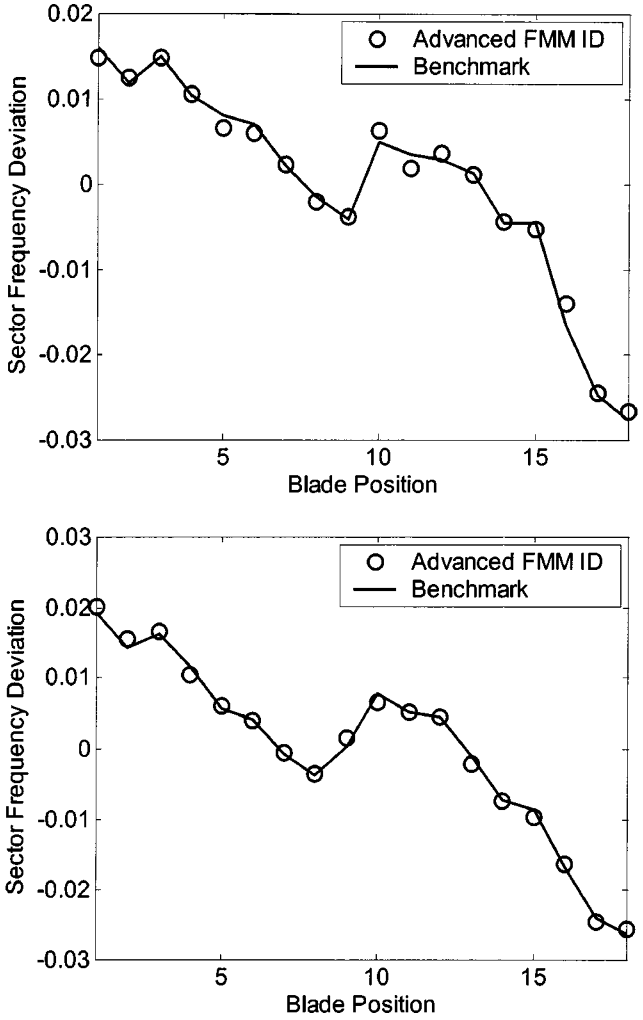

Fig. 9 Comparison of mistuning from FMM ID with benchmark results for torsion modes, (*a*) SN-1, (*b*) SN-3

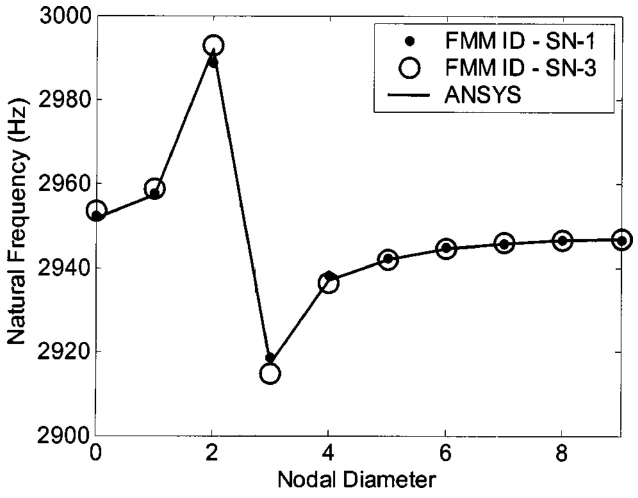

Fig. 10 Comparison of tuned system frequencies from FMM ID and FEM for torsion modes

3.3 FMM ID Results for Torsion Modes.

In this section we will examine FMM ID's ability to identify mistuning in the first torsion modes. Only the results for Advanced FMM ID are presented in order to conserve space.

Advanced FMM ID was applied to each test rotor's family of torsion modes. **Figure 9** compares the mistuning identified by FMM ID with the values inferred by our industrial partners from their geometric measurements. The agreement between the two methods for SN-1 is quite good, while the agreement for SN-3 is remarkable. In **Fig. 9,** the blades are numbered in the same order as in plots 6 and 7. Thus, the mistuning patterns in the torsion modes are very similar to those observed for the bending modes, e.g., the blades with the highest and lowest frequencies are the same for both sets of modes. This suggests that the mistuning in these systems may well be caused by relatively uniform thickness variations in the blades since this would affect the frequencies of both types of modes in a very similar manner.

In addition to identifying the mistuning in these rotors, Advanced FMM ID simultaneously inferred the tuned system frequencies of the system's torsion modes, as shown in Fig. 10. Again, the agreement is good. Thus, FMM ID worked well on both the torsion and bending modes of the test compressors.

4 Forced Response Prediction

In the previous section, we found that both forms of FMM ID inferred mistuning that agreed very well with benchmark data. In this section, the identified mistuning will be used to predict the forced response of the compressors to a traveling wave excitation. The results will be compared with measurements done by our industrial partners.

Pratt & Whitney has developed an experimental capability for simulating traveling wave excitation in stationary rotors. Their technique was applied to SN-1 in order to measure its first bending family's response to a 3E excitation. We then predicted the response of SN-1 with the methods developed here and in [1,4].

The issue is: do the 28 parameters (18 mistuned frequencies and 10 tuned system frequencies) identified by FMM ID from one set of transfer functions determine the system properties sufficiently well that we can accurately predict the traveling wave response? To make the prediction, we use the mistuning and tuned system frequencies from Advanced FMM ID as input to the FMM reduced-order model. FMM calculates the system's mistuned modes and natural frequencies. Then, we use modal summation to

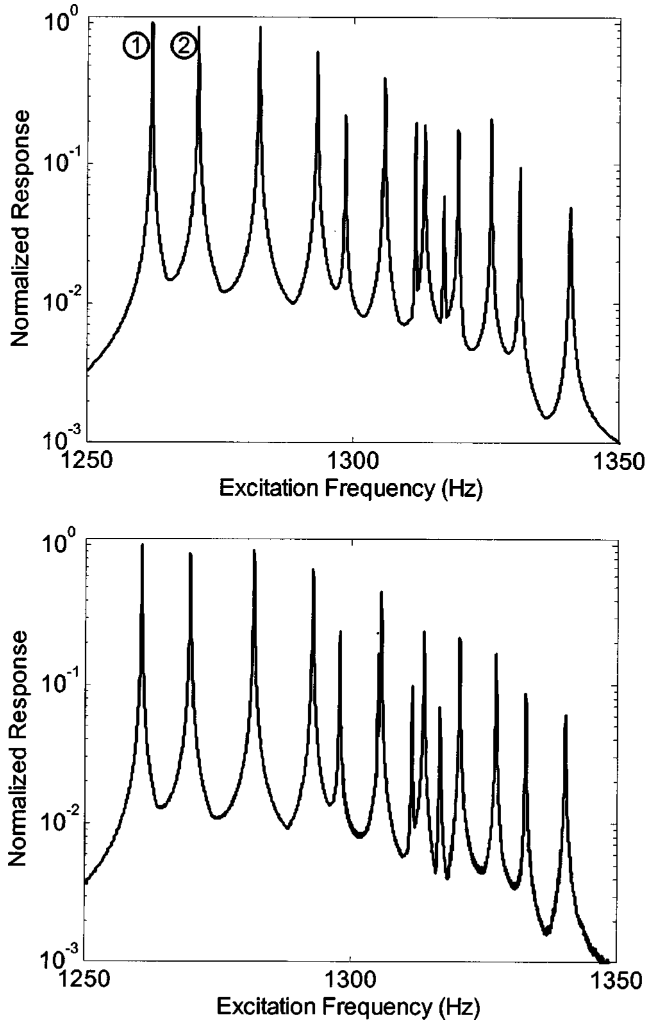

Fig. 11 Comparison of FMM based forced response with experimental data, (*a*) FMM, (*b*) experiment

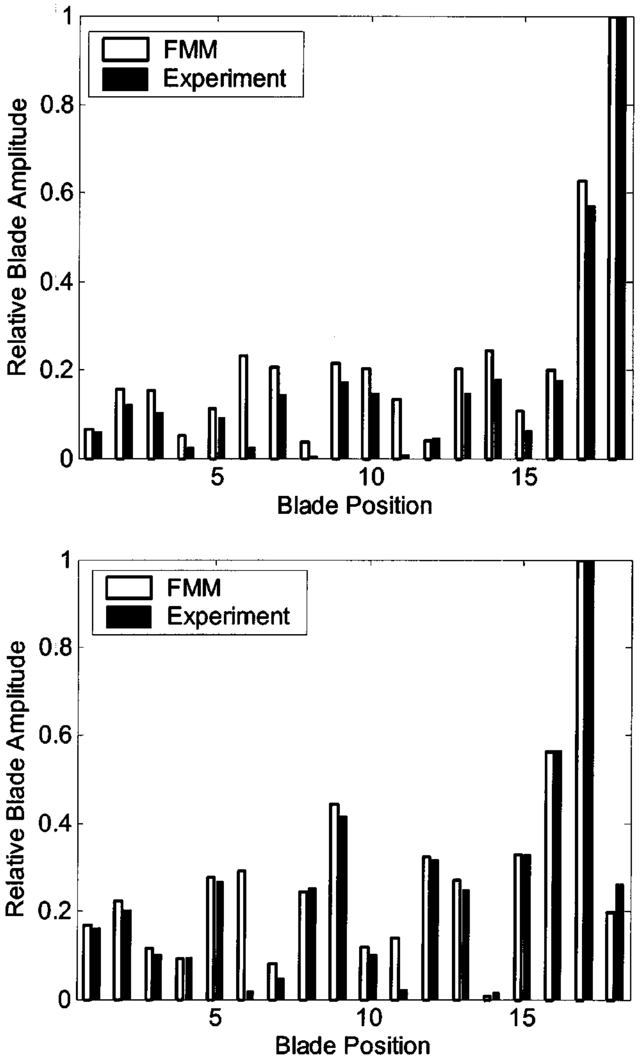

Fig. 12 Relative blade amplitudes at forced response resonance, (*a*) Resonance 1, (*b*) Resonance 2

calculate the response to a 3E excitation. The modal damping used in the summation was calculated from the half-power bandwidth of the transfer function peaks.

Figure 11 shows the comparison of the benchmark forced response results with that predicted by FMM. For clarity, only the envelope of the blade response is shown. Also, the plots have been normalized so that the maximum response is equal to one. In general, the two curves agree reasonably well. In order to observe how well the response of individual blades was predicted we have also compared the relative responses of the blades at two resonant peaks, the peaks labeled ① and ② in **Fig. 11.** The relative amplitude of each blade as determined by both methods is plotted for both resonant peaks in **Fig. 12.** The agreement is also reasonably good. Thus, the FMM based method not only captured the overall shape of the response, but also determined the relative amplitudes of the blades at the various resonances.

5 Cause and Implications of Repeated Mistuning Pattern

In the literature, the mistuning in bladed disks is generally considered to be a random phenomenon. However, in Section 3 we saw that both test rotors have very similar mistuning patterns that are far from random. If such repeated mistuning matters are found to be common among IBRs, it will have broad implications on the predictability of these systems. In Section 5.1 we discuss the cause of the repeated mistuning. Then in Section 5.2, we examine its implications on forced response predictability for a larger sample.

5.1 Possible Cause of Repeated Mistuning. The similarity between the mistuning patterns identified in SN-1 and SN-3 is highly suggestive that the mistuning was caused by a consistent manufacturing effect. In addition, we observed that the mistuning in the torsion modes follows the same trends as in the bending modes. Thus, the dominant form of mistuning is most likely caused by relatively uniform blade-to-blade thickness variations. One plausible explanation for the observed patterns is tool wear. Suppose that the blades were machined in descending order from blade 18 to blade 1. Then, due to tool wear, each subsequent blade will be slightly larger than the previous one. This effect would cause the sector frequencies to monotonically increase around the wheel. With the exception of the frequency jump observed at blade 9, this behavior matches the observed mistuning. Since there are 18 blades, the discontinuity at blade 9 could well be the result of a tool adjustment made halfway through the machining process.

5.2 Implications of Repeated Mistuning. The repeating mistuning patterns caused by such machining effects can significantly increase our ability to accurately predict the response of the fleet through probabilistic methods. For example, consider an en-

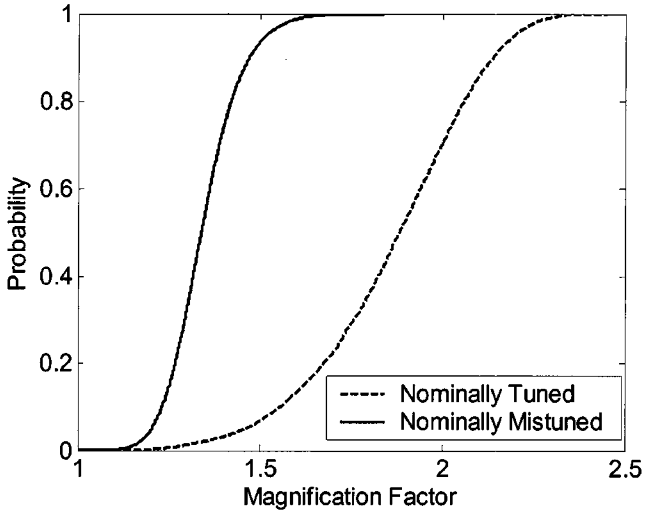

Fig. 13 CDF of peak blade amplitude for a nominally tuned and nominally mistuned compressor

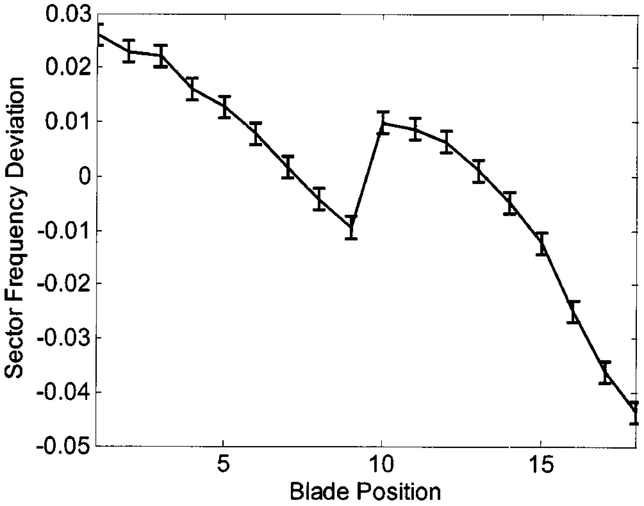

Fig. 14 Mean and standard deviation of each sector's mistuning for a nominally mistuned compressor

tire fleet of the transonic compressors studied in this paper. If we were to incorrectly assume that the mistuning in these rotors was completely random, then we would estimate that the sector frequency deviation of each sector has a mean of zero and a standard deviation of about 2%. Assuming these variations, we used FMM to perform 10,000 Monte Carlo simulations to represent how a fleet of engines would respond to a 3E excitation. We used the data to compute the cumulative distribution function (CDF) of the maximum blade amplitude on each compressor. The CDF of a fleet of engines with random mistuning have a standard deviation of 2% is shown as the dashed line in **Fig. 13.** Notice that the maximum amplitude varies widely across the fleet, ranging in magnification from 1.1 to 2.5.

However, these rotors are in fact nominally mistuned with a small random variation about the nominal pattern. Since the random variation is much smaller than that considered above, the fleet's response is actually far more predictable. To illustrate this point, we approximated the nominal mistuning pattern as the mean of the patterns measured for the two test rotors. Based on this pattern, we found that the sector frequency deviations differed from the nominal values with a standard deviation of only 0.2%, as shown in **Fig. 14.** Making use of the fact that the rotors are nominally mistuned, we repeated the Monte Carlo simulations. We then computed the CDF of the maximum amplitude on each rotor. The results are plotted as the solid line on **Fig. 13.** Notice that by accounting for nominal mistuning, the range of maximum amplitudes is significantly reduced. Thus, if we can measure and make use of nominal mistuning when it occurs then the fleet's behavior will be far more predictable.

6 Conclusions

A new method of identifying mistuning in bladed disks is demonstrated using actual hardware. The method is called FMM ID because it is based on the fundamental mistuning model (FMM), [4]. To test the FMM ID approach, we used it to identify the mistuning in a pair of modern transonic compressors and compared the results with values that were determined by Pratt & Whitney using a completely independent method.

FMM ID uses measurements of the system mode shapes and natural frequencies to infer the rotor's mistuning. The key concept behind FMM ID is that the high sensitivity of system modes to small variations in mistuning causes measurements of those modes themselves to be an accurate basis for mistuning identification. Since FMM ID does not require individual blade measurements, it is particularly suited to integrally bladed rotors. The method is only applicable to isolated families of modes. We have developed two forms of FMM ID: Basic FMM ID, and an advanced version that also identifies the frequencies of the tuned system.

We applied both forms of FMM ID to the two test rotors. To provide benchmark values of mistuning, our industrial partners in this research, Pratt & Whitney, also identified the mistuning in the rotors by measuring the geometry of each blade and then determining its natural frequencies through a finite element analysis. The results from both methods of identifying mistuning agreed very well. In addition to identifying mistuning, the advanced form of FMM ID can also infer the tuned system frequencies of the rotor. Except for a slight shift in their mean value, the identified tuned frequencies agreed well with finite element values. In practice, the ability of FMM ID to identify the tuned frequencies of the system could provide a useful method of confirming that the manufacturing process resulted in an IBR that is consistent with the original design.

We observed that the mistuning patterns in the two test rotors were very similar. This suggests that the mistuning was caused by a repeating feature of the manufacturing process, perhaps tool wear. The cause of the repeating mistuning pattern will be the subject of further investigation. If the mistuning in the two IBRs that we have tested are, in fact, representative of the manufacturing process, then a larger sample of rotors would exhibit similar behavior, i.e., they would have significant levels of nominal mistuning with small levels of random mistuning superimposed. In this case, the forced response of a fleet of these compressors would be far more predictable than might have been previously foreseen. If the manufacturing process can be understood and controlled, then we may be able to use optimization techniques such as those proposed in [5,6] to manufacture IBRs that have low, robust response.

The FMM ID method provides a simple approach for accurately identifying mistuning in integrally bladed rotors for isolated families of modes. In fact, because of its simplicity one version of the method requires only experimental data to determine the key parameters that characterize its response. Once determined, the mistuning can be used with the FMM reduced-order model, [4], to predict how much the mistuning will increase the stage's forced response to a traveling wave, engine order excitation. This technology is useful since it will allow test engineers to determine how the vibratory response of a specific IBR that is tested in a spin pit, rig test or engine relates to the vibratory response of the population as a whole. Ultimately, this technology should allow us to reduce the number of tests required to characterize the vibratory response of components and still have more durable engines.

Acknowledgments

The authors would like to acknowledge that this research was supported in part by the U.S. Air Force, contract number F33615-01-C-2186, under the direction of Dr. Charles Cross and by the GUIde Consortium.

The authors also would like to thank Mr. Robert J. Morris of Pratt & Whitney Aircraft for providing the experimental and analytical data on the two test compressors. We would also like to acknowledge that the IBRs were provided by Prof. S. Fleeter from Purdue University.

References

[1] Feiner, D. M., and Griffin, J. H., 2004, ‘‘Mistuning Identification of Bladed Disks Using a Fundamental Mistuning Model—Part I: Theory,’’ ASME J. Eng. Gas Turbines Power, **126**, pp. 150–158.
[2] Srinivasan, A. V., 1997, ‘‘Flutter and Resonant Vibration Characteristics of Engine Blades,’’ ASME J. Eng. Gas Turbines Power, **119**, pp. 742–775.
[3] Judge, J. A., Pierre, C., and Ceccio, S. L., 2002, ‘‘Mistuning Identification in Bladed Disks,’’ *Proceedings of the International Conference on Structural Dynamics Modeling*, Madeira Island, Portugal.
[4] Feiner, D. M., and Griffin, J. H., 2002, ‘‘A Fundamental Model of Mistuning for a Single Family of Modes,’’ ASME J. Turbomach., **124**, pp. 597–605.
[5] Jones, K. W., and Cross, C. J., 2002, ‘‘Reducing Mistuned Bladed Disk Forced Response Below Tuned Resonant Amplitudes,’’ *Proceedings of the 7th National Turbine Engine High Cycle Fatigue Conference*, Palm Beach Gardens, FL.
[6] Petrov, E., and Ewins, D., 2002, ‘‘Search for the Best Blade Arrangement in a Mistuned Bladed Disc Assembly,’’ *Proceedings of the 7th National Turbine Engine High Cycle Fatigue Conference*, Palm Beach Gardens, FL.

A. J. Sanders
e-mail: Al.Sanders@Honeywell.com

K. K. Hassan
e-mail: Khaled.Hassan@Honeywell.com

Honeywell Engines, Systems & Services,
111 South 34th Street, MS 301-134,
Phoenix, AZ 85034

D. C. Rabe
Air Force Research Laboratory,
1950 Fifth Street, Building 18D,
Wright Patterson AFB, OH
e-mail: Douglas.Rabe@afrl.af.mil

Experimental and Numerical Study of Stall Flutter in a Transonic Low-Aspect Ratio Fan Blisk

Experiments are performed on a modern design transonic shroudless low-aspect ratio fan blisk that experienced both subsonic/transonic and supersonic stall-side flutter. High-response flush mounted miniature pressure transducers are utilized to measure the unsteady aerodynamic loading distribution in the tip region of the fan for both flutter regimes, with strain gages utilized to measure the vibratory response at incipient and deep flutter operating conditions. Numerical simulations are performed and compared with the benchmark data using an unsteady three-dimensional nonlinear viscous computational fluid dynamic (CFD) analysis, with the effects of tip clearance, vibration amplitude, and the number of time steps-per-cycle investigated. The benchmark data are used to guide the validation of the code and establish best practices that ensure accurate flutter predictions. [DOI: 10.1115/1.1645532]

Introduction

Stall flutter has been one of the most difficult aeroelastic problems to predict in turbomachinery, with two distinct stall-side flutter regimes possible. Subsonic/transonic stall flutter occurs at part-speed operating conditions where the incidence angles are high and the inlet flow is high subsonic or transonic. The flutter response is typically the first torsion mode although cases of bending flutter have also been observed. Supersonic stall flutter occurs at high-speed operating conditions in which the inlet flow is supersonic and detached leading edge shocks are present, with the flutter response typically the first bending mode. Until recently, empirical and semi-empirical methods have been used with limited success to predict stall flutter for both of these regimes, [1–4].

Advances in unsteady computational fluid dynamic (CFD) techniques have provided considerable insight into the flow physics driving stall-side flutter. Shabata and Kaji [5] analyzed bending flutter for the tip section of a transonic fan using a linearized unsteady two-dimensional Euler analysis and found that the shock-induced unsteady aerodynamic loading on the airfoil suction surface produced the largest destabilizing force for unstarted supersonic inlet flows. Isomura and Giles [6] also concluded that unsteady shock oscillations rather than blade stall were the driving mechanism for a bending flutter instability observed in a transonic fan. They analyzed the tip section using a quasi three-dimensional viscous analysis and found that suction surface separation behind the shock actually exhibited a stabilizing effect, with the shock oscillating between started and unstarted conditions producing the dominant aerodynamic excitation.

Fully unsteady nonlinear three-dimensional Navier-Stokes analyses are also being used to predict the stall flutter characteristics of advanced fan and compressor designs. Silkowski et al. [7] describes how these CFD based techniques can be applied to solve a wide variety of aeroelastic problems during the design phase. Their flutter predictions for a transonic fan agreed fairly well with test data, including predicting the least stable nodal diameter pattern and the onset of flutter within 7.5% of the measured flow rate. Srivastava et al. [8] also utilized an unsteady three-dimensional Navier-Stokes analysis to investigate the flutter characteristics of an advanced forward swept fan design that encountered stall-side flutter. Several operating conditions were analyzed, with the analysis predicting that the aerodynamic damping rapidly decreased as the fan was throttled toward stall. However, negative aerodynamic damping was not calculated at the tested instability point, with numerical convergence difficulties encountered for operating conditions closer to the stall line.

As shown by the above examples, these advanced CFD based flutter predictions capture correct trends, but the accuracy of the predictions cannot be assured without properly validating the analyses with benchmark quality data. Since the unsteady aerodynamics are the driving mechanism for flutter, detailed unsteady surface pressure data that define the motion-induced unsteady aerodynamic loading are needed to determine if the relevant flow physics are being captured in the CFD analyses. Unfortunately, their has been little research to address this need, with most of the experimental investigations for two-dimensional linear cascades or low-speed research rigs.

Carta and St. Hilaire [9,10] and Carta [11] obtained unsteady surface pressure data on a low-speed linear cascade of NACA 65 series airfoils forced to undergo harmonic torsional oscillations. The experiments were performed over a range of incidence angles, reduced frequencies, and interblade phase angles, with the interblade phase angle found to be the single most important parameter affecting the stability of the cascade. Buffum et al. [12,13] obtained unsteady surface pressure data on a transonic linear cascade of airfoils also forced to undergo harmonic torsional oscillations. The airfoils were representative of a modern low-aspect ratio fan blade tip section and data were acquired over a range of inlet Mach numbers, incidence angles, and reduced frequencies for an interblade phase angle of 180 deg. Investigations have also been performed on low-speed rotating rigs in which unsteady surface pressure data were acquired for three-dimensional blades forced to undergo harmonic torsional oscillations, [14,15].

Unsteady surface pressure data that define the flutter response for realistic three-dimensional transonic fan designs is even more scarce, due in part to the inherent difficulty of acquiring rotating data in a high-speed machine. Stargardter [16] obtained unsteady surface pressure data in the tip region of a single-stage transonic

---

Contributed by the International Gas Turbine Institute and presented at the International Gas Turbine and Aeroengine Congress and Exhibition, Atlanta, GA, June 16–19, 2003. Manuscript received by the IGTI December 2002; final revision March 2003. Paper No. 2003-GT-38353. Review Chair: H. R. Simmons.

Table 1 90% span Kulite locations

ID	Blade	Surface	% Chord
B07PS15	7	PS	15
B07PS35	7	PS	35
B07PS55	7	PS	55
B07PS75	7	PS	75
B08SS15*	8	SS	15
B08SS25	8	SS	25
B08SS35	8	SS	35
B08SS55*	8	SS	55
B08SS75	8	SS	75
B16PS25	16	PS	25
B16PS45*	16	PS	45
B16PS65*	16	PS	65
B16PS85	16	PS	85
B17SS20	17	SS	20
B17SS30*	17	SS	30
B17SS45	17	SS	45
B17SS65	17	SS	65
B17SS85	17	SS	85

*Inoperative Transducer at Time of Test

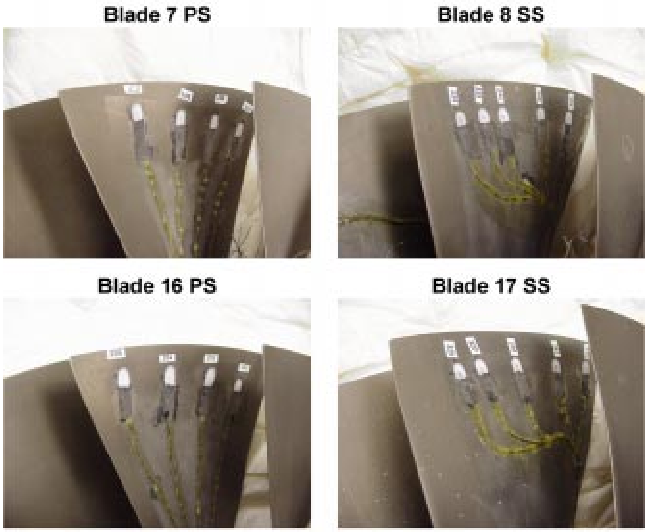
Blade 7 PS
Blade 8 SS
Blade 16 PS
Blade 17 SS

Fig. 1 Flush-mounted Kulites at 90% span

shrouded research fan that encountered torsion mode subsonic/transonic stall flutter. The data indicated that flutter only occurred at corrected fan speeds in which the flow was locally supersonic along the airfoil suction surface. However, the flow physics driving the flutter response could not be determined from the surface pressure data, with no distinct evidence of flow separation or shock oscillation contained in the data. Halliwell et al. [17] made similar unsteady pressure measurements for a shrouded transonic fan vibrating in a coupled bending-torsion mode in the unstalled supersonic flutter regime. Unfortunately, both of these investigations were for older generation fan designs that featured part-span shrouds and moderate to high-aspect ratios.

For modern shroudless low-aspect ratio fan designs, the only data typically available to help guide the CFD validation are conventional strain gage and performance measurements acquired during development rig and engine tests. These limited data, however, provide no insight into whether the unsteady CFD analyses are correctly predicting the flow physics that drive the flutter response. Since the unsteady aerodynamics are the driving mechanism for flutter, unsteady surface pressure data are also needed. This research was aimed at addressing this need, with detailed unsteady aerodynamic, vibratory response, and performance data acquired on a transonic low-aspect ratio shroudless fan blisk that experienced both subsonic/transonic and supersonic stall-side flutter. Miniature flush mounted high-response pressure transducers were used to measure the unsteady aerodynamic loading distribution in the tip region of the fan, with strain gages used to simultaneously measure the vibratory response at incipient and deep flutter operating conditions for each flutter regime.

These benchmark data were then compared with unsteady three-dimensional nonlinear viscous CFD simulations of the fan for several operating conditions that corresponded to both stable and incipient flutter operating conditions for each of the two flutter regimes. The effects of tip clearance, vibration amplitude, and the number of time steps-per-cycle were investigated, with the simulations compared with the benchmark data in order to quantify the impact of these parameters on the accuracy of the flutter predictions and define best practices.

Experimental Investigation

The test article for this investigation was a development fan blisk featuring 22 low-aspect ratio shroudless fan blades that was tested in the Air Force Research Laboratory (AFRL) Compressor Research Facility (CRF) at Wright Patterson Air Force Base. A total of two blade passages located approximately 180 degrees apart were instrumented at 90% span with high-response Kulite XCQ-062-20A flush mounted pressure transducers at the locations listed in **Table 1**. Note that the chordwise positions of the Kulites for the two passages differ from one another and have been staggered to provide greater spatial resolution along the airfoil chord. The transducer chip was built directly in a recessed pocket and was covered with a thin layer of RTV to protect the diaphragm, with epoxy potting compound used to blend the trenched area back to the original airfoil profile, **Fig. 1**. Acoustic ring signature (ARS) testing verified that machining pockets into the blisk to recess the Kulites had a negligible effect on the natural frequency of the flutter mode which was first bending.

Eight blades were also instrumented with strain gages sensitive to the first bending mode, with the strain gaged blades corresponding to the two passages instrumented with Kulites and the adjacent blades on each side of these two passages. The leads from the rotating instrumentation were transferred to the stationary reference frame using a forward mounted 100 channel slip ring unit, **Fig. 2**. The AC coupled strain gage and Kulite signals were recorded on analog tape at a speed of 30 inches per second (ips) to yield a frequency response of 30 kHz. This frequency response was more than sufficient to capture the 450 Hz flutter frequency which occurred at the high-speed operating condition. At the time of testing 13 out of the original 18 blade mounted Kulites and 6 out of the original 8 strain gages were functional and delivered high-quality data.

The performance instrumentation included total pressure and total temperature rakes both upstream and downstream of the fan stage, **Fig. 2**. Upstream kiel head rakes were also located in the inlet plenum and used to develop an empirical correlation to correct these data to the fan aerodynamic interface plane (AIP). This correlation allowed the 5 AIP rakes to be removed for the flutter testing, thereby providing a clean inlet flow field to the fan. For the flutter tests, two five-element inlet boundary layer rakes located 180 deg apart were installed in place of the AIP rakes to measure the shroud inlet boundary layer profile. The fan stage exit

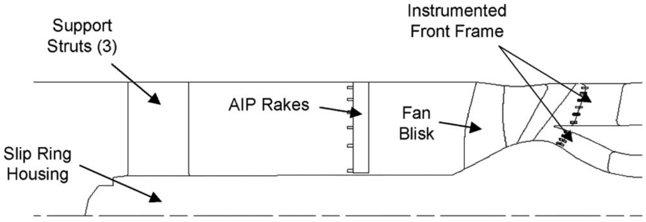

Fig. 2 Fan stage test section

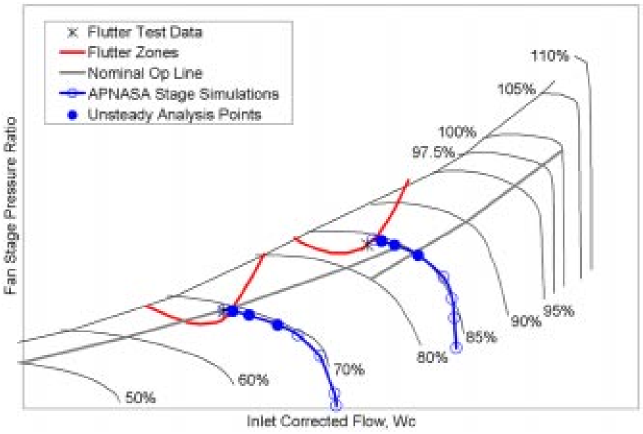

Fig. 3 Fan map with flutter test and analysis points

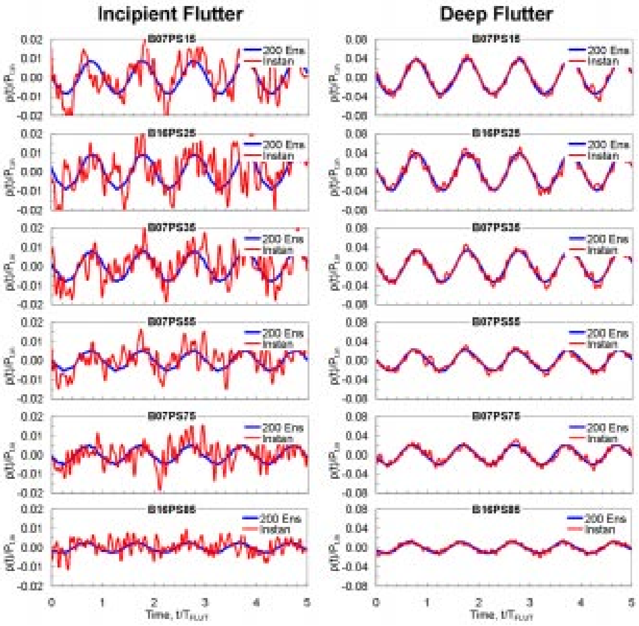

Fig. 4 Phase-lock averaged pressure surface waveforms

total pressure and total temperature profiles were measured in both the core and bypass streams using an instrumented front frame assembly. The strut leading edge instrumentation consisted of ten rakes (five total pressure and five total temperature) equally spaced around the annulus. Each rake had kiel head elements placed at the centers of equal annular areas, with six immersions used in the bypass and four in the core, with these data arithmetically averaged to define the fan operating point. Four equally spaced capacitance probes located near the rotor trailing edge plane were also used to measure the running tip clearance.

Previous development testing of this fan blisk identified the presence of two large flutter zones, with the first zone extending from 65–80% corrected speed and the second from 82–92% corrected speed, **Fig. 3**. In the present investigation, detailed performance, unsteady aerodynamic, and vibratory response data were acquired at both incipient and deep flutter operating conditions for each of these flutter zones at 70% and 85% corrected speed. This was accomplished by slowly throttling the fan up each of the speedlines while maintaining the desired bypass ratio and monitoring the strain gages for any signs of nonsynchronous activity indicative of flutter. The flutter boundary was defined as the location where the alternating stress was above the noise and below 5 ksi (34.5 MPa). Once the location of the flutter boundary had been identified, the core and bypass throttle valves were closed slightly to maintain the desired bypass ratio while moving the fan operating point just inside the flutter zone.

The high-response unsteady aerodynamic and vibratory response data were recorded on analog tape as the flutter boundary was penetrated, with the strain gages monitored and the throttle valves immediately opened once the stress on any blade exceeded predetermined vibration limits. Acquiring the data in this manner allowed the flutter response to be characterized as the amplitude of the unsteadiness developed from incipient to deep flutter operating conditions. Analysis of the strain gage data indicated the flutter response occurred in the first bending mode as a two nodal diameter forward traveling wave for both flutter regimes. Since the strain gage data were acquired only on specific blades, nonintrusive stress measurement system (NSMS) data were also acquired to quantify mistuning effects on the flutter response. These NSMS data, however, are not included in the present paper.

The data were digitized from the analog tape at a sampling rate of 18,750 Hz, with the Kulite data phase-lock averaged over 200 oscillation cycles using the strain gage signal on blade eight as the data initiation pulse to perform the averaging. During these 200 cycles the vibration amplitude was nearly constant, with the data windowed to select two distinct time intervals corresponding to both incipient (5 ksi) and deep (20 ksi) flutter operating conditions. Post-processing the data in this manner allowed the periodic component of the unsteady surface pressure generated by the blade motion to be recovered from the instantaneous signals. Additionally, all data was time shifted to blade eight using the measured vibration frequency and interblade phase angle (nodal diameter pattern) determined from the strain gage data, with these time-variant waveforms corresponding to sine-wave motion of the reference blade.

Figure 4 and **Fig. 5** show the phase-lock averaged unsteady pressure and suction surface waveforms normalized by the fan inlet total pressure for both the incipient and deep flutter operating conditions at 70% corrected speed. An instantaneous time trace at the center of the averaging window (cycle 100) is also shown for

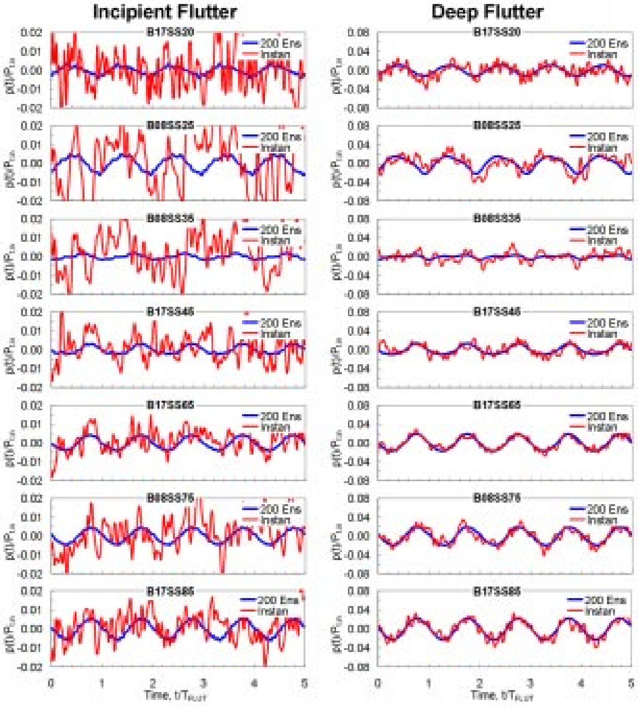

Fig. 5 Phase-lock averaged suction surface waveforms

reference. Even though the instantaneous signals at the incipient flutter operating condition are dominated by random noise, very clean periodic time traces are obtained for all chordwise locations using 200 ensembles to phase-lock average the data. Also notice that the phase-lock averaged waveforms for the two stress levels are in excellent agreement with one another along the entire chord, with the unsteady pressure at the deep flutter operating condition (20 ksi) nearly four times that occurring at the incipient flutter operating condition (5 ksi). Although not presented here, similar features were observed in the 85% corrected speed data.

To facilitate the comparison of the data with the CFD predictions, a Fourier analysis was performed on the phase-lock averaged surface pressure data to extract the harmonic component at the flutter frequency. These first harmonic unsteady surface pressure distributions were then normalized by the product of the fan inlet total pressure and the maximum vibratory tip deflection divided by the tip chord. An ANSYS finite element model of the fan blisk was used to convert the measured alternating stresses to equivalent vibratory tip deflections. The maximum uncertainty in the magnitude and phase angle of this normalized unsteady pressure coefficient is estimated to be 5.3% and 6.2 degrees, respectively.

Numerical Investigation

Unsteady three-dimensional viscous CFD simulations of the fan were performed using TURBO-AE v4.2 with a CMOTT k-ε turbulence model, [18], and nonreflecting inlet and exit boundary conditions. This code is a time-accurate three-dimensional Euler/Navier-Stokes flow solver for axial-flow turbomachinery under development at Mississippi State University and NASA Glenn Research Center, [19–22]. A single blade passage was modeled in the unsteady analysis using periodic phase-lag boundary conditions to simulate the desired interblade phase angle, i.e., nodal diameter pattern. To assess aeroelastic stability, the work-per-cycle determined from the analysis was converted to the critical damping ratio since this value was more physically meaningful, with both the unsteady normal pressure and viscous shear forces included in the work-per-cycle calculation. Since both mechanical and material damping are negligible for blisks, the fan is considered unstable if the aerodynamic damping is negative.

The grid was a single block smoothed H mesh with 122 points in the streamwise, 39 points in the blade-to-blade, and 51 points in the spanwise direction, with four cells spanning the clearance gap, **Fig. 6**. Clearance effects were modeled using a periodic boundary across the nongridded region between the blade tip and shroud similar to APNASA. This technique treats the clearance flow as an orifice flow with no change in mass, momentum, or energy across the blade tip. Steady CFD investigations have shown that this approach provides reasonable estimates of clearance effects as long as the mass flow through the tip gap is correctly predicted, [23–25]. The current best practice for steady simulations is to use half the measured clearance for transonic operating conditions, with the impact of this recommendation on the accuracy of the flutter predictions quantified in the present paper. The main benefit of modeling the clearance flow in this manner was that it is easy to implement and did not require a multiblock flow solver and additional computer resources to resolve the tip gap flow.

In the unsteady analyses, the motion of the blade was simulated by harmonically deforming the grid using the mode shape from an ANSYS finite element modal analysis of the blisk at each part-speed operating condition. The modal deflections for the airfoil portion of the blisk model are shown in **Fig. 7**, with the mode shape primarily bending with a torsional component due to the high hub slope. Unless otherwise noted, the modal deflections from the finite element model were scaled to yield a tip displacement of 0.27% tip chord and then mapped to the CFD grid using the NASA developed preprocessor AEPREP. This tip displacement corresponded to an alternating stress of 2.3 ksi (15.9 MPa) and is thus representative of the incipient flutter response. The reduced frequencies based on semi-chord for the 90% span section are 0.36 and 0.34 for the 70% and 85% corrected speed operating conditions, respectively.

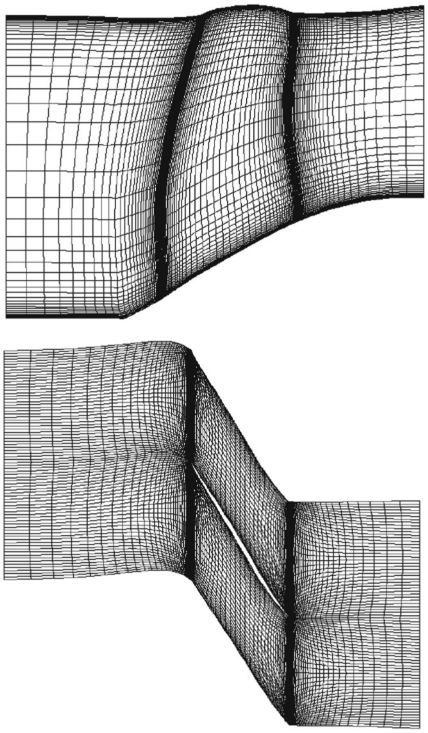

Fig. 6 CFD grid for unsteady TURBO-AE simulations

Comparison of Results

The measured tip clearance and shroud inlet boundary layer profiles from the test were used to define the boundary conditions for the CFD analyses. For each speed, an ANSYS static analysis was performed and the CFD geometry updated to reflect the true part-speed running condition. Steady APNASA stage (rotor and stator) simulations were performed since the instrumentation used to set the fan operating point in the test was located on the front frame assembly downstream of the fan stage. These APNASA stage simulations were used to define the rotor exit boundary conditions and initialize the flow field for the isolated rotor TURBO-AE simulations. The predicted speedlines for the APNASA stage simulations at 70% and 85% corrected speed are shown along with the tested operating conditions on the background fan map in **Fig. 3**.

Three operating points close to the measured flutter boundaries were analyzed with TURBO-AE for both 70% and 85% corrected speed, with these operating points shown by the solid symbols in

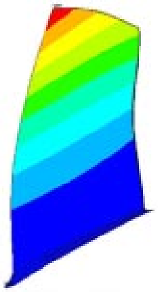

Fig. 7 Mode shape for unsteady TURBO-AE simulations

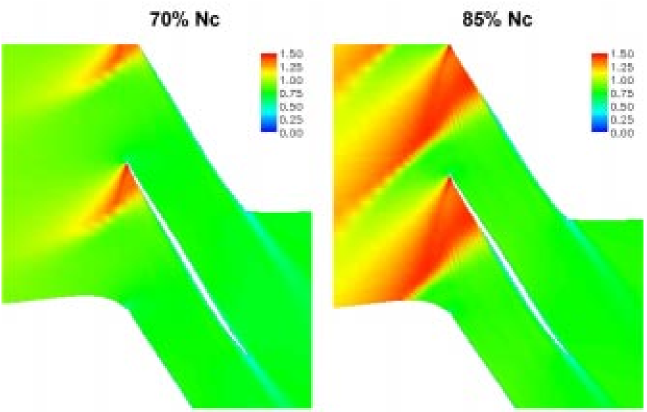

Fig. 8 Steady 90% span blade-to-blade Mach number

Fig. 3. In order to quantify the effects of tip clearance on the flutter predictions, the TURBO-AE simulations were performed using both half (0.54% tip chord) and full (1.07% tip chord) clearance. The time-accurate TURBO-AE simulations were initiated from converged steady solutions, with the unsteady analyses marched forward in time using 100 time steps-per-cycle for 15 cycles to obtain periodic time-dependent solutions. The number of Newton subiterations for each time step was determined by requiring the minimum density and total energy residuals to be less than −1.20, which typically required five to seven subiterations. Numerical studies have shown that a residual limit of −1.20 provides good convergence while keeping the number of subiterations at each time step within reasonable limits. To determine the least stable nodal diameter pattern, the unsteady simulations were performed for nodal diameters of −2, 0, +2, and +4. Unsteady simulations were also attempted for the higher back-pressure operating points just inside each flutter zone, but numerical convergence difficulties were encountered.

Figure 8 shows the steady rotor blade-to-blade relative Mach number contours for the half-clearance simulations at the grid plane located closest to the 90% span measurement location for the incipient flutter operating conditions at both 70% and 85% corrected speed. At 70% corrected speed, the inlet Mach number at 90% span is near sonic, with a supersonic bubble terminating into a shock in the leading edge region of the airfoil due to the high incidence angle. At 85% corrected speed, the inlet Mach number at 90% span is 1.2 and a strong unstarted shock wave is present in the leading edge region.

Figure 9 displays the aerodynamic damping as a function of nodal diameter for the lowest and highest of the three back-pressure operating conditions for the half and full-clearance simulations for each of the two speedlines. Recall that the lower back-pressures correspond to stable operating points while the higher back-pressures correspond to operating points right at the edge of the measured flutter boundary for each speed, **Fig. 3**. The low back-pressure operating points away from the measured flutter boundary for both speeds are predicted to be stable since the aerodynamic damping is positive for all nodal diameters. Similarly, the high back-pressure operating points near the measured flutter boundary are predicted to be unstable or on the verge of instability for both speeds, which is in excellent agreement with the test data. Also, clearance has a very small effect on the aerodynamic damping predictions at 70% corrected speed, with the damping curves for the half and full clearance simulations nearly collapsing. At 85% corrected speed, clearance effects are more pronounced with the full clearance simulations predicted to be slightly less stable than those at the half-clearance for both operating conditions.

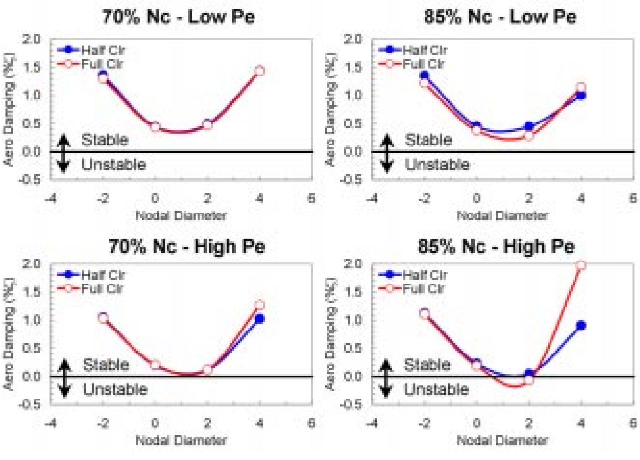

Fig. 9 Aerodynamic damping versus nodal diameter

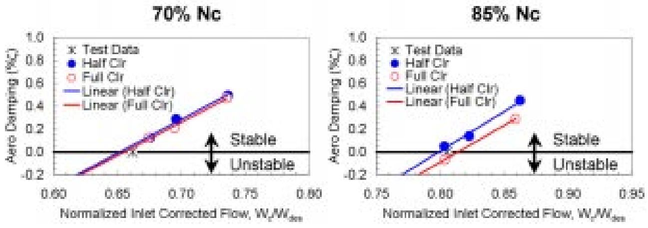

Fig. 10 Effect of tip clearance on flutter boundary predictions

The aerodynamic damping is predicted to be lowest in the 0 to +2 nodal diameter range, with the strain gage data indicating that flutter occurs in the +2 nodal diameter pattern. The reasons for the +2 nodal diameter pattern being the least stable in the test can be explained by examining the structural dynamic characteristics of the blisk. Specifically, through bench testing the 2 nodal diameter pattern was found to exhibit the lowest system mode frequency using the system identification technique of Feiner and Griffin [26,27]. Since the 2 nodal diameter forward traveling wave exhibits both the lowest frequency and the lowest aerodynamic damping of all system modes, it is the least stable pattern.

Figure 10 displays how the aerodynamic damping for the 2 nodal diameter forward traveling wave varies as the fan is throttled toward the flutter boundary for the half and full clearance simulations at both 70% and 85% corrected speed. Notice that the intermediate back-pressure operating condition for each speed has also been presented. The aerodynamic damping varies nearly linearly with inlet corrected flow for each speed, with a least-squares fit of damping versus flow also shown for the half and full clearance simulations. At 70% corrected speed, both the half and full clearance predictions of the flutter inception points using the least-squares fit are nearly identical and in excellent agreement with the data. At 85% corrected speed, decreasing the clearance causes the onset of flutter to occur at lower flows, with the half and full-clearance predictions bracketing the test data. Again, the predictions are in very good agreement with the data and also indicate that extrapolation of the aerodynamic damping predictions provides very accurate flutter boundary predictions.

Based on the aerodynamic damping alone, one might conclude that the flutter predictions are independent of clearance at 70% corrected speed whereas clearance has a noticeable effect on the predictions at 85% corrected speed. To determine which value of clearance most accurately captures the flow physics that drive the flutter response, the benchmark unsteady surface pressure data are compared with the CFD predictions for the 2 nodal diameter forward traveling wave at the incipient flutter point. The effects of vibration amplitude and the number of time steps-per-cycle on the

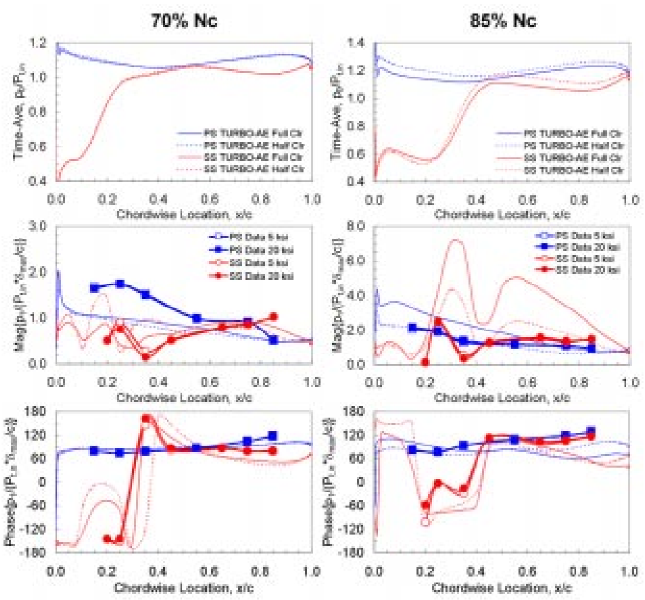

Fig. 11 Effect of tip clearance on loading predictions

unsteady surface pressure predictions are also investigated and compared with the benchmark data to establish optimum parameter settings.

Figure 11 shows the comparison of the data with the half and full clearance unsteady CFD simulations at the incipient flutter operating conditions, with the time-average and first harmonic unsteady pressure magnitude and phase angle displayed. In this figure the time-average pressure has been normalized by the fan inlet total pressure, and the unsteady pressure by the product of the fan inlet total pressure and the maximum vibratory tip deflection divided by the tip chord. No steady pressure data were acquired in the test due to problems with electrical drift effects, with only predictions shown for the steady loading. Also note that the scales for the unsteady surface pressure magnitude differ for the two speeds, with the predicted suction surface loading considerably larger for the supersonic stall flutter response at 85% corrected speed.

At 70% corrected speed, clearance has a negligible effect on the time-average loading predictions as evident by the collapse of the predictions for both the half and full-clearance simulations. Both the magnitude and phase angle of the unsteady suction surface loading distributions, however, are markedly different for the two simulations, with the full clearance predictions correlating much better with the data. It should be noted that these differences are due to unsteady flow effects since the time-average loading distribution is not affected by clearance. Also notice that whereas the suction surface predictions differ considerably for the half and full-clearance simulations, the pressure surface predictions are not affected. Here both the magnitude and phase angle of the pressure surface unsteadiness are nearly identical for the two clearances. Also notice that the phase angle predictions are in excellent agreement with the data across the entire chord, with the magnitude underpredicted across the front 50% chord although the agreement is still quite good.

At 85% corrected speed, clearance has a small but noticeable effect on the time-average surface pressure distribution, with the loading diagrams for the half and full clearance simulations slightly offset from one another. Even though the steady pressure gradients are very similar for both clearances, the unsteady suction surface loading distributions differ considerably for the half and full-clearance simulations. The trends with clearance also differ from those at 70% corrected speed. Here, increasing the clearance results in an increase in the magnitude of the suction surface unsteadiness whereas at 70% corrected speed the opposite was true. The magnitude of the suction surface unsteadiness is also nearly a factor of two larger for the full clearance simulation, with the half-clearance simulation in much better agreement with the data although the magnitude is still overpredicted. Similar behavior is also present in the pressure surface unsteady loading predictions, with the half-clearance magnitude and phase angle in much better agreement with the data along the entire chord. In fact, the magnitude of the half clearance prediction nearly falls on top of the data whereas the full-clearance simulation significantly overpredicts the magnitude of the unsteady loading.

The ''steady'' interaction of the tip clearance flow with the passage shock is thought to be the main reason why the half-clearance simulations provide more accurate predictions at 85% corrected speed. At 70% corrected speed this interaction does not occur since there is no passage shock (see **Fig. 8**), with the full-clearance simulation providing good agreement with the data. At 85% corrected speed, however, the interaction of the clearance flow with the passage shock is significant and a scaling of the tip gap is necessary for the unsteady pressure predictions to agree with the data. Steady CFD investigations have shown that this interaction has a significant effect on the flow field in the tip region of high-speed fans, with the clearance model of APNASA providing reasonable predictions of this interaction as long as the tip gap is scaled in the numerical simulation to account for the blockage introduced by the vena contracta of the actual flow in the clearance region, [23]. The present results confirm that accurate flutter predictions can be achieved using this simple clearance model as long as the tip gap is scaled for supersonic operating conditions. This is not a new concept as it has already been established as a best practice for steady CFD simulations, we are simply pointing that it is also valid for unsteady flows.

Also notice that both the magnitude and the phase angle of the pressure surface loading distributions are remarkably similar at both 70% and 85% corrected speed, with this behavior evident in both the data and the numerical simulations. Here the unsteadiness is highest in the leading edge region and monotonically decreases along the airfoil chord. Also notice the linear variation in the phase angle along the entire pressure surface of the blade. This behavior is in contrast to the suction surface loading distributions, with both the magnitude and phase angle of the suction surface unsteadiness noticeably different for the two flutter regimes due to changes in the suction surface shock structure as the inlet Mach number is increased (see **Fig. 8**). As the supersonic bubble transitions to a strong shock wave, there is a considerable increase in the magnitude of the unsteadiness very locally in the vicinity of the shock. Other than this, the magnitude of the suction surface loading is qualitatively very similar for both flow regimes, although there are significant differences in the phase angle due to the shock wave formation.

The collapse of the normalized unsteady surface pressure data for the incipient and deep flutter operating conditions indicates that the unsteady aerodynamics linearly scale with deflection amplitude. To investigate this behavior, additional CFD simulations were performed for vibratory deflection amplitudes of 0.80% tip chord (6.9 ksi) and 1.34% tip chord (11.5 ksi) using full clearance at 70% corrected speed and half-clearance at 85% corrected speed since these clearances were found to produce the best correlation with the data. For each speed, the 2 nodal diameter forward traveling wave was analyzed at three operating conditions along each speedline using 100 time steps-per-cycle, with the aerodynamic damping versus flow shown in **Fig. 12**.

As the vibration amplitude is increased, the onset of flutter appears to be moved toward lower flow rates, i.e., closer to the stall line. This behavior is numerical and is a consequence of the manner in which the flutter analyses are performed. Specifically, the blade is being forced to vibrate at a fixed amplitude, frequency, and interblade phase angle in the unsteady CFD simulations, with the resulting aerodynamic damping calculated

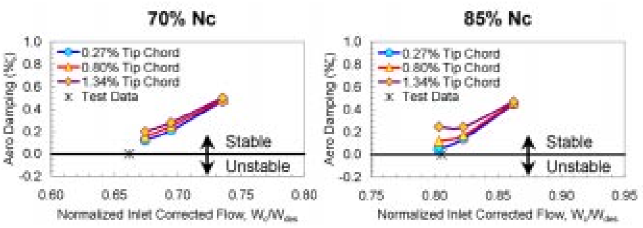

Fig. 12 Effects of vibration amplitude on flutter boundary predictions

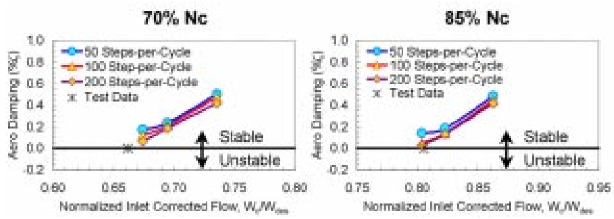

Fig. 14 Effect of number of time steps-per-cycle on flutter boundary predictions

due to this prescribed motion. Flutter, however, is initiated when the aerodynamic damping becomes zero for an infinitesimal motion of the airfoil. As the amplitude of the blade motion grows, nonlinear effects will cause the aerodynamic damping to increase such that the flutter response develops into a limit cycle oscillation at the flutter frequency. This precise behavior is being captured in the unsteady CFD simulations and demonstrates the need to specify small vibration amplitudes when performing the stability assessments using nonlinear time marching analyses.

The predicted time-average loading and first harmonic unsteady pressure magnitude and phase angle for the incipient flutter operating conditions are compared with the data in **Fig. 13** for the three vibration amplitudes at each speed. Increasing the vibration amplitude does not affect the time-average loading but does have a small effect on both the magnitude and phase angle of the unsteady loading for both speeds due to nonlinear effects. These predictions thus confirm that the unsteady surface pressure distributions nearly collapse at 90% span for all three vibratory deflection amplitudes which is consistent with the first harmonic unsteady surface pressure data. The small differences in phase angle, however, have a significant impact on the flow rate at which the onset of flutter is predicted to occur as evident in **Fig. 12**.

In order to quantify the impact of the number of time steps-per-cycle on the accuracy of the flutter predictions, additional simulations were performed using full clearance at 70% corrected speed and half-clearance at 85% corrected speed. For each speed, the 2 nodal diameter forward traveling wave was analyzed at the same three operating conditions as before for a vibratory deflection amplitude of 0.27% tip chord (2.3 ksi). **Figure 14** shows the results of simulations performed using 50, 100, and 200 time steps-per-cycle, with the number of subiterations at each time step determined by requiring the minimum residual to be below -1.20 which typically required five to seven iterations.

In general, the slope of the damping versus flow curves for both speeds become more linear as the number of time steps-per-cycle is increased, with the 100 and 200 time step-per-cycle flutter boundary predictions in good agreement with one another as well as the test data. The 50 time step-per-cycle damping versus flow curves tend to flatten out as the flutter boundary is approached for each of the two speeds giving the elusion that there is no flutter problem. This behavior, however, is numerical and even though the 50 time step-per-cycle simulations provide the fastest turnaround time they could erroneously lead one to believe that there is no risk of a flutter problem when in fact there is. Also, the 200 time step-per-cycle simulations provide only a marginal improvement in the accuracy of the flutter boundary predictions and are so computationally intensive that they could not be used for routine aeroelastic design. Thus, the 100 time step-per-cycle simulations are seen to yield the best compromise between accuracy and computational time for both flutter regimes.

Figure 15 shows the effect of increasing the number of time steps-per-cycle on the time-average and unsteady first harmonic loading predictions at 90% span for the incipient flutter operating conditions. Changing the number of time steps-per-cycle has a small, but noticeable, effect on the magnitude of the pressure and suction surface unsteadiness at both speeds. However, these differences are very small and the overall shape of the curves match the data very well across the entire chord for both speeds. The number of time steps-per-cycle is also seen to have a small effect

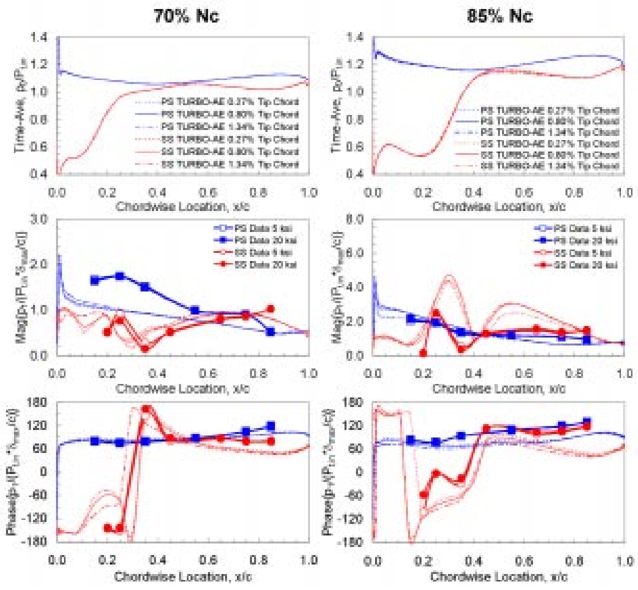

Fig. 13 Effects of vibration amplitude on loading predictions

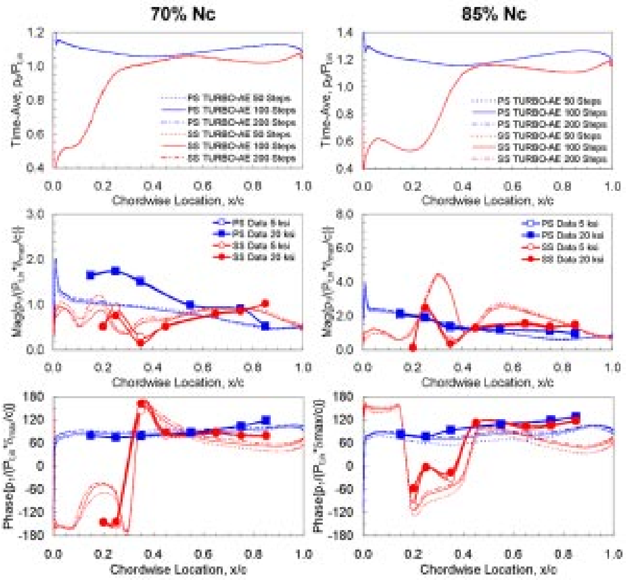

Fig. 15 Effect of number of time steps-per-cycle on loading predictions

on the phase angle of both the pressure and suction surface unsteadiness, with increasing the number of time steps-per-cycle resulting in slightly higher phase angle predictions along the entire airfoil chord for both surfaces. This behavior is present for both speeds, and although the differences in phase angle appear small, they do have a significant impact on the flutter boundary predictions as evident in **Fig. 14**. This is because the phase angle of the unsteady pressure determines if that region of the airfoil is stabilizing or destabilizing, with the magnitude of the unsteady pressure mainly affecting the magnitude of the stabilizing or destabilizing effect. A small shift in the phase angle distributions can thus have a significant impact on the stability assessment.

Summary and Conclusions

The stall-side flutter characteristics of a transonic low-aspect ratio shroudless fan blisk have been experimentally investigated, with detailed unsteady aerodynamic, vibratory response, and performance data acquired in both the subsonic/transonic and supersonic stall flutter regimes. High-response flush mounted miniature pressure transducers were utilized to measure the unsteady aerodynamic loading distribution in the tip region of the fan for both incipient and deep flutter operating conditions, with simultaneously acquired strain gage data defining the vibratory response characteristics of the fan blisk. This unique data provides a benchmark test case to guide the validation of unsteady CFD analyses for stall-side flutter prediction.

Unsteady TURBO-AE simulations of the fan were performed at a series of operating points along the 70% and 85% corrected speedlines to assess the accuracy of the flutter predictions. Both stable and unstable operating conditions were analyzed for each speed, with TURBO-AE predicting the fan to be stable for all nodal diameter patterns at operating conditions away from the measured flutter boundary. At the tested incipient flutter operating conditions, TURBO-AE predicted the two nodal diameter forward traveling wave to be the least stable pattern and the fan to be on the verge of flutter, which was in good agreement with the test data for both flutter regimes.

The predicted unsteady surface pressure distributions were compared to the measured unsteady loading at 90% span for the incipient flutter operating points at each speed in order to assess the accuracy of the flutter predictions. Clearance was found to have a marked impact on both the magnitude and phase angle of the predicted unsteady surface pressure distributions in the tip region of the fan for both flutter regimes. This result was very surprising since the effect of clearance on the time-average loading was small. For the subsonic/transonic flutter regime at 70% corrected speed, the full clearance simulation was found to provide very good correlation with the data whereas for the supersonic flutter regime at 85% corrected speed it was the half-clearance simulation that provided the better correlation. This indicated that the unsteady aerodynamics in the tip region of the fan were influenced by clearance effects to a much larger extent than the time-average flow field. The results also demonstrated that accurate flutter predictions were obtained using the simple tip clearance model of APNASA as long as the tip gap was scaled for supersonic operating conditions.

The normalized unsteady first harmonic surface pressure data at 90% span for the incipient and deep flutter operating conditions were found to linearly scale with deflection amplitude for both flutter regimes, with this behavior confirmed by the unsteady CFD simulations. The onset of flutter, however, was predicted to occur at significantly different flow rates depending on the amplitude of the prescribed blade motion. This was due to nonlinear unsteady aerodynamic effects causing a very small change in the phase angle of the surface pressure distributions that increased the net aerodynamic damping at the incipient flutter point. This result should be expected since flutter occurs when the aerodynamic damping becomes zero for infinitesimal harmonic motion of the airfoil, with nonlinear effects causing the damping to increase with the amplitude of vibration such that a limit cycle oscillation develops. Although expected, these results indicate that erroneous flutter boundary predictions can occur if the nonlinear time-accurate analyses are not used properly. Namely, small-amplitude vibratory motion must be specified in the unsteady CFD simulations to properly model the incipient flutter point. When small amplitude blade vibrations were modeled, it was found that accurate flutter boundary predictions were obtained by extrapolating the aerodynamic damping versus flow curve out to zero damping.

The effect of the number of time steps-per-cycle on the flutter predictions was investigated to determine optimal parameter settings. Even though increasing the number of time steps-per-cycle was found to have a small effect on the unsteady pressure distributions at 90% span, the flutter onset predictions were significantly impacted. This behavior was due to small changes in the phase angle of the surface pressure distributions, with the accuracy of the predictions increasing as the number of time steps was increased. The optimum time step size was found to be 100 steps-per-cycle in the present investigation, with the higher number of time steps significantly increasing the computational time while only yielding a minimal improvement in the accuracy of the predictions. Similarly, decreasing the number of time steps-per cycle below 100 significantly reduced the computational time but severely compromised the accuracy of the simulations and led to erroneous flutter boundary predictions.

Finally, both the data and the unsteady CFD analyses indicated that the character of the suction surface unsteadiness was markedly different for the two flutter regimes. This was in sharp contrast to the behavior on the pressure surface, with both the magnitude and phase angle of the pressure surface unsteadiness very similar for both flutter regimes. Thus, different unsteady aerodynamic mechanisms drive stall-side flutter for the subsonic/transonic and supersonic flow regimes, with the unsteady CFD analysis capturing the relevant flow physics for both flow regimes.

Acknowledgments

The authors would like to thank AFRL and Honeywell Engines, Systems & Services for permission to publish this paper. The fan test was supported under PRDA Contract No. F33615-98-C-2922 and the data reduction and CFD validation work under internal Honeywell funding. This support is most gratefully acknowledged. The authors would also like to thank the test team at the CRF, including Dr. Ron Fost of Battelle Memorial Institute, for their individual contributions during the experimental investigation.

References

[1] Jeffers, II, J. D., and Meece, Jr., C. E., 1975, ''F100 Stall Flutter Problem Review and Solution,'' AIAA J. Aircr., **12**(4), pp. 350–359.

[2] El-Aini, Y. M., Bankhead, H. R. and Meece, C. E., 1986, ''Subsonic/Transonic Stall Flutter Investigation of an Advanced Low Pressure Compressor,'' ASME Paper No. 86-GT-90.

[3] El-Aini, Y. M., and Capece, V. M., 1995, ''Stall Flutter Prediction Techniques for Fan and Compressor Blades,'' AIAA Paper No. 95-2652.

[4] Adamczyk, J. J., Stevans, W., and Jutras, R., 1982, ''Supersonic Stall Flutter of High-Speed Fans,'' ASME J. Eng. Power, **104**(3), pp. 675–682.

[5] Shibata, T., and Kaji S., 1998, ''Role of Shock Structures in Transonic Fan Rotor Flutter,'' *Proceedings of the 8th International Symposium of Unsteady Aerodynamics and Aeroelasticity of Turbnomachines*, Kluwer, Dordrecht, The Netherlands, pp. 733–747.

[6] Isomura, K., and Giles, M. B., 1998, ''A Numerical Study of Flutter in a Transonic Fan,'' ASME J. Turbomach., **120**, pp. 500–507.

[7] Silkowski, P. D., Rhie, C. M., Copeland, G. S., Eley, J. A., and Bleeg, J. M., 2001, ''CFD Investigation of Aeromechanics,'' ASME Paper No. 2001-GT-0267.

[8] Srivastava, R., Bakhle, M. A., Keith Jr., T. G., and Stefko, G. L., 2002, ''Flutter Analysis of a Transonic Fan,'' ASME Paper No. GT-2002-30319.

[9] Carta, F. O., and St. Hilaire, A. O., 1978, ''Experimentally Determined Stability Parameters of a Subsonic Cascade Oscillating Near Stall,'' ASME J. Eng. Power, **100**, pp. 111–120.

[10] Carta, F. O., and St. Hilaire, A. O., 1980, ''Effect of Interblade Phase Angle and Incidence Angle on Cascade Pitching Stability,'' ASME J. Eng. Power, **102**, pp. 391–396.

[11] Carta, F. O., 1983, ''Unsteady Aerodynamics and Gapwise Periodicity of Os-

cillating Cascaded Airfoils,'' ASME J. Eng. Gas Turbines Power, **105**, pp. 565–574.

[12] Buffum, D. H., Capece, V. R., King, A. J., and El-Aini, Y. M., 1996, ''Experimental Investigation of Unsteady Flows at Large Incidence Angles in a Linear Oscillating Cascade,'' AIAA Paper No. 96-2823.

[13] Buffum, D. H., Capece, V. R., King, A. J., and El-Aini, Y. M., 1996, ''Oscillating Cascade Aerodynamics at Large Mean Incidence,'' ASME Paper No. 96-GT-339.

[14] Hardin, L. W., Carta, F. O., and Verdon, J. M., 1987, ''Unsteady Aerodynamic Measurements on a Rotating Blade Row at Low Mach Number,'' ASME Paper No. 87-GT-221.

[15] Frey, K. K., and Fleeter, S., 1996, ''Oscillating Airfoil Aerodynamics of a Rotating Compressor Blade Row,'' AIAA Paper No. 96-2673.

[16] Stargardter, H., 1979, ''Subsonic/Transonic Stall Flutter Study,'' NASA CR-165256.

[17] Halliwell, D. G., Newton, S. G., and Lit, K. S., 1984, ''A Study of Unsteady Pressures Near the Tip of a Transonic Fan in Unstalled Supersonic Flutter,'' ASME J. Vib., Acoust., Stress, Reliab. Des., **106**, pp. 198–203.

[18] Shabbir, A., and Zhu, J., 1996, ''Assessment of Three Turbulence Models in a Compressor Rotor,'' ASME Paper No. 96-GT-198.

[19] Bakhle, M. A., Srivastava, R., and Keith Jr., T. G., 1997, ''A 3D Euler/Navier-Stokes Aeroelastic Code for Propulsion Applications,'' AIAA Paper No. 97-2749.

[20] Bakhle, M. A., Srivastava, R., and Keith Jr., T. G., 1998, ''Aeroelastic Calculations Based on Three-Dimensional Euler Analysis,'' AIAA Paper No. 98-3295.

[21] Chen, J. P., and Whitfield, D. L., 1993, ''Navier-Stokes Calculations for the Unsteady Flowfield of Turbomachinery,'' AIAA Paper No. 93-0676.

[22] Srivastava, R., Bakhle, M. A., and Keith Jr., T. G., 1999, ''Phase-Lagged Boundary Condition Methods for Aeroelastic Analysis of Turbomachines—A Comparative Study,'' ASME Paper No. 99-GT-19.

[23] Adamczyk, J. J., Celestina, M. L., and Greitzer, E. M., 1993, ''The Role of Tip Clearance in High-Speed Fan Stall,'' ASME J. Turbomach., **115**, pp. 28–38.

[24] Chima, R. V., 1998, ''Calculation of Tip Clearance Effects in a Transonic Compressor Rotor,'' ASME J. Turbomach., **120**, pp. 131–140.

[25] Van Zante, D. E., Strazisar, A. J., Wood, J. R., Hathaway, M. D., and Okiishi, T. H., 1999, ''Recommendations for Achieving Accurate Numerical Simulation of Tip Clearance Flows in Transonic Compressor Rotors,'' ASME Paper No. 99-GT-390.

[26] Feiner, D. M., and Griffin, J. H., 2003, ''Mistuning Identification of Bladed Disks Using a Fundamental Mistuning Model—Part 1: Theory,'' ASME Paper No. GT2003-38952.

[27] Feiner, D. M., and Griffin, J. H., 2003, ''Mistuning Identification of Bladed Disks Using a Fundamental Mistuning Model—Part 2: Application,'' ASME Paper No. GT2003-38953.

A Method for Use of Cyclic Symmetry Properties in Analysis of Nonlinear Multiharmonic Vibrations of Bladed Disks

E. P. Petrov
Center for Vibration Engineering,
Mechanical Engineering Department,
Imperial College London,
South Kensington Campus,
London SW7 2AZ, UK

An effective method for analysis of periodic forced response of nonlinear cyclically symmetric structures has been developed. The method allows multiharmonic forced response to be calculated for a whole bladed disk using a periodic sector model without any loss of accuracy in calculations and modeling. A rigorous proof of the validity of the reduction of the whole nonlinear structure to a sector is provided. Types of bladed disk forcing for which the method may be applied are formulated. A multiharmonic formulation and a solution technique for equations of motion have been derived for two cases of description for a linear part of the bladed disk model: (i) using sector finite element matrices and (ii) using sector mode shapes and frequencies. Calculations validating the developed method and a numerical investigation of a realistic high-pressure turbine bladed disk with shrouds have demonstrated the high efficiency of the method. [DOI: 10.1115/1.1644558]

Introduction

It is well known that in analysis of linear vibration, use of cyclically symmetric properties of bladed disks allows the analysis of a whole bladed-disk assembly to be reduced to analysis of its one sector, which usually comprises a blade, a disk sector and, possibly, parts of shrouds adjoined to the blade. Methods for use of the cyclic symmetry properties of linear mechanical structures in analysis of natural frequencies and mode shapes, and in forced response analysis, have been developed more than 30 years. Many papers on the subject including papers [1–3], together provide a theoretical basis and methods for analysis of linear vibrations of cyclically symmetric structures. It has been shown that cyclic symmetry allows a sector model to be used instead of a whole bladed disk model, which decreases number of degrees-of-freedom in the resulting equations by a factor equal to the number of blades in a bladed disk, without any compromise with modeling accuracy. Coupling of vibrations of all sectors can be accounted for by special boundary conditions imposed on the interfaces where a sector considered interacts with neighboring ones. This method of taking into account cyclic symmetry, for linear systems, has become conventional and numerous applications in analysis of linear vibrations of bladed disks and other structures have been developed. An option allowing use of cyclic symmetry has become a standard in the majority of commercial finite element programs.

In contrast to the case of linear systems for nonlinear systems, up to date, there has been no a rigorously formulated and universal method available in the literature that would take advantages of cyclic symmetry for analysis of strongly nonlinear vibrations in a consistent way.

There are very few papers on numerical analysis of strongly nonlinear vibration of cyclically symmetric structures but calculation techniques and investigations provided in papers [4,5] for a models with cubic nonlinear springs should be noticed.

One of first calculations of cyclically symmetric bladed disks with gaps was proposed in [6], where single degree-of-freedom and beam models of blades are explored. Later papers on analysis of bladed disks with underplatform dampers by [7,8] and shrouded bladed disks [9], differ from the above-mentioned paper by modeling the bladed disk and friction forces, but use similar approaches to account for the cyclic symmetry, which are based on assuming that excitation and vibrations are monoharmonic and leaving aside the question about applicability of the method developed for linear structures with cyclic symmetry to a nonlinear structure. Multiharmonic vibrations of bladed disks are analyzed in [10,11] although the method for calculation of the cyclically symmetric bladed disks is not elaborated in either paper.

In this paper an effective method for analysis of steady-state nonlinear vibrations of cyclically symmetric bladed disks subjected to arbitrary distributed in space and periodic in time loads is proposed.

At the beginning the possibility for reduction of calculation of vibrations of a whole bladed disk to analysis of its sector model is rigorously proved and conditions of the method applicability are derived. Types of forcing that can occur in practice of bladed disk analysis and satisfy to the conditions are discussed. Then the nonlinear equations of multiharmonic motion are formulated for a sector model for two cases: (i) using finite element matrices and (ii) using frequency response function matrices. Further decrease of computational efforts by exclusion of linear degrees-of-freedom is introduced for the latter case. A technique for using complex arithmetic for the calculation of the multiharmonic nonlinear equations of motion together with the necessary transformation into domain of real numbers for their solution is developed. Calculations validating the developed method are performed and a numerical investigation of a realistic high-pressure turbine bladed disk with shrouds is carried out.

Basis of the Method

Bladed Disks of Cyclically Symmetric Design: Sector and Order of Cyclic Symmetry. Bladed disks are designed in majority of cases to be cyclically symmetric. Cyclically symmetric bladed disks are such bladed disks for which it is possible to find a rotationally periodic, ‘‘cyclic’’ part of the structure which can form the whole bladed disk by simple rotations of this part relatively to the axis of the symmetry. The rotation angles have to be multiples of $2\pi/N$ where integer number N is so-called ‘‘order of the cyclic symmetry,’’ which is equal to the number of cyclic parts in the whole structure. This cyclic part is sometimes called also

---

Contributed by the International Gas Turbine Institute and presented at the International Gas Turbine and Aeroengine Congress and Exhibition, Atlanta, GA, June 16–19, 2003. Manuscript received by the IGTI December 2002; final revision March 2003. Paper No. 2003-GT-38480. Review Chair: H. R. Simmons.

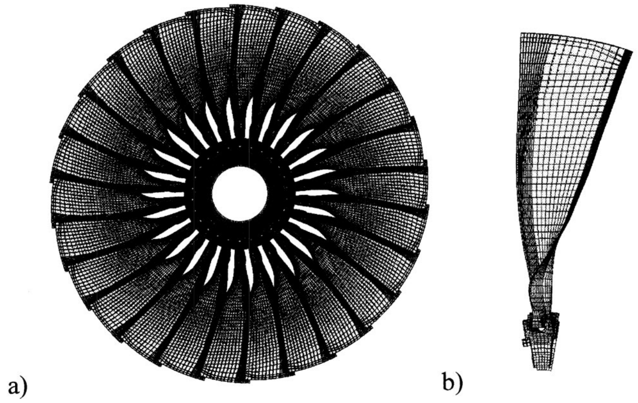

Fig. 1 A cyclically symmetric bladed disk; (*a*) a whole structure, (*b*) a sector

"sector" reflecting the fact that the cyclic part can be in many cases separated from the whole structure by two planes passing through the symmetry axis with angle $2\pi/N$ between them. The structure possesses all cyclic symmetry properties also for a general case when surfaces separating the cyclic part can have very complex and curved shapes. Because of that word "sector" is used in this paper in a general meaning assuming that there is no restrictions on shapes of the sector boundaries.

As evident all co-factors, N_j, of $N=N_1^* N_2^* N_3 \ldots$, if such exist, and all possible combinations of multiplication of these co-factors are also orders of cyclic symmetry. In order to take a maximum of advantages of using cyclic symmetry properties the largest possible order of cyclic symmetry is used in analysis. This choice of the cyclic symmetry order provides the smallest sector of the cyclically symmetric bladed disk and accordingly the smallest number of degrees-of-freedom in the sector model. Number of blades that has to be included into one sector depends on a design of a bladed disk. For bladed disks of gas turbine engines a sector can usually include only one blade (as shown in **Fig. 1**) and number of sectors, *N*, is equal to the number of blades, although there are cases when bladed disks have such design that the sector has to include two or more blades.

Major Relationships and Applicability Conditions. If a bladed disk is cyclically symmetric its equations of motion can be written in the following form:

$$\mathbf{K}\mathbf{q}_j+\mathbf{C}\dot{\mathbf{q}}_j+\mathbf{M}\ddot{\mathbf{q}}_j+\mathbf{f}_i(\mathbf{q}_j)+\mathbf{f}_l(\mathbf{q}_{j-1},\mathbf{q}_j)+\mathbf{f}_r(\mathbf{q}_j,\mathbf{q}_{j+1})=\mathbf{p}_j(t) \qquad (1)$$

where $j=\overline{1,N}$ is a sector number; **K**, **C**, and **M** are conventional linear stiffness, damping and mass matrices of one sector which are the same for all sectors of the cyclically symmetric system; $\mathbf{q}_j(t)$ is a vector of displacements of *j*-th sector; $\mathbf{p}_j(t)$ is a vector of excitation forces; $\mathbf{f}_i(\mathbf{q}_j)$ is a vector of nonlinear forces which are dependent only on displacements of the considered *j*th sector; $\mathbf{f}_l(\mathbf{q}_{j-1},\mathbf{q}_j)$ and $\mathbf{f}_r(\mathbf{q}_j,\mathbf{q}_{j+1})$ are forces of nonlinear interaction of *j*th sector and sectors adjacent to it from the left and from the right, they are dependent on displacements of the considered, *j*th sector and neighboring $(j-1)$th and $(j+1)$th sectors. Due to the cyclic symmetry the functional dependencies of vectors $\mathbf{f}_i(\mathbf{q}_j)$, $\mathbf{f}_l(\mathbf{q}_{j-1},\mathbf{q}_j)$ and $\mathbf{f}_r(\mathbf{q}_j,\mathbf{q}_{j+1})$ on the displacements are the same for all sectors, and, moreover, $\mathbf{f}_l(\mathbf{q}_j,\mathbf{q}_{j+1})=\mathbf{f}_r(\mathbf{q}_j,\mathbf{q}_{j+1})$, although different displacements can produce different force values.

Equation (1) represents a system of *N* matrix equations. In this system of equations subscript values 0 and $N+1$ appearing in $\mathbf{q}_{j\pm 1}$ for $j=1$ and $j=N$ are replaced by *N* and 1 accordingly since first sector interacts with *N*th sector. If arbitrary periodic excitation forces, $\mathbf{p}_j(t)$, applied to each *j*th sector are similarly distributed over sector nodes and different only in a fixed phase shift, δt, between adjacent sectors, then these excitation forces can be written in the form

$$\mathbf{p}_j(t)=\mathbf{p}(t+(j-1)\,\delta t) \qquad (2)$$

where $\delta t=\pm T/N$ and *T* is the period of the force variation, or $\delta t=0$ when the phase shift between the forces applied to different sector is 0.

For this kind of excitation and when linear and nonlinear properties of the bladed disk are cyclically symmetric it is possible to write explicit relationship between displacements of all sectors. This relationship has the form

$$\mathbf{q}_j(t)=\mathbf{q}(t+(j-1)\,\delta t) \qquad (3)$$

where **q** is the vector of displacements of first sector, which is also periodic with period *T*. The relationship given by Eq. (3) is the major relationship which allows all forces applied to a sector of the bladed disk including forces of interaction with adjacent sectors to be expressed in terms of its own displacements only. As a result the dynamic equation for a sector can be written in the form that describe vibrations of the whole bladed disk. Validity of this relationship can be proved by substitution of Eqs. (2) and (3) into Eq. (1). As a result of such substitution one obtains a system of *N* equations of identical form:

$$\begin{aligned}&\mathbf{K}\mathbf{q}(t_j)+\mathbf{C}\dot{\mathbf{q}}(t_j)+\mathbf{M}\ddot{\mathbf{q}}(t_j)+\mathbf{f}_i(\mathbf{q}(t_j))+\mathbf{f}_l(\mathbf{q}(t_j-\delta t),\mathbf{q}(t_j))\\&\quad+\mathbf{f}_r(\mathbf{q}(t_j),\mathbf{q}(t_j+\delta t))=\mathbf{p}(t_j) \qquad (4)\end{aligned}$$

where $t_j=t+(j-1)\,\delta t$ and *j* takes values from 1 to *N*. One can see that these equations differ for different sectors by the phase of the time variable only and the solution found, $\mathbf{q}(t)$, for one sector from Eq. (4) satisfies equations for all sectors.

Moreover, comparing in Eq. (4) $\mathbf{f}_l$ and $\mathbf{f}_r$ allows a relationship for forces of interaction between the considered sector and adjacent to it on left and right boundaries to be written in the following form:

$$\mathbf{f}_r(t)=\mathbf{f}_l(t+\delta t). \qquad (5)$$

This property together with Eq. (3) provides us a basis for calculation of forced response of the whole cyclically symmetric bladed disk using its sector model without introduction of any assumptions and loss of accuracy of the calculations even for the case of nonlinear vibrations with strong nonlinear forces of any kind.

Types of Forcing That can be Analyzed by the Method. The condition formulated for excitation forces by Eq. (2) together with the cyclic symmetry of the bladed disk are the only conditions that have to be satisfied to apply the method proposed. Types of the excitation forces that occur in analysis of vibration of bladed disks and satisfy to this condition are briefly discussed in this section.

Excitation of Traveling Wave Type. This type of excitation is one of the most customary in analysis of vibrations of bladed disks. It is typical for rotating bladed disks when they are excited by aerodynamic or other forces that travel relatively to the bladed disk due to the bladed disk rotation with constant speed while preserving their spatial distribution. In cylindrical coordinates, *r*, *z*, and φ, distribution and travelling of these forces can be expressed in the form: $p=p(r,z,\varphi\pm\omega t)$, where sign "$-$" corresponds to forward travelling wave and sign "$+$" correspond to backward travelling wave. All forces of this type satisfy to the condition given by Eq. (2). In our method no restrictions on distribution of the forces over a bladed disk are imposed and these forces can be distributed arbitrarily. Being expanded into Fourier series with respect to bladed disk circumferential coordinate, φ, they can comprise many harmonic components. The rotation speed, ω, determines the period of the excitation: $T=2\pi/\omega$ and phase shift is determined as $\delta t=\pm T/N$, where sign "$-$" correspond to the forces travelling forward and sign "+" corresponds to the forces travelling backward with respect to the bladed disk.

The conventional engine-order excitation is a particular kind of the travelling wave forcing considered here. For engine-order excitation the forces are distributed along the circumferential direction of the bladed disk as a sine or cosine function. A number of waves along the circumference is prescribed by the engine order.

Excitation That is Stationary in Space. This type of excitation is characteristic for analysis of bladed disk vibration when the bladed disk is immobile, as in static test rigs with shakers attached to the bladed disk, although it can also occur in rotating bladed disks under a special kind of excitation when the excitation forces are moving together with the rotating bladed disk. The stationary excitation forces can be expressed in the form $p = p_s(r,z,\varphi)p_t(t)$ where $p_s(r,z,\varphi)$ is a function of spatial distribution of the forces and $p_t(t)$ is a periodic function of the force variation in time. The conditions of the method applicability can be satisfied in the following cases.

1. A case when distribution of forces is the same for each of all sectors of the bladed disk, i.e., when the function of the spatial distribution, $p_s(r,z,\varphi)$, is periodic with the period equal to a sector angle, $T_\varphi = 2\pi/N$:

$$p_s(r,z,\varphi) = p_s(r,z,\varphi + T_\varphi). \tag{6}$$

For this case Eq. (2) is satisfied and phase shift between forces applied to different sectors is zero, i.e., $\delta t = 0$.

2. The method proposed can also be applied for a more complex case, when the function of the spatial distribution can differ for several sectors. However, to apply the method for this case a period for this spatial distribution has to exist. This period, T_φ, can stretch over a group that comprises several sectors, i.e., $T_\varphi = n_s 2\pi/N$ where n_s is the number of sectors in the group. In order to satisfy Eq. (2) the group of n_s sectors has to be considered as a new "super" sector. Number of such "super" sectors in the whole system is determined as $N^* = N/n_s$. This allows this case to be reduced to the case considered in the previous paragraph although with smaller magnitude of the order of the cyclic symmetry.

Multiharmonic Formulation of Equations of Motion Using a Sector Model

Multiharmonic Expansion of Displacements. In cases where the excitation forces are periodic, it is usually desirable to find steady-state, periodic regimes of response variation. For a search of the periodic vibration response the variation of all degrees-of-freedom (DOF) of the system in time can be represented as a restricted Fourier series, which can contain as many and such harmonic components as are necessary to approximate the sought solution, i.e.,

$$\mathbf{q}(t) = \mathbf{Q}_0 + \sum_{j=1}^{n} (\mathbf{Q}_j^{(c)} \cos m_j \omega t + \mathbf{Q}_j^{(s)} \sin m_j \omega t) \tag{7}$$

where $\mathbf{Q}_j^{(c)}$ and $\mathbf{Q}_j^{(s)}$ $(j = 1 \ldots n)$ are vectors of harmonic coefficients for system DOFs upon cosine and sine components marked by superscripts $^{(c)}$ and $^{(s)}$ accordingly; $\mathbf{Q}_0$ is a vector of constant components of the displacements; m_j $(j = 1 \ldots n)$ are specific numbers of harmonics that are kept in the displacement expansion in addition to the constant component. Equation (7) can be rewritten in more concise and convenient for our derivation form:

$$\mathbf{q}(\tau) = (\mathbf{H}^T \otimes \mathbf{I})\mathbf{Q} \tag{8}$$

where $\mathbf{H} = \{1, \cos m_1\tau, \sin m_1\tau, \ldots, \cos m_n\tau, \sin m_n\tau\}^T$ is a vector of harmonic functions used in the multiharmonic expansion; $\mathbf{Q} = \{\mathbf{Q}_0, \mathbf{Q}_1^{(c)}, \mathbf{Q}_1^{(s)}, \ldots, \mathbf{Q}_n^{(c)}, \mathbf{Q}_n^{(s)}\}^T$ is a total vector including all harmonic coefficients for the sector DOFs; $\tau = \omega t$ is dimensionless time, $\mathbf{I}$ is identity matrix of size equal to the number of DOFs in the sector; and $\otimes$ is a symbol of the Kronecker matrix product operator, [12]. This operator maps here vector $\mathbf{H}$ and matrix $\mathbf{I}$ into the following rectangular matrix:

$$\underset{(1+(2n+1))}{\mathbf{H}^T} \otimes \underset{(N_q \times N_q)}{\mathbf{I}} = \underset{(N_q \times (2n+1)N_q)}{[\mathbf{I}, \cos m_1 \tau \mathbf{I}, \sin m_1 \tau \mathbf{I}, \ldots, \cos m_n \tau \mathbf{I}, \sin m_n \tau \mathbf{I}]} \tag{9}$$

where N_q is size of vector $\mathbf{q}$.

Formulation Using a Finite Element Sector Model. In accordance with the multi-harmonic balance method, the expansion from Eq. (7) is substituted into the equation of motion (4), after this Eq. (4) is sequentially multiplied by $(\cos m_j \omega t)$ and $(\sin m_j \omega t)$ for all harmonics from the expansion and integrals over the vibration period, T, are calculated. As a result, the Eq. (4) of motion in time domain is transformed into a frequency domain equation in the following form:

$$\mathbf{Z}(\omega)\mathbf{Q} + \mathbf{F}(\mathbf{Q}) = \mathbf{P} \tag{10}$$

where $\mathbf{F}(\mathbf{Q}) = \{\mathbf{F}_0(\mathbf{Q}), \mathbf{F}_1^{(c)}(\mathbf{Q}), \mathbf{F}_1^{(s)}(\mathbf{Q}), \ldots, \mathbf{F}_n^{(s)}(\mathbf{Q})\}^T$ is a vector of harmonic components of nonlinear forces; $\mathbf{P} = \{\mathbf{P}_0, \mathbf{P}_1^{(c)}, \mathbf{P}_1^{(s)}, \ldots, \mathbf{P}_n^{(s)}\}^T$ is a vector of harmonic components of the excitation forces, and $\mathbf{Z}(\omega)$ is the dynamic stiffness matrix of the linear part of the system, constructed for all harmonic components, i.e.,

$$\mathbf{Z} = \mathrm{diag}[\mathbf{Z}_0, \mathbf{Z}_1, \ldots, \mathbf{Z}_n] \tag{11}$$

where

$$\mathbf{Z}_0 = \mathbf{K}; \quad \text{and} \quad \mathbf{Z}_j = \begin{bmatrix} \mathbf{K} - (m_j\omega)^2\mathbf{M} & m_j\omega\mathbf{C} \\ -m_j\omega\mathbf{C} & \mathbf{K} - (m_j\omega)^2\mathbf{M} \end{bmatrix}. \tag{12}$$

This equation is nonlinear with respect to the harmonic components of the displacements, $\mathbf{Q}$.

In order to take into account conditions imposed on the sector of cyclically symmetric bladed disk by Eqs. (3) and (5) one can partition the vector of sector displacements into three vectors: (i) a vector of displacements at nodes located at the left boundary of the sector, $\mathbf{q}_l$; (ii) a vector of internal displacements, $\mathbf{q}_i$, and (iii) a vector of displacements at nodes located at the right boundary of the sector, $\mathbf{q}_r$.

The major relationship, Eq. (3), imposes constraints on displacements of the nodes located at left, $\mathbf{q}_l$, and right, $\mathbf{q}_r$, boundaries of the sector where this sector interacts with adjacent ones.

$$\mathbf{q}_r(\tau) = \mathbf{q}_l(\tau + \alpha) \tag{13}$$

where $\alpha = \pm 2\pi/N$ and sign "+" or "−" is chosen here accordingly to the direction of the rotation of the excitation forces in Eq. (2).

These constraints can be formulated with respect to harmonic coefficients for displacements at the right, $\mathbf{Q}_r$, and left, $\mathbf{Q}_l$, boundaries with the help of Eq. (8) in the form

$$(\mathbf{H}^T(\tau) \otimes \mathbf{I})\mathbf{Q}_r = (\mathbf{H}^T(\tau + \alpha) \otimes \mathbf{I})\mathbf{Q}_l. \tag{14}$$

The vectors of the multiharmonic expansion, $\mathbf{H}(\tau)$, with a constant phase shift, α, are related as

$$\mathbf{H}(\tau + \alpha) = \mathbf{T}\mathbf{H}(\tau) \tag{15}$$

where matrix of the transformation, $\mathbf{T}$, takes the following form:

$$\mathbf{T} = \mathrm{diag}[t_0, \mathbf{t}_1, \ldots, \mathbf{t}_n] \tag{16}$$

where

$$t_0 = 1 \quad \text{and} \quad \mathbf{t}_j = \begin{bmatrix} \cos m_j\alpha & -\sin m_j\alpha \\ \sin m_j\alpha & \cos m_j\alpha \end{bmatrix} \quad \text{for } j = 1 \ldots n.$$

From Eq. (14) and Eq. (15) the following relationship between harmonic coefficients for the displacements at right and left boundaries can be derived:

$$\mathbf{Q}_r = (\mathbf{T} \otimes \mathbf{I})\mathbf{Q}_l \,. \tag{17}$$

Selecting from Eq. (17) expressions for each jth harmonic of the displacements one can write a relationship between coefficients of the multiharmonic expansion at left and right sector boundaries:

$$\begin{Bmatrix} \mathbf{Q}_r^{(c)} \\ \mathbf{Q}_r^{(s)} \end{Bmatrix}_j = \begin{bmatrix} \cos m_j\alpha\mathbf{I} & -\sin m_j\alpha\mathbf{I} \\ \sin m_j\alpha\mathbf{I} & \cos m_j\alpha\mathbf{I} \end{bmatrix} \begin{Bmatrix} \mathbf{Q}_l^{(c)} \\ \mathbf{Q}_l^{(s)} \end{Bmatrix}_j \tag{18}$$

and then harmonic coefficients of all sector displacements can be expressed through displacements at internal and left boundary nodes in the form

$$\begin{Bmatrix} \mathbf{Q}_l^{(c)} \\ \mathbf{Q}_i^{(c)} \\ \mathbf{Q}_r^{(c)} \\ \mathbf{Q}_l^{(s)} \\ \mathbf{Q}_i^{(s)} \\ \mathbf{Q}_r^{(s)} \end{Bmatrix}_j = \begin{bmatrix} \mathbf{I} & \mathbf{0} & \mathbf{0} & \mathbf{0} \\ \mathbf{0} & \mathbf{I} & \mathbf{0} & \mathbf{0} \\ \cos m_j\alpha\mathbf{I} & \mathbf{0} & -\sin m_j\alpha\mathbf{I} & \mathbf{0} \\ \mathbf{0} & \mathbf{0} & \mathbf{I} & \mathbf{0} \\ \mathbf{0} & \mathbf{0} & \mathbf{0} & \mathbf{I} \\ \sin m_j\alpha\mathbf{I} & \mathbf{0} & \cos m_j\alpha\mathbf{I} & \mathbf{0} \end{bmatrix} \begin{Bmatrix} \mathbf{Q}_l^{(c)} \\ \mathbf{Q}_i^{(c)} \\ \mathbf{Q}_l^{(s)} \\ \mathbf{Q}_i^{(s)} \end{Bmatrix}_j = \mathbf{G}_j \begin{Bmatrix} \mathbf{Q}_l^{(c)} \\ \mathbf{Q}_i^{(c)} \\ \mathbf{Q}_l^{(s)} \\ \mathbf{Q}_i^{(s)} \end{Bmatrix}_j . \tag{19}$$

Relationships for harmonic coefficients of the interaction forces are derived from Eq. (5) and their form is similar to Eqs. (17) and (19) but $\mathbf{F}$ should be written instead of $\mathbf{Q}$.

Cyclic symmetry properties are taken into account by substituting Eq. (19) into Eq. (10). This allows equation of motion of the sector to be obtained in terms of displacements of the one sector only whereas taking into account forces applied to the sector from adjacent parts of the bladed disk. Moreover, the number of unknowns in the equation is reduced by excluding displacements on right boundary of the sector and thus results in the following equation:

$$\mathbf{E}^{FE}(\mathbf{Q}) = \tilde{\mathbf{Z}}(\omega)\tilde{\mathbf{Q}} + \tilde{\mathbf{F}}(\tilde{\mathbf{Q}}) - \tilde{\mathbf{P}} = 0 \tag{20}$$

where $\tilde{\mathbf{Z}} = \mathbf{G}^T\mathbf{Z}\mathbf{G}$; $\tilde{\mathbf{F}}(\tilde{\mathbf{Q}}) = \mathbf{G}^T\mathbf{F}(\tilde{\mathbf{Q}})$; $\tilde{\mathbf{P}} = \mathbf{G}^T\mathbf{P}$; $\mathbf{G} = \operatorname{diag}[\mathbf{G}_0, \mathbf{G}_j, \ldots, \mathbf{G}_n]$ and $\mathbf{G}_j$ is a matrix used in Eq. (19) for expression of all sector DOFs through internal and left boundary DOFs for each harmonic.

Equation (20) represents a nonlinear set of equations with respect to $\tilde{\mathbf{Q}} = \{\mathbf{Q}_l, \mathbf{Q}_i\}^T$ which describes vibration of a whole bladed disk exactly using a finite element model for one sector only.

Formulation With Use of Complex Arithmetic. Special structure of matrix, $\mathbf{Z}$, allows the computational efforts necessary for evaluation of the vector of residuals, $\mathbf{E}(\mathbf{Q})$ to be reduced. This is achieved by formulation with a use of complex numbers, which allows all relationships to be simplified and, moreover, size of the matrices to be reduced by a factor of two. In order to make such formulation the complex vectors for each jth harmonics of displacements, $\mathbf{Q}_{jj}$, nonlinear forces, $\mathbf{F}_j$, and excitation forces, $\mathbf{P}_j$ are introduced in the following form:

$$\mathcal{Q}_j = \mathbf{Q}_j^{(c)} + i\mathbf{Q}_j^{(s)}; \quad \mathcal{P}_j = \mathbf{P}_j^{(c)} + i\mathbf{P}_j^{(s)}; \quad \mathcal{F}_j = \mathbf{F}_j^{(c)} + i\mathbf{F}_j^{(s)} \tag{21}$$

where $i = \sqrt{-1}$ and all complex quantities in order to differ them from their real counterparts are written here and further in the paper using a different font. A matrix of complex dynamic stiffness for each jth harmonics, $\mathbf{Z}_j$, is introduced as

$$\mathbf{Z}_j = [\mathbf{K} - (m_j\omega)^2\mathbf{M}] - i m_j\omega\mathbf{C}. \tag{22}$$

Equation (10) can now be rewritten, with taking into account the block diagonal structure of the matrix $\mathbf{Z}$, separately for each jth harmonics in the following form:

$$\mathcal{Z}_j\mathcal{Q}_j + \mathcal{F}_j(\mathbf{Q}) = \mathcal{P}_j; \quad (j = \overline{0,n}). \tag{23}$$

It should be noted that vector of jth harmonics of the nonlinear forces, $\mathcal{F}_j(\mathbf{Q})$, is dependent on all multiharmonic components of displacements, $\mathbf{Q}$, because of that all harmonics components of Eq. (23) are interdependent.

The expression given by Eq. (19) for all sector displacements through internal displacements and displacements of nodes located at left boundary is transformed into the following form:

$$\begin{Bmatrix} \mathcal{Q}_l \\ \mathcal{Q}_i \\ \mathcal{Q}_r \end{Bmatrix}_j = \begin{bmatrix} \mathbf{I} & \mathbf{0} \\ \mathbf{0} & \mathbf{I} \\ e^{im_j\alpha}\mathbf{I} & \mathbf{0} \end{bmatrix} \begin{Bmatrix} \mathcal{Q}_l \\ \mathcal{Q}_i \end{Bmatrix}_j = \mathcal{G}_j \begin{Bmatrix} \mathcal{Q}_l \\ \mathcal{Q}_i \end{Bmatrix}_j . \tag{24}$$

Matrix of this transformation, $\mathcal{G}_j$, allows Eq. (20) to be rewritten for each jth harmonic in the form:

$$\mathcal{E}_j^{FE}(\tilde{\mathbf{Q}}) = \tilde{\mathcal{Z}}_j\tilde{\mathcal{Q}}_j + \tilde{\mathcal{F}}_j(\tilde{\mathbf{Q}}) - \tilde{\mathcal{P}}_j = 0; \quad (j = \overline{0,n}) \tag{25}$$

where $\tilde{\mathcal{Z}}_j = \mathcal{G}_j^* \mathcal{Z}_j \mathcal{G}_j$; $\tilde{\mathcal{F}}(\tilde{\mathbf{Q}}) = \mathcal{G}^*\mathcal{F}(\tilde{\mathbf{Q}})$ and $\tilde{\mathcal{P}} = \mathcal{G}^*\mathcal{P}$ and an asterisk "*" denotes Hermitian conjugate. A relationship between vectors of residuals expressed in real numbers, $\mathbf{E}_j^{FE}$, and in complex numbers, $\mathbf{E}_j^{FE}$, takes the following form:

$$\mathbf{E}_j^{\mathrm{FE}} = \begin{Bmatrix} \operatorname{Re}(\mathcal{E}_j^{\mathrm{FE}}) \\ \operatorname{Im}(\mathcal{E}_j^{\mathrm{FE}}) \end{Bmatrix}. \tag{26}$$

Mutiharmonic Formulation Using Sector Frequency Response Function Matrices. For many practical cases a formulation based on a use of dynamic compliance or frequency response function (FRF) matrices can be significantly more efficient than the formulation which uses finite element (FE) matrices directly. These cases are, for example, when number of DOFs where nonlinear interaction occurs is much smaller that total number of DOFs in a sector model or when information about dynamic properties of a bladed disk with nonlinear interactions is provided by mode shapes and natural frequencies calculated by conventional FE software.

The multiharmonic formulation using sector FRF matrices can be made with a use of complex arithmetic. The dynamic stiffness matrices of the sector, $\tilde{\mathcal{Z}}_j(m_j\omega)$, used in Eq. (25) for each of the multiharmonic components describe linear forces. These matrices are independent on vibration amplitudes and Eq. (25) can be multiplied by $\tilde{\mathcal{A}}_j = \tilde{\mathcal{Z}}_j^{-1}(m_j\omega)$ order to obtain equations in the following form:

$$\mathcal{E}_j^{FRF}(\tilde{\mathbf{Q}}) = \tilde{\mathcal{Q}}_j + \tilde{\mathcal{A}}_j(\tilde{\mathcal{F}}_j(\tilde{\mathbf{Q}}) - \tilde{\mathcal{P}}_j) = 0; \quad (j = \overline{0,n}) \tag{27}$$

where $\tilde{\mathcal{A}}_j =$ is a sector FRF matrix determined for j-th harmonic of the multiharmonic expansion. This is a sector matrix that is customary used in analysis of linear vibration of bladed disks. It can be obtained by direction inversion of dynamic stiffness matrix of the sector, $\tilde{\mathcal{Z}}_j(m_j\omega)$. However for structures with large number of DOFs such calculation of the FRF matrix require large computational expenses, because of that special techniques are applied that are discussed in the following sections.

Exclusion of Linear Degrees-of-Freedom From the Nonlinear Equations. Usually in models of practical bladed disks a number of DOFs where nonlinear interaction forces are applied is much smaller than the total number of degrees-of-freedom in a sector. A use of the FRF matrices allows all DOFs where only linear forces are applied to be excluded easily and without any loss of accuracy and completeness of the model. As a result the resulting equation is formulated only with respect to DOFs where nonlinear forces are applied and size of this equation and accordingly computational expense are reduced usually in many times or orders.

In order to exclude linear DOFs Eq. (27) can be rewritten in the form where vector $\tilde{\mathcal{Q}}_j$ is partitioned into a vector of nonlinear DOFs, $\tilde{\mathcal{Q}}_j^{\mathrm{nln}}$, and a vector of linear DOFs, $\tilde{\mathcal{Q}}_j^{\mathrm{lin}}$:

$$\mathcal{E}_j^{\mathrm{FRF}}(\tilde{\mathbf{Q}})=\left\{\begin{matrix}\tilde{\mathcal{Q}}_j^{\mathrm{lin}}\\ \tilde{\mathcal{Q}}_j^{\mathrm{nln}}\end{matrix}\right\}+\left\{\begin{matrix}\mathbf{0}\\ \tilde{\mathcal{A}}_j^{\mathrm{nln}}\tilde{\mathcal{F}}_j(\tilde{\mathbf{Q}}^{\mathrm{nln}})\end{matrix}\right\}-\tilde{\mathcal{A}}_j\tilde{\mathcal{P}}_j=\mathbf{0} \qquad (28)$$

where $\tilde{\mathcal{A}}_j^{\mathrm{nln}}$ is a minor of matrix $\tilde{\mathcal{A}}_j$ corresponding to nonlinear DOFs. Selecting from Eq. (28) equations corresponding to nonlinear DOFs we obtain the sought for equation of significantly reduced size:

$$\mathcal{E}_j^{\mathrm{FRF}}(\tilde{\mathbf{Q}}^{\mathrm{nln}})=\tilde{\mathcal{Q}}_j^{\mathrm{nln}}+\tilde{\mathcal{A}}_j^{\mathrm{nln}}\tilde{\mathcal{F}}_j(\tilde{\mathbf{Q}}^{\mathrm{nln}})-\tilde{\mathcal{Q}}_{Pj}^{\mathrm{nln}}=\mathbf{0} \qquad (29)$$

where $\tilde{\mathbf{Q}}^{\mathrm{nln}}=\{\tilde{\mathbf{Q}}_0^{\mathrm{nln}},\tilde{\mathbf{Q}}_1^{\mathrm{nln}},\ldots,\tilde{\mathbf{Q}}_n^{\mathrm{nln}}\}$ is a vector comprising all nonlinear harmonic coefficients. $\tilde{\mathcal{Q}}_{Pj}^{\mathrm{nln}}=(\tilde{\mathcal{A}}_j\tilde{\mathcal{P}}_j)^{\mathrm{nln}}$ is a vector of complex amplitudes determined for nonlinear DOFs of the bladed disk excited by *j*-th harmonic of the excitation forces. These amplitudes are determined for a completely linear system when the nonlinear forces appearing at contact interfaces of the bladed disk are not taken into account. The vector of excitation forces, $\tilde{\mathcal{P}}_j$, can include forces applied to all DOFs of the structure, as linear and as nonlinear. FRF matrix including all DOFs, $\tilde{\mathcal{A}}_j$, is used to evaluate vector $\tilde{\mathcal{A}}_j\tilde{\mathcal{P}}_j$ and then components corresponding to nonlinear DOFs are selected from the resulting vector to form $\tilde{\mathcal{Q}}_{Pj}^{\mathrm{nln}}$.

Calculation of Sector Frequency Response Function Matrices. The sector FRF matrix can be efficiently generated from natural frequencies, ω_{rm_j}, and mode shapes, $\boldsymbol{\phi}_{rm_j}$, calculated for the sector for a harmonic number needed, m_j, in order to avoid very numerically inefficient operation of the matrix inverse

$$\tilde{\mathcal{A}}_j=\tilde{\mathcal{Z}}_j^{-1}(m_j\omega)\simeq\sum_{r=1}^{N_m}\frac{\boldsymbol{\phi}_{rm_j}\boldsymbol{\phi}^*_{rm_j}}{(1-i\,\eta_{rm_j})\omega^2_{rm_j}-(m_j\omega)^2} \qquad (30)$$

where subscript "r" is a number of the mode shape in a family of modes with m_j circumferential waves of displacements; η_{rm_j} is damping loss factor determined for *r*th mode of the family with m_j waves, and N_m is the number of modes that are used in the modal expansion. In many cases small numbers of modes, N_m, kept in the expansion provides sufficient accuracy in the FRF matrix calculation (analysis of the accuracy obtained for FRF matrices of bladed disks models is performed in [13]).

It should be noted that Eq. (30) is exact when all sector modes of the family of modes with m_j waves are included in the expansion and when the damping matrix, $\tilde{\mathbf{C}}$, represents 'proportional' damping (i.e., it can be expressed as a linear combination of the stiffness matrix and mass matrix).

The following form of presentation for the damping matrix describes as structural, frequency-independent damping and as viscous damping:

$$\tilde{\mathbf{C}}_j=\mu_1\frac{1}{m_j\omega}\tilde{\mathbf{K}}+\mu_2\tilde{\mathbf{K}}+\mu_3\tilde{\mathbf{M}} \qquad (31)$$

where first summand describes structural, hysteresis damping and two other summands correspond to damping of viscous type; here μ_k $(k=1,2,3)$ are coefficients that can be determined theoretically or experimentally. The modal damping loss factors can be then expressed through these coefficients in the form:

$$\eta_{rm_j}=\mu_1+m_j\omega(\mu_2+\mu_3/\omega^2_{rm_j}). \qquad (32)$$

Assuming here $\mu_2=\mu_3=0$ one can describe pure hysteresis damping, and when $\mu_1=0$ the damping is pure viscous. In many cases the modal damping loss factors, η_{rm_j}, are determined directly from experiments for each modes included into Eq. (30). The expansion given by Eq. (30) can be accurate enough in many practical cases even when damping is not "proportional" but level of linear damping described by matrix **C** and interaction between different modes caused by this damping are small.

The vector of complex amplitudes, $\tilde{\mathcal{Q}}_{Pj}^{\mathrm{nln}}$, introduced in Eq. (29) can be very efficiently calculated as

$$\tilde{\mathcal{Q}}_{Pj}^{\mathrm{nln}}=\sum_{r=1}^{N_m}\frac{\boldsymbol{\phi}^*_{rm_j}\tilde{\mathcal{P}}_j}{(1-i\,\eta_{rm_j})\omega^2_{rm_j}-(m_j\omega)^2}\,\boldsymbol{\phi}^{\mathrm{nln}}_{rm_j}. \qquad (33)$$

Multiplication of large vectors, $\boldsymbol{\phi}^*_{rm_j}\tilde{\mathcal{P}}_j$, involving all sector DOFs provides a single coefficient for each mode shape, which is usually called "a modal force." These modal forces take into account arbitrary distribution of the excitation forces over all nodes of the sector model. For a case when distribution of the excitation forces over a sector is preserved for all rotation frequencies additional decrease of computational efforts can be achieved since for this case calculation of the modal forces involving many degrees-of-freedom is carried out only one time. At the same time for this case values of the forces can be varied with variation of the rotation frequency when a coefficient of variation is common for forces applied to all DOFs. As a result calculations of $\tilde{\mathcal{Q}}_{Pj}^{\mathrm{nln}}$ for each current value of the rotation speed, ω, is performed by summation of mode shapes, $\boldsymbol{\phi}^{\mathrm{nln}}_{rm_j}$, containing only nonlinear DOFs, which usually represent a very small fraction of all DOFs in a sector model. In this summation each such mode, $\boldsymbol{\phi}^{\mathrm{nln}}_{rm_j}$, is multiplied by a simple coefficient which is product of the modal force and an explicitly given function of the rotation frequency.

Solution of Nonlinear Equations

Nonlinear Equations Formulated in Real Numbers. One of the most efficient methods for solution of the nonlinear equations is the Newton-Raphson method which possesses quadratic convergence when an approximation is close enough to the solution. An iterative solution process is expressed by the following formula:

$$\tilde{\mathbf{Q}}^{(k+1)}=\tilde{\mathbf{Q}}^{(k)}-\left[\frac{\partial\mathbf{E}(\tilde{\mathbf{Q}}^{(k)})}{\partial\tilde{\mathbf{Q}}}\right]^{-1}\mathbf{E}(\tilde{\mathbf{Q}}^{(k)}) \qquad (34)$$

where superscript $^{(\mathrm{k})}$ indicates the number of the current iteration. Vector of residuals, $\mathbf{E}(\tilde{\mathbf{Q}}^{(k)})$ can be taken for this equation as from FE and as from FRF formulation.

For a case of FE model performing differentiation of Eq. (20) with respect to $\tilde{\mathbf{Q}}$, one can obtain the following expression for derivatives of the residuals:

$$\frac{\partial\mathbf{E}(\tilde{\mathbf{Q}}^{(k)})}{\partial\tilde{\mathbf{Q}}}=\tilde{\mathbf{Z}}(\omega)+\frac{\partial\tilde{\mathbf{F}}(\tilde{\mathbf{Q}}^{(k)})}{\partial\tilde{\mathbf{Q}}}=\tilde{\mathbf{Z}}(\omega)+\tilde{\mathbf{K}}^{\mathrm{nln}}(\tilde{\mathbf{Q}}) \qquad (35)$$

where $\tilde{\mathbf{K}}^{\mathrm{nln}}(\tilde{\mathbf{Q}})$ represents a so-called "tangent" stiffness matrix, i.e., a stiffness matrix describing stiffness properties of the nonlinear contact interfaces in vicinity of current values of the displacements, $\tilde{\mathbf{Q}}$. An efficient method for analytical derivation which provides explicit, extremely fast and exact expressions of the stiffness matrices and the nonlinear forces at contact interfaces with friction forces, gaps and interferences can be found in papers, [14,15].

The case of a use of FRF sector matrices can be efficiently analyzed using complex arithmetic and is considered below.

Nonlinear Equations Formulated in Complex Numbers Although nonlinear equation of motion can be formulated and conveniently evaluated using complex arithmetic but at the stage of their iterative solution by Newton-Raphson method they have to be transformed back into domain of real numbers. This is very important and necessary requirement since residuals, $\mathcal{E}_j$, are not analytic functions of complex vectors, $\tilde{\mathcal{Q}}_j$, and as result of this their derivatives, $\partial\mathcal{E}_i/\partial\tilde{\mathcal{Q}}_j$ cannot be defined.

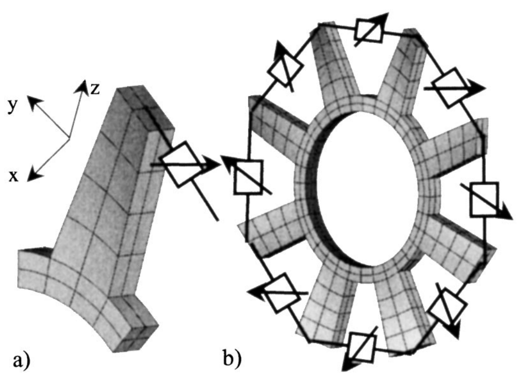

Fig. 2 Models of the bladed disk compared: (*a*) a sector model, (*b*) the whole structure

After calculation of complex residuals for a sector, $\mathbf{E}_j$, which can be made very efficiently using FRF formulation, vector of real residuals is calculated from their complex counterparts as

$$\mathbf{E}=\{\mathcal{E}_0,\mathrm{Re}(\mathcal{E}_1),\mathrm{Im}(\mathcal{E}_1),\ \ldots,\mathrm{Im}(\mathcal{E}_n)\}^T. \tag{36}$$

The matrix of derivatives of the residuals involved into Eq. (34) is calculated for the case when complex FRF sector matrices are used by the following way:

$$\frac{\partial \mathbf{E}^{\mathrm{FRF}}}{\partial \tilde{\mathbf{Q}}}=I+\begin{bmatrix} \mathbf{D}_{00} & \mathrm{Re}(\mathbf{D}_{01}) & \mathrm{Im}(\mathbf{D}_{02}) & \cdots & \mathrm{Im}(\mathbf{D}_{0,2n}) \\ \mathrm{Re}(\mathbf{D}_{10}) & \mathrm{Re}(\mathbf{D}_{11}) & \mathrm{Re}(\mathbf{D}_{12}) & \cdots & \mathrm{Re}(\mathbf{D}_{1,2n}) \\ \mathrm{Im}(\mathbf{D}_{10}) & \mathrm{Im}(\mathbf{D}_{11}) & \mathrm{Im}(\mathbf{D}_{12}) & \cdots & \mathrm{Im}(\mathbf{D}_{1,2n}) \\ \cdots & \cdots & \cdots & \cdots & \cdots \\ \mathrm{Im}(\mathbf{D}_{n0}) & \mathrm{Im}(\mathbf{D}_{n1}) & \mathrm{Im}(\mathbf{D}_{12}) & \cdots & \mathrm{Im}(\mathbf{D}_{n,2n}) \end{bmatrix} \tag{37}$$

where

$$\mathbf{D}_{00}=\mathcal{A}_i^{\mathrm{nln}}\frac{\partial \tilde{\mathcal{F}}_i}{\partial \mathbf{Q}_0};\quad \mathbf{D}_{i,2i}=\mathcal{A}_i^{\mathrm{nln}}\frac{\partial \tilde{\mathcal{F}}_i}{\partial \mathbf{Q}_i^{(c)}};\quad \mathbf{D}_{i,2i+1}=\mathcal{A}_i^{\mathrm{nln}}\frac{\partial \tilde{\mathcal{F}}_i}{\partial \mathbf{Q}_j^{(s)}}$$

for $i=\overline{0,n}$. As seen in first row of matrix, $\partial \mathbf{E}^{FRF}/\partial \tilde{\mathbf{Q}}$, real and imaginary parts of $\mathbf{D}_{0j}$ are alternating and all the other rows contain only real or imaginary parts of $\mathbf{D}_{ij}$ $(j=\overline{0,2n})$ and these rows are also alternating.

Numerical Results

Comparison of Results Obtained With the Proposed Method and With a Whole Bladed Disk Model. In order to validate the method forced response of cyclically symmetric systems obtained with proposed method was compared with results obtained using whole models of structures when cyclic symmetry properties were disregarded.

As an example of a bladed disk that was calculated using a sector model and a whole bladed disk model, is shown in Fig. 2. The whole bladed disk consists of eight sectors and is modeled by hexahedral finite elements with a total number of degrees-of-freedom in the model equal to 5760; the sector model comprises 720 DOFs. Excitation by first engine order harmonic is considered and the damping loss factor was accepted to be 0.003. Nonlinear interface elements are applied between adjacent blades at a middle node of blade tip faces and as illustrated in Fig. 2 by boxes with arrows.

The nonlinear interface elements produce forces that are dependent on relative displacements of the adjacent blades. Three different types of the nonlinear interface elements were examined: (i) a friction damper (with the friction coefficient 0.3; the normal force $2*10^5$ N and stiffness coefficient $4*10^4$ N/mm); (ii) a spring with cubic dependence, $f(x)=cx^3$, of the nonlinear interaction force, $f(x)$, on relative displacement, x, (stiffness coefficient, c, of the spring is taken to be 10^3 N/mm); (iii) a gap element, which does not produce any force unless the prescribed gap is closed and when the gap is closed then interaction force is proportional to the relative displacement (a gap value is taken to be 0.5 mm and stiffness coefficient when the gap is closed is equal to 10^5 N/mm). Explicit expressions for tangent stiffness matrix and for multiharmonic components of the interaction forces produced by these elements are used in for calculations in the form as they are analytically derived in papers [14,15]. For all these interface elements forced response of the bladed disk exhibits strongly nonlinear behavior. First five harmonics (from 0 to 4) are kept in multiharmonic expansion of the forced response and maximum displacements for all three coordinates, *x*, *y*, and *z*, of displacements at the nodes where the nonlinear interface elements were calculated. Results obtained by using the sector model and by using the whole bladed disk are identical. This is demonstrated in Fig. 3, where lines plot results obtained with the whole bladed disk model and results obtained with the proposed method are shown by circles, squares and triangles for *x*, *y*, and *z* coordinates accordingly.

Realistic High-Pressure Turbine Bladed Disk. As an example of a practical application a turbine high-pressure bladed disk shown in Fig. 4 is considered. The bladed disk comprises 92 shrouded blades. The damping loss factor is set to 0.003 and excitation by 4, 6, 8, and 16 engine orders is considered in the analysis. Natural frequencies of the high-pressure turbine disk normalized with respect to the first blade-alone frequency are shown in Fig. 5 for all possible nodal diameter numbers from 0 to 46. These frequencies are calculated for the case where there is no contact between shrouds.

Nonlinear forces can occur under certain circumstances during vibration as a result of contact interaction between blade shrouds. These nonlinear forces and nonlinear stiffness matrices of the contact interface were calculated using friction contact interface elements developed in [14]. The contact interface elements allow to take into account unilateral nature of the force normal to the contact surface, friction forces with accounting for the normal load variation and they also allow consistent determination of all stick-slip and contact-separation transitions that occur under the vibrations.

Eleven of the friction interface elements are distributed over nodes of left boundary and eleven interface elements on the right boundary of the sector shroud contacts (locations of the elements on the right sector boundary are shown by circles marked by letter ''A'' in Fig. 4(*c*).

Full finite element model of the bladed disk comprises about 15 millions DOFs and the finite single-sector model contains 162,708 degrees-of-freedom (DOFs). Number of DOFs in nonlinear equations is reduced to 66 by applying the developed method for exclusion of linear DOFs from resulting equation while preserving accuracy and all dynamic properties of the initial model since during this reduction there is no any loss of information about influence of the excluded DOFs. In all calculations performed the maximum displacement is determined as $\max_{\tau\in[0,2\pi]}\sqrt{x^2(\tau)+y^2(\tau)+z^2(\tau)}$. Ratio between amplitudes of all nodes of the bladed disk is varied with excitation frequency and is dependent on the shroud contact conditions but for the bladed disk analyzed the displacements have higher levels at the blade tip in the frequency ranges considered. Because of that the maximum displacement is plotted in all figures for a representative node located at the blade tip. The node is shown by a circle marked by letter ''B'' in Fig. 4(*c*).

In Fig. 6 the maximum displacement is shown as a function of excitation frequency for different values of clearances (Fig. 6*a*) and interferences (Fig. 6*b*) between shrouds of adjacent sectors. Excitation of engine order type by 4EO is applied to the bladed disk and 4th harmonic component is used in the displacement expansion. For comparison forced responses of linear systems are

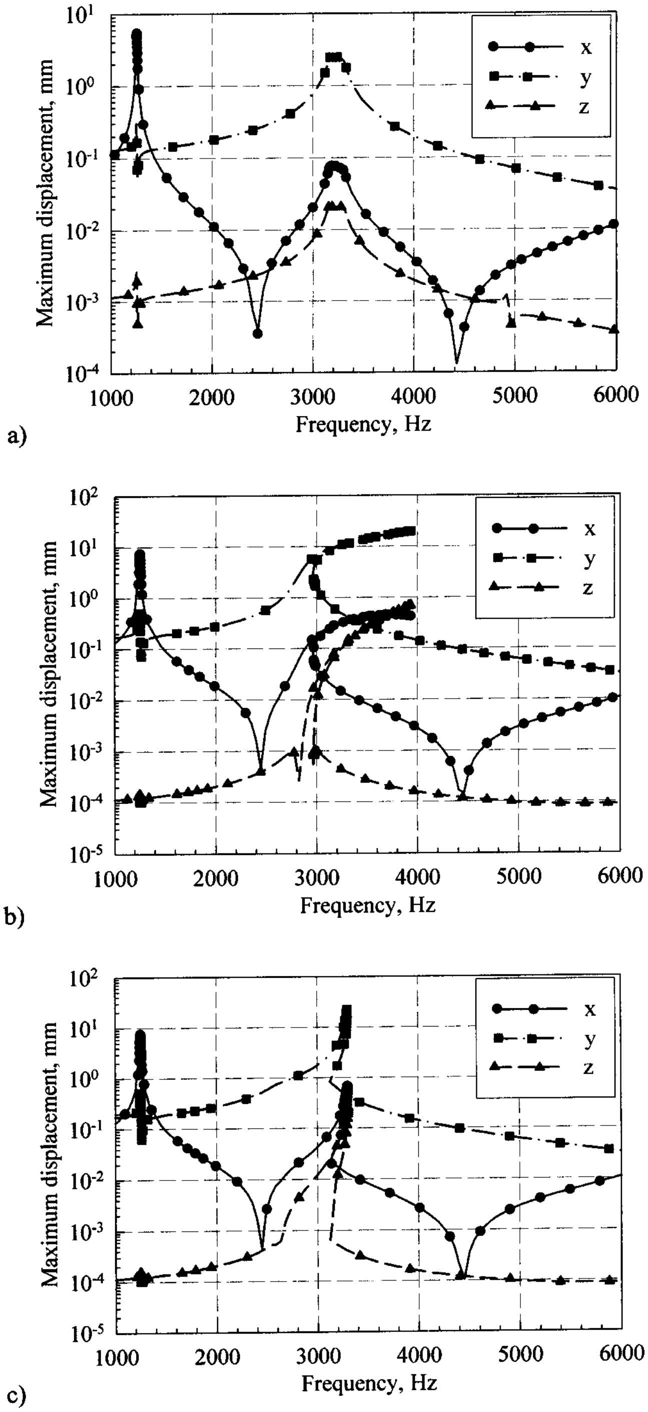

Fig. 3 Comparison of results obtained with the proposed method and with using the whole bladed disk model: (*a*) a case of friction dampers, (*b*) nonlinear spring elements with nonlinear cubic dependence of forces on displacements, (*c*) gap elements

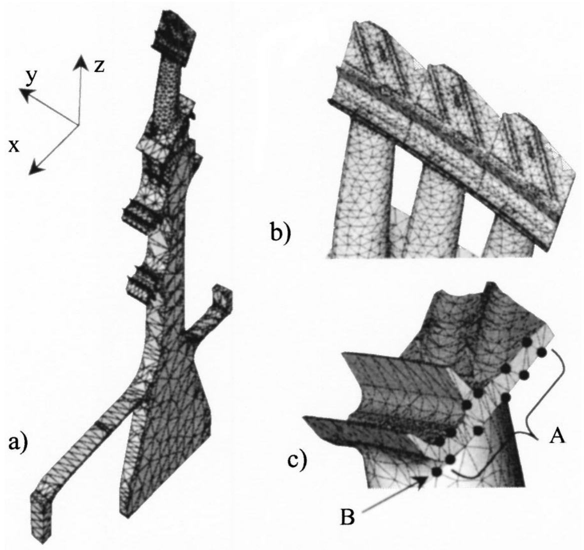

Fig. 4 Finite element model: (*a*) a sector of the bladed disk, (*b*) shroud of the sector model with shrouds adjacent to it, (*c*) interface nodes where friction and impact forces are considered

plotted also by thin lines: (i) in Fig. 6(*a*) forced response of the bladed disk without shroud contacts is plotted and (ii) in Fig. 6(*b*) forced response of the bladed disk when all nodes are always in full contact without slip is plotted. As seen for the bladed disk with clearances 10^{-2} mm and 10^{-3} mm the system starts exhibiting strongly nonlinear behavior in vicinities of resonance peaks where vibration displacement are large enough to close the clearance between shrouds. The nonlinear forced response has stiffening characteristics when with increase of amplitude resonance frequency is increasing. Far from resonances the amplitudes are so small that shrouds cannot contact during vibrations and the system has forced responses identical to the linear system. For clearance 10^{-4} mm the shrouds come to contact over the whole excitation frequency range. This causes significant reduction of the response level over the analyzed frequency range and even disappearance of one of three resonance peaks that the linear system without shroud contacts has. Moreover, the forced response characteristics takes a more complicated shape, as on can see for frequency range after first resonance and in vicinity of second resonance. For the latter zoomed view is shown to see the curve in more detail. For the bladed disk with interferences shown in Fig. 6(*b*) one can see that force response exhibits softening characteristics when increase of amplitudes is accompanied by decrease of resonance frequencies.

This happens because increase of amplitude of displacements causes more nodes at the shroud contact surfaces to go out of contact and to slip. For interference values 10^{-4}, 10^{-5}, and 10^{-6} mm nonlinear effects become evident in the vicinity of resonance and for their values $5*10^{-7}$, 10^{-7}, and 0 forced response is different from the linear system compared over the whole frequency range. For these small interference values the amplitudes are much higher that those of the linear system in frequencies ranges far from the resonance whereas they are many times lower

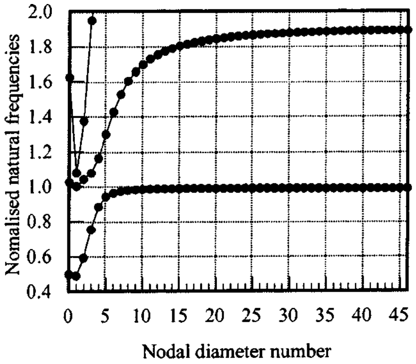

Fig. 5 Natural frequencies of a tuned bladed high-pressure turbine disk and the analyzed frequency range

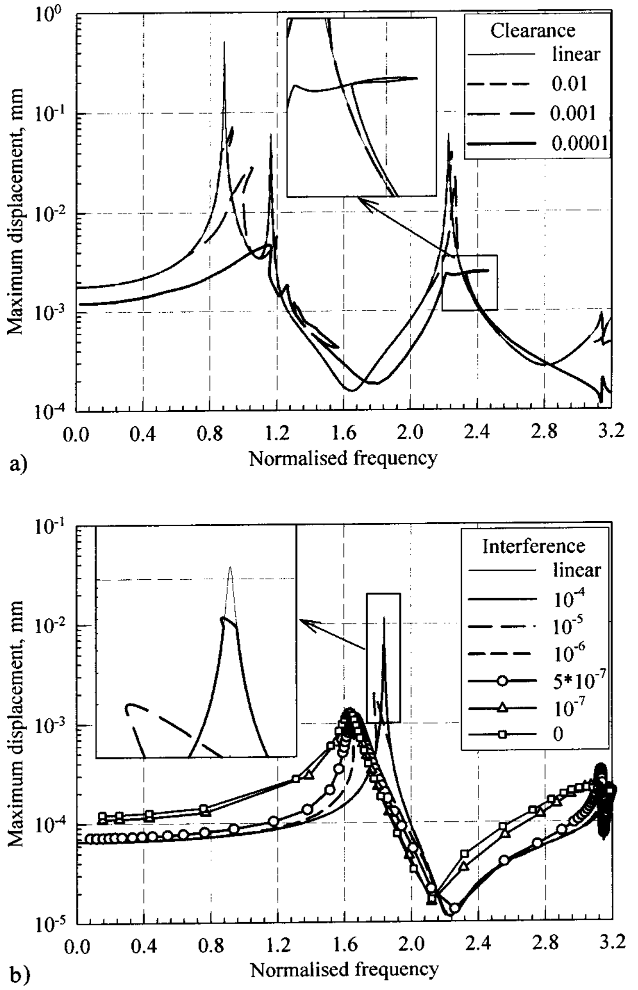

Fig. 6 Forced response of the bladed disk for excitation by 4EO: (*a*) a case of different clearance values, (*b*) a case of different interference values

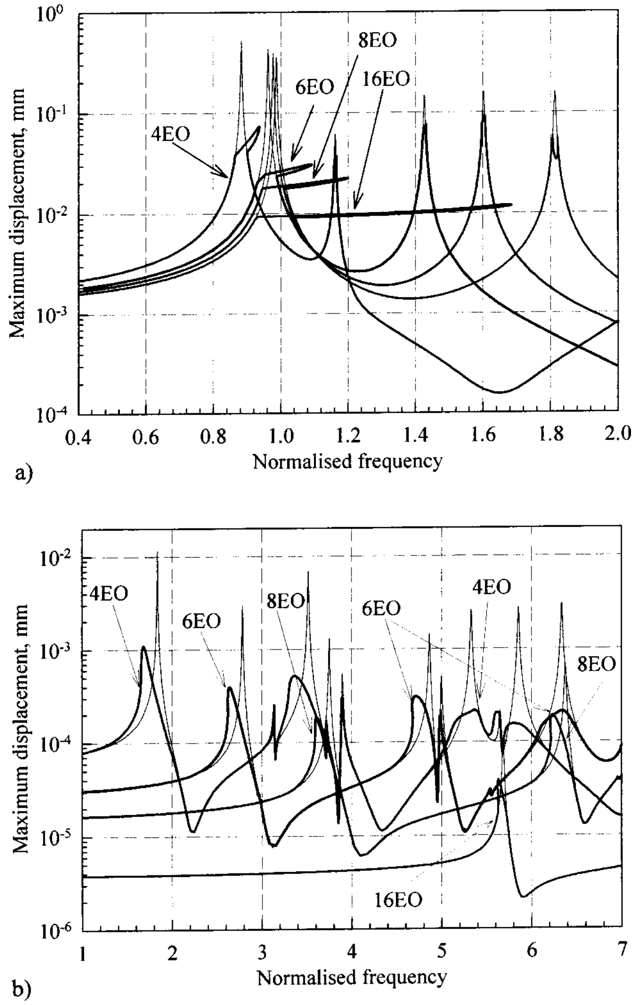

Fig. 7 Forced response of the bladed disk for excitation of different engine orders: (*a*) a case with gap between shrouds of 0.01 mm, (*b*) a case with interferences of 10^{-6} mm

than those of the linear system at the resonance. This observation is explained by different effects of the shroud nonlinear interaction for excitation frequencies far and close to the resonance. For out-of-resonance regimes the friction damping produced at shroud contact surfaces does not affect significantly level of amplitudes and major effect on the amplitudes is due to decrease of shroud contact stiffness when some or all of the contact nodes lose temporarily contact. For the resonance regime the friction damping is a major cause of the reduction of the amplitude level while change of the stiffness is also reflected in the decrease of the resonance frequency value.

Effects of the clearances and interferences on nonlinear forced response excited by different engine orders is demonstrated in Fig. 7 where cases of the clearance value 10^{-2} mm (Fig. 7(*a*)) and the interference value 10^{-6} mm (Fig. 7(*b*)) are analyzed. Forced responses of the corresponding linear systems are also plotted for comparison by thin lines. For the case of the system with the clearances one can see that the higher engine order number, the lower amplitude level when shroud contact occurs.

This is explained by the fact that to close the gap between adjacent shrouds their relative displacements have to be large enough. Amplitudes are the same for adjacent blades of the cyclically symmetric bladed disk but a phase shift between the dominant harmonics of the displacements is proportional to the excitation engine order number. For larger engine order numbers due to larger phase shift the relative displacements can be larger even when the absolute blade amplitudes are smaller. For both cases of the considered clearances and the interferences the friction damping is significant although for the case with the interferences its effect much more evident.

Conclusions

An effective method for analysis of periodic forced response of nonlinear cyclically symmetric structures has been developed.

A rigorous proof of the validity of the reduction of the whole nonlinear structure to a sector is provided for a general case of nonlinear forces of arbitrary character and nature. Types of bladed disk forcing permitting application of the method are discussed.

The method allows multiharmonic nonlinear forced response for a whole bladed disk to be calculated using a sector model without any loss of accuracy in calculations and modeling. A multiharmonic formulation for equations of motion has been derived for two widely used techniques of description of the linear part of a bladed disk model with the large number of degrees-of-freedom: (i) using sector finite element matrices; (ii) using sector natural mode shapes and frequencies. An approach for a use of complex arithmetic in the multiharmonic formulation and in the solution of the nonlinear equations of motion has been examined. A technique for reduction of size of the nonlinear multiharmonic equations by exclusion of linear DOFs from the resulting equations has been developed.

The numerical investigations show high efficiency of the proposed method. The identity of the results obtained with the developed method using a sector model and with a whole bladed disk model has been demonstrated for different types of nonlinear forces produced by nonlinear interfaces: (i) friction dampers; (ii) gaps; (iii) cubic nonlinear springs. A practical, large finite element model of a shrouded turbine bladed disk has been analyzed with accounting for friction forces, clearances, and interferences at nodes located at surfaces of shroud contacts.

Acknowledgments

The author is grateful to Rolls-Royce plc. for providing the financial support for this project and for giving permission to publish this work.

References

[1] Thomas, D. L., 1979, ''Dynamics of Rotationally Periodic Structures,'' Int. J. Numer. Methods Eng., **14**, pp. 81–102.

[2] Williams, F. W., 1986, ''An Algorithm for Exact Eigenvalue Calculations for Rotationally Periodic Structures,'' Int. J. Numer. Methods Eng., **23**, pp. 609–622.

[3] Wildheim, J., 1981, ''Vibrations of Rotating Circumferentially Periodic Structures,'' Q. J. Mech. Appl. Math., **36**, Part 2, pp. 213–229.

[4] Vakakis, A. F., 1992, ''Dynamics of a Nonlinear Periodic Structure With Cyclic Symmetry,'' Acta Mech., **95**, pp. 197–226.

[5] Samatanayake, S., and Bajaj, A. K., 1997, ''Subharmonic Oscillations in Harmonically Excited Mechanical Systems With Cyclic Symmetry,'' J. Sound Vib., **206**(1), pp. 39–60.

[6] Wagner, L. F., and Griffin, J. H., 1990, ''Blade Vibration With Nonlinear Tip Constraint: Model Development,'' ASME J. Turbomach., **112**, pp. 778–785.

[7] Csaba, G., 1998, ''Forced Response Analysis in Time and Frequency Domains of a Tuned Bladed Disk With Friction Dampers,'' J. Sound Vib., **214**(3), pp. 395–412.

[8] Panning, L., Sextro, W., and Popp, K., 2002, ''Optimization of the Contact Geometry Between Turbine Blades and Underplatform Dampers With Respect to Friction Damping,'' ASME Paper GT-20002-30429.

[9] Yang, B. D., Chen, J. J., and Menq, C. H., 1999, ''Prediction of Resonant Response of Shrouded Blades With Three-Dimensional Shroud Constraint,'' ASME J. Eng. Gas Turbines Power, **121**, pp. 523–529.

[10] Chen, J. J., and Menq, C. H., 1999, ''Prediction of Periodic Response of Blades Having 3D Nonlinear Shroud Constraints,'' ASME Paper 99-GT-289.

[11] Petrov, E., and Ewins, D., 2002, ''Analysis of Nonlinear Multiharmonic Vibrations of Bladed Disks With Friction and Impact Dampers,'' *Proc. of the 7th National Turbine Engine HCF Conference*, Universal Technology Corporation, Dayton, OH.

[12] Graham, A., 1981, *Kronecker Products and Matrix Calculus With Applications*, John Wiley and Sons, New York.

[13] Petrov, E. P., Sanliturk, K. Y., and Ewins, D. J., 2002, ''A New Method for Dynamic Analysis of Mistuned Bladed Disks Based on Exact Relationship Between Tuned and Mistuned Systems,'' ASME J. Eng. Gas Turbines Power, **122**, pp. 586–597.

[14] Petrov, E., and Ewins, D., 2002, ''Analytical Formulation of Friction Interface Elements for Analysis of Nonlinear Multiharmonic Vibrations of Bladed Disks,'' ASME Paper GT-20002-30325.

[15] Petrov, E. P., and Ewins, D. J., 2002, ''Robust Analysis of Periodic Vibration of Structures With Friction and Gaps Based on Analytical Derivation of Nonlinear Interface Elements,'' *Proceedings of 5th World Congress on Computational Mechanics*, July 7–12, Vienna University of Technology, Vienna, Austria.

Generic Friction Models for Time-Domain Vibration Analysis of Bladed Disks

E. P. Petrov

D. J. Ewins

Centre of Vibration Engineering,
Mechanical Engineering Department,
Imperial College London,
South Kensington Campus,
London SW7 2AZ, UK

New efficient models have been developed to describe dynamic friction effects in order to facilitate analysis of the vibration of bladed disks in the time domain. These friction models describe friction forces occurring at contact interfaces under time-varying normal load variations, including cases of separation. The friction models developed allow one to take into account time-varying friction contact parameters, such as friction coefficient and contact stiffness coefficients. Anisotropy and variation of the friction characteristics over the contact surfaces are included in the proposed models. The capabilities of the new friction models are demonstrated. Analysis of the friction forces is performed for different motion trajectories and different time variations of the normal load, and the effects of anisotropy, variation in time of the friction characteristics and normal load variation are discussed. A numerical analysis of transient vibrations of shrouded blades using the new models is presented. [DOI: 10.1115/1.1644557]

Introduction

Dry friction is one of the most important sources of damping in bladed disk assemblies. Friction forces appear during vibration under certain conditions at contact interfaces between different parts of the assembly: for example, at the contact surfaces in blade tang-disk joints; at contact surfaces of adjacent blade shrouds in a shrouded bladed disk and at contact surfaces in friction dampers which are special devices that are designed to increase dissipation of vibration energy through the friction damping.

In many cases service conditions (e.g., forcing, rotation speed, temperature, etc.) for bladed disks change so quickly that bladed disk vibrations are transient rather than steady-state and there is a need to analyze their vibration in the time domain.

Because of this, development of consistent friction models allowing accurate determination of in-time variation for the forces appearing at friction contact interfaces, taking into account history of relative motion of the contact interface, represents a very important problem: not only theoretical but also practical.

The problem of developing friction models is one of the oldest in mechanics and the model developed by Coulomb in 1785 is widely used in structural dynamics owing to its simplicity. However, Coulomb's friction model is discontinuous, and this causes numerical difficulties in its application for time-domain analysis. Moreover, it has inherent limitations when attempting to capture experimentally-observed friction effects found after Coulomb, and these drawbacks of Coulomb's friction model encourage the development of new friction models. Several so-called ''dynamic'' models have been developed which overcome the drawbacks in Coulomb's model to a large extent (and among these, the models developed in papers [1–3] should be noted). These dynamic friction models allow the history of the relative motion of the contact surfaces to be taken into account. However, existing dynamic models are devised mostly for cases where relative motion is one-dimensional, i.e., motion takes place along a line lying on the contact surface. Moreover, the problem of determining friction forces when the normal load is varied significantly has not been fully addressed. Comprehensive surveys of the current state of the problem of modeling friction forces are presented in [4,5] and a review on friction damping in bladed disks is given in [6].

Examples of friction models with constant normal load developed for the analysis of steady-state vibrations of bladed disks and two-dimensional, monoharmonic motion in the plane of the contact, can be found in Refs. [7,8].

Friction models for the case of variable normal load were first developed in [9] and then, with different consideration, in [10] for two-dimensional motion of contact interfaces. For the practically important case of periodic multiharmonic motion the expressions for stiffness matrices and contact forces are derived analytically in paper [10] allowing extremely robust and effective analysis of structures with friction in the frequency domain. A friction model for three-dimensional motion with variable normal load is developed in [11] where also anisotropy of contact stiffness coefficients (but not anisotropy of the friction coefficient) is accounted for. Friction forces are described in these papers by different sets of equations for the two possible states considered there: (i) for stick and (ii) for slip. In order to determine instants of transition from one of these states to the other, conditions of stick-slip transition have to be checked at each time instant and nonlinear equations have to be solved to find the time instants of these transitions. This can cause a difficulty for time-domain analysis of nonperiodic vibration, especially for the case of three-dimensional motion where, as derived in [11], to find times of the slip-to-stick transitions, nonlinear algebraic-differential equations have to be solved.

Modern contact mechanics gives an insight into the physics of friction contact interaction of rough surfaces, which consist of a multitude of micro-asperities and waviness at different scales (see, for example, [12,13]). For practical calculations, there is a need for phenomenological models of friction which provide a description of forces, appearing at contacting interfaces, resulting from motion of the contacting surfaces and defined in terms of parameters characterizing statistically roughness, material and other properties of the mating surfaces.

Manufacture and finishing treatment of the contact surfaces can produce differently shaped micro-asperities and different statistical distributions of the micro-asperities for different directions which results in anisotropic properties of all friction characteristics of the contact surface. Because of that friction and stiffness coefficients can be dependent on the direction of motion at every time instant. Moreover, inevitable variation of the surface roughness, temperature, local material properties, etc., can be a cause of inhomogeneity of the friction characteristics, i.e., their variation over the contact surface as a function of coordinates of the contact points.

Contributed by the International Gas Turbine Institute and presented at the International Gas Turbine and Aeroengine Congress and Exhibition, Atlanta, GA, June 16–19, 2003. Manuscript received by the IGTI December 2002; final revision March 2003. Paper No. 2003-GT-38475. Review Chair: H. R. Simmons.

Under certain regimes of a gas turbine engine the friction and stiffness coefficients vary rapidly with time, and their variation should be included in the friction models. It can happen, for example, when temperature of the contact surface is changing rapidly, or when high contact stresses causes wear of the contact surfaces.

In this paper, new generic models of dynamic friction effects are developed in order to facilitate predictive analysis of the vibration of bladed disk assemblies in the time domain. These models describe the friction forces occurring at contact interfaces under arbitrary motion of the contact surfaces and accounting for variation of the normal load. Normal load variations are arbitrary, and cases of separation of the contacting surfaces can be included.

The dynamic friction models developed here are the first known to the authors which allow formulation differential equations describing the friction forces over the whole process of motion, derived for arbitrary three-dimensional motion of contacting surfaces.

The differential equations derived describe variation of the friction forces as function of relative displacement of the contact surfaces, taking into account the history of the friction contact interaction. Friction forces are determined using general equations that are valid for all possible states of the friction contact, i.e., for stick, for slip and for stick-slip transitions. All possible states of the friction contact interface can be modelled although there is no necessity for explicit determination of slip-stick transition instants. The latter facilitates application of the friction models to time-domain analysis, and allows friction contact forces to be determined at any time by simple integration of the differential equations.

Moreover, the new models provide capabilities that have not existed to date for modeling friction forces in dynamic analysis of bladed disks:

1. accounting for time variations of friction contact parameters such as friction coefficient and contact stiffness coefficients;
2. accounting for variation and rate of variation of the friction characteristics as functions of coordinates over the contact surface;
3. accounting for anisotropic properties of the friction coefficient together with anisotropy of the contact stiffness coefficients.

An analysis of the friction models is performed and the dependence of the hysteresis loops produced by the new friction models on the trajectory of the motion and normal load variation is demonstrated. Simple conditions for possible occurrences of stick-slip transitions as a function of trajectory shape are proposed and new effects caused by normal load variations and variable friction characteristics are discussed. A numerical analysis of transient vibrations of shrouded blades using the new models is performed.

New Time-Domain Friction Models With Arbitrary Variation of the Normal Load

In this section new friction models are derived for the general case when not only the normal load is varied in time but so also can the characteristics of the contact surfaces, such as a friction coefficient, and contact stiffness coefficients, be varied with time, τ. Moreover, the possibility that these characteristics may vary as a function of coordinates of the contact point, X and Y, is also taken into account. Friction models for two cases of relative motion of the contacting surfaces are developed separately, namely: (i) for the case when motion in the plane of friction contact takes place along a line and (ii) for the more general case when the motion is an arbitrary planar motion. For the case of this planar motion, anisotropy of the contact surface characteristics is included in the consideration. The friction model for planar motion can include the case of motion along a line as a particular case.

Below, we shall derive a phenomenological friction model, which describes the friction phenomenon for purposes of analysis of vibration response of mechanical systems but which is not aimed at analysing physical mechanisms of friction. Nevertheless, some physical model is useful for the derivation of the mathematical model for the friction forces.

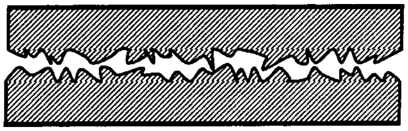

Fig. 1 Friction contact interaction of rough surfaces

Friction is produced as a result of contact interaction of a multitude of microscopic asperities of the rough contact surfaces (see **Fig. 1**). In order to develop a model for friction, we consider the contact interaction of one asperity with characteristics which represent statistically the microasperities over a contact patch.

The interaction of one moving surface over a fixed one is considered here for clarity and conciseness. However, this does not affect the generality of the friction models derived here, since for the case of two moving contact surfaces, all quantities (displacements, friction and stiffness coefficients, etc.) used in the friction models developed below can be interpreted as the quantities corresponding to the relative motion and characteristics of the contact interface for these surfaces.

Motion of a Contact Point Along a Line. For motion along a line we consider a contact interaction of one such asperity, as shown in **Fig. 2**. In this figure the letter "A" indicates a reference node which belongs to the moving body and the motion of this node is prescribed by the body displacement, $x(\tau)$, where the letter "S" indicates a point belonging to the tip of the asperity. The coordinate system is oriented in such way that the x axis is directed along the line of the tangential motion and the z-axis is directed along the positive normal to the contact surface. The force, f_x, is determined by friction and can be expressed in the following form:

$$f_x = \mathrm{sgn}(\dot{x}_S(\tau))\mu(\tau) f_z(\tau) \tag{1}$$

where $f_z(\tau)$ is the normal load, $\mu(\tau)$ is the friction coefficient at the point of contact, and a dot above x_S indicates a derivative with respect to time. This expression is similar, but not identical, to the Coulomb friction law since in the conventional Coulomb friction model the velocity of the reference node, $\dot{x}$, is used instead of the velocity of the asperity peak, $\dot{x}_S$, adopted in Eq. (1).

Moreover, we assume that the asperity in contact can be deformed linearly and elastically so that a stiffness coefficient, $k_t(\tau,X)$, of the asperity for deformation along a tangential direction is known as a function of time, τ, and a coordinate of the point of contact, X. Then, the interaction force, f_x, can be expressed as an elastic force caused by the asperity deformation

$$f_x = k_t(\tau,X)(x(\tau) - x_S(\tau)). \tag{2}$$

Equations (1) and (2) contain unknown quantity, $x_S(\tau)$, which has to be eliminated to allow the determination of the friction

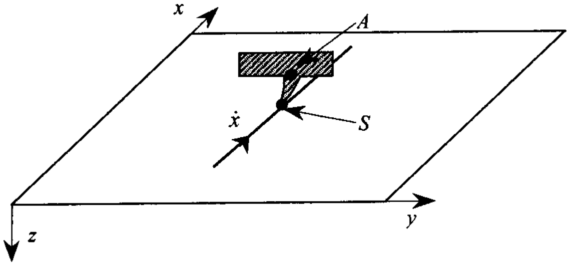

Fig. 2 Motion of the asperity model along a line

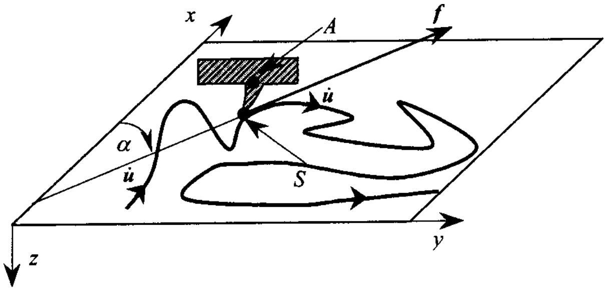

Fig. 3 Arbitrary planar motion of the asperity model

force through motion of the contacting bodies. In order to do this we introduce an approximation for the sign function, $\mathrm{sgn}(\dot{x})$, in the expression for the friction force given by Eq. (1). The approximation is used to smooth out the discontinuity of the sign function and to allow a solution of Eq. (1) with respect to $\dot{x}_S$. There are good approximations for this function and several examples of these, discussed in paper [14], are

$$\mathrm{sgn}(\dot{x}_S)\approx\frac{2}{\pi}\arctan(c\dot{x}_S)\approx\tanh(c\dot{x}_S)\approx\mathrm{erf}(c\dot{x}_S)\approx\frac{c\dot{x}_S}{1+c|\dot{x}_S|} \tag{3}$$

where the constant, c, controls the closeness of the approximation to the sign function: the larger the value chosen for c, the more accurate is the approximation. We choose from the set of the sign function approximations in Eq. (3) a function that has a simple inverse counterpart: $\mathrm{sgn}(\dot{x}_S)\approx 2\arctan(c\dot{x}_S)/\pi$. This expression is substituted into Eq. (1), and then the equation obtained is solved for $\dot{x}_S$. As a result, the following expression for asperity velocity is derived:

$$\dot{x}_S=\frac{1}{c}\tan\left(\frac{\pi f_x}{2\mu(\tau)f_z(\tau)}\right). \tag{4}$$

Differentiation of Eq. (2) with respect to time, followed by use of Eq. (4), gives the following differential equation for determination of the friction force:

$$\frac{df_x}{d\tau}=k_t(\tau)\left(\dot{x}(\tau)-\frac{1}{c}\tan\left(\frac{\pi f_x}{2\mu(\tau)f_z(\tau)}\right)\right)+\left(\frac{\partial k_t(\tau,X)}{\partial\tau}+\frac{\partial k_t(\tau,X)}{\partial X}\dot{x}\right)\frac{f_x}{k_t(\tau,X)}. \tag{5}$$

For the case when the variation of the stiffness coefficient, $k_t(\tau,X)$, in time and space can be neglected, the differential equation for determination of the friction force takes the following, simpler form:

$$\frac{df_x}{d\tau}=k_t\left(\dot{x}(\tau)-\frac{1}{c}\tan\left(\frac{\pi f_x}{2\pi(\tau)f_z(\tau)}\right)\right) \tag{6}$$

Planar Motion of a Contact Point. We consider a general case of arbitrary planar motion of the contacting surfaces in the plane of contact, which can be periodic or nonperiodic, and the trajectory of motion in this case can be a closed curve or an open curve (**Fig. 3**).

The friction force can be represented for this case by a vector of two coordinates:

$$\mathbf{f}=\{f_x,f_y\}^T. \tag{7}$$

The relative displacements of the reference node, A, and the motion of the asperity tip, S, in this plane are described by the following vectors:

$$\mathbf{u}=\{x(\tau),y(\tau)\}^T \quad \text{and} \quad \mathbf{u}_S=\{x_S(\tau),y_S(\tau)\}^T \tag{8}$$

and directions of the friction force vector, $\mathbf{f}$, and of the vector of asperity velocity, $\dot{\mathbf{u}}_S$, are assumed to be coincident, i.e.:

$$\dot{\mathbf{u}}_S/\|\dot{\mathbf{u}}_S\|=\mathbf{f}/\|\mathbf{f}\| \tag{9}$$

where $\|\dot{\mathbf{u}}_S\|=\sqrt{\dot{x}_S^2+\dot{y}_S^2}$ and $\|\mathbf{f}\|=\sqrt{f_x^2+f_y^2}$ are magnitudes of the vectors.

For the case of planar motion, Eq. (1) is transformed to the following form:

$$\|\mathbf{f}\|=\mathrm{sgn}(\|\dot{\mathbf{u}}_S\|)\mu(\tau,\dot{\mathbf{u}}_S/\|\dot{\mathbf{u}}_S\|)f_z(\tau) \tag{10}$$

where the friction coefficient, $\mu(\tau,\dot{\mathbf{u}}_S/\|\dot{\mathbf{u}}_S\|)$, is dependent, for the general case of anisotropic friction properties, on the direction of the motion, $\dot{\mathbf{u}}_S/\|\dot{\mathbf{u}}_S\|$, of the contact point, S.

Taking Eq. (9) into account, the dependence of the friction coefficient on the direction of motion can be rewritten in terms of the direction of the friction force vector in the following form:

$$\mu(\tau,\dot{\mathbf{u}}_S/\|\dot{\mathbf{u}}_S\|)=\mu(\tau,\mathbf{f}/\|\mathbf{f}\|)=\mu(\tau,\alpha(\mathbf{f}(\tau))) \tag{11}$$

where $\alpha(\mathbf{f}(\tau))$ is an angle characterising the direction of the friction force vector in the plane of contact. The angle is determined by its sine and cosine values: $\cos\alpha=f_x/\|\mathbf{f}\|$ and $\sin\alpha=f_y/\|\mathbf{f}\|$.

Using the approximation for the sign function, $\mathrm{sgn}(\|\dot{\mathbf{u}}_S\|)=2\arctan(c\|\dot{\mathbf{u}}_S\|)/\pi$, Eq. (10) can be resolved with respect to $\|\dot{\mathbf{u}}_S\|$ in the following way:

$$\|\dot{\mathbf{u}}_S\|=\frac{1}{c}\tan\left(\frac{\pi\|\mathbf{f}\|}{2\mu(\tau,\alpha(\mathbf{f}))f_z(\tau)}\right). \tag{12}$$

Considering elastic deformation of the asperity, the friction force vector can be expressed as follows:

$$\mathbf{f}=\mathbf{K}(\tau,\mathbf{X})(\mathbf{u}(\tau)-\mathbf{u}_S) \tag{13}$$

where

$$\mathbf{K}=\begin{bmatrix}k_{xx}(\tau,\mathbf{X}) & k_{xy}(\tau,\mathbf{X})\\ k_{yx}(\tau,\mathbf{X}) & k_{yy}(\tau,\mathbf{X})\end{bmatrix} \tag{14}$$

is a symmetrical matrix of stiffness coefficients which takes into account anisotropic properties of the elastic deformation of the asperity. The stiffness coefficients can be dependent on the vector of coordinates of the contact point, $\mathbf{X}=\{X,Y\}^T$ and be varied in time.

In order to derive the differential equations describing friction forces, Eq. (13) is differentiated with respect to time and then Eq. (9) is taken into account:

$$\begin{aligned}\frac{d\mathbf{f}}{dt}&=\mathbf{K}(\dot{\mathbf{u}}(\tau)-\dot{\mathbf{u}}_S(\tau))+\dot{\mathbf{K}}(\mathbf{u}(\tau)-\mathbf{u}_S(\tau))\\ &=\mathbf{K}\left(\dot{\mathbf{u}}(\tau)-\|\dot{\mathbf{u}}_S\|\frac{\mathbf{f}}{\|\mathbf{f}\|}\right)+\dot{\mathbf{K}}\mathbf{K}^{-1}\mathbf{f}\end{aligned} \tag{15}$$

where

$$\dot{\mathbf{K}}=\frac{\partial\mathbf{K}(\tau,\mathbf{X})}{\partial\tau}+\frac{\partial\mathbf{K}(\tau,\mathbf{X})}{\partial\mathbf{X}}\dot{\mathbf{u}}(\tau). \tag{16}$$

Substitution of Eq. (12) into Eq. (15) results in the following equation for determination of the friction forces for an arbitrary planar motion and arbitrary variation of the contact characteristics:

$$\frac{d\mathbf{f}}{dt}=\mathbf{K}\left(\dot{\mathbf{u}}(\tau)-\frac{1}{c}\tan\left(\frac{\pi\|\mathbf{f}\|}{2\mu(\tau,\alpha(\mathbf{f}))f_z(\tau)}\right)\frac{\mathbf{f}}{\|\mathbf{f}\|}\right)+\dot{\mathbf{K}}\mathbf{K}^{-1}\mathbf{f}. \tag{17}$$

For the case of isotropic and homogeneous properties of the contact surface with constant stiffness coefficients, the differential equation for the friction forces takes the simpler form:

$$\frac{d\mathbf{f}}{d\tau}=k_t\left(\dot{\mathbf{u}}(\tau)-\frac{1}{c}\tan\left(\frac{\pi\|\mathbf{f}\|}{2\mu(\tau)f_z(\tau)}\right)\frac{\mathbf{f}}{\|\mathbf{f}\|}\right). \tag{18}$$

The friction model for arbitrary plane motion includes the case of motion along a line as a particular case.

Determination of the Normal Load

The derived friction models given by differential Eqs. (5) and (17) allow the friction forces to be calculated under conditions of variable normal load, $f_z(\tau)$. The normal load has to be positive, i.e., $f_z(\tau)>0$ in order to ensure that the surfaces remain in contact, and if this condition is not satisfied then there is no contact and integration is not performed since the friction forces are then zero a priori.

The normal load can be defined in two ways: (i) prescribed as a known function of time; or (ii) determined from the relative motion of the contacting surfaces along the normal direction. For the second case, assuming elastic contact for motion along the normal direction, the normal force can be represented, in the form:

$$f_z = N_0 + k_n(\tau,\mathbf{X}) z^r(\tau) \tag{19}$$

where $z(\tau)$ is the displacement along the direction normal to the contact surface; $k_n(\tau,\mathbf{X})$ is the stiffness coefficient of the asperity for deformation along the normal direction; r is a constant characterising interaction along the normal direction, and N_0 is the preloaded static component of the normal load.

The time instants when the normal force is equal to zero correspond to transitions of the contact interface from contact to separation or from separation to contact. The sign of the rate of in-time variation of the normal force indicates which of this two transitions occur. Conditions for determination of the transition times are the following:

$$\begin{aligned} &f_z(\tau)=0 \ \text{ and } \ \dot{f}_z(\tau)<0 \rightarrow \text{contact to separation} \\ &f_z(\tau)=0 \ \text{ and } \ \dot{f}_z(\tau)>0 \rightarrow \text{separation to contact} \end{aligned} \tag{20}$$

where $\dot{f}_z = z^{r-1}(\tau)(\dot{k}_n(\tau,\mathbf{X})z(\tau) + r k_n(\tau,\mathbf{X})\dot{z}(\tau))$ is the rate of the normal load variation accounting for variation of the contact stiffness and $\dot{k}_n(\tau,\mathbf{X}) = \partial k_n(\tau,\mathbf{X})/\partial\tau + (\partial k_n(\tau,\mathbf{X})/\partial \mathbf{X})^T \dot{\mathbf{u}}$.

Numerical Aspects of the Friction Models

Integration of the differential Eqs. (5), (6), (17), and (18) allows the friction force to be determined at any time of interest. They belong to the class of stiff differential equations and can be efficiently integrated by a large variety of algorithms and computer codes available on the Internet or in different commercial software packages. Relative and/or absolute errors of the integration process have to be set to guarantee accuracy for determination of the friction forces such $\|\mathbf{f}\| < \mu(\tau) f_z(\tau)$ throughout the integration process.

Choice of the constant, c, used in the approximation for the sign function is determined by the following two considerations: (i) very large values give an approximation which is not smooth enough, and incur large efforts for numerical integration of the equations; (ii) too small values can make the approximation too different from the sign function, and this can produce smaller friction forces than expected. Effects of choice of the value for constant c in the approximation of the sign function, $2\arctan(cx)/\pi$, and hence on the hysteresis loops are illustrated in **Fig. 4**. The hysteresis loops are calculated here for the case of harmonic motion of the contact point along a line, with constant friction characteristics and constant normal load.

The differential equations allow friction forces to be determined for any level of normal load variation, including even the extreme case of temporary separation of the contact surfaces during vibration. When surfaces are separated the integration of the differential equations is performed separately for each time interval $[\tau_j, \tau_{j+1}]$ of the contact state. In order to resolve the singularities occurring at the ends of the interval in Eqs. (5) and (17), when $f_z(\tau_j) = f_z(\tau_{j+1}) = 0$, the integration is performed for this case over a slightly reduced interval $[\tau_j + \varepsilon_1, \tau_{j+1} - \varepsilon_1]$. The initial values for the friction forces required for such intervals of temporary contact are taken as $\mathbf{f} = (1-\varepsilon_2)\mu(\tau_j+\varepsilon_1) f_z(\tau_j+\varepsilon_1)\dot{\mathbf{u}}(\tau_j+\varepsilon_1)/\|\dot{\mathbf{u}}\|$, where ε_1 and ε_2 are small positive numbers.

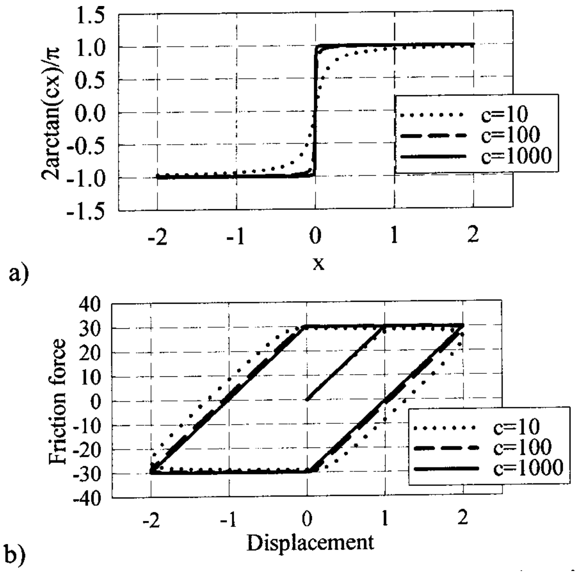

Fig. 4 Effects of different choice of the constant, *c*: (*a*) on the sign function approximation; (*b*) on hysteresis loop shapes

Capabilities of the New Friction Models

In this section, some of the capabilities of the friction models developed here are demonstrated, and properties of friction forces are explored, by prescribing the relative motion of the contact point and variation of the normal load and then calculating the friction forces corresponding to the given motion. Both types of relative motion are analyzed: (i) motion along a line and (ii) motion in the plane of contact.

Motion Along a Line

Influence of Normal Load Variation. For an example of the motion along a line given as $x=2\sin\tau$, contact surface characteristics: $k_t=30$ and $\mu=0.3$ are assumed, and a value, $c=1000$ is used for the constant of the sign function approximation, which provides an accurate approximation. In **Fig. 5**, the friction force, f_x, calculated by integration of Eq. (6), is shown as a function time (left column of the plots in **Fig. 5**) and as a function of relative displacement (right column in this figure), for different levels of the normal load variation.

The limiting friction force, $\pm\mu f_z$ is plotted by dashed lines in **Fig. 5**. Stick-to-slip transitions and back can be easily identified from the plots: the stick state corresponds to the larger slope of the curves and, in the slip state, the friction force is equal to the limiting force, $\pm\mu f_z(\tau)$. For the case of constant normal load (**Fig. 5(*a*)**), the hysteresis loop and time-variation of the friction force have the expected shapes. Introduction of a variation of the normal load causes changes of shape for the hysteresis loops, which then take on an unfamiliar form (**Fig. 5(*b*,*c*)**).

Influence of Phase Shift Between Normal Load and Displacement. The hysteresis loops are also dependent on the phase shift, ϕ, between the displacement and the normal load variation, which is demonstrated in **Fig. 6** by the results obtained for a normal load, $f_z = 100 + 80\sin(\tau+\phi)$ with different phase values.

Multiharmonic Vibrations. For cases when motion of the contact point and the normal load variation have more than one harmonic component the friction force variation and the hysteresis loop takes on more complex shapes. Examples of friction forces

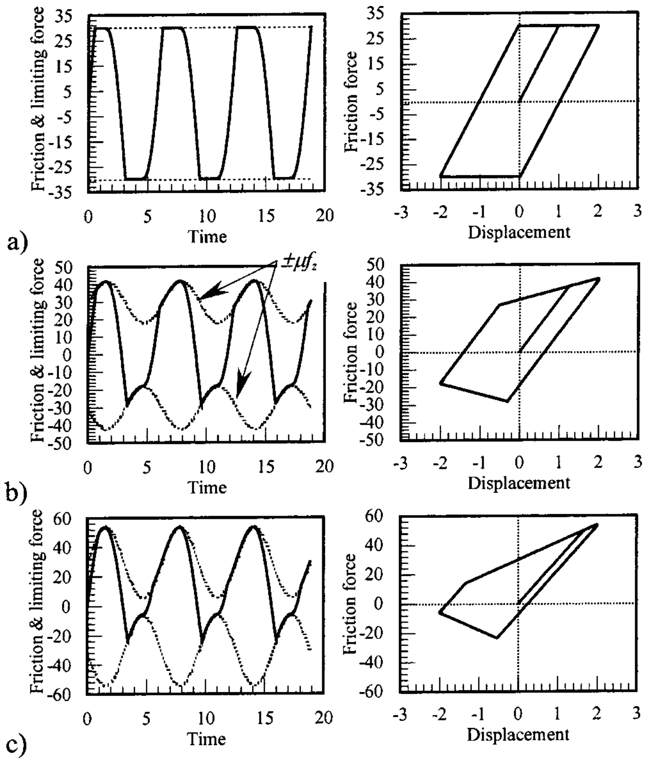

Fig. 5 The friction force and hysteresis loops for different levels of the normal load variation: (*a*) $f_z=100$; (*b*) $f_z=100+40\sin\tau$; (*c*) $f_z=100+80\sin\tau$

calculated for the case of $x=2\sin\tau+\cos 2\tau+0.8\sin 2\tau+0.5\cos 3\tau+\sin 3\tau$ and $f_z=100+40\sin\tau+32\sin(2\tau+\pi/4)$ are shown in **Fig. 7**.

For this case, the number of slip-to-stick transitions is different from the number of changes of the displacement velocity sign: Over a period of vibration one can see three stick states while there are four changes of the sign for $\dot{x}(\tau)$.

Variable Friction Parameters. The friction model developed also allows efficient determination of the friction forces when characteristics of the friction surface are varied in time. Examples of hysteresis loops obtained for varying friction characteristics are shown in **Fig. 8**.

Three cases of variation of the friction characteristics are compared here: (i) a case of varying friction and constant stiffness

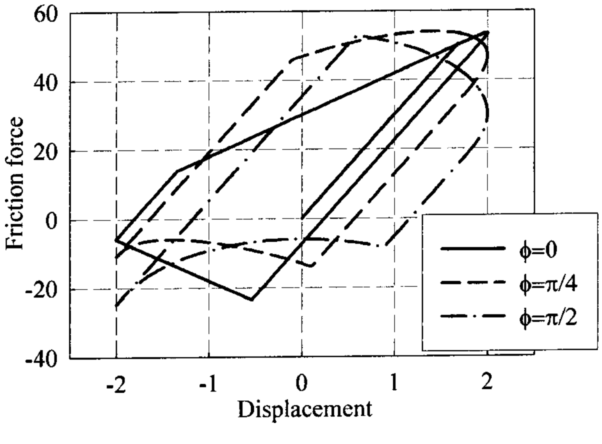

Fig. 6 Hysteresis loops for different phase values of the normal load variation: $f_z=100+80\sin(t+\phi)$

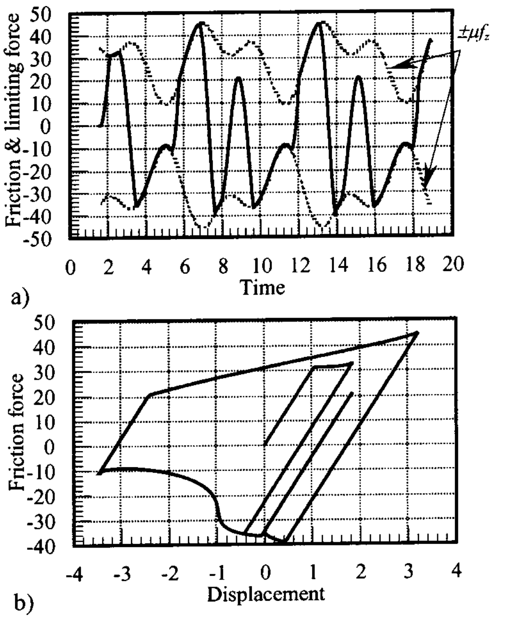

Fig. 7 Friction force with multiharmonic displacement and normal load variation

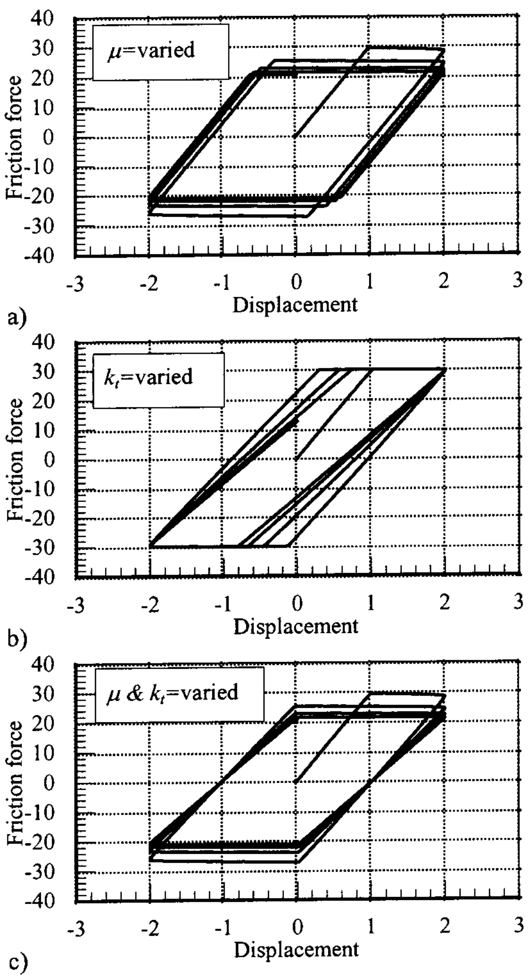

Fig. 8 Hysteresis loops for variable friction characteristics: (*a*) $\mu=1/3\mu_0(2+e^{-0.1\tau})$; $k_t=k_0$; (*b*) $\mu=\mu_0$; $k_t=1/3k_0(2+e^{-0.1\tau})$; (*c*) $\mu=1/3\mu_0(2+e^{-0.1\tau})$ and $k_t=1/3k_0(2+e^{-0.1\tau})$

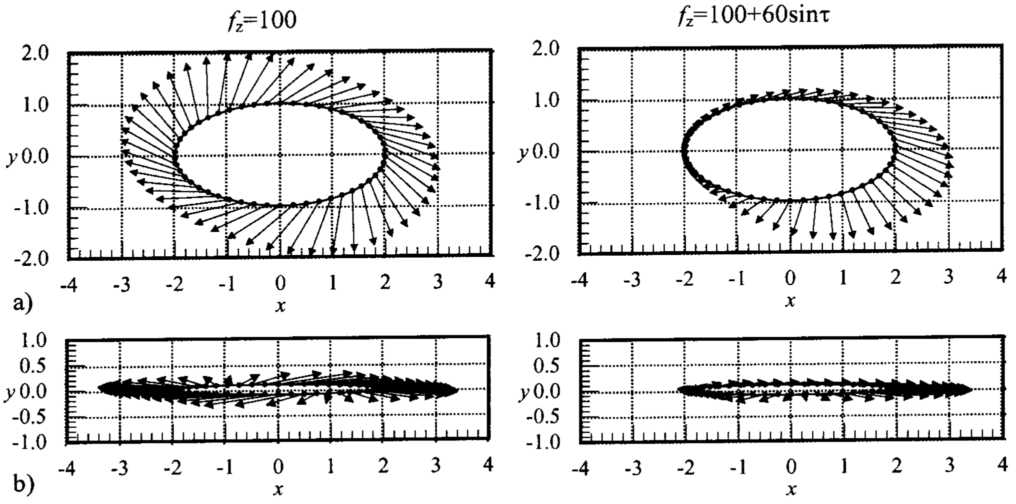

Fig. 9 Vectors of the friction force for different trajectories and normal load variation: (*a*) a case of an ellipse with the ratio of its axis lengths 2:1; (*b*) a case of an ellipse with the ratio 2:0.1

coefficients, (ii) a case of constant friction and varying stiffness coefficient, and (iii) a case when both coefficients are varied. The friction forces are calculated in the interval $[0,8\pi]$. One can see that the shape of the hysteresis loops is changing in time even for the case considered here of periodic motion. Variation of the displacement is assumed to be: $x=2\sin\tau$, and initial values for varying contact characteristics are: for the friction coefficient, $\mu_0=0.3$ and the stiffness coefficient, $k_0=30$. The normal load is constant: $f_z=100$, and functions of the friction parameter variation are specified in the caption for **Fig. 8**.

Planar Motion

Influence of the Trajectory of Motion. For planar relative motion, in contrast to the case of motion along a line, it is possible to have no slip-to-stick transitions in steady-state motion even when the vector of relative velocity reverses in direction. In order to illustrate this, relative motion is examined where the contact point circumscribes an elliptical trajectory: $x=2\sin\tau$ and $y=a\cos\tau$, and different values for the semi-minor axis are considered, namely, $a=1$, 0.5, 0.1. The friction properties are assumed to be isotropic and homogeneous and the values for the friction interface coefficients are: $k_t=100$ and $\mu=0.3$. In **Fig. 9** two trajectories of motion, (namely with $a=0.5$ and $a=0.1$) and the corresponding vectors of the friction force are plotted for cases of constant, $f_z=100$, and varied, $f_z=100+60\sin\tau$, normal load.

The magnitude of the friction force vector, $\|\mathbf{f}\|$, is plotted as a function of time for all three values of the ellipse semi-minor axis, *a*, in **Fig. 10**. Since, during slip, $\|\mathbf{f}\|$ has to be close to the limiting force, μf_z, and during stick, $\|\mathbf{f}\|$ can take values much smaller than the limiting force, then intervals with $\|\mathbf{f}(\tau)\| \ll \mu f_z(\tau)$ indicate a stick occurrence. Because of that, this type of plot is useful to determine the appearance of the stick state for planar relative motion. One can see that $\|\mathbf{f}(\tau)\|$ is very close to μf_z when $a=1$, and the smaller the value of *a*, the more distinctive is the reduc-

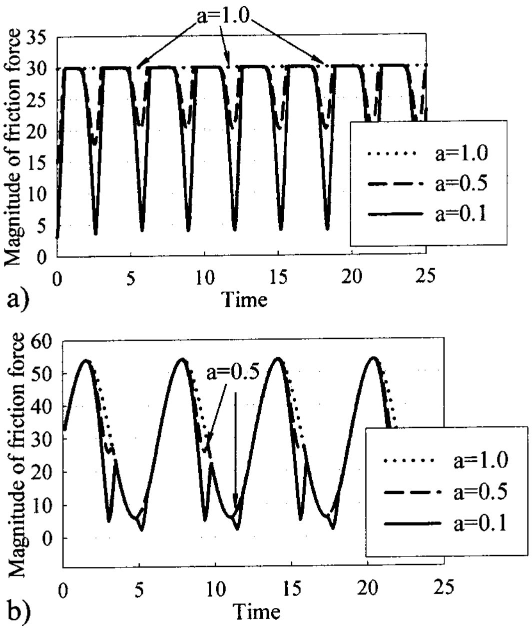

Fig. 10 Magnitude of the friction force vector for different trajectories: (*a*) $f_z=100$; (*b*) $f_z=100+60\sin\tau$

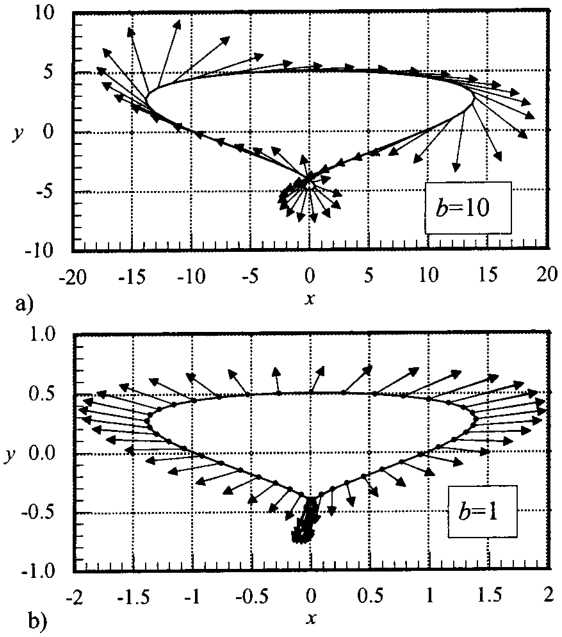

Fig. 11 Trajectory of motion and vectors of the friction force for different levels of displacements

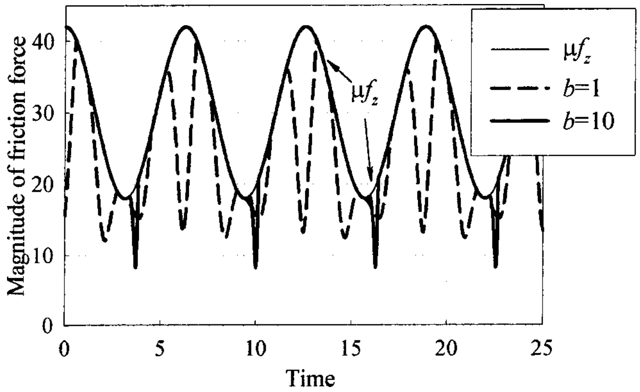

Fig. 12 Magnitude of the friction force vector for different levels of displacements

tion of $\|\mathbf{f}(\tau)\|$ indicating stick state. These stick states start at the time instants when the contact point is located at the point of minimum radius of curvature (i.e., $\tau_j = \pi(1/2+j)$ for the considered trajectory).

Friction forces were in this case also calculated for a more complex case of trajectory shape and normal load variation: $x = b(\sin\tau + 0.6\cos\tau)$; $y = 0.5b\cos\tau$ and $f_z = 100 + 40\cos\tau$. Results from these calculations are presented in **Figs. 11** and **12**. Two different levels of relative displacement are considered: $b = 10$ and $b = 1$, which provide the same shape of trajectory but give different values for the curvatures.

Trajectories of motion are plotted in **Fig. 11**, together with vectors of the friction force. As seen, the trajectories have a loop with small curvature radius near the point with co-ordinates $x = 0$ and $y = -5$ (for the case $b = 10$) or $y = -0.5$ (for the case $b = 1$). For the case of $b = 10$, shown in **Fig. 11(*a*)**, there are large parts of the trajectory where the direction of the friction force is close to the tangent to the trajectory and these parts correspond to large curvature radius. The displacement velocity vector, $\dot{\mathbf{u}}$, is directed at each point of a trajectory along the tangent direction, and hence the friction force vector is close to the direction of motion where the curvature radius has a large value. This fact correlates with the prediction of the conventional Coulomb's theory, although the latter requires coincidence of directions of the motion and of the friction force and not simply their closeness, as happens in our case. In the vicinity of the loop with a small radius of curvature, the friction forces can even be perpendicular to the direction of motion and, moreover, there are parts of the trajectory where the friction force vector transits from the tangent direction to directions with large angles between the motion and the friction force. For the case of $b = 1$ (see **Fig. 11(*b*)**, where all curvature radii are ten times smaller than for $b = 10$, there are large intervals of stick state. Time intervals of slip state are too short to allow the vector of friction force to change its direction from normal to tangent direction and, consequently, the angles between $\dot{\mathbf{u}}$ and $\mathbf{f}$ are large for all points on the trajectory.

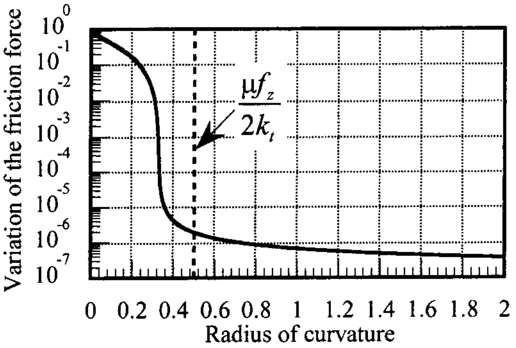

Fig. 13 Variation of the friction force as a function of radius of the minimum curvature

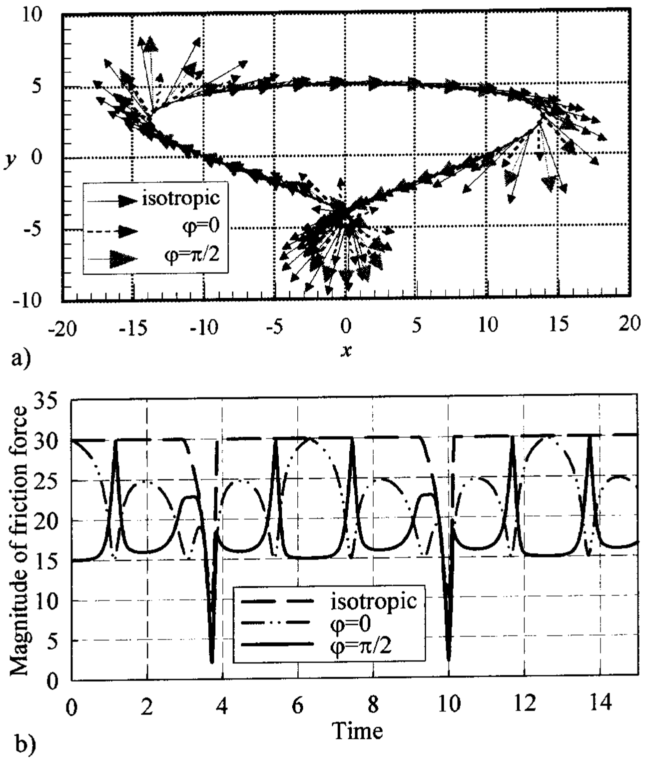

Fig. 14 Friction forces for different orientation of anisotropy axes for the friction coefficient, $\mu(\varphi)$: (*a*) friction force vector at different points of the trajectory; (*b*) magnitude of the friction vector

In **Fig. 12** time variations in the magnitude of the friction force vector, $\|\mathbf{f}(\tau)\|$, are shown. One can see that for $b = 10$ the magnitude of the friction force is close to μf_z over most of the time, except small intervals starting from time instants: $\tau^* = 3.43 + 2\pi j$. When the curvature radius reaches the minimum value, the magnitude of the friction force starts to deviate from the limiting value, μf_z, which indicates that the stick occurs at this point of the trajectory.

Simple Criteria of Possibility of Slip-to-Stick Transitions for Planar Motion. In **Fig. 13**, a function $\max_\tau(\mu f_z - \|\mathbf{f}\|)/\mu f_z$, which characterizes the variation of the module of the friction vector, is plotted with respect to the minimum curvature radius, calculated as $\rho_{\min} = \min_\tau(\dot{x}^2 + \dot{y}^2)^{3/2}/|\dot{x}\ddot{x} - \dot{y}\ddot{y}|$. Variation of $\rho_{\min}$ is achieved by changing the amplitude, a, of vibration along axis Y, $y = a\cos\tau$, from 10^{-7} to 2. As one can see, noticeable variation of $\|\mathbf{f}(\tau)\|$ occurs when $\rho_{\min} < \mu(\tau) f_z(\tau)/2k_t(\tau)$. This condition can be used as a simple criterion for the possibility of occurrence of the slip-to-stick transition for the general case of steady-state planar motion of the contacting surfaces. Another useful condition is the possibility of occurrence of the slip during vibration. Transition from stick to slip can occur if displacements are large enough to exceed the limiting force, μf_z, under elastic deformation of the asperity, i.e., when the following condition: $\max_\tau k_t(\tau)\|\mathbf{u}\|/\mu(\tau) f_z(\tau) \leq 1$ is violated.

Anisotropic Friction Characteristics. The importance of taking anisotropy of the friction characteristics into account is demonstrated in **Fig. 14**. The friction force vectors are shown for different points of the motion trajectory in **Fig. 14(*a*)**, and the magnitude of the friction force vector is plotted with respect to time in **Fig. 14(*b*)**. Different orientations of the anisotropy axes

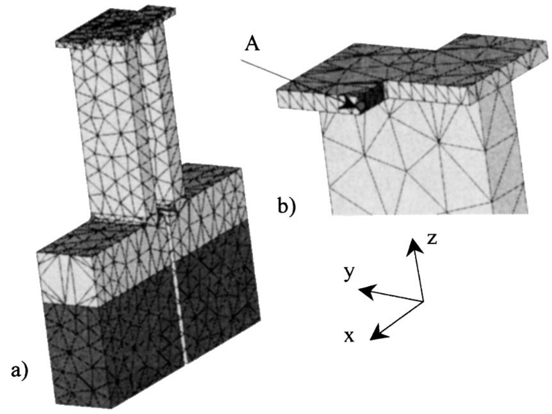

Fig. 15 Finite element model of the test rig, (*a*); and a patch where the blades have the friction contact interface, (*b*)

for the friction coefficient are examined and compared with the results obtained for a case of isotropic friction coefficient, $\mu=0.3$. For the cases of anisotropic friction coefficient, the following dependence of the anisotropic friction coefficient on the direction of the friction force, α, is assumed: $\mu=0.3^*(1-0.5|\sin(\alpha-\varphi)|)$ and two cases of orientation of the anisotropy axis are explored: (i) $\varphi=0$ and (ii) $\varphi=\pi/2$. Stiffness properties are isotropic with the stiffness coefficient value, $k_t=30$, and the normal load is constant: $f_z=100$. Displacements are assumed to be the same as in the previous case with $b=10$.

Analysis of Transient Forced Response

The friction models developed here have been applied to the analysis of vibrations of two blades interacting through their shrouds. The finite element model of the structure considered is shown in **Fig. 15(*a*)** where dark gray color indicates surfaces where the fixed restraints are imposed on all displacements. The patch where the shrouds can contact, and friction and normal interaction forces appear is marked in **Fig. 15(*b*)** in dark gray. Vibrations are excited by forces applied to one of the blades at its tip. The damping loss factor of the structure is assumed to be 0.0025 when the friction damping is not included. The frequency of excitation is varied linearly from 0.7 to 1 kHz during the time interval [0,0.1 sec]. Integration of the equations of motion is performed over this interval, i.e. while the forcing is applied. Components *x* and *y* of displacements calculated as functions of time are shown in **Fig. 16**.

The displacements are compared here for two cases: (i) a structure without accounting for friction forces at the interface patch; and (ii) a structure where, over nodes of the contact patch, the friction interface is described by the proposed friction model. One can see that the structure is much more heavily damped when the friction forces are included, and also has a higher resonance frequency. This latter fact can be observed by comparison of the time where amplitude levels are high in both cases because the excitation frequency is varied linearly within the time interval analyzed.

Predominant fiction force component, f_y, occurring at the node marked by letter 'A' in **Fig. 15** is shown in **Fig. 17(*a*)**, and hysteresis loops for this friction force are shown in **Fig. 17(*b*)**, for the whole analyzed history of the motion.

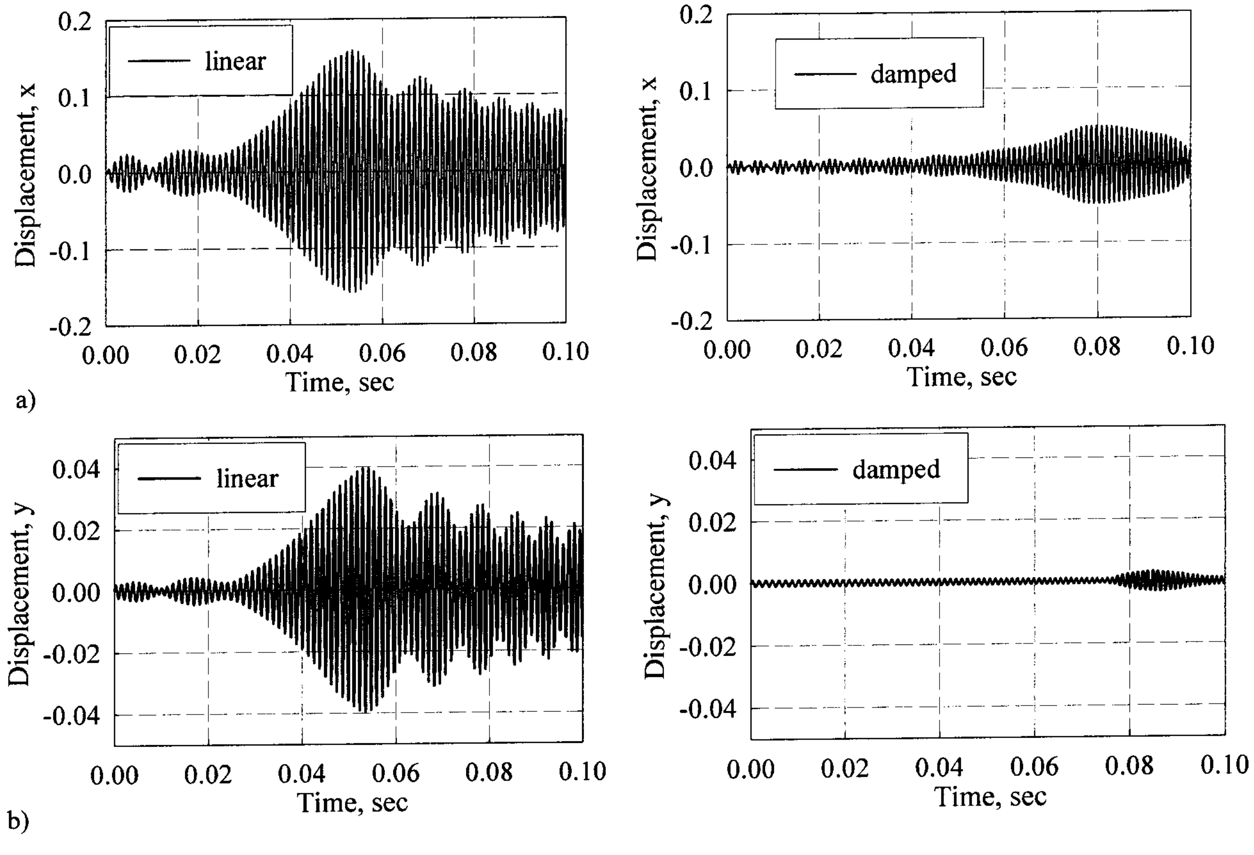

Fig. 16 Variation of displacement components over the time interval considered

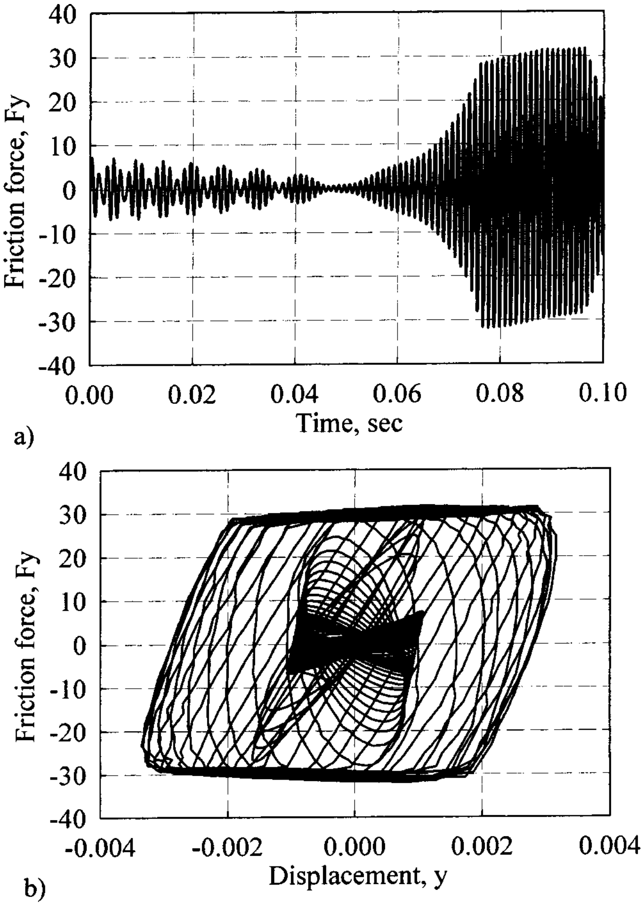

Fig. 17 Calculated friction force: (*a*) as functions of time; (*b*) hysteresis loops for the whole time range for friction force component f_y

Conclusions

The new models for friction dynamics developed here provide consistent and effective determination of the friction forces for time-domain analysis of vibrations of mechanical systems.

The models take into account a number of factors that have not been considered before, or have previously caused difficulty when applied to time-domain analysis.

The models allow arbitrary variation of the normal load, including the case of separation of the contacting surfaces. Arbitrary variation of the characteristics of the friction interface (e.g., friction coefficient, contact stiffness, etc.) in time can be also described.

Anisotropy and variation of the characteristics of the friction interface, as a function of coordinates of the contact surface, are accounted for.

Numerical examples of modelling the friction forces demonstrate the wide possibilities of the new friction models and give an insight into friction force behavior under variations of normal load and friction characteristics.

Acknowledgment

The authors are grateful to Rolls-Royce plc. for providing the financial support for this project and for giving permission to publish this work.

References

[1] Dahl, P. R., 1976, "Solid Friction Damping of Mechanical Vibrations," AIAA J., **14**(12), pp. 1675–1682.
[2] Gaul, L., and Lenz, J., 1997, "Nonlinear Dynamics of Structures Assembled by Joints," Acta Mech., **125**, pp. 169–181.
[3] de Wit, C. C., Olsson, H., Astrom, K. J., and Lischinsky, P., 1995, "A New Model for Control of Systems With Friction," IEEE Trans. Autom. Control, **40**(3), pp. 419–425.
[4] Armstrong-Helouvry, B., Dupont, P., and de Wit, C. C., 1994, *A* "Survey of Models, Analysis Tools and Compensation Methods for the Control of Machines With Friction," Automatica, **30**, pp. 1083–1138.
[5] Ibrahim, R. A., 1994, "Friction-Induced Vibration, Chatter, Squeal, and Chaos," Appl. Mech. Rev., **47**, "Part I: Mechanics of Contact and Friction," pp. 209–226, "Part II: Dynamic and Modeling," pp. 227–253.
[6] Griffin, J. H., 1990, "A Review of Friction Damping of Turbine Blade Vibration," Int. J. Turbo Jet Engines, (7), pp. 297–307.
[7] Sanliturk, K. Y., Imregun, M., and Ewins, D. J., 1997, "Harmonic Balance Vibration Analysis of Turbine Blades With Friction Dampers," ASME J. Vibr. Acoust., **119**, pp. 96–103.
[8] Sextro, W., 1996, "The Calculation of the Forced Response of Shrouded Blades With Friction Contacts and Its Experimental Verification," *Proc. of 2nd European Nonlinear Oscillation Conference*, Prague, Sept. 9–13.
[9] Yang, B. D., Chu, M. I., and Menq, C. H., 1998, "Stick-Slip-Separation Analysis and Non-linear Stiffness and Damping Characterization of Friction Contacts Having Variable Normal Load," J. Sound Vib., **210**(4), pp. 461–481.
[10] Petrov, E., and Ewins, D., 2004, "Analytical Formulation of Friction Interface Elements for Analysis of Nonlinear Multiharmonic Vibrations of Bladed Disks," ASME J. Turbomach., **126**, pp. 364–371.
[11] Yang, B. D., and Menq, C. H., 1998, "Characterization of 3D Contact Kinematics and Prediction of Resonant Response of Structures Having 3D Frictional Constraint," J. Sound Vib., **217**(5), pp. 909–925.
[12] Tabor, D., 1981, "Friction—The Present State of Our Understanding," ASME J. Lubr. Technol., **103**, pp. 169–179.
[13] Tworzydlo, W. W., Cecot, W., Oden, J. T., and Yew, C. H., 1998, "Computational Micro- and Macroscopic Models of Contact and Friction: Formulation, Approach and Applications," Wear, **220**, pp. 113–140.
[14] Mostanghel, N., and Davis, T., 1997, "Representations of Coulomb Friction for Dynamic Analysis," Earthquake Eng. Struct. Dyn., **26**, pp. 541–548.

A New Model for Boundary Layer Transition Using a Single-Point RANS Approach

D. Keith Walters[1]

James H. Leylek

Department of Mechanical Engineering,
Clemson University,
Clemson, SC 29634

This paper presents the development and implementation of a new model for bypass and natural transition prediction using Reynolds-averaged Navier-Stokes computational fluid dynamics (CFD), based on modification of two-equation, linear eddy-viscosity turbulence models. The new model is developed herein based on considerations of the universal character of transitional boundary layers that have recently been documented in the open literature, and implemented into a popular commercial CFD code (FLUENT) in order to assess its performance. Two transitional test cases are presented: (1) a boundary layer developing on a flat heated wall, with free-stream turbulence intensity (Tu_∞) ranging from 0.2 to 6%; and (2) flow over a turbine stator vane, with chord Reynolds number 2.3×10^5, and Tu_∞ from 0.6 to 20%. Results are presented in terms of Stanton number, and compared to experimental data for both cases. Results show good agreement with the test cases and suggest that the new approach has potential as a predictive tool. [DOI: 10.1115/1.1622709]

1 Introduction

Prediction of the heat-transfer characteristics in attached boundary layers is an example of a widely relevant application to which computational fluid dynamics (CFD) is currently applied. Laminar boundary layers lend themselves to straightforward computation, since there is no need to account for any turbulence effect. Somewhat more difficult are fully turbulent boundary layers. Recent advances in Reyolds-averaged Navier Stokes (RANS) based turbulence modeling have greatly improved predictive capability, even for arbitrary, complex geometries and relatively complex flow physics (e.g., streamline curvature and streamwise pressure gradients).

In many cases, the boundary layer is neither laminar nor turbulent, but undergoes transition. Transition is significant for many applications, especially when the local variation in heat transfer may be important. In the low-pressure turbines of modern gas turbine engines, for example, the boundary layer may remain laminar over a majority of the airfoil surface, and predictions using a fully turbulent approach could lead to inaccurate conclusions regarding heat-transfer design. It has also been recently shown that the prediction of film-cooling flows is particularly sensitive to the state of the approaching boundary layer, and that improper resolution of transition may have a significant impact on results [1,2].

RANS-based boundary-layer transition simulation lags appreciably behind turbulent flow simulation, and therefore represents a ''new frontier'' in CFD modeling research. A few notable attempts have been made to address the issue, with the various approaches summarized as follows: (1) use of zonal modeling, dividing the flowfield into separate laminar and turbulent regions based on some empirical reasoning; (2) use of unmodified low-Re versions of RANS-based turbulence models; and (3) use of low-Re RANS models in conjunction with intermittency functions, either empirical or calculated within the simulation. The first approach is most often used by CFD practitioners who have a familiarity with their application, and is rightly regarded as more ''art'' than ''science.'' The other two approaches, however, have been seriously examined as true predictive methods, although relatively few references are yet found in the open literature.

An early summary of low-Re turbulence models applied directly to transitional flows is given by Savill [3]. He documents a study in which a number of modelers implemented several different model forms to the problem of transition, as part of a large-scale research effort coordinated by the European Research Community on Flow Turbulence and Combustion (ERCOFTAC). Conclusions were mixed. No model was found to perform satisfactorily over a wide range of conditions, including varying free-stream turbulence and mainstream pressure gradients. In addition, almost all model forms were found to be highly dependent on the initial conditions and free-stream boundary conditions (parabolic solvers) and/or the inlet conditions (elliptic solvers). Many of the reported simulations were ''started'' within the developing boundary layer, and the turbulence quantities were applied there, instead of developing entirely from a free-stream prescription. Perhaps most significant is the fact that all of these approaches rely on a ''diffusion-controlled'' model of bypass transition. Conceptually, this interprets bypass transition as caused by the transport, or diffusion, of free-stream turbulent kinetic energy into the boundary layer, where it is acted upon by the mean shear, leading to transition. This not only results in the extreme sensitivity to boundary conditions mentioned above, but also does not allow the models to correctly reproduce the production of streamwise fluctuations in the nonturbulent, pre-transitional boundary layer.

More recent attempts to apply low-Re models directly to transition include the efforts of Wilcox [4], Craft et al. [5], Chen et al. [6], and Chernobrovkin and Lakshminarayana [7]. These studies include more advanced model forms beyond the linear k-ε, including the k-ω model [4] and nonlinear eddy-viscosity models to more accurately resolve the Reynolds-stress tensor [5–7]. At present, results remain mixed. These models still rely on ''diffusion-controlled'' bypass transition and do not specifically address the pre-transitional region. However, all of these studies have been significant in pushing the limits of RANS-based transition prediction, and would suggest that elliptic, single-point modeling may in fact be a reasonable approach for transitional flows.

The other approach most often found in the literature is the use of semiempirical techniques, most often using some type of intermittency factor to bridge the pre-transitional and turbulent bound-

---

[1] Present address: Department of Mechanical Engineering, Mississippi State University, Mississippi State, KS 39762.

Contributed by the International Gas Turbine Institute and presented at the 2002 International Mechanical Engineering Congress and Exposition. Manuscript received by the Heat Transfer Division, March 2002, final revision, July 2002. Paper No. 2002-HT-32740. Associate Editor: R. Bunker.

ary layer and to enforce transition. Recent papers by Suzen and Huang [8] and Steelant and Dick [9] utilize transport equations for the intermittency factor, although similar to the studies above they rely on a diffusion-controlled transition concept. Volino [10] and Baek et al. [11] have recently documented models that use empirical forms for the intermittency, but are significant in that they specifically address the growth of streamwise fluctuations in the pre-transitional region of the boundary layer. One disadvantage of the intermittency type models is that none are truly single-point techniques. All rely on nonlocal or integral parameters of the flow as inputs to the terms in the transport equations, including, for example, Reynolds number, boundary-layer height, wall shear stress, or free-stream turbulence parameters.

The present study documents a new approach to RANS-based transition prediction that seeks to combine the advantages of the above methods. It is a single-point, elliptic model providing the ease-of-use of low-Re eddy-viscosity models. At the same time, it specifically addresses the production of streamwise fluctuations in the pre-transitional boundary layer and their impact on the bypass transition process. This new model approach also eliminates the need for intermittency factors altogether.

2 New Model Development

This section documents in detail the development of the new model as part of the current study. Section 2.1 discusses the physical motivation and major concepts embodied in the model, and Sec. 2.2 presents the model equations in detail and discusses the physical relevance of individual terms.

2.1 Concept. The pre-transitional region of a boundary layer subject to free-stream turbulence (Tu_∞) resembles a laminar boundary layer in terms of the mean velocity profile. As Tu_∞ is increased, the profile becomes noticeably distorted from the typical Blasius layer, with an increase in momentum in the inner region and a decrease in the outer, even for Tu_∞ as low as about 1% [12]. This shift in mean velocity profile is accompanied by the development of relatively high-amplitude streamwise fluctuations, which can reach intensities several times the free-stream level [13]. This process results in an augmentation of skin friction and heat transfer in the pre-transitional region, and eventually leads to bypass transition through the eventual breakdown of the streamwise fluctuations [14].

It is important to note that these streamwise fluctuations are not ‘‘turbulence’’ in the usual sense of that word. This distinction was made for modeling purposes by Mayle and Schulz [15], who proposed a ‘‘laminar-kinetic-energy’’ equation to describe the development of such fluctuations. Structurally they are very different from turbulent fluctuations, since the energy is almost entirely contained in the streamwise component. Their dynamics are also considerably different. The familiar cascade of energy from larger to smaller scales is not present, instead fluctuations are amplified at certain scales determined by the boundary layer itself, and remain at relatively low frequency. Dissipation is therefore also expected to be relatively low, except very near the wall due to the no-slip condition. All of these considerations have led to an adoption of a second kinetic energy equation in the present work to describe these fluctuations. This is an extension of the original concept of Mayle and Schulz [15], and similarly, the energy of the fluctuations will be called laminar kinetic energy, k_L. Model equations are also included for the turbulent kinetic energy k_T and the far-field dissipation ε.

The dynamics of laminar kinetic energy production are not entirely understood at present, but a number of researchers—experimental, numerical, and analytical—have shed light on the subject. A review of the current literature seems to indicate a growing consensus that two aspects are critical: selectivity of the boundary layer to certain freestream eddy scales, and amplification of low-frequency disturbances in the boundary layer by the mean shear. The growth of k_L has been shown experimentally [16] and analytically [17] to correlate with low-frequency normal (v') fluctuations of the free-stream turbulence. The scale selectivity of the boundary layer was clearly demonstrated by Johnson and Ercan [18], who plotted amplification of six frequency bands in a pre-transitional boundary layer. Reasons for this selectivity and amplification are not yet completely understood.

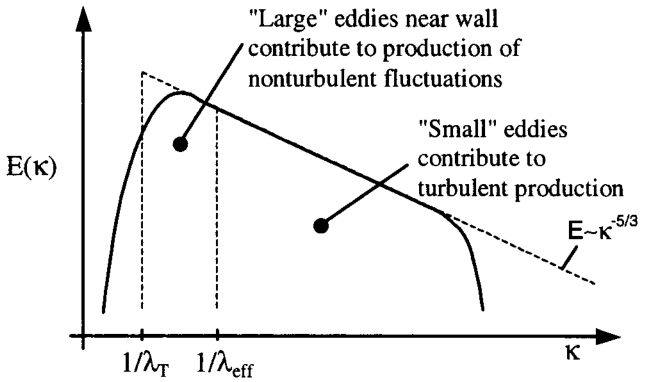

Fig. 1 Illustration of wall-limiting concept leading to “splat mechanism” for production of k_L

Volino [10] considered the possibility that growth of k_L is due to a ‘‘splat mechanism,’’ similar to that discussed by Bradshaw [19]. The wall redirects the normal fluctuation into a streamwise component, at the same time creating local pressure gradients in the boundary layer, and leading to disturbance amplification. This mechanism is decidedly different from typical turbulence production, and is adopted herein as a reasonable explanation of the development and amplification of k_L. Since ‘‘splats’’ are likely to occur only for eddies with large length scales relative to the wall distance, we have assumed that the turbulent energy spectrum can be divided into wall-limited (large scales) and non-wall-limited (small scales) sections in the near-wall region (Fig. 1), where the cutoff eddy size is designated λ_eff, since it is the effective turbulent length scale for the small scale turbulence. Scales smaller than λ_eff interact with the mean flow as typical turbulence and larger scales contribute to the production mechanism for k_L. The small scale component of k_T is dubbed $k_{\mathrm{T,s}}$, and the large-scale component is $k_{\mathrm{T,l}}$. Note that far from walls, in the free stream, $k_{\mathrm{T,s}} \rightarrow k_\mathrm{T}$ and $k_{\mathrm{T,l}} \rightarrow 0$, and the splat mechanism is nonexistent.

The dynamics of k_L have been found to be quite universal. Fluctuation energy grows linearly with Re_x for flat plate boundary layers, where the linearity constant depends on the level of free-stream turbulence [12,20]. The frequency content of k_L has also been found to be relatively independent of the forcing spectrum, provided the forcing is broadband [14,21]. Both of these observations suggest that a relatively simple modeling approach may be capable of resolving the fluctuation growth in the pre-transitional region.

Another region of interest is the transition zone itself. Jacobs and Durbin [14] showed that bypass transition is initiated by an instability of the upstream fluctuations, which leads to turbulent spot development and progression to full turbulence. It is not clear what initiates the instability. In the new model, a local transition parameter is implemented that depends on the turbulence energy, effective length scale, and fluid viscosity, based in part on observations of Andersson et al. [21]. Once this parameter reaches a certain value, transition is assumed to begin, which results in a transfer of energy from the streamwise fluctuations k_L to the turbulent fluctuations k_T. It is accompanied by a change in length scale of the turbulence, as would occur in actual spot breakdown processes.

Downstream of transition, the model predicts a fully turbulent boundary layer. Almost all of the fluctuation energy is turbulent, but a small amount of k_L is still present within the viscous sublayer. This agrees qualitatively with experimental observations indicating the presence of streamwise-oriented streaky structures in the viscous sublayer and buffer region that bear a resemblance to those in the pre-transitional region.

Although bypass transition is recognized to occur for Tu_∞ greater than 1%, the downstream location of transition is in fact shortened by turbulence intensities greater than about 0.1% [22]. This suggests that there is a ‘‘mixed’’ transition regime involving elements of both natural and bypass transition. In order to include natural and mixed mode transition into the new model, modifications must be made to both the k_L production terms and the transition ‘‘production’’ term that governs transfer of energy between streamwise fluctuations and turbulent energy. These modifications necessarily do not depend directly on turbulence quantities, but depend instead on the local mean flow and the laminar kinetic energy k_L.

2.2 Model Equations. The model developed in this study is a three equation, linear, eddy-viscosity type. In addition to the mean flow variables U_i, P, and θ, equations are solved for the turbulent kinetic energy k_T, laminar kinetic energy k_L, and far-field dissipation rate ε. The influence of turbulent and laminar fluctuations on the mean flow and energy equations is included through prescription of a total eddy viscosity and total eddy thermal diffusivity, respectively:

$$-\overline{u_i u_j} = \nu_{TOT}\left(\frac{\partial U_i}{\partial x_j}+\frac{\partial U_j}{\partial x_i}\right)-\frac{2}{3}k_{TOT}\delta_{ij} \tag{1}$$

$$-\overline{u_i \theta} = \alpha_{\theta,TOT}\frac{\partial \theta}{\partial x_i}. \tag{2}$$

As discussed above, the turbulent energy k_T is assumed in the near-wall region to be split into small scale energy $k_{T,s}$, which contributes directly to turbulence production, and large scale energy $k_{T,l}$, which contributes to production of laminar kinetic energy through the splat mechanism discussed in Sec. 2.1. The cutoff is the effective length scale, defined as

$$\lambda_{eff} = \mathrm{MIN}(C_\lambda d, \lambda_T), \tag{3}$$

where λ_T is the turbulent length scale:

$$\lambda_T = \frac{k^{3/2}}{\varepsilon}. \tag{4}$$

The energies are then calculated assuming the Kolmogorov inertial range spectrum applies over all wave numbers greater than $1/\lambda_T$:

$$k_{T,s} = k_T\left(\frac{\lambda_{eff}}{\lambda_T}\right)^{2/3}, \tag{5}$$

$$k_{T,l} = k_T\left[1-\left(\frac{\lambda_{eff}}{\lambda_T}\right)^{2/3}\right]. \tag{6}$$

The sum of Eqs. (5) and (6) is the turbulent kinetic energy k_T.

The transport equations for k_T, k_L, and ε are as follows, in their incompressible form:

$$\frac{Dk_T}{Dt} = P_T + R + R_{NAT} - \varepsilon - D_T + \frac{\partial}{\partial x_j}\left[\left(\nu+\frac{\alpha_T}{\sigma_k}\right)\frac{\partial k_T}{\partial x_j}\right], \tag{7}$$

$$\frac{Dk_L}{Dt} = P_L - R - R_{NAT} - D_L + \frac{\partial}{\partial x_j}\left[\nu\frac{\partial k_T}{\partial x_j}\right], \tag{8}$$

$$\frac{D\varepsilon}{Dt} = C_{\varepsilon 1}\frac{\varepsilon}{k_T}(P_T+R_{NAT}) + C_{\varepsilon R}R\frac{\varepsilon}{\sqrt{k_T k_L}} - C_{\varepsilon 2}\frac{\varepsilon^2}{k_T} - \frac{\varepsilon}{k_T}D_T + \frac{\partial}{\partial x_j}\left[\left(\nu+\frac{\alpha_T}{\sigma_\varepsilon}\right)\frac{\partial \varepsilon}{\partial x_j}\right]. \tag{9}$$

The first term on the right-hand side of Eq. (7) is the production of turbulence by turbulent fluctuations:

$$P_T = \nu_{T,s}S^2. \tag{10}$$

The small-scale turbulent viscosity $\nu_{T,s}$ is defined as

$$\nu_{T,s} = f_\nu f_{\tau,s} C_\mu \sqrt{k_{T,s}}\lambda_{eff}. \tag{11}$$

C_μ is the turbulent viscosity coefficient, taken to be 0.09 in the equilibrium region of a fully turbulent boundary layer. The importance of realizability for turbulence modeling is well established [23,24], and can be imposed through C_μ. The present work adopts a simplified form of that documented by Shih et al. [25]:

$$C_\mu = \frac{1}{A_0 + A_s\left(\frac{Sk_T}{\varepsilon}\right)}. \tag{12}$$

f_ν and $f_{\tau,s}$ are damping functions, the former to impose viscous effects, and the latter based on time scales, to account for the inability of slow turbulent eddies to couple with rapid strain rates in the boundary layer. Their forms are

$$f_\nu = 1-\exp\left(-\frac{\sqrt{\mathrm{Re}_{T,s}}}{A_\nu}\right), \tag{13}$$

$$f_{\tau,s} = 1-\exp\left[-C_{\tau,s}\left(\frac{\tau_m}{\tau_{T,s}}\right)^2\right], \tag{14}$$

where $\mathrm{Re}_{T,s}$ is the turbulent Reynolds number for the small, turbulence producing scales,

$$\mathrm{Re}_{T,s} = \frac{k_{T,s}^2}{\nu\varepsilon}, \tag{15}$$

and the mean and effective turbulent time scales in Eq. (14) are given by

$$\tau_m = \frac{1}{S}, \tag{16}$$

$$\tau_{T,s} = \frac{\lambda_{eff}}{\sqrt{k_{T,s}}}. \tag{17}$$

The first term on the right-hand side of Eq. (8) is the production of laminar kinetic energy by large-scale turbulent fluctuations:

$$P_L = \nu_{T,l}S^2. \tag{18}$$

If only bypass transition is considered, the large-scale turbulent viscosity $\nu_{T,l}$ is modeled as

$$\nu_{T,l} = f_{\tau,l}C_{11}\left(\frac{\Omega\lambda_{eff}^2}{\nu}\right)\sqrt{k_{T,l}}\lambda_{eff}, \tag{19}$$

where the damping function $f_{\tau,l}$ is similar to $f_{\tau,s}$ above:

$$f_{\tau,l} = 1-\exp\left[-C_{\tau,l}\left(\frac{\tau_m}{\tau_{T,l}}\right)^2\right], \tag{20}$$

$$\tau_{T\ell} = \frac{\lambda_{eff}}{\sqrt{k_{T,l}}}. \tag{21}$$

Equation (19) indicates that production of laminar streamwise fluctuations by large-scale turbulence requires wall proximity—since $k_{T,l}=0$ in the far field—as well as vorticity. Streamwise disturbances will not grow in the presence of irrotational straining alone (e.g., stagnation flow outside of the viscous near-wall layer).

Both the k_T and k_L equations include an explicit calculation of the near-wall dissipation that arises from the no-slip condition on turbulent and laminar fluctuations:

$$D_{\mathrm{T}}=2\nu\frac{\partial\sqrt{k_{\mathrm{T}}}}{\partial x_{\mathrm{j}}}\frac{\partial\sqrt{k_{\mathrm{T}}}}{\partial x_{\mathrm{j}}}, \tag{22}$$

$$D_{\mathrm{L}}=2\nu\frac{\partial\sqrt{k_{\mathrm{L}}}}{\partial x_{\mathrm{j}}}\frac{\partial\sqrt{k_{\mathrm{L}}}}{\partial x_{\mathrm{j}}}, \tag{23}$$

and the total dissipation rate of fluctuation energy $\varepsilon_{\mathrm{TOT}}$ is defined as

$$\varepsilon_{\mathrm{TOT}}=\varepsilon+D_{\mathrm{T}}+D_{\mathrm{L}}. \tag{24}$$

The term R that appears in Eqs. (7)–(9) represents the averaged effect of the breakdown of streamwise fluctuations into turbulence during bypass transition. It is specifically the rate of production of turbulent kinetic energy by laminar kinetic energy during the bypass transition process. It appears with opposite sign in Eqs. (7) and (8), resulting in no net change of total fluctuation energy. Its presence in Eq. (9) causes a decrease of turbulent length scale from the initial (approximately freestream) value to a value dependent on wall distance, since the length scale in the inertial range of a fully turbulent boundary layer scales linearly with wall distance. Since the breakdown process is modeled as production of turbulence by the laminar fluctuations, the R term is assumed proportional to the laminar fluctuation energy k_{L} and inverse to the effective turbulent time scale τ_{T}:

$$R=C_{\mathrm{R}}\beta_{\mathrm{BP}}\frac{k_{\mathrm{L}}}{\tau_{\mathrm{T}}}, \tag{25}$$

$$\tau_{\mathrm{T}}=\frac{\lambda_{\mathrm{eff}}}{\sqrt{k_{\mathrm{T}}}}. \tag{26}$$

The threshold function β_{BP} controls the bypass transition process:

$$\beta_{\mathrm{BP}}=1-\exp\left(-\frac{\phi_{\mathrm{BP}}}{A_{\mathrm{BP}}}\right), \tag{27}$$

$$\phi_{\mathrm{BP}}=\mathrm{MAX}\left[\left(\frac{\sqrt{k_{\mathrm{T}}}d}{\nu}-C_{\mathrm{BP,crit}}\right),0\right]. \tag{28}$$

It is assumed that laminar fluctuations break down whenever the turbulent kinetic energy is greater than some threshold value, relative to the wall distance and fluid kinematic viscosity. Put another way, transition initiates when the laminar streamwise fluctuations are transported a certain distance from the wall, where that distance is determined by the energy content of the free stream, and the kinematic viscosity. This concept is consistent with the observations of Jacobs and Durbin [14] regarding breakdown of backward jets (pre-transitional fluctuations) to small-scale turbulence near the top of the boundary layer. In order to induce a rapid reduction of the turbulence length scale during the early stages of transition, the coefficient $C_{\varepsilon\mathrm{R}}$ is assigned the form

$$C_{\varepsilon\mathrm{R}}=0.21*\left(\frac{1.5\lambda_{\mathrm{T}}}{\lambda_{\mathrm{eff}}}-1\right). \tag{29}$$

Modifications are included in order to allow prediction of natural and mixed transition modes in addition to bypass transition. The production of laminar fluctuations is governed by the large-scale turbulent viscosity $\nu_{\mathrm{T,l}}$ (Eq. (19)). To include development of Tollmein-Schlichting waves, an instability component is added that is independent of free-stream turbulence, and the modified form is

$$\nu_{\mathrm{T,l}}=f_{\tau,1}C_{11}\left(\frac{\Omega\lambda_{\mathrm{eff}}^{2}}{\nu}\right)\sqrt{k_{\mathrm{T,l}}}\lambda_{\mathrm{eff}}+\beta_{\mathrm{TS}}C_{12}\phi_{\mathrm{NAT}}d^{2}\Omega. \tag{30}$$

Equation (30) includes a Tollmien-Schlichting threshold function,

$$\beta_{\mathrm{TS}}=1-\exp\left(-\frac{\mathrm{MAX}(\phi_{\mathrm{NAT}}-C_{\mathrm{TS,crit}},0)^{2}}{A_{\mathrm{TS}}}\right), \tag{31}$$

and a natural transition parameter based on wall distance, strain rate, and kinematic viscosity:

$$\phi_{\mathrm{NAT}}=\frac{d^{2}S}{\nu}. \tag{32}$$

Additionally, the breakdown to turbulence due to instabilities is included as a separate natural transition "production" term:

$$R_{\mathrm{NAT}}=C_{\mathrm{R,NAT}}\beta_{\mathrm{NAT}}k_{\mathrm{L}}S, \tag{33}$$

$$\beta_{\mathrm{NAT}}=1-\exp\left[-\frac{\mathrm{MAX}(\phi_{\mathrm{NAT}}^{0.75}\phi_{\mathrm{MIX}}^{0.25}-C_{\mathrm{NAT,crit}},0)}{A_{\mathrm{NAT}}}\right], \tag{34}$$

$$\phi_{\mathrm{MIX}}=\frac{\sqrt{k_{\mathrm{L}}}d}{\nu}. \tag{35}$$

Note that neither the modified form of $\nu_{\mathrm{T,l}}$ (Eq. (30)) nor the expressions in Eqs. (31)–(35) depend directly on the turbulence quantities. However, in order to model the "mixed" transition mode, the level of laminar kinetic energy is assumed to influence the location of "natural" transition, as indicated by Eqs. (34) and (35).

In Eq. (9), the coefficient $C_{\varepsilon 1}$ is assigned the following functional form:

$$C_{\varepsilon 1}=2\left[1-\left(\frac{\lambda_{\mathrm{eff}}}{\lambda_{\mathrm{T}}}\right)^{4/3}\right]+1.44\left(\frac{\lambda_{\mathrm{eff}}}{\lambda_{\mathrm{T}}}\right)^{4/3}. \tag{36}$$

The effect of the modified $C_{\varepsilon 1}$ is to decrease the turbulent length scale in the presence of turbulence production, when close to the wall. Far from walls, the coefficient takes its typical high-Re value of 1.44, and turbulence production tends to increase the length scale.

The total eddy viscosity and eddy diffusivity included in Eqs. (1) and (2) are given by

$$\nu_{\mathrm{TOT}}=\nu_{\mathrm{T,s}}+\nu_{\mathrm{T,l}}, \tag{37}$$

$$\alpha_{\theta,\mathrm{TOT}}=\frac{\nu_{\mathrm{T,s}}}{\mathrm{Pr}_{\theta}}+C_{\alpha,\theta}\sqrt{k_{\mathrm{T,l}}}\lambda_{\mathrm{eff}}. \tag{38}$$

Finally, the turbulent scalar diffusivity in Eqs. (7) and (9) is given by

$$\alpha_{\mathrm{T}}=f_{\nu}C_{\mu,\mathrm{std}}\sqrt{k_{\mathrm{T,s}}}\lambda_{\mathrm{eff}}. \tag{39}$$

The inlet boundary conditions for k_{T} and ε are set as constant values, determined as for any form of k-ε model. If the inlet is located in the free stream, far from any solid boundary, then k_{L} is set to zero. At solid walls, all three model equations use zero-flux conditions:

$$\frac{\partial k_{\mathrm{T}}}{\partial\eta}=0, \tag{40}$$

$$\frac{\partial k_{\mathrm{L}}}{\partial\eta}=0, \tag{41}$$

$$\frac{\partial\varepsilon}{\partial\eta}=0, \tag{42}$$

where η is the local wall-normal coordinate direction. This choice of boundary condition eliminates any diffusive transport of fluctuation energy out of the domain. It also leads to very small finite values of k_{T} and k_{L} being computed at the wall in the simulations. These wall values do not directly influence the simulation and can be set to zero during post-processing without detriment. During processing of the simulation, the wall values of k_{T} and k_{L} used to compute the gradients in Eqs. (22) and (23) are set to zero.

The model constants are summarized in Table 1. These constants were determined based on numerical experiments with fully turbulent channel flow and flat-plate boundary layer simulations.

Table 1 Summary of model constants

$A_0=4.04$	$C_{\mathrm{CAT,crit}}=460$	$C_{\tau,s}=4360$
$A_{\mathrm{s}}=2.12$	$C_{\mathrm{TS,crit}}=1000$	$C_{\varepsilon 2}=1.92$
$A_\nu=5.5$	$C_{\mathrm{R,NAT}}=4$	$C_\lambda=2.495$
$A_{\mathrm{BP}}=8$	$C_{11}=0.0000034$	$C_{\mu,\mathrm{std}}=0.09$
$A_{\mathrm{NAT}}=120$	$C_{12}=6*10^{-11}$	$\mathrm{Pr}_\theta=1.5$
$A_{\mathrm{TS}}=2000$	$C_{\mathrm{R}}=0.21$	$\sigma_k=1$
$C_{\mathrm{BP,crit}}=35$	$C_{\tau,1}=4360$	$\sigma_\varepsilon=1.4$

3 Test Cases

The model described by the above equations was implemented into FLUENT version 6.0.12 (Fluent, Inc.) using user-modified subroutines. New primary variables were defined for k_{T}, k_{L}, and ε using the user-defined scalar capability available in FLUENT. The source terms and effective diffusivities were supplied through user-defined function (UDF) subroutines. Similarly, the effective turbulent viscosity and diffusivities in Eqs. (1) and (2) were prescribed using UDF's. This approach to model implementation in FLUENT has been tested by developing in-house UDF versions of both the standard k-ε (SKE) model and the realizable k-ε (RKE) model [25] at Clemson University. These models have been applied to numerous test cases, and been found to yield identical results to those obtained with the same models available internally in FLUENT.

3.1 Fully Turbulent Channel Flow. To be generally applicable to a wide range of problems, the model described above must yield the correct behavior in fully turbulent flows downstream of transition. A simple test case is available in fully developed turbulent flow in a nonrotating plane channel. The DNS data of Kim et al. [26] were used for comparison purposes, for the case of $\mathrm{Re}_\tau=395$. For this case, in addition to the FLUENT implementation, the model was tested using a one-dimensional (1D) channel code written and processed with MATLAB (MathWorks, Inc). This was intended as yet another check of the UDF implementation in FLUENT. Results from the two codes were identical.

Figure 2 shows the profiles of mean velocity and total fluctuation energy k_{TOT}. Results are compared to the DNS data, and also to results using the standard k-ε (SKE) model available in FLUENT with a two-layer near-wall treatment. It is apparent that the current model performs at least as well as the "industry standard" for this fully turbulent flow. Figure 3 shows the separate components of the total fluctuation energy for the current model. Even in fully turbulent flow, there is still evidence of laminar fluctuations very near the wall, although the magnitude is relatively small. This is likely due to the similarity between the viscous sublayer of the turbulent boundary layer and the pre-transitional boundary layer with high Tu_∞.

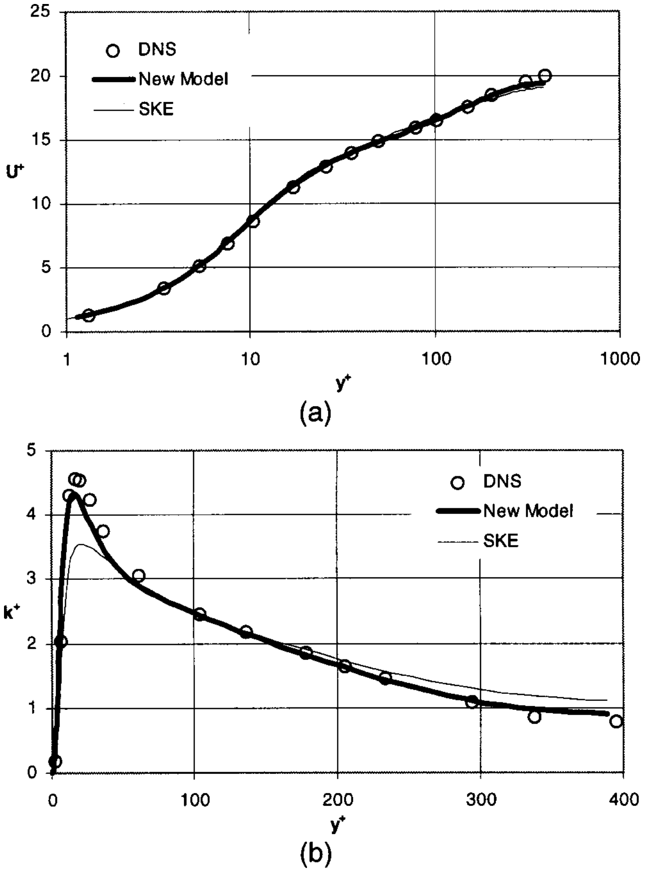

Fig. 2 Profiles of mean velocity (*a*) and total fluctuation kinetic energy (*b*) for fully developed turbulent channel flow

3.2 Flat-Plate Boundary Layer. The simplest test case for transition prediction is the 2D flat-plate boundary layer without curvature or streamwise pressure gradients. For this case the experimental data of Blair [27] were used for comparison purposes. Results were obtained for transitional boundary layers with varying Tu_∞ of 0.2%, 2.6%, and 6.2%. An additional computational test was run with very low Tu_∞ equal to 0.02%. The test case geometry is illustrated in Fig. 4. The computational domain extended 2.9 m downstream of the plate leading edge for the cases of Tu_∞ equal 2.6% and 6.2%, and 5.2 m for the cases of Tu_∞ equal 0.02% and 0.2%. This corresponded to a maximum Re_{x} of approximately 2×10^6 and 3.5×10^6, respectively, with an inlet velocity of 10 m/s. The domain extended 175 mm in the wall normal direction, and a symmetry condition was applied at the top. The resulting freestream acceleration over the entire length of the plate was for all cases less than 5%, and the reference freestream velocities in Re_{x} and St were adjusted accordingly. The computational inlet extended 50 mm upstream of the flat plate leading edge, and a symmetry plane was applied at the bottom of the domain, upstream of the leading edge. This allowed for a natural stagnation of the free-stream flow and boundary layer start. One of the advantages of the current model is the elimination of any need to prescribe initial boundary layer profiles. Both the experiments and computations included a relatively short unheated starting length that extended to $\mathrm{Re}_{\mathrm{x}}=8.31\times10^4$, and a constant heat flux was applied downstream of this point.

The simulations used a 2D Cartesian grid with 635 cells (high Tu_∞ cases) or 675 cells (low Tu_∞ cases) in the streamwise direction, and 105 cells in the wall-normal direction. Grid stretching

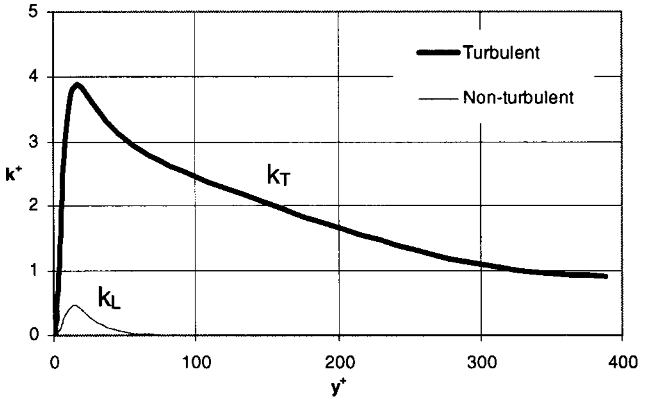

Fig. 3 Distribution of turbulent (k_{T}) and nonturbulent (k_{L}) fluctuations in fully developed turbulent channel flow

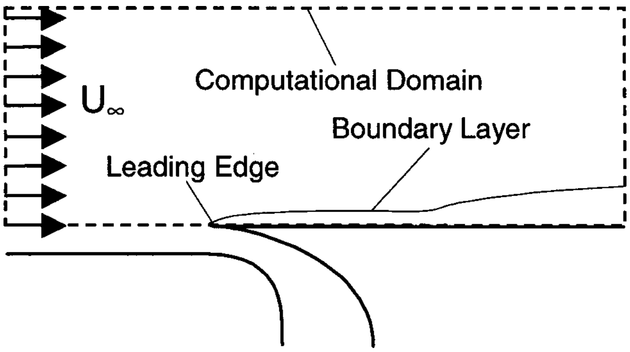

Fig. 4 Illustration of flat-plate boundary layer test case

was used to cluster cells near the wall and near the plate leading edge. The first cell sizing was such that y^+ was less than one everywhere.

The inlet values of k_T and ε for each case were chosen so that the downstream decay of free-stream turbulence exactly matched the results reported in Ref. [27]. As stated in Sec. 2.2, the laminar kinetic energy k_L was set to zero at the inlet.

The surface results are presented in Fig. 5. The plots show Stanton number versus Reynolds number, for each of the test conditions, along with measured data for the same conditions. The exact laminar solution is also shown for reference purposes. The new model indicates clear transition behavior, and the transition location moves upstream as Tu_∞ is increased. The overall levels of St are predicted fairly well, including the augmentation of heat transfer in the pre-transitional boundary layer for the cases with 2.6 % and 6.2 % free-stream turbulence. The worst agreement is in the downstream portion of the transition region for the two highest Tu_∞ cases. The model predicts a slight overshoot versus the measured data, but relaxes toward the turbulent asymptote farther downstream. The reasons for this are not known, but may be related to the manner in which the model accounts for the transfer of energy between k_L and k_T in the transition zone. Future work will address this issue. For comparison, the results with the RKE model [25] with a two-layer near-wall treatment [28] are also shown. The RKE model predicts a turbulent boundary layer from just downstream of the plate leading edge, regardless of Tu_∞. This should not be interpreted as a weakness in the RKE model, since it is not intended to resolve transition. The results are simply included as a reference for currently available single-point, eddy viscosity turbulence models, and to highlight the importance of resolving transition for heat transfer prediction.

Although it is not obvious from these plots, examination of the results revealed that the two highest Tu_∞ cases underwent a purely bypass transition while the 0.2% case underwent natural or "mixed" transition, according to the model. Whether this agrees with the experimental test case is uncertain, but it does indicate that the model performs as intended. Results are not shown for the case of Tu_∞ equal to 0.02%, since there is no experimental counterpart. However, the simulations indicate that natural transition onset occurs at $Re_x = 2.9 \times 10^6$, which agrees satisfactorily with the value of 2.8×10^6 documented in Schlichting [22].

Figure 6 shows the development of the nonturbulent streamwise fluctuations in the pre-transitional boundary layer, for the case of Tu_∞ equal to 2.6%. The figure shows k_L versus nondimensional wall distance at four downstream locations. The most significant aspect is the fact that the fluctuation energy grows approximately linearly with downstream Reynolds number, as determined experimentally and analytically by Matsubara and Alfredsson [12] and Luchini [20], respectively. Figure 7(*a*) shows plots of the total streamwise fluctuation intensity u' versus y/δ at four different downstream locations. Note that in the new model, all of the laminar fluctuation energy is assumed to be oriented in the streamwise direction, therefore $u' = \sqrt{\frac{2}{3}k_T + 2k_L}$. The results are compared to similar experimental results reported in Mayle and Schulz [15] for Tu_∞ in the range of 2–3%. In Fig. 7(*b*), the same results are plotted for the case of Tu_∞ equal to 6.2%, $Re_x = 4.3 \times 10^4$, and compared to experimental results [15] at the same Re_x and Tu_∞ equal to 5.4%. Both comparisons indicate that the current model reproduces pre-transitional fluctuations at levels comparable to those seen in experiments for flat plate boundary layers. The current simulations apparently slightly underpredict the total streamwise fluctuation strength, but this may be due to the fact that the turbulent contribution is assumed to be isotropic.

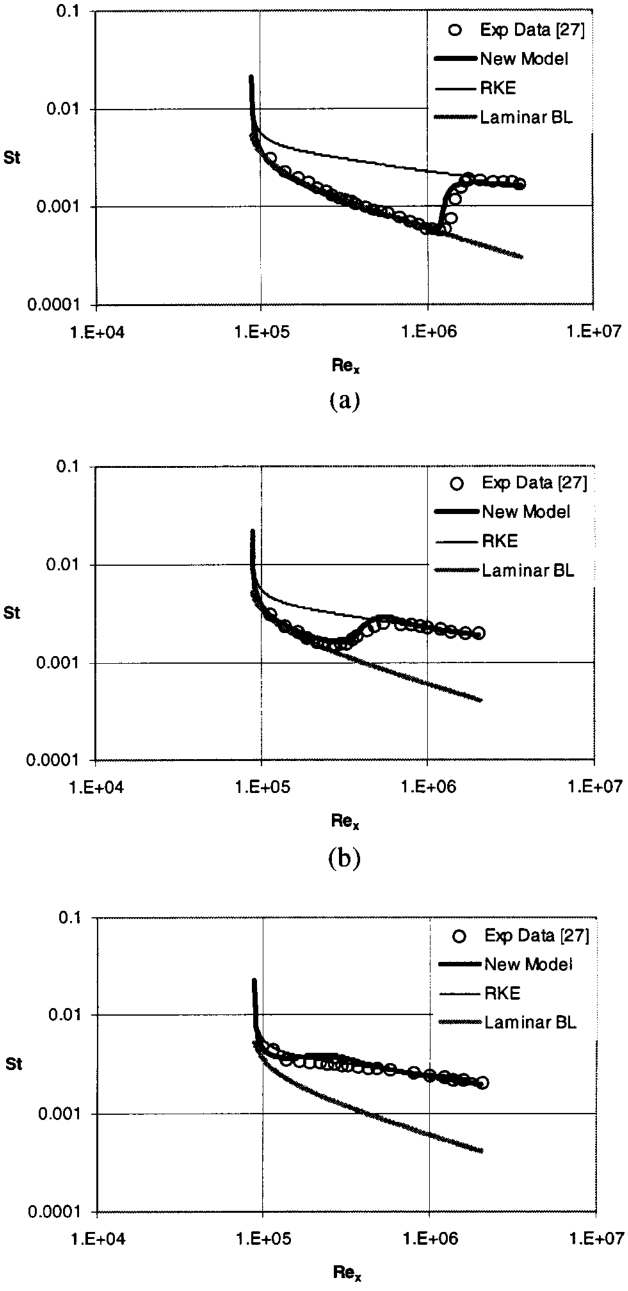

(a)

(b)

(c)

Fig. 5 Stanton number versus downstream Reynolds number for each of the three flat plate cases: $Tu_\infty = 0.2\%$ (*a*), $Tu_\infty = 2.6\%$ (*b*), and $Tu_\infty = 6.2\%$ (*c*)

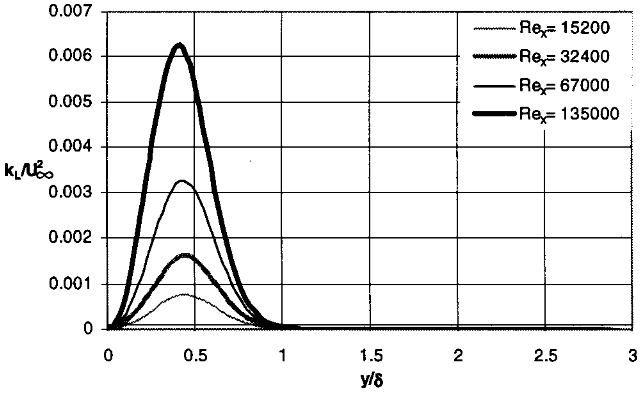

Fig. 6 Profiles of laminar kinetic energy k_L in the pre-transitional region of the boundary layer $Tu_\infty=2.6\%$. The peak value of k_L increases approximately linearly with downstream Reynolds number.

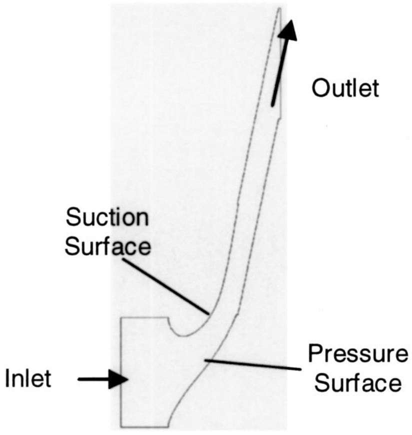

Fig. 8 Illustration of computational domain for nozzle guide vane test case, indicating high turning and acceleration of passage flow

3.3 Highly Loaded Turbine Airfoil. The final test case considered in this study was that of flow over a nozzle guide vane. This case is considerably more challenging than the flat plate considered above, since the flow undergoes significant turning and experiences relatively strong pressure gradients. In addition the range of Tu_∞ is much greater, from 0.6% to 19.5%. The validation case was documented by Radomsky and Thole [29,30], who performed experiments with the purpose of providing code-validation-quality data for CFD methods development. This experimental study is an excellent validation case since it provides data for a realistic, high turning guide vane, with turbulence levels comparable to those exiting the combustion chamber of actual gas turbines. Also significant is the fact that the study provides surface quantities—in the form of friction coefficient and Stanton number—as well as flow-field measurements in the freestream and within the boundary layer. The present work makes comparisons based on St alone; a more thorough comparison of both free-stream flow and boundary layer development is left for future study.

The 2D computational domain is shown in Fig. 8. The experimental study documented profiles of mean velocities, fluctuation energy, and turbulence length scale at the location indicated as the inlet in Fig. 8. The profiles showed little blade-to-blade variation, and so constant values for U_i, k_T, and ε were applied in the simulations, in order to match the average measured value of each of these quantities. A single blade-to-blade pitch was simulated, with periodic conditions applied at the boundary between adjacent airfoils, in order to model an infinite cascade. The airfoil surface was treated as a constant heat flux boundary condition, matching the experiments. The Reynolds number based on inlet velocity and chord length was 2.3×10^5. The maximum Mach number within the domain was less than 0.1, and so the flow was treated as incompressible. Further details of the geometry and experimental flow conditions may be found in Radomsky and Thole [29,30]. The computational grid for all of the airfoil simulations contained

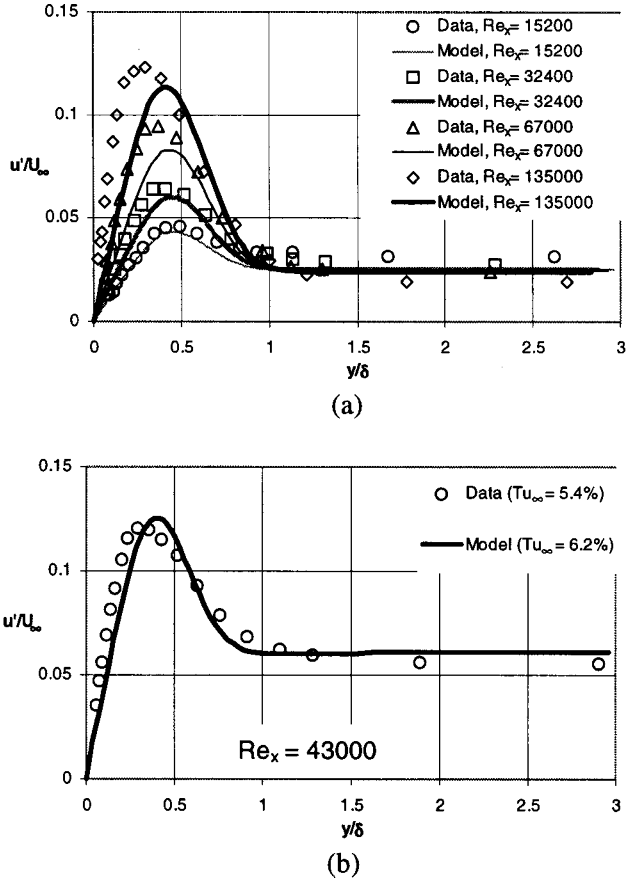

Fig. 7 Profiles of total fluctuation intensity in the pre-transitional region for $Tu_\infty=2.6\%$ (*a*) and $Tu_\infty=6.2\%$ (*b*). The model predicts fluctuation levels comparable to experimental data documented in Ref. [15].

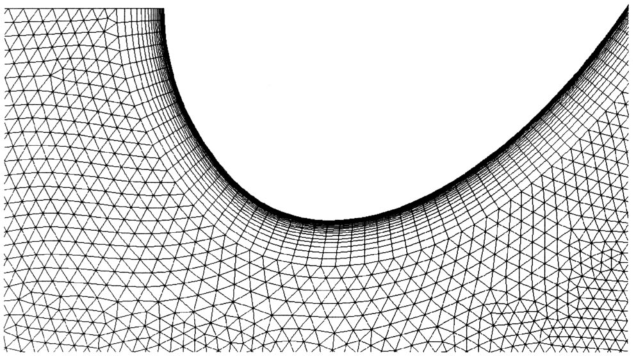

Fig. 9 Closeup of 2D grid near the leading edge on the suction surface, highlighting the multitopology mesh used to accurately resolve boundary-layer region

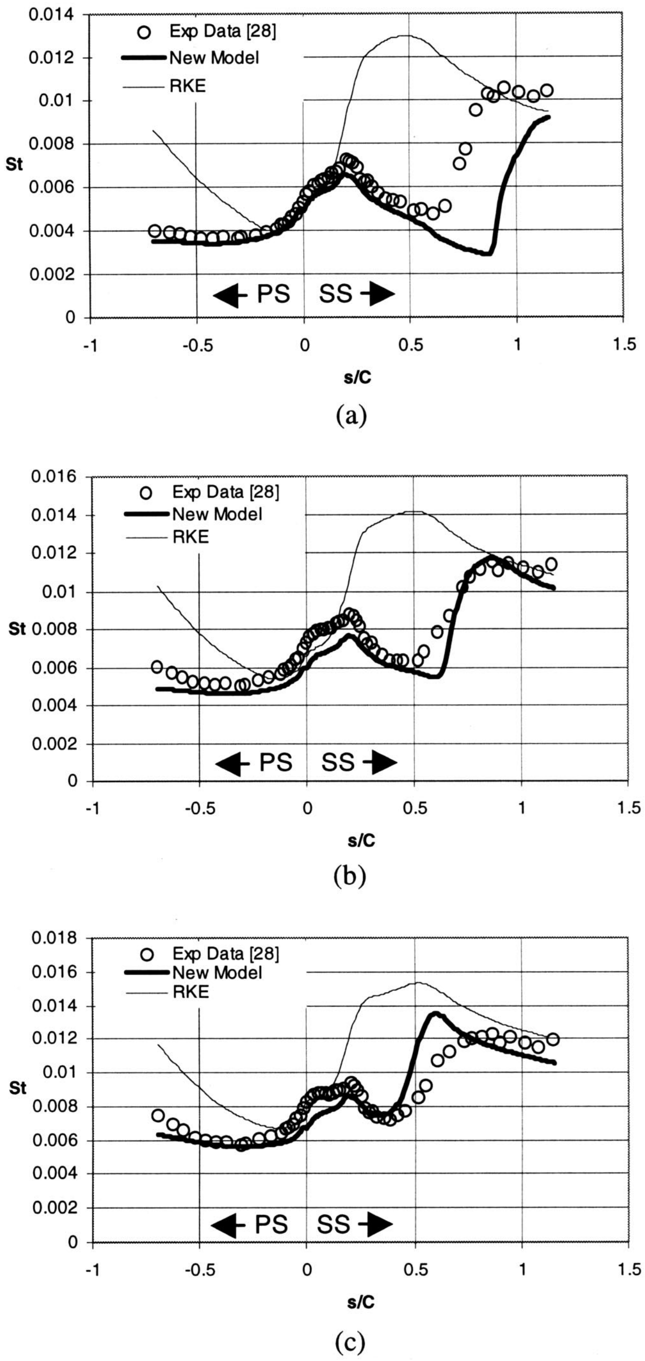

(a)

(b)

(c)

Fig. 10 Stanton number versus downstream distance for each of three airfoil cases considered in the present study: $\mathrm{Tu}_\infty=0.6\%$ (*a*), $\mathrm{Tu}_\infty=10\%$ (*b*), and $\mathrm{Tu}_\infty=19.5\%$ (*c*)

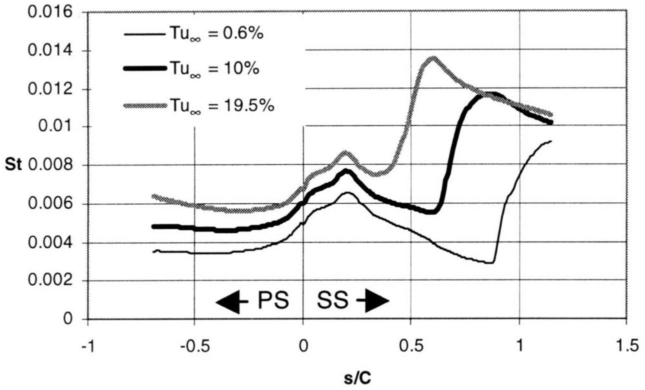

Fig. 11 Predicted Stanton number distribution for the three airfoil test cases, using the new model. The figure highlights the influence of freestream turbulence on the simulations.

approximately 32,000 cells, and utilized a hybrid topology, allowing stretched quadrilateral cells near the airfoil surface, and triangular cells in the irrotational free stream and in the downstream wake. An illustration of the grid near the leading edge on the suction surface is shown in Fig. 9.

Figures 10(*a*)–(*c*) show the Stanton number distribution along the airfoil on both the suction (SS) and pressure (PS) surfaces, for each of the three cases examined, corresponding to Tu_∞ equal to 0.6%, 10%, and 19.5%. Included in each plot are the measured data, the results from the current simulations, and the results obtained with the RKE model available in FLUENT. As in the flat plate simulations above, the new model clearly predicts transition behavior for all three cases, as compared to the RKE model, which as expected indicates a fully turbulent boundary layer from the leading edge onward.

In general, the new model correctly follows the trends of the experimental data. For the two highest turbulence cases, the model indicates that the suction surface boundary layer undergoes bypass transition, while the pressure surface boundary layer remains nonturbulent over the entire airfoil surface, similar to the experiments. The location of transition onset on the SS is shown to move upstream as Tu_∞ is increased. In the pre-transitional regions the model predicts the measured increase in heat transfer coefficient due to the freestream turbulence, though the levels are slightly lower than indicated by the experiments. The most significant disagreement is in the downstream portion of the transitional region for $\mathrm{Tu}_\infty=19.5\%$, where an overshoot is observed similar to the flat-plate cases in Section 3.2.

For the case of $\mathrm{Tu}_\infty=0.6\%$, the measured Stanton number distribution indicates transition onset on the suction surface at about $s/C=0.6$. However, the measured boundary-layer profiles reported in Ref. [30] show that the boundary layer is nonturbulent at $s/C=0.75$, in transition at $s/C=1.0$, and fully turbulent at $s/C=1.2$. For this low turbulence case, the transition location is highly sensitive to any free-stream or surface disturbances that may be present in the experiments. The discrepancy between the heat transfer [29] and boundary-layer profile [30] measurements is likely due to the use of two different vane test surfaces used for the two different sets of measurements [31]. Since any disturbances in the experiments are likely to shorten the transition onset length, it is especially encouraging that the new model agrees more closely with the boundary-layer profile measurements, even though it leads to an apparently significant disagreement with the St measurements in Fig. 10(*a*). For the higher turbulence cases discussed above, the transition location is dominated primarily by the free-stream fluctuations, and no discrepancy is present between the heat transfer and boundary-layer profile measurements [29–31]. For these cases, the new model shows better agreement with the experimental data.

Figure 11 shows the predicted Stanton number for all three airfoil cases. The figure highlights the predicted increase in St in the pre-transitional region due to the influence of freestream turbulence. It also clearly shows the transition location on the suction surface moving upstream as Tu_∞ increases. That the new model yields the correct trends for this complex test case is encouraging.

4 Summary and Conclusions

This paper has presented the development of a new turbulence modeling approach for prediction of boundary-layer transition. The model uses a relatively simple framework—eddy-viscosity

Reynolds-averaged Navier-Stokes—and is therefore easily implemented into existing in-house or commercial CFD codes, as demonstrated in the present study. There are two major concepts embodied in the current approach. First is the use of a new transport equation to represent the growth of nonturbulent, streamwise fluctuations in the pre-transitional boundary layer, an idea that builds upon the work of Mayle and Schulz [15]. Second is the incorporation of fluctuation growth due to a splat mechanism, as proposed by Volino [10]. Recent experimental and DNS studies of bypass transition have been used to determine universal features of the developing pre-transitional boundary layer, and to guide the model development in this study. In order to include natural and ‘‘mixed’’ mode transition, the equations that govern fluctuation growth and breakdown in bypass transition have been modified to account for the growth of Tollmien-Schlichting waves, and subsequent transition due to instabilities.

To the authors’ knowledge, this is the first truly single-point approach to transition modeling that specifically addresses pre-transitional fluctuation growth, the mechanism responsible for bypass transition [14]. The new model does not require any modification or user input based on integral or other nonlocal parameters. This is significantly different from other recently proposed models that include correlations based on downstream distance, boundary layer thickness, free-stream turbulence intensity, etc. The new approach differs from other single-point approaches, since these typically adopt a ‘‘diffusion-controlled’’ model of bypass transition, and are therefore highly sensitive to initial and free-stream conditions.

The new model was implemented into a popular commercial code (FLUENT) using user-modified subroutines, and applied to the test cases of fully developed channel flow, flat-plate boundary layer with varying levels of freestream turbulence, and a modern, highly loaded turbine airfoil with significant variation of free-stream turbulence. For the latter two test cases, the new model clearly predicted transition for all conditions, and indicated the proper response to increases in free-stream turbulence intensity. Perhaps most encouraging is that the model yields reasonable results, even for two cases that represent extremes in terms of pressure gradients, streamline curvature, and range of Tu_∞. Future work will include further development and refinement of the model, but these initial results highlight the potential of the new approach to provide predictive capability in transitional flows.

Acknowledgments

Special thanks to Dr. Karen Thole, Virginia Polytechnic Institute and State University, for providing the authors with details of the turbine vane experimental test case, and for assistance in data interpretation. The authors gratefully acknowledge the continued support of Fluent, Inc. personnel, with special thanks to Rick Lounsbury and John Straus. Thanks as well to Will Robinson, Clemson University College of Engineering and Science Computer & Network Services, for excellent support of computing systems.

Nomenclature

C = airfoil chord length
C_μ = turbulent viscosity coefficient
D_L = laminar kinetic energy near-wall dissipation
D_T = turbulent kinetic energy near-wall dissipation
d = wall distance
E = turbulent energy spectral density
f_ν = viscous damping function
f_τ = time-scale damping function
k_L = laminar kinetic energy
k_T = turbulent kinetic energy
k_TOT = total fluctuation energy, $k_\mathrm{L}+k_\mathrm{T}$
k^+ = nondimensional fluctuation energy, k_TOT/u_τ^2
P = mean (Reynolds-averaged) pressure
P_L = laminar kinetic energy production term
P_T = turbulent kinetic energy production term
PS = airfoil pressure surface
Pr_T = turbulent Prandtl number
R = bypass transition production term
R_NAT = natural transition production term
Re_T = turbulence Reynolds number
Re_x = Reynolds number based on distance downstream of leadinge edge and free-stream velocity at leading edge
Re_τ = Reynolds number based on channel height and wall friction velocity
S = magnitude of mean strain rate tensor, $\sqrt{2S_\mathrm{ij}S_\mathrm{ij}}$
s = downstream distance from leading edge stagnation point
S_ij = strain rate tensor, $\frac{1}{2}(\partial U_\mathrm{i}/\partial x_\mathrm{j}+\partial U_\mathrm{j}/\partial x_\mathrm{i})$
SS = airfoil suction surface
St = Stanton number based on inlet velocity
Tu = turbulence intensity, u'/U
U = mean (Reynolds-averaged) streamwise velocity
U_i = mean (Reynolds-averaged) velocity vector
$-\overline{u_\mathrm{i}u_\mathrm{j}}$ = kinematic Reynolds stress tensor
$-\overline{u_\mathrm{i}\theta}$ = kinematic heat flux vector
u' = average streamwise fluctuation
u_τ = friction velocity
v' = wall-normal fluctuation
y^+ = nondimensional wall distance, yu_τ/ν
α_T = turbulent diffusivity for turbulent quantities
$\alpha_{\theta,\mathrm{TOT}}$ = total (laminar+turbulent) diffusivity for θ
β_BP = bypass transition threshold function
β_TS = Tollmien-Schlichting threshold function
β_NAT = natural transition threshold function
δ = 99% boundary-layer thickness
ε = far-field dissipation
ϕ_BP = bypass transition parameter
ϕ_NAT = natural transition parameter
η = local wall-normal coordinate direction
κ = wave number
λ_eff = effective (wall-limited) length scale
λ_T = turbulent length scale
ν = molecular kinematic viscosity
ν_T = turbulent kinematic viscosity
ν_TOT = total (laminar+turbulent) eddy viscosity
Ω = magnitude of mean rotation tensor, $\sqrt{2\Omega_\mathrm{ij}\Omega_\mathrm{ij}}$
Ω_ij = rotation rate tensor, $\frac{1}{2}(\partial U_\mathrm{i}/\partial x_\mathrm{j}-\partial U_\mathrm{j}/\partial x_\mathrm{i})$
θ = mean (Reynolds-averaged) temperature
τ_m = mean flow time scale
τ_T = turbulent time scale

Subscripts

i,j = indices
s = small scale
l = large scale
∞ = free-stream condition

References

[1] Walters, D. K., and Leylek, J. H., 2000, ‘‘Impact of Film-Cooling Jets on Turbine Aerodynamic Losses,’’ ASME J. Turbomach., **122**, pp. 537–545.
[2] Walters, D. K., and Leylek, J. H., 2002, ‘‘Computational Study of Film-Cooling Effectiveness on a Low-Speed Airfoil Cascade—Part II: Discussion of Physics,’’ ASME Paper No. DETC2002/CIE-34422.
[3] Savill, A. M., 1993, ‘‘Some Recent Progress in the Turbulence Modelling of By-Pass Transition,’’ in *Near-Wall Turbulent Flows*, So, R. M. C., Speziale, C. G., and Launder, B. E. (eds.), Elsiver Science, New York, pp. 829–848.
[4] Wilcox, D. C., 1994, ‘‘Simulation of Transition with a Two-Equation Turbulence Model,’’ AIAA J., **32**, pp. 247–255.
[5] Craft, T. J., Launder, B. E., and Suga, K., 1997, ‘‘Prediction of Turbulent Transitional Phenomena with a Nonlinear Eddy-Viscosity Model,’’ Int. J. Heat Fluid Flow, **18**, pp. 15–28.
[6] Chen, W. L., Lien, F. S., and Leschziner, M. A., 1998, ‘‘Non-Linear Eddy-Viscosity Modelling of Transitional Boundary Layers Pertinent to Turbomachine Aerodynamics,’’ Int. J. Heat Fluid Flow, **19**, pp. 297–306.

[7] Chernobrovkin, A., and Lakshminarayana, B., 1999, ''Turbulence Modeling and Computation of Viscous Transitional Flows for Low Pressure Turbines,'' ASME J. Fluids Eng., **121**, pp. 824–833.

[8] Suzen, Y. B., and Huang, P. G., 2000, ''Modeling of Flow Transition Using an Intermittency Transport Equation,'' ASME J. Fluids Eng., **122**, pp. 273–284.

[9] Steelant, J., and Dick, E., 2001, ''Modeling of Laminar-Turbulent Transition for High Freestream Turbulence,'' ASME J. Fluids Eng., **123**, pp. 22–30.

[10] Volino, R. J., 1998, ''A New Model for Free-Stream Turbulence Effects on Boundary Layers,'' ASME J. Turbomach., **120**, pp. 613–620.

[11] Baek, S. G., Chung, M. K., and Lim, H. J., 2001, ''k-ε Model for Predicting Transitional Boundary-Layer Flows Under Zero-Pressure Gradient,'' AIAA J., **39**, pp. 1699–1705.

[12] Matsubara, M., and Alfredsson, P. H., 2001, ''Disturbance Growth in Boundary Layers Subjected to Free-Stream Turbulence,'' J. Fluid Mech., **430**, pp. 149–168.

[13] Klebanoff, P. S., 1971, ''Effects of Free-Stream Turbulence on a Laminar Boundary Layer,'' Bull. Am. Phys. Soc., **16**.

[14] Jacobs, R. G., and Durbin, P. A., 2001, ''Simulations of Bypass Transition,'' J. Fluid Mech., **428**, pp. 185–212.

[15] Mayle, R. E., and Schulz, A., 1997, ''The Path to Predicting Bypass Transition,'' ASME J. Turbomach., **119**, pp. 405–411.

[16] Volino, R. J., and Simon, T. W., 1997, ''Boundary Layer Transition Under High Free-Stream Turbulence and Strong Acceleration Conditions: Part 2—Turbulent Transport Results,'' ASME J. Heat Transfer, **119**, pp. 427–432.

[17] Leib, S. J., Wundrow, D. W., and Goldstein, M. E., 1999, ''Effect of Free-Stream Turbulence and Other Vortical Disturbances on a Laminar Boundary Layer,'' J. Fluid Mech., **380**, pp. 169–203.

[18] Johnson, M. W., and Ercan, A. H., 1999, ''A Physical Model for Bypass Transition,'' Int. J. Heat Fluid Flow, **20**, pp. 95–104.

[19] Bradshaw, P., 1994, ''Turbulence: The Chief Outstanding Difficulty of Our Subject,'' Exp. Fluids, **16**, pp. 203–216.

[20] Luchini, P., 2000, ''Reynolds-Number-Independent Instability of the Boundary Layer Over a Flat Surface: Optimal Perturbations,'' J. Fluid Mech., **404**, pp. 289–309.

[21] Andersson, P., Berggren, M., and Henningson, D. S., 1999, ''Optimal Disturbances and Bypass Transition in Boundary Layers,'' Phys. Fluids, **11**, pp. 134–150.

[22] Schlichting, H., 1968, *Boundary Layer Theory*, 6th Edition, McGraw Hill, New York, 1968.

[23] Durbin, P. A., 1996, ''On the k-ε Stagnation Point Anomaly,'' Int. J. Heat Fluid Flow, **17**, pp. 89–90.

[24] Moore, J. G., and Moore, J., 1999, ''Realizability in Turbulence Modeling for Turbomachinery CFD,'' ASME Paper No. 99-GT-24.

[25] Shih, T.-H., Liou, W. W., Shabbir, A., Yang, Z., and Zhu, J., 1995, ''A New k-ε Eddy Viscosity Model for High Reynolds Number Turbulent Flows,'' Comput. Fluids, **24**, pp. 227–238.

[26] Kim, J., Moin, P., and Moser, R. D., 1987, ''Turbulence Statistics in Fully Developed Channel Flow at Low Reynolds Number,'' J. Fluid Mech., **177**, pp. 133–186.

[27] Blair, M. F., 1983, ''Influence of Free-Stream Turbulence on Turbulent Boundary Layer Heat Transfer and Mean Profile Development, Part I—Experimental Data,'' ASME J. Heat Transfer, **105**, pp. 33–40.

[28] Wolfstein, M., 1969, ''The Velocity and Temperature Distribution of One-Dimensional Flow with Turbulence Augmentation and Pressure Gradient,'' Int. J. Heat Mass Transfer, **12**, pp. 301–318.

[29] Radomsky, R. W., and Thole, K. A., 2000, ''Flowfield Measurements for a Highly Turbulent Flow in a Stator Vane Passage,'' ASME J. Turbomach., **122**, pp. 255–262.

[30] Radomsky, R. W., and Thole, K. A., 2001, ''Detailed Boundary-Layer Measurements on a Turbine Stator Vane at Elevated Freestream Turbulence Levels,'' ASME Paper No. 2001-GT-0169.

[31] Thole, K. A., 2002, personal communications.

Sean Jenkins
e-mail: sjenkins@mail.utexas.edu

Krishnakumar Varadarajan
e-mail: krish_v@mail.utexas.edu

David G. Bogard
e-mail: dbogard@mail.utexas.edu

Mechanical Engineering Department,
The University of Texas at Austin,
Austin, TX 78712

The Effects of High Mainstream Turbulence and Turbine Vane Film Cooling on the Dispersion of a Simulated Hot Streak

This paper presents the combined effects of high turbulence and film cooling on the dispersion of a simulated hot streak as it passes over a scaled-up nozzle guide vane. Experimental data demonstrates a considerable decay in the strength of a hot streak due to turbulence effects alone. Film cooling further reduces the peak temperature values resulting in a reduction of the peak temperature in the hot streak on the order of 75% relative to the upstream peak temperature in the hot streak. Comparisons are made between high turbulence ($Tu=20\%$) and moderate turbulence ($Tu=3.5\%$) as well as between different blowing conditions for the suction side, showerhead, and pressure side film cooling holes on a simulated nozzle guide vane. [DOI: 10.1115/1.1643911]

Introduction

Nonuniform temperature profiles, or ''hot streaks'' exiting the combustor in a gas turbine engine play a large role in failures of the first stage nozzle guide vanes and rotor blades due to thermal loading. Since the engine designer must account for the highest temperature levels in any portion of the turbine section, a greater level of effort is required when strong temperature gradients or hot streaks exist in the flow. Depending on the position of the hot streak relative to the first stage nozzle guide vane, a greater amount of cooling may be required to maintain vane surface temperatures at acceptable levels. Similarly, interactions of the hot streak with the vane and coolant may change the resultant surface temperature distribution and therefore the cooling requirements of the first stage rotor blades. Since the maximum exit temperature from the combustor is one of the primary limiting factors in gas turbine efficiency, it is crucial to understand how the hot streak is attenuated by turbulence conditions. Additionally, it is important to quantify how turbine vane film cooling further attenuates the hot streak, thereby affecting the durability of the rotor blades with respect to thermal loading.

As highlighted in the review paper by Dorney et al. [1], there have been numerous studies of the hot streak in turbine flows. Although these have been primarily numerical simulations, there have been several experimental studies. As described in the review paper, experimental hot streak simulations have been conducted by NASA Glenn Research Center (Schwab et al. [2] and Stabe et al. [3]), the United Technologies Research Center (Butler et al. [4]), and Massachusetts Institute of Technology (Shang et al. [5] and Shang and Epstein [6]). These researchers studied hot streaks in simulated vane cascades of one or more stages with a variety of hot streak configurations.

Among these, the NASA CERTS experiments, [2–3], were the only ones to consider somewhat realistic inlet conditions by using a circumferential slot with mass injection giving radially varying temperature and total pressure profiles. Their hot streak temperature ratio was 1.2, with a measurement location less than one chord length upstream of the vane, and the shape of the hot streak was roughly parabolic in the spanwise direction. However, since measurements were only taken downstream of the rotor, it is not possible to determine the shape or the strength of the hot streak in the stator/rotor axial gap.

The United Technologies Research Center tests performed by Butler et al. [4] were conducted in a low speed, rotating rig comprised of one stage with components that were not cooled, in which the approach flow to the first vane passed through a contraction. The hot streak consisted of heated air at a temperature ratio of 2.0, which was seeded with CO_2, and was introduced through a pipe in the middle of the vane passage at a radial location 40% above the hub. At the inlet of the stator passage, the hot streak was reported as a mostly flat profile, with high gradients at the edges. Carbon dioxide was used for concentration measurements to track the migration of the hot streak and for wall concentration measurements such that surface heat transfer could be inferred. The major findings from this study were that the rotor flow field was significantly affected by the hot streak with hotter gas migrating to the pressure side of the rotor.

The experiments conducted by Shang and Epstein [6] at MIT used two different hot streak configurations. Their facility consisted of a one and a half stage vane cascade oriented radially in the same manner as the actual engine. A discrete circular hot streak with a diameter length scale of one vane pitch with a temperature ratio of 1.1 and a radially varying, but circumferentially uniform hot streak with a temperature ratio of 1.1 were used to evaluate the effect of the hot streak on the rotor surface. Their measurements include a gas temperature profile at the entrance to the rotor section (downstream of the vane), but do not reference this profile to the upstream condition. In addition, these researchers chose two distinct turbulence levels generated by a turbulence grid at 3% and 8%, measured just upstream of the vane.

Later experiments using the United Technologies Large-Scale Rotating Rig were performed by Roback and Dring [7], where hot, neutral, and cold streaks were generated. The streak was again introduced through a pipe in the middle of the vane passage. Their hot streak temperature ratio was 1.5 and had a similar inlet shape to that of Butler et al. [4]. Carbon dioxide was used as a trace gas and the results were presented as normalized trace gas concentrations on the surface of the first stage rotor. Results accounted for density ratio, variation in spanwise position, and position relative to the vane. The bulk of the data were taken on the surface of the first stage rotor, but no information was available to allow one to ascertain the strength of the hot (or cold) streak immediately downstream of the first stage vane. Attenuation lev-

---

Contributed by the International Gas Turbine Institute and presented at the International Gas Turbine and Aeroengine Congress and Exhibition, Atlanta, GA, June 16–19, 2003. Manuscript received by the IGTI December 2002; final revision March 2003. Paper No. 2003-GT-38575. Review Chair: H. R. Simmons.

els as the hot streak passed around the vane were also not possible to determine since profiles upstream of the vane were not given. However, concentration profiles taken across the span in the plane of the rotor leading edge showed both the shape and peak levels were the same for the hot streak impacting the leading edge of the vane versus passing through the passage at mid-pitch. A simulation of trailing edge cooling was performed by coolant ejection at several coolant to freestream velocity ratios. However, results were not given for the combination of a hot streak and trailing edge coolant at the rotor leading edge as were given for the impinging and non-impinging hot streak.

For the above experimental studies, turbulence levels were not given with the exception of Shang and Epstein [6]; however, current combustor designs result in much higher turbulence intensity levels than those used. As such, the study of the attenuation of a hot streak under engine-like conditions of high turbulence has not yet been addressed. Additionally, there have been no previous experimental studies that addressed the effects of the interaction of a hot streak with a film cooled nozzle guide vane.

The computational studies that have been conducted on hot streaks range from two-dimensional, steady, inviscid simulations to three-dimensional, viscous, unsteady simulations. In general, the three-dimensional viscous simulations were found to better agree with the rotor flow angle distribution, which was attributed to the strong secondary flows that develop in the rotor. These studies have also shown the hot gas segregation in the rotor section, which cause high heat transfer to occur on the pressure side.

These experimental studies and most numerical simulations have primarily introduced the hot streak so that it passed through the middle of the vane passage and have been focused on the effect of the hot streak on the heat load on the rotor downstream of the first vane. In contrast to the Roback and Dring [7] study, the numerical simulations done by Gundy-Burlet and Dorney [8] showed that ''clocking'' the hot streak so that it is positioned at the leading edge of the vane results in a diminishing of the effect of the hot streak on the downstream rotor as evidenced by decreased rotor surface temperatures. This was attributed to the deceleration and increased mixing of the hot streak as it interacted with wake of the vane. However, fluid temperatures in the wake region were not documented, so an attenuation of the hot streak by impact on the vane was not confirmed.

The ratios of the hot streak temperature to mainstream temperature that have been used in previous studies have ranged from $T/T_\infty = 1.1$ to 2.5. Using numerical simulation, Dorney et al. [9] investigated the effect of the hot streak temperature ratio for a range of $T/T_\infty = 1.5$ to 2.5. Increasing the temperature ratio from $T/T_\infty = 1.5$ to 2.0 was found to have very little effect on the predicted kinematics of the hot streak, while higher temperature ratios would be affected more strongly. Gundy-Burlet and Dorney [10] noted that $T/T_\infty = 1.1$ to 1.6 was typical of engine operating environments. However, since ground-based power generation engines are generally designed to have more uniform temperatures at the combustor exit, it is reasonable to expect that characteristic temperature ratios for the hot streak would be at the low end of this range.

It has been generally accepted that hot streaks exiting the combustor survive the first row of turbine guide vanes to impact the first stage rotors. There have been no previous studies investigating the effects of high mainstream turbulence on the attenuation of a hot streak. It is clear that the hot streak, a co-flowing heated jet, will attenuate much more under high turbulence than under low to moderate turbulence conditions, however, no previous attempts have been made to quantify this effect for actual engine operating conditions. Furthermore, the interaction of a hot streak with a film cooled first stage guide vane has not been previously investigated. Therefore, establishing how much attenuation of a hot streak is possible in a rigorous and quantitative fashion by impacting a highly film cooled vane under conditions of high mainstream turbulence has obvious importance for turbine designs.

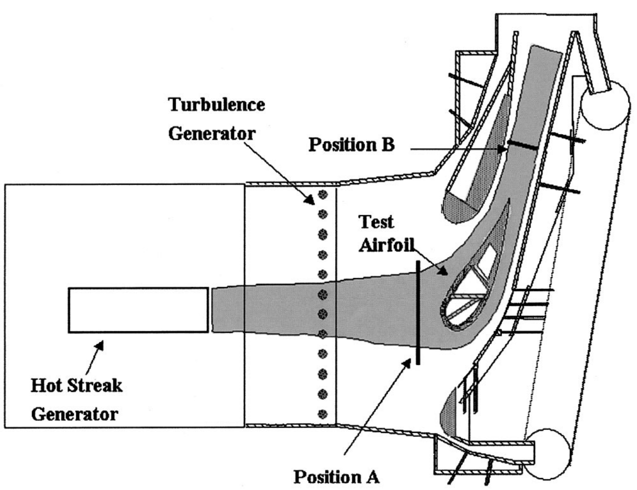

Fig. 1 Simulated vane cascade with hot streak generator

In the present study, experiments were conducted with a simulated hot streak to determine how mainstream turbulence, impact on the vane, and film cooling diminished the strength of the hot streak. The goal of the study was to determine how much the hot streak strength could be reduced by appropriate positioning of the hot streak and use of film cooling.

Facilities and Experimental Conditions

The test facility was a closed-loop, low-speed wind tunnel, driven by a 50 hp, variable pitch, variable speed fan. The test section, shown in **Fig. 1,** was a simulated three vane, two passage cascade with adjustable bleed and adjustable walls to maintain the proper flow around the test airfoil. A full description of the facility is given in Polanka [11].

The test airfoil was a scaled up model of a first stage turbine guide vane with the Reynolds number matched to actual engine operating conditions. The vane had a chord length of $C = 594\ \mathrm{mm}$, a span of $S = 550\ \mathrm{mm}$, and the pitch between airfoils was $P = 460\ \mathrm{mm}$. The mainstream approach velocity was $U_0 = 5.8\ \mathrm{m/s}$ for all experiments resulting in a Reynolds number of $\mathrm{Re} = 1.2 \times 10^6$ based on chord length and exit velocity. The test vane was constructed of polyurethane foam selected for strength and low thermal conductivity, with a value of $k = 0.048\ \mathrm{W/m \cdot K}$. For all coolant regions, the coolant hole diameter was $d = 4.11\ \mathrm{mm}$ and the pitch in the vertical, or spanwise, direction between coolant hole centerlines was $5.55d$.

Three separate regions of coolant holes were used in the present study. The showerhead region, shown in **Fig. 2(*a*),** had six rows of coolant holes with a row spacing of $3.33d$. These holes were oriented laterally, i.e., 90 deg to the streamwise direction, and had an injection angle of 25 deg relative to the surface. The pressure side film cooling holes are also shown in **Fig. 2(*a*),** consisting of two rows of coolant holes. These rows were located at $\mathbf{x}/d = -25$ and $\mathbf{x}/d = -45$, where $\mathbf{x}/d = 0$ is located at the stagnation line at the leading edge of the airfoil. The pressure side coolant holes had an injection angle of $\phi = 30$ deg and a streamwise angle of $\theta = 45$ deg. In addition to the showerhead and pressure side coolant holes, the film cooling schematic in **Fig. 2(*b*)** shows the three rows of suction side coolant holes. Their locations with respect to the stagnation line were $\mathbf{x}/d = 30$, $\mathbf{x}/d = 53$, and $\mathbf{x}/d = 84$. The injection angles were $\phi = 50$ deg, 45 deg, and 35 deg, respectively and the streamwise angles were $\theta = 0$ deg, 45 deg, and 45 deg, respectively. The nominal mainstream temperature was 300 K and coolant consisted of cryogenically cooled air supplied at 187.5 K resulting in a density ratio of 1.6. Each coolant region had a separate pressure plenum providing coolant supply as

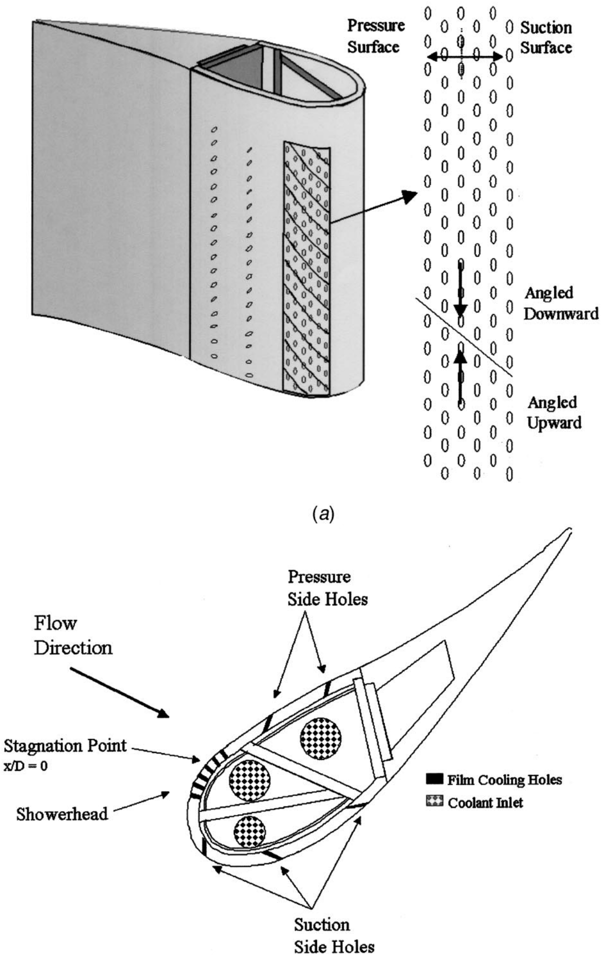

Fig. 2 (*a*) Showerhead and pressure side cooling holes (*b*) Schematic of film cooling hole configuration

shown in **Fig. 2(*b*).** A full description of the film cooling supply and of the construction of the film cooling holes is given in Cutbirth and Bogard [12].

The hot streak generator section was installed upstream of the test section as shown in **Fig. 1.** The hot streak generator consisted of a metal duct and electrical resistance heating elements, supported by six metal rods on each side, and provided 7 kW of heating which could be run at full and half power. The heating elements were enclosed in a square metal duct, 200 mm by 200 mm in cross section and 406 mm in length, followed by a transition section leading to a 200 mm diameter exit. The transition section was 200 mm in length and its exit was located $1.7C$ upstream of the vane leading edge. The hot streak generator was positioned vertically, or spanwise, in the center of the tunnel and was fully adjustable across the pitch so that the hot streak could be positioned to impact various positions on the vane or pass through the center of the passage between vanes. The hot streak generator was designed to give a temperature ratio of $T/T_\infty = 1.1$ under high turbulence conditions. As mentioned earlier, this temperature ratio should be a good representation of ground-based engines.

In order to obtain a uniform total pressure profile across the test section downstream of the hot streak generator in both the spanwise and pitchwise direction, an array of rods was installed in the space surrounding the hot streak generator. These rods provided an aerodynamic resistance similar to the resistance to the flow passing through the hot streak generator. Various numbers of rods, rod diameters and locations were tested until a final configuration, shown in **Fig. 3,** was obtained. The resulting mean velocity profiles over a vertical span downstream of the hot streak generator and downstream of the resistance rod to the side of the generator are shown in **Fig. 4.** The velocity, V, was normalized by $V_{\max}$, the maximum velocity measured across the hot streak generator with no hot streak. These mean velocity profiles were measured at a standard reference position shown in **Fig. 1** as Position A, $0.21C$ upstream of the stagnation point. The profiles were uniform within $\pm 4\%$. The velocity profile was also measured with the hot streak generator activated, and the velocities within the hot streak were found to increase as shown in **Fig. 4.** The increased velocities followed the relation $V_{hs} = V_\infty^*(T_{hs}/T_\infty)^{1/2}$, consistent with a conserved total pressure.

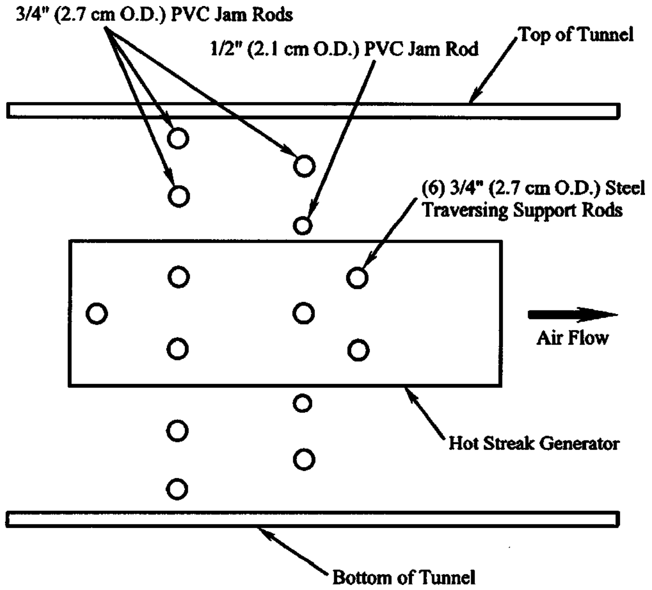

Fig. 3 Final positions and sizes of resistance rods, horizontal view of hot streak generator section

Since the resistance rods located in the hot streak generator section produced a moderate level of turbulence, a fine mesh screen was positioned between the hot streak generator section and the test section to reduce turbulence levels as the flow approached the vane. Turbulence intensity and integral length scales

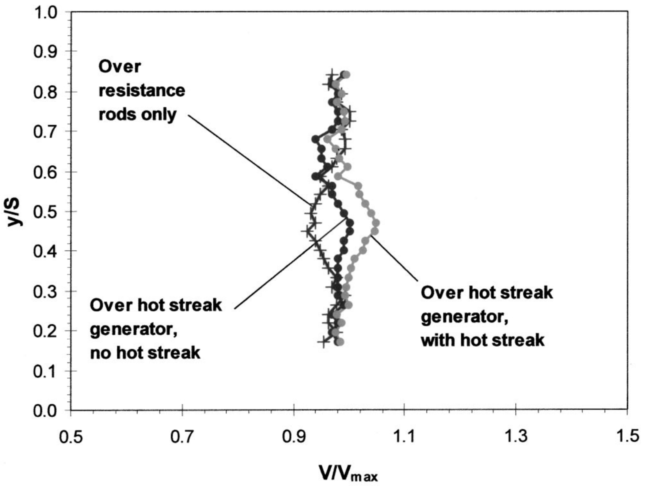

Fig. 4 Normalized velocity distribution for vertical traverse over the resistance rods and over the hot streak generator measured at Position A, *Tu*=3.5

were established using hot-wire anemometer measurements at Position A. Downstream of the centerline of the hot streak generator, at this reference position, the turbulence intensity was $Tu = 3.5\%$ with an integral length scale $\Lambda_f = 19$ mm. Downstream of the resistance rods the turbulence intensity was $Tu = 3.5\%$ with an integral length scale $\Lambda_f = 30$ mm. High mainstream turbulence was generated using an array of 38 mm diameter vertical rods, spaced 85 mm apart, and located 0.88C upstream of the stagnation point as shown in **Fig. 1.** The turbulence generator produced a turbulence intensity of $Tu = 20\%$ with an integral length scale of $\Lambda_f = 33$ mm at Position A. This level of turbulence intensity has been shown to be representative of actual engine operating conditions, [13]. The turbulence generation rods were constructed of a material with very low thermal conductivity to avoid interference with the hot streak. Additional details of the turbulence generator are available in Cutbirth [14].

The hot streak temperature profile was measured using a thermocouple rake consisting of 6 E-type thermocouples spaced 14.2 mm apart. Temperature readings from the thermocouple rake and thermocouples placed in the mainstream were acquired using a National Instruments multiplexer and A/D module, and LabVIEW software and time-averaged over a 6 second time span. For some results, the temperature data were normalized by the mainstream temperature to produce temperature ratios, T/T_∞, where T_∞ was the mainstream temperature. For other results, the use of a normalized temperature ratio, Θ_R, was found to be more appropriate. The normalized ratio, Θ_R, was defined based on the peak hot streak temperature, $T_{0,hs}$, measured at the standard reference Position A, shown in Eq. (1) as follows:

$$\Theta_R = \frac{T_{hs} - T_\infty}{T_{0,hs} - T_\infty} \tag{1}$$

The thermocouple rake was traversed vertically in increments of 1.27 cm between approximately 5 cm from the top and bottom of the tunnel for all tests.

Based on statistical analysis of the temperature measurements, the precision uncertainty (95% confidence interval) of the time averaged temperature values ranged between ±0.1 K at the mainstream temperature to ±0.4 K at the peak hot streak temperature. This error was random error resulting from the data acquisition system. Bias error between the rake thermocouples and the mainstream thermocouple was found to be insignificant. The error in the temperature ratio, T/T_∞ was calculated to be ±0.001 and the error in the normalized temperature ratio, Θ_R, was calculated to be ±0.02.

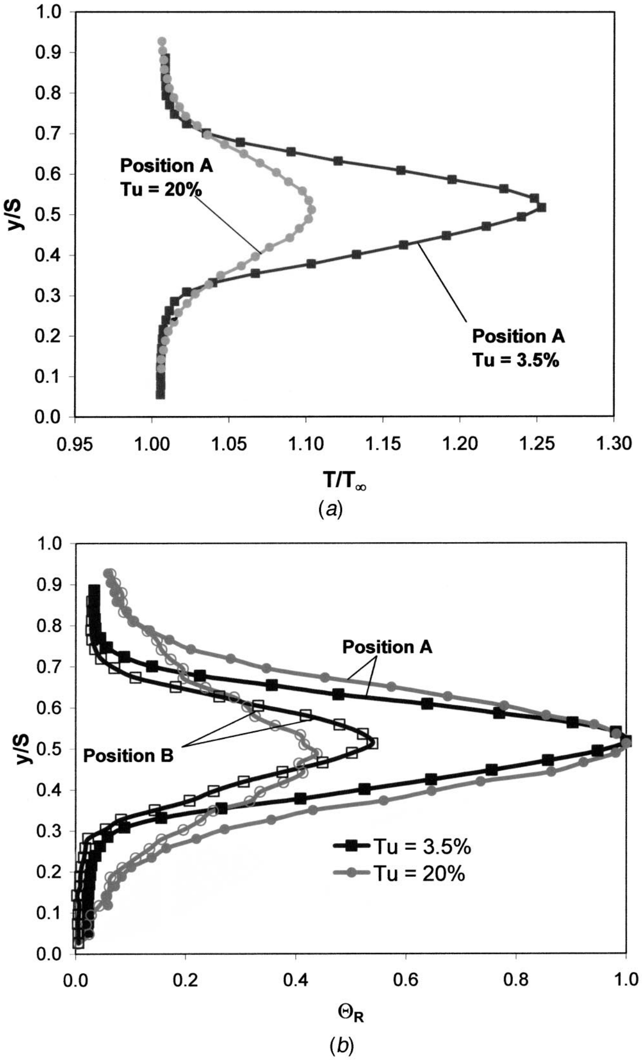

Fig. 5 (***a***) **Peak temperature ratio profiles at Position A for** $Tu=20\%$ **and 3.5%** (***b***) **Peak normalized temperature ratio** (Θ_R) **profiles at Position A and B for** $Tu=20\%$ **and 3.5% for the hot streak through the mid-passage**

Results

The hot streak temperature profile was measured in several locations: 0.21C upstream of the stagnation point (Position A); along the surface of the vane; and 0.32C downstream of the trailing edge (Position B). Measurements were made at these locations under conditions of moderate and high turbulence to quantify the added effects of high turbulence on the attenuation of the hot streak. The effect of film cooling on the attenuation of the hot-streak was studied with the hot streak impacting the stagnation point of the vane and with high mainstream turbulence conditions. For these tests coolant was ejected from the showerhead, suction side, and pressure side film cooling holes both individually and in combination.

Attenuation of the Hot Streak With No Film Cooling. To establish the attenuation of the hot streak as it interacted with the vane or passed through the vane passage, the hot streak temperature profiles were measured at Position A as shown on **Fig. 1,** which is 0.21C upstream of the stagnation point. Time-averaged temperature profiles for the moderate and high mainstream turbulence conditions are shown in **Fig. 5(*a*).** At this position, the hot streak was nominally circular. The profiles in the figure were taken across the peak in a vertical or spanwise traverse. Immediately apparent is the much smaller peak temperature for the high mainstream turbulence case. For the high turbulence case the hot streak passed through the turbulence generation bars located 0.88C upstream, and presumably the decreased hot streak temperature was primarily due to the increased dispersion due to the higher turbulence levels. For moderate mainstream turbulence the peak mean temperature of $T/T_\infty = 1.26$ was only slightly decreased from the peak temperature of $T/T_\infty = 1.30$, which was measured 1.03C upstream of the stagnation point (this position was slightly upstream of the turbulence generator as shown in **Fig. 1).** Since the maximum temperature for the hot streak at Position A varied significantly for moderate and high mainstream turbulence conditions, a normalized temperature ratio, Θ_R, was used that scaled the temperature values relative to the peak temperature at the reference position and the mainstream temperature. The mean temperature profiles in terms of Θ_R are shown in **Fig. 5(*b*).** At Position A, $\Theta_R = 1$ at the peak due to the definition of Θ_R. However, the Θ_R profile for the high turbulence case was broader in the spanwise direction as would be expected due to the increased dispersion of the hot streak. Also shown in **Fig. 5(*b*)** are the Θ_R profiles at Position B, located 0.32C downstream of the trailing edge (see **Fig. 1**) for the hot streak passing through the

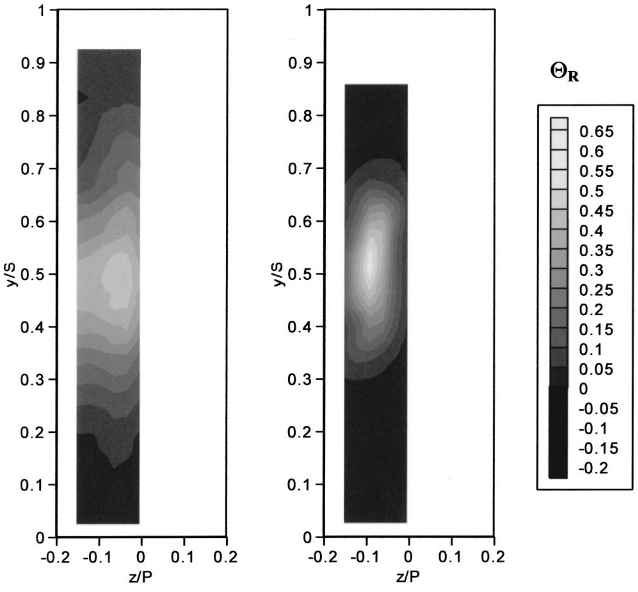

(*a*) (*b*)

Fig. 6 Normalized temperature ratio (Θ_R) plot at Position B with hot streak through the mid-passage; (*a*) high turbulence (20%), (*b*) low turbulence (3.5%)

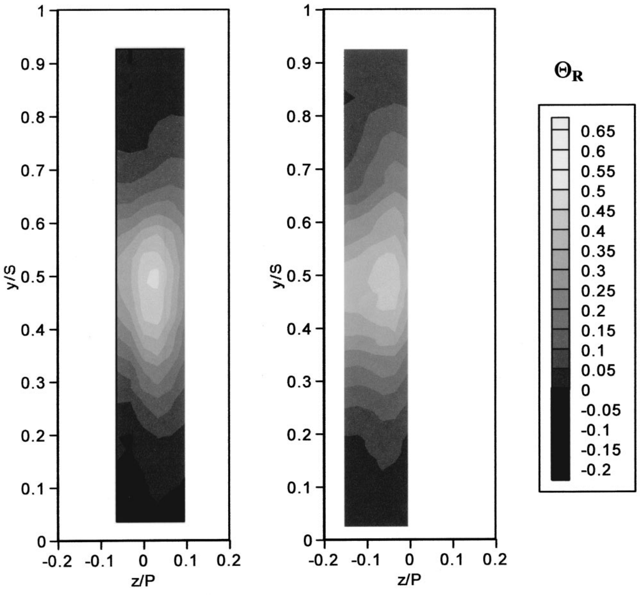

(*a*) (*b*)

Fig. 7 Normalized temperature ratio (Θ_R) plot at Position B, high turbulence (20%), with hot streak; (*a*) impacting the stagnation point, (*b*) through the mid-passage

mid-passage. Both moderate and high mainstream turbulence caused a significant decrease in the peak temperature of the hot streak. These profiles showed the greater decrease in the peak Θ_R value for the high mainstream turbulence case, where $\Theta_R = 0.44$, relative to the moderate mainstream turbulence case, where $\Theta_R = 0.54$. However, there was only a 20% difference in peak Θ_R values for the two turbulence cases.

The extent of the spreading of the hot streak is shown by normalized temperature contours in the y-z plane. The Θ_R contours for the moderate and high mainstream turbulence cases at Position B (downstream of the trailing edge) are shown in **Fig. 6.** In this figure $z/P = 0$ corresponds to a streamline originating from the trailing edge of the vane, with negative and positive z/P values corresponding to the suction side and pressure side of the test vane, respectively. Furthermore, $z/P = \pm 0.2$ correspond to the wall and vane on either side of the test vane (see **Fig. 1).** Naturally, at Position B, the hot streak was contracted in the pitch-wise direction due to the factor of five narrowing of the passage in this direction. Immediately apparent in comparing the hot streaks for the moderate and high mainstream turbulence cases is the much greater spread of the hot streak for the high turbulence case. Although the peak temperature for the high turbulence case was only 20% lower than the moderate turbulence case, the greater spread of the hot streak resulted in much lower temperature gradients for the high turbulence case. This difference would be important when predicting the effect of the hot streak on the downstream rotor stage.

The effect of impacting the hot streak on the vane, with the hot streak centered on the stagnation line, was evaluated by measuring the hot streak profile at Position B for an impacting and nonimpacting hot streak. These results, presented in Fig. 7, show that the thermal profiles for impacting and non-impacting hot streaks are very similar. The peak value with the hot streak impacting the stagnation point was $\Theta_R = 0.46$ with a slightly lower value for the hot streak passing through the mid-passage. This result is consistent with the observation of Roback and Dring [7] who found the peak strength of hot streaks impacting the vane and passing through the passage were the same. Note that for this study the vane was adiabatic, i.e. there was no thermal interaction between the hot streak and the vane. Consequently this test provided insight into the potential for increased dispersion of the hot streak due to boundary layer flows on the vane, and due to the wake behind the vane. The thermal profiles shown in **Fig. 7** do show a distinctly larger spreading of the hot streak for the hot streak passing through the center of the passage. This indicates a decreased dispersion for the hot streak impacting the vane rather than an increase due to boundary layer and wake effects. This apparent discrepancy can be explained when recognizing the effect of the vane on the mainstream turbulence. Because the mainstream turbulence is large scale, $\Lambda_f = 33$ mm, the turbulence within 33 mm or $0.07P$ of the surface will be suppressed by the interaction with the surface. Evidently this suppression of the mainstream turbulence near the vane results in a more cohesive thermal profile for the hot streak impacting the vane.

Direct measurements of the attenuation of the hot streak as it passed around the vane are presented in **Figs. 8** and **9** for the suction and pressure sides, respectively. These measurements were for the high mainstream turbulence case with the hot streak impacting the stagnation point, with thermal profiles measured at 1/3 and 2/3 of the total length along the suction and pressure side. Recall that at Position A, the peak temperature ratio for the high mainstream turbulence case was $T/T_\infty = 1.104$. **Figure 8** shows the thermal profiles compressed towards the surface on the suction side. Peak temperature ratios for the hot streak on the suction surface were $T/T_\infty = 1.063$ at $s/L_S = 0.33$ and $T/T_\infty = 1.052$ at $s/L_S = 0.67$, where L_S was the distance measured along the surface of the suction side from the stagnation point to the trailing edge. In the wake behind the vane the peak temperature ratio was $T/T_\infty = 1.048$. Using the peak upstream temperature ratio as a reference, the peak dropped by 39% at $0.33L_S$, by 50% at $0.67L_S$, and finally by 54% in the wake at Position B. Consequently, the greatest attenuation of the hot streak on the suction side occurred as it passed around the first third of the suction side length.

A distinctly different rate of attenuation of the hot streak was found on the pressure side, shown in **Fig. 9.** At $s/L_P = 0.33$ the hot streak was much wider on the pressure side as compared to the suction side. This can be attributed to the convergence of the streamlines around the pressure and suction sides. Here L_P is measured in the same fashion as L_S, but on the pressure side. As

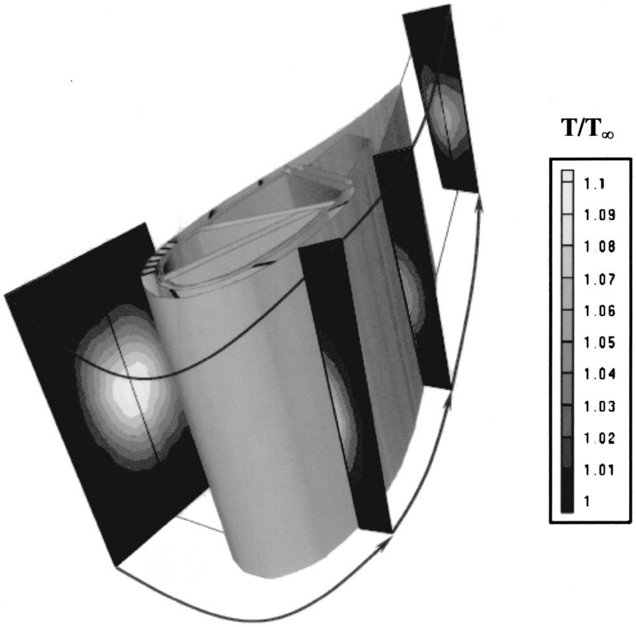

Fig. 8 Temperature ratio (T/T_∞) plots around suction side from Position A to $0.33L_S$ to $0.66L_S$ to Position B for high turbulence with hot streak impacting the stagnation point

seen in **Fig. 10** (obtained from Thole [15]), streamlines originating from the same distance on either side of the stagnation streamline show a much greater rate of convergence on the suction side at a position of $s/L=0.33$ than on the pressure side. On the pressure side the peak temperature ratio at $s/L_P=0.33$ was $T/T_\infty=1.078$, reducing to $T/T_\infty=1.070$ at $s/L_P=0.67$. Hence, the reduction of the peak hot streak strength at $s/L_P=0.33$ on the pressure side was only 25% compared to the 39% reduction on the suction side. This may be attributed to the greater length of travel of the hot streak on the suction side to reach $s/L=0.33$ as compared to the pressure side.

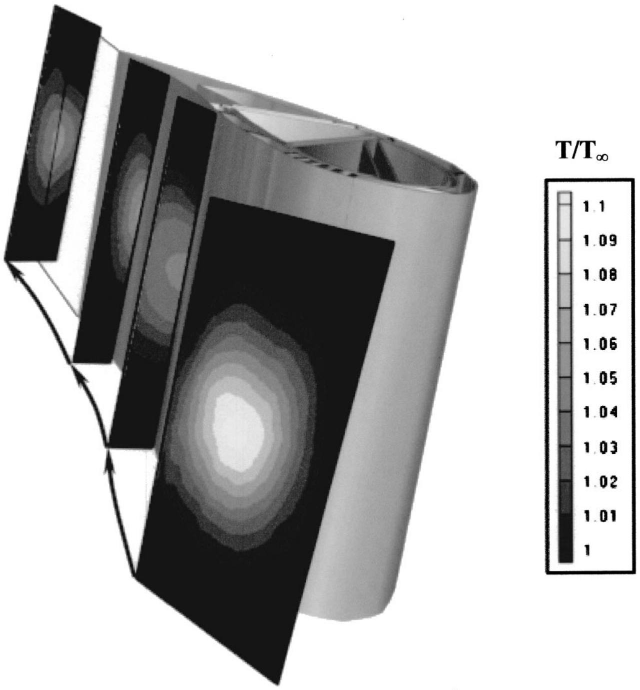

Fig. 9 Temperature ratio (T/T_∞) plots around pressure side from Position A to $0.33L_P$ to $0.66L_P$ to Position B for high turbulence with hot streak impacting the stagnation point

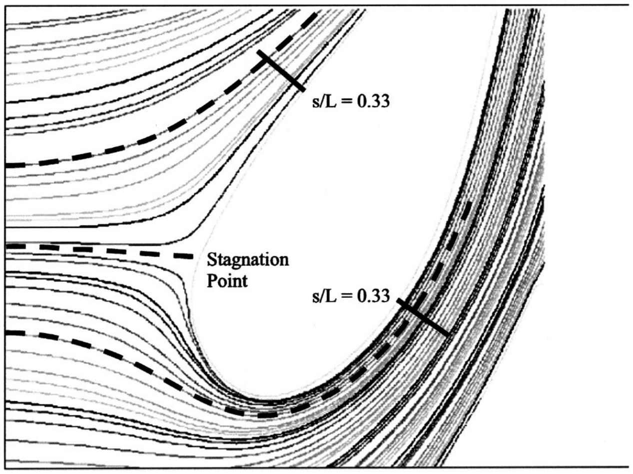

Fig. 10 Streamlines passing around the vane on the suction and pressure side to a position of $s/L=0.33$

Attenuation of the Hot Streak With Film Cooling. The additional attenuation of the hot streak due to film cooling injection was studied for the high mainstream turbulence condition. Coolant hole regions used in these experiments were: the showerhead with six rows of coolant holes; the suction side with three rows of holes; and the pressure side with two rows of holes. Experiments were conducted with each region of coolant holes used individually, and with all three regions combined. This made it possible to isolate the contribution of each coolant injection region in attenuating the hot streak. Blowing ratios used for these experiments were at a level corresponding to the maximum blowing ratio that still provided reasonable adiabatic effectiveness. In all cases the hot streak was centered to impact the vane at the stagnation line, and for each operating condition the hot streak thermal profile was measured in the wake downstream of the vane at Position B.

A comparison of the thermal profiles with no film cooling and with coolant injection from the showerhead region only is presented in **Fig. 11.** For this test, the blowing ratio from the showerhead was $M^*=2.0$ with a density ratio of $DR=1.6$. A significant level of attenuation of the hot streak by the showerhead coolant injection is immediately apparent in **Fig. 11.** With showerhead blowing, the peak was reduced to $\Theta_R=0.33$, compared to $\Theta_R=0.46$ with no blowing and the hot streak impacting the stagnation point.

Blowing from suction side coolant holes alone had a substantially different effect. For this test the overall blowing ratio for the three rows of holes was set at $M=1.4$ with a density ratio of $DR=1.6$. Since a common pressure plenum was used for all three rows of holes on the suction side (seen in **Fig. 2(*b*)),** the blowing ratio for each row varied according to the local external flow conditions at that row. For this test the blowing ratios for the three rows were $M=1.9$, 1.2, and 1.1 for the 1st, 2nd, and 3rd row of holes respectively. As shown in **Fig. 12,** the hot streak was diminished substantially on the suction side of the trailing edge leaving a much narrower portion on the pressure side. The maximum temperature ratio here was $\Theta_R=0.37$, but this was on the pressure side of the wake that was not directly affected by the suction side blowing. The total mass flow rate of coolant for the suction side alone was 75% of the mass flow rate from the showerhead alone.

The effect of blowing from the pressure side alone is shown in **Fig. 13** with an overall blowing ratio for the pressure side of $M=1.4$ with the same density ratio of $DR=1.6$. Again, a common

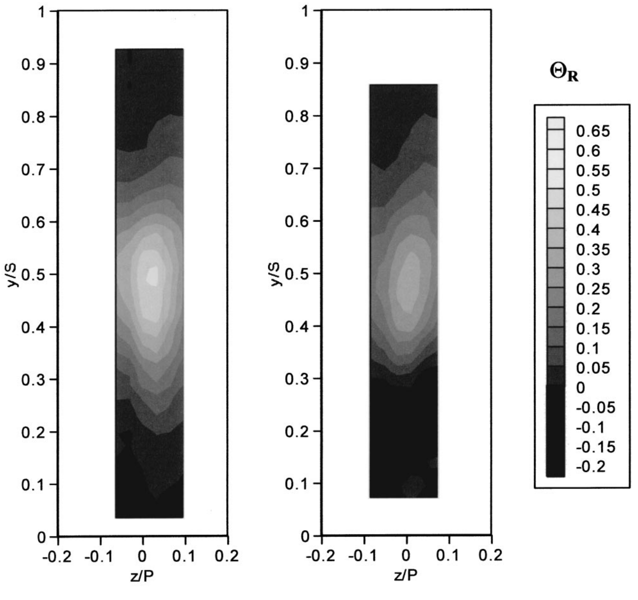

(*a*) (*b*)

Fig. 11 Normalized temperature ratio (Θ_R) plot at Position B with streak impacting the stagnation point, high turbulence (20%); (*a*) no coolant, (*b*) showerhead on, $M^*=2.0$, $DR=1.6$

pressure plenum supplied both rows of holes and here the individual row blowing ratios were $M=1.7$ and 1.1 for the 1st and 2nd row of holes, respectively. Evident from **Fig. 13** is that blowing from the pressure side alone had very little effect on the hot streak. Even though the blowing ratios were relatively large on the pressure side, the total mass flow rate of coolant was only 31% of the mass flow rate from the showerhead. This was due to the lower local freestream velocities at the pressure side rows of holes.

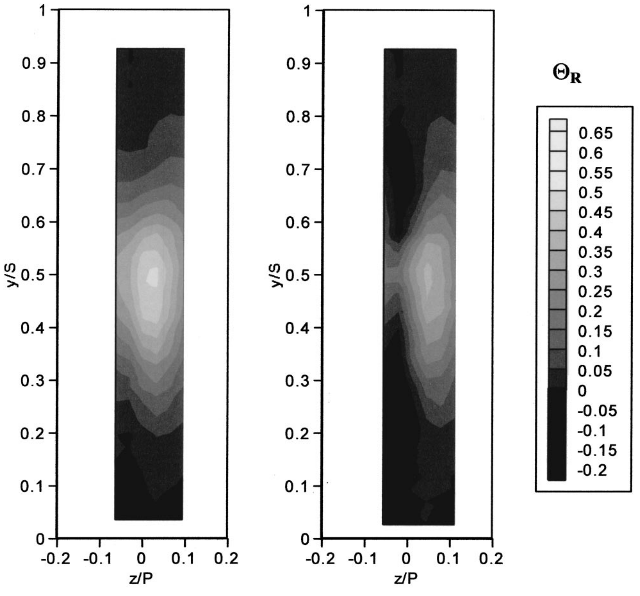

a. b.

Fig. 12 Normalized temperature ratio (Θ_R) plot at Position B with hot streak impacting the stagnation point, high turbulence (20%); (*a*) no coolant, (*b*) suction side on, $M=1.4$, $DR=1.6$

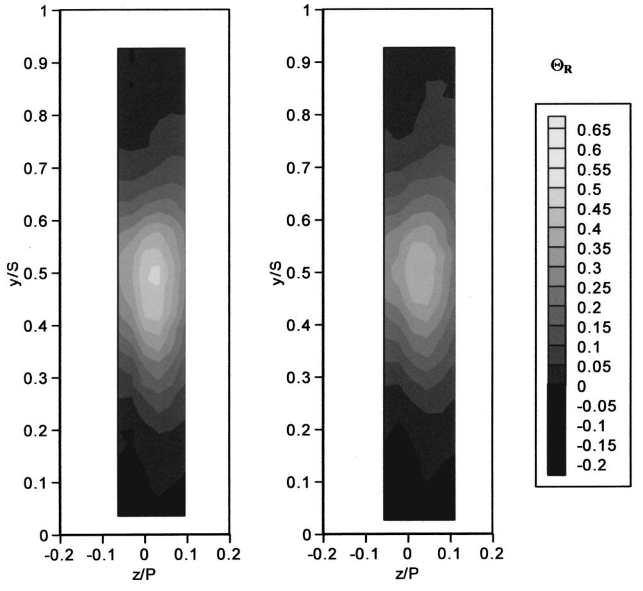

(*a*) (*b*)

Fig. 13 Normalized temperature ratio (Θ_R) plot at Position B with hot streak impacting the stagnation point, high turbulence (20%); (*a*) no coolant, (*b*) pressure side on, $M=1.4$, $DR=1.6$

Reviewing the attenuation of the hot streak induced by each of the coolant injection regions independently, injection from the suction side had the strongest effect, virtually eliminating the portion of the hot streak that flowed along the suction side. Coolant injection from the showerhead had a moderate effect, and from the pressure side virtually no effect. There are several factors that would account for the much stronger effect on the suction side relative to the pressure side. One important factor is the difference in mass flow rates, where the pressure side flow rate was only 41% of the suction side flow rate. Additionally, the hot streak on the suction side had a much steeper temperature gradient than the pressure side, partially due to the compression of streamlines on the suction side, and attenuation levels appeared to be stronger along the suction side due to turbulence effects alone. This steeper gradient allowed both turbulence effects and coolant to significantly reduce the hot streak on the suction side. The penetration depth of the coolant, as a result of coolant hole angles and hot streak width, also played a part in the reduction of the peak hot streak temperature. The first row of suction side holes had an injection angle relative to the surface of 50 deg, and was oriented in the streamwise direction. In contrast, the holes on the pressure side had an injection angle of only 30 deg and were oriented with an angle of 45 deg to the streamwise direction. Consequently, the penetration distance of the coolant jets from the pressure side would have been much less. Showerhead film cooling had a broader effect with the lower portion of the hot streak mostly reduced to mainstream temperatures. The showerhead interacted with the approaching hot streak, which split in half over the stagnation point. On either side of the stagnation point, the hot streak had not been compressed as it was on the suction side and showerhead holes interacted with an effectively ''wider'' hot streak. This helps to explain the moderate performance of the showerhead blowing alone relative to the suction side alone.

For the experiment with all regions of coolant injection on the vane fully operational, the blowing ratios were reduced from those values used for a single region alone. These lower blowing ratios were closer to the blowing ratios for optimum adiabatic effectiveness performance for each region. The blowing ratios used were $M^*=1.4$ for the showerhead, and the suction and pressure sides were each set at an overall blowing ratio of $M=1.0$. For the

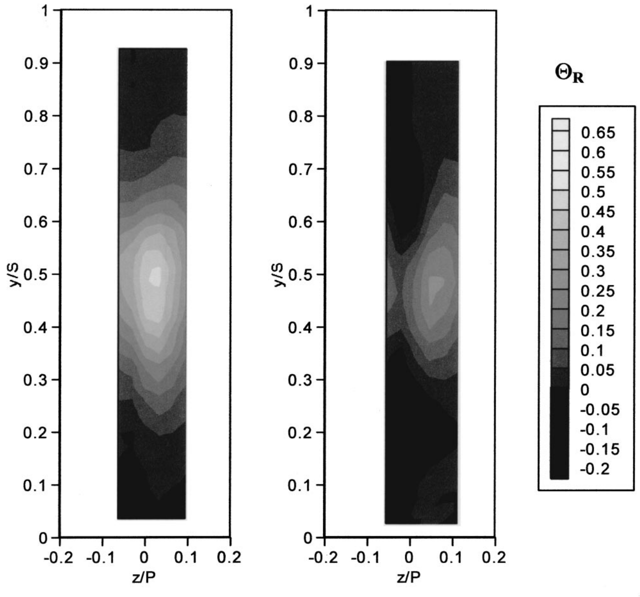

(*a*) (*b*)

Fig. 14 Normalized temperature ratio (Θ_R) plot at Postion B with hot streak impacting the stagnation point, high trubulence (20%); (*a*) no coolant, (*b*) showerhead on $M^*=1.4$, pressure side on, $M=1.0$, suction side on, $M=1.0$, $DR=1.6$

suction side, this overall blowing ratio corresponded to $M=1.4$, 0.9, and 0.8 for the 1st, 2nd, and 3rd row of holes, respectively. Likewise, on the pressure side, the overall blowing ratio of $M=1.0$ corresponded to $M=1.2$ and 0.8 for the 1st and 2nd row of holes. The effect of a fully film cooled vane on the hot streak is evident in **Fig. 14.** The hot streak was eliminated entirely on the suction side for $z/P<0.0$, and reduced to a peak level of $\Theta_R=0.26$ on the pressure side of the wake. Recall that the peak level of the hot streak with no blowing was $\Theta_R=0.46$, hence coolant injection resulted in an additional 56% reduction in peak hot streak temperature compared with the no blowing case.

Conclusions

The effects of mainstream turbulence and film cooling on the attenuation of a hot streak were found to be significant. Changes in the shape and size of the hot streak and of the peak temperature were found under various conditions of mainstream turbulence and film cooling.

The present study found that positioning the hot streak to impact the leading edge of an uncooled vane did not diminish its strength or peak temperature under conditions of high turbulence. For the high turbulence condition, the additional turbulence existing in the wake region did not appear to have a significant effect on the attenuation of the hot streak. In fact, suppression of mainstream turbulence near the surface of the vane decreased the dispersion rate slightly for the impacting case, resulting in a more coherent hot streak.

It was found that high turbulence levels were responsible for the higher level of attenuation seen downstream of an uncooled vane, although the peak temperature ratio in the wake under high turbulence conditions was only 20% lower than with moderate turbulence. However, under conditions of moderate turbulence the hot streak remained much more compact, with higher temperature gradients than for high turbulence.

High turbulence levels combined with film cooling had a substantial effect on the attenuation of a hot streak. In combination, the peak hot streak temperature was reduced by 74% relative to the reference value upstream at 0.21 chord lengths upstream of the vane, using film cooling from all regions. Comparing individual regions, the showerhead acting alone had an overall diminishing effect where the lower portion of the hot streak was significantly reduced. On the other hand, the suction side coolant alone nearly eliminated the hot streak on that side of the vane, leaving a substantial hot streak on the pressure side. The pressure side coolant alone had a very slight effect, somewhat reducing hot streak temperatures on an overall basis. Due to differences in the mass flow rates, injection angles, and the local hot streak thickness, the suction side coolant had the largest effect between the three film cooling regions.

Acknowledgments

We are most grateful to the sponsors of this work, the U.S. DOE National Energy Technology Laboratory through the South Carolina Institute of Energy Studies at Clemson University, and Pratt & Whitney. We would also like to thank Pratt & Whitney for supplying the turbine vane geometry.

Nomenclature

C = vane chord length, 594 mm
d = film cooling hole diameter, 4.11 mm
DR = density ratio of coolant to mainstream, ρ_c/ρ_∞
K = thermal conductivity
L_P = length measured along pressure side of vane from the stagnation point to the trailing edge
L_S = length measured along suction side of vane from the stagnation point to the trailing edge
M = blowing ratio for the suction and pressure side, where U_∞ is the local freestream velocity at the hole location, $\rho_c U_c/\rho_\infty U_\infty$
M^* = blowing ratio for the showerhead region, where U_0 is the approach velocity to the vane, $\rho_c U_c/\rho_0 U_0$
p = film cooling hole pitch in the spanwise direction
P = pitch between vanes, 460 mm
S = span length of vane, 550 mm
s = distance along vane surface
T_{hs} = hot streak temperature at a point in the flow
$T_{0,hs}$ = upstream peak hot streak temperature at the reference location
T_∞ = mainstream temperature
Tu = turbulence intensity, $u_{\mathrm{rms}}/U\times 100\%$
U_0 = approach velocity to the vane
U_∞ = local freestream velocity
V = local streamwise velocity
$V_{\max}$ = maximum streamwise velocity
y = vertical coordinate originating at the tunnel floor
z = spanwise coordinate originating at the trailing edge (negative towards suction side of test vane, positive towards pressure side of test vane)

Greek Symbols

ϕ = injection angle with respect to the surface plane
Λ_f = turbulence integral length scale
Θ_R = normalized temperature ratio, $(T_{hs}-T_\infty)/(T_{0,hs}-T_\infty)$
θ = streamwise injection angle
ρ = density

Subscripts

c = coolant
hs = hot streak value
P = along pressure side
R = normalized
rms = root-mean-square
S = along suction side
∞ = mainstream
0 = approach condition

Superscripts

$*$ = showerhead (blowing ratio)

References

[1] Dorney, D. J., Gundy-Burlet, K. L., and Sondak, D. L., 1999, ''Survey of Hot Streak Experiments and Simulations,'' International J of Turbo and Jet Engines, **16**(1), pp. 1–15.

[2] Schwab, J. R., Stabe, R. G., and Whitney, W. J., 1983, ''Analytical and Experimental Study of Flow Through an Axial Turbine Stage With Nonuniform Inlet Radial Temperature Profiles,'' NASA Technical Memorandum 83431, AIAA 83-1175.

[3] Stabe, R. G., Whitney, W. J., and Moffitt, T. P., 1984, ''Performance of a High-Work Low Aspect Ratio Turbine Tested With a Realistic Inlet Radial Temperature Profile,'' NASA Technical Memorandum 83655, AIAA Paper No. 84-1161.

[4] Butler, T. L., Sharma, O. P., Joslyn, H. D., and Dring, R. P., 1989, ''Redistribution of an Inlet Temperature Distortion in an Axial Flow Turbine Stage,'' J. Propul. Power, **5**(1), pp. 64–71.

[5] Shang, T., Guenette, G. R., Epstein, A. H., and Saxer, A. P., 1995, ''The Influence of an Inlet Temperature Distortion on Rotor Heat Transfer in a Transonic Turbine,'' AIAA Paper 95-3042.

[6] Shang, T., and Epstein, A. H., 1996, ''Analysis of Hot Streak Effects on Turbine Rotor Heat Load,'' ASME Paper No. 96-GT-118.

[7] Roback, R. J., and Dring, R. P., 1993, ''Hot Streaks and Phantom Cooling in a Turbine Rotor Passage: Part 1—Separate Effects,'' ASME J. Turbomach., **115**(4), pp. 657–666.

[8] Gundy-Burlet, K. L., and Dorney, D. J., 1997, ''Three-Dimensional Simulations of Hot Streak Clocking in a 1–1/2 Stage Turbine,'' International Journal of Turbo and Jet Engines, **14**(3), pp. 123–132.

[9] Gundy-Burlet, K. L., and Dorney, D. J., 1998, ''Effects of Radial Location on the Migration of Hot Streaks in a 1–1/2 Stage Turbine,'' AIAA Paper Number 98-3578.

[10] Dorney, D. J., 1997, ''Investigation of Hot Streak Temperature Ratio Scaling Effects,'' International J. of Turbo and Jet Engines, **14**, pp. 217–227.

[11] Polanka, M. D., 1999, ''Detailed Film Cooling Effectiveness and Three Component Velocity Field Measurements on a First Stage Turbine Vane Subject to High Freestream Turbulence,'' Ph.D. dissertation, The University of Texas at Austin.

[12] Cutbirth, J. M., and Bogard, D. G., 2002, ''Evaluation of Pressure Side Film Cooling with Flow and Thermal Field Measurements, Part I: Showerhead Effects,'' ASME Paper No. GT-2002-30174.

[13] Kuotmos, P., and McQuirk, J. J., 1989, ''Isothermal Flow in a Gas Turbine Combustor—A Benchmark Experimental Study,'' Exp. Fluids, **7**, pp. 344–354.

[14] Cutbirth, J. M., 2000, ''Turbulence and Three-Dimensional Effects on the Film Cooling of a Turbine Vane,'' Ph.D. dissertation, The University of Texas at Austin.

[15] Thole, K. A., 2003, personal communication.

Pressure and Flow Characteristics in a Rotating Two-Pass Square Duct With 45-Deg Angled Ribs

Tong-Miin Liou[1]
Professor and Dean,
College of Engineering,
Feng Chia University,
Taichung, Taiwan, ROC
Fellow ASME

Guang-Yuan Dai
Graduate Student,
Department of Power Mechanical Engineering,
National Tsing Hua University,
Hsinchu, Taiwan, ROC
e-mail: d853708@oz.nthu.edu.tw

Measurements are presented of the local velocity and wall static-pressure distributions by using laser-Doppler velocimeter and pressure transducers, respectively, in a rotating two-pass square duct with ribs placed on the leading and trailing walls at an angle of 45 deg to the main stream. The ribs were square in cross section and in a parallel mode of arrangement. The rib-height/duct-height ratio and the pitch/rib-height ratio were 0.136 and 10, respectively. The duct Reynolds number was 1×10^4 and rotation number Ro ranged from 0 to 0.2. Results are addressed in terms of the evolutions of both main flow and cross-stream secondary flow, the distributions of the pressure coefficient, and the variation of friction factor with Ro. In addition, the relationships between the regional averaged Nusselt number, transverse and convective mean velocity component, and turbulent kinetic energy are documented. Simple expressions are obtained to correlate friction factor with Ro, which are lacking in the published literature for ducts ribbed with 45-deg ribs. The 45-deg ribs are found to reduce the friction loss to 60% of the 90-deg ribs for rotating duct under the same operating conditions. For CFD reference, the fully developed flow condition is absent for the rotating ribbed duct investigated. The measured evolution of complex secondary flow vortices is believed to be a challenge to numerical simulations. [DOI: maximum]

Introduction

Among the cooling techniques for metal blades of a gas turbine engine, enhanced internal cooling is the focus of the present study. Cooling air bled from the compressor section is fed to the root section of the rotating blade and subsequently directed to one or several radial internal passages connected by 180-deg sharp turns. Angled ribs are often arranged on the leading and trailing wall of these passages to induce the spanwise and longitudinal vortices, trip the boundary layer and disturb the core flow, and elevate turbulence level. As a result, surface heat transfer is augmented with the penalty of increased pressure loss. Thus, numerous studies have been undertaken to find an appropriate rib arrangement for a better compromise between the heat transfer enhancement and pressure loss. Most of these studies were mainly emphasized on the heat transfer outcome without complementary flow dynamic investigations. The reason is partly that measuring fluid flow in a rotating coolant duct is a challenging.

Since a state-of-the-art list of flowfield measurements in rotating smooth ducts by various research groups, [1–5], had been given in the study of Liou et al. [6], only the measurements made in ribbed rotating ducts are addressed below. Tse and Steuber [7] investigated flow characteristics in a rotating ribbed serpentine (four-pass) coolant duct with a square cross section using laser-Doppler velocimetry (LDV). Their ribs having a semi-circular cross section were skewed −45 deg and +45 deg, respectively, to the radially outward and inward main stream and arranged in a staggered mode. The rib pitch/height (Pi/H) and rib height/hydraulic diameter (H/D_H) were, respectively, 5 and 0.1. Reynolds number and rotational number were fixed at 25,000 and 0.24, respectively. In the first passage within 5 D_H upstream of the turn the secondary flow was found to be characterized by a counterclockwise swirl on the trailing side and a corner recirculation at the inner corner of the leading side. Within 3 D_H after the first turn the secondary flow was featured by a clockwise swirl on the leading side and a corner recirculation zone at the inner corner of the trailing side. Liou et al. [8] studied the fluid flow in a rotating two-pass square duct with in-line 90-deg ribs. Their LDV data were presented for $Pi/H=10$ and $H/D_H=0.136$ with Reynolds number fixed at 1×10^4 and Ro varied from 0 to 0.2. The rotating ribbed duct flow was found to produce higher $U_{\max}/U_b$ and $u'_{\max}/U_b$, stronger total averaged secondary flow, and higher heat transfer enhancement. In recent years measurements of flow structure in two-pass square ducts with 45-deg rib turbulators were also performed by Schabacker et al. [9] and Chanteloup et al. [10] using particle image velocimetry; nevertheless, the ducts were all stationary.

Numerically, Prakash and Zerkle [11] showed that flow in a rectangular duct with normal strips was featured by a two-vortex structure for Ro=0.12 and Coriolis effects were less pronounced in a ribbed passage compared to a smooth wall passage. They concluded that a low Reynolds number model and a Reynolds stress model, respectively, should be adopted to capture the practical aircraft gas turbine engine conditions and anisotropic turbulence effects. Iacovides and Raisee [12] assessed four turbulence models for predicting fluid flow and heat transfer characteristics in serpentine cooling ducts with 90-deg ribs. They found that the isotropic eddy viscosity model and the widely used wall function approach are unable to capture physically reasonable heat transfer and flow field features since the presence of the turn and ribs usually generates flow separation and anisotropic turbulence. Jang et al. [13] computed flow and heat transfer in a rotating square duct with 45-deg ribs using a Reynolds stress turbulence model. Their results revealed that the 45-deg ribs induced longitudinal vortices, rotating buoyancy, and Coriolis forces generate strong anisotropic turbulent stresses and heat fluxes. Obviously, the computational studies cited above all suggest the necessity of detailed fluid flow measurements in a rotating multipass ribbed duct with 180-deg sharp turning.

Heat transfer measurements in rotating serpentine ribbed ducts, [8,14–20] are more abundant than the corresponding fluid flow measurements. Taslim et al. [14] studied the heat transfer charac-

---

[1] Address correspondence to Professor Tong-Miin Liou, Department of Power Mechanical Engineering, National Tsing Hua University, Hsinchu, Taiwan 300, ROC. e-mail: tmliou@pme.nthu.edu.tw

Contributed by the International Gas Turbine Institute and presented at the International Gas Turbine and Aeroengine Congress and Exhibition, Atlanta, GA, June 16–19, 2003. Manuscript received by the IGTI Dec. 2002; final revision Mar. 2003. Paper No. 2003-GT-38346. Review Chair: H. R. Simmons.

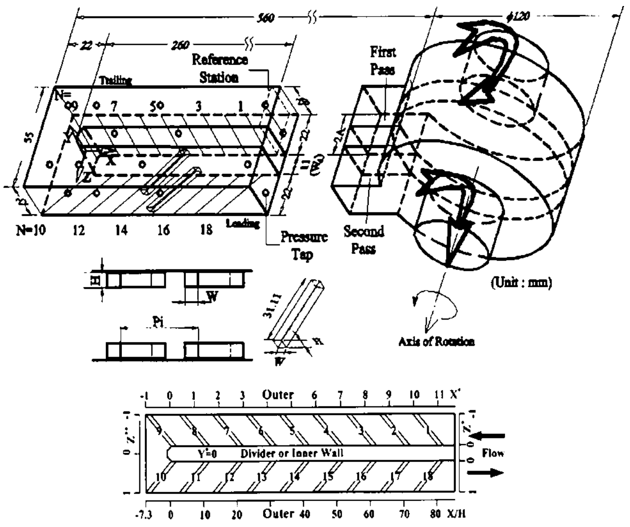

Fig. 1 Sketch of configuration, coordinate system, and dimension of test section

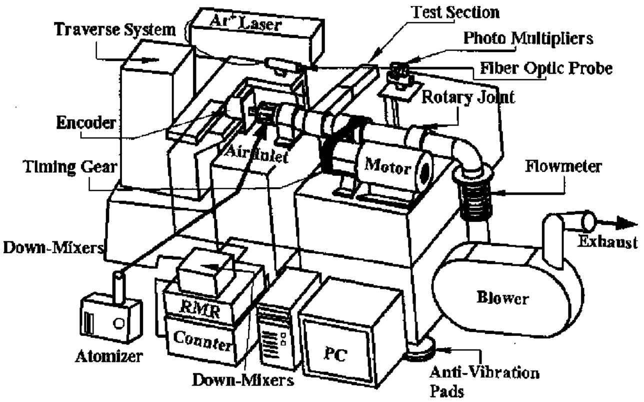

Fig. 2 Schematic drawing of flow system and LDV facility

teristics in rotating one-pass channels with 45-deg angled ribs arranged in a criss-cross mode on the leading and trailing walls. They found that rotational effects were more pronounced in ribbed channels with a higher aspect ratio and a lower rib blockage ratio. Johnson et al. [18] investigated the effects of buoyancy and Coriolis forces on heat transfer coefficient distribution of four-pass square channel with 45-deg ribs. Fann et al. [19] produced local heat transfer measurements in rotating serpentine (four-pass) passage with ribbed surfaces. They concluded that both rotation and ribs improved the local heat transfer, and 45-deg ribs performed the best in both the stationary and rotating cases. Note that in a nonrotating square channel with two opposite in-line ribbed walls, Han et al. [20] also reported that the 45-deg angled ribs were more effective in heat transfer augmentation than the ribs placed normal to the flow. Recently, Azad et al. [21] performed experimental heat transfer results in a two-pass rectangular channel with smooth and ribbed surfaces for two rib angles and channel orientations. The results showed that 45-deg parallel ribs produced a better heat transfer augmentation than 45-deg cross ribs, and a 90-deg channel orientation produced higher heat transfer effect over a 135-deg orientation.

From the references cited above, it is clear that the cross-stream secondary flow induced by rotation-generated Coriolis and centrifugal forces makes the fluid flow and heat transfer distributions in rotating coolant ducts rather different from those in nonrotating ducts. Although aforementioned studies have provided valuable information, most of them were focused only on heat transfer part without including velocity field and pressure gradient that drive the forced convective heat transfer. Hence, there is a need to explore the local velocity and pressure distributions. The information gathered is believed to provide a useful reference in designing an efficient cooling system and validating the CFD codes.

Experimental Facility and Conditions

Test Section and Conditions. **Figure 1** depicts the configuration, coordinate system, and dimensions of the test section made of acrylic sheets 20 mm thick for optical access. The hydraulic diameter of the square cross-sectional flow path was $D_H = 22$ mm and the divider-wall thickness was $0.5\,D_H$. At the turn, the clearance between the tip of the divider wall and the duct outer wall was fixed at 1 D_H. The 45-deg transverse Plexiglas ribs with a thermal conductivity 0.195 W/mK were mounted on the leading and trailing walls and directly opposite (not staggered). Nine pairs of ribs were installed in each pass. The tips of the first rib pair were located at 13.8 mm downstream of the front edge of the test section. H/D_H and Pi/H were 0.136 and 10, respectively, in each pass. The Reynolds number, based on the bulk mean air velocity of 7.58 m/s and hydraulic diameter, was fixed at 1.0×10^4. The rotation number varied from 0 to 0.20, corresponding to rotational speeds from 0 to 660 rpm. Note that for comparison purposes the above conditions were selected from those reported by Liou et al. [8] for 90-deg angled ribs case.

The LDV measurements were undertaken in the region 1.5 rib pitches upstream to 1.5 rib pitches downstream of the turn along the longitudinal central plane of each pass, i.e., $Z^* = \pm 0.5$. At each X station the LDV measurements were made at 9 to 14 locations. The wall static pressures were measured at 16 locations indicated in **Fig. 1** along the leading and trailing walls of the two-pass ducts with a 180-deg sharp turn.

Experimental Facility. **Figure 2** depicts the experimental facility that consists of flow system and optical system. The inlet air firstly flowed radially outward in the first pass, made a 180-deg sharp turn, and flowed radially inward in the second pass. The air was sucked from the test section to amblent by a 2.2 KW turbo-blower controlled by a frequency converter. A micro-differential transducer (Kyowa PDL-40GB) connected to 16 pressure taps on the leading and trailing walls (**Fig. 1**) measured the wall static pressures. The pressure transducer was located on the wall of hollow shaft (**Fig. 1**), i.e., at a radius of 60 mm. These signals were subsequently amplified and fed via the slip ring to the PC for storage. Note that the microdifferential pressure transducer was referenced to pressure tap located at the inlet reference station, $X^* = 11.6$ or $X/H = 85$ in **Fig. 1**. It used a foil strain gage as its detector element and permits high precision measurement of very small differential pressure. Its accuracy was within ±0.1% of the 400 mmAq (3922 N/m^2) full-scale value. The principles of LDV have been described in detail in authors' previous studies, [3,6].

Data Uncertainty

The statistical errors in the mean velocity and turbulence intensity are less than 1.8 and 3.1 percent, respectively, for a 95% confidence level. More detailed uncertainty estimates and velocity bias correlations are included in Liou et al. [3]. For the range of atomizer pressure settings, the saline solution was mixed producing particles from 0.5 to 1.2 μm. This particle diameter range is able to follow turbulence frequencies exceeding 1 KHz (Durst et al., [22]).

The uncertainties in the pressure loss measurements are ±0.1, ±0.5, and ±0.1% associated with the pressure transducer temperature effect on output, the slip ring noise, and the amplifier noise, respectively. A resultant uncertainty of ±0.52% is thus estimated for the pressure loss data. The corresponding uncertainty in C_p is ±0.64%.

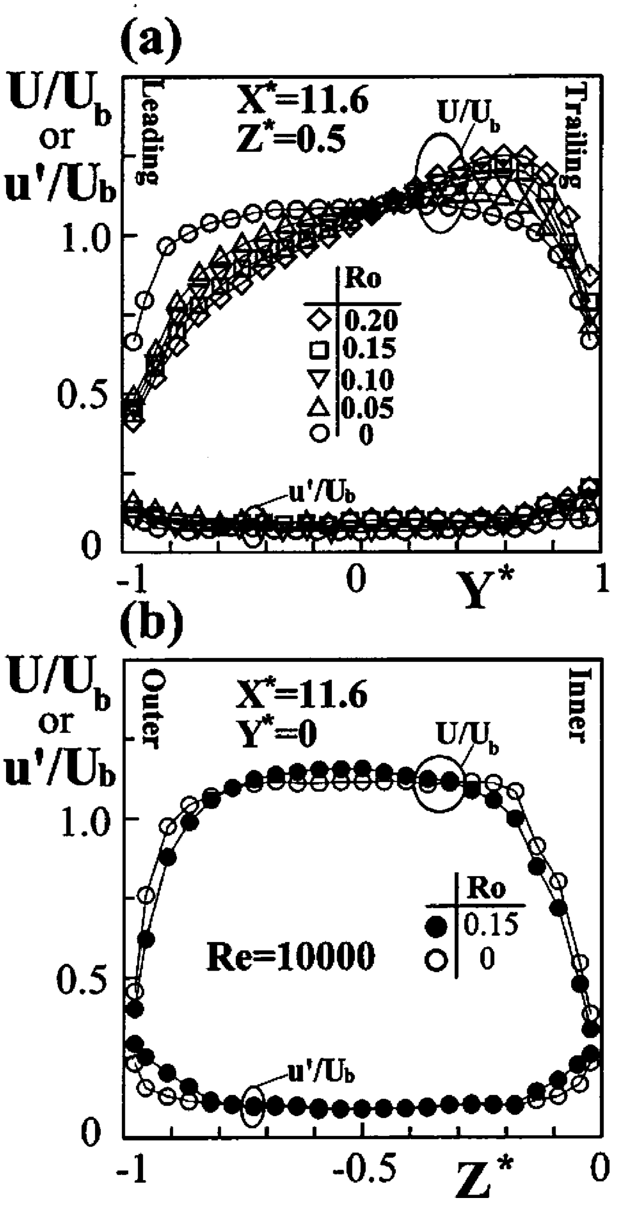

Fig. 3 Streamwise mean velocity and turbulence intensity profiles at inlet reference station $X^*=11.6$ (or $X/H=85$) of the first pass in (*a*) $Z^*=-0.5$ and (*b*) $Y^*=0$ planes

Results and Discussion

Inflow at Reference Station. The inlet reference station was selected at $X^*=11.6$ (or $X/H=85$) which is located at $5H$ distance upstream of the first rib pair ($N=1$ in **Fig. 1**) in the first outward duct. **Figure 3**(*a*) shows the variation of streamwise mean X-component velocity and turbulence intensity profiles with Ro at inlet reference station in $Z^*=-0.5$ plane. The U/U_b and u'/U_b profiles are rather symmetric for Ro=0. As Ro is increased from 0 to 0.2, the skewness of U/U_b and u'/U_b increases monotonically due to the increase of the Coriolis force directed toward the trailing wall ($Y^*=1$) and, in turn, the steeper mean velocity gradient near the trailing wall. The U and u' peaks can be as high as $1.24U_b$ and $0.20U_b$, respectively, for Ro=0.2. The uniform parts of u'/U_b profiles extend to (with respect to $Y^*=0$) 70% of the channel height and have values of 9.0%±0.5%. For CFD reference, the boundary layer thickness defined at 95% $U_{\max}$ is $\delta_{95}/H=1.5/1.5$, 3.4/1.1, 3.9/1.1, 4.1/0.9, 4.3/0.9 along the leading/trailing wall for Ro=0, 0.05, 0.10, 0.15, and 0.2, respectively. The corresponding U/U_b and u'/U_b profiles in $Y^*=0$ plane are depicted in Fig. 3(*b*) for Ro=0 and 0.15. Because the span plane $Y^*=0$ is perpendicular to the Coriolis force, all the profiles are very symmetric to the central plane $Z^*=-0.5$. The peak U and u', respectively, increase from $1.05U_b$ and $0.20U_b$ at Ro=0 to $1.10U_b$ and $0.25U_b$ at Ro=0.15. The boundary layer thickness is $\delta_{95}/H=1.1/1.1$ and 1.6/1.6 along the inner/outer wall for Ro=0 and 0.15, respectively.

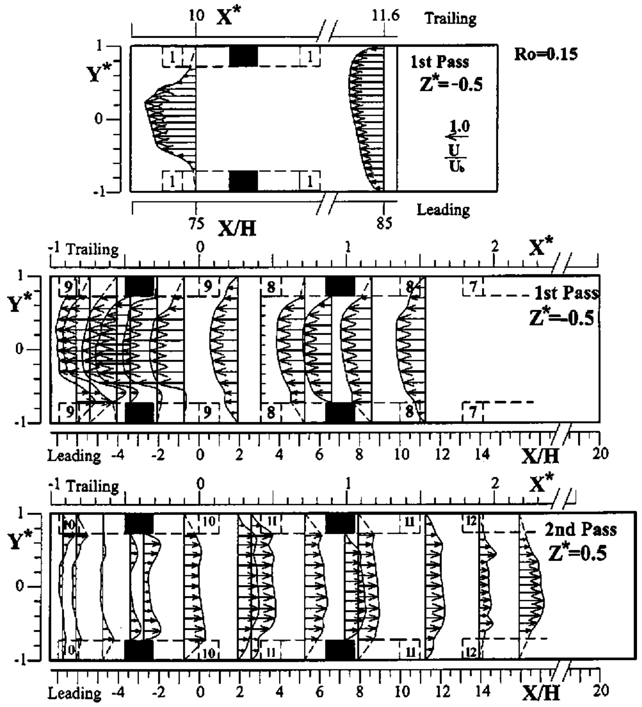

Fig. 4 Evolution of longitudinal mean velocity component in $Z^*=-0.5$ and $Z^*=0.5$ planes

Evolution of Mean Flow. In the following discussion, the case of Ro=0.15 is selected as an example among the range of Ro investigated to illustrate the evolution of the mean velocity profile along the $Z^*=-0.5$ and $Z^*=+0.5$ plane in **Fig. 4**. As the fluid flows radially outward over the first 45-deg angled rib pair, the U/U_b at $X^*=10$ station in between the $N=1$ and $N=2$ rib pair decreases in the region $|Y^*|\geqslant 0.5$ due to the blockage of ribs but increases in the region $|Y^*|<0.5$ due to mass conservation. The profile is still skewed toward the trailing wall as a result of the Coriolis force. The peak U is $1.85U_b$ while $U_{\max}=1.49U_b$ for the case of 90-deg ribs at the same Ro [8]. It is obvious that a 45-deg rib has a longer streamwise cross section than a 90-deg rib, giving a longer nozzle formed by the in-line opposite ribs on the leading and trailing wall and, therefore, a higher $U_{\max}$ than the 90-deg rib case.

The longitudinal mean velocity profiles in between $N=7\sim 9$ or $X^*=2.2\sim -1$ along $Z^*=-0.5$ plane and $N=10\sim 12$ or $X^*=-1\sim 2.2$ along $Z^*=+0.5$ plane are used to demonstrate the flow characteristics around the turn. **Figure 5** of the mean velocity vector plots unveils the slant impingement of fluid flow upon the first-pass trailing wall and second-pass leading wall directed by the Coriois force. Specific examples are the slant velocity vectors in the region $1.5<X^*<1.8$ adjacent to the trailing wall of the first pass and in the region $11<X/H<13$ adjacent to the leading wall of the second pass. The corresponding heat transfers on these two walls are to be augmented. Note that LDV measurements within a rib height (3 mm) distance to the wall were generally not attainable due to rib's blockage of laser beams. Exceptions are the two

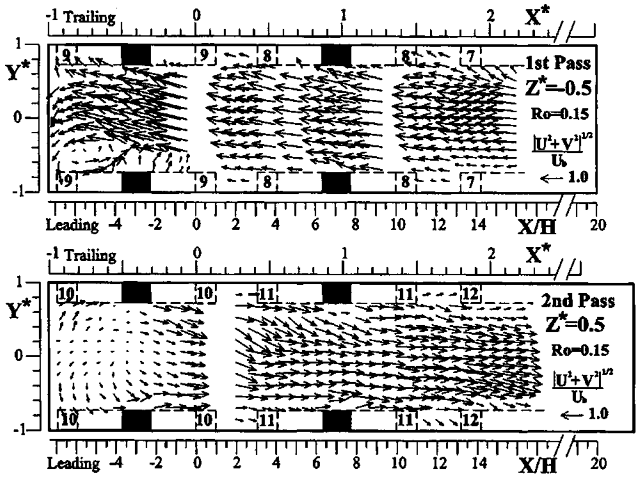

Fig. 5 Mean velocity vector plots around the turn for Re=1.0 $\times 10^4$ and Ro=0.15 in *X-Y* plane of the (*a*) first and (*b*) second pass

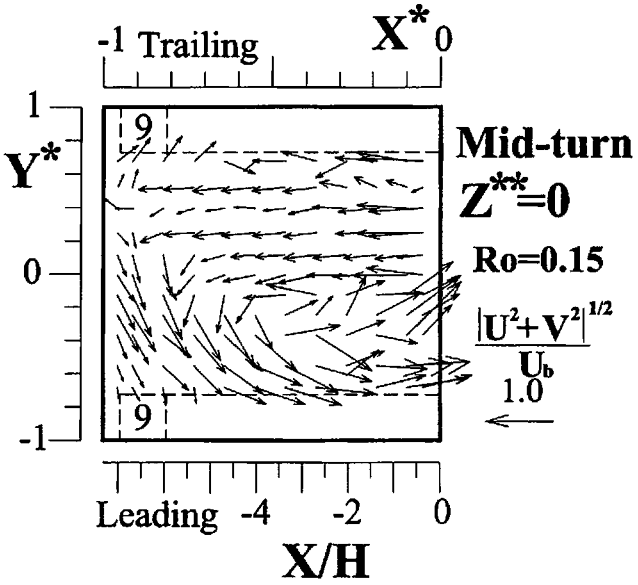

Fig. 6 Mean velocity plot on the midturn cross section for Re $=1.0\times 10^4$ and Ro=0.15

rib-height gap between the consecutive 45-deg angled rib pairs. Inside the 180-deg sharp turn ($-1<X^*<0$ or $-7.3<X/H<0$) and in the $Z^*=-0.5$ plane of the first pass (**Figs. 4** and **5**), the curvature and rotation make the flow pattern form a strongly skewed Dean-type vortex flow. More specifically, the Dean vortices degenerate into a single vortex located near the duct tip and leading wall. The velocity component normal to the leading or trailing wall plays an important role in augmenting heat transfer. Inside the turn ($-1<X^*<0$) on the first outward duct side, the near wall mean velocity vectors in the region ($Y^*=1$ and $-1<X^*<-0.5$) have larger Y-component and are directed toward the trailing wall ($Y^*=1$). The downwash effect is expected to markedly increase the heat transfer rate. In contrast, the near-wall mean velocity vectors in the region ($Y^*=-1$ and $-0.5<X^*<0$) have larger Y-component but are directed away from the leading wall. The upwash effect is not expected to contribute to the heat transfer enhancement. Inside the turn ($-1<X^*<0$) on the second pass side (in the $Z^*=-0.5$ plane), the U/U_b profiles in **Fig. 4** clearly indicate the presence of a pair of counterrotating skewed Dean-type vortices. In addition, the velocity vectors in **Fig. 5** are more inclined toward the leading wall. Hence, one expects that heat transfer enhancement inside the turn on the second pass side is higher on the leading wall than on the trailing wall.

Secondary Flow. Secondary flow can be induced by the geometric turn as shown in **Fig. 6** in terms of mean velocity vectors pattern on the midturn cross-sectional plane. The counterrotating Dean vortices pair is skewed by duct rotation as mentioned above. Core flow impingement on the large portion of leading wall is clearly unveiled. Secondary flow can also be generated by angled ribs. In general, a 45-deg angled rib generates an angled vortex with a vorticity vector $\vec{\Omega}$ behind and parallel the rib. The $\vec{\Omega}$ has a longitudinal component $\vec{\Omega}_x$, as shown on the top schematic diagrams of **Figs. 7** and **8**, giving the secondary flow pattern on the cross-sectional plane. At a given X^* station in the first radially outward duct (say, $X^*=9.81$ in between rib pairs $N=1$ and $N=2$, **Figs. 7** and **1**) the in-line 45-deg rib pair generates the secondary flow consisting of two counterrotating vortices that drive fluid from the duct center towards the inner (or divider) wall ($Z^*=0$) along the center plane and to the outer wall ($Z^*=-1$) along the ribbed trailing ($Y^*=1$) and leading ($Y^*=-1$) walls. However, duct rotation also induces secondary flow consisting of two counterrotating vortices that steer fluid from the duct center towards the trailing wall along the center plane and to the leading wall along the inner and outer wall. Hence, the double-cell longitudinal counterrotating vortex patterns, respectively, induced by the angled rib pair and duct rotation are perpendicular to one another. The outcomes of the combined effect of the in-line 45-deg rib pair and duct rotation on the secondary flows in the first and second passage are depicted in **Figs. 7** and **8**, respectively. It is seen from **Fig. 7** that at $X^*=9.81$ between $N=1$ and $N=2$, i.e., the front portion of the ribbed first pass, the upper half of the cross section is dominated by one of the 45-deg parallel rib induced double vortices mentioned above. Nevertheless, the lower half of the cross section is predominated by the aforementioned rotation-

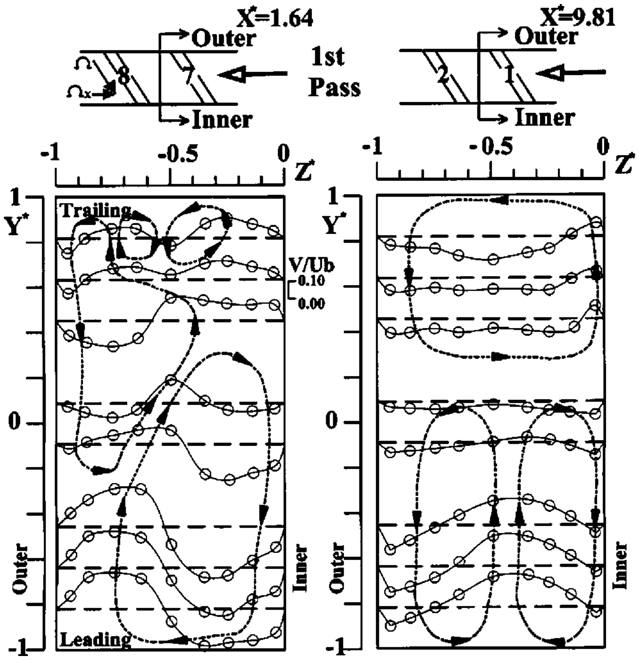

Fig. 7 Distributions of transverse mean velocity on the cross-sectional planes in between rib pairs $N=1$ and $N=2$ (near the entrance) and $N=7$ and $N=8$ (near the 180-deg turn) of the first ribbed passage

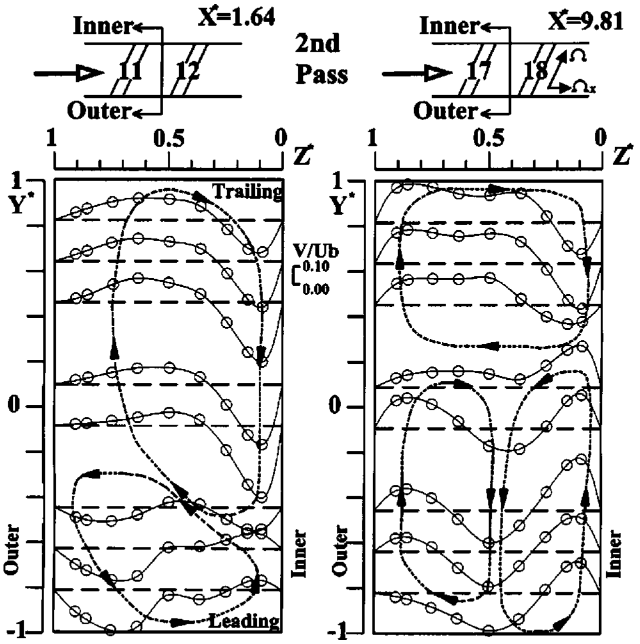

Fig. 8 Distributions of transverse mean velocity on the cross-sectional planes in between rib pairs $N=11$ and $N=12$ (near the 180-deg turn) and $N=17$ and $N=18$ (near the exit) of the second ribbed passage

induced double vortices. Note that all the secondary flow patterns are viewed from the downstream towards upstream direction and, hence, the divider or inner wall ($Z^*=0$) is always on the right-hand side. As the flow proceeds to the rear portion of the ribbed first pass, $X^*=1.64$ between $N=7$ and $N=8$, the subsonic flow senses the presence of the geometric turn and makes some adjustments. It responds with an upward movement and a distortion of the rotation-induced counterclockwise vortex, an expansion of the rotation-induced clockwise vortex, and a compression and breakup of the 45-deg rib induced counterclockwise vortex into two smaller counterrotating vortices. Inside the turn (between $N=9$ and $N=10$) the secondary flow has the familiar pattern of Dean-type double vortex with the upper vortex cell squeezed by the rotation effect as has been shown in **Fig. 6**. Note that the angled ribs and geometry curvature have similar effects on the secondary flow pattern: directing the central core flow towards the outer wall ($X^*=-1$). Immediately after the turn at $X^*=1.64$ between $N=11$ and $N=123$, **Fig. 8** depicts that the secondary flow still keeps the Dean vortices pattern with, however, the lower vortex cell squeezed by the reversed Coriolis force. Note that the fluid flow is radially inward in the second passage. Far downstream near the outlet at $X^*=9.81$ between $N=17$ and $N=18$ of the second passage, the secondary flow (right portion of **Fig. 8**) recovers the pattern (right portion of **Fig. 7**) at corresponding X^* station of the first passage. Nevertheless, all the vortexes rotate in opposite directions due to reversed Coriolis force.

It should be pointed out that the measured secondary flow patterns presented above are far more complicated than what can be imagined purely from a conceptual view. In addition, from the evolutions of the longitudinal velocity component profile and cross-sectional secondary flow pattern presented above, a fully developed flow condition is never attained in the rotating duct investigated. **Figure 9** provides an example to illustrate this observation in terms of a comparison of the longitudinal mean velocity profiles at a fixed station $X_N/H=3.5$ but in different pitches $(X_{N+1}-X_N)$, $N=4$ to 7 in the first passage and $N=13$ to 16 in the second passage. The data shown are away from the entrance of the first passage, the 180-deg turn, and the exit of the second passage. It is seen that the maximum differences between any two consecutive profiles are from 16% U_b to 23% U_b and 12% U_b to 31% U_b in the first and second passage, respectively. This result is contrary to that found in a similar two-pass duct under stationary condition, [23]. Bonhoff et al. [23] in their PIV measurements of stationary ribbed duct flows reported the attainment of the fully developed condition after eight and three rib modules for staggered 45-deg and 90-deg ribs, respectively. These facts pose a challenge to the CFD predictions. The resultant secondary flow pattern at a specific cross section is a synthesis of the effects of duct rotation and 45-deg rib pair (also the effect of the geometric turn for fluid flow inside the turn and in the second passage). These effects compete with one another and the dominant one has the largest influence on the resultant secondary flow pattern. For instance, in the rotating four-pass square duct flow with 45-deg staggered ribs studied by Tse and Steuber [7] the rib-to-duct height ratio, $H/2B=0.1$, and rotation number, Ro=0.24, are respectively lower and higher than those ($H/2B=0.136$ and Ro $=0.15$) of the present case. Thus, they reported that the rotation-induced counterrotating vortices prevailed over the whole cross sections located within 1 to 4 D_H distances after the entrance of

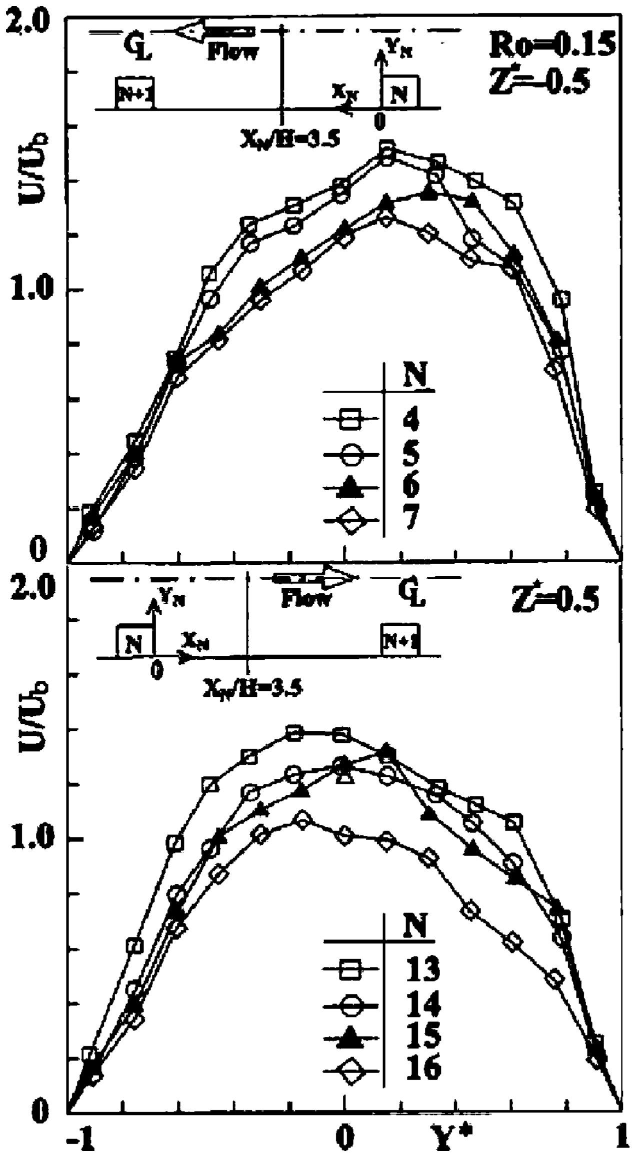

Fig. 9 Examination of periodic fully developed flow condition by comparing U/U_b profiles at $X_N/H=3.5$ in various pitches

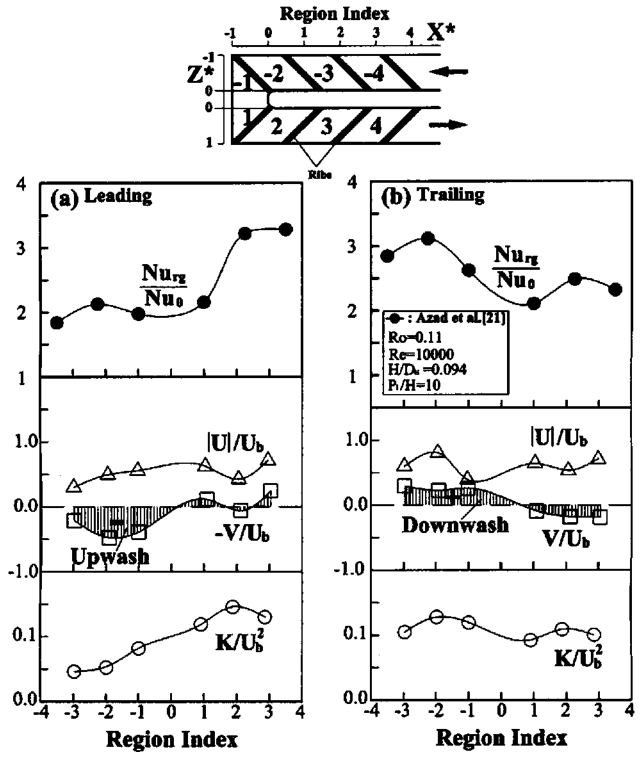

Fig. 10 Relationships between mean velocity components, turbulent kinetic energy, and regional averaged surface heat transfer coefficient

the first pass, instead of the secondary flow at $X^*=9.81$ shown in **Fig. 7**. Further, the secondary flow on the midturn cross section was predominated by a single vortex only, instead of that shown in **Fig. 6**. Quantitatively, the maximum positive/negative transverse mean velocities of the secondary flow on the cross-sectional planes examined reach $+0.14U_b/-0.18U_b$ and $+0.20U_b/-0.26U_b$ at $X^*=9.81$ and $X^*=1.64$ of the first passage, respectively. They attain the values of $+0.13U_b/-0.39U_b$ and $+0.30U_b/-0.25U_b$ at $X^*=1.64$ and $X^*=9.81$ of the second passage, respectively.

Fluid Flow and Surface Heat Transfer. It is important to relate the flow dynamics to the heat transfer. The upper part of **Fig. 10** shows the region averaged Nusselt number ratio reported by Azad et al. [21] in their thermocouple measurements of surface heat transfer for 45-deg angled parallel ribs under rotating condition. The X and Y mean velocity components (U/U_b, V/U_b) and turbulent kinetic energy K/U_b^2 at 1.5 mm away from the leading and trailing wall measured in the present study are respectively depicted in the middle and lower part of **Fig. 10**. Although the heat transfer experiment of Azad et al. was made in a two-pass rotating ribbed "rectangular" channel, they found a similar result as was observed in a two-pass rotating ribbed "square" channel from the previous studies in the existing literature. That is, heat transfer coefficient distributions in the first and second pass show different dependence on rotation, primarily due to the reversal of the Coriolis forces acting on the moving fluid in radially outward and inward rotating flow, as shown in the upper part of **Fig. 10**. The present fluid flow results further reveal that the distributions of K/U_b^2 (**Fig. 10**, lower part) are approximately correlated with those of Nu_{rg}/Nu_0 (**Fig. 10**, upper part) within measurement uncertainties. In other words, turbulence enhances the heat transfer, as expected. The magnitude and direction of the mean transverse velocity component V are also essential to the heat transfer enhancement on the leading and trailing wall. In the middle part of

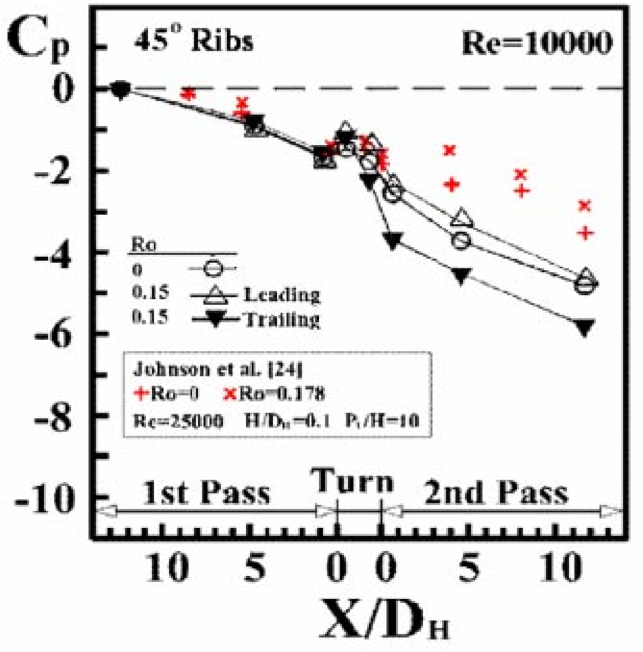

Fig. 11 Variation of dimensionless wall static pressure with X/D_H at various rotation numbers (+ and ×: measured along the outer and inner side walls of the first and second passage, respectively)

Fig. 10 the positive values of $-V/U_b$ and V/U_b near the leading and trailing wall, respectively, denote the downwash (or impingement) effect on the heat transfer surface whereas the negative values indicate the upwash effect, as a result of the secondary flow induced by the Coriolis force, 45-deg angled ribs, and geometric turn (for flow inside the turn and in the second passage). Near the first pass (region indices: -3, -2, -1) leading wall and the second pass trailing wall (region indices: 1, 2, 3), the upwash effect of the secondary flow lowers the heat transfer enhancement on the corresponding walls. In contrast, the downwash effect of the secondary flow increases the heat transfer enhancement on the first pass trailing wall and second pass leading wall. Thus, the shapes of K/U_b^2 curves once modulated by the downwash and upwash effects of the secondary flow tend to correlate very well with those of the Nu_{rg}/Nu_0 curves. As for the convective effect denoted by U/U_b, **Fig. 10** shows it uniformly contributes to the heat transfer enhancement on both the leading and trailing wall.

Local Pressure Coefficient and Average Friction Factor The data bank of local pressure distributions along rotating two-pass coolant ducts is scarce in open literature to date although knowledge of the coolant duct pressure loss will help in designing an efficient rotating cooling system. Measurements of streamwise wall static pressure distributions along the leading and trailing wall are thus performed and the results are plotted in **Fig. 11**. It is seen that the trend is similar to the familiar pressure distribution along the "outer" wall of a stationary curved duct. That is, the streamwise pressure gradient is adverse over the leading and trailing walls for the front part of the turn, but for the later part of the turn is on the contrary. Upstream of the turn in the first pass and downstream of the turn in the second pass, C_p decreases approximately linearly with increasing X/D_H as that observed in a straight smooth duct. Owing to the presence of the streamwise pressure gradient inside the turn (**Fig. 11**), the streamwise mean velocity generally displays deceleration near the "outer" wall for the front part of the turn, but for the latter part of the turn it is reversed, as what known from the stationary curved duct flows. As a check, attention is directed to **Fig. 1** that shows the locations of the two pressure taps inside the turn are nearer the "outer" wall. That illustrates the above trend. On the other hand, the trend shown in **Fig. 11** is different from that obtained from the smooth ducts in that immediately after the turn there exists a sudden drop of C_p for the smooth ducts due to turn induced flow separation, [6,22], while it is absent for the ducts roughened by 45-deg angled ribs due to the absence of turn induced flow separation, [9].

Figure 11 depicts that the C_p distributions on the leading and trailing wall for $\mathrm{Ro}=0.15$ are on the opposite sides of $\mathrm{Ro}=0$ case. It also shows that upstream of the turn in the first passage frictional losses are insignificantly affected by rotation. For flow inward downstream of the 180-deg turn, the pressure is lower on the trailing wall than the leading wall. In other words, it takes at least one-pass distance to accumulate noticeable difference between the values of C_p on the leading and trailing wall. For a given cross-sectional plane in the second passage, the Coriolis force is directed towards the leading wall. An inverted pressure gradient is thus established on this plane to balance the Coriolis force. Since both the Coriolis force and the inverted pressure gradient increase with increasing Ro, the C_p on the leading and trailing wall of the second passage increase and decrease with increasing Ro, respectively (not shown in **Fig. 11** but will be evidenced from the friction-loss results presented below). The pressure loss results measured by Johnson et al. [24] in a rotating square duct ribbed by 45-deg semicircular ribs for $H/D_H=0.1$, $P_i/H=10$, $\mathrm{Ro}=0.178$, and $\mathrm{Re}=2.5\times10^4$ are also included in **Fig. 11** for comparison. It should be pointed out that their pressure taps were, respectively, arranged on the outer and inner side wall of the first and second duct. These side walls are smooth. Thus, their data (cross in **Fig. 11**) show a pressure loss smaller than the present case. Moreover, since the side wall is perpendicular to the Coriolis force, their data, [24], (not included in **Fig. 11**) indicated a different response to the rotation rate.

Figure 12 depicts the rotation number dependence of average friction factor f in the smooth and 45-deg ribbed duct flows. Previous results made by authors, [8], in 90-deg ribbed duct flow are also included in **Fig. 12** for comparison. The results show an increase of *f* with increasing Ro on the trailing wall for all cases but a decrease and an increase of *f* with increasing Ro on the leading wall for the 45 deg/90 deg ribbed and smooth duct case, respectively. The above trend on the trailing wall is because of the aforementioned decrease of C_p with increasing Ro on the trailing wall of the second inward duct. In contrast, the decrease of f with increasing Ro on the leading wall for the cases of the 45 deg/90 deg ribbed duct is due to the increase of C_p with increasing Ro on the leading wall of second inward duct toward which the Coriolis force is directed. The reason for the increase of *f* with increasing Ro in the case of the smooth duct is that the diminution of the 180-deg turn induced separation bubble with increasing Ro [9] results in the decrease of C_p on the leading wall of second inward duct.

Also shown in **Fig. 12** is that a replacement of 90-deg angled ribs with 45-deg angled ribs diminishes the friction losses to about 60% of the 90-deg ribbed case under the same operating conditions. The reason is that the 45-deg angled ribs have a smaller angle of attack and, in turn, less resistance to the main stream. For engineering reference, the Ro dependences of *f* are expressed as compact correlations of linear increase or decrease in **Fig. 12** for the range of parameters examined. The average deviations in the correlations from the measured data are ±0.8/±0.6 (trailing wall/leading wall), ±3.2/1.3, and ±1.9/±2.2%, respectively, for the smooth-walled, 90-deg ribbed, and 45-deg ribbed duct flows.

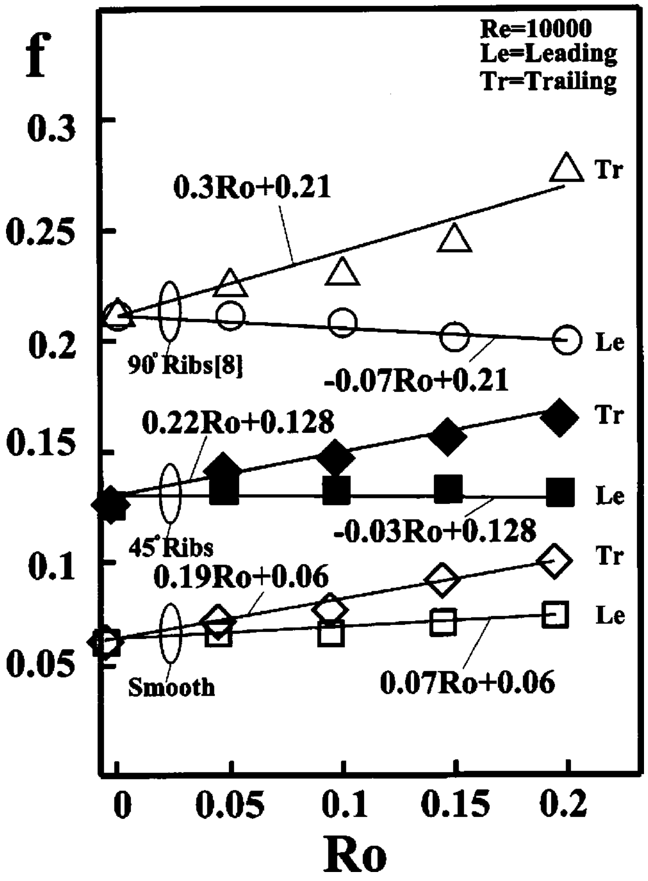

Fig. 12 Friction factor versus rotation number

Summary and Concluding Remarks

The following main results are drawn from the data presented:

1 In contrast to the results previously reported from the stationary ribbed (45 deg and 90 deg, staggered) duct flows, the measured evolutions of main and secondary flows indicate the absence of a fully developed flow condition in the rotating ribbed (45 deg, in-line) two-pass square duct of 12.8 hydraulic diameters in length investigated in the present study.

2 The cross-stream secondary flow evolves from three into four vortices as the flow progresses from the front to rear portion of the ribbed first passage. Inside the turn the secondary flow pattern consists of a large and a squeezed vortex. Immediately after the turn the secondary flow pattern has the form opposite to that inside the turn. In the latter portion of the second passage the secondary flow pattern recovers the three-vortex structure except the reverse of rotating directions. The number of vortices at a given cross section mentioned above tends to decrease as Ro is increased beyond 0.15. The above evolution of the complex secondary flow structure is believed to pose a challenging to the CFD simulations.

3 It is found that the streamwise distributions of region averaged Nussult number ratio on the leading and trailing wall reported previously by other researchers can be well illustrated by the corresponding distributions of region averaged turbulent kinetic energy and the magnitude and direction of the transverse mean velocity reported in the present study.

4 For flow outward in the first passage, the pressure coefficient C_p on the leading and trailing walls are approximately equal. This trend remains in the front-half of the 180-deg turn. In the rear-half of the turn and for flow inward downstream of the 180-deg turn, the C_p is lower on the trailing wall than the leading wall. The difference of C_p between the two walls first increases with distance from the mid-turn and then maintains the same in the second passage.

5 For engineering reference, simple expressions are developed to linearly correlate the friction factor with rotation number. A replacement of 90 deg with 45-deg angled ribs diminishes the friction losses to about 60% of the 90-deg ribbed case under the same operating conditions.

Acknowledgment

Support for this work was partially provided by the National Science Council of the Republic of China under contract NSC 91-2212-E-007-081.

Nomenclature

A = half-width of duct (m)
B = half-height of duct (m)
C_p = pressure coefficient, $(P-P_0)/0.5\rho U_b^2$
D_H = hydraulic diameter, $4AB/(A+B)$ (m)
f = friction factor, $(\Delta P/\Delta X)\cdot D_H/(\rho U_b^2/2)$
h = heat transfer coefficient ($\mathrm{Wm^{-2}\,K^{-1}}$)
H = rib height (m)
k = turbulent kinetic energy $(\overline{u^2}+\overline{v^2})/2$ ($\mathrm{m^2\,s^{-2}}$)
k_a = thermal conductivity of air ($\mathrm{Wm^{-1}\,K^{-1}}$)
Nu = local Nusselt number, $h\cdot D_H/k_a$
Nu_0 = Nusselt number in fully developed tube flow$=.023\cdot \mathrm{Re}^{0.8}\cdot \mathrm{Pr}^{0.4}$
Nu_{rg} = regional averaged Nu
P_0 = pressure at $X/H=88$ in first pass ($\mathrm{Nm^{-2}}$)
Pi = rib pitch (m)
Pr = Prandtl number of air, ν/α
Re = Reynolds number, $U_b D_H/\nu$
Ro = rotation number, $\omega D_H/U_b$
U = streamwise mean velocity ($\mathrm{ms^{-1}}$)
U_b = duct bulk mean velocity ($\mathrm{ms^{-1}}$)
u = streamwise velocity fluctuation ($\mathrm{ms^{-1}}$)
u' = rms value of streamwise velocity fluctuation, $\sqrt{\overline{u^2}}$ ($\mathrm{ms^{-1}}$)
V = transverse mean velocity ($\mathrm{ms^{-1}}$)
v = transverse velocity fluctuation ($\mathrm{ms^{-1}}$)
v' = rms value of transverse velocity fluctuation, $\sqrt{\overline{v^2}}$ ($\mathrm{ms^{-1}}$)
W = rib width (m)
W_d = divider thickness (m)
X = streamwise coordinate, **Fig. 1** (m)
X^* = normalized streamwise coordinate, X/D_H
X_N = streamwise coordinate in a pitch, Fig. 9 (m)
Y = transverse coordinate, **Fig. 1** (m)
Y^* = normalized transverse coordinate, Y/B
Y_N = transverse coordinate in a pitch, Fig. 9 (m)
Z = spanwise coordinate, **Fig. 1** (m)
Z^*, Z^{**} = normalized spanwise coordinate; (i) $X<0$, $Z^{**}=Z/(2A+W_d/2)$ (in the turn), (ii) $X\geqslant 0$, $Z<0$, $Z^*=(Z+W_d/2)/2A$ (in the first pass), (iii) $X\geqslant 0$, $Z>0$, $Z^*=(Z-W_d/2)/2A$ (in the second pass)

Greek Symbols

ρ = air density ($\mathrm{kg/m^3}$)
ν = kinematic viscosity of air ($\mathrm{m^2/s}$)
α = thermal diffusivity of air ($\mathrm{m^2/s}$)
Ω = vorticity ($\mathrm{s^{-1}}$)
ω = rotating speed ($\mathrm{rad\,s^{-1}}$)

Subscripts

b = bulk
max = maximum value
w = wall

References

[1] Elfer, M., 1993, ‘‘The Effect of Rotation and Buoyancy on Flow Development in a Rotating Circular Channel,’’ *2nd International Symposium on Engineering Turbulence Modelling and Measurements*, May 31–June 2, Florence, Italy.

[2] Cheah, S. C., Iacovides, H., Jackson, D. C., Ji, H., and Launder, B. E., 1996, ‘‘LDA Investigation of the Flow Development Through Rotating U-Ducts,’’ ASME J. Turbomach., **118**, pp. 590–596.

[3] Liou, T. M., and Chen, C. C., 1999, ‘‘LDV Study of Developing Flows Through a Smooth Duct With 180-deg Straight-Corner Turn,’’ ASME J. Turbomach., **121**, pp. 167–174.

[4] Servouze, Y., 1998, ‘‘3D Laser Anemometry in a Rotating Cooling Channel,’’ ASME Paper 98-GT-123.

[5] Bons, J. P., and Kerrebrock, J. L., 1999, ‘‘Complementary Velocity and Heat Transfer Measurements in a Rotating Cooling Passage With Smooth Walls,’’ ASME J. Turbomach., **121**, pp. 651–662.

[6] Liou, T. M., Chen, C. C., and Chen, M. Y., 2003, ‘‘Rotating Effect on Fluid Flow in Two Smooth Ducts Connected by a 180-Degree Bend,’’ ASME J. Fluids Eng., **125**, pp. 327–335.

[7] Tse, G. N., and Steuber, G. D., 1997, ‘‘Flow in a Rotating Square Serpentine Coolant Passage With Skewed Trips,’’ ASME Paper 97-GT-529.

[8] Liou, T. M., Chen, M. Y., and Tsai, M. H., 2001, ‘‘Fluid Flow and Heat Transfer in a Rotating Two-Pass Square Duct With In-Line 90° Ribs,’’ ASME J. Turbomach., **177**, pp. 255–264.

[9] Schabacker, J., Bolcs, A., and Johnson, B. V., 1999, ‘‘PIV Investigation of the Flow Characteristics in an Internal Coolant Passage With 45° Rib Arrangement,’’ ASME Paper 99-GT-120.

[10] Chanteloup, D., Juaneda, Y., and Bolcs, A., 2002, ‘‘Combined 3D Flow and Heat Transfer Measurements in a 2-Pass Internal Coolant Passage of Gas Turbine Airfoil,’’ ASME Paper GT-2002-30214.

[11] Prakash, C., and Zerkle, R., 1995, ‘‘Prediction of Turbulent Flow and Heat Transfer in a Ribbed Rectangular Duct With and Without Rotation,’’ ASME J. Turbomach., **177**, pp. 255–264.

[12] Iacovides, H., and Raisee, M., 1999, ‘‘Recent Progress in the Computation of Flow and Heat Transfer in Internal Cooling Passages of Turbine Blades,’’ Int. J. Heat Fluid Flow, **20**, pp. 320–328.

[13] Jang, Y. J., Chen, H. C., and Han, J. C., 2000, ‘‘Flow and Heat Transfer in a Rotating Square Channel With 45° Angled Ribs by Reynolds Stress Turbulence Model,’’ ASME Paper 2000-GT-0229.

[14] Taslim, M. F., Rahman, A., and Spring, S. D., 1991, ‘‘An Experimental Investigation of Heat Transfer Coefficients in a Spanwise Rotating Channel With Two Opposite Rib-Roughened Walls,’’ ASME J. Turbomach., **113**, pp. 75–82.

[15] Taslim, M. F., Bondi, L. A., and Kercher, D. M., 1991, ‘‘An Experimental Investigation of Heat Transfer Coefficients in a Spanwise Rotating Channel With Two Opposite Rib-Roughened Walls,’’ ASME J. Turbomach., **113**, pp. 75–82.

[16] Wagner, J. H., Johnson, B. V., Graziani, R. A., and Yeh, F. C., 1992, ‘‘Heat Transfer in Rotating Serpentine Passages With Trips Normal to the Flow,’’ ASME J. Turbomach., **114**, pp. 847–857.

[17] Parsons, J. A., Han, J. C., and Zhang, Y. M., 1994, ‘‘Wall Heating Effect on Local Heat Transfer in a Rotating Two-Pass Square Channel With 90° Rib Turbulators,’’ Int. J. Heat Mass Transfer, **37**, pp. 1411–1420.

[18] Johnson, B. V., Wagner, J. H., Steuber, G. D., and Yeh, F. C., 1994, ‘‘Heat Transfer in Rotating Serpentine Passage With Trips Skewed to the Flow,’’ ASME J. Turbomach., **116**, pp. 113–123.

[19] Fann, S., Yang, W. J., and Zhang, N., 1994, ‘‘Local Heat Transfer in a Rotating Serpentine Passage With Rib-Roughened Surfaces,’’ Int. J. Heat Mass Transfer, **37**(2), pp. 217–228.

[20] Han, J. C., Zhang, Y. M., and Lee, C. P., 1991, ‘‘Augmented Heat Transfer in Square Channels With Parallel, Crossed, V-Shaped Angled Ribs,’’ ASME J. Heat Transfer, **113**, pp. 590–596.

[21] Azad, G. S., Uddin, Mohammad J., and Han, J. C., 2001, ‘‘Heat Transfer in a Two-Pass Rectangular Channel With 45° Angled Rib Turbulators,’’ ASME Paper 2001-GT-186.

[22] Durst, F., Melling, A., and Whitelaw, J. H., 1976, *Principles and Practice of Laser-Doppler Anemometry*, Academic Press, New York.

[23] Bonhoff, B., Schabacker, J., Parneix, S., Leusch, J., Johnson, B. V., and Bolcs, A., 1999, ‘‘Experimental and Numerical Study of Developed Flow and Heat Transfer in Coolant Channels With 45° and 90° Ribs,’’ ASME Paper 99-GT-123.

[24] Johnson, B. V., Wagner, J. H., and Steuber, G. D., 1991, ‘‘Effects of Rotation on Coolant Passage Heat Transfer—Vol. II, Coolant Passages With Trips Normal and Skewed to the Flow,’’ *NASA Contract Report 4396*, pp. 103–108.